energies

Special Issue Reprint

Thermal Behaviour, Energy Efficiency in Buildings and Sustainable Construction

4th Edition

Edited by
Paulo Santos

mdpi.com/journal/energies

MDPI

Thermal Behaviour, Energy Efficiency in Buildings and Sustainable Construction: 4th Edition

Thermal Behaviour, Energy Efficiency in Buildings and Sustainable Construction: 4th Edition

Guest Editor

Paulo Santos

MDPI

Basel • Beijing • Wuhan • Barcelona • Belgrade • Novi Sad • Cluj • Manchester

Guest Editor
Paulo Santos
Department of Civil
Engineering
University of Coimbra
Coimbra
Portugal

Editorial Office
MDPI AG
Grosspeteranlage 5
4052 Basel, Switzerland

This is a reprint of the Special Issue, published open access by the journal *Energies* (ISSN 1996-1073), freely accessible at: https://www.mdpi.com/journal/energies/special_issues/JBB4ERQ49K.

For citation purposes, cite each article independently as indicated on the article page online and as indicated below:

Lastname, A.A.; Lastname, B.B. Article Title. *Journal Name* **Year**, *Volume Number*, Page Range.

ISBN 978-3-7258-5913-9 (Hbk)
ISBN 978-3-7258-5914-6 (PDF)
https://doi.org/10.3390/books978-3-7258-5914-6

Contents

About the Editor

Paulo Santos

Paulo Santos is currently an Associate Professor at the Department of Civil Engineering (DEC) of the Faculty of Sciences and Technology, University of Coimbra (FCTUC), as well as a Research Member of the Institute for Sustainability and Innovation in Structural Engineering (ISISE), Functional Performance (FP) research group.

The main actual research topics are Thermal Behaviour, Energy Efficiency in Buildings, and Sustainable Construction, with main focus on the Lightweight Steel-Framed (LSF) construction system and sustainable construction materials. As a result of his research, he is author of around 225 publications, including 4 books, 2 dissertations, 4 book editions, 17 journal special editions, 5 book chapters, 87 articles published in peer-reviewed scientific journals, and 109 papers published in proceedings of scientific conferences, with 101 publications indexed and listed in the Web of Science Core Collection.

He has around 3,620 citations and 91,650 reads on Research Gate (Berlin), with an h-index of 29. He was supervisor of 57 doctoral and master's theses already completed within his research topics.

He participated in around 16 funded European and national research projects within his research areas, as the Principal Investigator of the Tyre4BuildIns research project. He was a member of the scientific committee and/or organizer of several national and international scientific conferences. He is an editorial board member of 20 international scientific journals, for which he already has 822 verified Web of Science editor records. He reviewed, by request of the editors, around 130 articles submitted to international journals. He was also a member of the scientific evaluation committee of several national and international research projects proposed for funding.

Preface

Currently, energy and sustainability are two of the major concerns worldwide. Given the relevant energy consumption share of the buildings sector, it is very important to search for innovative design solutions and for the optimal thermal performance of buildings in order to reduce energy bills and greenhouse gas emissions while maintaining the comfort levels of the occupants. Additionally, given the environmental burdens of the construction sector, seeking more environmentally responsible processes and a more efficient use of resources is currently attracting more attention.

The fourth edition of this Special Issue, published in the *Energies* journal, is dedicated to the analysis of the recent advances on the following topics: (1) the thermal behaviour improvement of a building's elements (e.g., walls, roofs, floors, doors, windows, etc.); (2) energy efficiency in buildings; and (3) sustainable construction. The main goal is to compile scientific works within these topics making use of different possible research approaches, such as theoretical, experimental, numerical, computational, analytical, case studies, and their combinations. This reprint collects a set of original research works of an excellent academic standard and of complete scientific soundness.

The Guest Editor would like to extend their heartfelt gratitude to the contributors whose expertise and dedication have enriched this compilation, as well as to the reviewers who have significantly contributed to improving the quality of the manuscripts. As editor, it is my sincere hope that this collection inspires dialogue, sparks creativity, and serves as a catalyst for transformative action in the pursuit of highly energy-efficient buildings and more sustainable construction practices.

Paulo Santos
Guest Editor

energies

MDPI

Article

Thermophysical Properties of Compressed Earth Blocks Incorporating Natural Materials

Chiara Turco [1], Mohammadmahdi Abedi [1,2], Elisabete Teixeira [1] and Ricardo Mateus [1,*]

[1] Institute for Sustainability and Innovation in Structural Engineering (ISISE), Advanced Production and Intelligent Systems Associated Laboratory (ARISE), Department of Civil Engineering, University of Minho, Campus de Azurém, Av. da Universidade, 4800-058 Guimarães, Portugal; id9631@alunos.uminho.pt (C.T.); id8012@alunos.uminho.pt (M.A.); elisabeteteixeira@civil.uminho.pt (E.T.)

[2] Fibrenamics, Institute of Innovation on Fibre-Based Materials and Composites, University of Minho, Campus de Azurém, Av. da Universidade, 4800-058 Guimarães, Portugal

* Correspondence: ricardomateus@civil.uminho.pt

Abstract: Building materials are responsible for significant CO_2 emissions and energy consumption, both during production and operational phases. Earth as a building material offers a valuable alternative to conventional materials, as it naturally provides high hygrothermal comfort and air quality even with passive conditioning systems. However, disadvantages related to high density, conductivity, and wall thickness prevent its effective inclusion in the mainstream. This research explores enhancing the thermophysical properties of compressed earth blocks (CEBs) by using locally sourced natural materials. The study is framed in the Portuguese context and the natural materials involved are wheat straw (WS) as a by-product of wheat harvesting, cork granules (CGs) from bottle caps, and ground olive stone (GOSs) residues from olive oil production. Blocks were produced with different mixtures of these materials and the thermal response was examined in a hot box apparatus. Best results include a 20 and 26% reduction in thermal conductivity for mixtures with 5v.% CG and 10v.% GOS, respectively, and an associated reduction in bulk density of 3.8 and 5.4%. The proposed approach therefore proves to be effective in improving the key thermophysical characteristics of CEBs. The article includes a comparative analysis of the experimental data from this study with those from the literature. The study contributes to the growing knowledge of sustainable materials, providing insights for researchers and practitioners looking for innovative solutions for low-carbon and energy-efficient materials.

Keywords: compressed earth blocks; natural materials; thermal properties; hot box testing; sustainable construction

1. Introduction

The construction sector has a significant impact on the planet. To deliver infrastructure and buildings, it consumes a large amount of natural resources and non-renewable energy [1]. According to the European Commission, accounting for materials and operations, buildings are responsible for 40% of energy consumption and 36% of greenhouse gas emissions [2]. Furthermore, it is estimated that this industry produces more than 35% of the total waste in Europe [3]. Therefore, the quest for energy-efficient and environmentally conscious building materials and methods has become paramount. In the ever-evolving landscape of sustainable construction, a crucial aspect is the integration of technologies that facilitate thermal energy storage and passive cooling systems [4]. Traditional building materials often struggle to adapt to external temperature fluctuations, leading to an increased reliance on energy-intensive climate control systems. In this context, earth as a building material is experiencing a renaissance as it naturally guarantees high hygrothermal comfort and indoor air quality with low or no energy requirements for conditioning [5–7].

Compressed earth blocks (CEBs) are unfired masonry blocks made from locally sourced earth and compressed with a manual or hydraulic press. The stages of raw material extraction, transportation, and production are characterised by minimal energy consumption, making them highly environmentally sustainable building materials. In a 2020 study, Dabaieh et al. [8] found that eliminating the firing process (in favour of sun-drying) leads to the reduction of about 6 tonnes of CO_2 and over 5000 MJ of embodied energy to produce 1000 clay bricks. Fernandes et al. [9] quantified 0.39 kg of CO_2 emissions and 3.94 MJ of total embodied energy per CEB. In the cradle-to-gate analysis of walls, the authors found that the use of earth-based materials (CEBs and rammed earth) reduced the environmental impact by 50% compared to the use of conventional materials (fired clay bricks and concrete blocks). According to Ben-Alon et al. [10], earthen wall assemblies reduce environmental impact by 62–99% compared to conventional assemblies such as timber frame and concrete blocks. At the end of their life cycle, CEBs can be reused, recycled [11], or possibly disaggregated and returned to the natural environment. These characteristics are critical for the assessment of the environmental performance of the product, positioning CEBs as promising candidates to contribute to the decarbonisation of the construction sector and the promotion of a circular economy in the building materials cycle [12].

In addition to their environmental advantages, from a technical point of view CEBs have high thermal mass, meaning they can store and release heat slowly, acting as a natural reservoir of heat. According to [13], for different moisture levels, the capacity of earth to absorb it is fifteen and ten times higher than that of concrete blocks and fired clay, respectively. These properties help to stabilise indoor temperatures and reduce fluctuations and the need for active cooling systems [14]. Nevertheless, the regulatory frameworks geared towards conventional building materials and the physical limitations associated with the material itself (high thermal conductivity, heaviness, and wall thickness, among others) prevent it from being effectively included in the mainstream [15,16].

The thermal conductivity of earthen building elements lies in the range of 0.60–1.20 W/mK [17], with corresponding bulk density values typically between 1700 and 2000 kg/m^3. These values are higher than those of insulation materials, which are characterised by very low densities and thermal conductivity of less than 0.10 W/mK. At the same time, they are superior to or comparable with conventional building materials such as concrete blocks, fired clay bricks, and stones, yet stronger. Therefore, to achieve a satisfactory level of thermal insulation, the earthen building envelope can reach significant thicknesses. On the other hand, from a mechanical point of view, typical compressive strength values in the 1.0–2.0 MPa range (unstabilised or slightly stabilised mixtures) allow the safe use of CEBs for one- or two-storey constructions (maximum two in seismic areas) [18], or higher if combined with other load-bearing structures. Though, such cases are still rare.

However, in light of the environmental, economic, hygrometric, and non-toxicity advantages, the wide availability of the material, and considering the pressing demand for housing due to the growing population, complying with the EU 2050 climate neutrality target [19], the scientific effort pursued aims to mitigate the described limitations by modifying the basic mixtures with other materials.

This study responds to a very specific research question: is it possible to improve the thermophysical properties of CEBs without compromising their quality and keeping environmental impact and costs low? To answer this question, the proposed experimental strategy is to use local natural materials with low density and low thermal conductivity in the mixture. In this category, residues and by-products are prime candidates.

In a previous study [20], we reviewed the research published from 2015 to 2021 on the use of materials of natural origin for the optimisation of CEBs. The abundant quantities of natural residues generated daily by agricultural, textile, and food industry processes are routinely dumped in landfills or, at best, used as biofuels. However, depending on their form and composition, their potential can be better exploited. Fibres and straws improve the ductility of the blocks, mitigate cracking and shrinkage, and elevate the thermal properties. Nevertheless, their hydrophilic nature entails disadvantages such as increased water

absorption rate, which compromises the mechanical and adhesion properties between the fibre and the matrix, and hence the durability [21]. To counter this, surface chemical treatment of fibres can be implemented [21,22], albeit at the expense of sustainability. Examining the studies, the fibres and straws involved ranged from bamboo, hemp, date palm, banana, kenaf, and jute fibres to fonio, lavender, barley, wheat, and rice straw. In general, plant fibres exhibit low density and lightweight properties. Overall, the studies reveal that, when introduced into the soil mixture, intrinsic properties and constituents, aspect ratio, concentration, orientation, and bonding capacity must be considered as key factors in achieving effective composite behaviour. Natural aggregates, such as argan nutshell, olive stone, shea butter residue, and sawdust, share a composition with fibres, consisting of natural polymers (cellulose, hemicellulose, and lignin). They exhibit high porosity and lightweight properties, making them ideal for enhancing thermal characteristics. Powders or ashes of natural origin, with distinct purposes, often contribute to stabilisation. Examples are eggshell or mussel powders [23,24], and sawdust, wood, rice husk, and sugarcane bagasse ashes. While aggregates are usually derived by simple grinding, powders and ashes derive from more complex processes such as thermal treatments (e.g., calcination). The presence of oxides such as CaO, SiO_2, and Al_2O_3 confers them a certain degree of reactivity allowing for pozzolanic reaction in the presence of water and over time [25,26]. Therefore, their use could improve the compressive strength, durability, and overall quality of the blocks.

Considering the above, the use of local waste and by-products to enhance the properties of earthen building materials fosters a virtuous chain of values in terms of environmental regeneration and the circular economy. The use of local resources is now necessary to counter the environmental and social problems of our time, as advocated by the 17 Sustainable Development Goals claimed by the United Nations [27]. The proposed solution also contributes to mitigating their accumulation and reducing the extraction of raw soil. However, the inherent diversity of the materials involved makes the response of new products very difficult to predict [28]. Uncertainties in the interaction between soil and different natural materials represent one of the main limitations of this research topic. Furthermore, the literature review revealed a lack of data on thermal properties, with only one-third of the research addressing these aspects, compared to more than 80% of the research addressing mechanical aspects [20]. Other limitations are related to the wide variability of the available data, which makes it difficult to compare results. The limited data available and the multiple methods of measuring thermal properties adopted (stationary and non-stationary methods) result in an overall fragmented and heterogeneous picture. Therefore, to be fully understood, the topic must still be investigated. As this approach helps mitigate the thermophysical limitations of CEBs and has the advantage of proposing new local waste streams, this type of research has recently been strongly encouraged in the literature [13,20,29–31]. It is believed that feeding the literature with more data can provide a less heterogeneous picture and clarify the extent to which these differences should be adequately considered. In addition, procedures and criteria for the reference mix design are outlined that can support the setting of standards, government policies, and social acceptance, all of which are essential factors to support the true dissemination of materials incorporating waste [32].

This study provides experimental data on CEBs incorporating separately and in various percentages three different natural materials. It is framed in the Portuguese context and the natural materials to modify the mixtures were selected according to local availability. These are wheat straw (WS), cork granules (CGs) and ground olive stones (GOSs). While straw is more widely used in soil-based mixtures, even traditionally [33], little data have been found in the literature on the use of cork granules [34,35] and olive oil residues [36]. Therefore, this study could be seen as confirmatory research.

The blocks used as reference for this study are produced by a company in the south of the country and are commercially available. Their properties were analysed in a previous work [35], in which another variable that largely governs thermophysical behaviour, the particle size of the soil, was studied. The key attributes are: bulk density—1850 kg/m^3;

open porosity—32%; natural moisture content—0.60%; thermal resistance—0.23 m^2K/W; thermal conductivity—0.65 W/mK; thermal diffusivity—3.99 $\times$ 10^{-7} m^2/s; compressive strength—2.03 MPa; E-Modulus—46.21 MPa; ultrasound pulse velocity—1079.09 m/s; flexural strength—0.21 MPa; coefficient of capillarity absorption—0.15 $g/(cm^2\sqrt{min})$; electrical resistivity—1.57 kΩcm and; water absorption by total immersion—16% (refer to the R2-180D mixture).

Based on this reference, the objective of this research is to improve the thermophysical properties of these CEBs by using locally sourced natural materials. By selecting WS, CGs, and GOSs, a new waste stream management is proposed for southern Portugal. The experimental results presented here are part of a comprehensive study, including analyses of mechanical strength and durability, the results of which will be presented in future studies.

2. Materials and Methods

This section introduces and characterises the raw materials used and describes sample preparation. Subsequently, the experimental methods for investigating the blocks are presented.

2.1. Raw Materials and Sample Preparation

CEBs used as reference for this study consist of a mixture of soil, hydraulic lime as stabiliser, and water. The blocks were produced by a company in the south of Portugal with long experience in earthen construction, Betão e Taipa. The company supplied these materials.

Natural materials used for the experimentation are wheat straw (from wheat harvesting), cork granules (from recycling bottle stoppers) and ground olive stones (from olive oil production). These materials were selected according to local availability and the producers who supplied them. As the aim is to keep raw materials minimally processed, they were not subjected to any treatment aimed at changing their surface or microstructural attributes.

2.1.1. Soil Characteristics

The soil was quarried in the region of Serpa, Alentejo, Portugal. The main characteristics were deduced from common physical and geotechnical testing methods. Complementary analyses such as X-ray diffraction (XRD) and thermogravimetric analysis (TGA) provided microstructural insights.

The primary characteristics are given in Table 1, along with the standards followed.

Table 1. Physical and geotechnical characteristics of the soil used.

	Characteristics	Test Methods	Standards
Consistency limits [1]	w_L = 29.5%, w_P = 18.5%, IP = 11%	Atterberg limits	NP-143 [37]
Particle density [1]	2.71 g/cm^3	Pycnometer test	NP-83 [38]
Specific heat (at 26.85 °C) [1,2]	883.93 J/kg°C	DSC	ASTM E1269 [39]
Maximum dry density	2.01 g/cm^3	Proctor test	E 197 [40]
Optimum water content	12.0%		
Sand content	18.80%	Sand equivalent test	NP EN933-8 [41]
Activity of clay minerals	0.67 mg/g	Blue methylene test	NP EN933-9 [42]
Organic content	3.50%	Loss on ignition	ASTM D2974 [43]

[1] This test is standardised for a maximum particle size of 4.75 mm. [2] Due to the apparatus's calibration, it was impossible to obtain reliable measurements at 20 °C.

Based on this characterisation, the soil is classified as 'sandy'. Figure 1 illustrates the particle size distribution, showing adequate clay content to produce CEBs (~10%) [44].

XRD analysis, used for mineral identification, was conducted using a Locked Coupled configuration on a Bruker AXS D8 Discover diffractometer (Bruker, Billerica, MA, USA) equipped with Cu-Kα radiation (λ = 1.54060 Å) at 40 kV and 40 mA. Scanning was performed between 5° and 82° with a step size of 0.04°s^{-1} and a step time of 3 s. Phase

identification was performed using EVA analytical software (v. 4.2.2). Crystalline phases were indexed in the International Centre for Diffraction Data (ICDD) database. Quantitative phase analysis was attained employing Rietveld refinements with TOPAS software (v. 3).

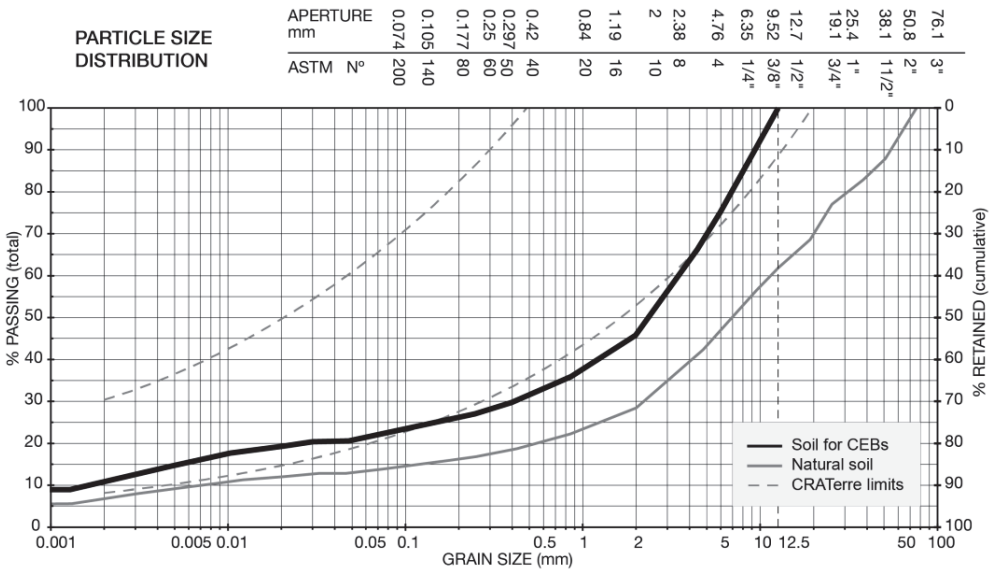

Figure 1. Particle size distribution curve of the soil used.

The obtained XRD pattern is presented in Figure 2. Peak-matching analysis reveals the presence of three plausible main crystalline phases: quartz (13%), muscovite (55%), and clinochlore (32%).

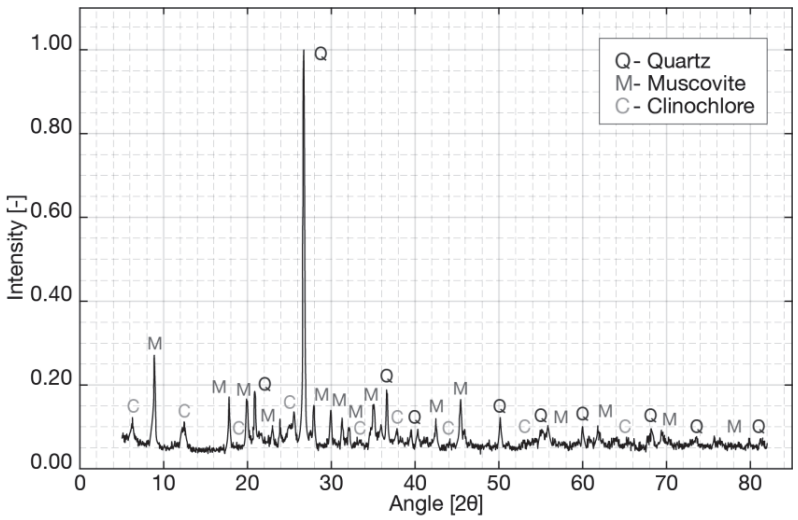

Figure 2. X-ray diffraction pattern of the soil sample analysed.

Quartz (SiO_2) belongs to one of the most significant and common classes of minerals, and its presence is expected in sandy soils. This element suggests a significant granitic and metamorphic influence on the soil. Muscovite and clinochlore are phyllosilicates, minerals consisting of parallel sheets of hydrated silicate tetrahedra with water or hydroxyl groups attached. Muscovite ($KAl_2[(AlSi_3O_{10})(OH)_2]$) is the most common dioctahedral mica characterised by perfect basal cleavage [45]. Clinochlore ($Mg_5Al[(AlSi_3O_{10})(OH)_2]$) is a Mg-dominant species belonging to the chlorite group (clay mineral group). Generally green, with a pearly to glassy lustre, it is relatively soft and has a scaly, platy appearance [45]. On visual examination and touch, the presence of such soft and relatively soft minerals as muscovite and clinochlore is evident.

Soil characterisation is finally completed with TGA. The analysis was performed by an SDT Q600 V20.9 Build 20 apparatus (TA Instruments, New Castle, DE, USA). The temperature program set was a linear ramp with an increase of 10.0 °C/min up to 1100.0 °C. The mass loss of each analysed sample is recorded against the increase in temperature. The first derivative of the gravimetric curve is then plotted to identify the peaks corresponding to the reactions in the sample. The soil gravimetric curve and its first derivative are shown in Figure 3.

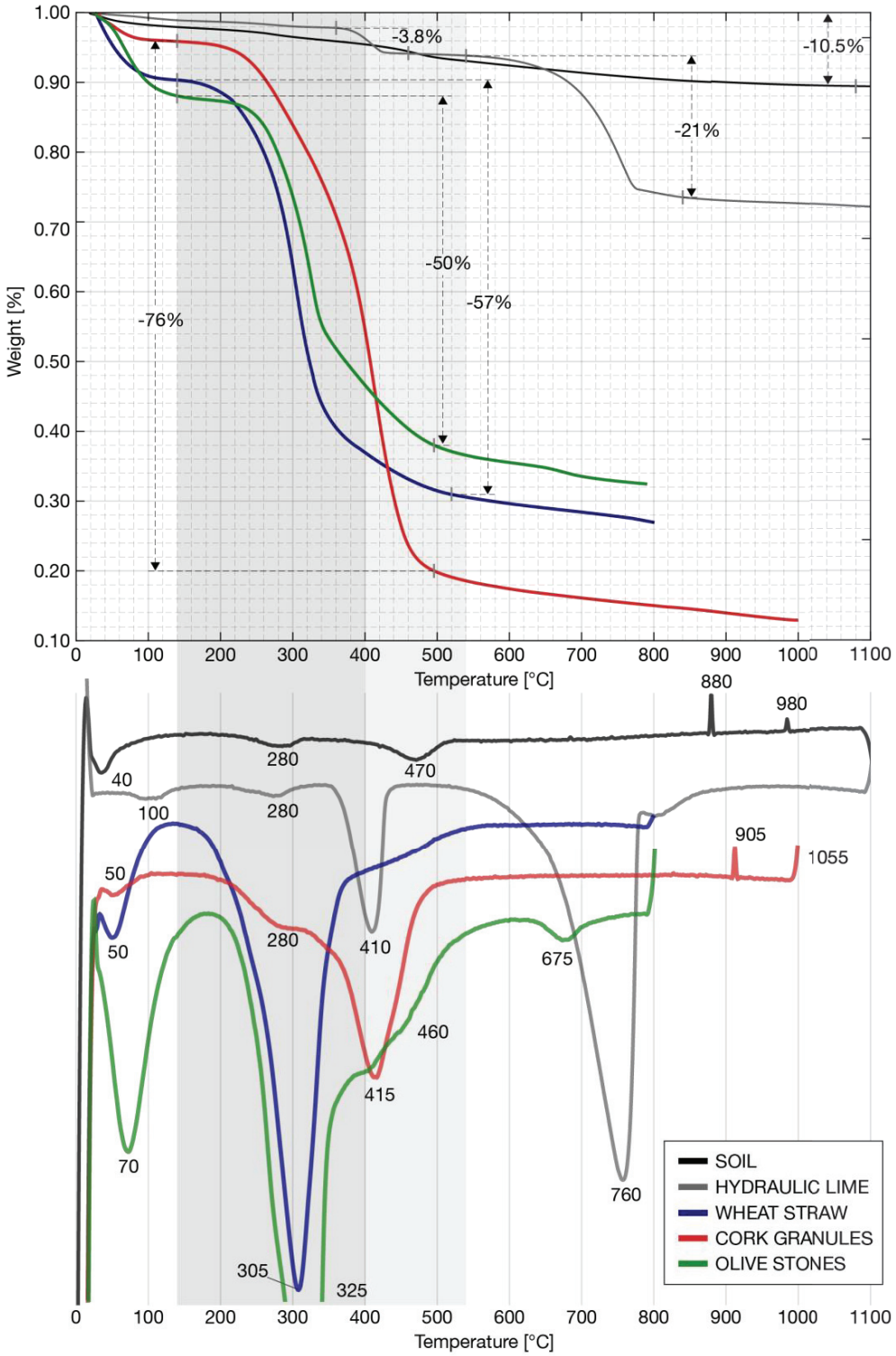

Figure 3. Thermograms of the raw materials involved: at the top the thermogravimetric curves (TG), at the bottom their first derivative (DTG) for peak identification.

It is anticipated that, for a more direct comparison, Figure 3 shows the thermograms of all the raw materials involved in this study. Please refer to the specific sections (Sections 2.1.2 and 2.1.3) for the discussion about these results.

The first derivative (DTG) of the soil thermogravimetric (TG) curve revealed five distinctive peaks. The initial weight loss below 100–140 °C corresponds to hygroscopic water loss (free water between clay particles). This loss continues to increase at higher temperatures due to water being bound to exchangeable cations in the minerals. In the temperature range 200–400 °C (low), decomposition of organic matter occurs first, followed by oxidation of the carbon content. Therefore, the peak identified at 280 °C possibly represents the dehydroxylation or decarboxylation of organic compounds. However, it could also represent the loss of hydroxyl groups from gibbsite ($Al(OH)_3$) or the dehydroxylation of goethite (FeO(OH)), which occurs in the 290–330 °C range and whose possible presence is based on visual inspection of the soil sample (characteristic iron-red colour). In the temperature range of 400–500 °C (moderate), a peak at 470 °C suggests the decomposition of more complex organic compounds or the presence of clay minerals (most likely the presence of the latter, as the same peak was detected in the analysis of soil samples free of organics). Finally, carbon thermal degradation occurs in the high-temperature range above 600 °C. Peaks at 880 °C and 980 °C may correspond to mineral decomposition and oxidation processes, respectively. It is reported in the literature that phyllosilicates detected by XRD (muscovite and clinochlore), for example, show a simple dehydroxylation reaction in the temperature range 820–920 °C, compatible with the peak found [46]. The presence of quartz, with its characteristic peak at 573 °C corresponding to phase transition α-β, was not found [47,48].

2.1.2. Natural Hydraulic Lime

As sandy soils may lack of cohesion, 5% by volume (5v.%) of Natural Hydraulic Lime (NHL5) was used for stabilisation. The grey TG and DTG curves in Figure 3 form the fingerprint of hydraulic lime with the two main peaks at 410 °C and 760 °C. The first one is associated with the dehydroxylation of $Ca(OH)_2$, while the second indicates the thermal decomposition of $CaCO_3$ to form CaO and CO_2 [49].

2.1.3. Natural Materials

This study defines 'natural materials' as all raw materials of plant or animal origin, such as fibres, straw, leaves and any aggregate, powder or ash derived from fruit stones, shells, and wood. To be considered residues and by-products, these materials must derive from other processes and not be extracted directly. In this study, three were selected on the basis of their local availability. These are wheat straw, cork granules, and ground olive stones.

Wheat straw (WS) is an agricultural by-product of wheat cultivation represented by the residual stalk, which includes stems and leaves. Cellulose, hemicellulose, and lignin are the main components of its fibrous structure. Observing Figure 3, the weight loss in the 140–540 °C range and the peak at 305 °C in the DTG curve are indeed related to the release of condensable vapours (acetic acid, methanol, and wood tar) and incondensable gas (CO, CO_2, CH_4, H_2, and H_2O) deriving from their decomposition (pyrolysis) [50]. The lightweight and porosity characteristics of straw fibres make them suitable for inclusion in composite materials designed for construction purposes. In this study, the WS was chopped into pieces 3 to 5 cm long.

Cork granules (CGs) are a recycled product from bottle stoppers. Along with Spain, Algeria, and California, Portugal is one of the leading countries producing commercial cork. For its ease of availability in the local market and outstanding properties (low density and permeability, elasticity, resiliency, acoustic and thermal insulation, chemical and biological inertia, and fire resistance [51–53]), this material emerges as a valuable candidate for enhancing the thermal performance of CEBs. As a natural aggregate, unlike fibres, CGs are used as a partial substitute for soil. The TGA (Figure 3) shows that, like straw, the most

prominent mass loss occurs in the 140–540 °C range. In this region, a smaller peak around 280 °C corresponding to the degradation of polysaccharides composed of cellulose and hemicellulose can be noticed. However, a second, more important reaction is noticeable at 415 °C, corresponding to more stable aromatic structures, such as lignin and suberin. Above 540 °C, the mass loss rate is slow until the cork reduces to ash [54].

Ground olive stones (GOSs) are the residual by-products of olive oil production. GOSs are composed mainly of the hard, inner seeds crushed during olive oil processing and exhibit a durable and granular structure, rich in lignin and cellulose, also confirmed by TG analysis. Figure 3 shows that the most significant mass loss occurs in the 140–540 °C range. Identified peaks at about 325 °C and 460 °C are due to the cellulose. The long tail corresponds to the thermal decomposition of lignin, which indeed decomposes, overlapping the cellulose [55]. The physical properties of GOSs include a low density and high porosity, making them ideal candidates for enhancing materials' thermal and structural characteristics.

Table 2 provides the main characteristics of selected natural materials.

Table 2. Characteristics of the natural materials involved in this study.

	Thermal Conductivity [W/mK]	Moisture Content [%]	Bulk Density [g/cm^3]	Porosity [%]	Absorption [%]
Wheat straw (WS)	0.041–0.049 [1] [56]	5.02–7.79% [57]	0.98–1.77 [57]; 0.104 [29]	–	–
Cork granules (CGs)	0.036 [35]	–	0.70 [35]	51% [35]	2.40 [35]
Olive stones (GOSs)	–	–	0.65; 0.70 [36]	83% [36]	4.60 [36]

[1] This range was calculated on wheat straw bales. Note: If not calculated, data in the table were taken from the specific literature referenced. Due to the highly variable composition, materials' properties do not have an unambiguous value but fall within a range of values.

Pictures in Figure 4 show their appearance.

(**a**) (**b**) (**c**)

Figure 4. Appearance of the natural materials selected: (**a**) WS—wheat straw (WS); (**b**) CGs—cork granules; (**c**) GOSs—ground olive stones.

2.1.4. Preparation of the Samples

The block samples were prepared at the company's premises, following company practice. Regarding preparation conditions, some important information about the production process should be highlighted: (i) at the company scale, it was not possible to oven-dry the raw soil before mixing; therefore, the water content was defined for each mixture based on the producer's experience and may not reflect the optimal content deduced from the Proctor test; (ii) as for company uses, all mixtures were prepared on a volumetric basis; (iii) the blocks produced do not have the same volume (block height varies slightly depending on the mixture).

To produce CEBs, raw materials were mixed 'dry' first to ensure an even distribution. Water was added gradually until the dropping ball test conditions were satisfied [33,58,59].

This field test, which consists of dropping a ball of moist earth from a height of 1 metre and observing how it breaks, is considered adequate for non-plastic earthen techniques [17].

In this study, the reference blocks are CEBs consisting of soil, 5% by volume (v.%) hydraulic lime addition, and water. This basic mixture is identified here as 'REF'. The designed mixtures covered by this study are those shown in Table 3.

Table 3. Designed mixtures.

		Soil	Hydraulic Lime [v.%]	Natural Material [v.%]	Mixing Water [v.%]
Reference mixture—REF [1]	REF	100%	5%	-	10%
Mixtures with addition of wheat straw—WS	WS5	100%	5%	5%	13%
	WS10	100%	5%	10%	12%
	WS15	100%	5%	15%	11%
Mixtures with replacement of soil with cork granules—CGs	CG1	99%	5%	1%	16%
	CG3	97%	5%	3%	15%
	CG5	95%	5%	5%	14%
Mixtures with replacement of soil with ground olive stones—GOSs	GOS10	90%	5%	10%	15%
	GOS15	85%	5%	15%	14%

[1] The blocks used as reference for this study were characterised in their main thermophysical, mechanical and durability attributes in a previous study [60], see batch 'R2-180D'.

According to the above-presented mixes, CEBs were produced using a hydraulic press machine (Eco Máquinas, São Domingos, Brazil—Eco Master 7000 Turbo II) at 10 MPa (Figure 5a). Blocks have standard dimensions of 300 mm × 150 mm × 80 mm (length × width × average height). After compression, the blocks were stored in a sheltered area, sprayed with water twice a day for the first week and covered with a plastic sheet. They were cured for 180 days before testing (Figure 5b).

(**a**) (**b**)

Figure 5. (**a**) Freshly manufactured blocks and (**b**) batch of blocks (mixture WS15) ready for curing.

2.2. Experimental Methods

The experimental investigation consisted of characterising the physical–geometric and thermal attributes of the CEBs. For each mixture, the batch of blocks produced comprises at least eighteen blocks. Due to the inherent variability of the material, to provide the best representative value, the physical and geometric attributes refer to the average measurement of the entire batch. Thermal tests were instead performed on a sample of three blocks.

2.2.1. Physical Characterisation of the Blocks

The volume and mass of each block was measured at natural moisture content. The bulk density, expressed in kg/m^3, is estimated according to Equation (1):

$$\gamma = m/V, \tag{1}$$

where m and V are the measured mass and volume of the block, respectively. The dry bulk density (γ_d) is estimated through Equation (1), by replacing the mass m with the dry mass (m_d). The blocks were considered dry when their mass stabilised after several days in the oven at 40 °C. An estimation of the percentage of open porosity (φ) and natural moisture content (ω) can be then obtained through equations:

$$\varphi = 1 - (\gamma_d/\gamma_s), \text{ and} \tag{2}$$

$$\omega = (\gamma - \gamma_d)/\gamma \tag{3}$$

where γ_s is the soil particle density (see Table 1).

2.2.2. Thermal Characterisation of the Blocks

The thermal characterisation of the blocks was performed in a hot box apparatus. The primary output of the hot box is the thermal resistance. The thermal resistance was measured under steady-state conditions according to ASTM C1363-11:2011 [61] and ISO 9869-1:2014 [62]. Each block was placed between two sensors in a temperature-controlled enclosure while a known temperature difference was applied. The sensors measured the heat flux. Steady-state conditions are assumed to occur when the percentage change in heat flux throughout the sample is $\leq$5% at 24 h intervals and after a minimum of 72 h of testing. For a detailed description of the apparatus, please refer to [63].

The thermal resistance, expressed in m^{2}K/W, is defined by Equation (4):

$$R = \Delta T/q, \tag{4}$$

where ΔT is the applied temperature difference, and q is the heat flux across the sample. From it, thermal conductivity (W/mK) can be deduced according to Equation (5):

$$\lambda = d/R, \tag{5}$$

where d is the thickness of the product (wall thickness), and R is the thermal resistance.

3. Results and Discussion

3.1. Physical Properties of the Blocks

The average bulk density values calculated for the entire batch of CEBs produced for each mixture are presented in Figure 6a. The graph of Figure 6b shows the estimated open porosity associated with each mixture.

The reference CEBs (REF) are characterised by a bulk density of 1848.0 kg/m^3 and an estimated open porosity of 32.6%. In the histograms, the dashed line indicates these reference values, while the percentages on each bar represent the variation from the reference. As a general tendency, the incorporation of natural materials reduces the bulk density as their concentration increases. In the case of WS, the effect is less pronounced as the fibres were added to the mixture rather than replacing a portion of soil. In fact, mixtures containing 5 and 10v.% WS only marginally reduced bulk density to 1841.2 and 1842.5 kg/m^3, respectively—less than 1% of the reference. Porosity is estimated to be 32.4% for WS5 and 31.7% for WS10. The mixture with 15v.% WS recorded a slightly lower bulk density (1825.5 kg/m^3), and higher porosity (34.9%).

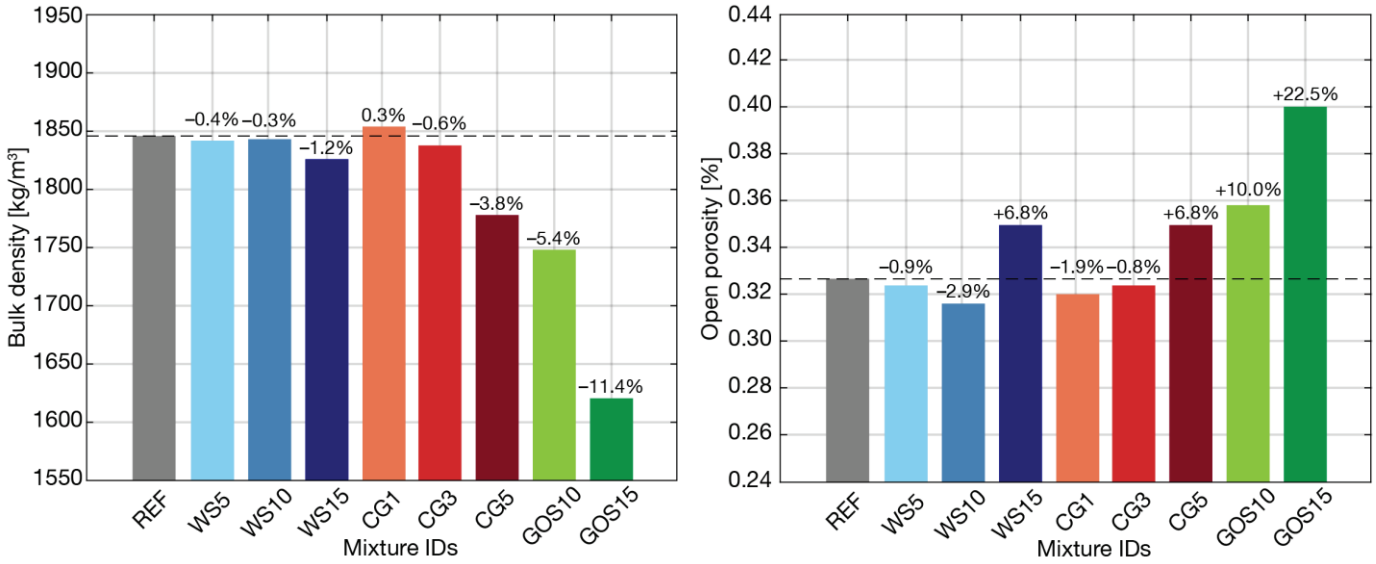

Figure 6. Bulk density (**a**) and open porosity (**b**) of CEBs incorporating different natural materials.

The replacement of 1 and 3v.% of soil with CGs had an almost negligible impact on the bulk density, with values of 1853.3 and 1837.1 kg/m^3 respectively—both still varying within 1%. Porosity is estimated to be 32.0% for CG1 and 32.4% for CG3. Incorporating 5v.% CG resulted instead in 4% lower bulk density (1777.5 kg/m^3), and higher porosity (34.9%). These results, particularly those for CG1 and CG3, are due to the minimum substitution rate examined. Unfortunately, it was not possible to go any further as, for concentrations above 5v.%, a degradation of the blocks' quality was observed during production. As shown in Figure 7, beyond this threshold, the blocks exhibited poor quality and a lack of cohesion that made them prone to crumbling immediately after compaction. It can be said that 5v.% represents the upper limit for effective soil replacement with CGs.

Figure 7. CEBs incorporating 10v.% CG broke down (**a**) and cracks (**b**) immediately after compaction.

Mixtures incorporating GOSs exhibited more remarkable results. Replacing 10 and 15v.% of soil with GOSs reduced the bulk density to 1747.8 and 1636.7 kg/m^3: in percentage, 5.4 and 11%, respectively. The estimated porosity raised up to 35.9% for GOS10 and 40% for GOS15. Unlike CG, even at higher concentrations, GOS mixtures encountered no significant issues during the production process. This disparity may be attributed to the differences

between the two natural aggregates. Although both are characterised by considerable lightness and porosity, the hardness of the olive kernel and the surface's roughness prove to be more akin to soil particles compared to the soft and resilient honeycomb structure of cork. Therefore, GOSs exhibit a superior affinity than CGs for replacing a portion of the soil in mixtures intended for CEBs.

With the exception of GOS15 blocks, the bulk density of the CEBs examined falls within the typical range disclosed in the literature—from 1700 to 2000 kg/m^3 [20]. It should be noted that there are no regulatory requirements on this aspect in most parts of the world. Only Indian and Sri Lankan standards have set a minimum bulk density of 1750 kg/m^3 [30,64,65]. This notwithstanding, despite lower density values in the range 1600–1650 kg/m^3, blocks with 15v.% GOS showed no discernible problems during the production process (as in the case of blocks with >5v.% CG).

Finally, in the reference CEBs as in those with natural materials, the natural moisture content at 180 days was always around 0.6%.

3.2. Thermal Properties of the Blocks

The average results of thermal tests performed in the hot box apparatus are presented in Figure 8. As in the previous graphs, the dashed lines indicate the reference values, while the percentages on each bar represent the variation from this reference.

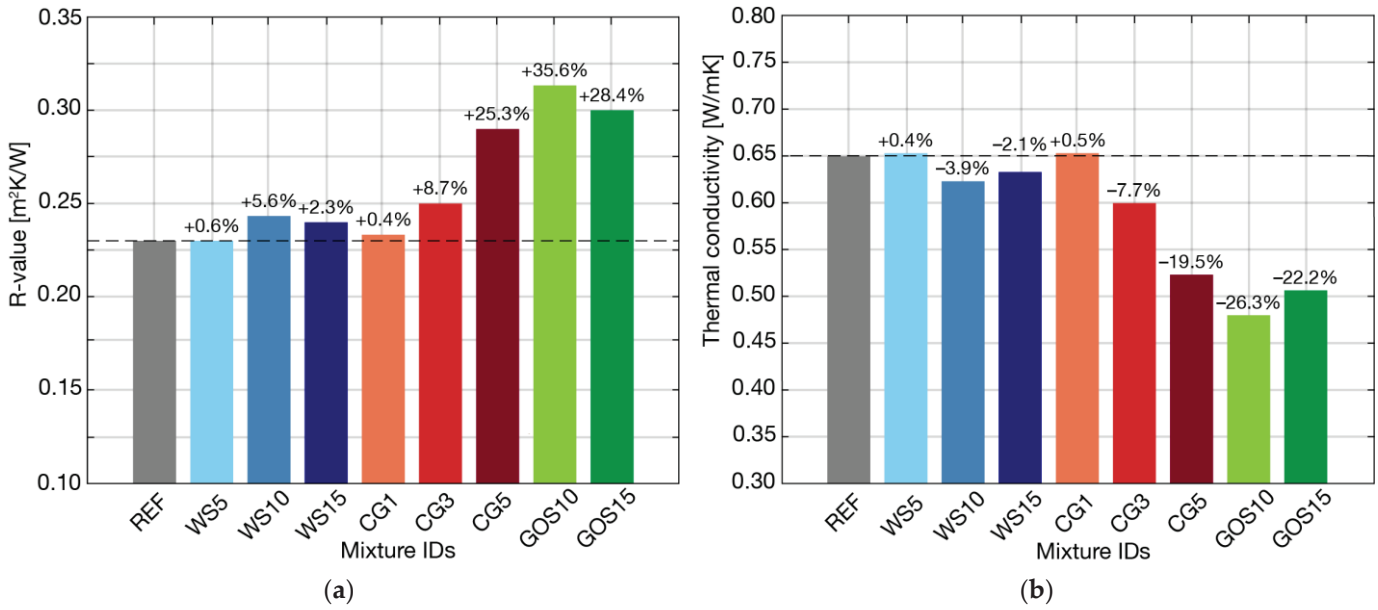

Figure 8. Thermal resistance (**a**) and conductivity (**b**) of CEBs incorporating different natural materials.

Reference CEBs are characterised by a thermal resistance of 0.23 m^{2}K/W. The incorporation of WS did not lead to any significant alterations of the thermal response: in the case of 5v.% addition, the increase in resistance is below 1%; in the case of 15v.%, it is slightly above 2%. A modest increase of 5.6% can be noted for a concentration of 10v.% (WS10: R-0.24 m^{2}K/W). However, it would be premature to attribute this result to the presence of fibres for two reasons: the first is that the relatively low percentages considered can make the soil thermal response dominant over the presence of straw; the second is that mixing on a volumetric basis and producing blocks on a large scale (company scale) increases data scattering. Similar to the WS5 blocks, the CG1 blocks include an extremely small percentage of CGs (1v.%), essentially incapable of modifying the thermal resistance. On the other hand, the other CG mixtures exhibit a sharper response. Replacing 3 and 5v.% of the soil with CGs brings the thermal resistance of the blocks to 0.25 and 0.29 m^{2}K/W, corresponding to an increase of 8.7 and 25.3% for CG3 and CG5, respectively. However, the best results are obtained for CEBs incorporating GOSs. The R-value increases by 35.6%,

reaching 0.31 m^2K/W in the case of a 10v.% GOS concentration (GOS10), and by 28.4%, reaching 0.30 m^2K/W, in the case of a 15v.% GOS concentration (GOS15). Overall, the incorporation of natural materials increases the thermal resistance of the blocks, enhancing their insulating potential. Note that, according to the actual laying in masonry walls, the blocks were measured in flat position and, therefore, the R-values correspond to a wall-thickness of 15 cm. Regardless of the thickness, Figure 8b represents the thermal conductivity of each mixture experimented.

As in the case of thermal resistance, the same non-linear trend is observed for the reciprocal thermal conductivity in blocks with WS and GOS mixtures (Figure 8b). In fact, in the case of these mixtures, the results show an initial improvement in the thermal properties (see WS10 and GOS10) followed by their decay (see WS15 and GOS15), in line with the literature findings suggesting a maximum concentration threshold limiting the benefits related to the presence of natural materials [20]. Interestingly, the CG mixtures exhibit a more linear trend: the thermal conductivity, as well as the bulk density (Figure 6a), decrease steadily as the concentration of CGs increases. This response may be attributed to the presence of non-hygroscopic water associated with the microstructure of the natural materials involved. In fact, for dry soils, relatively small increases in water content can substantially increase the thermal contact between soil particles, resulting in a non-linear increase in thermal conductivity [66]. As evidenced by the thermograms in Figure 3, the water content (mass lost below 140 °C) exceeds 10% in the case of WS and GOSs, while for CGs it remains below 4%. Experimental data are provided in Table 4.

Table 4. Thermophysical properties of CEBs incorporating natural materials [1].

	γ_d [kg/m^3] [2]	R-Value [m^{2}K/W]	λ [W/mK]
REF	1831.53 ± 4.72 (0.26%)	0.231 ± 0.01 (4.13%)	0.650 ± 0.03 (4.11%)
WS5	1835.31 ± 13.14 (0.72%)	0.232 ± 0.03 (12.28%)	0.653 ± 0.09 (13.08%)
WS10	1805.36 ± 68.06 (3.77%)	0.243 ± 0.04 (14.45%)	0.625 ± 0.08 (13.60%)
WS15	1816.43 ± 32.24 (1.77%)	0.236 ± 0.02 (6.35%)	0.636 ± 0.04 (6.59%)
CG1	1771.21 ± 41.65 (2.35%)	0.232 ± 0.03 (12.85%)	0.653 ± 0.08 (12.32%)
CG3	1848.86 ± 76.02 (4.11%)	0.251 ± 0.02 (7.94%)	0.600 ± 0.05 (8.32%)
CG5	1748.36 ± 7.21 (0.41%)	0.289 ± 0.04 (12.15%)	0.523 ± 0.06 (11.54%)
GOS10	1737.31 ± 16.21 (0.93%)	0.313 ± 0.01 (4.17%)	0.479 ± 0.02 (4.14%)
GOS15	1626.84 ± 50.87 (3.13%)	0.297 ± 0.01 (3.24%)	0.506 ± 0.02 (3.21%)

[1] This table shows the average data with their standard deviation and, in brackets, the coefficient of variation. [2] These data refer to the average dry bulk density of only the CEBs used for the thermal tests (three). Therefore, they may differ from the values shown in the histogram of Figure 6a, as those values were calculated by averaging the entire batch of blocks produced (eighteen per mixture) to obtain a more robust measurement.

3.3. Comparison and Analysis

In the graph of Figure 9, the experimental data are presented along with data from the literature. As the compression process entails some substantial changes in soil particle packing and heat transfer, it is worth mentioning that these data were collected within the context of a previous study [20] focusing exclusively on the case of CEBs incorporating natural materials. These materials are indicated in the legend.

Experimental data of this study fit well into the broader framework collected, being in the range of both conventional density and thermal conductivity values. Although one cannot speak of a linear dependency relationship between the two variables—statistical analyses have estimated very low coefficients of determination (in the range 0.2–0.4, see Figure 9, top left-hand corner)—a certain increase in the thermal conductivity as the bulk density increases is noticeable. It is legitimate to query whether more data availability could support this hypothesis which remains an open issue [45].

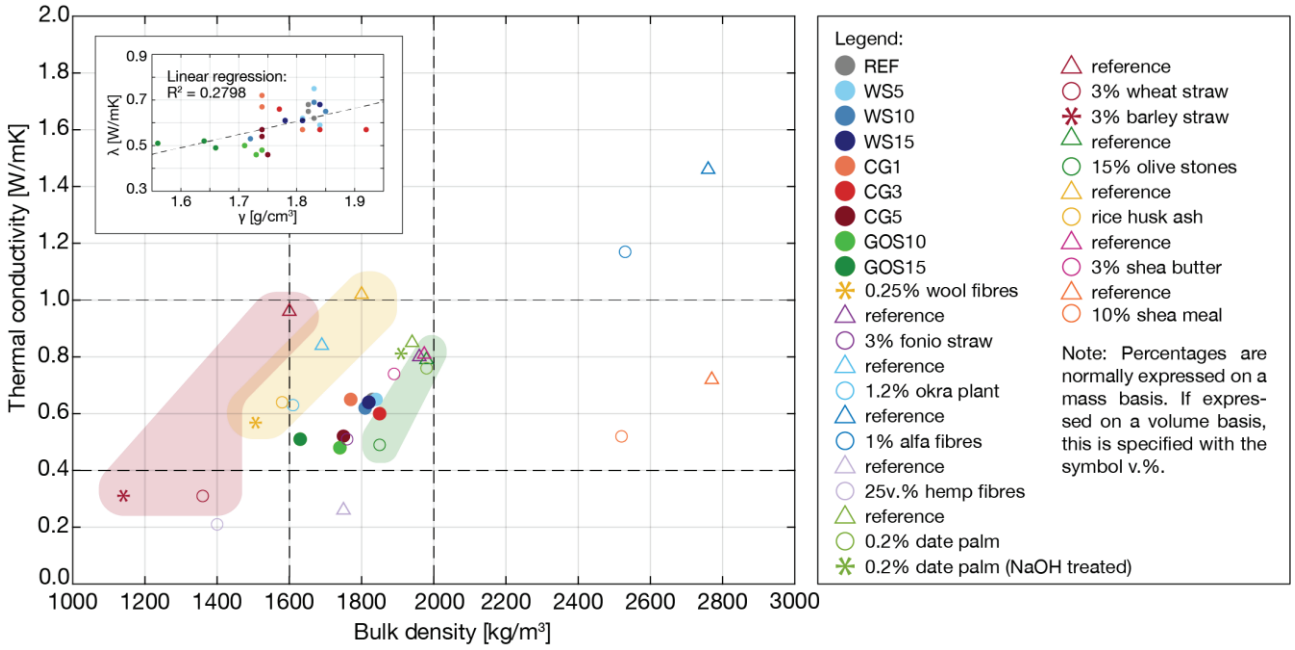

Figure 9. Comparison of the experimental data with the literature data. The main graph shows average values, while the zoom in the top left-hand corner presents the raw data and the linear regression.

However, data reassure on the effectiveness of the natural materials considered in improving thermal properties of CEBs. Observing the graph and the highlighted cases, the consistent reduction in thermal conductivity of mixtures modified with natural materials compared to those unmodified can be noted. The most significant reduction in thermal conductivity, exceeding 50%, was observed in mixtures containing 3% by mass of wheat and barley straw [67] (highlighted in red). This notable achievement can be attributed to the significant amount of fibres used (calculated on a mass basis), fairly above the concentrations considered in this study (calculated on a volumetric basis). Without compromising the essential mechanical strength and durability of the blocks, these results suggest the possibility of exploring even higher proportions.

Other noteworthy examples showcased reductions in thermal conductivity exceeding 35%, particularly in mixtures incorporating rice husk ash [25] (highlighted in yellow) and olive stones (highlighted in green) [36]. In this regard, the results of the present study concerning GOS mixtures align consistently with those reported by [36] and other studies not included in the review article [68,69].

In the case of CGs, the results of this study still find consensus with the literature, but outside of that included in the review article [34,35]. The thermal conductivity as well as the bulk density of mixtures incorporating CGs decreased with a linear trend. The authors agree on attributing this result to the low density and low thermal conductivity of this natural aggregate. However, within the scope of this study, production problems were observed for concentrations above 5v.% CG. Above this threshold, in fact, the blocks crumbled and broke immediately after demoulding.

In conclusion, continuing to explore the potential of natural materials to improve the thermal characteristics of CEBs has proven beneficial. The increase in thermal resistance improves the insulation potential of the material, allowing a reduction in the thickness of the building envelope. Many natural materials inherently exhibit a lightweight and porous structure, making them particularly well suited for achieving this purpose. When sourced from production processes, such as those in the agro-food industry, the utilization of these materials not only presents a substantial opportunity for improving thermal behaviour but also contributes significantly to waste reduction. The findings underscore the feasibility of simultaneously attaining diverse objectives that could generate a positive environmental and economic impact for the building industry [70].

4. Conclusions

This study investigates enhancing the thermophysical properties of compressed earth blocks (CEBs) by incorporating locally sourced natural materials. The experimental design involved formulating eight different mixtures with varying volume concentrations (v.%) of wheat straw (WS—5, 10 and 15v.%), cork granules (CGs—1, 3, and 5v.%), and ground olive stones (GOSs—10 and 15v.%). The resulting blocks were tested using a hot box apparatus and characterised in their thermophysical attributes. The findings reflect the distinct impact of adding natural fibres (as seen with WS) or substituting soil with natural aggregates (the case observed with CGs and GOSs) on the mixtures' properties. Notably, the variations in properties were more pronounced with natural aggregates. Certain mixtures showed superior thermal properties compared to standard blocks (REF: R—0.23 m^2K/W and λ—0.65 W/mK). The best mixture incorporating WS, albeit with modest improvements, achieved a 4% decrease in thermal conductivity at a 10v.% concentration (WS10: R—0.24 m^2K/W and λ—0.63 W/mK). In contrast, mixtures with 5v.% CG and 10v.% GOS reduced conductivity by approximately 20 and 26%, respectively (CG5: R—0.29 m^2K/W and λ—0.52 W/mK; GOS10: R—0.31 m^2K/W and λ—0.48 W/mK). These findings underscore the potential of these materials to enhance the thermal properties of earth-based mixtures while also contributing to waste reduction and minimising raw material extraction.

Some observations:

- Further research is warranted to refine the material ratios and manufacturing processes to achieve optimal thermal performance in mixtures incorporating WS. Contrary to the existing literature [67], this study did not observe an improvement in thermal properties.
- Utilising CGs from bottle stoppers showcases the recycling and reusing potential of this natural material. However, concentrations exceeding 5v.% were found to compromise block quality, as evidenced by immediate block crumbling post compaction.
- The inclusion of GOSs in mixtures is a promising alternative for enhancing earth's insulating properties and overall energy efficiency, while also proposing a sustainable waste management technique. Positive results from their use align with the existing literature [36], marking a significant milestone. Further experimentation in other producing countries would be beneficial.
- The investigation did not reveal a linear correlation between density reduction and thermal conductivity reduction. Two considerations: the introduction of natural materials into the soil matrix, whose properties diverge from those of the soil grains, lead to non-linearities in the heat flux paths. Accurately describing this problem using analytical models is difficult without significant simplifications. On the other hand, numerical approaches employing random discrete-element modelling could simulate the behaviour of the mixed granular medium, albeit with computational cost. Despite low coefficients of determination indicating weak correlations, a certain pattern is still decipherable. Consequently, while more data can increase confidence in navigating the survey space, the creation of a comprehensive database could make it easier to exploit the potential of artificial intelligence.

Enhancing our understanding and refining the thermophysical properties of earth-based building materials incorporating natural elements is an essential prerequisite for their advancement. Therefore, continued research in this area is strongly encouraged.

In the comprehensive evaluation of the proposed new products, following studies will present the analysis of mechanical and durability aspects as well as the life cycle assessment in terms of environmental impact and cost. Further investigations will focus on the possibility of using materials of natural origin for soil stabilisation, thus eliminating traditional binders (cement or lime, as in the case of this study).

Future prospects should encompass conducting experimental thermo-hygrometric investigations on walls and simulations to evaluate their performance across different climate zones, thus enabling the transition from product to building scale.

This study represents a foundational yet indispensable step towards the implementation of a closed-loop approach that positions earth as a central component of sustainable and regenerative building solutions. The integration of residues and by-products of natural origin not only enhances thermal performance, but also sets the stage for a transformative shift in the use of unconventional materials in the construction industry.

Author Contributions: Conceptualization, C.T., E.T. and R.M.; methodology, C.T., E.T. and R.M.; investigation, C.T., M.A. and E.T.; data curation, C.T.; writing—original draft preparation, C.T.; writing—review and editing, C.T., E.T. and R.M.; visualization, C.T.; supervision, E.T. and R.M.; project administration, R.M.; funding acquisition, R.M. All authors have read and agreed to the published version of the manuscript.

Funding: This work is funded by national funds through FCT, Foundation for Science and Technology, under grant agreement UIBD/150874/2021 (https://doi.org/10.54499/UI/BD/150874/2021, accessed 23 April 2024), attributed to the first author. The work is partly financed by Fundação "La Caixa" (Programa Promove) under the project BTCpro with the reference PV20-00072. The work is also partly financed by FCT/MCTES through national funds (PIDDAC) under the R&D Unit Institute for Sustainability and Innovation in Structural Engineering (ISISE), reference UIDB/04029/2020 (https://doi.org/10.54499/UIDB/04029/2020, accessed 23 April 2024), and under the Associate Laboratory Advanced Production and Intelligent Systems ARISE, reference LA/P/0112/2020.

Data Availability Statement: Data will be made available upon request to the first author.

Conflicts of Interest: The authors declare no conflicts of interest.

References

1. Huang, L.; Krigsvoll, G.; Johansen, F.; Liu, Y.; Zhang, X. Carbon emission of global construction sector. *Renew. Sustain. Energy Rev.* **2018**, *81*, 1906–1916. [CrossRef]
2. In Focus: Energy Efficiency in Buildings—European Commission, (n.d.). Available online: https://commission.europa.eu/news/focus-energy-efficiency-buildings-2020-02-17_en (accessed on 20 February 2024).
3. Buildings and Construction—European Commission, (n.d.). Available online: https://single-market-economy.ec.europa.eu/industry/sustainability/buildings-and-construction_en (accessed on 26 January 2024).
4. Ben-Alon, L.; Rempel, A.R. Thermal comfort and passive survivability in earthen buildings. *Build. Environ.* **2023**, *238*, 110339. [CrossRef]
5. Fabbri, A.; Aubert, J.-E.; Bras, A.A.; Faria, P.; Gallipoli, D.; Goffart, J.; McGregor, F.; Perlot-Bascoules, C.; Soudani, L. Hygrothermal and Acoustic Assessment of Earthen Materials. In *Testing and Characterisation of Earth-Based Building Materials and Elements*; Springer: Cham, Switzerland, 2022; pp. 83–126. [CrossRef]
6. McGregor, F.; Heath, A.; Maskell, D.; Fabbri, A.; Morel, J.-C. A review on the buffering capacity of earth building materials. *Proc. Inst. Civ. Eng.-Constr. Mater.* **2016**, *169*, 241–251. [CrossRef]
7. Giuffrida, G.; Caponetto, R.; Nocera, F. Hygrothermal properties of raw earth materials: A literature review. *Sustainability* **2019**, *11*, 5342. [CrossRef]
8. Dabaieh, M.; Heinonen, J.; El-Mahdy, D.; Hassan, D.M. A comparative study of life cycle carbon emissions and embodied energy between sun-dried bricks and fired clay bricks. *J. Clean. Prod.* **2020**, *275*, 122998. [CrossRef]
9. Fernandes, J.; Peixoto, M.; Mateus, R.; Gervásio, H. Life cycle analysis of environmental impacts of earthen materials in the Portuguese context: Rammed earth and compressed earth blocks. *J. Clean. Prod.* **2019**, *241*, 118286. [CrossRef]
10. Ben-Alon, L.; Loftness, V.; Harries, K.A.; Hameen, E.C. Integrating Earthen Building Materials and Methods into Mainstream Construction Using Environmental Performance Assessment and Building Policy. *IOP Conf. Ser. Earth Environ. Sci.* **2019**, *323*, 012139. [CrossRef]
11. Bruno, A.W.; Scott, B.; D'Offay-Mancienne, Y.; Perlot, C. Recyclability, durability and water vapour adsorption of unstabilised and stabilised compressed earth bricks. *Mater. Struct.* **2020**, *53*, 1–15. [CrossRef]
12. Mateus, R.; Fernandes, J.; Teixeira, E.R. *Environmental Life Cycle Analysis of Earthen Building Materials*; Elsevier Ltd.: Amsterdam, The Netherlands, 2020. [CrossRef]
13. Zhang, Y.; Jiang, S.; Quan, D.; Fang, K.; Wang, B.; Ma, Z. Properties of Sustainable Earth Construction Materials: A State-of-the-Art Review. *Sustainability* **2024**, *16*, 670. [CrossRef]
14. Wakil, M.; El Mghari, H.; Kaitouni, S.I.; El Amraoui, R. Thermal energy performance of compressed earth building in two different cities in Moroccan semi-arid climate. *Energy Built Environ.* **2023**, *5*, 800–816. [CrossRef]
15. Goodhew, S.; Griffiths, R. Sustainable earth walls to meet the building regulations. *Energy Build.* **2005**, *37*, 451–459. [CrossRef]
16. Ben-Alon, L.; Loftness, V.; Harries, K.A.; Hameen, E.C.; Bridges, M. Integrating earthen building materials and methods into mainstream construction. *J. Green Build.* **2020**, *15*, 87–106. [CrossRef]

17. Fabbri, A.; Morel, J.-C.; Aubert, J.-E.; Bui, Q.-B.; Gallipoli, D.; Reddy, B.V.V. *Testing and Characterisation of Earth-Based Building Materials and Elements*; Springer: Cham, Switzerland, 2022. [CrossRef]
18. Fabbri, A.; Morel, J.C.; Aubert, J.-E.; Bui, Q.-B.; Gallipoli, D.; Ventura, A.; Reddy, V.B.V.; Hamard, E.; Pelé-Peltier, A.; Abhilash, H.N. An overview of the remaining challenges of the RILEM TC 274-TCE, testing and characterisation of earth-based building materials and elements. *RILEM Tech. Lett.* **2021**, *6*, 150–157. [CrossRef]
19. 2050 Long-Term Strategy—European Commission, (n.d.). Available online: https://climate.ec.europa.eu/eu-action/climate-strategies-targets/2050-long-term-strategy_en (accessed on 12 April 2024).
20. Turco, C.; Paula Junior, A.C.; Teixeira, E.; Mateus, R. Optimisation of Compressed Earth Blocks (CEBs) using natural origin materials: A systematic literature review. *Constr. Build. Mater.* **2021**, *309*, 125140. [CrossRef]
21. Samanth, M.; Bhat, K.S. Conventional and unconventional chemical treatment methods of natural fibres for sustainable biocomposites. *Sustain. Chem. Clim. Act.* **2023**, *3*, 100034. [CrossRef]
22. Li, X.; Tabil, L.G.; Panigrahi, S. Chemical treatments of natural fiber for use in natural fiber-reinforced composites: A review. *J. Polym. Environ.* **2007**, *15*, 25–33. [CrossRef]
23. Poorveekan, K.; Ath, K.M.S.; Anburuvel, A.; Sathiparan, N. Investigation of the engineering properties of cementless stabilized earth blocks with alkali-activated eggshell and rice husk ash as a binder. *Constr. Build. Mater.* **2021**, *277*, 122371. [CrossRef]
24. Lejano, B.A.; Gabaldon, R.J.; Go, P.J.; Juan, C.G.; Wong, M. Compressed earth blocks with powdered green mussel shell as partial binder and pig hair as fiber reinforcement. *Int. J. GEOMATE* **2019**, *16*, 137–143. [CrossRef]
25. Nshimiyimana, P.; Messan, A.; Courard, L. Physico-mechanical and hygro-thermal properties of compressed earth blocks stabilized with industrial and agro by-product binders. *Materials* **2020**, *13*, 3769. [CrossRef]
26. Nshimiyimana, P.; Messan, A.; Zhao, Z.; Courard, L. Chemico-microstructural changes in earthen building materials containing calcium carbide residue and rice husk ash. *Constr. Build. Mater.* **2019**, *216*, 622–631. [CrossRef]
27. THE 17 GOALS | Sustainable Development. Available online: https://sdgs.un.org/goals (accessed on 8 April 2024).
28. Turco, C.; Funari, M.F.; Teixeira, E.; Mateus, R. Artificial Neural Networks to Predict the Mechanical Properties of Natural Fibre-Reinforced Compressed Earth Blocks (CEBs). *Fibers* **2021**, *9*, 78. [CrossRef]
29. Laborel-Préneron, A.; Aubert, J.E.; Magniont, C.; Tribout, C.; Bertron, A. Plant aggregates and fibers in earth construction materials: A review. *Constr. Build. Mater.* **2016**, *111*, 719–734. [CrossRef]
30. Jannat, N.; Hussien, A.; Abdullah, B.; Cotgrave, A. Application of agro and non-agro waste materials for unfired earth blocks construction: A review. *Constr. Build. Mater.* **2020**, *254*, 119346. [CrossRef]
31. Turco, C.; de Paula Junior, A.; Teixeira, E.; Mateus, R. Authors closure to the Discussion of the Review article "Optimisation of Compressed earth blocks (CEBs) using natural origin materials: A systematic literature review". *Constr. Build. Mater.* **2022**, *325*, 126888. [CrossRef]
32. Zhang, L. Production of bricks from waste materials–A review. *Constr. Build. Mater.* **2013**, *47*, 643–655. [CrossRef]
33. Minke, G. *Building with Earth: Design and Technology of a Sustainable Architecture*; De Gruyter: Berlin, Germany, 2009.
34. Guettala, S.; Bachar, M.; Azzouz, L. Properties of the Compressed-Stabilized Earth Brick Containing Cork Granules. *J. Earth Sci. Clim. Chang.* **2016**, *7*, 353. [CrossRef]
35. Bachar, M.; Azzouz, L.; Rabehi, M.; Mezghiche, B. Characterization of a stabilized earth concrete and the effect of incorporation of aggregates of cork on its thermo-mechanical properties: Experimental study and modeling. *Constr. Build. Mater.* **2015**, *74*, 259–267. [CrossRef]
36. Djadouf, S.; Chelouah, N.; Tahakourt, A. The influence of the addition of ground olive stone on the thermo-mechanical behavior of compressed earth blocks. *Mater. Tech.* **2020**, *108*, 1–9. [CrossRef]
37. *LNEC NP 143*; Solos. Determinação dos Limites de Consistencia-Soils. Determination of Consistency Limits. LNEC: Lisbon, Portugal, 1969. (In Portuguese)
38. *LNEC NP-83*; Solos. Determinação da Densidade das Partículas-Soils. Determination of Particle Density. LNEC: Lisbon, Portugal, 1965. (In Portuguese)
39. *E1269-11*; Standard Test Method for Determining Specific Heat Capacity by Differential Scanning Calorimetry. ASTM: West Conshohocken, PA, USA, 2011.
40. *LNEC E 197*; Solos. Ensaio de Compactação-Soils. Compaction Test. LNEC: Lisbon, Portugal, 1966. (In Portuguese)
41. *NP EN 933-8*; Ensaios das Propriedades Geométricas dos Agregados: Parte 8: Determinação do Teor de Finos: Ensaio do Equivalente de Areia-Tests for Geometrical Properties of Aggregates: Part 8: Assessment of Fines: Sand Equivalent Test. IPQ: Caparica, Portugal, 2002. (In Portuguese)
42. *NP EN 933-9*; Ensaios das Propriedades Geométricas dos Agregados: Parte 9: Determinação do teor de Finos: Ensaio do Azul de Metileno-Tests for Geometrical Properties of Aggregates: Part 9: Assessment of Fines: Methylene Blue Test. IPQ: Caparica, Portugal, 2002. (In Portuguese)
43. *ASTM D 2974*; Standard Test Methods for Moisture, Ash, and Organic Matter of Peat and Other Organic Soils. ASTM International: West Conshohocken, PA, USA, 2014.
44. Delgado, M.C.J.; Guerrero, I.C. The selection of soils for unstabilised earth building: A normative review. *Constr. Build. Mater.* **2007**, *21*, 237–251. [CrossRef]
45. Jolyon Ralph, Mindat.org—Mines, Minerals and More, The Hudson Institute of Mineralogy (n.d.). Available online: https://www.mindat.org/ (accessed on 19 February 2024).

46. Fo, M. *Handbook of Thermogravimetric System of Minerals and Its Use in Geological Practice*; Geological Institute of Hungary: Budapest, Hungary, 2011.
47. Klimesch, D.S.; Ray, A. The use of DTA/TGA to study the effects of ground quartz with different surface areas in autoclaved cement: Quartz pastes. Use of the semi-isothermal thermogravimetric technique. *Thermochim. Acta* **1997**, *306*, 159–165. [CrossRef]
48. Ringdalen, E. Changes in Quartz During Heating and the Possible Effects on Si Production. *JOM* **2015**, *67*, 484–492. [CrossRef]
49. Shanmugavel, D.; Dubey, R.; Ramadoss, R. Use of natural polymer from plant as admixture in hydraulic lime mortar masonry. *J. Build. Eng.* **2020**, *30*, 101252. [CrossRef]
50. Csanády, D.; Fenyvesi, O.; Nagy, B. An empirical model of heat-treated straw bulks' thermal conductivity based on changes in mass and chemical composition. *J. Therm. Anal. Calorim.* **2023**, *148*, 3731–3749. [CrossRef]
51. Gibson, L.J.; Easterling, E.; Ashby, M.F. The Structure and Mechanics of Cork. *Proc. R. Soc. Lond. A Math. Phys. Sci.* **1981**, *377*, 99–117. Available online: https://www.jstor.org/stable/2397034 (accessed on 6 November 2023).
52. Motte, J.C.; Delenne, J.Y.; Barron, C.; Dubreucq, É.; Mayer-Laigle, C. Elastic properties of packing of granulated cork: Effect of particle size. *Ind. Crops Prod.* **2017**, *99*, 126–134. [CrossRef]
53. Chanut, J.; Wang, Y.; Cin, I.D.; Ferret, E.; Gougeon, R.D.; Bellat, J.P.; Karbowiak, T. Surface properties of cork: Is cork a hydrophobic material? *J. Colloid Interface Sci.* **2022**, *608*, 416–423. [CrossRef] [PubMed]
54. Martins, C.I.; Gil, V. Processing–Structure–Properties of Cork Polymer Composites. *Front. Mater.* **2020**, *7*, 572353. [CrossRef]
55. Caballero, J.A.; Marcilla, A.; Conesa, J.A. Thermogravimetric analysis of olive stones with sulphuric acid treatment. *J. Anal. Appl. Pyrolysis* **1997**, *44*, 75–88. [CrossRef]
56. Ashour, T.; Korjenic, A.; Korjenic, S.; Wu, W. Thermal conductivity of unfired earth bricks reinforced by agricultural wastes with cement and gypsum. *Energy Build.* **2015**, *104*, 139–146. [CrossRef]
57. Zhang, Y.; Ghaly, A.E.; Li, B. Physical Properties of Wheat Straw Varieties Cultivated Under Different Climatic and Soil Conditions in Three Continents. *Am. J. Eng. Appl. Sci.* **2012**, *5*, 98–106. [CrossRef]
58. Rigassi, V. *Compressed Earth Blocks: Manual of Production*; Deutsche Development Agency: Bonn, Germany, 1985.
59. *NZS 4298*; Materials and Workmanship for Earth Buildings. New Zealand Standard: Wellington, New Zealand, 1998.
60. Turco, C.; Junior, A.P.; Jacinto, C.; Fernandes, J.; Teixeira, E.; Mateus, R. Influence of Particle Size on Compressed Earth Blocks Properties and Strategies for Enhanced Performance. *Appl. Sci.* **2024**, *14*, 1779. [CrossRef]
61. *ASTM C1363-11*; Standard Test Method for Thermal Performance of Building Materials and Envelope Assemblies by Means of a Hot Box Apparatus. American Society for Testing Materials: West Conshohocken, PA, USA, 2014.
62. *BSI, ISO 9869-1:2014*; Thermal Insulation—Building Elements—In Situ Measurement of Thermal Resistance and Thermal Transmittance; Part 1: Heat Flow Meter Method. ISO: Geneva, Switzerland, 2014.
63. Teixeira, E.R.; Machado, G.; de, P. Junior, A.; Guarnier, C.; Fernandes, J.; Silva, S.M.; Mateus, R. Mechanical and Thermal Performance Characterisation of Compressed Earth Blocks. *Energies* **2020**, *13*, 2978. [CrossRef]
64. *IS 1725*; Specification for Soil Based Blocks Used in General Building Constructuion. Indian Standard: New Delhi, India, 1982.
65. *SLS 1382*; Compressed Stabilized Earth Blocks. Sri Lankan Standard: Colombo, Sri Lankan, 2009.
66. Ochsner, T. *Rain or Shine: An Introduction to Soil Physical Properties and Processes*; Oklahoma State University: Stillwater, OK, USA, 2019. [CrossRef]
67. Laborel-Préneron, A.; Aubert, J.-E.; Magniont, C.; Bertron, A. Influence of straw content on the mechanical and thermal properties of bio-based earth composites. *Acad. J. Civ. Eng.* **2015**, *33*. [CrossRef]
68. Barreca, F.; Fichera, C.R. Use of olive stone as an additive in cement lime mortar to improve thermal insulation. *Energy Build.* **2013**, *62*, 507–513. [CrossRef]
69. Vicente-Navarro, A.S.; Mendívil-Giro, M.; Los Santos-Ortega, J.; Fraile-García, E.; Ferreiro-Cabello, J. Alternative Use of the Waste from Ground Olive Stones in Doping Mortar Bricks for Sustainable Façades. *Buildings* **2023**, *13*, 2992. [CrossRef]
70. He, J.; Jie, Y.; Zhang, J.; Yu, Y.; Zhang, G. Synthesis and characterization of red mud and rice husk ash-based geopolymer composites. *Cem. Concr. Compos.* **2013**, *37*, 108–118. [CrossRef]

energies

MDPI

Article

Envelope Deficiencies and Thermo-Hygrometric Challenges in Warehouse-Type Buildings in Subtropical Climates: A Case Study of a Nori Distribution Center

Yue Xu [1], Hiroatsu Fukuda [1,*], Xindong Wei [2] and Tingting Yin [1]

[1] Department of Architecture, Faculty of Environmental Engineering, The University of Kitakyushu, Kitakyushu 808-0135, Japan; yue.xu205@outlook.com (Y.X.); e3dbb001@eng.kitakyu-u.ac.jp (T.Y.)
[2] School of International Education, Jilin Jianzhu University, Changchun 130118, China; weixindong@jlju.edu.cn
* Correspondence: fukuda@kitakyu-u.ac.jp

Abstract: Enhancing the energy efficiency and climate resilience of existing buildings is crucial amid growing environmental challenges. While extensive research has focused on non-residential buildings, studies on thermo-hygrometric conditions in warehouse-type buildings, particularly in subtropical climates, remain limited. This study investigated the impact of building envelope deficiencies on indoor thermal and moisture regulation at the Nori Distribution Center. Using infrared thermal imaging and long-term environmental monitoring, significant thermo-hygrometric fluctuations were identified, primarily due to design and construction deficiencies. Poor insulation, inadequate sealing, and the lack of moisture barriers contributed to unstable indoor temperature and humidity. Seasonal analysis showed that during summer, the median second-floor air temperature reached 28.8 °C, peaking at 39.2 °C, with relative humidity exceeding 70% for 45% of the time. First-floor relative humidity surpassed 70% for 72% of the time. While condensation risk remains low year-round, it increases significantly with air infiltration through gaps in the building envelope. This study recommends enhancing the sealing of the building envelope, upgrading insulation materials and moisture barriers, particularly in the roof, and optimizing the HVAC system to improve energy efficiency and storage conditions. These findings offer valuable recommendations for retrofitting warehouse-type buildings in subtropical climates to improve energy efficiency and climate resilience.

Keywords: building envelope; thermo-hygrometric control; subtropical climates; deficiency detection; insulation; warehouse-type buildings

1. Introduction

As the built environment faces growing demands for sustainability, optimizing the energy performance of existing buildings is crucial for reducing energy consumption and carbon emissions [1,2]. In reflecting on the current capabilities and the possibilities for improving the building stock, it is essential to design buildings that can adapt to climate changes throughout their entire life cycle [3]. Adapting buildings to local climatic conditions—characterized by high humidity, significant temperature fluctuations, and intense solar radiation—presents considerable challenges [4–6]. These conditions stress traditional building methods and severely impact indoor thermo-hygrometric conditions, which are essential for occupant comfort [7–10], material integrity preservation [11,12], and energy efficiency [13].

The built environment plays a crucial role in addressing climate change, particularly in urban areas where dense populations and high levels of human activity intensify environmental pressures. The concentration of population in cities makes them more vulnerable to the externalities of emissions and the impacts of climate change [14]. As a result, cities have become central to both mitigation and adaptation efforts [15]. Mitigation strategies

aimed at reducing greenhouse gas emissions are essential for improving energy efficiency and minimizing the environmental impact of buildings [16]. At the same time, buildings in edge-of-city or suburban areas, while exposed to different environmental conditions, face equally significant challenges as cities expand to incorporate rural and industrial zones [17]. Therefore, targeted strategies are necessary to ensure both energy efficiency and the long-term performance of buildings in these regions.

In the context of climate-responsive building design, distinguishing between mitigation and adaptation strategies is critical. Mitigation measures address the root causes of climate change by reducing greenhouse gas emissions and improving energy efficiency [1]. In contrast, adaptation measures aim to enhance a building's capacity to endure the effects of climate change, maintaining functionality under shifting environmental conditions [18]. To comprehensively address the complexities of climate-related challenges, adaptation must be given equal priority alongside mitigation [19].

With the intensification of these environmental challenges, prioritizing the maintenance, renovation, and retrofitting of existing buildings has emerged as a key strategy to enhance their resilience and sustainability [2,20,21]. By mitigating the impacts of climate on building integrity and functionality and subsequently maintaining optimal thermo-hygrometric conditions, we can ensure the long-term sustainability of the built environment [22,23].

Adaptation strategies of buildings to diverse climatic conditions have been extensively researched, predominantly focusing on residential buildings [24–28]. Although significant attention has been directed toward non-residential buildings [29–33], challenges specific to warehouse-type buildings in subtropical climates are less studied [34]. This research gap is particularly evident in the specific structural and environmental control requirements of warehouse-type buildings, especially in maintaining optimal thermo-hygrometric conditions.

In hot and torrid climates, the internal heat load of commercial and industrial buildings is mainly determined by solar heat gain through the roof, walls, and floors [35,36]. However, the loads that most influence internal temperatures, apart from those entering from opaque structures, are the solar loads entering through windows [37]. Such facilities are typically characterized by large open spaces and high ceilings, which contribute to significant vertical temperature gradients and increase infiltration heat loads due to their small shape factor [38,39]. Additionally, warehouse-type buildings often utilize metal roof panels and lack surrounding shading structures, frequently exposing roofs to prolonged direct sunlight, exacerbating temperature and humidity fluctuations and causing overheating [40,41]. Under subtropical climate conditions, these factors can lead to condensation and mold growth, compromising the structural integrity of the building and reducing product quality [42–45].

Non-destructive in situ investigations are increasingly recognized as essential for the thermal characterization of building envelopes. These techniques offer significant advantages by allowing the evaluation of thermal performance without causing damage to the structure [46]. Key parameters for thermal characterization include heat flux, which measures the rate of thermal energy transfer per unit area, and thermal transmittance, which quantifies the rate of heat transfer through building materials. Accurate measurement of these parameters is critical for assessing the performance of building envelope components and identifying areas where energy efficiency can be improved [47]. Recent studies have demonstrated the effectiveness of direct and indirect heat flux measurement techniques and highlighted the environmental impact of conducting such tests in existing buildings [48,49].

However, in many existing buildings, due to equipment and cost limitations, in situ measurements can be challenging. In such cases, theoretical methods that calculate thermal resistance and transmittance based on material properties offer a practical alternative [50]. While these methods may not match the accuracy of in situ measurements, they remain useful when direct measurement is not feasible. Furthermore, infrared thermography has been widely applied as a non-destructive testing method for both qualitative analysis and quantitative analysis [51–53].

The thermal and moisture management capabilities of the building envelope are crucial for maintaining indoor comfort, especially in regions with challenging climate conditions such as high humidity and temperature variability [54,55]. Improper design or construction can exacerbate the impact of external environmental stresses, leading to heat loss and moisture infiltration in the building envelope, which, in turn, increases energy consumption and accelerates material degradation [51,56]. Therefore, an optimally designed building envelope is essential to withstand harsh environmental stresses and ensure the internal environment necessary for maintaining optimal conditions [53,57,58].

Given the essential role of a well-designed building envelope in maintaining optimal conditions, many industrial facilities are turning to thermal retrofitting and renovation strategies to enhance overall energy efficiency [36,38,59]. However, the variability in the design and operation of warehouse-type buildings, often tailored to specific materials and products, complicates fair comparisons of energy efficiency across different facilities [60,61]. Given these complexities, effective state monitoring and building diagnostics are crucial for ensuring the long-term performance and safety of buildings [51,62]. In summary, managing thermo-hygrometric conditions and mitigating building envelope deficiencies are critical for the long-term stability and efficiency of such facilities, particularly in subtropical climates.

An illustrative example of these challenges is the Nori (dried seaweed) Distribution Center, located in a subtropical zone. This facility is specifically designed to manage the storage, quality control, and pricing of nori—a product highly sensitive to environmental conditions [63,64]. It exemplifies the critical need for building envelope solutions. Inherent deficiencies in its design and construction amplify environmental challenges [65], making the Center an ideal case study to evaluate how the building envelope impacts the operational efficacy, functionality, and long-term viability of warehouse-type buildings in subtropical climates. The building envelope's role as a key determinant of a facility's climate responsiveness was a pivotal focus of this research [17].

This study conducted a comprehensive empirical analysis of the Nori Distribution Center, focusing on how deficiencies in the building envelope affect the performance and functionality of the facility under subtropical conditions. It aimed to identify specific deficiencies in the building envelope, analyze their impact under high humidity and temperature fluctuations, and develop targeted improvement strategies. These strategies were designed to significantly enhance the indoor thermo-hygrometric environment, along with the energy efficiency and sustainability of the facility, ensuring that it is better equipped to withstand the climatic conditions of its region. While this study primarily focused on adaptation strategies to improve the ability of the building to cope with the hot and humid subtropical climate, some of the proposed measures, such as enhanced insulation and sealing, also contribute to mitigation efforts by reducing energy consumption and associated emissions. Before beginning renovations, it is crucial to conduct a detailed evaluation of the existing building conditions to accurately determine the necessary modifications and interventions.

The insights derived from this research are intended to provide architects, engineers, and policymakers with actionable, evidence-based information to aid in making informed decisions about adapting warehouse-type buildings to the environmental and energy challenges of subtropical climates.

2. Materials and Methods

2.1. Study Case

This study examined a Nori Distribution Center constructed in 2017 in Kumamoto, Kyushu, Japan. The two-story facility has a total floor area of approximately 4990.76 m^2 and a building footprint of 2692.76 m^2. It features a steel frame structure with a standing seam interlocking roof made of color-coated Galvalume steel sheets and exterior walls composed of corrugated color-coated Galvalume steel sheets (Figure 1). The facility is located in a predominantly residential and agricultural area, situated away from any high-rise buildings.

Figure 1. Building selected for the case study. The red dashed circle highlights the location of the Nori Distribution Center.

The thermal properties of the opaque building envelope components are summarized in Table 1, while the thermal properties of the transparent components (windows) are detailed in Table 2. The calculation of thermal parameters is referenced in Appendix A.

Table 1. Thermal properties of the opaque building envelope components.

Element	Thermal Transmittance (U-Value/Heat Transfer Coefficient) (W/m^2·K)	Layer Composition (from Inner Side to Outer Side in the Zone)	Layer Thickness (mm)	Thermal Conductivity (λ) (W/(m·K))
Roof	3.70	High flame retardant foam Galvalume steel sheet	4 0.6	0.029 45
Wall	0.59	Calcium silicate board Glass wool Non-closed air layer Polyethylene foam Galvalume steel sheet	8 50 - 4 0.5	0.14 0.038 - 0.037 45
Floor 2	2.56	Polyvinyl chloride flooring sheet Concrete Galvanized Steel Sheet	2 130 1.2	0.19 1.60 45
Floor 1	3.33	Concrete	180	1.60
Roller Shutter	6.67	Steel sheet	1.6	55

Note: the thermal property of the non-closed air layer was set as thermal resistance (=0.07 m^2·K/W).

Table 2. Thermal properties of the windows.

Element	Type of Glass	Glass Layer Composition (Layer Thickness (mm))	Glass Thermal Transmittance (W/(m^2·K))	Solar Heat Gain Coefficient	Window (Glass with Frame) Thermal Transmittance (W/(m^2·K))
W1	Single-glazed glass	Single-glazed glass (4)	6	0.88	6.3
W2	Double-glazed glass	Transparent glass (5) air gap (6) transparent glass (5)	3.3	0.79	4.2

The primary functions of the facility are the storage, quality assessment, and pricing of nori. From late November to April, nori is stored on the ground floor in cardboard boxes

and plastic bags, while the second floor contains a specialized inspection room for quality evaluation. Due to the variability of nori quality influenced by weather conditions, the facility urgently needs to maintain strict temperature and humidity controls to standardize the bidding process. This ensures competitive bidding and potentially higher prices for fishermen, promoting improved production techniques and quality management [66].

However, the steel-framed construction, with its corrugated sheet roofing, faces significant challenges in Kyushu's humid and rainy climate, requiring effective climate control measures. Records indicate issues such as nori shrinkage and the occurrence of condensation, emphasizing the need to address building deficiencies through inspections and corrective actions to improve thermo-hygrometric management and maintain optimal conditions in this subtropical environment.

2.2. Study Area and Climate Condition

Kumamoto, located at 32°48′ N and 130°42′ E, exemplifies the Köppen Cfa climate category, characterized by a humid subtropical climate prevalent in Japan's Kyushu region (Figure 2). This climate features warm, humid summers and mild winters, consistent with other humid subtropical zones, as evidenced by TMYx data obtained from the online repository https://climate.onebuilding.org/ (accessed on 5 September 2024) [67] and shown in Table 3.

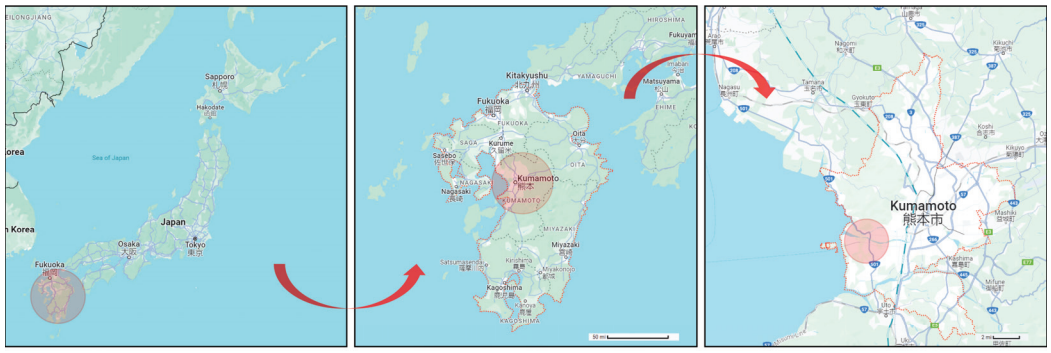

Figure 2. Location of Kumamoto City.

Table 3. Climatic data for Kumamoto City.

Month	Mean T_a (°C)	Max T_a (°C)	Min T_a (°C)	Mean *RH* (%)	Max *RH* (%)	Min *RH* (%)
January	6.02	15	−4	70.91	100	36
February	7.68	20.3	−2.9	68.04	95	27
March	9.78	23.2	−1.7	70.91	100	36
April	15.55	27.8	2.9	75.00	100	28
May	20.04	30	7	66.95	100	26
June	23.47	33.8	13.9	78.52	99	38
July	27.26	35.6	21.1	80.27	100	46
August	27.92	34.7	20.9	74.97	99	40
September	24.95	33.5	15.5	69.59	93	30
October	19.72	28.6	8.8	69.24	98	30
November	13.03	22	3.6	71.55	100	36
December	8.23	18.5	0.9	71.57	96	37

The TMYx data reveal significant monthly precipitation variations (Figure 3). June sees the highest average precipitation at 448.5 mm during the 'tsuyu' period [56], markedly contrasting with January's low of 57.2 mm. Seasonal variations in solar radiation are significant, with a peak of 18.4 MJ/m^2 in May and a low of 8.1 MJ/m^2 in December. In

June, during the rainy season, sunshine duration significantly decreases to 130.8 h due to increased cloud cover and precipitation, while the peak in August reaches 206.0 h.

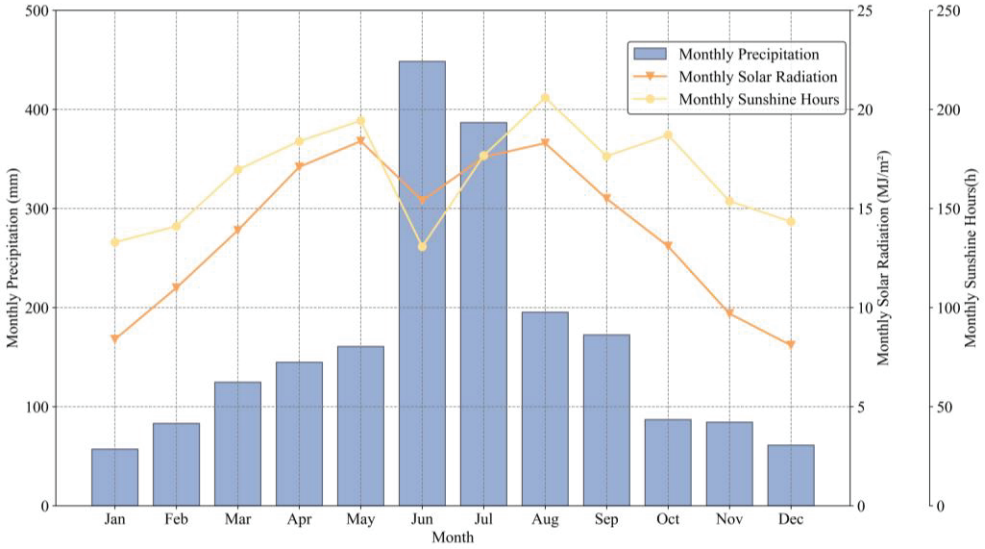

Figure 3. Monthly climatic trends in kumamoto city: precipitation, solar radiation, and sunshine hours.

The TMYx data further show that Kumamoto's winter air temperature (T_a) typically remains above 0 °C, suggesting a short and moderate winter. In contrast, during the summer, T_a frequently exceeds 30 °C, accompanied by high relative humidity (*RH*) and a significant increase in precipitation, especially in June. This pattern aligns with the East Asian rainy season, locally termed 'tsuyu', which is characterized by extensive rainfall, as illustrated in Figure 3, and high *RH*, as shown in Table 3.

2.3. Data Collection

This study evaluated the interaction between the building envelope and the thermal-humid environment to assess the impact of the subtropical climate on building performance. The details of the instruments used, including their measurement ranges and accuracies, are provided in Table 4. Initially, we used the FLIR ONE Pro infrared thermography camera, sourced from FLIR Systems, Inc., Wilsonville, OR, USA, to conduct preliminary inspections of the first-floor storage room and the second-floor inspection room, aiming to identify potential thermal bridges and areas of moisture accumulation. Additionally, this study involved a comprehensive evaluation of the design and construction quality of the building envelope. Detailed checks focused on the compliance of materials, accuracy of construction, and integrity of the insulation layer, aiming to address key issues that could undermine the building's thermal efficiency and indoor comfort [68,69].

Table 4. Instrumentation for Parameter Measurements.

Measurement Parameter	Measurement Instrument	Range of Measurement	Accuracy	Measurement Resolution
Surface temperature	FLIR ONE Pro	−20 °C~400 °C	±3 °C	0.1 °C
Air temperature Air relative humidity	T&D TR-72nw	T_a: 0 to 55 °C *RH*: 10 to 95% RH	±0.5 °C, ±5% RH at 25 °C, 50% RH	0.1 °C 1% RH
Surface temperature	T&D TR-71A	−40 to 110 °C	Avg. ±0.3 °C at −20 to 80 °C	0.1 °C

The core of the research focused on continuous monitoring of key environmental parameters. These parameters include outdoor air temperature ($T_{a,ex}$) and outdoor relative

humidity (RH_{ex}), as well as indoor air temperature ($T_{a,in}$) and indoor relative humidity (RH_{in}) for the first-floor warehouse ($T_{a,in,1}$ and $RH_{in,1}$) and the second-floor inspection room ($T_{a,in,2}$ and $RH_{in,2}$). Surface temperature (T_s) measurements were taken for the floors in the first-floor warehouse ($T_{s,in,f,1}$) and second-floor inspection room ($T_{s,in,f,2}$), the internal surfaces of the external walls in both rooms ($T_{s,in,w,1}$ and $T_{s,in,w,2}$), and the roof ceiling and beam in the second-floor inspection room ($T_{s,in,r,2}$ and $T_{s,in,b,2}$). These parameters are critical for maintaining the quality of nori and optimizing the building's thermal performance. By analyzing the building's thermo-hygrometric behavior across different time periods, annual monitoring results were obtained, covering seasonal, monthly, and typical weekly patterns. Furthermore, the measurement of T_a and T_s, along with RH, is a well-established diagnostic method for identifying defects [70]. The first-floor warehouse was selected as the main monitoring point due to its location on the ground floor and its frequent operations, which increase its susceptibility to moisture ingress and temperature and humidity fluctuations. Additionally, the first-floor warehouse and the second-floor inspection room are the two largest spaces in the building. The second-floor inspection room, located directly beneath the roof, is prone to solar heat gain, making it a critical area for observing thermal behavior in warehouse-type buildings.

To monitor environmental conditions continuously, a T&D series of high-precision temperature and humidity sensors, including the T&D TR-72nw and T&D TR-71A models, sourced from T&D Corporation, Matsumoto, Japan, were deployed, recording data at 10 min intervals. To ensure the accuracy and consistency of data collection while minimizing disruptions to the routine operations within the facility sensors were strategically positioned (Figure 4).

Despite over a year of continuous monitoring, we encountered challenges with data loss, primarily due to equipment failures and restrictions on building access during the COVID-19 pandemic. The initial infrared thermography survey was conducted on 4 June 2021, and continuous temperature and humidity monitoring commenced in July 2021. Following these initial data collection efforts, starting from the winter of 2021, we initiated additional monitoring of the $T_{s,in,r,2}$ and $T_{s,in,b,2}$ to refine our methodologies. Due to data loss in June 2022, we replicated the monitoring and data collection in June 2023 to supplement the missing information and finalize our annual analysis. Additionally, during this period, we conducted a supplementary assessment of the T_a and RH near the roof ceiling in the second-floor inspection room ($T_{a,in,r,2}$ and $RH_{in,r,2}$). On 26 January 2023, a further infrared thermography survey was performed. In the same month, we implemented temperature and humidity monitoring following the same protocols that we planned for June 2023 to enhance our data collection for the winter season.

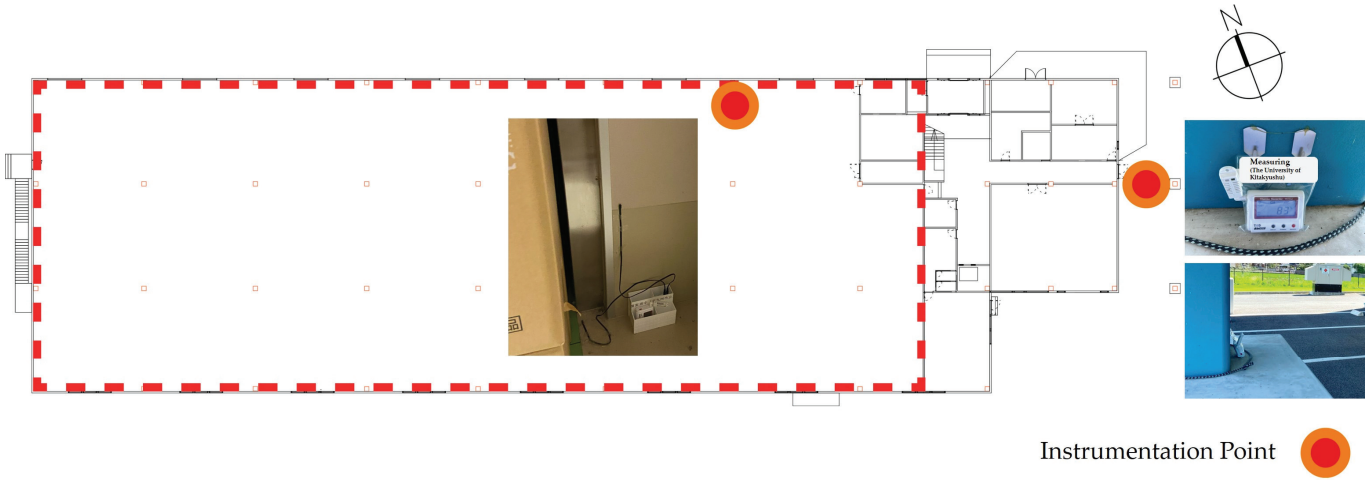

(**a**)

Figure 4. *Cont.*

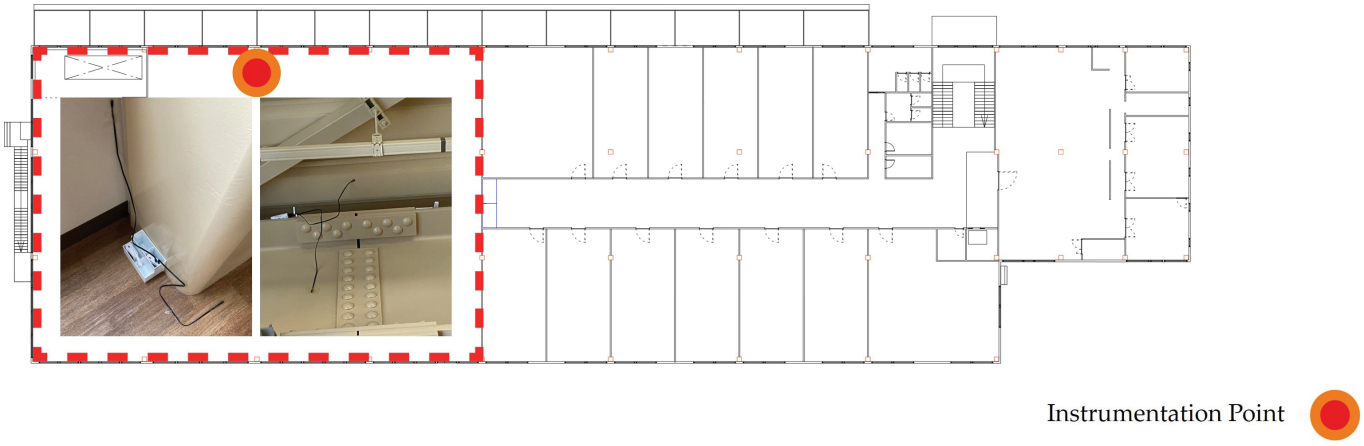

(**b**)

Figure 4. Layout and instrumentation points for thermal-humidity assessment: (**a**) first-floor warehouse, (**b**) second-floor inspection room.

2.4. Data Processing and Analysis

After completing data collection, this study utilized Microsoft Excel (version 2021) and Python (version 3.11.5) for data processing, analysis, and visualization. Descriptive statistics were employed to summarize key features of the data, while correlation analyses were conducted to rigorously explore relationships and patterns among the variables.

2.4.1. Calculation Methodology for Air Dew Point Temperature and Humidity Variables

The air dew point temperature (DP) and the absolute humidity (AH) were calculated from the measured parameters using the Tetens (1930) [71] equation as follows:

$$DP = \frac{237.3 \times \log_{10}(6.1078/e_a)}{\log_{10}(e_a/6.1078) - 7.5}, \quad (1)$$

where DP is the dew point temperature in the unit of °C, and e_a is the actual vapor pressure in the unit of hPa.

The actual vapor pressure (e_a) was calculated using the following equations:

$$e_a = e_s \times \frac{RH}{100}, \quad (2)$$

$$e_s = 6.1078 \times 10^{\frac{7.5 \times T_a}{T_a + 237.3}}, \quad (3)$$

where e_s is the saturation vapor pressure in the unit of hPa, RH is the relative humidity in the unit of %, and T_a is the air temperature in the unit of °C.

The absolute humidity (AH) was calculated as follows:

$$AH = a_s \times \frac{RH}{100}, \quad (4)$$

$$a_s = \frac{217 \times e_s}{T_a + 273.15}, \quad (5)$$

where a_s is the saturation vapor density in the unit of g/m^3, and AH is the absolute humidity in the unit of g/m^3.

2.4.2. Assessment of Hygrothermal Stability Using Monthly Average Diurnal Range

In building preservation and nori storage, maintaining a stable hygrothermal environment is essential. The Monthly Average Diurnal Range (MADR) serves as an effective indicator for quantifying the stability of hygrothermal conditions. The MADR measures

the average daily variation in environmental parameters, representing the diurnal thermal and moisture stability in a building. The calculation is expressed as follows:

$$\text{MADR} = \frac{1}{n}\sum_{i=1}^{n}(m_{\max,i} - m_{\min,i}), \tag{6}$$

where $m_{\max,i}$ denotes the peak daily value, $m_{\min,i}$ represents the lowest daily value, and n is the number of days in the month.

2.4.3. Analysis of Condensation Risk via Vapor Pressure Ratios

This study investigated the condensation risk (CR) on interior surfaces by analyzing vapor pressure ratios using a bifurcated approach, evaluating both the indoor air vapor pressure relative to the saturation vapor pressure at the interior surface temperature and the outdoor air vapor pressure relative to the saturation vapor pressure at the equivalent surface temperature. Although HVAC systems are installed in the warehouse and inspection room, they are used infrequently. In the facility's daily operations, the HVAC system is only used from November to April, for four days each month during bidding sessions on the second floor, to optimize indoor conditions. The frequent operation of rolling shutters leads to considerable natural air exchange. In this study, we assumed that the vapor pressure of outdoor air remains unchanged when it enters the indoor environment. While temperature and humidity differences can affect vapor pressure, this assumption simplified our analysis, allowing us to focus on how air exchange impacts CR. This study categorized condensation risk into four levels [58] based on the ratio of actual vapor pressure to saturation vapor pressure:

- Category I, where ratios between 95% and 100% indicate a high likelihood of condensation;
- Category II, with ratios up to 95% suggesting potential condensation;
- Category III, ratios from 85% to 90% denoting probable condensation in the event of significant environmental changes;
- Category IV, where ratios at or below 85% present a low risk of condensation.

3. Results and Discussion

3.1. Qualitative Analysis

This section conducts a qualitative analysis to evaluate the thermal performance and identify potential insulation deficiencies within the nori distribution center. Utilizing infrared thermal imaging surveys, visual inspections, and an extensive review of building design documents, this study uncovered several critical insights. Table 5 outlines the external environmental parameters recorded during the thermal imaging measurement period, with data sourced from the Japan Meteorological Agency [72].

Table 5. External environmental parameters during the thermal imaging measurement period.

Date	Mean T_a (°C)	Max T_a (°C)	Min T_a (°C)	Mean *RH* (%)	Min *RH* (%)
4 June 2021	20.8	23.5	19.2	97.0	88.0
26 January 2023	2.3	7.6	−3.4	68	48

The initial infrared thermal imaging survey, carried out on 4 June 2021, after daytime rainfall and conducted in the evening, revealed that, despite the absence of significant thermal gradients, yellow linear streaks were observed along the roll-up door edges on the first floor (Figure 5(I-a)), indicating air leaks through visible gaps [51]. $T_{s,in,f,1}$ and $T_{s,in,w,1}$ were lower than $T_{s,in,c,1}$ (Figure 5(I-b)), while $T_{s,in,f,2}$ was higher than $T_{s,in,r,2}$ (Figure 5(I-d)). Additionally, the first-floor foundation rises displayed distinct yellow hues in the thermal images (Figure 5(I-b)), which, upon verification against building design documents, confirmed the absence of insulation material in this area.

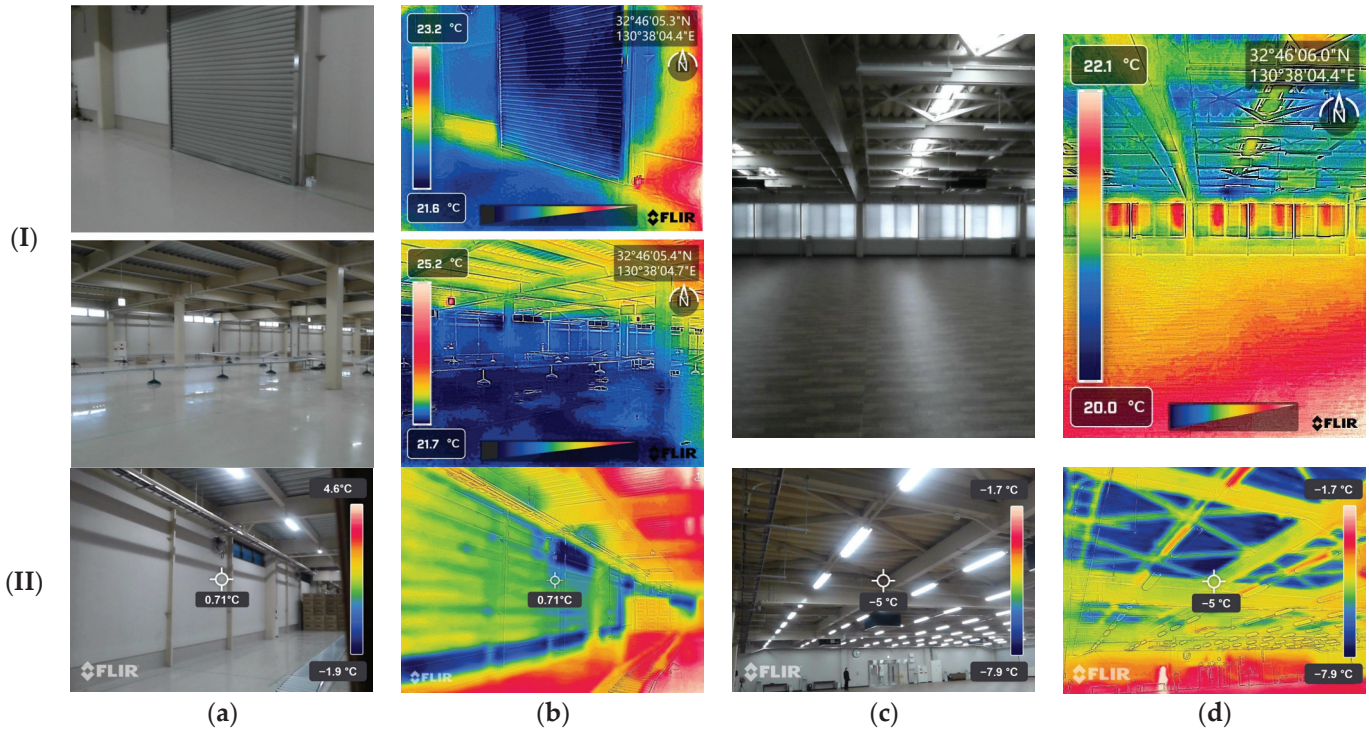

Figure 5. Qualitative detection of thermal characteristics: (**I**) 4 June 2021; (**II**) 26 January 2023; (**a**,**b**) first-floor warehouse visible image and thermal image; (**c**,**d**) second-floor inspection room visible image and thermal image.

A subsequent thermal survey was conducted on the morning of 26 January 2023, following the coldest day of the year. This survey revealed pronounced thermal anomalies at the first-floor foundation rise and windows (Figure 5(II-b)), suggesting insulation deficiencies. Thermal imaging of the second-floor inspection room (Figure 5(II-d)) showed that $T_{s,in,r,2}$ was lower than other T_s, indicating inadequate insulation in the roof structure. The building's design document indicates that the insulation layer beneath the steel plate roof in the second-floor inspection room is only 4mm thick, with a calculated U-value of 3.70 W/(m^2·K), corresponding to a thermal resistance (R-value) of approximately 0.27 m^2·K/W. However, the insulation standard for roofs in this type of building in the region requires a minimum R-value of 1.35 m^2·K/W, indicating that the current insulation performance falls significantly short of the required standard [73]. Visual inspections also revealed gaps at the joints of the insulation materials.

Additionally, although the exterior walls of the first-floor warehouse and the second-floor inspection room are equipped with breathable waterproof membranes, the absence of moisture barriers undermines the overall moisture control, potentially compromising the effectiveness of insulation and increasing humidity-related issues [74]. Meanwhile, the first floor's flooring comprises a durable, low-maintenance concrete base with a coated finish designed to support substantial loads, making it ideal for warehouse use. However, the inherent high thermal conductivity of concrete, without adequate insulation, is likely to lead to increased energy consumption and reduced energy efficiency in the building [75]. To enhance energy efficiency and regulate temperature, integrating an insulating layer or thermal barrier is recommended. Additionally, in conditions of high RH_{in} and low $T_{a,in}$, the concrete's propensity to retain cold can lead to condensation formation on the floor surface, further complicating temperature management.

3.2. Indoor and Outdoor Air Temperature and Humidity

Continuous monitoring allowed for the detection of subtle environmental variations, particularly near the roll-up door on the north side of the first-floor storage area and in the corresponding second-floor inspection room.

3.2.1. Air Temperature

A statistical analysis was conducted to assess thermal distribution in the outdoor environment, first-floor warehouse, and second-floor inspection room under subtropical humid conditions across seasons. During summer, no active HVAC systems are used, emphasizing the building's reliance on passive cooling and insulation. Table 6 highlights the significant seasonal T_a variations.

Table 6. Seasonal air temperature distributions in various locations.

Season	$T_{a,ex}$ (°C)					$T_{a,in,1}$ (°C)					$T_{a,in,2}$ (°C)				
	Mean	**Median**	σ	**Min**	**Max**	**Mean**	**Median**	σ	**Min**	**Max**	**Mean**	**Median**	σ	**Min**	**Max**
Summer	27.27	27.2	3.57	17.7	36.8	26.65	26.9	2.28	20.8	31	28.97	28.8	4.01	19.7	39.2
Autumn	20.99	22.3	6.97	4.4	34.7	22.46	24.3	4.7	12.6	29.7	22.13	22.9	6.65	7.5	35.8
Winter	7.73	7.6	3.84	−2.1	19.9	9.38	9.2	2.29	3.4	15.3	9.15	8.8	3.51	1.1	22.9
Spring	17.59	18	5.41	1.7	30.9	17.01	17.5	3.94	5.4	23.9	18.84	19	5.22	3.8	32.1

Note: σ represents the standard deviation of temperature values.

$T_{a,in}$ records indicate that, relative to the second floor, the first floor demonstrates a modest level of thermal stability; however, passive thermal management remains inadequate, particularly during periods of peak summer T_a. The second-floor inspection room faces significant challenges, with median $T_{a,in,2}$ reaching 28.8 °C during summer and $T_{a,in,2}$ spikes up to 39.2 °C. These extreme $T_{a,in,2}$ continue into the transitional seasons, with $T_{a,in,2}$ peaking at 35.8 °C in autumn and 32.1 °C in spring. Although there are no specific regulations for warehouse-type buildings, researchers caution that Japan's recommended summer maximum $T_{a,in}$ of 28 °C, may be insufficient to ensure occupant comfort [10,76].

During the transitional seasons of spring and autumn, while the extremes in T_a are less severe compared with the harsh summer and winter months, the considerable variability within these periods indicates that the current passive environmental control systems struggle to adequately moderate these fluctuations. The consistently higher standard deviations (σ) in $T_{a,in,2}$ across all seasons highlight its increased sensitivity to external climatic conditions. By enhancing insulation, particularly on the second floor, peak $T_{a,in,2}$ can be reduced, mitigating the risk of overheating during the hot summer months [57,77].

The violin plots shown in Figure 6 present the monthly T_a data across different locations. A violin plot combines elements of a box plot and a kernel density plot, providing a comprehensive view of both the distribution range and the density of the data. The median is represented by a thicker dashed line, while the first and third quartiles (Q1 and Q3) are indicated by thinner dashed lines. The width of each violin plot reflects the density of the temperature recordings, clearly illustrating the frequency distribution within specific temperature ranges.

In August, the median $T_{a,ex}$ reaches 27.4 °C, with peaks up to 36.8 °C, indicating the presence of extreme heat. January contrasts sharply, with median $T_{a,ex}$ falling to 7.3 °C and lows nearing −2.1 °C, heralding the winter's chill. Transitional months such as April and October exhibit more moderate $T_{a,ex}$ fluctuations, with median $T_{a,ex}$ at 17.6 °C and 22 °C, respectively.

On the first floor, the warehouse experiences a median August $T_{a,in,1}$ of 28.1 °C, slightly above the external air, peaking at 31 °C. January's median $T_{a,in,1}$ of 9 °C, with a low of up to 4.3 °C, illustrates some capacity for heat retention, though not markedly superior to external conditions. The first-floor warehouse displays a more concentrated T_a distribution with smaller variations.

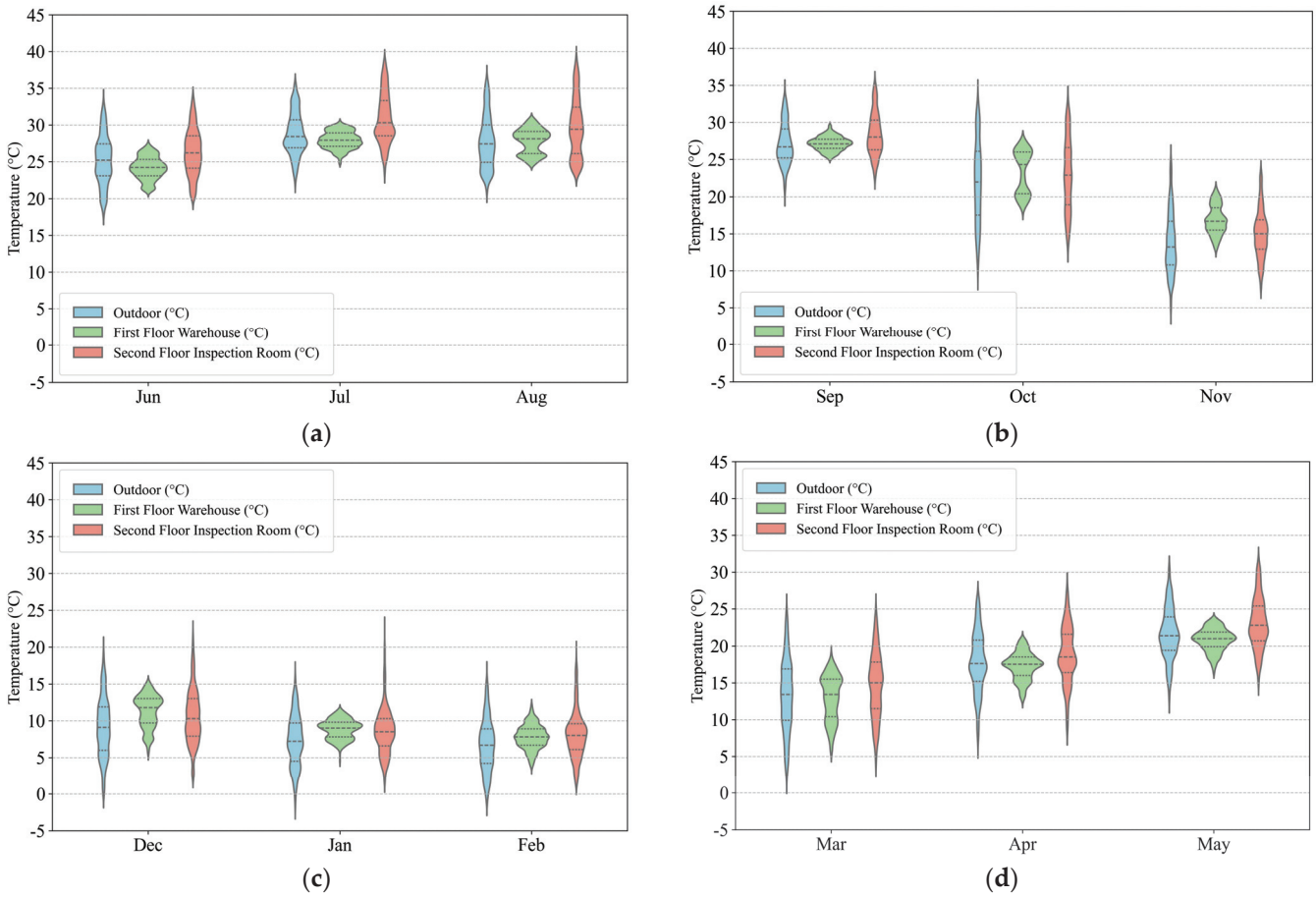

Figure 6. Monthly T_a distribution of indoor and outdoor environments: (**a**) Summer: June to August, (**b**) Autumn: September to November, (**c**) Winter: December to February, (**d**) Spring: March to May.

The second-floor inspection room shows consistently higher median T_a throughout the year. In August, the median $T_{a,in,2}$ reaches 29.4 °C, with highs surging to 39.2 °C, considerably above both $T_{a,ex}$ and $T_{a,in,1}$. This heightened vulnerability to heat is partly due to its elevated position and inadequate roof insulation [35]. In January, the median $T_{a,in,2}$ slightly surpasses $T_{a,ex}$ at 8.5 °C, with a minimum of 1.4 °C. Throughout the year, the extensive $T_{a,in,2}$ variations observed in the second-floor violin plots highlight a marked sensitivity to $T_{a,ex}$, necessitating a critical reassessment of both insulation and cooling strategies to enhance comfort and operational efficiency [78,79].

3.2.2. Relative Humidity

A year-long analysis at the facility highlighted significant challenges in humidity management. Figure 7 illustrates the monthly distribution of *RH* values, showing notable seasonal and locational variations.

While there are no specific standards for RH_{in}, it is crucial to avoid prolonged periods of excessive humidity above 70%, which can increase moisture load and damage the building structure [80,81]. Additionally, it is recommended to maintain RH_{in} below 60%, ideally between 30% and 50%, to ensure optimal conditions and prevent compromises to the quality of nori [82].

In June, July, and August, $RH_{in,1}$ exceeded 70% for 80%, 55%, and 79% of the time, respectively. $RH_{in,2}$ exceeded 70% for 52%, 30%, and 53% of the time, respectively. Additionally, in June, 4% of the time, $RH_{in,1}$ exceeded 90%, while in August, $RH_{in,2}$ exceeding 90% for 14% of the time.

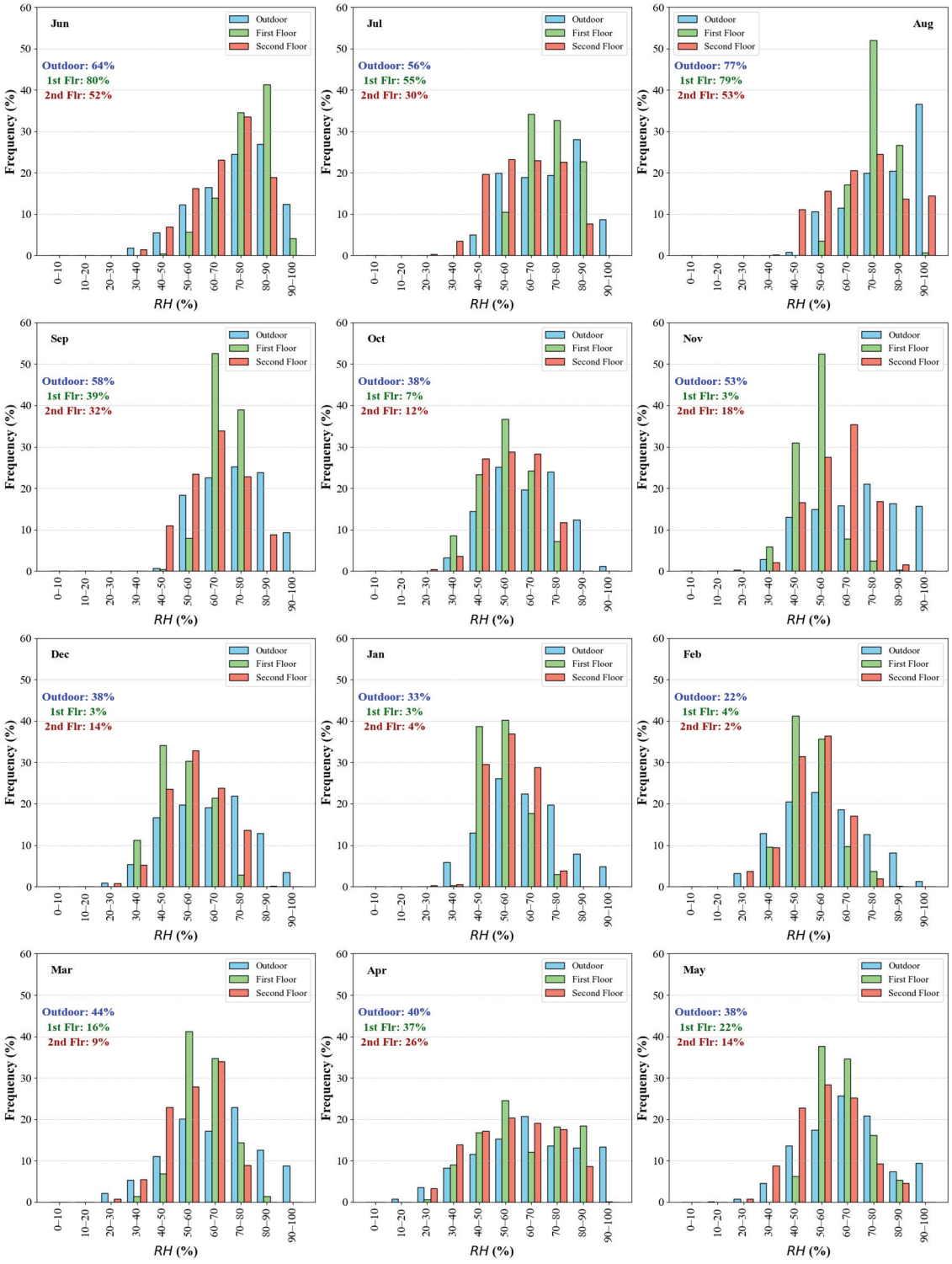

Figure 7. Monthly frequency distribution of indoor and outdoor *RH* values. The top left corner values in the figure highlight the frequency of *RH* reaching the critical high-humidity range (70–100%) across different zones. Blue values show RH_{ex}, green values represent $RH_{in,1}$, and red values indicate $RH_{in,2}$, representing the proportion of time in each month when the *RH* exceeded 70%.

As temperatures decreased in autumn, 24% of the $RH_{in,1}$ in October fell within the 60–70% range, with 7% of the time exceeding 70%, underscoring the urgency of enhanced dehumidification efforts before the storage season. The November readings similarly reflected this demand, with 53% of the readings falling in the 50–60% range, necessitating

continuous dehumidification. From November to February, the proportion of high $RH_{in,1}$ significantly decreased. However, $RH_{in,2}$ exceeded 70% for 18% and 14% of the time in November and December, respectively.

From March to May, *RH* levels rose in both rooms, with $RH_{in,1}$ experiencing a higher percentage of time with excessive *RH* levels compared with $RH_{in,2}$.

The transition from monthly to seasonal trend analysis highlights that challenges in humidity control are both persistent and seasonally variable. Table 7 shows the seasonal frequency of *RH* exceeding 50% for both indoor and outdoor environments in the facility.

Table 7. Seasonal frequency distribution of indoor and outdoor *RH* values.

Season	RH_{ex} (%)					$RH_{in,1}$ (%)					$RH_{in,2}$ (%)				
	50–60	60–70	70–80	80–90	90–100	50–60	60–70	70–80	80–90	90–100	50–60	60–70	70–80	80–90	90–100
Summer	13	16	21	25	19	9	19	40	30	2	18	22	27	13	5
Autumn	20	19	23	17	9	32	28	16	0	0	27	33	17	3	0
Winter	22	19	18	10	3	35	17	3	0	0	36	23	7	0	0
Spring	18	21	19	11	10	34	27	16	8	0	27	23	13	4	0

During summer, $RH_{in,1}$ frequently surpassed critical thresholds, with 40% of readings falling within the 70–80% range and 30% within the 80–90% range, posing significant risks of hygrothermal stress to building materials. Similarly, $RH_{in,2}$ experienced excessive humidity, with 45% of $RH_{in,2}$ readings exceeding 70%.

In autumn, while RH_{ex} levels declined, $RH_{in,1}$ and $RH_{in,2}$ still exceeded 70% for 16% and 20% of the time, respectively. Additionally, 28% of $RH_{in,1}$ and 33% of $RH_{in,2}$ readings were in the 60–70% range. These findings highlight the need for proactive humidity management to prevent *RH* from approaching or exceeding the critical 70% threshold, which poses risks to both structural integrity and product quality.

During winter, high humidity levels decreased, though occasional *RH* peaks of 70–80% were still observed (3% of $RH_{in,1}$ and 7% of $RH_{in,2}$). Despite these peaks, 52% of $RH_{in,1}$ and 59% of $RH_{in,2}$ remained in the 50–70% range, exceeding optimal conditions for nori storage.

As spring approached, humidity levels increased again, with 61% of $RH_{in,1}$ and 50% of $RH_{in,2}$ falling within the 50–70% range. $RH_{in,1}$ exceeded 70% for 24% of the time, while $RH_{in,2}$ exceeded 70% for 17% of the time.

From November to April, air conditioning was used on the second floor for four days each month to optimize indoor conditions for preservation. Despite these efforts, the data indicate ongoing challenges in controlling *RH*. To maintain seaweed quality, *RH* levels should be kept below 50% in spring and winter and below 70% in summer and autumn to prevent moisture-related damage to both the facility and the product.

3.2.3. Absolute Humidity

During the analysis, it became evident that examining *RH* levels alone did not fully capture the facility's indoor moisture conditions. Since *RH* is heavily influenced by temperature fluctuations, it was necessary to introduce *AH* levels to obtain a more precise quantification of the actual water vapor content in the air. This approach is supported by studies that emphasize the advantages of using *AH* for more accurate moisture assessment in environments with temperature variability [83,84].

A detailed boxplot analysis of *AH* levels, including outdoor *AH* (AH_{ex}), *AH* in the first-floor warehouse ($AH_{in,1}$), and *AH* in the second-floor inspection room ($AH_{in,2}$), recorded within the facility, is presented in Figure 8, highlighting pronounced seasonal fluctuations. The observed peak in humidity levels during the summer aligns with a scheduled pause in preservation activities, likely attenuating any immediate detrimental effects on product quality. Nonetheless, this period of elevated humidity could compromise the structural integrity of the facility, posing long-term risks.

The data from the boxplots show a clear reduction in $AH_{in,1}$ and $AH_{in,2}$ during the colder months. As temperatures rise, both *AH* levels and their variability increase, reflecting the complex indoor environmental dynamics. During key preservation months, the

boxplot analysis highlights that, although AH levels decrease, the small difference between $AH_{\text{in},1}$, $AH_{\text{in},2}$, and AH_{ex} indicates deficiencies in the building's insulation and climate control systems.

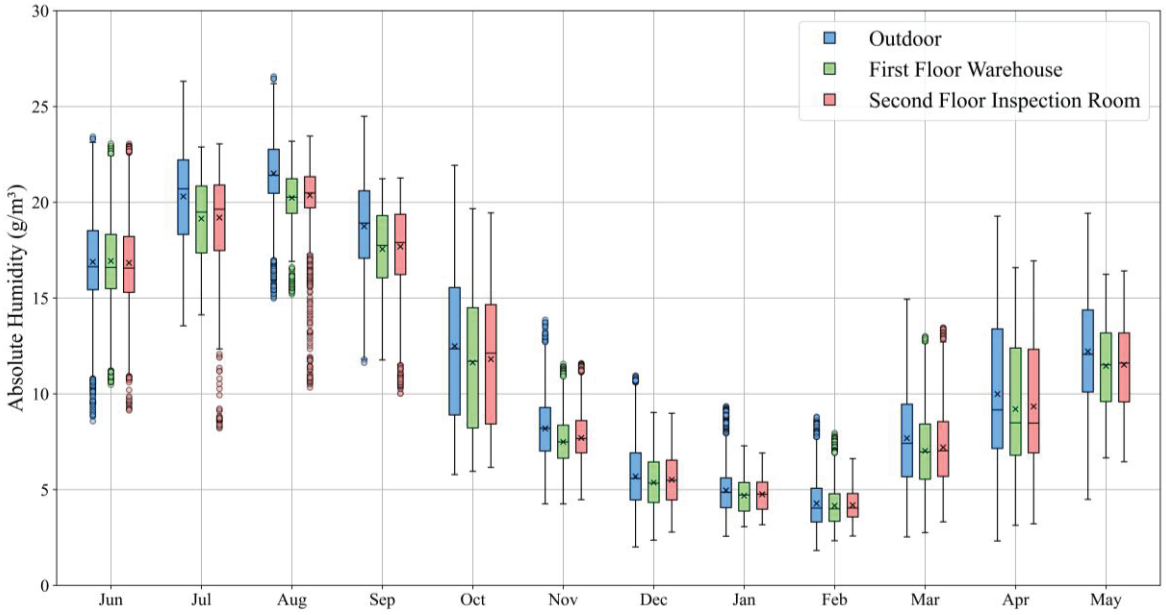

Figure 8. Monthly Absolute Humidity for Indoor and Outdoor Environments.

Table 8 provides a detailed monthly overview of the differences in AH between indoor and outdoor environments. Specifically, ΔAH_1 represents the difference in absolute humidity between the first-floor warehouse and the outdoors, while ΔAH_2 denotes the difference between the second-floor inspection room and the outdoors.

Table 8. Monthly variability in absolute humidity differences between indoor and outdoor environments.

Month	ΔAH_1 (g/m^3)							ΔAH_2 (g/m^3)						
	>0 g/m^3 (% of Time)	Min	25%	50%	75%	Max	Mean	>0 g/m^3 (% of Time)	Min	25%	50%	75%	Max	Mean
June	54	−3.78	−0.42	0.06	0.43	3.95	0.05	48	−8.00	−0.70	−0.03	0.50	4.84	−0.05
July	9	−5.09	−1.66	−1.08	−0.56	3.52	−1.13	14	−10.39	−1.70	−1.03	−0.33	3.98	−1.07
August	6	−5.15	−1.78	−1.25	−0.78	3.69	−1.28	14	−10.17	−1.72	−1.08	−0.46	3.95	−1.15
September	8	−5.31	−1.71	−1.16	−0.63	1.86	−1.18	17	−8.68	−1.74	−0.98	−0.29	3.69	−1.05
October	8	−4.39	−1.28	−0.74	−0.38	1.68	−0.86	23	−9.79	−1.21	−0.56	−0.05	3.14	−0.68
November	8	−3.11	−1.05	−0.64	−0.29	2.75	−0.70	24	−3.97	−0.95	−0.48	−0.01	3.43	−0.49
December	25	−2.74	−0.54	−0.28	−0.01	1.32	−0.32	39	−2.88	−0.55	−0.21	0.30	2.03	−0.17
January	24	−2.62	−0.40	−0.20	0.00	1.25	−0.28	37	−3.21	−0.45	−0.14	0.19	2.28	−0.21
February	42	−1.77	−0.35	−0.07	0.17	1.81	−0.12	49	−2.98	−0.49	−0.03	0.41	2.39	−0.09
March	23	−6.74	−0.99	−0.47	−0.03	4.51	−0.66	29	−3.85	−0.98	−0.45	0.14	4.25	−0.48
April	20	−4.77	−1.42	−0.59	−0.11	3.45	−0.79	27	−4.15	−1.41	−0.60	0.07	3.54	−0.65
May	17	−5.05	−1.36	−0.73	−0.25	4.79	−0.76	24	−4.81	−1.46	−0.71	−0.02	4.93	−0.69

In the early summer month of June, during the rainy season, ΔAH_1 exceeds 0 for 54% of the time and ΔAH_2 for 48% of the time. By July and August, the occurrence of ΔAH_1 exceeding 0 falls below 10%, while ΔAH_2 does so for 14% of the time. Throughout the year, the median values for ΔAH_2 are consistently higher than those for ΔAH_1.

During the crucial seaweed storage season from November to April, the air conditioning system, operational for only four days each month on the second floor, has minimal impact on changing the monthly AH differences between indoor and outdoor settings. During this period, the average values of ΔAH_1 range from -0.79 g/m^3 to -0.12 g/m^3 and ΔAH_2 from -0.65 g/m^3 to -0.09 g/m^3. Indoor AH levels are slightly lower than outdoor levels.

Additionally, both ΔAH_1 and ΔAH_2 recorded maximum values exceeding 3 g/m^3 during the summer and spring, indicating occasional substantial exceedances of indoor

over outdoor AH levels. These peaks highlight potential challenges in indoor climate control management.

The current indoor climate control measures seem inadequate in creating a noticeable difference in humidity levels between indoor and outdoor environments, likely due to factors such as limited HVAC operating time, poor insulation, high air exchange with the outside, and the absence of a vapor barrier, all of which make it more challenging to maintain optimal conditions for nori preservation.

3.2.4. Correlation Analysis

The correlation analysis was performed using Python, calculating Spearman correlation coefficients to assess the relationships between environmental variables. This approach provides robust and reliable insights into the data patterns. Heatmaps were generated to illustrate the strength of these correlations, with values ranging from −1.0 to 1.0, representing the Spearman correlation coefficient (ρ). A coefficient close to −1.0 indicates a strong negative correlation, close to 0 indicates no correlation, and close to 1.0 indicates a strong positive correlation. These values are clearly visualized in Figures 9 and 10. In the seasonal analysis, summer (Figure 9a) exhibited an inverse correlation between $T_{a,ex}$ and RH_{ex}, which was more pronounced than in other seasons, highlighting the increased air moisture capacity during warmer periods. In contrast, other seasons showed a weaker $T_{a,ex}$—RH_{ex} correlation but a stronger link between $T_{a,ex}$ and AH_{ex}.

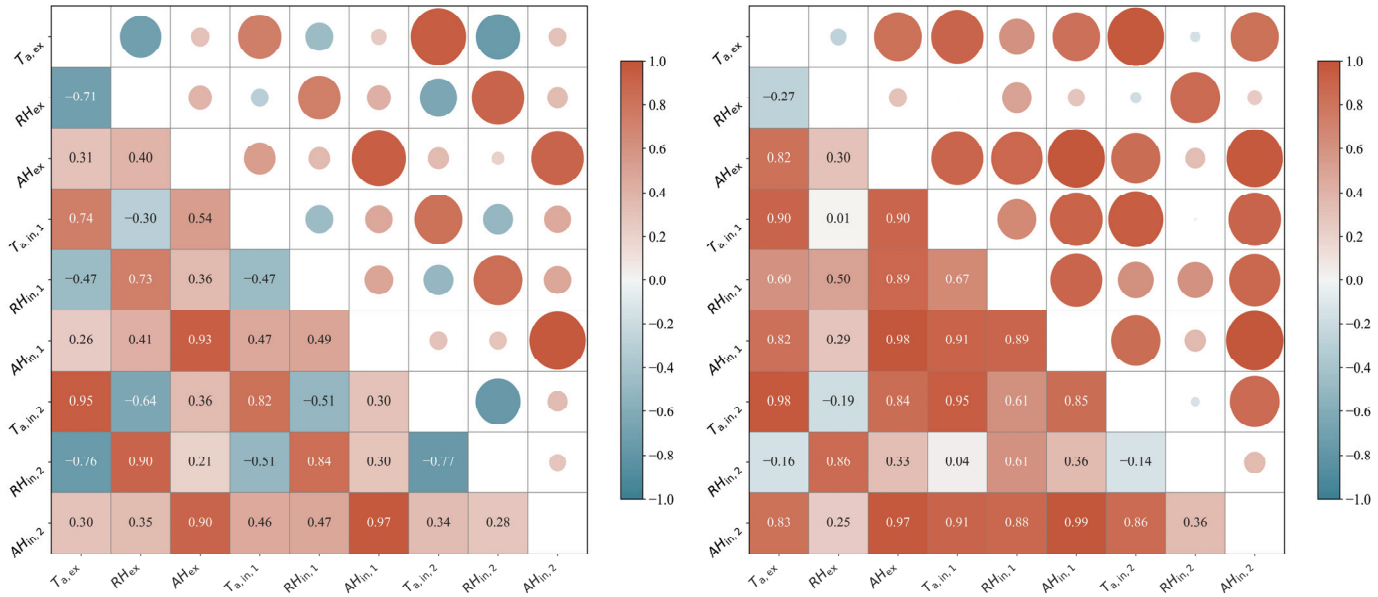

Figure 9. Correlation analysis of various environmental parameters: (**a**) summer, (**b**) autumn.

In summer, there was a moderate correlation between $T_{a,ex}$ and $T_{a,in,1}$ with $\rho = 0.74$, while $T_{a,ex}$ and $T_{a,in,2}$ showed a stronger correlation of $\rho = 0.95$, indicating that $T_{a,in,2}$ is more sensitive to $T_{a,ex}$ changes, likely due to inadequate roof insulation.

As shown in Figure 9b, in autumn, $AH_{in,1}$ demonstrated a significant positive correlation with AH_{ex} at $\rho = 0.98$, indicating a marked responsiveness to AH_{ex} fluctuations. The exceptionally high correlation coefficient of $\rho = 0.99$ between the $AH_{in,1}$ and $AH_{in,2}$ suggests a uniform humidity response throughout the building. Additionally, $T_{a,in,2}$ demonstrates a robust positive correlation with $T_{a,ex}$ at $\rho = 0.98$, and $RH_{in,2}$ shows a substantial correlation with RH_{ex} at $\rho = 0.86$.

In winter (Figure 10a), the correlation between $T_{a,in}$ and $T_{a,ex}$ diminishes, with the first floor at $\rho = 0.66$ and the second floor at $\rho = 0.81$. The decrease may be influenced by various factors. However, without further investigation, it remains unclear whether the

HVAC system adjustments—specifically, four days of heating per month to accommodate winter conditions on the second floor—played a significant role. Additionally, the strong correlation between $AH_{in,1}$ and AH_{ex} (ρ = 0.97) and between $AH_{in,2}$ and AH_{ex} (ρ = 0.90) highlights significant challenges in regulating indoor humidity.

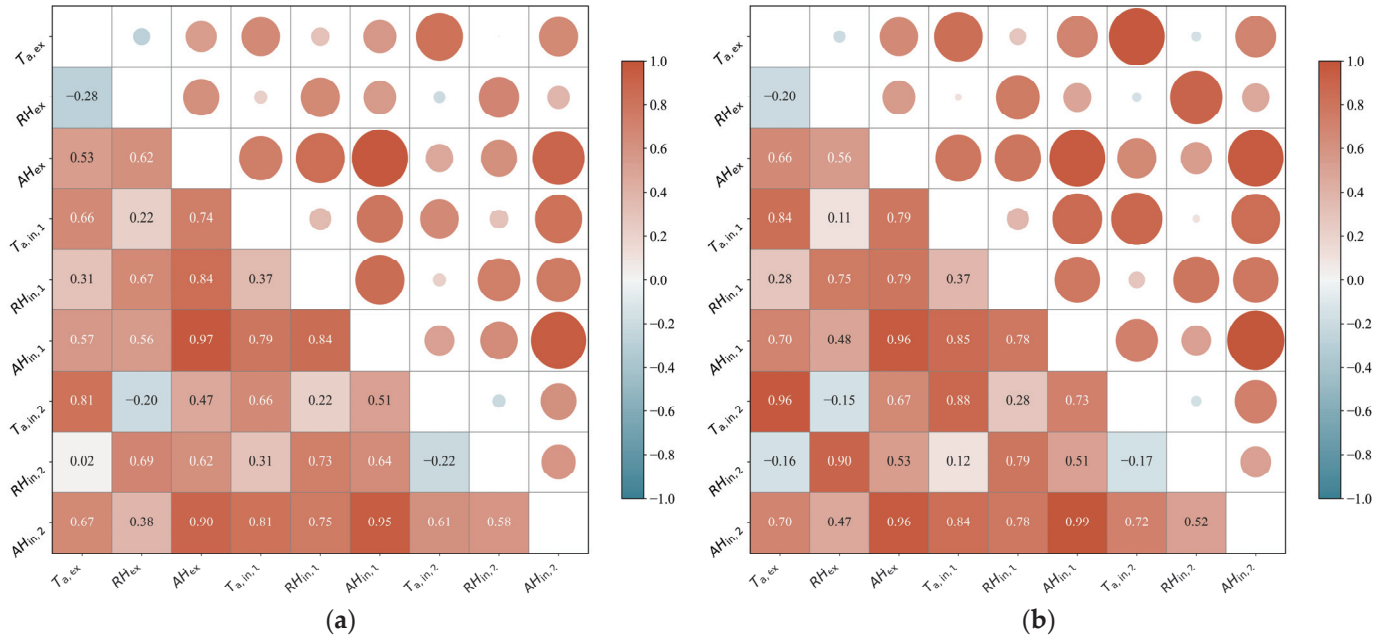

Figure 10. Correlation analysis of various environmental parameters: (**a**) winter, (**b**) spring.

In spring, as illustrated in Figure 10b, $T_{a,in,1}$ (ρ = 0.84) and $T_{a,in,2}$ (ρ = 0.96) demonstrate strong positive correlations with $T_{a,ex}$, indicating the building's significant thermal response to external temperature fluctuations. Notably, $RH_{in,2}$ exhibits a pronounced correlation with RH_{ex} at ρ = 0.90, highlighting its heightened sensitivity to springtime humidity changes. Despite the air conditioning system being operational for four days each month on the second floor during March and April to modulate the indoor climate, the persistent strong correlations, particularly with *RH*, suggest that intermittent HVAC operation has limited effect on modifying springtime indoor humidity levels. This pattern suggests that intrinsic structural attributes, such as insulation quality and moisture management efficiency, play a pivotal role in shaping the indoor climate.

The precise correlations between indoor and outdoor conditions show that deficiencies in insulation and moisture control exacerbate the impact of external environmental variations. $T_{a,in,2}$ and $T_{a,ex}$ and $RH_{in,2}$ and RH_{ex} consistently show stronger correlations compared with $T_{a,in,1}$ and $T_{a,ex}$ and $RH_{in,1}$ and RH_{ex}, indicating that the second floor is more sensitive to external fluctuations. A previous study [85] used correlation analysis to focus on the energy demands and thermal performance of opaque building elements. In contrast, our research examined the relationship between indoor and outdoor conditions, specifically how temperature and humidity interact with insulation performance and moisture control, with attention to seasonal variations and their effect on indoor climate stability.

3.2.5. Stability Analysis

In the depiction of the MADR of T_a in Figure 11, significant outdoor diurnal temperature fluctuations are observed, peaking at 10.61 °C in October. The MADR of $T_{a,in,1}$ varies from 1.57 °C to 2.94 °C, with its annual peak occurring in December. Notably, during the critical seaweed storage period from November to April, the first-floor warehouse exhibits elevated MADR of $T_{a,in,1}$. In the second-floor inspection room, there is even greater temperature variability during the spring months, with the maximum MADR of $T_{a,in,2}$,

recorded at 8.49 °C in April. This pronounced thermal volatility on the second floor, present throughout the year, is primarily due to inadequate insulation in the building envelope, leading to increased heat gain and heat loss. Similar findings have been noted in studies on building envelope deficiencies, which highlight the significant impact of poor insulation on indoor temperature fluctuations and energy efficiency [53,86].

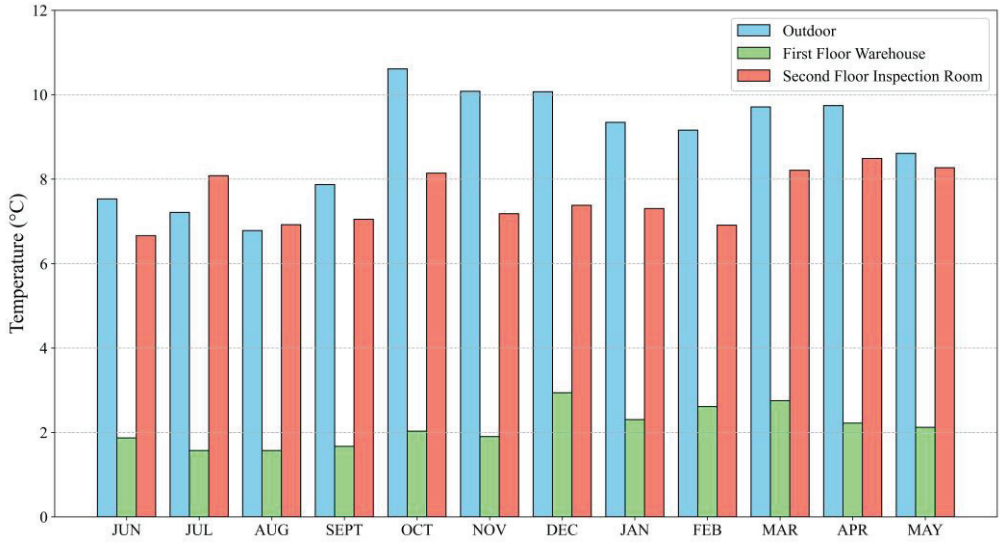

Figure 11. MADR of T_a.

As shown in Figure 12, the MADR of RH_{ex} fluctuates significantly throughout the year, peaking at 45%. This high variability persists during the critical seaweed storage months. $RH_{in,1}$ exhibits a MADR ranging from 8% to 15%, aligning with the external trend. In contrast, $RH_{in,2}$ experiences a broader range of 18% to 28%, underscoring ongoing challenges in maintaining humidity stability. This issue of humidity variability has also been observed in other studies that focus on moisture management in non-residential buildings, where insufficient insulation and air leakage can lead to significant humidity fluctuations and increased moisture load [58,87].

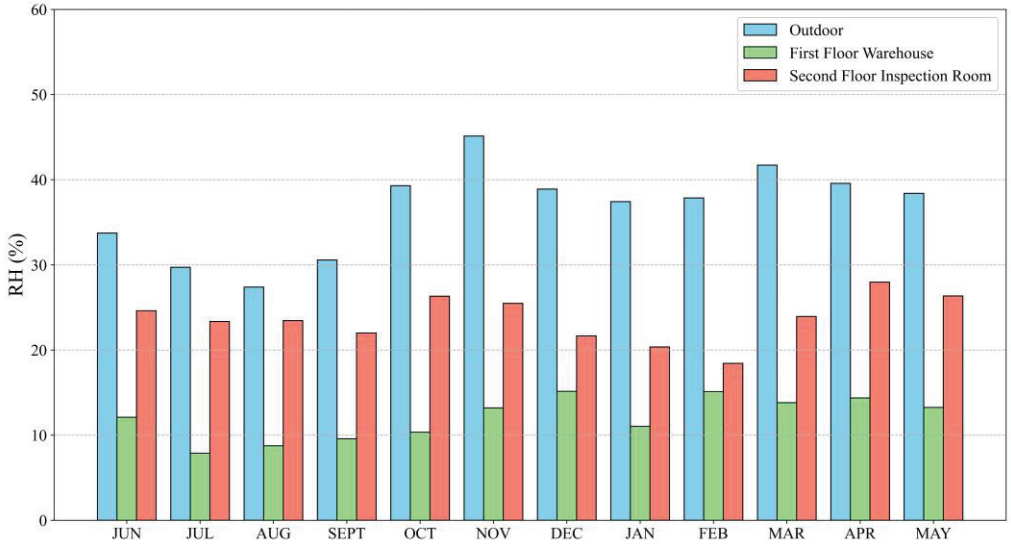

Figure 12. MADR of *RH*.

The MADR of *AH*, measured in g/m^3 and presented in Figure 13, displays notable variability outdoors, spanning from 1.98 g/m^3 to 4.73 g/m^3, with a notable peak in May. Indoors, the *AH* MADR values exhibit an increasing trend of variability from winter to

spring. The differences between the $AH_{in,1}$ MADR and the $AH_{in,2}$ MADR are relatively minimal, with values spanning from 1.06 g/m^3 to 2.27 g/m^3 and 1.21 g/m^3 to 2.59 g/m^3, respectively.

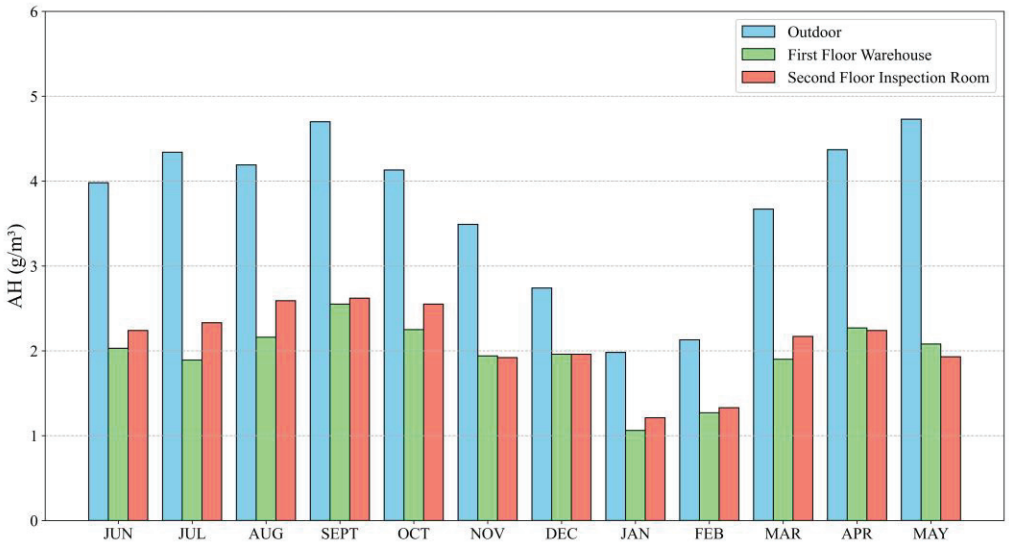

Figure 13. MADR of *AH*.

The MADR analysis for T_a, *RH*, and *AH* reveals that the second-floor inspection room consistently experiences greater environmental variability than the first-floor warehouse, subjecting stored goods and building materials to heightened environmental stress. The disparity between the first and second floors underscores the critical need for advanced hygrothermal management strategies, especially for upper floors that are more exposed to dynamic external conditions. Previous studies [12,39] have emphasized the need for improved hygrothermal regulation in buildings exposed to vertical environmental gradients and external stressors, highlighting the importance of both thermal and moisture management in maintaining a stable indoor climate.

3.3. Analysis of Indoor Condensation

3.3.1. Air Dew Point Temperature (*DP*) and Surface Temperature (T_s)

Figure 14 illustrates the cumulative distribution functions (CDFs) for *DP* and T_s across summer (Figure 14a) and autumn (Figure 14b). Higher *DP* indicates a greater amount of moisture in the air, indirectly reflecting humidity levels [88].

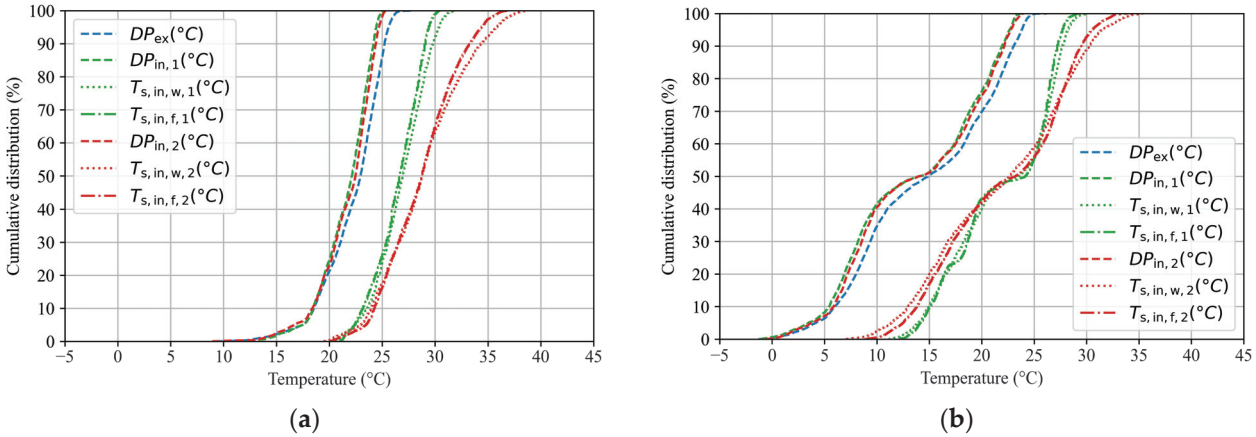

Figure 14. Cumulative distribution functions of *DP* and T_s: (**a**) summer, (**b**) autumn.

In summer, the median outdoor *DP* (DP_{ex}) of 22.95 °C reflects the season's high humidity, as shown in Figure 14a. Inside the building, the median *DP* on the first floor ($DP_{in,1}$) is 22.15 °C, and the median *DP* on the second floor ($DP_{in,2}$) is slightly higher at 22.48 °C, indicating marginally lower indoor humidity levels compared with outdoors. The median $T_{s,in,w,1}$ and median $T_{s,in,f,1}$ were 27.0 °C and 26.7 °C, respectively, while the median $T_{s,in,w,2}$ and $T_{s,in,f,2}$ maintained a consistent 28.7 °C. With $T_{s,in,w,2}$ reaching a peak of 38.7 °C and $T_{s,in,f,2}$ reaching 36.8 °C, this indicates severe overheating due to poor insulation, far exceeding comfort and functional requirements, and compromising overall thermal management.

Entering autumn, the median DP_{ex} decreased to 14.87 °C, reflecting the season's cooler, drier air, as depicted in Figure 14b. Internally, the building mirrors this trend, with a median $DP_{in,1}$ of 14.03 °C and $DP_{in,2}$ slightly lower at 13.98 °C. Despite cooler external temperatures, the surfaces in the second-floor inspection room maintain relatively high temperatures, with median $T_{s,in,w,2}$ at 22.6 °C and median $T_{s,in,f,2}$ at 23.2 °C.

In the winter analysis, as depicted in Figure 15a, the minimum DP_{ex} dropped to −12.57 °C. The median $DP_{in,1}$ was slightly lower than the outdoor condition at −0.12 °C, while the median $DP_{in,2}$ was 0.03 °C. Critical minimum T_s were recorded at 3.3 °C for $T_{s,in,w,1}$ 4.1 °C for $T_{s,in,f,1}$, and 0.6 °C for $T_{s,in,w,2}$ and 2.2 °C for $T_{s,in,f,2}$. The proximity of these temperatures, as shown in Figure 15a, underscores the necessity for improved insulation or targeted heating interventions to prevent cold spots and mitigate the risk of internal condensation, especially when humid air enters the building.

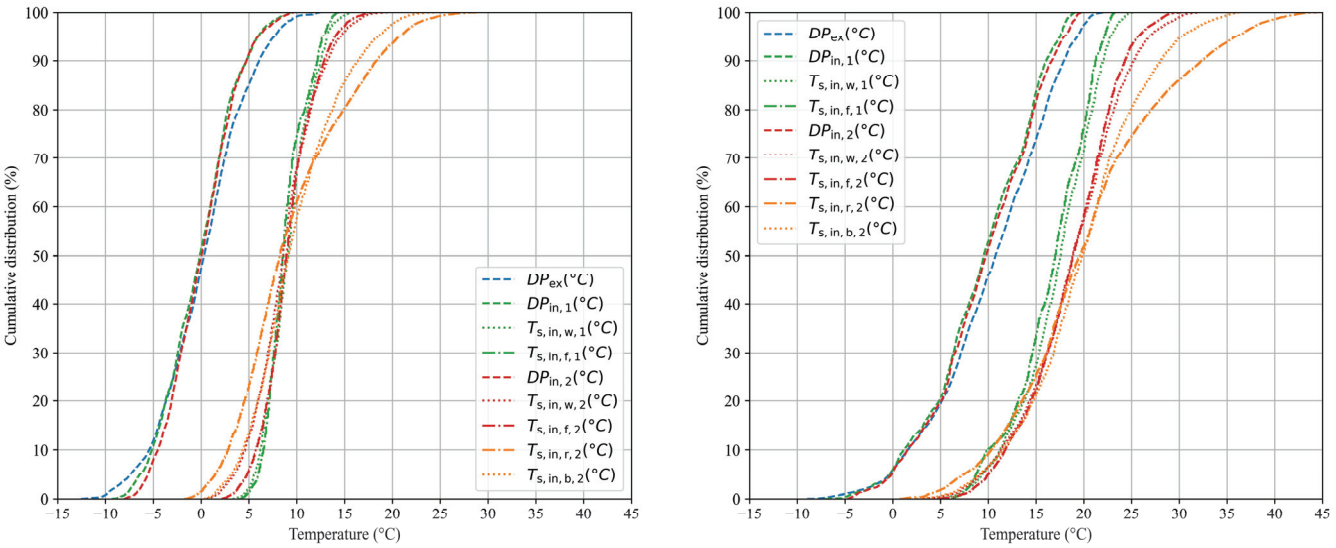

Figure 15. Cumulative distribution functions of *DP* and T_s: (**a**) winter, (**b**) spring.

Transitioning into spring, the median DP_{ex} rose to 10.74 °C, reflecting the shift towards warmer and more humid conditions, as illustrated in Figure 15b. This increase in humidity necessitates a thorough examination of the building's capacity to maintain a condensation-free environment. The spring minimum surface temperatures—5.1 °C for $T_{s,in,w,1}$ and 6.2 °C for $T_{s,in,f,1}$ and 3.2 °C for $T_{s,in,w,2}$ and 4.7 °C for $T_{s,in,f,2}$—underscore the challenges posed by these conditions.

The analyses for winter and spring include an examination of $T_{s,in,r,2}$ and $T_{s,in,b,2}$. The $T_{s,in,r,2}$ exhibits extreme fluctuations, highlighting the issue of insufficient roof insulation. The lack of adequate insulation and moisture barriers exacerbates indoor thermal and humidity issues.

3.3.2. Condensation Risk

Assess the risk of condensation with a comprehensive seasonal analysis conducted on wall and floor surfaces within spaces that typically do not use HVAC systems. This evaluation involves both indoor and outdoor air conditions and includes calculating the following:

1. The ratio of indoor air vapor pressure to the saturation vapor pressure at the interior surface temperature;
2. The ratio of ventilated outdoor air vapor pressure to the saturation vapor pressure at the same interior surface temperature.

Data from these calculations were then categorized into four distinct risk levels, from Category I—indicating the highest risk of condensation—to Category IV—representing the lowest risk, as depicted in Figure 16 (note: Category IV is omitted in the figure). This approach and categorization follow the analysis detailed in Section 2.4.3, where vapor pressure ratios were used to evaluate CR levels.

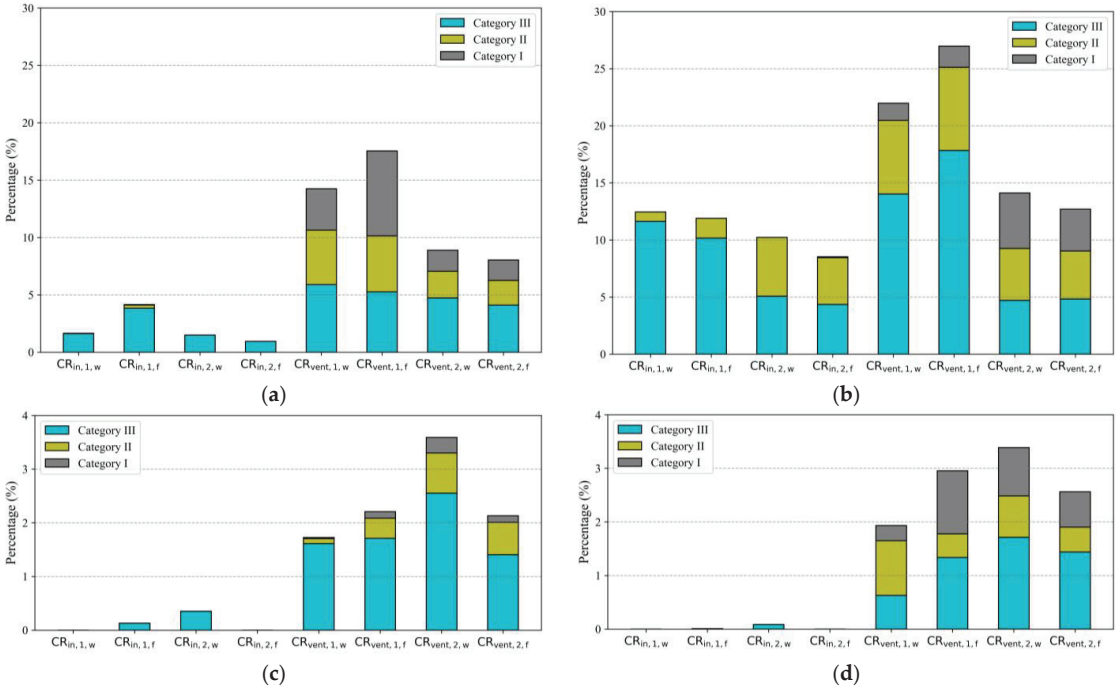

Figure 16. Frequency statistics of CR categories on indoor surfaces by season: (**a**) spring, (**b**) summer, (**c**) autumn, (**d**) winter. 'in' denotes indoor air and 'vent' stands for ventilated outdoor air. '1' and '2' refer to the first-floor warehouse and the second-floor inspection room, respectively. 'w' represents walls, and 'f' denotes floors.

Seasonal changes significantly impact the risk of condensation within the building. In spring observations, as shown in Figure 16a, $CR_{in,1,w}$ and $CR_{in,1,f}$, as well as $CR_{in,2,w}$ and $CR_{in,2,f}$, predominantly fell into Category IV, representing minimal risk, with frequencies nearing 98% or higher. However, the influence of ventilated outdoor air, denoted by 'vent', indicates an increased risk of condensation. For instance, $CR_{vent,1,f}$ rose to 7.404%, markedly contrasting with its counterparts influenced by indoor air.

During summer, as illustrated in Figure 16b, CR values vary; most indoor surfaces remain within lower-risk categories. $CR_{in,1,w}$, $CR_{in,1,f}$, $CR_{in,2,w}$, and $CR_{in,2,f}$ generally fall into Category IV, with frequencies ranging from 87.55% to 91.47%. However, surfaces exposed to ventilated outdoor air exhibit noticeable Category I risks, notably for $CR_{vent,2,w}$ and $CR_{vent,2,f}$, with respective frequencies of 4.86% and 3.67%. Category II and III risks also appear, with $CR_{vent,2,w}$ and $CR_{vent,2,f}$ recording 4.55% and 4.21% in Category II and slightly higher in Category III at 4.71% and 4.83%, highlighting potential CR under conditions such as open doors and windows that raise humidity levels.

In autumn, Figure 16c shows a predominance of Category IV across various surfaces, indicating a very low risk of condensation overall. While most surfaces marked with 'vent' remain in Category IV, the 2.55% Category III risk for $CR_{vent,2,w}$, underscores the subtle impact of external factors on increasing CR.

During winter, the CR on indoor surfaces predominantly falls within Category IV, as illustrated in Figure 16d. However, surfaces influenced by ventilated outdoor air, particularly $CR_{vent,1,f}$ and $CR_{vent,2,w}$, exhibit slight increases in higher-risk categories. Specifically, these surfaces exhibit marginal Category I risks at 1.18% for $CR_{vent,1,f}$ and 0.90% for $CR_{vent,2,w}$, respectively. Although these percentages are minimal, they underscore that the infiltration of cold outdoor air can escalate the risk of condensation during the colder months [33].

3.4. Typical Weeks

Typical weeks are selected based on regional climate characteristics and patterns, ensuring that the architectural design and assessment fully account for the impacts of climatic conditions on building performance. The data from Figures 17–20 demonstrate variations in T_a, *RH*, and *AH* during these weeks across different seasons at the Nori Distribution Center, emphasizing the significant influence of climate on the building's environmental functionality.

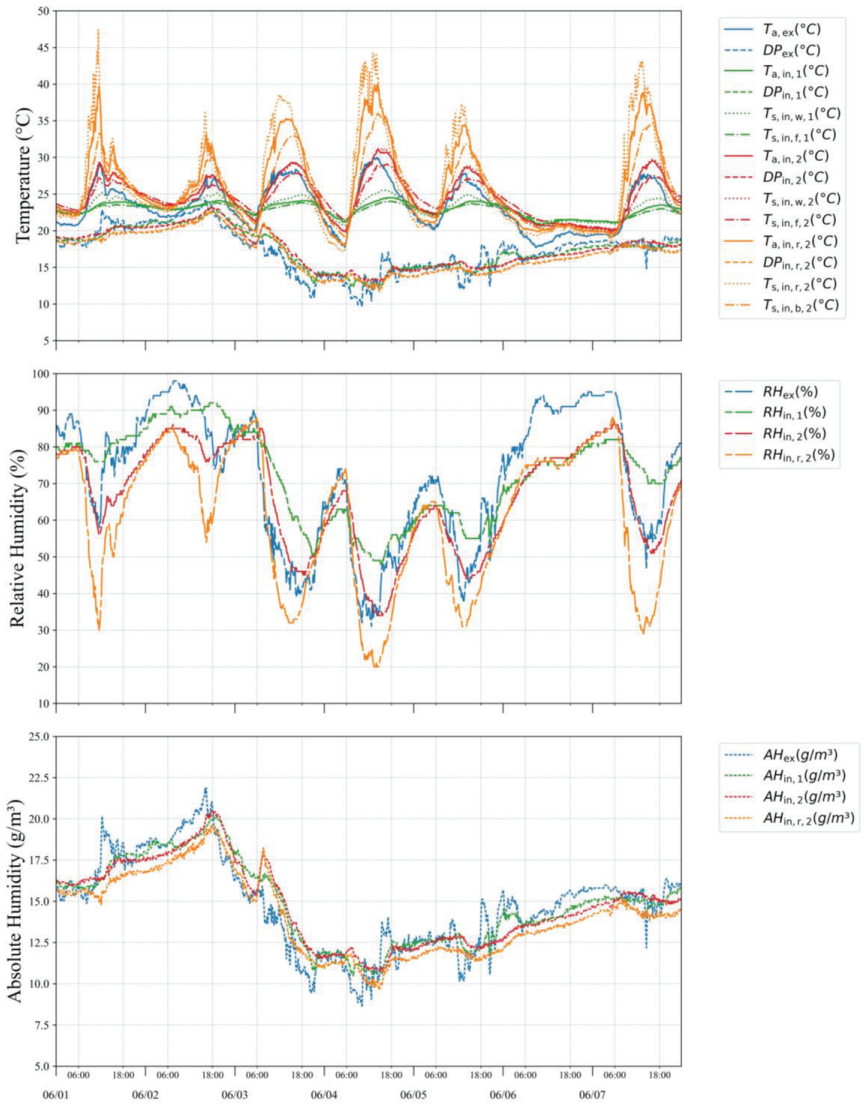

Figure 17. Variation in environmental parameters during early summer (rainy season), 1–7 June 2023.

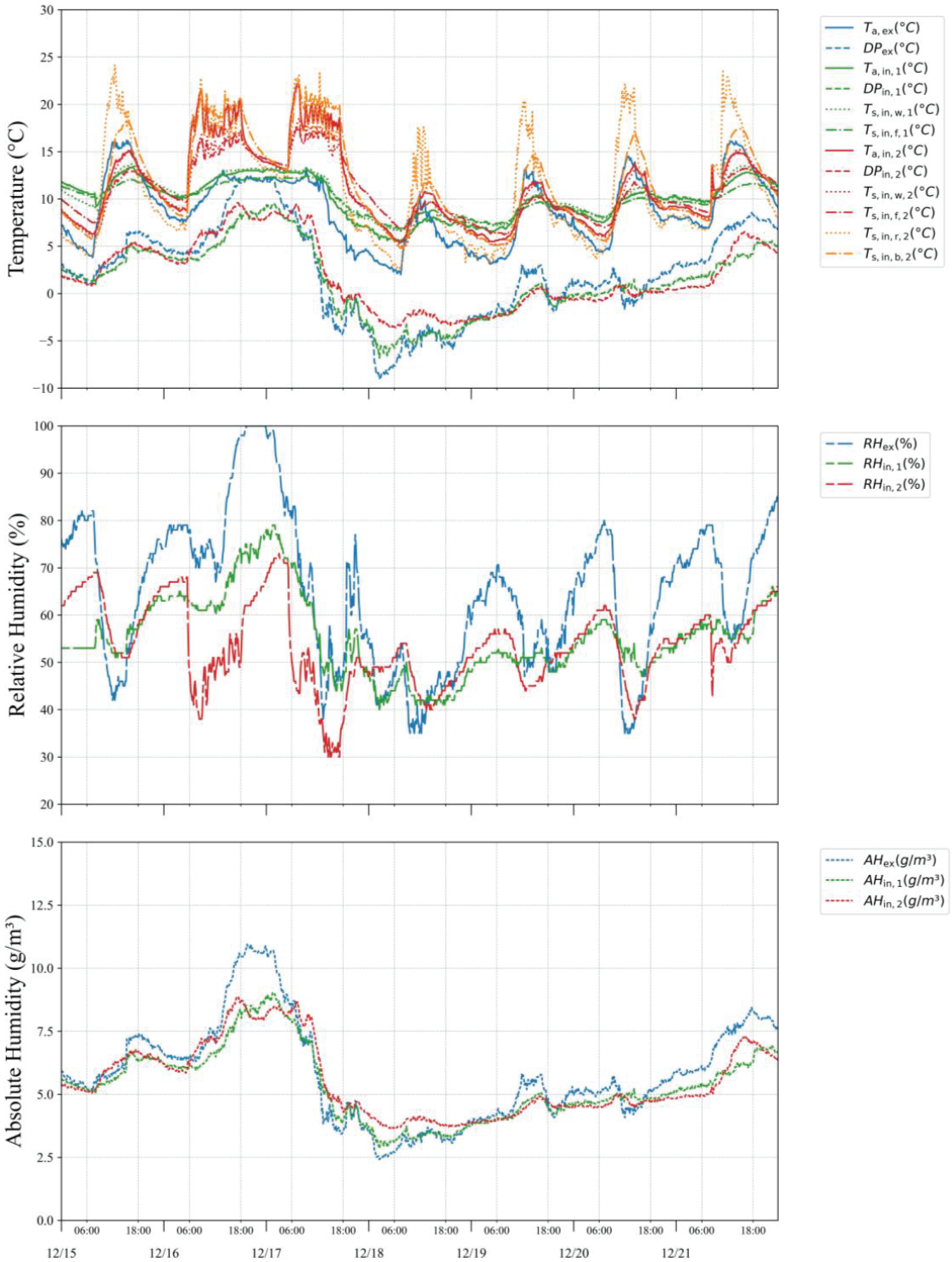

Figure 18. Variation in environmental parameters during winter (including heating days), 15–21 December 2021.

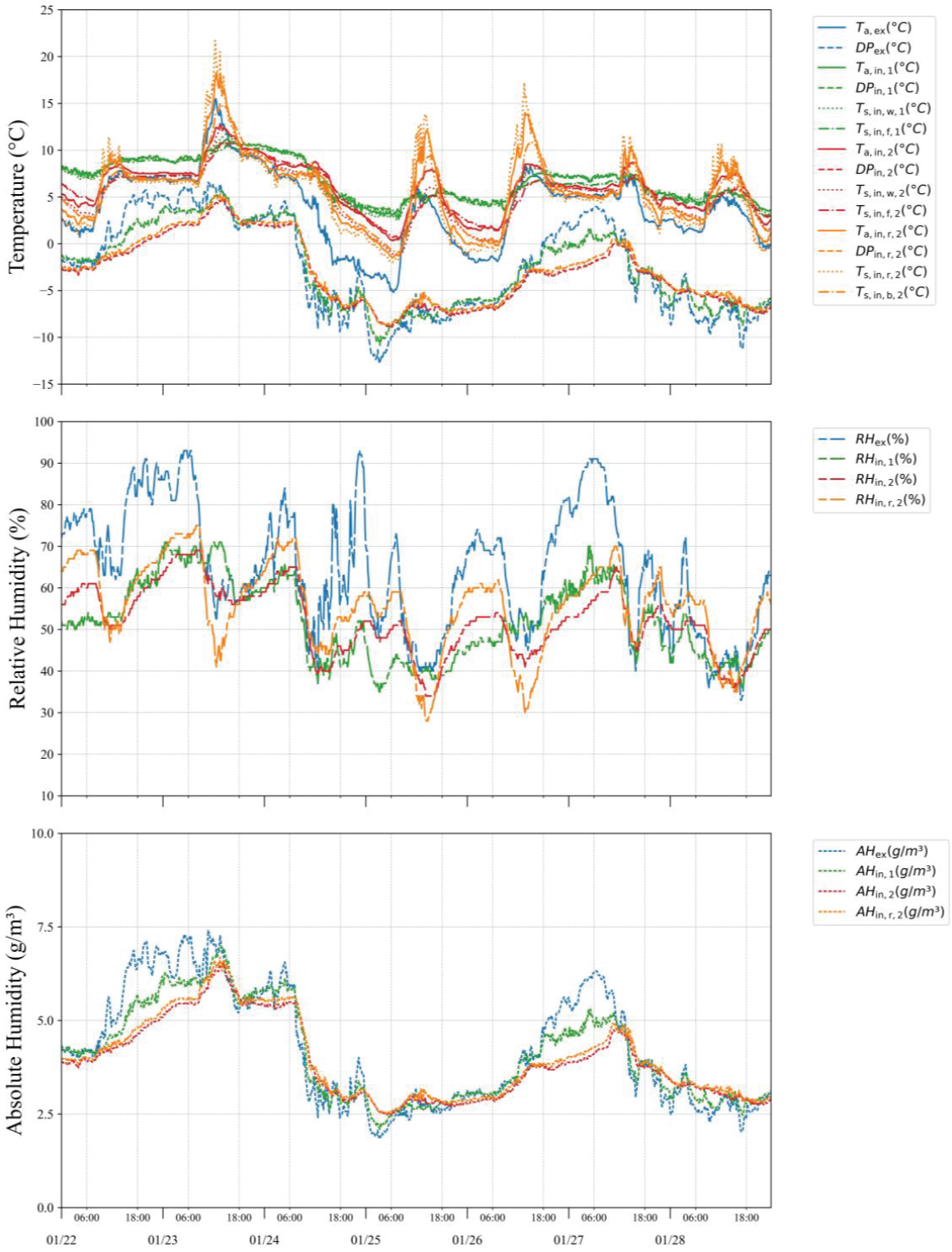

Figure 19. Variation in environmental parameters during winter, 22–28 January 2023.

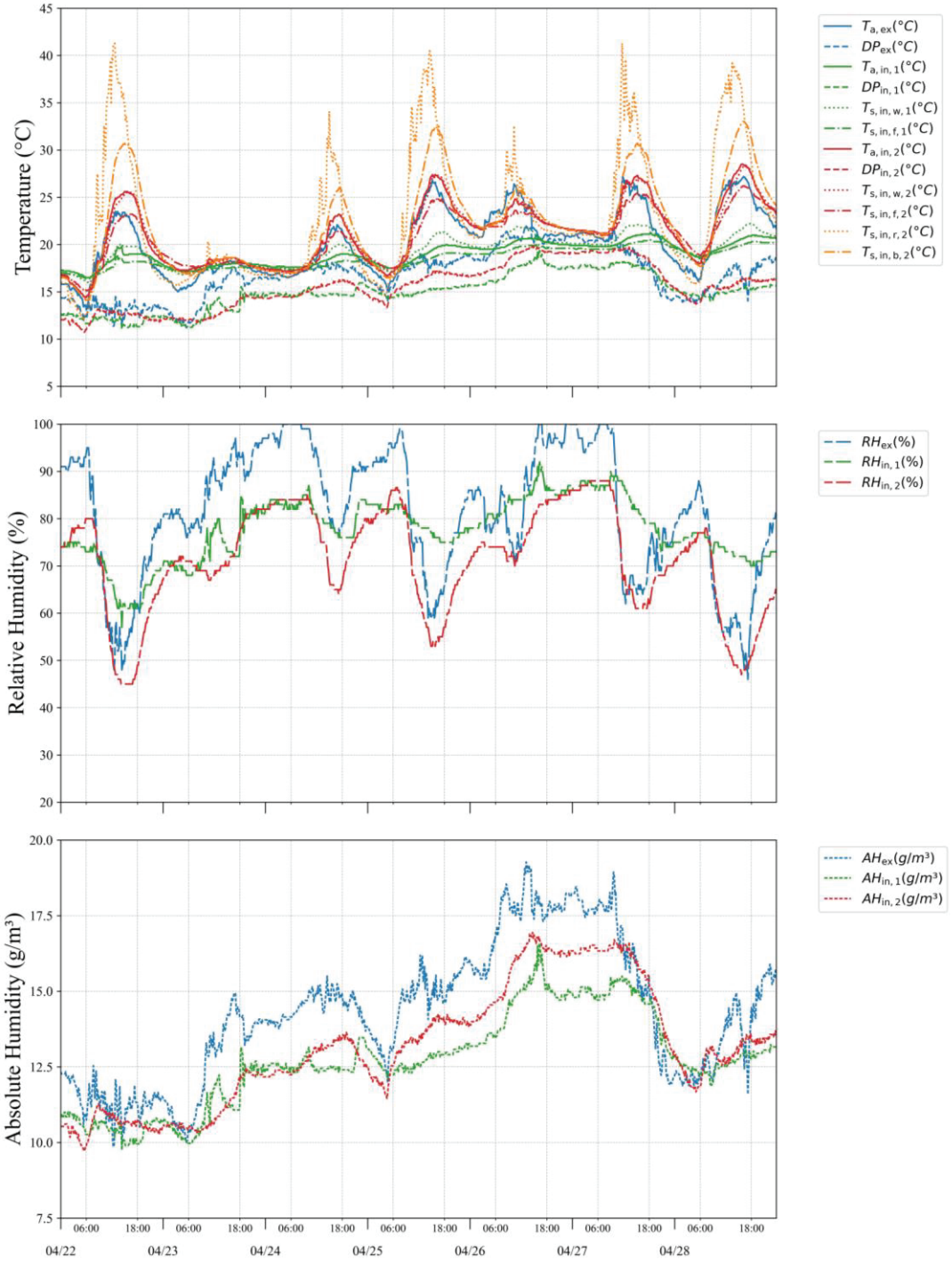

Figure 20. Variation in environmental parameters during spring, 22–28 April 2022.

3.4.1. Early Summer (Rainy Season)

During the early summer rainy season, data depicted in Figure 17 indicate that the HVAC system was inactive within the building. $T_{a,ex}$ showed significant fluctuations, peaking at 30.0 °C, with an average of 23.3 °C and a nocturnal low of 17.7 °C. Inside, the first-floor warehouse maintained a relatively stable thermal environment, with an average $T_{a,in,1}$ of 22.9 °C. In contrast, the second-floor inspection room recorded a higher average $T_{a,in,2}$ of 24.6 °C and exhibited greater temperature variability than the first-floor warehouse. These data clearly highlight significant thermal stratification within the building, particularly near the second-floor roof ceiling, where $T_{a,in,r,2}$ soared to 40 °C and $RH_{in,r,2}$ reached 88%.

The fluctuations in T_s of the walls were greater than those of the floors. $T_{s,in,r,2}$ peaked at 47.4 °C, primarily due to direct solar radiation and inadequate roof insulation. Such high temperatures, combined with high humidity, create localized hot zones within the building, thereby increasing the demand for cooling. The *AH* levels inside the building were very close to those outside, indicating that indoor humidity is significantly influenced by outdoor conditions. On days with elevated RH_{ex}, the indoor *DP* closely approached both the $T_{a,in}$ and $T_{s,in}$, indicating a concerning level of moisture accumulation.

3.4.2. Winter

During the observed week in winter, as depicted in Figure 18, the building's second-floor air conditioning system executed significant heating cycles on the 16th and 17th during daytime hours.

$T_{a,ex}$ varied between 2.0 °C and 16.2 °C, with an average of 8.9 °C. RH_{ex} averaged 65%, reaching full saturation at its peak. Inside, the first floor maintained an average $T_{a,in,1}$ of 10.0 °C, slightly above the $T_{a,ex}$, suggesting a stable yet minimally insulated environment. $RH_{in,1}$ levels were consistently above the optimal level most of the time, necessitating the implementation of dehumidification measures for the warehouse.

During HVAC operations on the second floor, significant temperature fluctuations were observed, especially a rapid cooling phase after reaching the set temperature and switching to air supply mode. These abrupt fluctuations indicate the weak thermal mass of the building envelope and poor insulation performance [86].

The winter T_a, *RH* and *AH* data, as shown in Figure 19, reveal significant deficiencies in environmental control, failing to meet the strict requirements for nori storage. $T_{a,ex}$ showed significant variations, averaging 3.9 °C, ranging from −5.2 °C to 15.5 °C. $T_{a,in,1}$ exhibited a narrower range of 2.7 °C to 11.2 °C, averaging 6.8 °C. In contrast, the fluctuations in $T_{a,in,r,2}$ were greater, ranging from −1.5 °C to 18.3 °C. The indicating that strong solar radiation during the day leads to increased temperatures, while radiative cooling at night exacerbates heat loss.

$RH_{\mathbf{ex}}$ also varied significantly, between 33% and 93%, with an average of 64%. RH_{in} levels frequently exceeded the optimal 50% threshold for nori storage, with $RH_{in,1}$ averaging 52% and peaking at 71%. $RH_{in,r,2}$ averaged 56%, reaching highs of 75%. Figure 19 demonstrates that RH_{in} closely mirrors outdoor variations. However, compared with the second floor, the first floor exhibits more frequent fluctuations in humidity, indicating an inability to maintain stable conditions within the building. This disparity highlights the urgent need to improve environmental management strategies to ensure humidity control across all floors.

3.4.3. Spring

Throughout the observed week in spring, the building's environment, as depicted in Figure 20, experienced varied conditions reflective of typical spring weather.

$T_{a,ex}$ ranged between 13.1 °C and 27.2 °C, indicative of moderate to warm days with cooler nights. Notably high $RH_{\mathbf{ex}}$, averaging 82% and occasionally reaching full saturation at 100%, was mirrored indoors, especially with average $RH_{\mathbf{in},1}$, recorded at 78%. These conditions underscore the challenges of managing indoor humidity in a persistently moist external environment, particularly in areas lacking adequate moisture control measures.

During this period, a significant condensation event was recorded around 08:50 a.m. on 27 April, following an afternoon of rainfall on 26 April that continued into the early morning. This saturation of the outdoor atmosphere, coupled with cooler nighttime and early morning temperatures, heightened the risk of condensation. Despite relatively stable $T_{a,in,1}$, DP_{ex} surpassed $T_{a,in,1}$ and $T_{s,in,f,1}$ from approximately 06:00 a.m. on 26 April to 10:00 a.m. on 27 April. This disparity, together with high external humidity, fostered conditions conducive to moisture condensation on cooler surfaces within the warehouse. The occurrence of condensation also underscored structural vulnerabilities in the building, such as inadequate vapor barriers and air leakage points, particularly around roll-up doors.

These deficiencies facilitated the ingress of humid external air, which, when meeting the cooler internal surfaces, led to condensation.

The observed data highlight the critical need for enhanced environmental management strategies to ensure stable humidity levels across different building zones and to mitigate structural vulnerabilities that exacerbate moisture issues.

Autumn was not included in the detailed weekly analysis because its temperature and humidity levels are not as extreme as those observed in other seasons. This relative mildness diminishes its impact on energy efficiency and thermo-hygrometric conditions, making it less relevant for in-depth study.

4. Conclusions

This study examined the impact of building envelope deficiencies in warehouse-type buildings situated in subtropical climates using a nori distribution center as a case study. Employing infrared thermography alongside continuous monitoring of temperature and humidity, complemented by both qualitative and quantitative analyses, this research delineated how such deficiencies compromise indoor thermal and humidity stability. This, in turn, impairs energy efficiency and the preservation of sensitive products.

Deficiencies in insulation, sealing, and moisture barriers during design and construction substantially compromise temperature and humidity control. The negligence of warehouse building managers in limiting the operating time of HVAC systems (in the context of misunderstood "savings") and the lack of care for proper thermal insulation and humidity control can lead to inappropriate food storage conditions and related financial losses.

Infrared thermography was employed to qualitatively assess thermal anomalies in the building envelope. The thermal images revealed air leaks, insufficient sealing, and thermal bridges, particularly around the roll-up doors and wall joints. These images clearly identified locations of heat loss and air infiltration, especially on the roof. Such qualitative data guided the identification of areas requiring immediate retrofitting. To complement the infrared thermography, U-value calculations were performed to quantify the thermal transmittance of key building components. The U-value for the roof was measured at 3.70 $W/m^2 \cdot K$, which significantly exceeds the regional standards. This discrepancy underscores the urgent need for improvements in insulation. Inadequate insulation in the roof, walls, and floors leads to significant heat accumulation and loss.

Seasonal analysis indicates that during the summer, the average temperature on the second floor reaches 28.8 °C, peaking at 39.2 °C. Surface temperatures on the wall and the floor reach maximum values of 38.7 °C and 36.8 °C, respectively. During transitional seasons, temperatures can reach up to 35.8 °C in spring and 32.1 °C in autumn. Temperature monitoring of the ceiling and beams on the second floor shows pronounced fluctuations exceeding those of other indoor surfaces, underscoring the inadequate roof insulation. Although the first floor exhibits more stable temperatures than the second floor, its thermal performance remains deficient.

The risk of condensation remains generally low; however, it is significantly exacerbated by the frequent opening of entrances and the infiltration of warm, humid air through gaps in the building envelope due to sealing deficiencies. High humidity poses a major concern during summer, with the first floor exceeding 70% relative humidity 72% of the time and the second floor 45% of the time. This issue is similarly pronounced during spring and autumn. Correlation analysis highlights the building's heightened sensitivity to external climate variations. Mean Absolute Daily Range analysis demonstrates significant fluctuations in indoor temperature and humidity, underscoring the building's instability due to structural deficiencies. By analyzing the building's thermo-hygrometric behavior across different time periods, annual monitoring results were obtained, covering seasonal, monthly, and typical weekly patterns.

To address these challenges, we recommend comprehensively sealing gaps in the building envelope to prevent the ingress of warm, moist air. Upgrading the insulation

materials and installing effective moisture barriers will further enhance the building's ability to regulate indoor temperature and humidity. Optimizing the existing HVAC systems will improve energy efficiency and reduce operational costs. These measures are expected to create better conditions for storing temperature-sensitive products like nori. Focusing on the roof is particularly important, as it plays a pivotal role in managing the thermal and humidity environment of warehouse-type buildings.

In conclusion, this study highlights the broader implications of building envelope deficiencies for warehouse-type buildings in subtropical climates. Prior to implementing targeted retrofitting and design improvements, conducting low-cost assessments of existing deficiencies is essential to inform targeted interventions. This preliminary assessment ensures that any proposed retrofits are based on a thorough understanding of the existing problems, thus enhancing the functionality, sustainability, and environmental resilience of these facilities.

5. Limitations and Future Works

This study identified several key areas where future research could expand upon the findings. First, while the thermal properties of the opaque elements of the building were the primary focus of this investigation, future studies should consider more detailed monitoring of window surface temperatures. Given the significant role that windows play in heat gain, a comprehensive assessment of their contribution to indoor temperature fluctuations could offer valuable insights into improving overall building performance.

Second, employing more advanced non-destructive in situ heat flux measurement techniques can more accurately analyze thermal bridging and heat flow patterns in building envelope components. This approach helps identify potential weak points that may exacerbate energy inefficiency and indoor discomfort, thereby facilitating more targeted building interventions.

Lastly, future research could explore the implementation of improved insulation materials, vapor barriers, and HVAC strategies specifically tailored to the needs of warehouse-type buildings in subtropical climates. Simulations and case studies based on the findings of this study could provide a clearer understanding of the long-term energy efficiency gains and thermal comfort improvements achievable through targeted building envelope enhancements.

Author Contributions: Conceptualization, Y.X. and H.F.; methodology, Y.X. and H.F.; software, Y.X. and T.Y.; validation, Y.X. and H.F.; investigation, Y.X. and H.F.; resources, H.F.; data curation, Y.X. and T.Y.; writing—original draft preparation, Y.X.; writing—review and editing, Y.X., H.F. and X.W.; visualization, Y.X.; supervision, H.F.; project administration, H.F.; funding acquisition, H.F. All authors have read and agreed to the published version of the manuscript.

Funding: This research received no external funding.

Data Availability Statement: The data presented in this study are available on request from the corresponding author.

Conflicts of Interest: The authors declare no conflict of interest.

Appendix A

The heat transfer coefficient $U_{i,k}$ is given by the formula [89]:

$$U_{i,k} = \frac{1}{R_{se,i} + R_{si,i} + \sum_i R_{i,k,l}},$$

where the following is true:

$U_{i,k}$ is the heat transfer coefficient (W/m^2·K);

$R_{se,i}$ is the external surface heat transfer resistance (m^2·K/W);

$R_{si,i}$ is the internal surface heat transfer resistance (m^2·K/W);

$R_{i,k,l}$ is the thermal resistance of layer l in part k of section i ($m^2 \cdot K/W$), calculated as follows:

$$R_{i,k,l} = \frac{d_{i,k,l}}{\lambda_{i,k,l}},$$

where $d_{i,k,l}$ is the thickness of layer l (m), and $\lambda_{i,k,l}$ is the thermal conductivity of layer l (W/mK).

Therefore, the surface heat transfer resistance on the external boundary $R_{se,i}$ of the general section i and the surface heat transfer resistance on the internal boundary $R_{si,i}$ of the general section i are values defined in Tables A1 and A2, based on the Japanese Energy Conservation Law for Buildings (current version) [90].

Table A1. Surface Thermal Resistance.

Element	Internal Surface Thermal Resistance ($m^2 \cdot K/W$)	External Surface Thermal Resistance ($m^2 \cdot K/W$)—Direct Air Exposure	External Surface Thermal Resistance ($m^2 \cdot K/W$)—Other Conditions
Roof	0.09	0.04	0.09 (e.g., air gap)
Ceiling	0.09	-	0.09 (e.g., attic space)
External Wall	0.11	0.04	0.11 (e.g., air gap)
Floor	0.15	0.04	0.15 (e.g., subfloor layer)

Table A2. Surface Thermal Resistance (Boundary and Floor Partitions).

Element	Surface Thermal Resistance (Target Zone Side) ($m^2 \cdot K/W$)	Surface Thermal Resistance (Adjacent Zone Side) ($m^2 \cdot K/W$)
Boundary Wall	0.11	0.11
Upper Floor Partition	0.09	0.09
Lower Floor Partition	0.15	0.15

References

1. Hashempour, N.; Taherkhani, R.; Mahdikhani, M. Energy Performance Optimization of Existing Buildings: A Literature Review. *Sustain. Cities Soc.* **2020**, *54*, 101967. [CrossRef]
2. Li, Q.; Zhang, L.; Zhang, L.; Wu, X. Optimizing Energy Efficiency and Thermal Comfort in Building Green Retrofit. *Energy* **2021**, *237*, 121509. [CrossRef]
3. Díaz-López, C.; Verichev, K.; Holgado-Terriza, J.A.; Zamorano, M. Evolution of Climate Zones for Building in Spain in the Face of Climate Change. *Sustain. Cities Soc.* **2021**, *74*, 103223. [CrossRef]
4. Wang, X.; Zhang, L.; Su, X.; Yang, H. Daylighting and Energy Performance of the Window with Transparent Insulation Slats in the Humid Subtropical Climate Zone. *Energy Build.* **2023**, *300*, 113685. [CrossRef]
5. Zhou, Y.; Herr, C.M. A Review of Advanced Façade System Technologies to Support Net-Zero Carbon High-Rise Building Design in Subtropical China. *Sustainability* **2023**, *15*, 2913. [CrossRef]
6. He, Y.; Wang, Z.; Wong, H.M.; Chen, G.; Ren, C.; Luo, M.; Li, Y.; Lee, T.; Chan, P.W.; Ho, J.Y.; et al. Spatial-Temporal Changes of Compound Temperature-Humidity Extremes in Humid Subtropical High-Density Cities: An Observational Study in Hong Kong from 1961 to 2020. *Urban Clim.* **2023**, *51*, 101669. [CrossRef]
7. Nasrollahzadeh, N. Comprehensive Building Envelope Optimization: Improving Energy, Daylight, and Thermal Comfort Performance of the Dwelling Unit. *J. Build. Eng.* **2021**, *44*, 103418. [CrossRef]
8. Sung, W.-P.; Chen, T.-Y.; Liu, C.-H. Strategy for Improving the Indoor Environment of Office Spaces in Subtropical Cities. *Buildings* **2022**, *12*, 412. [CrossRef]
9. Haddad, S.; Paolini, R.; Synnefa, A.; De Torres, L.; Prasad, D.; Santamouris, M. Integrated Assessment of the Extreme Climatic Conditions, Thermal Performance, Vulnerability, and Well-Being in Low-Income Housing in the Subtropical Climate of Australia. *Energy Build.* **2022**, *272*, 112349. [CrossRef]
10. Takasu, M.; Ooka, R.; Rijal, H.B.; Indraganti, M.; Singh, M.K. Study on Adaptive Thermal Comfort in Japanese Offices under Various Operation Modes. *Build. Environ.* **2017**, *118*, 273–288. [CrossRef]
11. Coelho, G.B.A.; Rebelo, H.B.; De Freitas, V.P.; Henriques, F.M.A.; Sousa, L. Current and Future Geographical Distribution of the Indoor Conditions for High Thermal Inertia Historic Buildings across Portugal via Hygrothermal Simulation. *Build. Environ.* **2023**, *245*, 110877. [CrossRef]

12. Annila, P.J.; Hellemaa, M.; Pakkala, T.A.; Lahdensivu, J.; Suonketo, J.; Pentti, M. Extent of Moisture and Mould Damage in Structures of Public Buildings. *Case Stud. Constr. Mater.* **2017**, *6*, 103–108. [CrossRef]
13. Chen, X.; Yang, H.; Zhang, W. Simulation-Based Approach to Optimize Passively Designed Buildings: A Case Study on a Typical Architectural Form in Hot and Humid Climates. *Renew. Sustain. Energy Rev.* **2018**, *82*, 1712–1725. [CrossRef]
14. Creutzig, F.; Agoston, P.; Minx, J.C.; Canadell, J.G.; Andrew, R.M.; Quéré, C.L.; Peters, G.P.; Sharifi, A.; Yamagata, Y.; Dhakal, S. Urban Infrastructure Choices Structure Climate Solutions. *Nat. Clim. Change* **2016**, *6*, 1054–1056. [CrossRef]
15. Grafakos, S.; Trigg, K.; Landauer, M.; Chelleri, L.; Dhakal, S. Analytical Framework to Evaluate the Level of Integration of Climate Adaptation and Mitigation in Cities. *Clim. Change* **2019**, *154*, 87–106. [CrossRef]
16. Daioglou, V.; Mikropoulos, E.; Gernaat, D.; Van Vuuren, D.P. Efficiency Improvement and Technology Choice for Energy and Emission Reductions of the Residential Sector. *Energy* **2022**, *243*, 122994. [CrossRef]
17. Barbaresi, A.; Bovo, M.; Torreggiani, D. The Dual Influence of the Envelope on the Thermal Performance of Conditioned and Unconditioned Buildings. *Sustain. Cities Soc.* **2020**, *61*, 102298. [CrossRef]
18. Stagrum, A.E.; Andenæs, E.; Kvande, T.; Lohne, J. Climate Change Adaptation Measures for Buildings—A Scoping Review. *Sustainability* **2020**, *12*, 1721. [CrossRef]
19. Sharifi, A. Co-Benefits and Synergies between Urban Climate Change Mitigation and Adaptation Measures: A Literature Review. *Sci. Total Environ.* **2021**, *750*, 141642. [CrossRef]
20. Li, J.; Ng, S.T.; Skitmore, M. Review of Low-Carbon Refurbishment Solutions for Residential Buildings with Particular Reference to Multi-Story Buildings in Hong Kong. *Renew. Sustain. Energy Rev.* **2017**, *73*, 393–407. [CrossRef]
21. Zheng, W.; Wei, F.; Su, S.; Cai, J.; Wei, J.; Hu, R. Effect of the Envelope Structure on the Indoor Thermal Environment of Low-Energy Residential Building in Humid Subtropical Climate: In Case of Brick–Timber Vernacular Dwelling in China. *Environ. Technol. Innov.* **2022**, *28*, 102884. [CrossRef]
22. Xia, D.; Xie, W.; Guo, J.; Zou, Y.; Wu, Z.; Fan, Y. Building Thermal and Energy Performance of Subtropical Terraced Houses under Future Climate Uncertainty. *Sustainability* **2023**, *15*, 12464. [CrossRef]
23. Li, M.; Cao, J.; Xiong, M.; Li, J.; Feng, X.; Meng, F. Different Responses of Cooling Energy Consumption in Office Buildings to Climatic Change in Major Climate Zones of China. *Energy Build.* **2018**, *173*, 38–44. [CrossRef]
24. Ouanes, S.; Sriti, L. Regression-Based Sensitivity Analysis and Multi-Objective Optimisation of Energy Performance and Thermal Comfort: Building Envelope Design in Hot Arid Urban Context. *Build. Environ.* **2024**, *248*, 111099. [CrossRef]
25. Liu, S.; Kwok, Y.T.; Lau, K.K.-L.; Ouyang, W.; Ng, E. Effectiveness of Passive Design Strategies in Responding to Future Climate Change for Residential Buildings in Hot and Humid Hong Kong. *Energy Build.* **2020**, *228*, 110469. [CrossRef]
26. Li, B.; Du, C.; Yao, R.; Yu, W.; Costanzo, V. Indoor Thermal Environments in Chinese Residential Buildings Responding to the Diversity of Climates. *Appl. Therm. Eng.* **2018**, *129*, 693–708. [CrossRef]
27. Jalali, Z.; Shamseldin, A.Y.; Ghaffarianhoseini, A. Impact Assessment of Climate Change on Energy Performance and Thermal Load of Residential Buildings in New Zealand. *Build. Environ.* **2023**, *243*, 110627. [CrossRef]
28. Avanzini, M.; Pinheiro, M.D.; Gomes, R.; Rolim, C. Energy Retrofit as an Answer to Public Health Costs of Fuel Poverty in Lisbon Social Housing. *Energy Policy* **2022**, *160*, 112658. [CrossRef]
29. Azimi Fereidani, N.; Rodrigues, E.; Gaspar, A.R. A Review of the Energy Implications of Passive Building Design and Active Measures under Climate Change in the Middle East. *J. Clean. Prod.* **2021**, *305*, 127152. [CrossRef]
30. De Azevedo Correia, C.M.; Amorim, C.N.D.; Santamouris, M. Use of Passive Cooling Techniques and Super Cool Materials to Minimize Cooling Energy and Improve Thermal Comfort in Brazilian Schools. *Energy Build.* **2024**, *312*, 114125. [CrossRef]
31. Nguyen, A.T.; Rockwood, D.; Doan, M.K.; Dung Le, T.K. Performance Assessment of Contemporary Energy-Optimized Office Buildings under the Impact of Climate Change. *J. Build. Eng.* **2021**, *35*, 102089. [CrossRef]
32. Chen, Y.; Ren, Z.; Peng, Z.; Yang, J.; Chen, Z.; Deng, Z. Impacts of Climate Change and Building Energy Efficiency Improvement on City-Scale Building Energy Consumption. *J. Build. Eng.* **2023**, *78*, 107646. [CrossRef]
33. Cho, W.; Iwamoto, S.; Kato, S. Condensation Risk Due to Variations in Airtightness and Thermal Insulation of an Office Building in Warm and Wet Climate. *Energies* **2016**, *9*, 875. [CrossRef]
34. Banti, N. Existing Industrial Buildings—A Review on Multidisciplinary Research Trends and Retrofit Solutions. *J. Build. Eng.* **2024**, *84*, 108615. [CrossRef]
35. Seifhashemi, M.; Capra, B.R.; Millller, W.; Bell, J. The Potential for Cool Roofs to Improve the Energy Efficiency of Single Storey Warehouse-Type Retail Buildings in Australia: A Simulation Case Study. *Energy Build.* **2018**, *158*, 1393–1403. [CrossRef]
36. Zhou, B.; Wang, D. Integrated Performance Optimization of Industrial Buildings in Relation to Thermal Comfort and Energy Consumption: A Case Study in Hot Summer and Cold Winter Climate. *Case Stud. Therm. Eng.* **2023**, *46*, 102991. [CrossRef]
37. Mustafa, J.; Alqaed, S.; Sharifpur, M.; Meyer, J. Optimization of Window Solar Gain for a Building with Less Cooling Load. *Case Stud. Therm. Eng.* **2024**, *53*, 103890. [CrossRef]
38. Chen, Y.; Liu, J.; Pei, J.; Cao, X.; Chen, Q.; Jiang, Y. Experimental and Simulation Study on the Performance of Daylighting in an Industrial Building and Its Energy Saving Potential. *Energy Build.* **2014**, *73*, 184–191. [CrossRef]
39. Liu, X.; Liu, X.; Zhang, T.; Ooka, R.; Kikumoto, H. Comparison of Winter Air Infiltration and Its Influences between Large-Space and Normal-Space Buildings. *Build. Environ.* **2020**, *184*, 107183. [CrossRef]
40. Tian, D.; Zhang, J.; Gao, Z. The Advancement of Research in Cool Roof: Super Cool Roof, Temperature-Adaptive Roof and Crucial Issues of Application in Cities. *Energy Build.* **2023**, *291*, 113131. [CrossRef]

41. Xu, J.; Li, Y.; Wang, R.Z.; Liu, W.; Zhou, P. Experimental Performance of Evaporative Cooling Pad Systems in Greenhouses in Humid Subtropical Climates. *Appl. Energy* **2015**, *138*, 291–301. [CrossRef]
42. Riahinezhad, M.; Hallman, M.; Masson, J.-F. Critical Review of Polymeric Building Envelope Materials: Degradation, Durability and Service Life Prediction. *Buildings* **2021**, *11*, 299. [CrossRef]
43. You, S.; Li, W.; Ye, T.; Hu, F.; Zheng, W. Study on Moisture Condensation on the Interior Surface of Buildings in High Humidity Climate. *Build. Environ.* **2017**, *125*, 39–48. [CrossRef]
44. Ma, Z.; Cui, S.; Chen, J. Demand Response through Ventilation and Latent Load Adjustment for Commercial Buildings in Humid Climate Zones. *Appl. Energy* **2024**, *373*, 123940. [CrossRef]
45. Li, Z.; Chen, W.; Deng, S.; Lin, Z. The Characteristics of Space Cooling Load and Indoor Humidity Control for Residences in the Subtropics. *Build. Environ.* **2006**, *41*, 1137–1147. [CrossRef]
46. Gaspar, K.; Casals, M.; Gangolells, M. A Comparison of Standardized Calculation Methods for in Situ Measurements of Façades U-Value. *Energy Build.* **2016**, *130*, 592–599. [CrossRef]
47. Bienvenido-Huertas, D. Assessing the Environmental Impact of Thermal Transmittance Tests Performed in Façades of Existing Buildings: The Case of Spain. *Sustainability* **2020**, *12*, 6247. [CrossRef]
48. Evangelisti, L.; Barbaro, L.; Guattari, C.; De Cristo, E.; De Lieto Vollaro, R.; Asdrubali, F. Comparison between Direct and Indirect Heat Flux Measurement Techniques: Preliminary Laboratory Tests. *Energies* **2024**, *17*, 2961. [CrossRef]
49. Evangelisti, L.; Barbaro, L.; De Cristo, E.; Guattari, C.; D'Orazio, T. Towards an Improved Thermometric Method: Convective and Radiative Heat Transfer for Heat Flux Measurement through an Indirect Approach. *Therm. Sci. Eng. Prog.* **2024**, *49*, 102479. [CrossRef]
50. Nardi, I.; Lucchi, E. In Situ Thermal Transmittance Assessment of the Building Envelope: Practical Advice and Outlooks for Standard and Innovative Procedures. *Energies* **2023**, *16*, 3319. [CrossRef]
51. Kim, H.; Lamichhane, N.; Kim, C.; Shrestha, R. Innovations in Building Diagnostics and Condition Monitoring: A Comprehensive Review of Infrared Thermography Applications. *Buildings* **2023**, *13*, 2829. [CrossRef]
52. Tardy, F. A Review of the Use of Infrared Thermography in Building Envelope Thermal Property Characterization Studies. *J. Build. Eng.* **2023**, *75*, 106918. [CrossRef]
53. Bailo, C.M.; Matud, C.C.; García-Ballano, C.J.; Ruiz-Varona, A. Evaluation Thermal of the Building Envelope: Rehabilitated Building versus Non-Rehabilitated. *Case Stud. Constr. Mater.* **2024**, *20*, e02846. [CrossRef]
54. Chowdhury, A.A.; Rasul, M.G.; Khan, M.M.K. Parametric Analysis of Thermal Comfort and Energy Efficiency in Building in Subtropical Climate. In *Thermofluid Modeling for Energy Efficiency Applications*; Elsevier: Amsterdam, The Netherlands, 2016; pp. 149–168. ISBN 978-0-12-802397-6.
55. Chernousov, A.A.; Chan, B.Y.B. Numerical Simulation of Thermal Mass Enhanced Envelopes for Office Buildings in Subtropical Climate Zones. *Energy Build.* **2016**, *118*, 214–225. [CrossRef]
56. Nardi, I.; Lucchi, E.; de Rubeis, T.; Ambrosini, D. Quantification of Heat Energy Losses through the Building Envelope: A State-of-the-Art Analysis with Critical and Comprehensive Review on Infrared Thermography. *Build. Environ.* **2018**, *146*, 190–205. [CrossRef]
57. Kumar, D.; Alam, M.; Zou, P.X.W.; Sanjayan, J.G.; Memon, R.A. Comparative Analysis of Building Insulation Material Properties and Performance. *Renew. Sustain. Energy Rev.* **2020**, *131*, 110038. [CrossRef]
58. Xue, Y.; Fan, Y.; Wang, Z.; Gao, W.; Sun, Z.; Ge, J. Facilitator of Moisture Accumulation in Building Envelopes and Its Influences on Condensation and Mould Growth. *Energy Build.* **2022**, *277*, 112528. [CrossRef]
59. Gourlis, G.; Kovacic, I. A Study on Building Performance Analysis for Energy Retrofit of Existing Industrial Facilities. *Appl. Energy* **2016**, *184*, 1389–1399. [CrossRef]
60. Lewczuk, K.; Kłodawski, M.; Gepner, P. Energy Consumption in a Distributional Warehouse: A Practical Case Study for Different Warehouse Technologies. *Energies* **2021**, *14*, 2709. [CrossRef]
61. Gu, J.; Goetschalckx, M.; McGinnis, L.F. Research on Warehouse Design and Performance Evaluation: A Comprehensive Review. *Eur. J. Oper. Res.* **2010**, *203*, 539–549. [CrossRef]
62. El Masri, Y.; Rakha, T. A Scoping Review of Non-Destructive Testing (NDT) Techniques in Building Performance Diagnostic Inspections. *Constr. Build. Mater.* **2020**, *265*, 120542. [CrossRef]
63. Tolstorebrov, I.; Senadeera, W.; Eikevik, T.M.; Bantle, M.; Sæther, M.; Petrova, I. Study on Drying of Seaweeds and Importance of Glass Transition and Stabilization. *Processes* **2024**, *12*, 373. [CrossRef]
64. López-Pérez, O.; Picon, A.; Nuñez, M. Volatile Compounds and Odour Characteristics of Seven Species of Dehydrated Edible Seaweeds. *Food Res. Int.* **2017**, *99*, 1002–1010. [CrossRef] [PubMed]
65. Faqih, F.; Zayed, T. Defect-Based Building Condition Assessment. *Build. Environ.* **2021**, *191*, 107575. [CrossRef]
66. Hikuma, M. Development of the Distribution Mechanism in the Processed Seafood Industry. *J. Jpn. Soc. Distrib. Sci.* **2018**, *41*, 33–46. (In Japanese) [CrossRef]
67. Climate.Onebuilding.Org. Available online: https://climate.onebuilding.org/ (accessed on 5 September 2024).
68. Barbosa, M.T.G.; Rosse, V.J.; Laurindo, N.G. Thermography Evaluation Strategy Proposal Due Moisture Damage on Building Facades. *J. Build. Eng.* **2021**, *43*, 102555. [CrossRef]
69. Li, Z.; Jin, Y.; Liang, X.; Zeng, J. Thermography Evaluation of Defect Characteristics of Building Envelopes in Urban Villages in Guangzhou, China. *Case Stud. Constr. Mater.* **2022**, *17*, e01373. [CrossRef]

70. Pereira, C.; De Brito, J.; Silvestre, J.D. Harmonising the Classification of Diagnosis Methods within a Global Building Inspection System: Proposed Methodology and Analysis of Fieldwork Data. *Eng. Fail. Anal.* **2020**, *115*, 104627. [CrossRef]
71. Tetens, O. Über einige meteorologische Begriffe. *Z. Geophys.* **1930**, *6*, 297–309.
72. Japan Meteorological Agency. Available online: https://www.jma.go.jp/jma/indexe.html (accessed on 6 September 2024).
73. Ministry of Land, Infrastructure, Transport and Tourism (MLIT). *Overview of the Energy Conservation Standards Revision*; MLIT: Tokyo, Japan, 2016; Available online: https://www.mlit.go.jp/common/001012880.pdf (accessed on 20 August 2024). (In Japanese)
74. Bastien, D.; Winther-Gaasvig, M. Influence of Driving Rain and Vapour Diffusion on the Hygrothermal Performance of a Hygroscopic and Permeable Building Envelope. *Energy* **2018**, *164*, 288–297. [CrossRef]
75. Asadi, I.; Shafigh, P.; Abu Hassan, Z.F.B.; Mahyuddin, N.B. Thermal Conductivity of Concrete—A Review. *J. Build. Eng.* **2018**, *20*, 81–93. [CrossRef]
76. Draganova, V.Y.; Yokose, H.; Tsuzuki, K.; Nabeshima, Y. Field Study on Nationality Differences in Adaptive Thermal Comfort of University Students in Dormitories during Summer in Japan. *Atmosphere* **2021**, *12*, 566. [CrossRef]
77. Khoukhi, M.; Hassan, A.; Abdelbaqi, S. The Impact of Employing Insulation with Variant Thermal Conductivity on the Thermal Performance of Buildings in the Extremely Hot Climate. *Case Stud. Therm. Eng.* **2019**, *16*, 100562. [CrossRef]
78. Zilberberg, E.; Trapper, P.; Meir, I.A.; Isaac, S. The Impact of Thermal Mass and Insulation of Building Structure on Energy Efficiency. *Energy Build.* **2021**, *241*, 110954. [CrossRef]
79. Guo, L.; Liao, Y.; Cheng, Z.; Zheng, H.; Guo, L.; Long, E. Experimental Study on Dynamic Effect of External Insulation on Indoor Thermal Environment and Energy Consumption. *Energy Build.* **2022**, *274*, 112299. [CrossRef]
80. Brambilla, A.; Sangiorgio, A. Mould Growth in Energy Efficient Buildings: Causes, Health Implications and Strategies to Mitigate the Risk. *Renew. Sustain. Energy Rev.* **2020**, *132*, 110093. [CrossRef]
81. *ASHRAE 62.1-2013*; Ventilation for Acceptable Indoor Air Quality. American Society of Heating, Refrigerating and Air-Conditioning Engineers, Inc.: Atlanta, Georgia, 2013.
82. United States Environmental Protection Agency. Mold Course Chapter 2. Available online: https://www.epa.gov/mold/mold-course-chapter-2 (accessed on 6 September 2024).
83. Raunima, T.; Laukkarinen, A.; Kauppinen, A.; Kiviste, M.; Tuominen, E.; Ketko, J.; Vinha, J. Indoor Air Temperature and Relative Humidity Measurements in Finnish Schools and Day-Care Centres. *Build. Environ.* **2023**, *246*, 110969. [CrossRef]
84. Ferrantelli, A.; Vornanen-Winqvist, C.; Mattila, M.; Salonen, H.; Kurnitski, J. Positive Pressure Effect on Moisture Performance in a School Building. *J. Build. Phys.* **2019**, *43*, 121–142. [CrossRef]
85. Summa, S.; Remia, G.; Di Perna, C. Comparative and Sensitivity Analysis of Numerical Methods for the Discretization of Opaque Structures and Parameters of Glass Components for EN ISO 52016-1. *Energies* **2022**, *15*, 1030. [CrossRef]
86. Jia, C.; Zhang, Z.; Wang, M.; Han, S.; Cao, J.; Rong, Y.; Du, C. Investigation on Indoor Thermal Environment of Industrial Heritage during the Cooling Season and Its Impacts on Thermal Comfort. *Case Stud. Therm. Eng.* **2023**, *52*, 103769. [CrossRef]
87. Chae, Y.; Kim, S.H. Selection of Retrofit Measures for Reasonable Energy and Hygrothermal Performances of Modern Heritage Building under Dry Cold and Hot Humid Climate: A Case of Modern Heritage School in Korea. *Case Stud. Therm. Eng.* **2022**, *36*, 102243. [CrossRef]
88. Bui, A.; Johnson, F.; Wasko, C. The Relationship of Atmospheric Air Temperature and Dew Point Temperature to Extreme Rainfall. *Environ. Res. Lett.* **2019**, *14*, 074025. [CrossRef]
89. *ISO 6946:2017*; Building components and building elements—Thermal resistance and thermal transmittance—Calculation methods. ISO: Geneva, Switzerland, 2017. Available online: https://www.iso.org/standard/65708.html (accessed on 3 October 2024).
90. Japanese Energy Conservation Law for Buildings, Section 3: Thermal Transmittance and Linear Thermal Transmittance. Available online: https://www.kenken.go.jp/becc/documents/house/3-3_240401_v22.pdf (accessed on 3 October 2024).

energies

MDPI

Article

Lumped-Parameter Models Comparison for Natural Ventilation Analyses in Buildings at Urban Scale

Yasemin Usta [1], Lisa Ng [2], Silvia Santantonio [1] and Guglielmina Mutani [1,*]

[1] Department of Energy, Politecnico di Torino, 10129 Torino, Italy; yasemin.usta@polito.it (Y.U.); silvia.santantonio@outlook.it (S.S.)
[2] National Institute of Standards and Technology, Gaithersburg, MD 20899, USA; lisa.ng@nist.gov
* Correspondence: guglielmina.mutani@polito.it

Abstract: This study validates a three-zone lumped-parameter airflow model for Urban Building Energy Modeling, focusing on its accuracy in estimating air change rates caused by natural ventilation, referred to here as air change rate. The model incorporates urban-scale variables like canyon geometry and roughness elements for the accurate prediction of building infiltration, which is an important variable in building energy consumption. Air change rate predictions from the three-zone lumped-parameter model are compared against results from a three-zone CONTAM model across a range of weather scenarios. The study also examines the impact of building level of detail on air change rates. Results demonstrate that the three-zone lumped-parameter model achieves reasonable accuracy, with a maximum Mean Absolute Error of 0.1 h^{-1} in winter and 0.03 h^{-1} in summer compared to three-zone CONTAM model, while maintaining computational efficiency for urban-scale energy consumption simulations. However, its applicability is limited to buildings within urban canyons rather than detached structures, due to the assumptions made in the methodology of the three-zone lumped-parameter model. The results also showed that the model had lower errors for low to mid-rise buildings since the simplification of a detailed high-rise building into a three-zone model alters the buoyancy effect; a 4-story building showed Mean Absolute Percentage Error of 7% and 5% for a typical winter and summer day respectively when a detailed and simplified three-zone models are compared, while the error for a 16-story building were 18% and 12%. The results of building air change rates are used as input data in an hourly energy consumption model at urban scale and validated against measured hourly consumption to test the effect of the calculated urban-scale hourly air change rates.

Keywords: building ventilation; infiltrations; lumped-parameter model; ACR; CONTAM; Urban Building Energy Modeling; place-based approach

1. Introduction

Building energy consumption represents the largest share of urban energy use. According to the International Energy Agency (IEA), operational energy use in buildings accounts for about 30% of global final energy consumption [1]. In the United States, buildings are responsible for 40% of total energy use, including 75% of all electricity use [2].

Building energy modeling (BEM) has emerged as a powerful decision-support tool, enabling the assessment of energy efficiency strategies and identifying conditions that cause higher energy consumption. For instance, the U.S. Department of Energy highlights BEM's adaptability, remarking on its applications, both for new buildings and retrofit design, to develop building energy-efficiency codes and decision policies [3]. However, BEM usually

focuses on individual buildings and detailed energy systems, but the complexity of the urban environment—particularly the influence of surrounding elements such as buildings and trees—demands more comprehensive modeling approaches.

Urban Building Energy Modeling (UBEM) addresses this gap by extending energy analysis to an urban scale, accounting for physical surroundings, microclimatic conditions, and building-specific characteristics. Recent reviews have highlighted both the significance and potential of UBEMs, while also addressing the challenges they face and suggesting ways to enhance their robustness [4,5]. UBEM incorporates factors such as shading effects, wind dynamics, and urban density to provide a comprehensive understanding of energy consumption and production. For example, shadows from different urban elements can impact the effectiveness of solar technologies [6], while modifications in wind speed caused by surrounding structures or roughness elements can influence ventilation and airflow rates [7–9]. Recent studies have also emphasized the critical role of occupant behavior in urban-scale modeling, highlighting the need for detailed, data-driven occupancy models to reduce simulation uncertainties and enhance the accuracy of energy demand predictions [10]. These interdependencies highlight the importance and potential of UBEM in identifying scenarios that improve an efficient use of energy at urban scale.

Given the complexity of urban environments and the volume of data required for large-scale analysis, a flexible, time-efficient, and scalable modeling framework is essential for analyzing large urban environments. In this context, process-driven UBEM provides an effective approach to calculate building energy use based on physical descriptions and local weather data. These models can rely on available open-source data for building details such as thermal transmittance and geometric data and often implement the assumption of fixed air change rate (ACR) that are based on a building permeability which is associated with construction period.

However, the assumption of a constant ACR does not reflect real-world conditions, as air infiltration is influenced by factors not only related to building envelope airtightness but also by issues such as the wind pressure on the building envelope and indoor-outdoor temperature gradients. A study that compared experimental methods for estimating infiltration rates highlighted the variability introduced by wind speed, wind direction, and temperature gradients [11]. The results emphasized that while experimental methods, such as CO_2, decay provide valuable insights on infiltration, they cannot fully account for the complexities of urban environments, including the influence of urban geometry on wind patterns.

The presented work contributes to broader research that aims to enhance the performance of an hourly process-driven and place-based UBEM. Initial efforts were made to improve ACR calculations focused on scenarios that involve using fixed ACR values, day/night adjustments, and adding window operation schedule, which all demonstrated significant impacts on energy consumption [6]. The second step refines ACR calculations by correcting wind speed inside the urban canyon to incorporate the effects of urban geometry on airflow dynamics. Lastly, the model is further developed to calculate energy consumption by representing each building as three interconnected zones, which is intended to better predict performance in large scales applications in conjunction with urban effects [12]. Validating this modeling approach will mark a critical step toward improving urban-scale energy consumption analysis.

Finally, in this work, the term **air change rate (ACR)** is used to describe the rate of air flow due to natural infiltration. While Air Change per Hour (ACH) is frequently applied in both mechanical and natural ventilation contexts, ACR specifically refers to air changes resulting from natural forces such as wind and temperature differences, providing a more accurate description of the phenomenon under consideration.

2. Objective of the Work

The primary aim of this analysis is to assess the accuracy of an already existing simplified three-zone lumped-parameter model [12] by comparing its results with CONTAM, a multizone airflow and contaminant transport simulation program [13]. The methodology presented in [12] calculated the ACR for a simplified building geometry by considering the surrounding built environment, which affects wind speed inside urban canyons due to urban roughness elements, as well as indoor conditions inside buildings.

The novelty of this work lies in analyzing the impact of building level of detail (LoD) on building ACR calculations and evaluating whether the three-zone lumped-parameter model, with its simplified representation of building geometry, is effective in estimating ACR for energy use prediction. This assessment will help define the applicability and limitations of the three-zone lumped-parameter model's methodology in urban scale natural ventilation load assessment.

The broader goal of this analysis is to support strategies to effectively use energy in urban areas. This will be enabled by developing an effective model for calculating hourly ACR as a function of urban geometry and local weather conditions, which can be then used as an input for energy consumption modeling at urban scale, while also optimizing simulation costs. By incorporating the effects of urban street canyons on wind speed and airflow dynamics, this methodology seeks to provide a more accurate building ACR input for UBEM, replacing widely used fixed assumptions.

3. Methods

The workflow followed in this analysis is outlined in Figure 1. The buildings used in the analysis are provided in Section 3.1. The study begins with providing a Level of Detail (LoD) analysis (Section 3.2) using CONTAM. This analysis aims to highlight the effect of simplifying a detailed building into three zones on the results of building ACR.

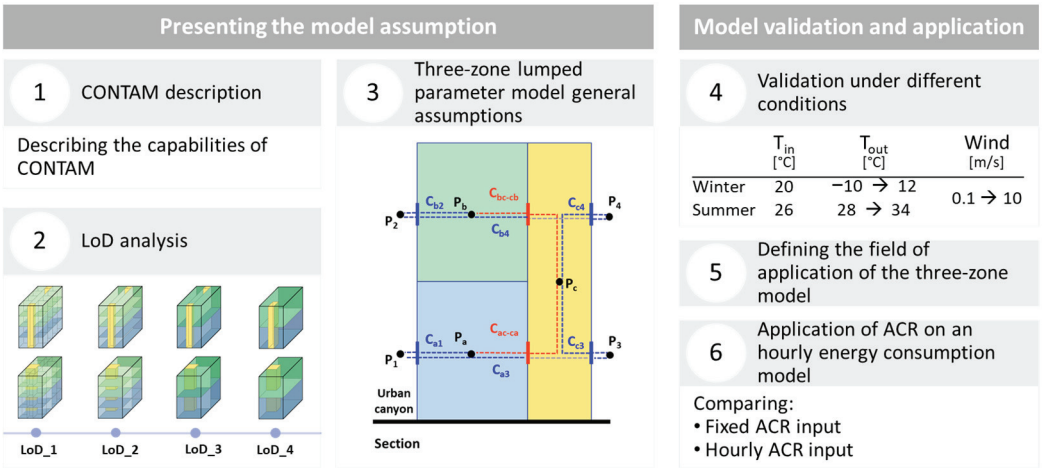

Figure 1. Manuscript workflow.

Section 3.3 provides an overview of the general assumptions made in the existing three-zone lumped-parameter model [12], and the boundary conditions used for the validation: 10 different indoor-outdoor temperature scenarios are tested under 12 wind speeds. The results of the defined boundary conditions from the three-zone lumped parameter model are compared with a three-zone CONTAM model. The results of both the LoD analysis and the validation are discussed in Section 4.

Following the validation, the study explores the potential applications of the proposed modeling approach, including its limitations, in Section 4.3.

Finally, Section 4.4 demonstrates the application of using an hourly ACR from a three-zone lumped-parameter model in estimating hourly energy consumption for space heating in residential buildings by comparing it against using fixed ACR values. The hourly energy consumption results of using hourly and fixed ACR are compared with real measured consumption data.

3.1. Analyzed Buildings

3.1.1. Midrise Prototype Building

The midrise prototype building is selected from the detailed CONTAM models developed by the National Institute of Standards and Technologies (NIST) and derived from U.S. Department of Energy (DOE) reference building models [14].

Figure 2 shows the typical floor plan of the prototype building. In this building the corridor divides the apartments/office across two opposite facades, thus, there is no cross ventilation for a single unit. The staircase and elevator are located at each end of the corridor resulting in two shafts. The building has 4 floors, each with a height of 3.05 m.

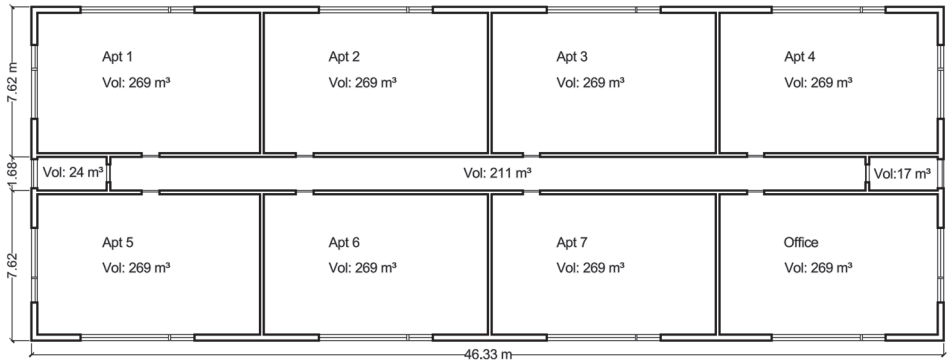

Figure 2. Typical floor plan for the midrise prototype building.

3.1.2. Turin Building

The building is a typical condominium built before 1918, located on a large street canyon (approximately 45 m wide), with adjacent buildings on both sides. It has two opposing facades: a canyon façade and a courtyard façade on the same side of the buildings as the staircase, which provides each apartment with cross ventilation. Unlike the prototype building, the staircase and the elevator are in a single shaft.

The building consists of 5 floors: a ground floor with vehicle access to the courtyard and 4 floors with layout as shown in Figure 3. The ground floor is excluded from the ACR calculations, as it is generally not used for residential purposes. The floor height for the typical floors is 3.3 m.

3.2. Level of Detail (LoD) Analysis

3.2.1. CONTAM

CONTAM (version 3.4.0.1) is a multizone modeling software, developed at the National Institute of Standards and Technology (NIST) [15]. CONTAM accounts for room-to-room, infiltration, and exfiltration airflows driven by temperature-induced pressures (i.e., stack effect), wind pressures acting on the building exterior, and mechanically-driven pressure differences (i.e., heating, ventilation, and air-conditioning system flows). The meteorological variables considered in the calculation of airflow rates are the ambient temperature [K], barometric pressure [Pa], wind speed [m/s], and wind direction [°].

CONTAM is able to perform whole-building simulations for periods of up to one year with an assumption that pressures only vary hydrostatically. Thus, its computational requirements are not as intensive as using other airflow simulation methods like

Computational Fluid Dynamics (CFD). CONTAM has been validated in terms of program integrity [16], laboratory experiments [17], and field studies in residential buildings [18,19]. It was also used to compare real-time infiltration estimates between detailed and simplified (e.g., single zone) models of two residential test houses at NIST [20]. Depending on the tightness of the test house and the simulated weather, the simplified models could capture the whole-building infiltration rate as well as the detailed model for the buildings studied.

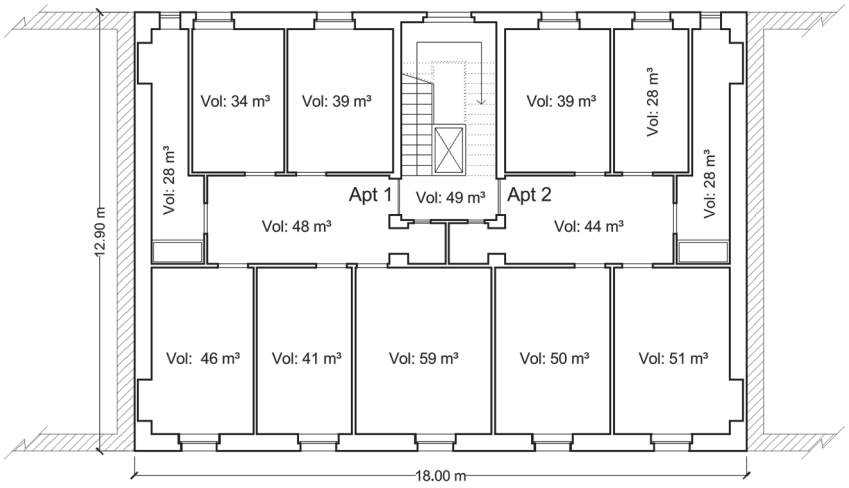

Figure 3. Typical floor plan for Turin building.

3.2.2. LoD Steps

The LoD analysis is performed using CONTAM and aims to evaluate the impact of building simplification into three zones by comparing the ACR results between a detailed building geometry and a simplified three-zone building: two heated zones representing the upper and lower levels of the building and an unheated shaft connecting them.

The building geometry is simplified according to the schematization provided in Figure 4, which outlines the LoD steps used for both buildings. The aim of including two buildings in the LoD analysis is to test the effects of building simplification on models with different floor plans and climate zones.

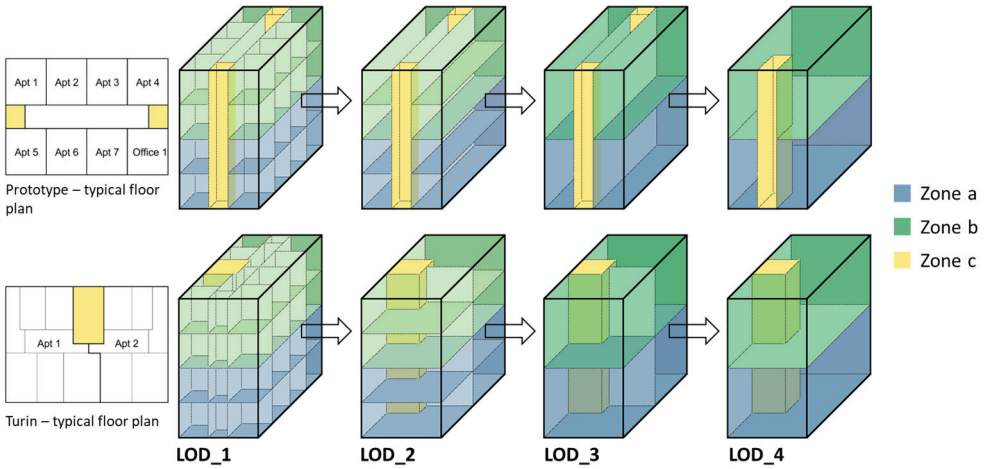

Figure 4. Level of Detail steps to achieve three-zone model.

The simplification starts with a detailed building geometry, considering all airflow elements that represent a real case (including leakages from windows, floors, internal/external walls, and roof). Then the building geometry is progressively reduced, arriving at the

three-zone model. In the detailed building step (LoD_1), the internal doors within each apartment are assumed to be open, while the apartment/shaft doors are considered closed.

For the prototype building, the simplification starts with removing the partitions between the apartments in LoD_2, followed by merging the building floors into two levels in LoD_3, and finally removing the corridor and merging the shafts into single shaft to arrive at three-zones in LoD_4.

For the building in Turin, the process starts by removing the internal partitions within each apartment in LoD_2, followed by merging the building floors into two levels in LoD_3, and finally removing the partition between the apartments in LoD_4.

Although the simplification steps differ between the two buildings, the main approach remains consistent: both buildings are simplified into a three-zone model, with two zones representing the upper and lower levels of the building and one shaft connecting them [21]. The results of this building simplification on ACR values are provided in Section 4.1.

3.2.3. LoD Models in CONTAM

For each analyzed building, the four LoD steps are modeled in CONTAM. Figures 5 and 6 provide CONTAM models for LoD_1 and LoD_4 only, to allow the direct comparison between the detailed and simplified models. The figures provide the models for both buildings with areas and volumes of each zone before and after the simplification (Figure a and b respectively). The airflow elements considered in this analysis are mainly the leakage from the envelope (in blue), the closed-door leakage (in red) and the floor leakage (in green). However, it should be highlighted that in the three-zone lumped-parameter model there is no leakage from the horizontal elements (floors, roof). To account for this behavior, it is represented as LoD_4″, which is the same as LoD_4 but excludes the leakage from the roof and between floors of the apartments.

In the prototype building, as shown in Figure 5a, there are no partitions within each apartment. Consequently, the only internal doors are the apartment/shaft doors (in red).

For the building in Turin, Figure 6a, there are two internal door types: within each apartment (in pink), which are considered open, and the apartment/shaft doors (in red), which are considered closed.

The leakage from the building envelope is obtained from available references related to whole building airtightness testing results [22], which are usually provided as normalized airflow rates, e.g., L/s/m^2 @75Pa.

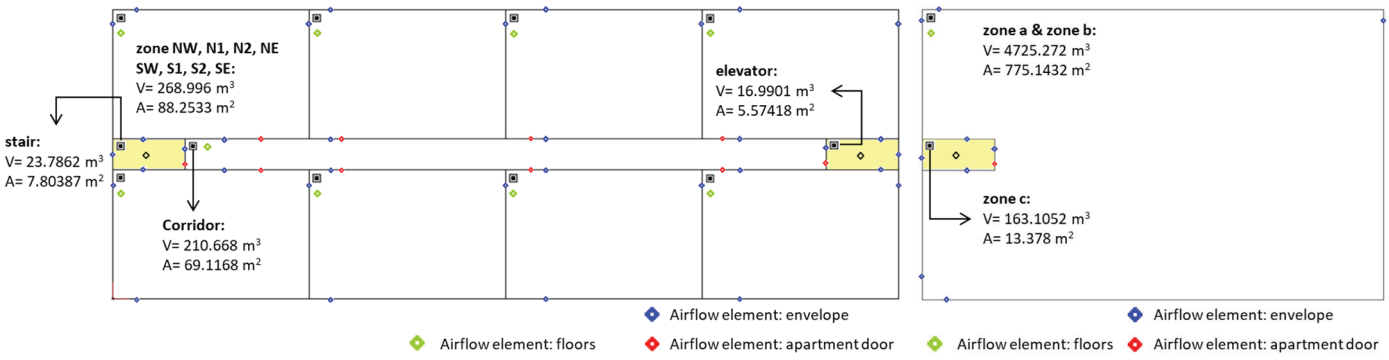

LoD_1 (**a**) LoD_4 (**b**)

Figure 5. Prototype building CONTAM model for LoD_1 (**a**) and LoD_4 (**b**).

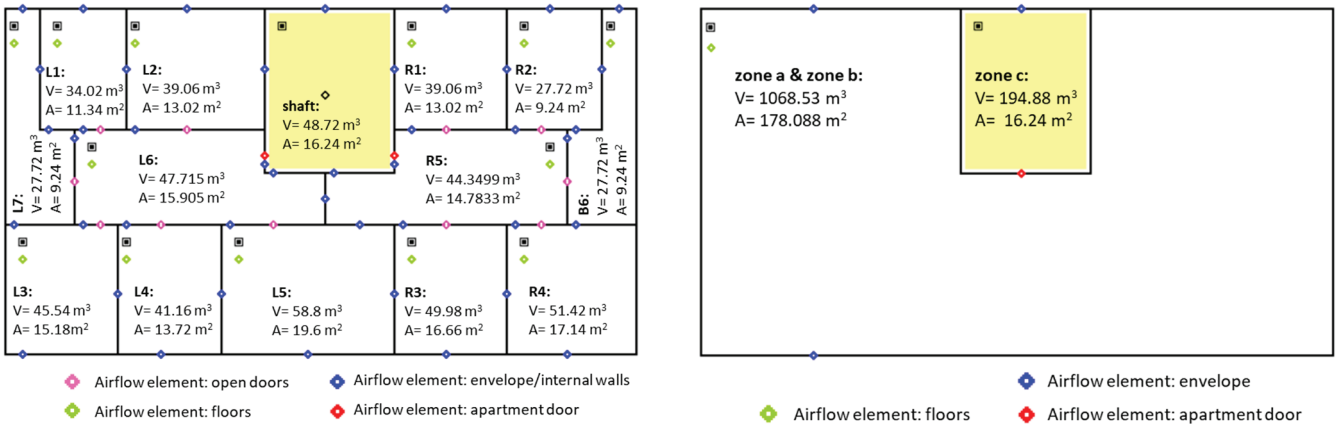

LoD_1 (**a**) LoD_4 (**b**)

Figure 6. Turin building CONTAM model for LoD_1 (**a**) and LoD_4 (**b**).

Having this normalized value, it was possible to calculate the leakage area A_L (cm^2/m^2) as an input for the flow elements in CONTAM using Equation (1) [14]. This leakage area is typically provided under reference test conditions, which include the discharge coefficient (C_d), flow exponent (n), and pressure difference (ΔP).

$$Q = \frac{C_d A_L}{10000} \cdot \sqrt{\frac{2}{\rho}} \cdot (\Delta P_r)^{0.5-n} \cdot \Delta P^n \quad (1)$$

where:

Q_r is the predicted airflow rate at ΔP_r (from pressurization test data) [$L/s/m^2$]
C_d is the discharge coefficient [-], used here as 1
A_L is the leakage area [cm^2/m^2]
ρ is the air density [kg/m^3]
ΔP_r is the reference pressure difference (from pressurization test data) [Pa]
n is the flow exponent [-], used here as 0.65
ΔP is the pressure difference, used here as 4 Pa.

The value of the flow exponent depends on the type of opening, whether it is large or small [15]. Generally, the values are near 0.65 for small cracks, which can be used to represent the leakage from window, door, and wall cracks [15,22]. For the discharge coefficient (C_d), one of the common reference conditions for small leakage areas is 1.0 at ΔP = 4 Pa [15,22]. Although these values can be used for small openings, Equation (1) can be used to convert reference building airflow rates for the required boundary conditions.

For the prototype building, the airtightness value used is 3.83 $L/s/m^2$ @75 Pa. For the building in Turin, the whole building airtightness value is 3.09 $L/s/m^2$ @75 Pa, which is the average value for multi-unit residential buildings (MURBs), determined from airtightness tests performed on 113 buildings [22].

Table 1 provides the leakage elements used in CONTAM for each building. The closed apartment/shaft doors in the prototype building are modeled in CONTAM using the Powerlaw Model: Orifice airflow element type.

Table 1. Leakage data of the analyzed buildings.

Envelope (walls, floors, roof): Powerlaw Model: Leakage area			
	Prototype	Turin	
Leakage per unit area [cm^2/m^2]	2.208	1.783	
Discharge coefficient [-]	1	1	
Flow exponent [-]	0.65	0.65	
Pressure difference [Pa]	4	4	
Internal doors			
Prototype		Turin	
Apartment/shaft doors: Powerlaw Model: Orifice		Internal doors (within apartments): Two-way Model: Single-opening	
Cross-sectional area [m^2]	0.023	Height [m]	2.2
Flow exponent [-]	0.5	Width [m]	0.9
Discharge coefficient [-]	0.6	Discharge coefficient [-]	0.78
Hydraulic diameter [m]	0.172	Apartment/shaft doors: Powerlaw Model: $F = C(\Delta P)^n$	
Reynold number [-]	30	Flow coefficient (C) [-]	Equation (2)
		Flow exponent (n) [-]	0.65

For the building in Turin, having two internal door elements, the open doors within each apartment are modeled using two-way model: Single-opening, and for the closed apartment/shaft doors using a Powerlaw Model: $F = C(\Delta P)^n$. For the latter, the flow exponent (n) is 0.65 and the flow coefficient (C) is calculated using Equation (2) assuming a typical leakage area of 12 cm^2/m^2 for each door. This estimate represents a loosely sealed element, considering construction period of the building [23,24].

The flow coefficient $C_{opening}$ [$kg \cdot s^{-1} \cdot Pa^{-n}$] for the shaft door in the Turin building is calculated using Equation (2). It is related to the leakage area ($A_{leakage}$) calculated using the typical leakage area values (A_L) available in standards or local databases [22–24].

$$C_{opening} = C_{d,opening} \cdot A_{leakage} \cdot (2 \cdot \rho)^{\frac{1}{2}} A_{leakage} = A_L \cdot A_{opening} \quad (2)$$

where:

$C_{d,opening}$ is the discharge coefficient of the opening [-], used here as 0.65
$A_{leakage}$ is the leakage area of the opening [m^2]
ρ is the air density [kg/m^3]
A_L is the leakage area [cm^2/m^2], used here as 12 cm^2/m^2
$A_{opening}$ is the opening area of the airflow element [m^2], used here as 1.98 m^2.

3.2.4. LoD Indoor Temperature and Weather Data

For the LoD analysis, a simulation for a representative winter and summer day with a one-hour timestep is used to calculate the hourly ACR. Although the overall simulation is annual, each hourly interval is solved under steady-state conditions.

The setpoint temperatures for the heated zones are 20 °C in winter and 26 °C in summer, while for the shaft the temperature is calculated using the equation provided in Table 2. These temperature schedules are assigned to each zone using continuous value files (.cvf) in CONTAM.

Table 2. Internal conditions of the analyzed buildings.

Season	Temperature [°C]	
	Heated Zones (a&b)	Shaft (Zone c)
Winter	20	$T_{sh} = T_{out} + b_{tr,u} \cdot (T_{in} - T_{out})$ *
Summer	26	

* $b_{tr,u}$: correction factor for confined spaces (shaft with one wall facing outwards), equals to 0.4 (Table 5 in the Appendix A of the Italian standard UNI/TS 11300-1: 2014 [25]).

The weather data used for both buildings are sourced from the EnergyPlus weather database [26], and subsequently converted from ".epw" format to CONTAM-compatible ".wth" format using the CONTAM weather file creator [27].

Figure 7 provides the outdoor air temperature (in red) and wind speed (in black) for a representative winter and summer day. These graphs show that the results of the three-zone model simplification will be analyzed considering different weather conditions: tropical (with hot and humid summers) in Miami for the prototype building and continental temperate in Turin. Both analyzed buildings, midrise and Turin, are simulated using the two weather files to compare the effects of climate and building geometry on the ACR results.

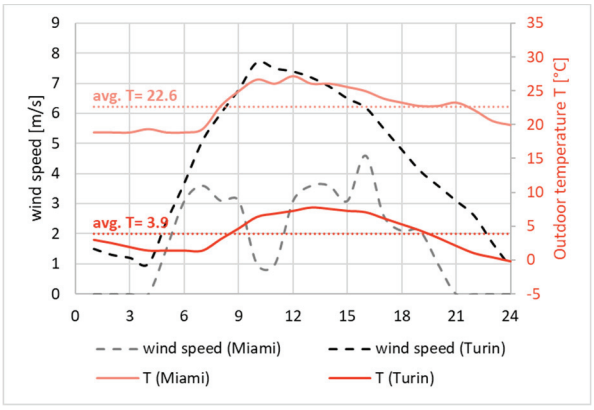

(**a**) Winter

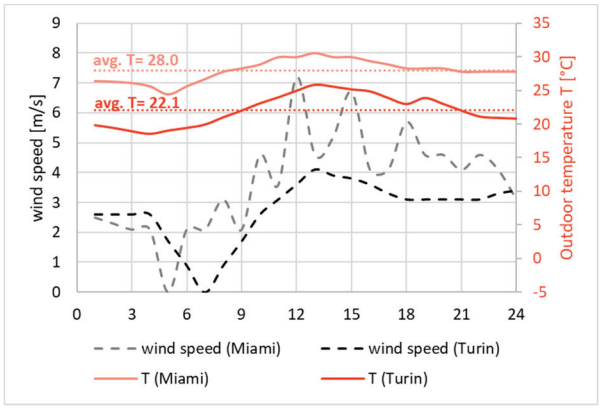

(**b**) Summer

Figure 7. Hourly weather data for Turin and Miami used in LoD analysis.

The wind pressure coefficients used in this vary as a function of the angle of the envelope flow paths relative to wind direction only [28], i.e., coefficients do not vary with height.

3.3. Three-Zone Lumped-Parameter Model

3.3.1. General Aim

The main aim of the three-zone lumped-parameter model being validated was to simplify a building into three zones to enable urban scale natural ventilation load assessments in energy consumption calculations, while minimizing simulation costs [12]. The existing model was used in this work with few impoorvements, e.g., neglecting the dynamic component of the pressure in the internal zones. The results of this simplification of the building geometry on the ACR results are discussed in Section 4.2.

The three-zone lumped-parameter model is used to consider outdoor airflow dynamics within urban street canyons, which are significantly influenced by the urban geometry (i.e., height-to-width ratio H/W).

3.3.2. Corrected Wind Speed

In this model, a Geographic Information System (GIS)-based approach is used to calculate aerodynamic roughness parameters that influence wind dynamics within urban areas. QGIS (Quantum Geographic Information System) is an open-source tool used to analyze and visualize spatial data. It supports a wide range of geospatial formats and provides various tools for geoprocessing and spatial analysis. To calculate the aerodynamic and morphometric parameters, the Urban Multi-scale Environmental Predictor (UMEP) plug-in within QGIS was employed [29]. This tool calculates aerodynamic and morphometric parameters using a 3D representation of the urban environment, i.e., digital surface models (DSM) and digital elevation models (DEM). To calculate the aerodynamic parameters, including the displacement height (z_d) and roughness length (z_0), the Morphometric Calculator tool within the plugin applies six different roughness calculation methods based on morphometric parameters [30]. Depending on the selected method, the calculation incorporates one or more morphometric parameters: plan area density (λp), frontal area ratio (λf), average building height (zH), maximum building height (zHmax), and height variability (zHstd). Among the six methods, the Kanda method is suggested for dense urban environments, as it incorporates all five morphometric parameters for the calculation of z_d and z_0 [31].

The primary parameter obtained from UMEP is the displacement height (z_d), which is determined as a function of the built environment and wind direction. Knowing the displacement height (z_d) in front of each building, the wind speed can be adjusted using the logarithmic law for buildings above z_d, where the flow is less turbulent and CFD simulations for buildings below z_d, in which turbulent flows occur. Most buildings in dense urban environments have turbulent airflow inside the canyon, thus requiring CFD simulations for the wind speed adjustment [32].

Considering the high simulation costs of CFD, this wind speed correction methods used to reduce the number of simulations by categorizing wind effects related to urban canyons according to height-to-width ratio (H/W). Generally, the canyons in a city can be defined as large, medium, and narrow. These canyon categories and weather scenarios for the CFD simulations are presented in Figure 8. The simulations are performed for four effects considering the presence or absence of wind and temperature gradient between opposing building facades in the urban canyon, four representative seasons, and four positions of the building surfaces with respect to wind direction and solar irradiation; windward/leeward with warm/cold façade. Thus, as illustrated in Figure 8, 192 CFD simulations are performed, i.e., 64 simulations for each canyon geometry category. The results of the CFD simulations are used as boundary conditions to calculate the ACR for each building in the city considering its canyon category, building position, and the weather conditions during each hour simulated.

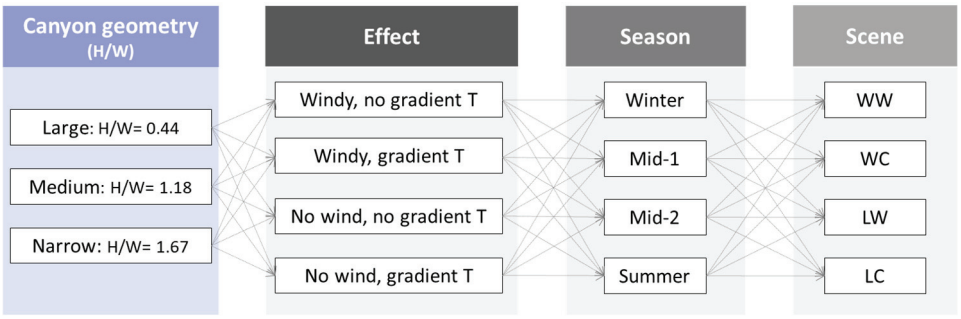

Figure 8. CFD simulation scenarios: WW: windward warm façade, WC: windward cold façade, LW: leeward warm façade, LC: leeward cold façade.

3.3.3. Three-Zone Building Simplification

Geometrical Simplification

The corrected wind speed explained previously is used as input data for a three-zone representation of each building in a city. The three interconnected zones shown in Figure 9 include two heated zones that correspond to the lower and upper apartment levels (zone a and b) and an unheated shaft connecting them (zone). The airflow connections between zones are depicted as thick lines (red for internal and blue for envelope connections) that are labeled with their flow coefficient (e.g., C_{a1}). The nodes represented as black dots in Figure 9 are characterized by steady-state conditions and air pressures, following the available multizone airflow modeling tools, e.g., CONTAM and COMIS [33], as well as to simplify the modeling approach which will be applied on urban scale.

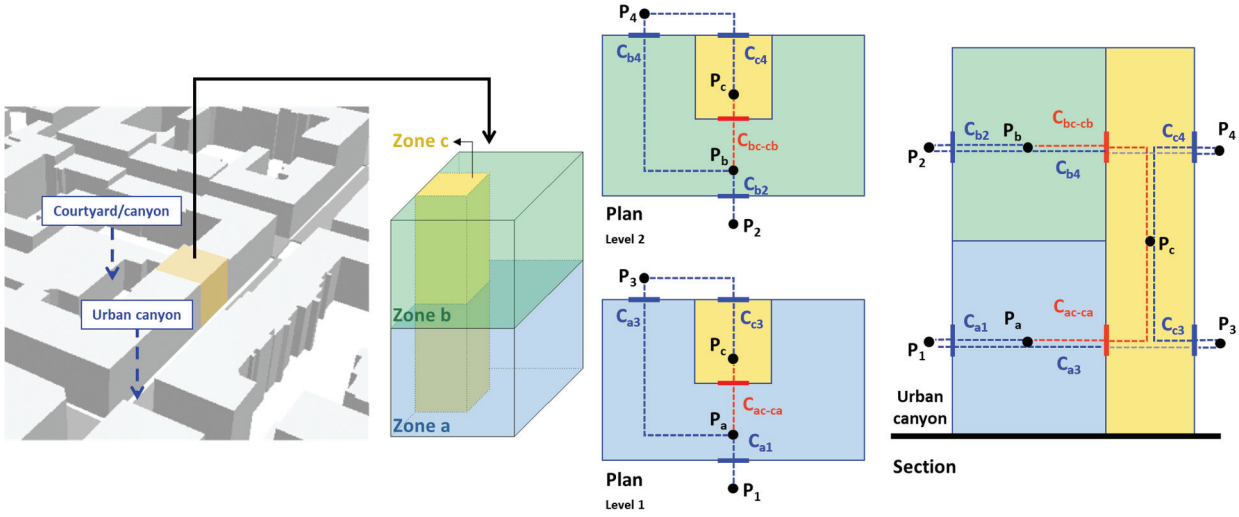

Figure 9. Three-zone lumped-parameter model schematization.

It was assumed that there was no airflow between zones a and b, the roof of zone b and c, and between the common walls of each building with its adjacent buildings. Thus, the stack effect is accounted for only in zone c. This assumption reduces the number of airflow path links, thereby minimizing simulation time for urban-scale analysis.

Physical Assumptions

In order to solve for the unknown internal zone pressures (P_a, P_b, P_c), a set of steady-state mass airflow conservation equations were applied as shown in Equations (3) and (4). The flow coefficient (C) is calculated for each link using Equation (2) provided previously. This three-zone, nonlinear system of equations was solved using MATLAB (version R2023b) applying the *fsolve* function and setting initial values and tolerance criteria [12,34].

$$\begin{cases} \dot{m}_{a1} + \dot{m}_{a3} + \dot{m}_{ac} = 0 \\ \dot{m}_{b2} + \dot{m}_{b4} + \dot{m}_{bc} = 0 \\ \dot{m}_{ca} + \dot{m}_{cb} + \dot{m}_{c3} + \dot{m}_{c4} = 0 \end{cases} \quad (3)$$

$$\begin{cases} C_{a1}\,(\Delta P_{a1})^n + C_{a3}\,(\Delta P_{a3})^n + C_{ac}\,(\Delta P_{ac})^n = 0 \\ C_{b2}\,(\Delta P_{b2})^n + C_{b4}\,(\Delta P_{b4})^n + C_{bc}\,(\Delta P_{bc})^n = 0 \\ C_{ca}\,(\Delta P_{ca})^n + C_{cb}\,(\Delta P_{cb})^n + C_{c3}\,(\Delta P_{c3})^n + C_{c4}\,(\Delta P_{c4})^n = 0 \end{cases} \quad (4)$$

where:

C is the flow coefficient [$kg \cdot s^{-1} \cdot Pa^{-n}$]
$\dot{m}$ is the airflow rate [kg/s]
ΔP is the total pressure difference [Pa].

The presented two-step approach—CFD simulations to calculate outside wind speed within the urban canyon, followed by a three-zone airflow model to estimate ACR—links urban-scale wind dynamics and building-level airflow rates, enabling the assessment of building infiltration in dense urban environments.

Validation with CONTAM

The validation aims to test the three-zone lumped-parameter model, explained in the previous section, with a three-zone CONTAM model to test the accuracy of the implemented model. For this validation, the building in Turin is used.

The validation is performed with a steady-state simulation using a range of weather data, which is derived from the hourly weather data presented previously in Section 3.2.4. This range is defined to ensure that the model is tested under different conditions, including extreme temperature cases (T_{out}), i.e., −10 °C to 34 °C and extreme wind velocity cases (W_s), i.e., 10 m/s as provided in Table 3.

Table 3. Weather data used for the model validation.

			Winter					**Summer**		
T_{out} [°C]	−10	−5	0	3	7	12	24	28	30	34
W_s [m/s]	0.1, 0.5, 1 → 10 (with an increment of 1 for each simulation)									

The indoor setpoint temperatures remain the same as 20 °C and 26 °C for winter and summer, respectively, for the heated zones, while for the shaft it is calculated using the equation provided previously in Table 2.

4. Results

This section presents the performance of the three-zone lumped-parameter model, implemented for urban scale energy analysis, through two steps. First, analyzing the impact of LoD on building ACR results, then validating the three-zone lumped-parameter model with a three-zone CONTAM model under a range of weather conditions. This is followed by highlighting the field of application of the presented methodology. Finally, an example application of this methodology on a residential building for space heating is provided in Section 4.4.

To assess the model's performance, the Mean Absolute Error (MAE) and the Mean Absolute Percentage Error (MAPE) are calculated using Equation (5). These metrics are applied to compare the difference in ACR results between a detailed CONTAM building model (LoD_1) and three-zone CONTAM models (LoD_4 and LoD_4″) and to assess the difference in building ACR between the three-zone lumped-parameter model and a three-zone CONTAM model.

$$MAE = \frac{1}{n}\sum_{i=1}^{n}|y - \hat{y}| MAPE = \frac{1}{n}\sum_{i=1}^{n}\left|\frac{y - \hat{y}}{y}\right| \times 100 \quad (5)$$

where:

y is the actual value
$\hat{y}$ is the predicted value
n is the total number of observations.

4.1. Level of Detail (LoD) Analysis Using CONTAM

4.1.1. Midrise Prototype Building Results

The results of the ACR analysis for different LoD are presented in Figures 10 and 11, for typical winter and summer days, in Miami. LoD_1 and LoD_2 exhibit similar results, indicating that internal partitions have a negligible effect on the ACR. The most significant change occurs in LoD_3, where the building floors are merged into two representative zones (upper and lower levels). This simplification increases the ACR overall due to the absence of internal obstructions. Additionally, it likely alters the buoyancy effect, as leakage in the detailed representation is assumed to occur at the midpoint of each floor height, whereas in LoD_3, leakage is assumed to occur at the midpoint of the merged zones, significantly changing the buoyancy-driven airflow.

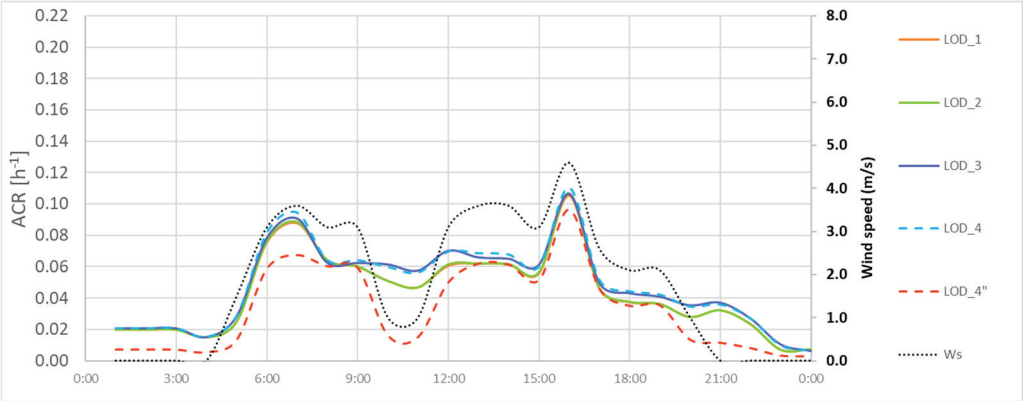

Figure 10. Hourly LoD effect on ACR (winter) for the midrise prototype building.

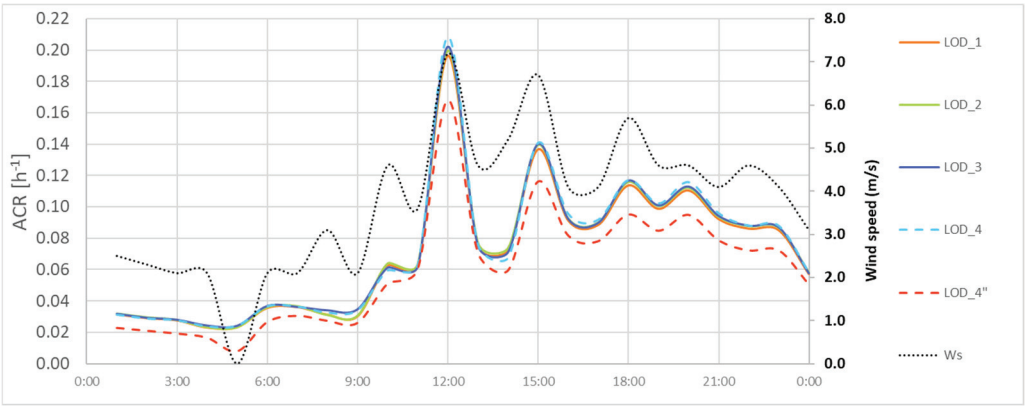

Figure 11. Hourly LoD effect on ACR (summer) for the midrise prototype building.

In LoD_4, where the corridor is removed and the shafts are merged into a single shaft, the ACR values became slightly higher compared to LoD_3. However, the results of LoD_4″, a variation of LoD_4 where leakages from internal floors and roofs are excluded as it is assumed in the three-zone lumped-parameter model, are generally lower than all LoD steps. The average daily building ACR with floor and roof leakage (LoD_4) is 1.5 times higher in winter and 1.2 in summer compared to LoD_4″.

The hourly absolute difference is provided in Figure 12 by directly comparing LoD_1 with LoD_4, and LoD_1 with LoD_4″ (which excludes the roof leakage). The hourly trend reveals that in winter, the error increases as wind speed decreases, while in summer, the error mostly followed the hourly wind speed trend. Moreover, the results demonstrate that excluding floor and roof leakage significantly impacts the ACR values by underestimating the ACR of a detailed model (LoD1).

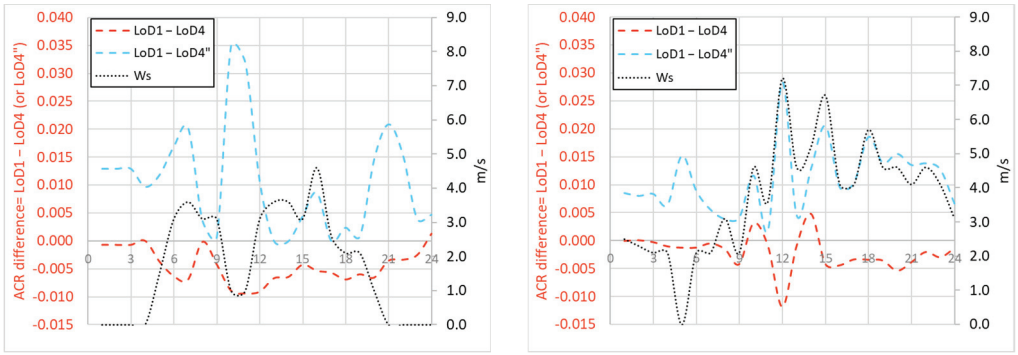

Figure 12. Hourly ACR difference comparing LoD_1 with LoD_4 (in red) and LoD_1 with LoD_4″ (in blue) for the midrise prototype building.

For LoD_4, the average daily MAE is 0.005 h^{-1} and 0.003 h^{-1} for winter and summer respectively, while for LoD_4″, the MAE" increases to 0.01 h^{-1} in both seasons. Using MAPE, the average daily error with floor and roof infiltrations included is 12% and 4% for winter and summer respectively, while excluding the infiltrations from the floor and roof resulted in 35% and 18% MAPE. Given that ACR measurements are low in magnitude, the MAE provides the error values in the actual units and avoids errors' overestimation that occur with MAPE when small differences are compared. Thus, the comparison of ACR values in the following sections is made using the MAE.

4.1.2. Turin Building Results

The LoD results for the building in Turin closely resemble those for the prototype building, with the most significant difference occurring in LoD_3 and LoD_4 as represented in Figures 13 and 14 for winter and summer, using Turin weather data. Like the prototype building, merging the floors into two levels, from LoD_2 to LoD_3, alters the buoyancy effect, resulting in higher ACR values. Moreover, the building in Turin showed low ACR results when the partition between the two apartments is removed: from LoD_3 to LoD_4.

Excluding the leakage from floors and roof (LoD_4″) results in considerable decrease in ACR values in this building; the average daily ACR with roof leakage (LoD_4) is 1.8 higher in winter and 1.6 in summer compared to the LoD_4″.

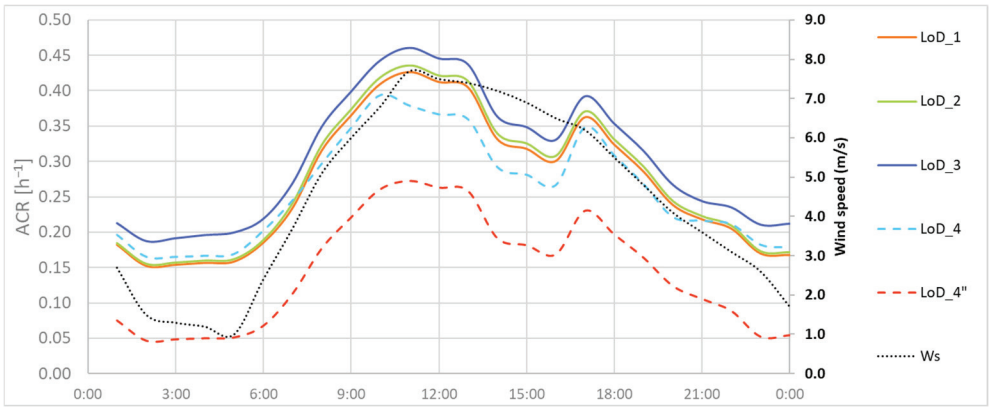

Figure 13. Hourly LoD effect on ACR (winter) for the building in Turin.

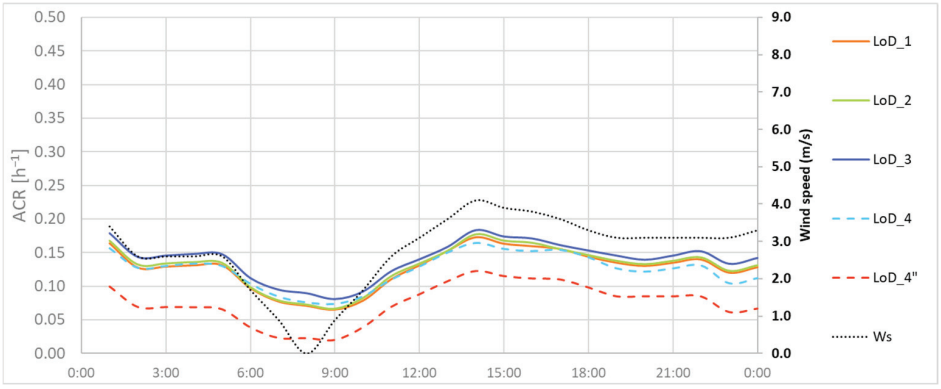

Figure 14. Hourly LoD effect on ACR (summer) for the building in Turin.

Figure 15 presents the hourly ACR difference between the detailed model LoD1 and the three-zone model (LoD_4 and LoD_4″)

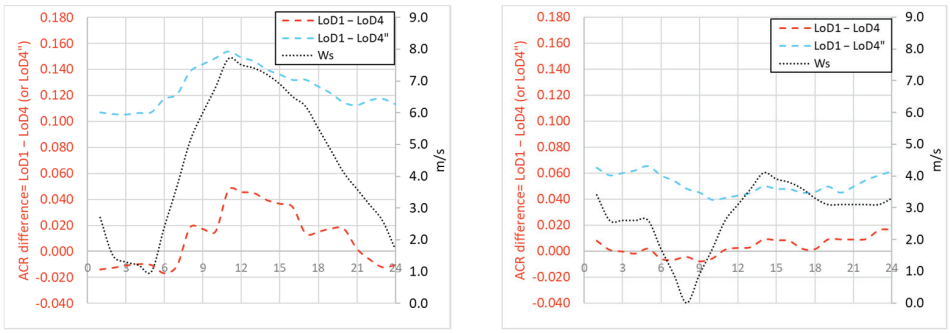

MAE (winter) MAE (summer)

Figure 15. Hourly ACR difference comparing LoD_1 with LoD_4 (in red) and LoD1 with LoD_4″ (in blue) for the building in Turin.

Excluding floor and roof leakage (LoD_4″) significantly reduces the ACR values resulting in underestimation for the building in Turin. Comparing LoD_1 with LoD_4, the MAE for average daily building ACR is 0.02 h^{-1} and 0.006 h^{-1} for winter and summer respectively, while for LoD_4″, the MAE increases to 0.1 h^{-1} and 0.05 h^{-1}. Accounting for roof infiltration, by adding airflow links for the roof in zone b and c, would increase the ACR, improving the simplified model's alignment with the detailed one. This can be done by introducing two flow elements in Equation (3), i.e., $\dot{m}_{br}$ and $\dot{m}_{cr}$ with the correct flow coefficients (C).

4.1.3. Summary

When each building was tested under different climate conditions, the overall trend in results remained unchanged, indicating that building zoning primarily determined the accuracy of the simplified model (LoD_4) compared to the detailed model (LoD_1). The mid-rise building, which included a corridor and two shafts in the detailed model, had different results compared to Turin building, which had no corridor and only a single shaft. While the mid-rise building overestimated the ACR in the three-zone model in both climates, the Turin building underestimated it, considering the average daily ACR.

Overall, the LoD analysis results for both buildings indicate a good balance between the ACR differences observed between LoD_1 and LoD_4, despite the simplification of a detailed building into only three representative zones. These findings suggest that this simplified approach is effective for representing building volumes across a city, provided that all leakage elements are accurately calculated (as in LoD_4). This finding offers a practical and efficient for urban-scale simulations.

4.2. Three-Zone Lumped-Parameter Model Validation with CONTAM

For the validation, the building in Turin was used to test 10 various indoor/outdoor air temperature scenarios under 12 wind speed conditions. Table 4 presents the MAE values comparing the three-zone lumped-parameter model with the three-zone CONTAM model.

Table 4. The absolute difference in ACR [h^{-1}] between three-zone CONTAM and lumped-parameter model for the tested weather conditions.

[°C]	T_{out}	−10	−5	0	3	7	12	24	28	30	34
	T_{in}	20							26		
	T_{shaft}	2	5	8	9.8	12.2	15.2	24.8	27.2	28.4	30.8
	ΔT $\lvert T_{out} - T_{in} \rvert$	30	25	20	17	13	8	2	2	4	8
Wind speed [m/s]	0.1	0.0005	0.0004	0.0016	0.0026	0.0044	0.0071	0.0128	0.0159	0.0154	0.0151
	0.5	0.0005	0.0004	0.0016	0.0017	0.0005	0.0007	0.0063	0.0095	0.0106	0.0132
	1	0.0036	0.0023	0.0008	0.0002	0.0019	0.0023	0.0053	0.0066	0.0103	0.0067
	2	0.0132	0.0108	0.0049	0.0066	0.0047	0.0030	0.0036	0.0042	0.0049	0.0066
	3	0.0309	0.0107	0.0056	0.0092	0.0081	0.0075	0.0006	0.0013	0.0021	0.0037
	4	0.0099	0.0156	0.0120	0.0128	0.0120	0.0111	0.0053	0.0027	0.0016	0.0004
	5	0.0408	0.0168	0.0179	0.0171	0.0160	0.0149	0.0081	0.0079	0.0066	0.0039
	6	0.0457	0.0243	0.0225	0.0216	0.0203	0.0189	0.0101	0.0093	0.0090	0.0085
	7	0.0448	0.0294	0.0274	0.0263	0.0248	0.0231	0.0122	0.0112	0.0107	0.0098
	8	0.0373	0.0349	0.0326	0.0313	0.0296	0.0275	0.0145	0.0132	0.0126	0.0114
	9	0.0434	0.0406	0.0379	0.0364	0.0344	0.0321	0.0168	0.0153	0.0146	0.0132
	10	0.0496	0.0465	0.0435	0.0417	0.0395	0.0368	0.0193	0.0176	0.0167	0.0151

The results indicate that at lower wind speeds, the absolute differences of ACR are generally low, particularly when the temperature difference is high (e.g., in winter). As wind speed increases, the error rises across all temperature scenarios, with a more obvious effect in winter. For instance, at ΔT = 30 °C, the error is significantly higher at a wind speed of 2 m/s compared to 0.1 m/s. Beyond 5 m/s, the error stabilizes across different temperatures, ranging from 0.014 h^{-1} to 0.05 h^{-1}, suggesting a low influence of temperature differences on ACR estimation. Wind speeds higher than 5 m/s are generally extreme cases in high-density urban environments. Considering the average wind speed for winter and summer in Turin were 1.26 m/s and 1.58 m/s, respectively, for the period 2015–2023, our analysis shows that the lumped-parameter model could be applied with relatively low errors in Turin.

Overall, the absolute differences remain low, with a maximum of 0.05 h^{-1} across all tested weather conditions. These findings demonstrate that the implemented model performs effectively with optimized *fsolve* settings for reduced simulation costs. The model reliably estimates ACR under varying weather conditions, making it a suitable and practical tool for large-scale infiltration analysis in urban environments.

4.3. Field of Application Analysis

The three-zone model presented in this work is applicable to certain building configurations, based on the assumptions of the lumped-parameter model. It is particularly suitable for buildings located in continuous urban canyons with homogeneous building height, as commonly found in Turin and in city centers generally. This approach, detailed

in Section 3.3.2, involves categorizing urban canyons into specific H/W classes to facilitate CFD simulations of airflows in the urban canyon. As a result, the model is not suitable for detached buildings. In such configurations, the lack of neighboring structures on all sides complicates the application of CFD simulations. This is because, in detached buildings, boundary conditions for the simulations become more challenging to define. Consequently, CFD simulations in these scenarios would be less efficient and less representative of urban-scale dynamics, making this model unsuitable for detached buildings.

Moreover, the results of the LoD analysis indicate that the most significant changes occur when the building is simplified into two representative zones for the apartments, which substantially alter the buoyancy effect. This finding makes the model more suitable for low-rise buildings, as applying such simplifications to high-rise buildings can modify the buoyancy effect significantly, potentially leading to inaccuracies in ACR calculations.

Figure 16 illustrates the airflow connection heights for LoD_1 and LoD_4, emphasizing the impact of building height in the simplified model. The variations in airflow opening heights representing the upper and lower zones highlight how simplifying a high-rise building into just three zones can intensify discrepancies in the buoyancy effect.

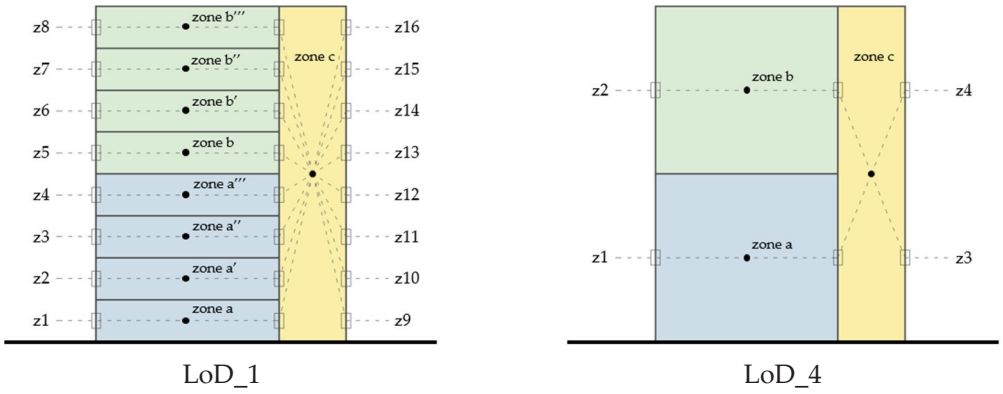

Figure 16. Airflow element heights in the detailed and schematized building models.

Figures 17 and 18 presents the hourly ACR for LoD_1 and LoD_4 for a typical winter and summer day considering different building heights. The results demonstrate that as building height increases, the ACR value decreases. This trend aligns with findings in the literature [35,36] and can be also attributed to the reduced surface-to-volume (S/V) ratio in taller buildings, which lowers the heat loss surface area.

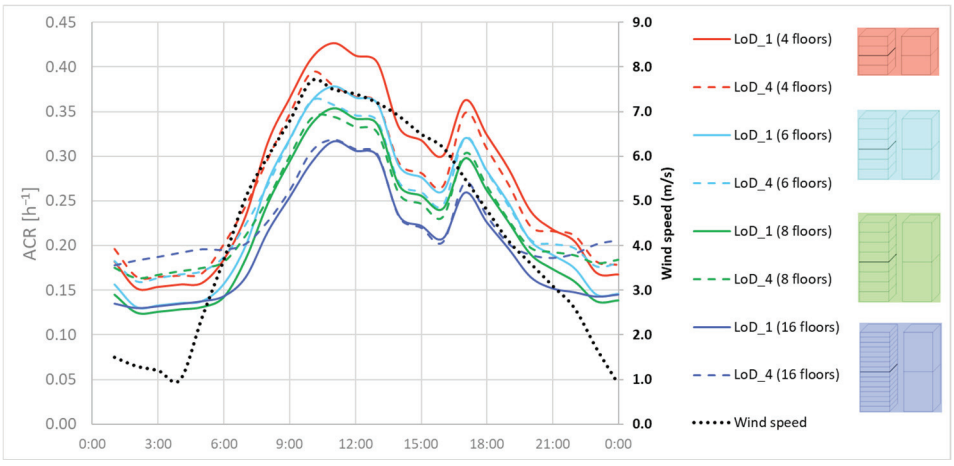

Figure 17. Hourly LoD effect on ACR (winter) considering different building heights.

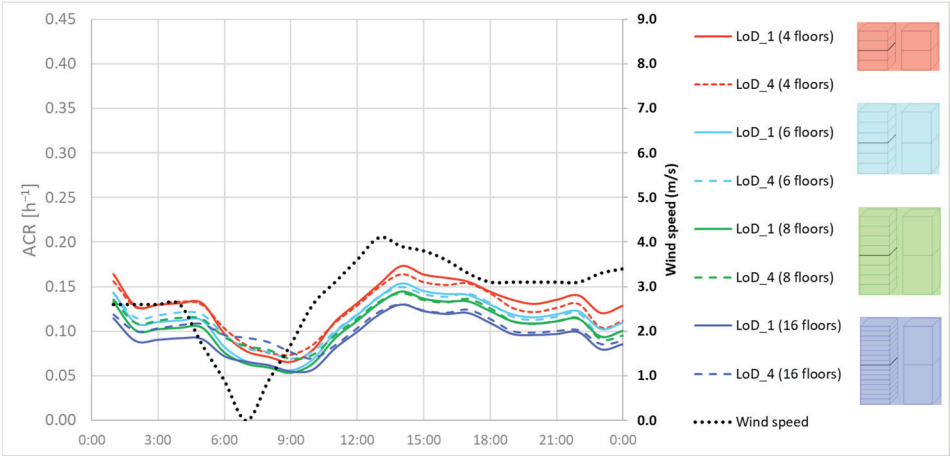

Figure 18. Hourly LoD effect on ACR (summer) considering different building heights.

For the detailed building model, LoD_1, the average daily ACR decreased by 26% in winter and 27% in summer when comparing a 16-story building with a 4-story building. While considering the three-zone model, LoD_4, this decrease is 13% in winter and 18% in summer when comparing a 16-story building with a 4-story one.

Figure 19 provides the absolute difference between LoD_1 and LoD_4 for each analyzed building height. The data clearly shows that shorter buildings generally yield lower differences, which becomes higher under low wind speed conditions. The average daily MAE increases significantly with taller buildings; 1.4 times higher MAE for both winter and summer when comparing a 16-story building with a 4-story one.

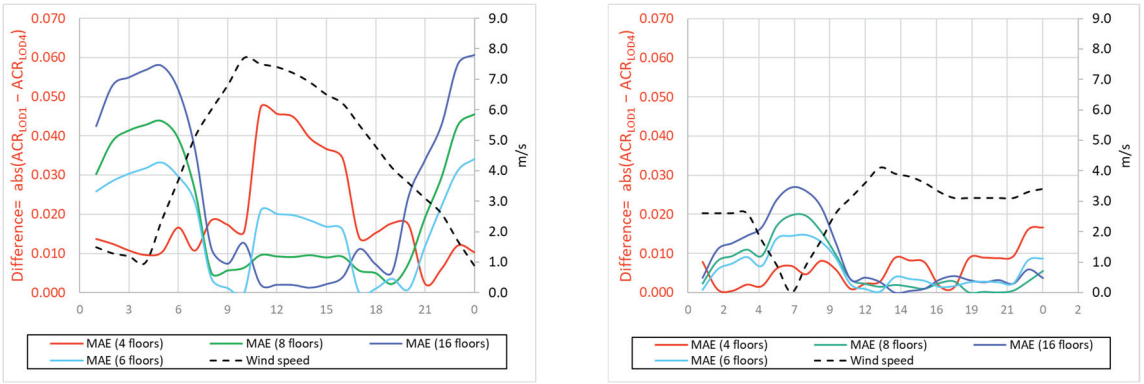

(winter) (summer)

Figure 19. Absolute ACR difference comparing LoD_1 and LoD_4 for different building heights.

The three-zone model was initially designed for residential buildings, which are generally not high-rise structures. Improving the three-zone model for high rise buildings would primarily require detailing the airflow elements for zone c (shaft), which would complicate the system of nonlinear equations (Equations (3) and (4)). A comprehensive analysis on the effect on building internal zones on the ACR results, has shown that the contribution of the number of internal zones on ACRs is higher than detailing of the airflow elements across the façade [37].

Overall, the results showed higher errors for the 16-story building compared to the 4-story building, however the average daily MAE between the LoD_1 and LoD_4 of a 16-story building is 0.03 h^{-1} in winter and 0.01 h^{-1} in summer. This MAE would still be accepted for urban scale applications if needed.

4.4. Example Application: Energy Consumption for Space Heating

4.4.1. Selected Building

In this section, the methodology of the three-zone lumped-parameter model, previously presented, is applied to an hourly GIS-based engineering model for calculating the energy consumption for space heating in residential buildings [6]. Among the buildings examined, a case study building with available hourly consumption data has been selected.

The objective of this application is to evaluate the contribution of the hourly ACR as input data for the energy model, compared to using a constant ACR value, in estimating hourly energy consumption. Both will be compared to the real heating season consumption data during the examined period.

First, the case study building was selected from the zones in the city of Turin that correspond to the application field of the presented methodology. The chosen building is located close to the city center of Turin, built between 1919 and 1945, and has available real hourly energy consumption data. As shown in Figure 20, the examined building is in a narrow canyon, oriented NE-SW (30°N), and positioned on the left side of the canyon. The hourly energy consumption data were collected from the local district heating company and correspond to the heating season of 2022–2023 (15 October 2022–15 April 2023).

Figure 20. The examined building located in a narrow canyon, NE-SW (30°N) oriented, and left positioned.

Mutani et al. (2020) provided a detailed description of a dynamic engineering model with three thermodynamic systems (TSs), which form the foundation of the GIS-based UBEM [6]. In line with this work, the main input data for the hourly energy consumption model can be summarized into three key categories: building characteristics, local weather data, and heating schedule.

- Building characteristics including the construction period (i.e., 1919–1945), the associated ACR value, and thermal properties, such as thermal capacity (C_t) and thermal transmittance (U) for both opaque (walls, roof, ground) and transparent (glazing) building envelopes, the window-to-wall ratio (WWR), heating system efficiency (η). Reference data are provided in Table 5, with the selected building's construction period highlighted.
- Local weather data includes hourly outdoor air temperature, humidity, pressure, solar radiation, and sun altitude, recorded by the weather station of Politecnico di Torino [38]

for the period from May 2022 to April 2023, in which the hourly consumption data are available.

- Heating schedule, which details the building's occupancy patterns and the operation of the centralized heating system. In the analyzed scenarios, the system operates according to national and local regulations, with the internal air temperature of 19 °C during the day from 6 am to 9 pm with two interruptions at 9 am and 2 pm.

Table 5. Thermo-physical characteristics and ACR values according to construction period.

Period	WALL		ROOF	GROUND	GLAZING			ACR	η
	$C_{envelope}$	U_{wall}	U_{roof}	U_{floor}	U_g	WWR	g-Value	h^{-1}	
	$kJ \cdot m^{-2} \cdot K^{-1}$	$W \cdot m^{-2} \cdot K^{-1}$	$W \cdot m^{-2} \cdot K^{-1}$	$W \cdot m^{-2} \cdot K^{-1}$	$W \cdot m^{-2} \cdot K^{-1}$	-	-	-	-
<1918	504	1.45	1.80	1.75	4.85	0.13	0.85	0.5	0.78
1919–45	**504**	**1.35**	**1.80**	**1.58**	**4.75**	**0.13**	**0.85**	**0.5**	**0.78**
1946–60	283	1.18	1.80	1.23	4.40	0.20	0.85	0.5	0.78
1961–70	283	1.13	2.20	1.30	4.90	0.20	0.85	0.5	0.79
1971–80	257	1.04	2.20	1.00	3.80	0.25	0.75	0.5	0.80
1981–90	264	0.78	1.18	0.95	3.80	0.20	0.75	0.5	0.82
1991–00	274	0.7	0.68	0.80	2.15	0.20	0.67	0.5	0.84
2001–05	274	0.7	0.68	0.80	2.15	0.20	0.67	0.3	0.84
2006–12	267	0.42	0.38	0.41	2.60	0.20	0.50	0.3	0.92
2013–15	267	0.34	0.30	0.33	2.20	0.20	0.50	0.3	0.92
2016–19	267	0.30	0.25	0.30	1.80	0.20	0.35	0.3	0.92

4.4.2. Application Results

This section provides the results of the hourly energy consumption model, considering the scenarios presented in Table 6. All scenarios are then compared to the real consumption data of the case study building.

Table 6. Infiltration scenarios and ACR.

	Scenario	Building Permeability	ACR
1	*cons*	Based on construction period	0.5 constant during the day
2	*cons+(d&n)*	Same as 1, with less permeability during the night for window shutters	0.5 during the day and 0.3 during the nigh
3	*cons+(d&n)+W*	Same as 2, with additional window opening for three times of the day	For 3 h, with windows opening, ACR was calculated by a correlation [6] considering 15 min of windows opening
4	*hourly*	Air infiltration depends on the weather conditions. It was considered an average airtightness of masonry buildings, i.e., 4.58 $L/s/m^2$ @75	ACR was calculated from the three-zone lumped-parameter model in each hour of the year

In the constant scenario "*cons*", the ACR for the analyzed building is set at 0.5 h^{-1}, based on its construction period (see Table 5). In the second scenario "*cons+(d&n)*" a day-night variation is introduced to account for closed window shutters at night by reducing the ACR to 0.3 h^{-1} from 9 p.m. to 8 a.m. In the third scenario "*cons+(d&n)+W*", window shutters are closed at night and windows are opened for 15 min three times per day [6].

The final scenario uses the hourly ACR (named "*hourly*") as a result of the three-zone lumped-parameter model presented previously, with an airtightness value of 4.58 $L/s/m^2$

@75 Pa, representing the average airtightness for masonry buildings based on a sample of 152 buildings [22].

The main output of the energy model is the heat loss through ventilation (Q_v) [kWh], which directly depends on the ACR values. Figure 21a,b provide Q_v for selected days during the heating season, comparing the different analyzed ACR scenarios for two representative days. Figure 21c,d present the hourly energy consumption for space heating for the same days.

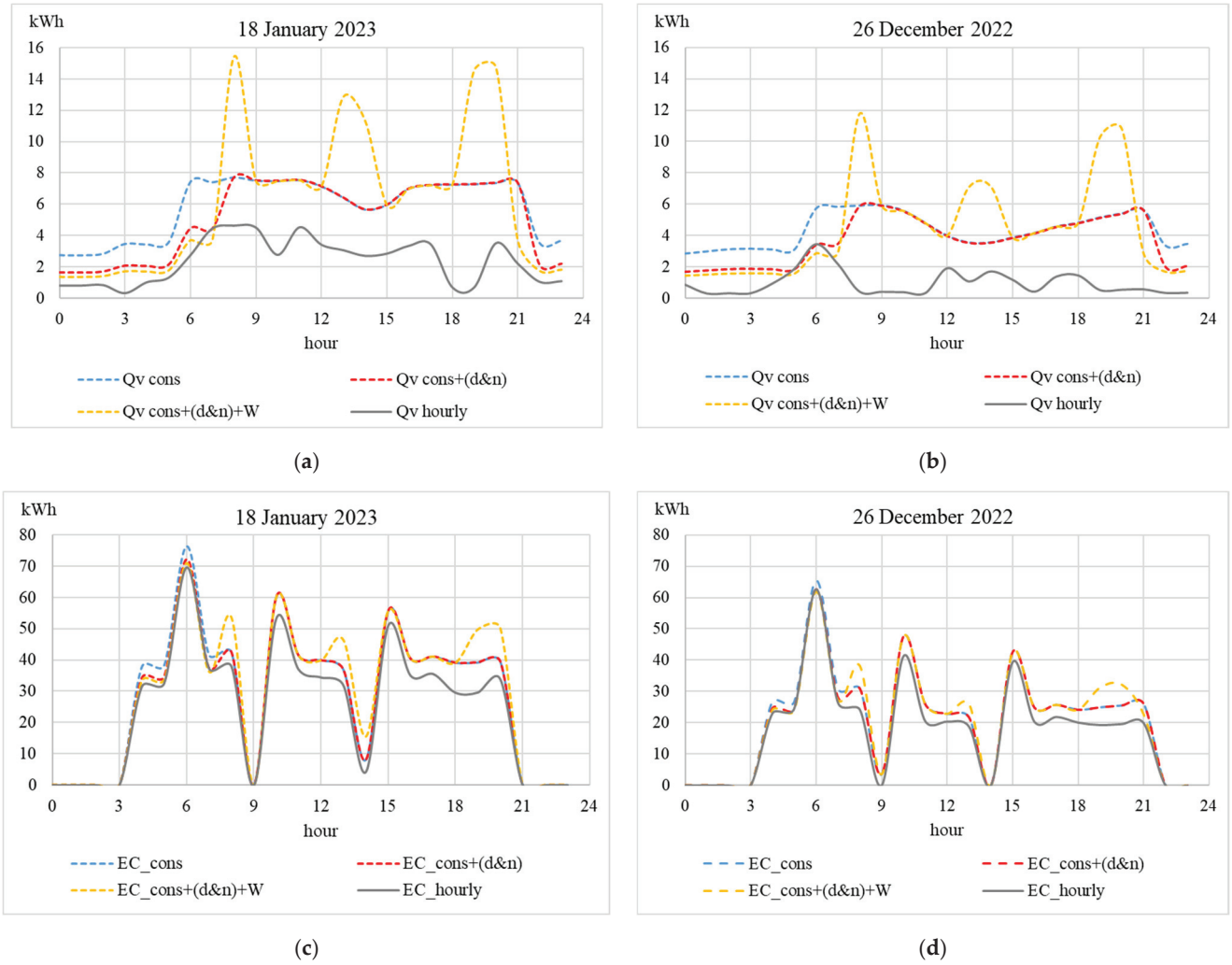

Figure 21. Hourly heat loss by ventilation Q_V [kWh] (**a**,**b**) and hourly energy consumption (EC) for space heating (**c**,**d**) for selected days in the heating season for the analyzed scenarios.

By examining the hourly profiles of the ventilation load in Figure 21a,b, it is evident that all constant ACR scenarios, particularly *cons+(d&n)+W*, show higher values compared to the *hourly* ACR scenario. This suggests that the *hourly* ACR scenario may be influenced by: the wind speed adjustment within the urban canyon (which is low), the low infiltration value used in the three-zone lumped-parameter model (which could not reflect the real situation), and finally the lack of roof infiltration considered in the three-zone lumped-parameter model.

As seen in Figure 21c,d, the energy consumption using the *hourly* ACR scenario shows, overall, lower values compared to the other three scenarios that use constant ACR. This demonstrates the direct impact of building ACR on space heating energy consumption.

Figure 22 shows the calculated and measured energy consumption for selected days in each month of the heating season. As this engineering model is directly influenced by

the building physical characteristics and weather data, the use of hourly ACR presents a more accurate approach compared to fixed values, especially with natural ventilation.

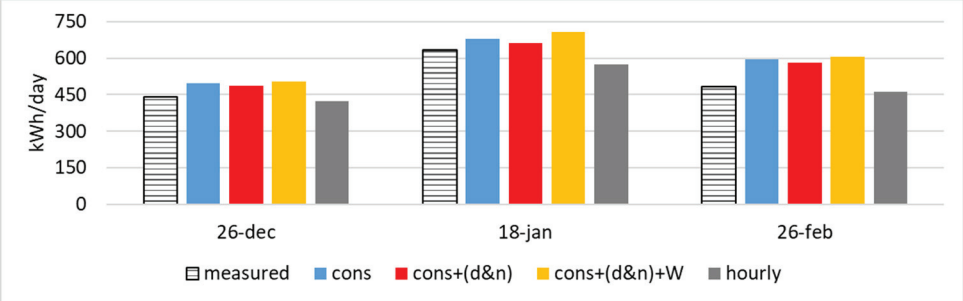

Figure 22. Daily energy consumption for space heating representative days during the heating season comparing the ACR scenarios and the measured consumption data.

For each scenario and day examined in Figure 22, Table 7 provides the MAPE. Among the analyzed scenarios, the *hourly* MAPE was lower, indicating that the three-zone lumped-parameter model provided better estimates of the ACR values. However, the *cons+(d&n)* scenario showed the lowest MAPE for 18 January, highlighting the role of unpredictable user behavior or system performance. Generally, on the analyzed days, MAPE results were low under conditions of low wind speed, aligning with the findings previously presented in Table 4.

Table 7. MAPE of the different ACR scenarios in predicting the daily energy consumption for space heating in representative days of the heating season.

Scenario	26-Dec	18-Jan	26-Feb
cons	12.6%	7.2%	22.9%
cons+(d&n)	10.3%	4.7%	19.6%
cons+(d&n)+W	14.5%	11.9%	25.4%
hourly	4.3%	7.6%	4.7%
Tout [°C]	6.83	5.44	5.96
Ws [m/s]	1.88	0.97	1.93

Figure 23 compares the hourly energy consumption for space heating [kWh] using both the *cons* ACR (solid red line) and *hourly* ACR (dotted red line), against the measured hourly consumption (dashed red line) for two selected days during the heating season. The figures also provide other relevant heat losses and gains [kWh] in the energy consumption model, which are: the heat loss by ventilation Q_v (blue line), the heat gain by internal gains Q_I (violet line), the heat loss by transmission from opaque envelope $Q_{t,e}$ (light green line), the heat loss by transmission from transparent envelope $Q_{t,g}$ (dark green line), the heat gain by solar irradiation Q_{sol} (yellow line). In addition, the solar irradiance $I_{sol,h}$ [$W \cdot m^{-2}$] is also shown (dotted orange line).

Analyzing the two graphs, both the *cons* and *hourly* ACR scenarios align closely with the real measured data (dashed red line), but generally the *cons* scenario overestimates the consumption compared to the *hourly* scenario. However, as provided previously in Table 7, the average daily MAPE for the presented two days in Figure 23 was lower for the *hourly* scenario in December and slightly lower for *cons* scenario in January.

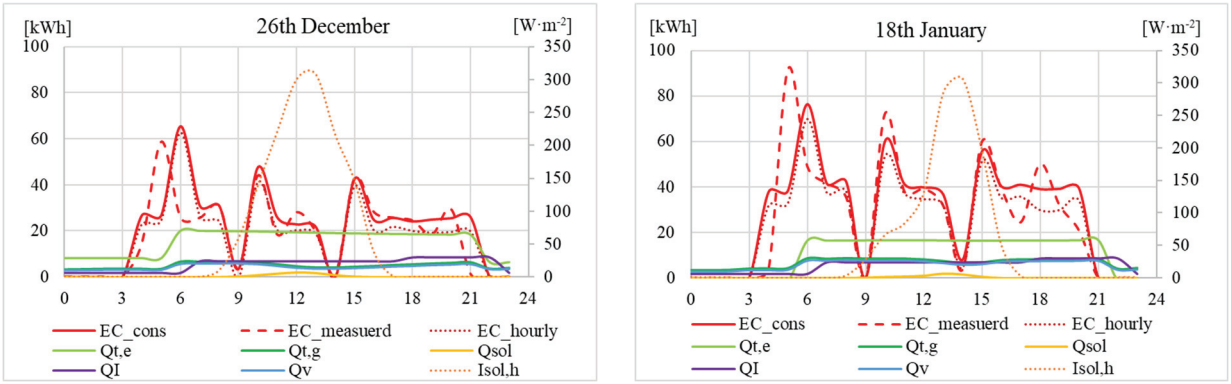

Figure 23. Hourly profiles of the energy consumption for space heating for selected two days comparing the measured data (dashed red line) with the ACR constant (solid red line) and the ACR hourly (dotted red line) scenarios.

Generally, the *hourly* scenario is underestimating energy consumption compared to the real measured data, which could be highly associated with the lack of roof infiltration in the current three-zone lumped parameter model. As mentioned earlier, the three-zone lumped-parameter model used in this study simplifies the building geometry by excluding infiltration from the roof and internal floors. This simplification was done to reduce simulation costs when solving the system of nonlinear equations. However, the model can be improved to include two extra links to the current system of nonlinear equations (Equation (3)) to account for roof infiltration from zones b and c. Nevertheless, the relatively small difference between the measured energy consumption and the consumption based on the *hourly* ACR, as presented in Figure 23, suggests that this methodology is promising. It effectively accounts for the influence of the built environment and corrected wind speed, which are critical for analyzing building airflow from natural ventilation and estimating energy consumption at urban scale.

5. Conclusions

This study assesses the accuracy of a steady-state three-zone lumped-parameter model by analyzing first the effect of simplifying a building into three-zones and then by validating the implemented three-zone lumped-parameter model with a three-zone CONTAM model. The lumped-parameter model accounts for natural infiltration in buildings and incorporates the effects of the surrounding environment by adjusting outside wind speed within urban canyons using CFD simulations for defined urban canyon and weather scenarios.

The comparison across different LoDs revealed that while internal partitions had a minor impact, simplifications—such as merging floors into representative zones—had a greater influence on ACR values, particularly by altering the buoyancy effect. Additionally, the exclusion of infiltration through floors and roofs led to a notable reduction in ACR, emphasizing the significance of including these elements in building infiltration modeling. The effect of including leakages from the floor and roof on the average daily building ACR was found to be 1.5 times higher in winter and 1.2 in summer for the prototype building, while for the building in Turin it was 1.8 times higher in winter and 1.6 in summer.

The results of comparing the three-zone lumped-parameter model with CONTAM using the building in Turin showed higher MAE in winter, with higher wind speed and higher ΔT.

Applying this model to a real case study and comparing its results with measured data confirmed that ACR values derived from the three-zone lumped-parameter model were lower compared to the constant ACR value. This finding underscores the necessity of accounting for all infiltration elements in buildings to improve model accuracy.

Despite these limitations, the proposed three-zone lumped-parameter model remains a computationally efficient tool for estimating ACR in urban-scale energy modeling. Future enhancements—such as refining the representation of infiltration pathways—could further improve its accuracy. These refinements hold significant potential in enabling more accurate assessments of ACR from natural ventilation at urban scale, which plays a crucial role in building energy loads. The ultimate goal in enhancing energy consumption modeling is to develop effective strategies for utilizing energy tailored to dense urban environments.

Author Contributions: Conceptualization, G.M. and S.S.; methodology, G.M. and S.S.; software, Y.U.; validation, Y.U.; formal analysis, Y.U.; investigation, L.N. and G.M.; resources, G.M.; data curation, S.S.; writing—original draft preparation, Y.U. and S.S.; writing—review and editing, G.M. and L.N.; visualization, Y.U.; supervision, G.M. All authors have read and agreed to the published version of the manuscript.

Funding: This research received no external funding.

Data Availability Statement: The raw data supporting the conclusions of this article will be made available by the authors on request.

Conflicts of Interest: The authors declare no conflict of interest.

References

1. IEA. Buildings—Energy System. Available online: https://www.iea.org/energy-system/buildings (accessed on 28 January 2025).
2. NREL Researchers Reveal How Buildings Across United States Do—and Could—Use Energy. Available online: https://www.nrel.gov/news/features/2023/nrel-researchers-reveal-how-buildings-across-the-united-states-do-and-could-use-energy.html (accessed on 28 January 2025).
3. U.S Department of Energy. Building Energy Modeling. Available online: https://www.energy.gov/eere/buildings/building-energy-modeling (accessed on 28 January 2025).
4. Ali, U.; Shamsi, M.H.; Hoare, C.; Mangina, E.; O'Donnell, J. Review of urban building energy modeling (UBEM) approaches, methods and tools using qualitative and quantitative analysis. *Energy Build.* **2021**, *246*, 111073. [CrossRef]
5. Kamel, E. A Systematic Literature Review of Physics-Based Urban Building Energy Modeling (UBEM) Tools, Data Sources, and Challenges for Energy Conservation. *Energies* **2022**, *15*, 8649. [CrossRef]
6. Mutani, G.; Todeschi, V.; Beltramino, S. Energy Consumption Models at Urban Scale to Measure Energy Resilience. *Sustainability* **2020**, *12*, 5678. [CrossRef]
7. Javanroodi, K.; Mahdavinejad, M.; Nik, V.M. Impacts of urban morphology on reducing cooling load and increasing ventilation potential in hot-arid climate. *Appl. Energy* **2018**, *231*, 714–746. [CrossRef]
8. Santantonio, S.; Mutani, G. QGIS-Based Tools to Evaluate Air Flow Rate by Natural Ventilation in Buildings at Urban Scale. In Proceedings of the BSA Conference 2022 IBPSA-Italy, Bozen-Bolzano, Italy, 29 June–1 July 2022; Volume 5, pp. 331–339. Available online: https://publications.ibpsa.org/conference/paper/?id=bsa2022_9788860461919_42 (accessed on 6 January 2025).
9. Todeschi, V.; Boghetti, R.; Kämpf, J.H.; Mutani, G. Evaluation of Urban-Scale Building Energy-Use Models and Tools—Application for the City of Fribourg, Switzerland. *Sustainability* **2021**, *13*, 1595. [CrossRef]
10. Dabirian, S.; Panchabikesan, K.; Eicker, U. Occupant-centric urban building energy modeling: Approaches, inputs, and data sources—A review. *Energy Build.* **2022**, *257*, 111809. [CrossRef]
11. Taddeo, P.; Ortiz, J.; Salom, J.; Segarra, E.L.; González, G.V.; Ruiz, G.R.; Bandera, C.F. Comparison of Experimental Methodologies to Estimate the Air Infiltration Rate in a Residential Case Study for Calibration Purposes, 2018. Available online: https://www.semanticscholar.org/paper/Comparison-of-experimental-methodologies-to-the-air-Taddeo-Ortiz/437eab49b3304179d102167876f74733caff6be4 (accessed on 28 January 2025).
12. Santantonio, S.; Dell'Edera, O.; Moscoloni, C.; Bertani, C.; Bracco, G.; Mutani, G. Wind-driven and buoyancy effects for modeling natural ventilation in buildings at urban scale. *Energy Effic.* **2024**, *17*, 95. [CrossRef]
13. National Institute of Standards and Technology. CONTAM Introduction. Available online: https://www.nist.gov/el/energy-and-environment-division-73200/nist-multizone-modeling/software/contam (accessed on 15 December 2024).
14. Ng, L.C.; Musser, A.; Persily, A.K.; Emmerich, S.J. *Airflow and Indoor Air Quality Models of DOE Prototype Commercial Buildings*; National Institute of Standards and Technology: Gaithersburg, MD, USA, 2019. [CrossRef]

15. Dols, W.S.; Polidoro, B. *CONTAM User Guide and Program Documentation Version 3.4*; National Institute of Standards and Technology: Gaithersburg, MD, USA. Available online: https://www.nist.gov/publications/contam-user-guide-and-program-documentation-version-34 (accessed on 18 December 2024).
16. Haghighat, F.; Megri, A.C. A Comprehensive Validation of Two Airflow Models—COMIS and CONTAM. *Indoor Air* **1996**, *6*, 278–288. [CrossRef]
17. Chung, K.-C. Development and Validation of a Multizone Model for Overall Indoor Air Environment Prediction. *HVAC&R Res.* **1996**, *2*, 376–385. [CrossRef]
18. Emmerich, S.J.; Howard-Reed, C.; Nabinger, S. Validation of multizone IAQ model predictions for tracer gas in a townhouse. *Build. Serv. Eng. Res. Technol.* **2004**, *25*, 305–316. [CrossRef]
19. Emmerich, S.J. *Validation of Multizone IAQ Modeling of Residential-Scale Buildings: A Review*; No. Pt.2; National Institute of Standards and Technology: Gaithersburg, MD, USA, 2001; Volume 107. Available online: https://www.nist.gov/publications/validation-multizone-iaq-modeling-residential-scale-buildings-review (accessed on 18 December 2024).
20. Ng, L.C.; Zimmerman, S.M.; Good, J.; Tool, B.; Emmerich, S.; Persily, A. *Estimating Real-Time Infiltration for Use in Residential Ventilation Control*; National Institute of Standards and Technology: Gaithersburg, MD, USA, 2019. Available online: https://www.nist.gov/publications/estimating-real-time-infiltration-use-residential-ventilation-control (accessed on 18 December 2024).
21. IEA. Annex 23—An International Effort in Multizone Air Flow Modeling | Smarter Small Buildings. Available online: https://smartersmallbuildings.lbl.gov/publications/annex-23-international-effort (accessed on 18 March 2025).
22. RDH Building Science, Study of Part 3 Building Airtightness. Available online: https://www.rdh.com/resource/study-of-part-3-building-airtightness/ (accessed on 9 December 2024).
23. UNI EN 12207:2017—UNI Ente Italiano di Normazione. Available online: https://store.uni.com/uni-en-12207-2017 (accessed on 17 November 2024).
24. Mckeen, P.; Liao, Z. The Influence of Building Airtightness on Airflow in Stairwells. *Buildings* **2019**, *9*, 208. [CrossRef]
25. UNI/TS 11300-1:2014 —Determinazione del Fabbisogno di Energia Termica Dell'edificio per la Climatizzazione Estiva ed Invernale. Available online: https://store.uni.com/uni-ts-11300-1-2014 (accessed on 15 November 2024). (In Italian)
26. EnergyPlus. Available online: https://energyplus.net/weather-location/north_and_central_america_wmo_region_4/USA/FL/USA_FL_Southwest.Florida.Intl.AP.722108_TMY3 (accessed on 16 December 2024).
27. National Institute of Standards and Technology. CONTAM Weather File Creator 2.0. 2018. Available online: https://www.nist.gov/el/energy-and-environment-division-73200/nist-multizone-modeling/software/contam-weather-file (accessed on 24 January 2025).
28. Florida Solar Energy Center; Chandra, S. Procedures for Calculating Natural Ventilation Airflow Rates in Buildings. 03-87. FSEC Energy Research Center®, 1987. Available online: https://stars.library.ucf.edu/fsec/988 (accessed on 16 December 2024).
29. Kent, C.W.; Lindberg, F.; Offerle, B.; Grimmond, S.; Krave, N. Urban Morphology and Morphometric Calculator (Grid), UMEP Documentation, 2023. Available online: https://umep-docs.readthedocs.io/en/latest/pre-processor/Urban%20Morphology%20Morphometric%20Calculator%20(Grid).html (accessed on 17 February 2025).
30. Kent, C.W.; Grimmond, S.; Barlow, J.; Gatey, D.; Kotthaus, S.; Lindberg, F.; Halios, C.H. Evaluation of Urban Local-Scale Aerodynamic Parameters: Implications for the Vertical Profile of Wind Speed and for Source Areas. *Bound.-Layer Meteorol.* **2017**, *164*, 183–213. [CrossRef] [PubMed]
31. Kanda, M.; Inagaki, A.; Miyamoto, T.; Gryschka, M.; Raasch, S. A New Aerodynamic Parametrization for Real Urban Surfaces. *Bound.-Layer Meteorol.* **2013**, *148*, 357–377. [CrossRef]
32. Javanroodi, K.; Nik, V.M. Interactions between extreme climate and urban morphology: Investigating the evolution of extreme wind speeds from mesoscale to microscale. *Urban Clim.* **2020**, *31*, 100544. [CrossRef]
33. Feustel, H.E. COMIS—An international multizone air-flow and contaminant transport model. *Energy Build.* **1999**, *30*, 3–18. [CrossRef]
34. Fsolve. Available online: https://it.mathworks.com/help/optim/ug/fsolve.html (accessed on 10 January 2025).
35. Emmerich, S.J.; Persily, A.; Mcdowell, T. Impact of Infiltration on Heating and Cooling Loads in U.S. Office Buildings, Building and Fire Research Laboratory, National Institute of Standards and Technology. Available online: https://www.researchgate.net/publication/265919110_Impact_of_Infiltration_on_Heating_and_Cooling_Loads_in_US_Office_Buildings (accessed on 10 January 2025).
36. Emmerich, S.J.; Persily, A.K. U.S commercial building airtightness requirements and measurements. In Proceedings of the AIVC Conference 2011, Brussels, Belgium, 12–13 October 2011. Available online: https://www.aivc.org/resource/us-commercial-building-airtightness-requirements-and-measurements (accessed on 30 January 2025).

37. Herring, S.J.; Batchelor, S.; Bieringer, P.E.; Lingard, B.; Lorenzetti, D.M.; Parker, S.T.; Rodriguez, L.; Sohn, M.D.; Steinhoff, D.; Wolski, M. Providing pressure inputs to multizone building models. *Build. Environ.* **2016**, *101*, 32–44. [CrossRef]
38. LivingLAB@polito.it—Ambiente Esterno. Available online: https://smartgreenbuilding.polito.it/monitoraggio/esterno.asp (accessed on 16 December 2024).

energies

MDPI

Article

Numerical Research on Mitigating Soil Frost Heave Around Gas Pipelines by Utilizing Heat Pipes to Transfer Shallow Geothermal Energy

Peng Xu [1,*] and Yuyang Bai [1,2]

[1] Beijing Key Lab of Heating, Gas Supply, Ventilating and Air Conditioning Engineering, Beijing University of Civil Engineering and Architecture, Beijing 100044, China
[2] Beijing Institute of Public Utilities Science Co., Ltd., Beijing 100011, China; byy_0616@163.com
* Correspondence: xupeng@bucea.edu.cn

Abstract: Frost heave in seasonally frozen soil surrounding natural gas pipelines (NGPs) can cause severe damage to adjacent infrastructure, including road surfaces and buildings. Based on the stratigraphic characteristics of seasonal frozen soil in Beijing, a soil–natural gas pipeline–heat pipe heat transfer model was developed to investigate the mitigation effect of the soil-freezing phenomenon by transferring shallow geothermal energy utilizing heat pipes. Results reveal that heat pipe configurations (distance, inclination angle, etc.) significantly affect soil temperature distribution and the soil frost heave mitigation effect. When the distance between the heat pipe wall and the NGP wall reaches 200 mm, or when the inclined angle between the heat pipe axis and the model centerline is 15°, the soil temperature above the NGP increases by 9.7 K and 17.7 K, respectively, demonstrating effective mitigation of the soil frost heave problem. In the range of 2500–40,000 W/(m·K), the thermal conductivity of heat pipes substantially impacts heat transfer efficiency, but the efficiency improvement plateaus beyond 20,000 W/(m·K). Furthermore, adding fins to the heat pipe condensation sections elevates local soil temperature peaks above the NGP to 274.2 K, which is 5.5 K higher than that without fins, indicating enhanced heat transfer performance. These findings show that utilizing heat pipes to transfer shallow geothermal energy can significantly raise soil temperatures above the NGP and effectively mitigate the soil frost heave problem, providing theoretical support for the practical applications of heat pipes in soil frost heave management.

Keywords: gas pipeline; soil frost heave; heat pipes; shallow geothermal energy

1. Introduction

High-pressure gas is transported from the upstream pipeline to the city gate station and then enters the urban gas pipeline network after pressure reduction. During this process, the rapid expansion of natural gas in pressure-regulating valves causes a sharp temperature drop in the pipeline due to the Joule–Thomson effect [1]. Consequently, the downstream natural gas temperature may fall below the soil freezing point, inducing frost heave in surrounding soils alongside the natural gas pipelines (NGPs). In view of the destructive impacts of soil frost heave on public infrastructure, researchers have proposed various mitigation strategies, such as soil replacement, adiabatic thermal insulation, preheating, isolation, and drainage methods [2,3]. While these measures can partially alleviate the soil frost heave problem, they often fail to achieve the expected effect due to the high cost in

practice. Consequently, developing more efficient and sustainable solutions to mitigate frost heave around NGPs remains imperative.

In recent years, a growing number of scholars have started to explore the use of renewable energy as a means to mitigate the issue of soil frost heave. Zhang et al. [4] employed a solar cycle heating embankment system for roadbed frost heave mitigation. Li et al. [5] utilized electric heating cables to balance soil temperatures around pipelines. Huang et al. [6,7] investigated geothermal energy applications for similar purposes. However, these approaches typically rely on heat pumps for heat transfer, facing challenges such as system complexity, high energy consumption, and limited environmental adaptability. To further enhance heat transfer efficiency, emerging studies attempted to combine heat pipes with heat pumps to achieve more efficient heat transfer and soil frost heave management.

As an efficient heat conductor, the heat pipe consists of three functional segments: the evaporation section, the adiabatic section, and the condensation section. In the evaporation section, the liquid working fluid undergoes a phase change to a gaseous state by absorbing heat from the outside heat source and flows toward the condensation section. After exchanging heat with the cold outside environment, it condenses back to the liquid phase, returns to the evaporation section by gravity, and continues to absorb heat in the evaporation section, thus repeating the cycle [8]. Heat pipes have gained prominence in geothermal applications, renowned for their exceptional thermal conductivity, working without external energy, temperature self-regulation, long-term stability, environmental resilience, compact structure, and easy maintenance, etc. [9–11]. Aiming at the geological and meteorological characteristics of China's cold regions, Wu et al. [12] analyzed the heat transfer and freezing process of heat pipe technology for preventing and controlling foundation freezing through numerical simulation, focusing on the effects of climatic conditions, soil properties, and heat pipe geometry on seasonal freezing, which provided a design basis for the application of heat pipe technology. Li et al. [13] established a thermo-hydro-mechanical coupled model for simulating geothermal heat transfer in saturated frozen soils under varying stress levels. Hu [14] established a distributed heating system combining heat pipes with geothermal heat pumps to sustainably mitigate soil frost heave in a 20 m railway subgrade subjected to seasonal freeze–thaw cycles. Deng et al. [15] designed a gravity heat pipe system utilizing shallow geothermal energy to solve the problem of frost damage in the root zone of grapes in Ningxia. Numerical simulations showed that the heat pipe formed a medium-temperature impact zone in the soil with a horizontal diameter of 30.8 cm and a vertical diameter of 32.8 cm, which warmed the soil in the root zone by an average of 7.0 °C and significantly reduced the frost damage.

Despite these advancements, direct utilization of shallow geothermal energy via heat pipes for soil frost heave mitigation around NGPs remains underexplored. Shallow geothermal energy refers to the energy source stored in soils, rocks, and groundwater within a certain depth of the ground that maintains stable temperatures, typically ranging from 10 °C to 25 °C [16]. By using heat pipes, the shallow geothermal energy can be transferred from underground to the soil around NGPs to increase the local soil temperature, thus alleviating the phenomenon of soil freezing, which is of practical significance for guaranteeing the safety and stability of buildings, roads, and other infrastructures.

This work focuses on the investigation of the direct use of shallow geothermal energy by utilizing heat pipes to address soil frost heave around NGPs. Through an in-depth investigation into the operational characteristics of heat pipes in shallow geothermal energy transfer, their coupling relationship with soil frost heave, and the optimal design of heat pipe systems, Fluent software was employed to simulate heat pipes under various positions and parameters. This study provides an efficient and sustainable novel approach for preventing frost heave in gas transmission pipelines while offering theoretical support

for the application of heat pipe heat conduction as a solution to mitigate seasonal soil frost heaving.

2. Modeling

2.1. Geometric Configuration

Based on geological conditions in actual frost heave zones around NGPs, a soil–NGP–heat pipe heat transfer model is developed, as shown in Figure 1. The spatial domain of the geometric model is 10 m × 5 m × 12 m (L × W × H). According to the requirements of the Chinese National Standard GB50028-Code for the design of city gas engineering, the design burial depth of urban gas buried pipelines should ensure that the thickness of the soil covering the top of the pipe (the vertical distance from the original soil layer surface to the top of the pipe) is not less than 0.9 m., In accordance with the actual conditions of certain buried high-pressure pipelines in Beijing, the pipe diameter in the geometric model is specified as DN500, with a burial depth of 2 m, and the heat pipes are inserted into the soil on both sides along the NGP.

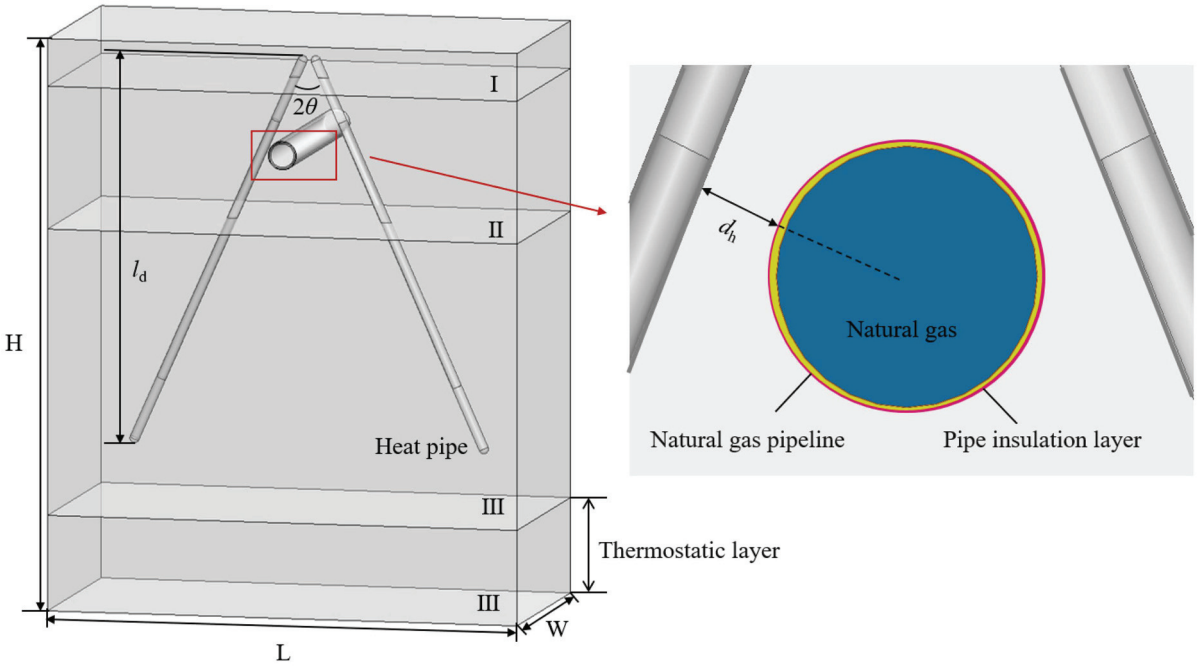

Figure 1. Soil–NGP–heat pipe heat transfer model. (I. silty clay; II. sandy clay–silty clay α; III. sandy clay–silty clay β).

To enhance the heat transfer performance of the heat pipes, fins can be added to their condensation section to increase the contact area with the surrounding soil. To further enhance the heat transfer performance of the heat pipe, additional fins were added to the heat pipe to increase the heat transfer contact area between the heat pipe and the soil, as shown in Figure 2. The spacing and number of fins were meticulously calculated to optimize the heat transfer efficiency of the heat pipe.

To avoid the overlap of heating areas around heat pipes with added fins, the fin spacing should be large enough. Meanwhile, the total thermal resistance of fins can be minimized with an optimized fin spacing. The specific calculation formula [17] is as follows:

$$R_{fin} = \frac{1}{\eta_{fin} h_{fin} A_{fin}} \quad (1)$$

$$\eta_{fin} = \frac{\tanh_{fin}(nL_{fin})}{nL_{fin}} \tag{2}$$

where R_{fin}, η_{fin}, A_{fin}, h_{fin}, L_{fin}, and n are the thermal resistance, efficiency, total surface area, convective heat transfer coefficient , height, and form factor of the fins, respectively.

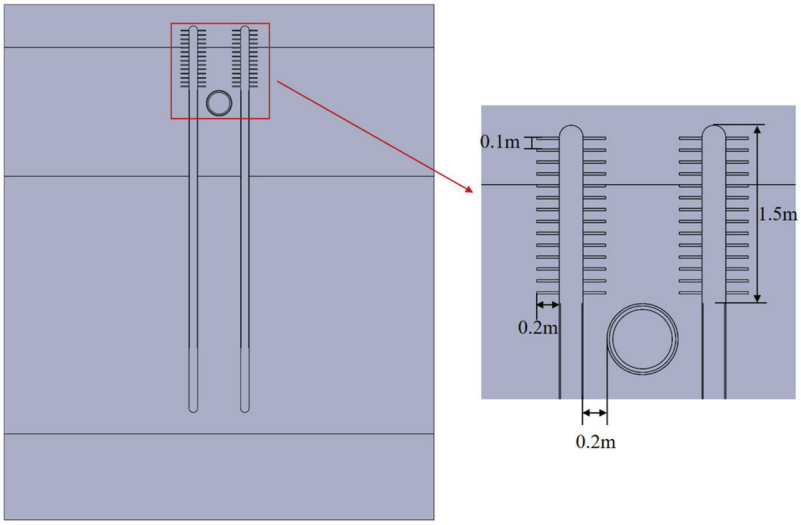

Figure 2. Simplified model of heat pipes with added fins.

There exists an appropriate fin spacing, which can be specifically calculated as follows [18]:

$$b = \frac{1}{\sqrt{\frac{1}{h_{fin}} \times \frac{2\delta_{fin}}{k_{fin}} \times \tanh_{fin}(nL_{fin})}} \tag{3}$$

$$n = \sqrt{\frac{h_{fin}P}{k_{fin}\delta_{fin}}} \tag{4}$$

where b, δ_{fin}, and k_{fin} are the spacing, thickness, and thermal conductivity of the fins, respectively.

Based on the above calculation, the optimal fin pitch is determined as 100 mm, and 15 fins are equidistantly installed along the 1.5 m condensation section to maximize the heat transfer process.

2.2. Assumptions

1. The flow velocity of the working fluid liquid film in the heat pipe is typically low, constrained by the pipe wall, and is generally characterized as being in a laminar flow regime.
2. At the macroscopic scale, soil is approximated as an isotropic porous medium with physical properties independent of spatial orientation.
3. The particles in the soil are considered as rigid, with negligible volume changes during the freezing process.
4. Moisture migration in soil occurs at a sufficiently slow rate, which exerts a negligible impact on the heat transfer process.
5. The latent heat effects from ice–water phase change in frozen soil layers are insignificant to the overall heat transfer process.
6. Within heat pipes, vapor flow is relatively independent of liquid film flow, so its effect on the liquid film flow is neglected.

7. Under normal operating conditions, the vapor is typically in a saturated state, and it is assumed that its temperature distribution is uniform.

These basic assumptions appropriately balance model simplification with result reliability, which reduces the computational demands while maintaining physical validity for subsequent frost heave mitigation simulations.

2.3. Heat Transfer Process

The heat transfer process can be categorized into the following three stages.

2.3.1. Heat Transfer Within the Soil

A porous medium heat transfer model is employed to describe heat transfer within the soil. The governing equations are derived from energy conservation principles, incorporating heat exchange between the liquid and solid phases, as well as thermal conduction effects within the porous medium. The equations are as follows.

(a) Energy Equation:

$$\frac{\partial}{\partial t}[(\rho c_p)_{eff,s} T_s] + \frac{\partial}{\partial x}[(\rho c_p)_{eff,s} u_x] + \frac{\partial}{\partial y}[(\rho c_p)_{eff,s} u_y] + \frac{\partial}{\partial z}[(\rho c_p)_{eff,s} u_z] = \frac{\partial}{\partial x}(k_{eff,s}\frac{\partial T_s}{\partial x}) + \frac{\partial}{\partial y}(k_{eff,s}\frac{\partial T_s}{\partial y}) + \frac{\partial}{\partial z}(k_{eff,s}\frac{\partial T_s}{\partial z}) \quad (5)$$

(b) Continuity Equation:

$$\frac{\partial \rho_w}{\partial t} + \frac{\partial(\rho_w u_x)}{\partial x} + \frac{\partial(\rho_w u_y)}{\partial y} + \frac{\partial(\rho_w u_z)}{\partial z} = 0 \quad (6)$$

(c) Momentum Equations:

Z-direction:

$$\frac{\rho_w}{\varepsilon}\frac{\partial u_z}{\partial \tau} + \frac{\rho_w}{\varepsilon^2}(u_z\frac{\partial u_z}{\partial z} + u_r\frac{\partial u_z}{\partial r}) = \frac{\mu_w}{\varepsilon}(\frac{\partial^2 u_z}{\partial z^2} + \frac{\partial^2 u_z}{\partial r^2}) - \frac{\partial p}{\partial z} + S_z + S_b \quad (7)$$

R-direction:

$$\frac{\rho_w}{\varepsilon}\frac{\partial u_r}{\partial \tau} + \frac{\rho_w}{\varepsilon^2}(u_z\frac{\partial u_r}{\partial z} + u_r\frac{\partial u_r}{\partial r}) = \frac{\mu_w}{\varepsilon}(\frac{\partial^2 u_r}{\partial z^2} + \frac{\partial^2 u_r}{\partial r^2}) - \frac{\partial p}{\partial r} + S_r \quad (8)$$

where $(\rho c_p)_{eff,s}$, $k_{eff,s}$ are the effective volumetric heat capacity and the effective thermal conductivity of the soil, respectively; $u_{x,y,z}$ is the velocity of the pore water in the x, y, and z directions; x, y, z, and r are the axial and radial coordinates; ρ_w, μ_w are the density and dynamic viscosity of the water, respectively; p is the pressure; ε is the porosity of the soil; S is the source term (values referenced from the literature [19]).

The key parameters include the effective volumetric heat capacity and effective thermal conductivity of the soil, which can be calculated as follows:

$$(\rho c_p)_{eff,s} = \theta_s \rho_s C_s + (1-\theta_s)\rho_p c_p \quad (9)$$

$$\rho_p = \rho_i + H(T) \times (\rho_w - \rho_i) \quad (10)$$

$$C_p = C_i + H(T) \times (C_w - C_i) \quad (11)$$

$$k_p = k_i + H(T) \times (k_w - k_i) \quad (12)$$

$$k_{eff,s} = k_s^{\theta_s} \times k_p^{(1-\theta_s)} \quad (13)$$

where θ_s is the volume fraction of the soil, c_s is the specific heat capacity of dry soil, ρ_s is the density of dry soil, c_p is the specific heat capacity of water or ice in soil pores, ρ_p is

the density of water or ice in the pores of the soil, k_s is the thermal conductivity of dry soil, c_w is the specific heat capacity of water, c_i is the specific heat capacity of ice, ρ_i is the density of ice, k_p is the thermal conductivity of water or ice in soil pores, k_w is the thermal conductivity of water, k_i is the thermal conductivity of ice, and $H(T)$ is the step function with temperature as an independent variable [20].

2.3.2. Heat Transfer Between the Soil and the Heat Pipes

Heat transfer between the heat pipe and the soil relies mainly on convective heat transfer between the air around the heat pipe and the air and moisture in the soil. The formula is as follows:

$$q = -\overline{h}\Delta T \tag{14}$$

where q is the heat transfer between heat pipes and soil per unit time, $\overline{h}$ is the average convective heat transfer coefficient of a heat pipe, and ΔT is the temperature difference.

The average convective heat transfer coefficient is calculated as follows [21]:

$$\overline{h} = \frac{1}{L}\int_0^L hdl = 0.943\left\{\frac{\rho_l g\lambda_l^3(\rho_l - \rho_v)\left[h_{fg} + 0.68c_{pl}(T_{sat} - T_w)\right]}{\mu_l L(T_{sat} - T_w)}\right\} \tag{15}$$

where L is the effective length of heat transfer from a heat pipe, h is the local convective heat transfer coefficient of a heat pipe, ρ_l is the density of the liquid working fluid, ρ_v is the density of the steam working fluid, λ_l is the thermal conductivity of the liquid film, c_{pl} is the specific heat capacity of the working fluid, T_{sat} is the saturation temperature of the working fluid, and T_w is the wall temperature.

The fundamental heat transfer equation for heat pipes is

$$Q = \dot{m} \cdot h_{fg} \tag{16}$$

$$\dot{m} = \frac{\rho_l A_l \mu_l}{1 - v} \tag{17}$$

where Q is the capacity of heat transfer, $\dot{m}$ is the circulating mass flow rate of working fluid, h_{fg} is the latent heat of vaporization of working fluid, A_l is the cross-sectional area of the liquid working fluid flow, μ_l is the velocity of the liquid working fluid, and v is the volume fraction of the steam working fluid.

2.3.3. Heat Transfer Inside the Heat Pipes

A multiphase flow model was adopted to simulate the heat transfer process inside the heat pipes. The governing equations include the following:

(a) Continuity Equation:

$$\frac{\partial A_{pipe}\rho_l}{\partial t} + \nabla_t(A\rho_l u_l \vec{e_t}) = 0 \tag{18}$$

(b) Equation for Conservation of Momentum:

$$\rho_l \frac{\partial u_l}{\partial t} = -\nabla_t p_l \vec{e_t} - \frac{1}{2} f_D \frac{\rho_l}{d_{pipe}} |u_l| u_l \tag{19}$$

(c) Equation for conservation of energy:

$$\rho_l A_{pipe} c_{pl} \frac{\partial T_l}{\partial t} + \rho_l A c_{pl} u_l \vec{e_t} \nabla_t T_l = \nabla_t \times (A k_l \nabla_t T_l) + \frac{1}{2} f_D \frac{\rho_l A}{d_{pipe}} |u_l| u_l^2 + Q_{wall} \quad (20)$$

where $\vec{e_t}$ is the tangential vector in the direction of the pipe, ∇_t is a differential operator in the pipe coordinates, f_D is the friction factor that depends on the Reynolds number, d_{pipe} is the diameter of the heat pipe, p_{pipe} is the pressure inside the heat pipe, T_l is the temperature of the liquid working fluid, and Q_{wall} is the rate of heat transfer per unit length through the pipe wall.

2.4. Mesh Partitioning and Independence Testing

The simulation domain is discretized with a mixture of triangular and quadrilateral cells, as shown in Figure 3. Typically, the refinement of mesh cells will be beneficial for obtaining simulation results that are closer to reality, but it will lead to higher computational costs. To balance the calculation accuracy and cost, grid independence tests were carried out on the established model and the research problem. Soil temperature at 1 m depth along the model centerline is selected as a criterion of mesh quality, as shown in Figure 4, and its temperature convergence diagram is shown in Figure 5.

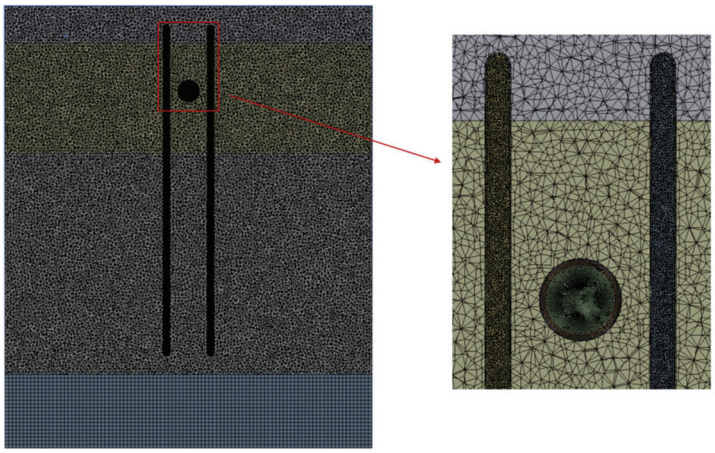

Figure 3. Meshing view.

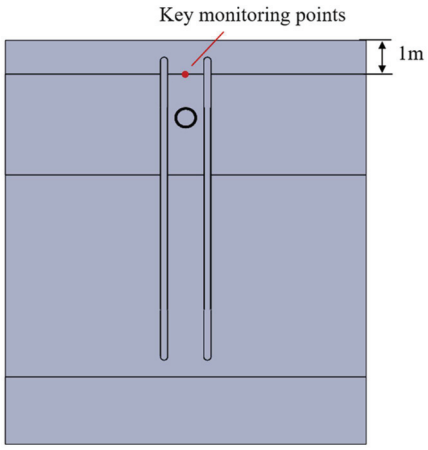

Figure 4. Schematic diagram of key monitoring points for mesh quality comparison.

The results show that when the total mesh count exceeds 5.02 million, temperature variations at the monitoring point are below 0.1% (Figure 6). Further mesh refinement yields no significant computational accuracy improvement but will increase the computational

cost. So, the mesh system with 5.02 million cells is optimal for the problem investigated in this work.

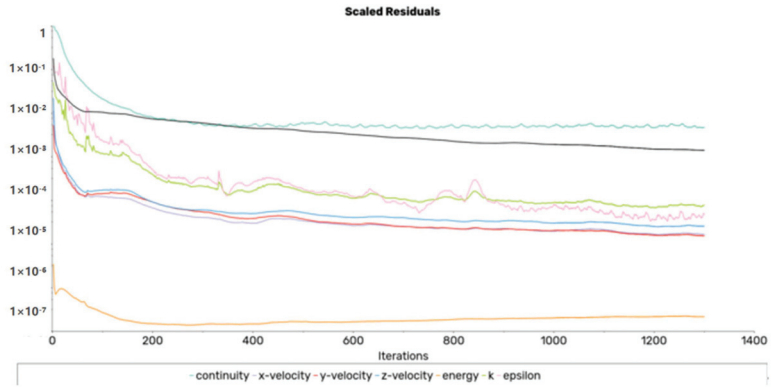

Figure 5. Convergence plot of temperatures at key monitoring points.

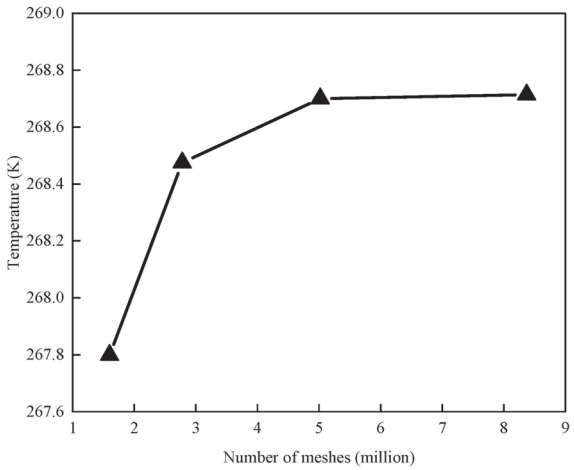

Figure 6. Mesh independence test.

3. Results and Discussion

3.1. Setting of the Working Conditions

Taking the Beijing area as a case study, the soil distribution in the frost heave zones surrounding NGPs primarily consists of clayey silt (fill) and clayey sandy silt. The stratigraphic configuration is illustrated in Figure 7, with the specific soil property parameters for different strata listed in Table 1 [22].

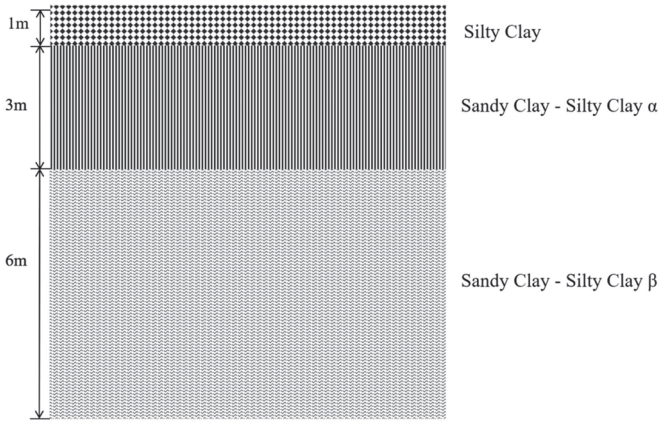

Figure 7. Selected soil stratigraphic characteristics [19,20].

Table 1. Soil characteristic parameter [22].

Soil Types	Density (kg/m^3)	Specific Heat Capacity (J/(kg·K))	Thermal Conductivity (W/(m·K))	Porosity
Silty Clay	1950	1460	1.695	0.43
Sandy Clay–Silty Clay α	1970	1370	1.627	0.68
Sandy Clay–Silty Clay β	1970	1370	1.627	0.73

By integrating the literature [23] and relevant data from the Chinese Soil Database, it can be concluded that when the soil depth in Beijing reaches 15 m, the soil temperature remains stable and is no longer influenced by fluctuations in ambient air temperature. Based on simulation analysis (as shown in Figure 8), a constant-temperature soil layer at a depth of 10–12 m with a temperature of 10 °C was ultimately selected as the heat source.

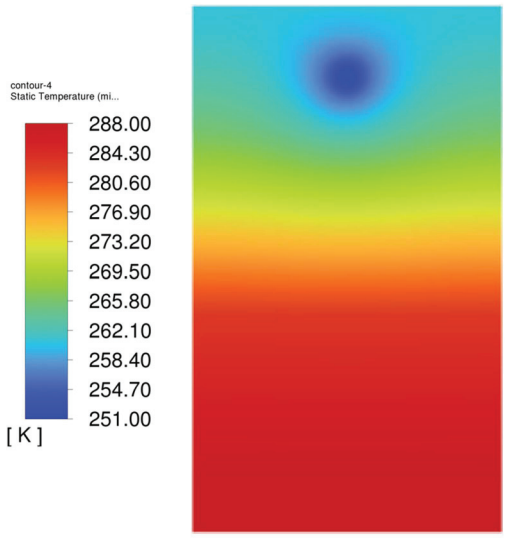

Figure 8. Temperature distribution map of the frost heave area of the soil around the gas pipeline at a depth of 0–15 m.

The specific parameters of NGPs are shown in Table 2.

Table 2. Specific parameters of gas pipelines [24].

Name	Material	Density (kg/m^3)	Specific Heat Capacity (J/kg·K)	Thermal Conductivity (W/m·K)	Thickness (mm)
Gas pipeline	Carbon steel	7850	480	52	16
Insulation layer	Polyurethane foam	45	1.72	0.022	8

The heat pipes employed in the work are made of copper, with the key geometric parameters of the heat pipes being an outer diameter of 200 mm, total length of 9 m (1.5 m in condensation section, 1.5 m in evaporation section, and 6 m in adiabatic section), and thermal conductivity of 20,000 W/(m·K). Ethanol is selected as the working fluid inside the heat pipes, with its physical properties being listed in Table 3.

Table 3. Physical properties of ethanol [25].

Specific Heat Capacity (kJ/kg·K)	Boiling Point (K)	Freezing Point (K)	Latent Heat of Vaporization (kJ/kg)	Viscosity (mPa·s)
2.42	280.8 [1]	159.1	831	0.594

[1] The data are taken at 90% of the standard atmospheric pressure in a vacuum.

Natural gas will experience a sudden temperature drop due to the Joule–Thomson effect when passing through the throttling valve at the gas gate station. The coefficient of Joule Thomson coefficient is defined as

$$\mu_{JT} = \frac{T_{\mathrm{m}} - T_b}{P_{\mathrm{m}} - P_{\mathrm{b}}} \tag{21}$$

where μ_{JT} is the coefficient of Joule–Thomson coefficient, T_m is the temperature of the gas before passing through the throttle valve, T_b is the temperature of the gas after passing through the throttle valve, P_m is the pressure of the gas before passing through the throttle valve, P_b is the pressure of the gas after passing through the throttle valve.

According to the gas pressure difference and ambient temperature before and after the throttle valve, μ_{JT} can be determined as 3.713 K/MPa from the check table [26]. Substituting into Equation (21), the post-throttling gas temperature is calculated as -22 °C.

In this work, the influences and mitigation effects of heat pipes on the seasonal soil frost heave problem are evaluated from the following five perspectives:

To analyze the mitigation effects of the distance between pipeline and heat pipe (DPHP) on the soil frost heave problem, eight simulation scenarios with DPHP values from 50 mm to 400 mm at 50 mm intervals were conducted.

1. To see the mitigation effects of the angle between the central axis of the heat pipe and the model centerline (AHPAMC) on the soil frost heave problem, six simulation cases with the AHPAMC ranging from 15° to 30° at 3° increments were conducted.
2. To explore the mitigation effects of heat source temperatures caused by different heat pipe insertion depths (HPIDs) on the soil frost heave problem, seven simulation cases with HPID changing from 9 m to 15 m at 1 m intervals were studied.
3. To evaluate the effects of heat pipe thermal conductivity (HPTC) on the soil frost expansion problem, five scenarios were simulated with HPTC values starting at 2500 W/(m·K) and increasing by factors of two, four, eight, and sixteen successively.
4. To analyze the mitigation effects of extra added fins on the soil frost heave problem, a typical scenario with a DPHP of 200 mm was simulated, where extra fins were added in the condensation section of the heat pipes.

3.2. Effects of Heat Pipe Positioning and Parameters on Soil Temperature Distribution

3.2.1. Effect of Thermal Conductivity

Figure 9 illustrates the temperature distribution along the model centerline under various HPTC conditions. From the single curve with HPTC of 2500 W/(m·K), it can be seen that in the depth range of 0–1 m, the soil temperature shows an increasing trend, which is due to the release of heat from the condensing section of the heat pipe, which raises the soil temperature. In the 1–2 m depth range, the soil temperature starts to decrease, which is due to the high speed transportation of low temperature gas in the NGP, which releases cold. It can be seen that a local temperature peak appears in the soil above NGPs at a depth of 1 m. Beyond 2.5 m depth, the soil temperature gradually increases with depth but at a diminishing rate. Thereafter, the temperature rise accelerates significantly beyond 9 m depth, and then stabilizes near the thermostatic layer at 10 m depth.

Further comparison demonstrates that the heat transfer capacity of heat pipes can be enhanced with the increase in HPTC. The local soil temperature peak above the NGP (around 1 m depth) rises from 261.9 K to 269.3 K when HPTC is increased from 2500 W/(m·K) to 40,000 W/(m·K). However, the differences in local temperature peak are only increasing by 0.6 K when HPTC is 20,000 W/(m·K) and 40,000 W/(m·K), indicating that the sensitivity of soil temperature to HPTC decreases when it is already at a high level. That is to say, the further increase in HPTC has a reduced enhancement on improving the heat transfer process. Thus, it is crucial to appropriately select HPTC for optimizing soil temperature fields around NGPs and thus to mitigate frost heave problems with an affordable requirement of heat pipes.

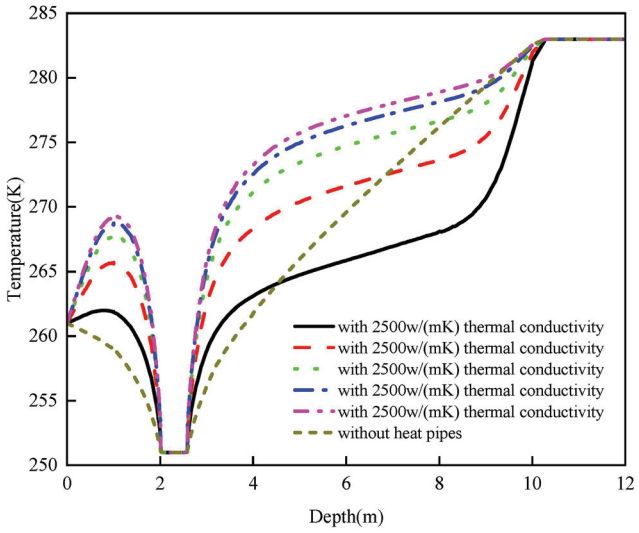

Figure 9. Soil temperature distribution at the model centerline under various HPTC conditions.

Considering the manufacturing costs and technical challenges in achieving ultra-high conductivity, heat pipes with thermal conductivity of 20,000 W/(m·K) were selected for the subsequent investigations.

3.2.2. Effect of Heat Pipe Insertion Depth

Figure 10 shows the temperature distribution contours under different HPID (l_d) conditions. When l_d is 8.5 m, the relatively low soil temperature at the evaporation section of heat pipes limits the heat exchange efficiency with the surrounding soil, so that the soil temperature around the NGP is not significantly elevated. With the increase of HPID, the soil temperature in the localized area above the NGP increases.

The optimal heating state of heat pipes occurs when l_d is increased to 14.5 m, where the soil temperature at 1 m depth is significantly higher than that when l_d is only 8.5 m. It can be found from Figure 10 that when l_d is larger than 9.5 m, heat pipes can effectively elevate the soil temperatures around the NGP, thus guaranteeing the soil temperature stability here and reducing the soil freezing potential.

Figure 11 plots the soil temperature distribution along the model centerline under various HPID conditions. It is revealed that with the increase of HPID, the local peak soil temperature above the NGP shows an upward trend, rising from 266.7 K to 271.4 K when l_d is increased from 8.5 m to 14.5 m. When l_d is increased to 14.5 m, the local peak soil temperature above the NGP is 12.4 K higher than that without heat pipes. Comparatively, when l_d is only 8.5 m, the local peak soil temperature at the same location is only 4.7 K higher than that without heat pipes. With the increase of HPID, the bottom of the heat pipe gets deeper, and the soil temperature at the evaporation section is higher, so more

heat can be absorbed by the evaporation section. So, the elevation of soil temperature above NPG is higher when HPID is increased. However, the increased amplitude in the local peak soil temperature gradually decreases when HPID is continuously increased. This indicates that there exist threshold effects of HPID on soil temperature improvement, when HPID is increased to a certain value, its further increase in depth tends to have a weak effect on soil temperature at a depth of 1 m above the NGP. Considering the rising construction complexity with the increase of HPID, l_d of 9.5 m is selected as the optimal insertion depth of heat pipes in this work. With this insertion depth, the relatively high soil temperature at the bottom of the heat pipes can be effectively utilized to enhance the heat transfer characteristics of the heat pipe, to achieve acceptable regulation of soil temperature above the NGP. Meanwhile, the excessive increase in cost and construction difficulty due to larger insertion depth can be avoided.

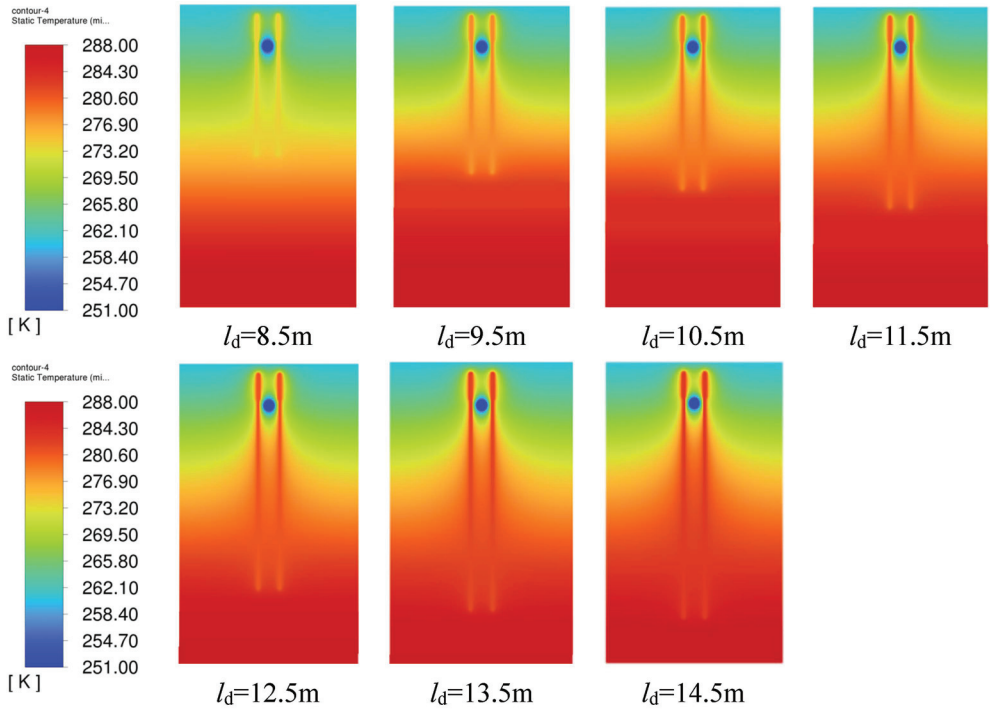

Figure 10. Temperature contour under various HPID conditions.

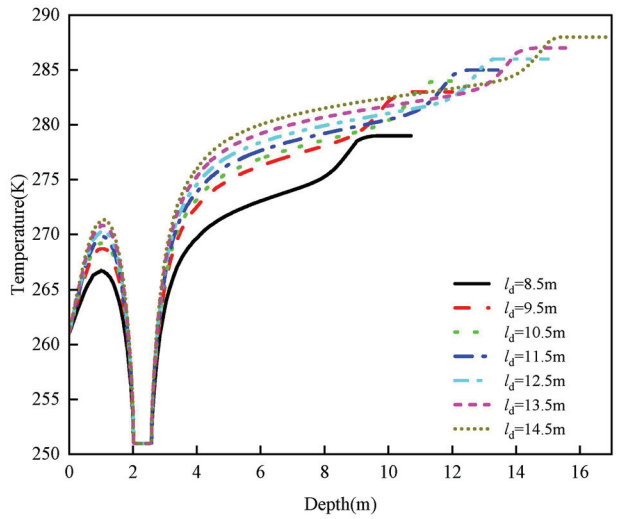

Figure 11. Soil temperature distribution at the model centerline under various HPID conditions.

3.2.3. Effect of Heat Pipe Insertion Depth

Figure 12 presents the temperature distribution contours under different DPHP (d_h) conditions. When d_h is set as 200 mm, the thermal influence zones of heat pipes on the two sides of the NGP start to overlap. When dh is reduced to 50 mm, the heating effect is the best, and the local peak soil temperature at 1 m depth is increased by 12.6 K compared with that without a heat pipe.

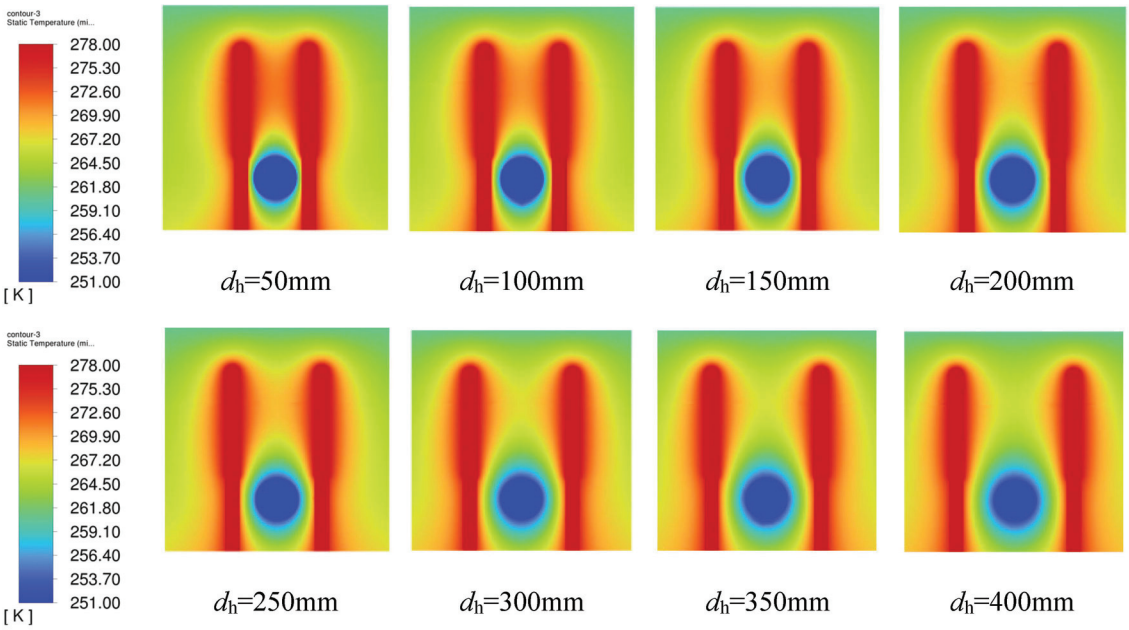

Figure 12. Local temperature contour under various DPHP conditions.

Figure 13 shows the soil temperature distribution along the model centerline under various DPHP conditions, where the local peak soil temperature above the NGP increases significantly with the decrease of the DPHP. When the DPHP is decreased from 400 mm to 50 mm, the local peak soil temperature above the NGP increases from 266.0 K to 271.6 K. The reason is that when the DPHP is decreased, the heat transferred by heat pipes is more concentrated in a small region above the NGP; thus, a more pronounced temperature increase here can be witnessed. However, although the heating effect of heat pipes on the soil above the NGP is most significant when d_h is 50 mm, heat absorption at the bottom of the heat pipes is too concentrated. Since the simulation domain is limited in this work, the heat of the thermostatic layer is difficult to fully make up for the missing heat, which tends to form a large temperature gradient near the heat pipe. Furthermore, in the practical application process, this will lead to a significant temperature difference between the soil near and far away from the heat pipes, thus resulting in a series of potential problems, such as non-uniformity of soil thermal stress, reduction of the heat transfer efficiency of heat pipes, and eventually, the possible performance degradation of heat pipes in long-term operation.

With comprehensive consideration of the effects of DPHP on soil temperature distribution, heat transfer efficiency of heat pipe, and the temperature recovery characteristics of the thermostatic layer, d_h of 200 mm is more reasonable for the investigated condition. With this distance, the heating effect of heat pipes to the soil can be ensured, with the local peak soil temperature above the NGP reaching 268.7 K. Meanwhile, the problem of excessively concentrated heat absorption at the bottom of the heat pipe can be avoided, to ensure the long-term stable operation of the heat pipe system.

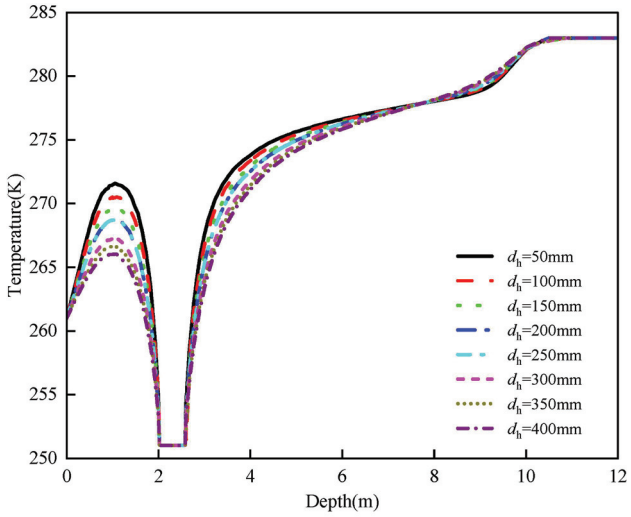

Figure 13. Soil temperature distribution at the model centerline under various DPHP conditions.

3.2.4. Effect of the Angle Between the Central Axis of the Heat Pipe and the Model Centerline

Figure 14 plots the local soil temperature distribution contours under different AHPAMC (θ) conditions. When θ is set as 15°, an obvious high-temperature zone is formed at the ends of heat pipes and around the NGP, indicating that the heat transported from the bottom thermostatic layer is mainly concentrated near the heat pipes and NGP. When θ is increased to 30°, the heating region is no longer confined to a specific small area. This indicates that with the increase in the AHPAMC, the heating area of heat pipes expands, and the high-temperature zone is not concentrated in a narrow area.

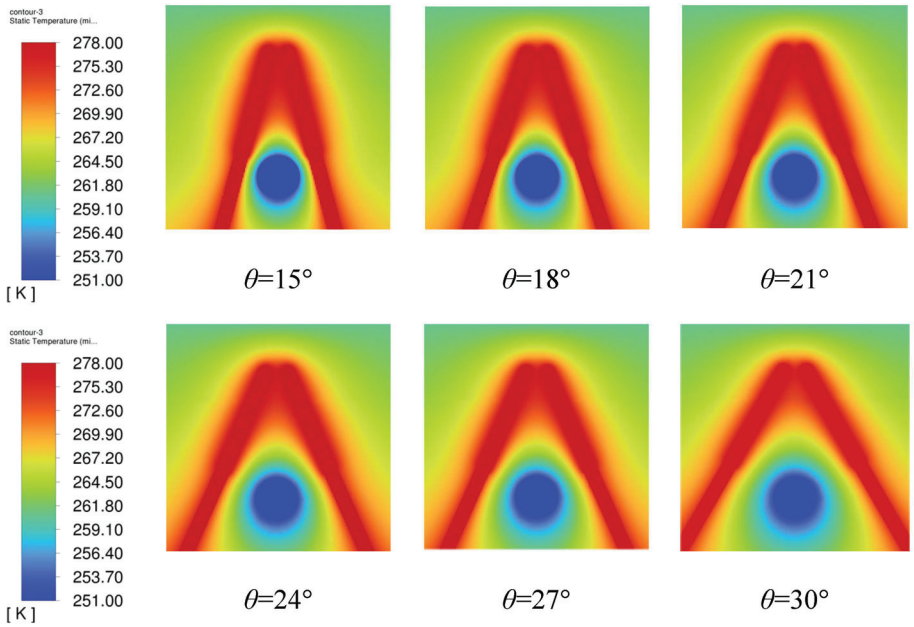

Figure 14. Local temperature contour under various AHPAMC conditions.

Figure 15 plots the soil temperature distribution along the model centerline under different DPHP conditions. It is clear that a local peak soil temperature appears above the NGP at a depth of 0.6 m. Beyond 2.5 m depth, the soil temperature gradually increases as the soil depth continues to increase, and then stabilizes until it reaches the thermostatic temperature at 10 m depth.

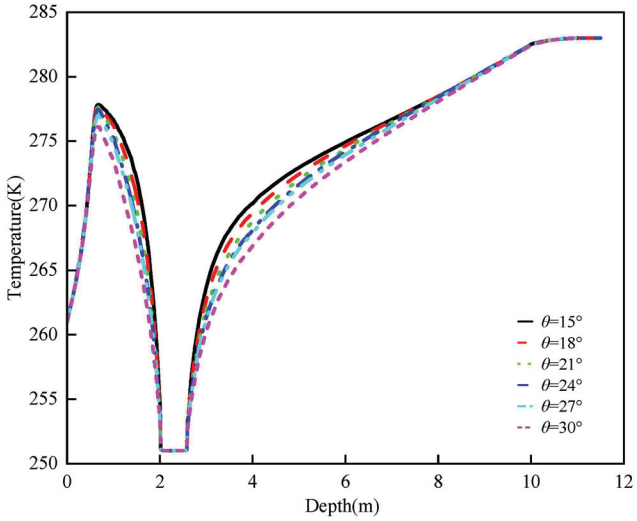

Figure 15. Soil temperature distribution at the model centerline under various AHPAMC conditions.

With the increase in θ, the increased amplitude of soil temperature above the NGP shows a decreasing trend. Beyond 2 m depth, the variation trend of the temperature curve under different conditions remained consistent, although slight differences still exist in the temperature recovery rates. When θ is 15°, the local peak soil temperature above the NGP is 276.7 K, which is 17.7 K higher than that without heat pipes. Meanwhile, compared with the condition with θ of 30°, the local peak soil temperature is 1.7 K higher, and the soil temperature at 1 m depth is 3.2 K higher.

It can be concluded from the above analysis that the smaller the AHPAMC is, the more concentrated the heat transferred by heat pipes is, and the stronger its ability to alleviate the soil frost heave problem above the NGP. So, for the investigated scenarios, θ of 15° is recommended.

3.2.5. Effect of Adding Fins to the Heat Pipe

Figure 16 shows the local soil temperature distribution contours in the longitudinal section of the model centerline (width direction of the simulation domain). The red zone represents the concentrated heating area by the heat pipes, and the blue striped zone represents the low-temperature flow area inside the NGP. Due to the high-speed movement of natural gas inside the NGP and the strong thermal inertia of soil, the natural gas temperature change in the NGP is small, which almost remains at 251 K. It can be observed that when the heat transfer area is enlarged by the addition of fins, the heat transfer process is significantly promoted, and the soil temperature above the NGP is improved to a greater extent.

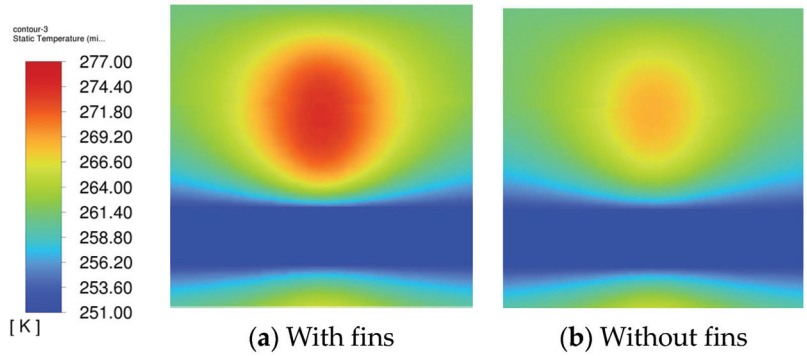

Figure 16. Local temperature contour under whether or not to add fins conditions.

The soil temperature along the model central line is further quantitatively plotted in Figure 17. At a depth of 1 m, the soil temperature above the NGP reaches 274.2 K after adding fins, which is 15.2 K higher than that without a heat pipe and is also 5.5 K higher than that without adding fins. These results demonstrate that the addition of fins can remarkably improve the heat transfer efficiency of heat pipes, thus increasing the soil temperature level above the NGP, which is of great significance in alleviating the soil from frost heave problems.

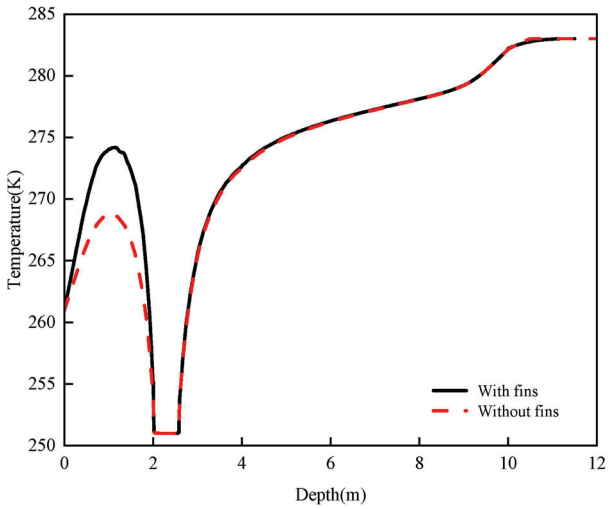

Figure 17. Soil temperature distribution at the model centerline with or without fin conditions.

4. Conclusions

A method of using heat pipes to transfer shallow geothermal energy to mitigate the frost heave problem in seasonal frozen soil around NGPs was proposed, and a soil–NGP–heat pipe heat transfer model was developed to analyze the effects of various parameters on the heat transfer performance and frost heave mitigation effects. Key findings are as follows.

The minimum distance (l_d) between the wall of the heat pipe and the gas pipe wall, the angle (θ) formed between the central axis of the heat pipe and the central axis of the model, as well as the depth (d_h) of the heat pipe's insertion into the ground, all significantly influence the soil temperature distribution and the effectiveness of frost heave mitigation. When l_d is 200 mm or θ is 15°, the heating effect of heat pipes is the most significant, which elevates the local peak soil temperature above the NGP by 9.7 K and 17.7 K, respectively, when compared with that without heat pipes.

The thermal conductivity of heat pipes is vital for soil frost heave mitigation. Simulation analyses revealed that the heat transfer capacity of heat pipes increases as the thermal conductance coefficient rises. However, when the thermal conductance coefficient reaches 20,000 W/(m·K), the enhancement in heat transfer efficiency begins to plateau.

Adding fins to the heat pipe can significantly enhance its heat transfer efficiency. When fins are incorporated, the local peak temperature of the soil above the NGP reaches 274.2 K, which is 5.5 K higher than that without fins.

These findings have demonstrated that the application of heat pipes in frost-heaving soil surrounding NGPs can effectively mitigate soil frost heave. Additionally, the geometric arrangement critically determines performance. At optimal values (l_d = 200 mm, d_h = 9.5 m, adding fins), peak soil temperature rises by 15.2 K, and the soil frost heave displacement is 36% higher compared to the condition with heat pipes. Nevertheless, their specific implementation must be carefully analyzed in conjunction with site-specific conditions to achieve optimal heat transfer performance.

Author Contributions: Conceptualization, P.X.; methodology, P.X. and Y.B.; validation, P.X. and Y.B.; writing—original draft preparation, P.X. and Y.B.; writing—review and editing, P.X.; visualization, P.X. and Y.B. All authors have read and agreed to the published version of the manuscript.

Funding: This research received no external funding.

Data Availability Statement: Data will be made available on request.

Conflicts of Interest: Yuyang Bai was employed by the Beijing Institute of Public Utilities Science Co., Ltd. The remaining author declares that the research was conducted in the absence of any commercial or financial relationships that could be construed as a potential conflict of interest.

References

1. Marić, I. The Joule–Thomson effect in natural gas flow-rate measurements. *Flow Meas. Instrum.* **2005**, *16*, 387–395. [CrossRef]
2. Deng, F.; Lu, J.; Wan, X.; Liu, B.; Zhang, B.; Fu, H. Mitigating frost heave of a soil stabilized with sisal fiber exposed to freeze-thaw cycles. *Geotext. Geomembr.* **2025**, *53*, 394–404. [CrossRef]
3. Tai, B.; Wu, Q.; Yue, Z.; Xu, H. Ground temperature and deformation characteristics of anti-freeze-thaw embankments in permafrost and seasonal frozen ground regions of China. *Cold Reg. Sci. Technol.* **2021**, *189*, 103331. [CrossRef]
4. Zhang, W.; Zhang, D.; Guo, L.; Dong, T.; Wang, J.; Wang, J.; Yu, Q. Experimental study on heating performance of a solar circulating heated embankment system for the treatment of frost heave disease in seasonally frozen regions. *Sol. Energy* **2022**, *248*, 41–50. [CrossRef]
5. Li, X.; Wu, Q.; Jin, H.; Shi, R.; Wu, G.; Cao, Y. Numerical evaluation of the effectiveness of frost heave mitigation strategies for chilled arctic gas pipelines. *Res. Cold Arid Reg.* **2022**, *14*, 338–345. [CrossRef]
6. Chen, J.; Huang, W.; Cen, J.; Li, Z.; Li, F.; Li, A.; Sun, H.; Lin, W.; Ma, Q.; Jiang, F. Operational characteristics of the super-long gravity heat pipe for geothermal energy exploitation. *Appl. Therm. Eng.* **2024**, *236*, 121530. [CrossRef]
7. Huang, W.; Cen, J.; Chen, J.; Cao, W.; Li, Z.; Li, F.; Jiang, F. Heat extraction from hot dry rock by super-long gravity heat pipe: A field test. *Energy* **2022**, *247*, 123492. [CrossRef]
8. Jose, J.; Kumar Hotta, T. A comprehensive review of heat pipe: Its types, incorporation techniques, methods of analysis and applications. *Therm. Sci. Eng. Prog.* **2023**, *42*, 101860. [CrossRef]
9. Liu, W.; Liu, X.; Chow, T.; Hao, Y.; Lau, W.; Pan, C. Thermal characteristics of heat-pipe-ring embedded building façades as both building-integrated and building-attached solar collectors. *Case Stud. Therm. Eng.* **2024**, *60*, 104621. [CrossRef]
10. Alhuyi Nazari, M.; Kumar, R.; Mukhtar, A.; Yasir, A.S.H.M.; Ahmadi, M.H.; Al-Bahrani, M. Geothermal energy for preheating applications: A comprehensive review. *J. Cent. South Univ.* **2023**, *30*, 3519–3537. [CrossRef]
11. Alsagri, A.S.; Chiasson, A.; Shahzad, M.W. Geothermal Energy Technologies for Cooling and Refrigeration Systems: An Overview. *Arab. J. Sci. Eng.* **2022**, *47*, 7859–7889. [CrossRef]
12. Wu, C.; Sun, Z.; Pan, Y. Theoretic study on the technology of applying heat pipe to solving frost heaving. *Chin. J. Geotech. Eng.* **2002**, *24*, 347–350.
13. Li, Z.; Jiang, R.; Tang, A.; Zhu, R. Heat-water-stress Coupling Model for Saturated Frozen Soil under Different Stress Levels. *KSCE J. Civ. Eng.* **2024**, *28*, 4897–4910. [CrossRef]
14. Hu, T.; Zhao, L.; Wang, T.; Yue, Z.; Yuan, Y.; Zhang, Y. Geothermal heat pump solutions for frost heave control in railway subgrades. *Geothermics* **2025**, *127*, 103244. [CrossRef]
15. Deng, G.; Yang, J.; Ma, X.; Kang, N.; He, J.; Li, J. Analysis of temperature response and thermal performance of hybrid gravity heat pipes for winter soil warming of grapevine root systems. *Trans. Chin. Soc. Agric. Eng.* **2025**, *41*, 230–237.
16. Sanner, B. Shallow geothermal energy—History, development, current status, and future prospects. In Proceedings of the European Geothermal Congress 2016, Strasbourg, France, 19–24 September 2016.
17. Yin, J.; Xing, Y.; Wang, S.; Hou, X.; Wang, Z.; Xu, Z. Temperature Response Calculation Model of Energy Storage Finned Tube Based on Thermal Network. *J. Aerosp. Power* **2023**, *38*, 2395–2406.
18. Gan, B. Experimental study on the effect of fin spacing on the heat transfer and flow resistance of plate fin-and-tube heat exchangers. *Energy Res. Inf.* **2018**, *34*, 97–101.
19. Yang, Q.; Yang, T.; Yang, Y.; Shen, J. Numerical and experimental investigations on the effect of skeleton shapes and heat transfer directions on water freezing in porous media. *Int. J. Heat Mass Transf.* **2025**, *236*, 126392. [CrossRef]
20. Wang, G.; Lin, C.; Zhu, L.; Feng, D.-C.; Xin, Y.-Y.; Zhang, F. Performance analyses of two-phase closed thermosyphons for road embankments in the high-latitude permafrost regions. *J. Mt. Sci.* **2023**, *20*, 3138–3153. [CrossRef]
21. Malitha, C.; Rajapaksha, M.; Shankar, V.; Senadheera, S. Improved empirical convection heat transfer coefficient model to predict flexible pavement layer temperatures. *Constr. Build. Mater.* **2024**, *411*, 134206.

22. Zou, M.; Wang, Y.; Liu, Y. The present status and problems of the research on Beijing urban green space soil. *Soil Fertil. Sci. China* **2012**, *3*, 1–6.
23. Wang, W.; Wang, G.; Zhu, X.; Liu, Z. Characteristics and potential of shallow geothermal resources in provincial capital cities of China. *Geol. China* **2017**, *44*, 1062–1073.
24. Zhang, X.; Wang, Z.; Ding, S.; Wang, Z.; Xie, H. Fabrication of Flame-Retardant Ammonium Polyphosphate Modified Phytic Acid-Based Rigid Polyurethane Foam with Enhanced Mechanical Properties. *Polymers* **2024**, *16*, 2229. [CrossRef] [PubMed]
25. Engineers, R.A. ASHRAE handbook: Fundamentals. In *Ashrae Handbook Fundamentals*; ASHRAE (American Society of Heating, Refrigerating and Air-Conditioning Engineers): Atlanta, GA, USA, 2021.
26. Ernst, G.; Keil, B.; Wirbser, H.; Jaeschke, M. Flow-calorimetric results for the massic heat capacitycpand the Joule–Thomson coefficient of CH4, of ($0.85CH_4 + 0.15C_2H_6$), and of a mixture similar to natural gas. *J. Chem. Thermodyn.* **2001**, *33*, 601–613. [CrossRef]

energies

MDPI

Article

Assessment of Sustainable Building Design with Green Star Rating Using BIM

Mazharuddin Syed Ahmed [1,*] and Rehan Masood [2,*]

[1] Department of Engineering & Architectural Studies, ARA Institute of Canterbury, Christchurch 8140, New Zealand
[2] School of Construction Management & Quantity Surveying, Otago Polytechnic, Dunedin 9016, New Zealand
* Correspondence: mazharuddin.syedahmed@ara.ac.nz (M.S.A.); rehan.masood@op.ac.nz (R.M.)

Abstract: Globally, construction is among the leading sectors causing carbon emissions. Sustainable practices have become the focus, which aligns with the nation's commitments to the Paris Agreement by targeting a 30% reduction in emissions from the 2005 levels by 2030. However, evaluation for sustainability is critical, and the Green Star certification provides assurance. Building information modelling has emerged as a transformative technology, integrating environmental sustainability into building design and construction. This study explores the use of BIM to enhance green building outcomes, focusing on optimising stakeholder engagement, energy efficiency, waste control, and environmentally sustainable design. This study employed a case study of an educational building, illustrating how BIM frameworks support Green Star certifications by streamlining design analysis, enhancing project value, and improving compliance with sustainability metrics. Findings highlight BIM's role in advancing low-carbon, energy-efficient building designs while fostering collaboration across disciplines. This research investigates the foundational approach required to establish a framework for implementing the Green Star certification in non-residential, environmentally sustainable designs. Further, this study underscores the importance of integrating BIM in achieving Green Star benchmarks and provides a roadmap for leveraging digital modelling to meet global sustainability goals. Recommendations include expanding BIM capabilities to support broader environmental assessments and operational efficiencies.

Keywords: building information modelling; green star rating; sustainability; energy efficiency; stakeholder engagement

1. Introduction

The rapid development of New Zealand's construction industry, particularly in the Canterbury region following the 2011 earthquake, has raised concerns about the environmental impact of new buildings and infrastructure [1]. Furthermore, there is also a need to minimize the effects of climate change on buildings, which is possible by reducing greenhouse gas emissions [2]. Sustainable buildings have proven economically viable throughout their whole lifetime by reducing waste and efficiently using resources. Nevertheless, these provide a value case for New Zealand [3]. However, the construction of sustainable buildings is mainly influenced by central and local governments, client demand, and social awareness [4]. As a technological factor for sustainable buildings, energy efficiency focuses on energy generation and energy-saving features [5]. However, improving energy efficiency depends on how much of the whole-of-life embodied carbon emission is reduced, but there is limited awareness within the New Zealand construction

industry [6,7]. Similarly, the sustainability rating tools are still in their infancy, such as the Green Star NZ by the New Zealand Green Building Council (NZGBC) [8,9]. Green Star NZ only focus on the environmental aspect of sustainability and is considered the weakest among the building sustainability assessment tools [10]. There are constraints to adopting Green Star NZ, such as the complexity of the certification system, limited supporting policies, and issues related to material supply [11].

The manual operation of the Green Star rating system has several challenges, such as the need for experts, the requirement for documentation, and the assessment of the breadth of the six-star band [12]. It was reported that only half of the accreditation points cover energy, emission, and IEQ, which requires a lot of information to process and evaluate [13]. Nonetheless, automation of the Green Star rating system streamlines the process and is likely to help in the adoption of sustainability practices [14]. Building information modelling (BIM), a digital intervention in building sustainability assessment, provides a 'one-stop shop' to meet the requirements of the sustainability criteria [15], and Green Star is not exceptional. Most common analyses through BIM are related to energy and material [16]. Hence, BIM is still not fully oriented to sustainable buildings, requiring a more integrated approach [14], from conceptual to empirical evidence. In New Zealand, BIM adoption is still in transition due to limited awareness [17] about achieving its potential to improve practices [16], but leadership is inevitable [18]. Nevertheless, BIM can potentially increase the uptake of Green Star [18].

This study aims to map the integration between Green Star rating and BIM functionalities to assess the sustainability of existing and new buildings. Firstly, the studies on the topic were critically reviewed to report on the extent of the work performed. Secondly, an existing sustainable building was selected to assess the potential integration. The Green Star rating was initially scored. Thirdly, the possible support of BIM functionalities was checked. A detailed BIM model was developed for the case building. The findings were reported and discussed in detail. This study aims to automate the sustainability evaluation of new and existing buildings towards achieving a zero-carbon footprint.

2. Literature Review

BIM offers significant advantages over traditional building design methods by enabling early-stage design analysis and simulation, which can reduce project costs and mitigate risks before physical construction or energy rating approval. It transforms traditional design into a sustainable one, with a focus on low-carbon, energy-saving, and emission reduction principles [19,20]. Implementing BIM and a sustainability strategy connects buildings, spaces, people, and communities, resulting in broader benefits [21]. While green BIM strategies are adopted globally, the relationship between BIM and green design requires further exploration [22,23]. Nonetheless, BIM has proven to be a fundamental trend of true sustainability [24]. BIM is now a standard practice in the construction industry, recognized for its contributions to sustainable strategies, becoming an integral part of the project lifecycle for sustainable building design deliverables. For projects in New Zealand, even if official green rating certification is not sought, utilizing a tool framework like Green Star is recommended to identify sustainability objectives and establish a common language for the design and construction teams [25].

Several studies have highlighted the integration of BIM tools and the Green Star rating system. Client demand plays a vital role in urging the exploration of the BIM and Green Star rating, which requires a high level of understanding to establish relationships [26]. Theoretically, BIM supports 75% of the Green Star criteria, but energy efficiency is the main criterion [14], with the optimisation option. Lu et al. [21] reviewed BIM support for green building assessment for Green Star Australia and reported that 64 out of 110 credits

are achievable, but there is no minimum requirement. BIM partially supports site, transportation, energy, and atmosphere/emission-related credits. However, it highly supports water, materials, waste, and indoor environment quality-related credits. There was no BIM support for innovation. Similarly, other studies highlight the limitations of covering sustainability areas such as water, land, biodiversity, acoustics, socioeconomics, and ecology in studies integrating BIM and green building certification [27], as well as culture [28]. Interestingly, stakeholder perception varied towards the potential of BIM applications for Green Star approaches [29].

There is a strong correlation between sustainability and morphological elements in the built environment [30]. However, there is no clearly defined relationship between BIM and Green Star. This created a space for a new criterion to determine the building sustainability. Nevertheless, there are barriers to integrating BIM and Green Star, including distinct processes, a lack of understanding, insufficient client demand, the requirements of Green Star submissions, and a low Level of Development (LoD) in BIM [31]. Gandhi and Jupp [32] presented a case study of a commercial building to evaluate gaps in BIM applications for green building certification. There was misalignment between design activities, certification criteria, and issues around internal project coordination. Ly and Kiroff [33] conducted a case study on six green star-rated head office in Auckland and found no or weak connection between green building certification and BIM. There were issues of low-quality modelling, inefficient procurement, and a lack of coordination at multi-disciplinary levels. Li et al. [34] used a cloud-based BIM platform for a case study to validate the envelope thermal transfer value calculation, as a key criterion for the green mark score. Further, simulation tools of BIM were used for the energy and daylight performance through design and operational phase optimisation [35].

The development of Green Star tools follows 'district' to 'product' (from macro to micro), but for BIM, the focus is on 'product' to 'element' to 'entity' and 'precinct' (from micro to macro) [36]. There is research confusion when investigating the integration of BIM tools with the Green Star rating system, as to which direction of support is more beneficial; however, the most common is BIM support [37]. However, this integration makes the overall process towards sustainability more standardised and agile [38]. The concept of Level of Development (LoDev) is crucial for Green Star rating, encompassing both Level of Detail (graphical representation) and Level of Information (properties of the object). For Green Star assessment, LoDev is suggested as the sum of LoI and LOD. BIM provides benefits across various dimensions, from 1D (research, concept design) to 6D (performance assessment, value engineering, save estimation, re-design) [39]. The architectural, structural, and MEP (mechanical, electrical, and plumbing) BIM models provide specific information essential for Green Star assessments. For example, architectural BIM defines the building's footprint, exterior, internal design, roofs, and sun shading. Structural BIM includes foundations, load-bearing walls, openings, and framing. MEP BIM covers cooling and heating pipework, HVAC services, lighting, and waste/waterworks [40].

The BIM framework leads this integration, and its adoption eventually overcomes the barrier [41]. The BIM and Green Star integration helps the designers gain awareness of the specific green building rating system, ultimately improving the design for sustainable buildings [42]. By aligning project designs with Green Star principles, teams can establish a common language and objectives for a sustainable outcome [43]. The adoption of Green Star ratings in New Zealand reflects a commitment to environmental sustainability and resilience in building design. By leveraging BIM's capabilities, projects can achieve higher performance ratings, minimise waste, and optimise energy consumption [44]. This framework also ensures compliance with evolving regulatory requirements and global environmental targets, reinforcing BIM's role as a fundamental element of modern sustain-

able design practices [45]. The integration of BIM with Green Star certification provides significant benefits by offering a strong platform for documenting, analysing, and improving compliance with the rating system's requirements [46]. This study helps to develop an evaluation criterion for comparing existing and newly constructed buildings.

Nevertheless, there was no clear standard or uniformity for integrating BIM and Green Star in relevant studies to develop a holistic framework. Limited studies provide empirical evidence of integration using proper case studies. Furthermore, there is no clarity about mapping the integrations. This study starts with exploring sustainable design options within the context of BIM. The Green Star rating system is applied to identify the potential sustainability credits achievable through BIM. The influence of BIM on sustainability outcomes and ratings is then assessed. The strategies proposed are to incorporate Green Star principles into the project workflow. This study reports on the benefits of achieving Green Star certification through BIM applications.

3. Research Methodology

3.1. Selection of the Case Building

This study focuses on leveraging BIM to meet Green Star certification requirements for the Ara Institute of Canterbury's Kahukura Block (K Block), refer to Figure 1a,b, located in the inner city of Christchurch, New Zealand, with an area of 6500 sqm and three floors. This is a public building, and the data for this property are accessible through an official request. This project was unique due to sustainability considerations from the start, aligning with institutional values. The project cost was around 38 million and was completed between 2014 and 2017. This project employed an early contractor involvement procurement strategy, suitable for complex projects [39], which resulted in timely completion and budget adherence through the use of BIM for scheduling quantities and administering project costs, as well as design authoring, review, and engineering analysis [47]. This building won several awards for educational facility, green building, timber design, spatial built environment, and public and institutional space [48]. The case building is selected for public use (educational) based on access to key information, documentation, and stakeholders.

(**a**)

Figure 1. *Cont.*

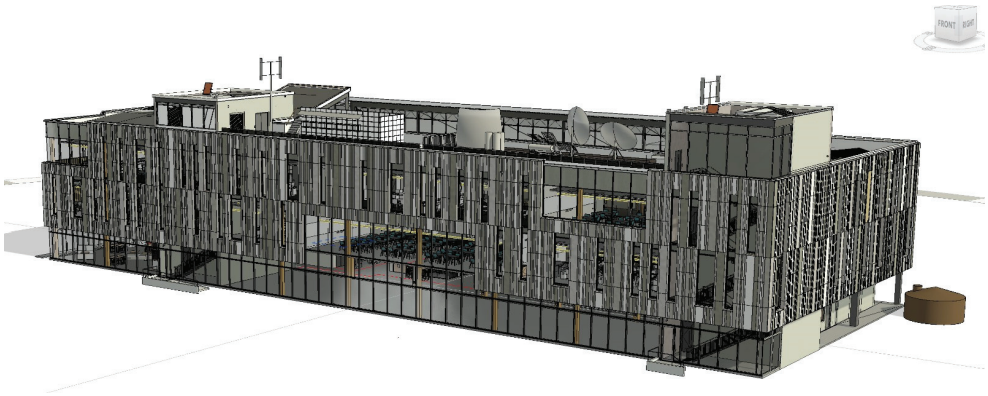

(**b**)

Figure 1. K Block building views (Source: authors' own work). (**a**) Real view photograph. (**b**) BIM 3D-model view.

3.2. Green Star Rating Calculation

The Green Star rating system, developed by the NZGBC, offers a systematic approach to evaluate and certify sustainable building performance. It uses a point-based system across nine categories, with each category including specific credits that indicate compliance with sustainability criteria [49]. Achieving Green Star certification requires meeting a minimum point threshold. Ratings from Four Stars to Six Stars indicate increasing excellence in sustainable practices.

The Green Star rating system promotes sustainable building practices by encouraging resource efficiency, energy and water savings, reduced operational costs, and healthier work environments [44]. It evaluates projects across nine categories, awarding star ratings based on total credits achieved, ranging from four stars to six stars, as shown in Figure 2. This system ensures that all project team members actively engage with sustainability goals by assigning documentation responsibilities and compliance tracking. Green Star Accredited Professionals play a critical role by coordinating teams and verifying documentation during various project stages.

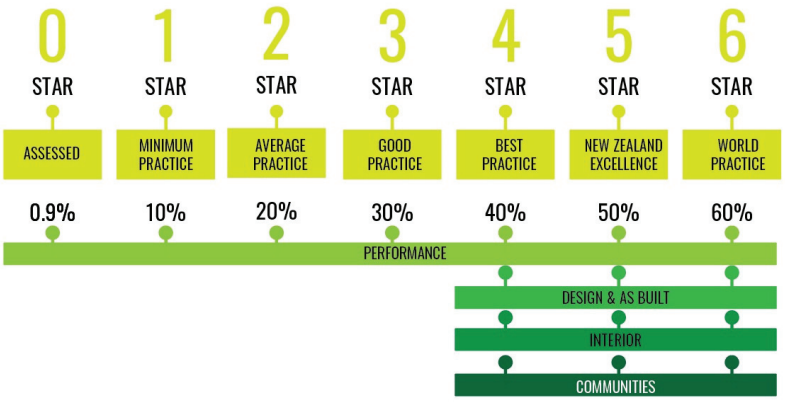

Figure 2. Green star rating system (adapted from [49]).

The Green Star framework and its associated categories are pivotal to the sustainable objectives of this research. The scope of this study encompasses four primary categories [50], excluding land use and ecology and emissions:

Management: it includes commissioning processes, building tuning, metering and monitoring, and operational waste management strategies.

Indoor Environment Quality (IEQ): it focuses on improving indoor air quality (ventilation), acoustics, lighting, and visual comfort, minimizing indoor pollutants, and optimizing thermal comfort.

Energy: it considers thermal envelope performance, mechanical systems, lighting efficiency, and on-site renewable energy generation (e.g., solar energy).

Materials: this section addresses the use of low-environmental-impact materials, including steel, concrete, timber, adhesives, sealants, flooring, ceilings, applied coatings, insulation, PVC, and furniture.

The Green Star certification process imposes specific requirements for services across multiple disciplines, including mechanical, electrical, hydraulic, civil, and fire systems [51]. These requirements, detailed in the Green Star Office Interiors, emphasize promoting sustainable building practices by establishing a common language and demonstrating the tangible benefits of green buildings [52].

The Green Star rating assessment involves a structured methodology that identifies achievable sustainability credits aligned with specific project goals, constraints, and regulatory requirements. Detailed technical simulations and modelling, such as energy, thermal comfort, and daylight analyses, are then conducted to substantiate the targeted credits. Comprehensive supporting documentation—including drawings, product certifications, and performance calculations—is prepared and submitted for rigorous review by an independent expert panel appointed by the New Zealand Green Building Council (NZGBC). This panel verifies compliance, finalises scores, and determines the project's Green Star rating.

In this study, documentation was analysed for a Green Star rating. This includes 2D drawings (architectural, structural, and mechanical, electrical, and plumbing), a schedule of quantities, and specifications. Maximum points available for the Green Star rating were identified, and target points also met the four-star rating for K Block.

3.3. Building Information Modelling

BIM has emerged as a transformative digital technology in the construction industry, offering a comprehensive platform. It has revolutionized the construction industry by providing a unified model integrating physical and functional building characteristics. Since its emergence in the late 20th century, BIM has become a central repository of knowledge, facilitating well-informed decisions throughout a building's lifecycle, from initial design to decommissioning [53]. BIM adoption is determined through n-dimensions (nD) of BIM, demonstrating different functionalities, which include 3D and 4D scheduling and sequencing, 5D cost estimating, 6D procurement, 7D facilities management, 8D risk assessment, 9D lean construction, and 10D prefabrication and continuing [54].

The design model, developed on Revit 2017 with LOF350, was initially received from the consultant; see Figure 3. Revit has a proven BIM tool to integrate well with green building assessment systems [38]. An as-built model was then developed based on real-time information about the building features. The model was checked for sanity, tagging, annotation, and connectivity. It was cleaned for errors to maintain its integrity. The graphical and material information was also checked.

The BIM process for the K Block project involved several iterative stages, beginning with creating an initial conceptual BIM model. The model was initially developed with basic geometric representations and general spatial configurations to outline project feasibility and preliminary sustainability goals. Throughout the design development phase, detailed elements such as structural frameworks, interior partitions, and facade components were progressively refined, enhancing the model's graphical accuracy and completeness [55].

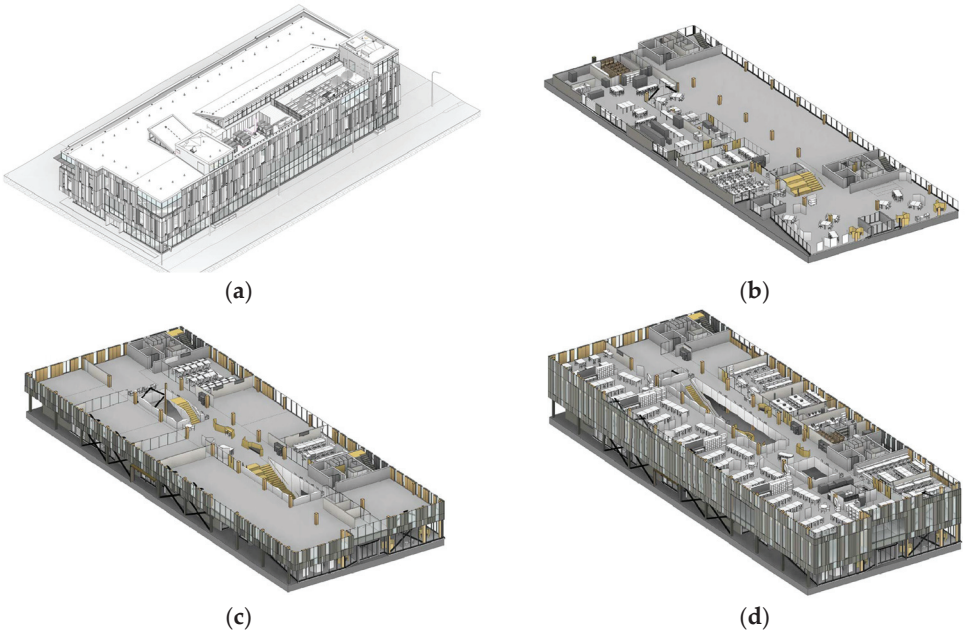

Figure 3. BIM model views for K building. (**a**) Building isometric view. (**b**) First floor plan with section view. (**c**) Second floor plan with section view. (**d**) Third floor plan with section view.

Significant changes were implemented before the sustainability analyses, including the integration of specific material specifications, energy-related properties, and detailed mechanical, electrical, and plumbing (MEP) systems. Adjustments to the model involved optimising window-to-wall ratios, updating insulation specifications, refining HVAC system designs, and incorporating precise occupancy and operational schedules. These refinements ensured the BIM model accurately reflected the building's anticipated real-world performance, providing robust input data for subsequent analyses using tools like Autodesk Insight and Green Building Studio (GBS) [56]. Ultimately, these updates facilitated accurate energy performance simulations and supported the project's compliance with Green Star sustainability requirements.

3.4. BIM Utilisation for Green Star Rating

BIM enables projects to meet Green Star requirements through advanced modelling frameworks such as Levels of Development, which integrates Level of Detail and Level of Information, as mentioned in Table 1. Architectural, structural, and mechanical, electrical, and plumbing BIM models capture vital design details, including demolition, HVAC systems, lighting fixtures, and structural elements, providing a comprehensive framework for sustainability assessment. BIM helps in an interoperable automation approach for certification [57]. BIM cloud helps to synchronize design models for different disciplines [58].

Table 1. BIM methodology and LOD for Green Star process.

Green Star Process	BIM Methodology	LoD
Meet the requirements	BIM approach and plan	100–200
Design and submission	BIM development and coordination	200–400
Assessment	BIM documentation review and management	200–500
Certification	Add value through the BIM lifecycle	100–500

A three-stage framework for integrating BIM with Green Star certification includes the following: developing a matrix to correlate BIM technologies with Green Star criteria,

validating the matrix through case studies, and auditing as-built BIM models for compliance [51]. This structured approach underscores BIM's role in achieving certification efficiency by reducing manual documentation and improving stakeholder coordination. The Green Star framework acknowledges local considerations, reflecting a commitment to advancing sustainable construction practices in the region. One approach, for non-residential projects, is to understand the Green Star rating and then explore the relationship with BIM through analysis of the criteria, followed by a case study for illustration [31]. Another approach is to apply Green Star design principles during the BIM process and to monitor and evaluate Green Star rating outcomes through BIM tools and workflows [59].

The model was then analysed with Autodesk Insight for building performance [60]. Autodesk Insight provides a comprehensive platform for analysing building energy and environmental performance. Its cloud-based accessibility enables team members to collaborate and review projects from any device. Early-stage design reviews using Insight help address sustainability concerns, with energy analysis data generated in Green Building Studio and displayed on an intuitive dashboard. This functionality allows users to identify design inefficiencies and implement energy-saving measures early.

Revit offers a familiar drafting and modelling environment, seamlessly transitioning from concept design to construction and facility management. Its built-in tools enable users to simulate building performance, meeting standards such as LEED and ASHRAE while predicting sustainable outcomes. Revit's energy analysis options assist in aligning projects with Green Star rating requirements, facilitating informed design decisions.

Autodesk GBS is a cloud-based energy analysis tool designed to optimise energy efficiency and reduce the carbon footprint of building designs [31]. GBS directly integrates with BIM data from Revit models, ensuring a streamlined workflow for performance evaluations. By incorporating energy engineering at the project's inception, GBS ensures that sustainability objectives are addressed during the design phase rather than as post-design modifications. This proactive approach maximises the value of BIM in achieving Green Star credits and highlights how Revit can model energy settings for sustainable outcomes [61].

The selection of Autodesk GBS software (version 2023) for sustainability analysis in the K Block project was based on its ability to integrate and analyse BIM data directly from Revit models efficiently. GBS offers a streamlined, cloud-based platform that significantly enhances the accuracy and speed of energy simulations and carbon footprint analyses. It is particularly suitable for detailed energy assessments required by the New Zealand Green Star certification process [11]. Moreover, GBS's intuitive interface facilitates early-stage engagement with sustainable design, enabling rapid evaluations of energy-efficient measures and fostering real-time collaboration among architects, engineers, and sustainability consultants. The software's capability to seamlessly generate comprehensive performance data directly from BIM models simplifies compliance documentation, enhances decision making, and ultimately supports higher Green Star ratings [62].

Autodesk GBS significantly supports the Green Star certification process through its integration with BIM. GBS efficiently generates precise energy and carbon footprint analyses by directly processing BIM data from Revit models. Its cloud-based platform facilitates early design assessments and collaborative evaluations, enabling project teams to test and optimise sustainability measures rapidly. Furthermore, GBS's automated and streamlined documentation simplifies compliance verification and reduces potential errors. This ensures a more reliable, efficient path toward achieving higher Green Star certification levels, ultimately enhancing overall project sustainability outcomes.

4. Results and Discussion

4.1. Green Star Rating for Case Building

The case building was evaluated using the Green Star rating tool. Achieving a preliminary score of 56 points, surpassing the 45-point threshold for a four-star rating, as reported in Table 2. The Green Star scoring for the K Block project was calculated by systematically assigning points across multiple sustainability categories based on the detailed Green Star rating sheet. This rating sheet, provided by the NZGBC, served as a structured framework outlining specific sustainability criteria and associated credits across nine primary categories: management, indoor environment quality, energy, transport, water, materials, land use and ecology, emissions, and innovation. Each category includes defined credits, and each credit is awarded a set number of points upon successful documentation and compliance verification. The cumulative total of these points determines the project's final Green Star rating, with thresholds for ratings clearly specified (e.g., 45–59 points for a four-star rating, indicating the best practice) [63].

Table 2. Green Star rating.

Category	Maximum Points Available	K Block Target Points
Management	15	10
Indoor Air Quality	17	10
Energy	22	12
Transport	10	7
Water	12	5
Total	76	44

In the K Block example, scoring involved detailed evaluations, technical modelling (including energy performance and thermal comfort analyses), and comprehensive documentation demonstrating compliance with each targeted credit. Autodesk Green Building Studio (GBS) and other BIM-integrated tools were instrumental in providing precise evidence required for these credits.

Challenges encountered during the Green Star rating process primarily concerned coordination and accurate data management. Specific difficulties included ensuring comprehensive documentation aligned precisely with Green Star requirements, maintaining consistency and accuracy across multiple interdisciplinary inputs, and handling revisions necessitated by changing project specifications or outcomes from technical simulations. Additionally, effectively managing the alignment between BIM model data and Green Star documentation requirements proved challenging, emphasizing the need for meticulous data tracking and robust interdisciplinary communication throughout the project lifecycle.

4.2. BIM and Green Star Integrations

There is no guidance available to determine the suitability of a software package for the Green Star rating system [27]. This study reported key integrations of the Green Star rating and BIM dimensions.

The K Block project's Green Star scoring was calculated using the Green Star rating sheet provided by the NZGBC. This structured framework outlines sustainability criteria across nine categories: management, indoor environment quality, energy, transport, water, materials, land use and ecology, emissions, and innovation. Each category comprises specific credits, and points are awarded based on thorough documentation and compliance verification. The cumulative total of points determines the project's final Green Star rating.

The integration of BIM and Green Star significantly enhances sustainability assessments by providing a centralized platform for managing graphical and non-graphical data,

streamlining documentation, and ensuring real-time data updates, ultimately promoting sustainable construction practices nationwide. This comprehensive approach not only improves project coordination and minimizes risks but also facilitates the achievement of targeted Green Star rating points through advanced analysis and simulation tools. A total of 297 integrations were mapped. There were 41 integrations for 'management', 36 for 'indoor environment quality', 13 for 'energy', 2 for 'transport', 5 for 'water', 18 for 'materials', 2 for 'land ecology and use', 9 for 'emissions', and 29 for 'innovations'. This study demonstrates that BIM supports 52% of the Green Star criteria using extended BIM dimensions, whereas previously, theoretically, BIM supported 75% [14].

The BIM integration analysis for each Green Star criterion followed these steps:

1. Management: BIM models facilitated comprehensive management strategies, incorporating building information commissioning and tuning, environmental management plans, and ongoing monitoring through precise BIM data tracking and reporting.
2. Indoor Environment Quality: Simulations conducted through BIM tools ensured optimal air quality, hazardous material management, thermal comfort, acoustic performance, and visual comfort, verifying compliance through detailed model simulations.
3. Energy: Autodesk GBS and BIM-enabled energy modelling validated greenhouse gas emission reductions and optimized peak electricity demand, ensuring efficiency criteria were robustly met.
4. Transport: BIM helped visualize and plan alternative transportation programs, enhancing accessibility and efficiency through integrated transport mode surveys and simulations.
5. Water: Water conservation strategies were validated through BIM-based simulations of potable water use and fire protection services, demonstrating significant reductions against baseline consumption.
6. Materials: BIM facilitated sustainable procurement processes, waste management during construction, and refurbishment phases by embedding environmental product declarations directly into the BIM model.
7. Land Use and Ecology: The ecological value and biodiversity contributions were assessed using BIM tools to plan and optimize site landscaping and maintenance practices.
8. Emissions: Stormwater management, light pollution control, and refrigeration impact assessments were modelled and analysed through BIM, ensuring adherence to Green Star emission reduction criteria.
9. Innovation: Innovative technologies, processes, and strategies for global sustainability benchmarks were identified, modelled, and documented through advanced BIM functionalities.

Table 3 outlines the aspirations and contributions of BIM processes across Green Star rating categories. These contributions encompass management practices such as commissioning and tuning, ongoing monitoring, and environmental management. For indoor environment quality, BIM supports improvements in air quality, lighting, thermal comfort, and acoustics through detailed modelling and simulation. The energy category benefits from reductions in greenhouse gas emissions and peak electricity demand, achieved through optimised building designs and systems, while alternative transportation programs and surveys support transport credits. Additionally, BIM facilitates sustainable procurement, operational waste reduction, and refurbishment management under the materials category. The integration of BIM into green building design optimizes design from initial stages, leading to more sustainable and economically efficient outcomes [64]. BIM-driven methodologies also enhance contributions to biodiversity, emissions control, and innovation, such as adopting transformative technologies.

Table 3. BIM and Green Star integrations.

Green Star Rating Subcategory	BIM Functionalities								
	BEP	**GBS**	**Insight**	**2D**	**3D**	**4D**	**5D**	**6D**	**7D**
1. Management									
Green Star Accredited Professional	✔	✔	✔	✔	✔	✔	✔	✔	✔
Building Information	✔	✔	✔	✔	✔	✔	✔	✔	✔
Commissioning & Tuning		✔	✔	✔	✔			✔	
Ongoing Monitoring & Metering	✔	✔	✔	✔	✔			✔	
Environmental Management	✔	✔	✔	✔	✔			✔	✔
Green Cleaning	✔	✔	✔	✔	✔			✔	✔
Commitment to Performance	✔	✔	✔	✔	✔			✔	✔
2. Indoor Environment Quality									
Quality of Indoor Air	✔	✔	✔	✔	✔			✔	
Hazardous Materials	✔	✔	✔	✔	✔			✔	
Lighting Comfort	✔	✔	✔	✔	✔			✔	
Daylight & Views	✔	✔	✔	✔	✔			✔	
Thermal Comfort	✔	✔	✔	✔	✔			✔	
Acoustic Comfort	✔	✔	✔	✔	✔			✔	
Occupancy Comfort Survey	✔	✔	✔	✔	✔			✔	
3. Energy									
Greenhouse Gas Emissions	✔	✔	✔	✔	✔	✔		✔	✔
Peak Electricity Demand		✔	✔	✔	✔			✔	
4. Transport									
Alternative Transportation Program				✔					
Transportation Modes Survey				✔					
5. Water									
Potable Water			✔	✔	✔				
Fire Protection Services				✔	✔				
6. Materials									
Procurement & purchasing	✔	✔	✔	✔	✔	✔	✔		
Waste from Operations		✔	✔	✔	✔	✔	✔	✔	
Waste from Refurbishments	✔	✔	✔	✔	✔	✔	✔		✔
7. Land Use									
Biodiversity and Ecological Value				✔					
Groundskeeping Practices				✔					
8. Emissions									
Stormwater Control				✔	✔			✔	
Light Pollution				✔	✔			✔	
Impacts from Refrigeration				✔	✔			✔	

Table 3. *Cont.*

Green Star Rating Subcategory	BIM Functionalities								
	BEP	GBS	Insight	2D	3D	4D	5D	6D	7D
9. Innovation									
Innovative Technology or Process	✔			✔	✔	✔	✔	✔	✔
Market Transformation	✔			✔	✔			✔	✔
Improving Green Star Benchmarks		✔	✔	✔		✔		✔	✔
Global Sustainability		✔	✔	✔			✔		✔
Innovation Challenge		✔	✔	✔			✔	✔	✔

BIM's contextual excellence, enabled by rich information within a collaborative 3D environment, ensures effective project coordination and minimises risks across all project phases. The ability to selectively target Green Star rating points through the BIM process, using advanced analysis and simulation tools, further strengthens its role in advancing sustainable design while minimizing impacts on the design and construction program. The integration of BIM and Green Star ratings represents a significant step forward in achieving sustainability goals for the construction industry, promoting more efficient, environmentally responsible, and economically viable building practices [65].

4.3. Performance Evaluation

Integrating BIM on the K Block project significantly improved the Green Star rating process. BIM enhanced the overall efficiency and effectiveness of sustainability assessments by streamlining data management and facilitating precise simulation analyses. The intervention of BIM significantly reduced the time required for conducting critical sustainability analyses, including energy performance, daylight optimisation, and thermal comfort, by enabling real-time model adjustments and immediate feedback [56].

Resourcefulness improved markedly as the BIM model consolidated essential documentation and facilitated accurate, cross-disciplinary data sharing, eliminating redundant processes and minimizing errors. This integration led to efficient resource use, enabling project teams to focus more directly on sustainability improvements than on administrative tasks [66].

Furthermore, conduit modelling, a specific application within BIM, provided precise visualisation and planning capabilities for mechanical, electrical, and plumbing services [67]. This capability improved accuracy in resource allocation, reduced material waste, and optimised service layouts, enhancing building performance and compliance with Green Star rating criteria. Overall, BIM intervention dramatically streamlined the certification process, enhanced accuracy, and improved resource efficiency throughout the project lifecycle.

5. Conclusions

This study evaluates the potential improvements and value that BIM offers in achieving Green Star certification. Through the case of the K Block project, this research demonstrates how the integration of BIM enhances Green Star rating credits, facilitating sustainable construction practices. The findings underscore the advantages of implementing BIM for Green Star-certified buildings, including its ability to provide a shared data environment for enhanced data access and collaboration, reduce risks during the design and construction phases by enabling better clash detection and issue resolution, create a rich and accurate record of the project lifecycle for improved facility management, and increase efficiency in the Green Star certification process [68]. The study demonstrated that integrating BIM significantly enhances the efficiency, accuracy, and overall effectiveness of achieving Green

Star certification. BIM streamlined the assessment process by enabling precise sustainability simulations, effective resource management, and improved cross-disciplinary coordination, collectively facilitating higher sustainability ratings.

The study's scope was limited to the educational building, focusing primarily on the management, indoor environment quality, energy, and materials categories. The exclusion of other Green Star categories, such as land use and ecology and emissions, restricts the broader applicability of findings. Additionally, reliance on a single case study limits the generalizability of the conclusions. This study reveals 155 integrations, indicating 52% coverage of the Green Star rating.

Theoretically, this research contributes to existing knowledge by demonstrating how BIM can be instrumental in achieving sustainability goals systematically within building certification frameworks. It reinforces BIM's potential in facilitating integrated design practices that align with sustainability certification criteria.

The findings provide actionable insights for architects, engineers, and sustainability consultants on effectively leveraging BIM for Green Star certification. The demonstrated methodology offers a practical framework for streamlining the sustainability certification process, potentially reducing project timelines and costs.

The integration of BIM significantly improved the efficiency, accuracy, and effectiveness of achieving Green Star certification for the K Block building at the Ara Institute of Canterbury. The building, a key subject of this assessment, successfully demonstrated compliance with specific Green Star sustainability criteria, such as management, indoor environment quality, energy, and materials. The positive assessment signifies that K Block has achieved substantial sustainability benchmarks, including optimized energy performance, improved indoor environmental conditions, efficient resource management, and effective cross-disciplinary collaboration.

This positive outcome confirms K Block as an exemplar of sustainable educational facility design, meeting and exceeding the stringent sustainability requirements outlined by the NZGBC. Practically, this demonstrates the robust capability of BIM tools to streamline sustainability certification processes, reduce administrative burdens, and enhance resource efficiency. Theoretically, this research reinforces BIM's critical role in aligning building design and construction practices with contemporary sustainability objectives.

Future research should explore BIM integration in broader sustainability categories not covered in this study, such as land use and ecology and emissions. Comparative analyses across multiple diverse building projects are recommended to enhance generalizability. Additionally, further investigation into the integration of advanced BIM technologies, such as digital twins and real-time monitoring systems, would provide deeper insights into enhancing sustainability performance throughout a building's lifecycle.

Author Contributions: Conceptualization, M.S.A.; methodology, M.S.A.; software, M.S.A.; validation, R.M.; formal analysis, M.S.A.; investigation, M.S.A.; resources, M.S.A. and R.M.; writing—original draft preparation, M.S.A. and R.M.; writing—review and editing, R.M.; visualization, M.S.A.; supervision, M.S.A.; project administration, M.S.A. All authors have read and agreed to the published version of the manuscript.

Funding: This research received no external funding.

Data Availability Statement: The article presents all the research data. However, the Revit model is kept confidential as the property of the Ara Institute of Canterbury.

Acknowledgments: The authors acknowledge Ara Institute of Canterbury for providing the resources for case building. Authors appreciate the support of graduate diploma student Mike Li in BIM analysis.

Conflicts of Interest: The authors declare no conflicts of interest.

Abbreviations

The following abbreviations are used in this manuscript:

BEP	Building Energy Modelling
BIM	Building Information Modelling
GBS	Green Building Studio
IEQ	Indoor Environment Quality
NZGBC	New Zealand Green Building Council

References

1. Dyason, D. Disasters and investment: Assessing the performance of the underlying economy following a large-scale stimulus in the built environment. *J. Risk Financ. Manag.* **2022**, *15*, 263. [CrossRef]
2. Bui, T.T.P.; Wilkinson, S.; Domingo, N. Climate change adaptation in New Zealand's building sector. In Proceedings of the 54th International Conference of The Australian and New Zealand Architectural Science Association (ANZAScA), Auckland, New Zealand, 26–28 November 2020; pp. 236–245.
3. Fullbrook, D.; Jackson, Q.; Finlay, G. Value case for sustainable building in New Zealand. In *Report for the Ministry for the Environment*; Ministry for the Environment: Wellington, New Zealand, 2006.
4. Li, X.; Liu, Y.; Wilkinson, S.; Liu, T. Driving forces influencing the uptake of sustainable housing in New Zealand. *Eng. Constr. Archit. Manag.* **2019**, *26*, 46–65. [CrossRef]
5. Cielo, D.; Subiantoro, A. Net zero energy buildings in New Zealand: Challenges and potentials reviewed against legislative, climatic, technological, and economic factors. *J. Build. Eng.* **2021**, *44*, 102970. [CrossRef]
6. Finnie, D.A.; Masood, R.; Goldsworthy, S.; Harding, B. Embodied Carbon in New Zealand Commercial Construction. *Energies* **2024**, *17*, 2629. [CrossRef]
7. Nidhin, B.K.S.N.; Domingo, N.; Bui, T.T.P.; Wilkinson, S. Construction stakeholders' knowledge on zero carbon initiatives in New Zealand. *Int. J. Build. Pathol. Adapt.* **2025**, *43*, 512–527. [CrossRef]
8. Smith, J. Implementation of a Building Sustainability Rating Tool: A Survey of the New Zealand Building Industry. Masters's thesis, Open Access Te Herenga Waka-Victoria University of Wellington, Wellington, New Zealand, 2008.
9. Doan, D.T.; Wall, H.; Ghaffarian Hoseini, A.; Ghaffarianhoseini, A.; Naismith, N. Green building practice in the New Zealand construction industry: Drivers and limitations. *Int. J. Technol.* **2021**, *12*, 946–955. [CrossRef]
10. Doan, D.T.; Ghaffarianhoseini, A.; Naismith, N.; Zhang, T.; Ghaffarianhoseini, A.; Tookey, J. A critical comparison of green building rating systems. *Build. Environ.* **2017**, *123*, 243–260. [CrossRef]
11. Liang, J.; Vishnupriya, V.; Le, A.; Shen, X. Future directions for advancing Green Star NZ to achieve zero-carbon goals: Insights from industry professionals. *Int. J. Build. Pathol. Adapt.* **2025**, *43*, 41–58. [CrossRef]
12. Smith, R.; Reid, V.; Smith, D.; Rodwell, J.; Rayburg, S.; Neave, M. Reorienting Green Ratings Towards the Big Problems Rather than Business as Usual: A Review of Pragmatic Issues. *Buildings* **2025**, *15*, 1915. [CrossRef]
13. Byrd, H.; Rasheed, E.O. The Productivity Paradox in Green Buildings. *Sustainability* **2016**, *8*, 347. [CrossRef]
14. GhaffarianHoseini, A.; Tien Doan, D.; Naismith, N.; Tookey, J.; GhaffarianHoseini, A. Amplifying the practicality of contemporary building information modelling (BIM) implementations for New Zealand green building certification (Green Star). *Eng. Constr. Archit. Manag.* **2017**, *24*, 696–714. [CrossRef]
15. Wong, J.K.W.; Zhou, J. Enhancing environmental sustainability over building life cycles through green BIM: A review. *Autom. Constr.* **2015**, *57*, 156–165. [CrossRef]
16. Carvalho, J.P.; Bragança, L.; Mateus, R. A systematic review of the role of BIM in building sustainability assessment methods. *Appl. Sci.* **2020**, *10*, 4444. [CrossRef]
17. Doan, D.T.; GhaffarianHoseini, A.; Naismith, N.; Ghaffarianhoseini, A.; Zhang, T.; Tookey, J. Examining critical perspectives on building information modelling (BIM) adoption in New Zealand. *Smart Sustain. Built Environ.* **2021**, *10*, 594–615. [CrossRef]
18. Doan, D.T.; Ghaffarianhoseini, A.; Naismith, N.; Ghaffarianhoseini, A.; Tookey, J. Developing a framework for building information modelling (BIM) adoption in New Zealand. *Built Environ. Proj. Asset Manag.* **2024**, *14*, 490–506. [CrossRef]
19. Płoszaj-Mazurek, M.; Ryńska, E. Artificial intelligence and digital tools for assisting low-carbon architectural design: Merging the use of machine learning, large language models, and building information modeling for life cycle assessment tool development. *Energies* **2024**, *17*, 2997. [CrossRef]
20. Cao, Y.; Kamaruzzaman, S.N.; Aziz, N.M. Green building construction: A systematic review of BIM utilization. *Buildings* **2022**, *12*, 1205. [CrossRef]
21. Lu, Y.; Wu, Z.; Chang, R.; Li, Y. Building Information Modeling (BIM) for green buildings: A critical review and future directions. *Autom. Constr.* **2017**, *83*, 134–148. [CrossRef]

22. Uddin, M.N.; Wei, H.H.; Chi, H.L.; Ni, M.; Elumalai, P. Building information modeling (BIM) incorporated green building analysis: An application of local construction materials and sustainable practice in the built environment. *J. Build. Pathol. Rehabil.* **2021**, *6*, 13. [CrossRef]
23. Hajj, E.C.I.; Montes, G.M. Examining green building practices: The influence on building information modeling function diffusion. *Sustainability* **2025**, *17*, 3843. [CrossRef]
24. Krygiel, E.; Nies, B. *Green BIM: Successful Sustainable Design with Building Information Modeling*; John Wiley & Sons: Hoboken, NJ, USA, 2008.
25. Gonzalez, R.E.; Stephens, M.T.; Toma, C.; Dowdell, D. Incorporating potential environmental impacts in building seismic design decisions. *Bull. Earthq. Eng.* **2023**, *21*, 4385–4428. [CrossRef]
26. Peng, W.; Feng, Z. The applications of building information modelling for the lifecycle performance of green buildings: A systematic literature review. In Proceedings of the 7th New Zealand Built Environment Research Symposium (NZBERS), Auckland, New Zealand, 17–18 February 2022.
27. Olanrewaju, O.I.; Enegbuma, W.I.; Donn, M.; Chileshe, N. Building information modelling and green building certification systems: A systematic literature review and gap spotting. *Sustain. Cities Soc.* **2022**, *81*, 103865. [CrossRef]
28. Kamaruzzaman, S.N.; Salleh, H.; Lou, E.; Edwards, R.; Wong, P.F. Assessment schemes for sustainability design through BIM: Lessons learnt. In Proceedings of the 4th International Building Control Conference, Kuala Lumpur, Malaysia, 7–8 March 2016; p. 80.
29. Abdelaal, F.; Guo, B.H. Stakeholders' perspectives on BIM and LCA for green buildings. *J. Build. Eng.* **2022**, *48*, 103931. [CrossRef]
30. Mobaraki, A.; Nikoofam, M.; Mobaraki, B. The Nexus of Morphology and Sustainable Urban Form Parameters as a Common Basis for Evaluating Sustainability in Urban Forms. *Sustainability* **2025**, *17*, 3967. [CrossRef]
31. Doan, D.T.; Ghaffarianhoseini, A.; Naismith, N.; Ghaffarianhoseini, A.; Zhang, T.; Tookey, J. Examining Green Star certification uptake and its relationship with Building Information Modelling (BIM) adoption in New Zealand. *J. Environ. Manag.* **2019**, *250*, 109508. [CrossRef]
32. Gandhi, S.; Jupp, J. BIM and Australian green star building certification. In Proceedings of the Computing in Civil and Building Engineering (2014), Orlando, FL, USA, 23–25 June 2014; pp. 275–282.
33. Ly, L.; Kiroff, L. BIM use in green building certification processes. In Proceedings of the International Structural Engineering and Construction, Chicago, IL, USA, 11–18 August 2023; pp. 1–6.
34. Liu, Z.; Wang, Q.; Gan, V.J.; Peh, L. Envelope thermal performance analysis based on building information model (BIM) cloud platform—Proposed green mark collaboration environment. *Energies* **2020**, *13*, 586. [CrossRef]
35. Renganathan, R. Investigating the Role of BIM and Simulation Tools in Promoting Energy Efficiency for Green Building Certification. *Renew. Energy* **2025**, *1*, 50–70. [CrossRef]
36. Gelder, J.; Agrawal, M.; Miller, J. *Green Star Communities Rating Tool: An Assessment*; CRC Low Carbon Living: Sydney, Australia, 2018.
37. Ferdosi, H.; Abbasianjahromi, H.; Banihashemi, S.; Ravanshadnia, M. BIM applications in sustainable construction: Scientometric and state-of-the-art review. *Int. J. Constr. Manag.* **2023**, *23*, 1969–1981. [CrossRef]
38. Alves Tenório de Morais, G.; RS de MS Nascimento, C.; dos Santos, E.B.; MN de Souza, K.; Fernandes, B.S.; Palha, R.P. Integration potential between REVIT and LEED: A review. *Archit. Eng. Des. Manag.* **2024**, *20*, 510–525. [CrossRef]
39. Alfalah, G.; Al-Sakkaf, A.; Abdelkader, E.M. On the exploration of building information modeling capabilities for promoting sustainability-related practices in construction projects: Case studies in china and usa. *WSEAS Trans. Environ. Dev.* **2021**, *17*, 764–786. [CrossRef]
40. Al Aamri, A.M.S.; Evdorides, H.; Baniotopoulos, C. Barriers and Opportunities for the Adoption of Building Information Modelling in the Design of Buildings: Case Study of Oman. *Sustainability* **2025**, *17*, 3510. [CrossRef]
41. Fauzi, M.A.; Anuar, K.F.; Mohd Zainudin, N.; Ahmad, M.H.; Wider, W. Building information modeling (BIM) in green buildings: A state-of-the-art bibliometric review. *Int. J. Build. Pathol. Adapt.* **2023**. [CrossRef]
42. Arbabi, A.; Taherkhani, R.; Ansari, R. A novel approach for integrating BIM and green building rating systems in the construction projects design phase. *Eng. Constr. Archit. Manag.* **2024**. [CrossRef]
43. Nwaogbe, G.; Urhoghide, O.; Ekpenyong, E.; Emmanuel, A. Green construction practices: Aligning environmental sustainability with project efficiency. *Int. J. Sci. Res. Arch.* **2025**, *14*, 189–201. [CrossRef]
44. Abdelaal, F. Integrating Building Information Modelling (BIM) and Whole Building Life Cycle Assessment (WBLCA) for Green Building Rating Systems. Ph.D. Thesis, University of Canterbury, Christchurch, New Zealand, 2021.
45. Alves, J.L.; Palha, R.P.; de Almeida Filho, A.T. BIM-Based Framework for Photovoltaic Systems: Advancing Technologies, Overcoming Challenges, and Enhancing Sustainable Building Performance. *Sustainability* **2025**, *17*, 3695. [CrossRef]
46. Tabrizi, A. Sustainable construction, LEED as a green rating system and the importance of moving to NZEB. *E3S Web Conf.* **2021**, *241*, 02001. [CrossRef]

47. BIMinNZ. ARA Institute of Canterbury Kahukura Block. Available online: https://www.biminnz.co.nz/casestudies/2017/ara-institute-of-canterbury-kahukura-block (accessed on 3 February 2025).
48. Jasmax. Kahukura—A Mass Timber and Net Zero-Ready Learning Building for Ara. Available online: https://jasmax.com/projects/ara-institute-kahukura (accessed on 3 February 2025).
49. NZGBC. Green Star Certification. Available online: https://nzgbc.org.nz/introduction-to-green-star (accessed on 3 February 2025).
50. Doocy, L.E.; Zarmehr, A.; Kider, J.T., Jr. A critical review of the effectiveness of the Sustainability Tracking, Assessment & Rating System (STARS) framework on campus sustainability. *Build. Simul.* **2021**, *17*, 629–635.
51. Maskil-Leitan, R.; Gurevich, U.; Reychav, I. BIM management measure for an effective green building project. *Buildings* **2020**, *10*, 147. [CrossRef]
52. Narcida, L.; O'Dell, M.; Pacheco, M.; Perla, C.; Ramirez, V.; Sanchez, D.; Shoemaker, J.; Songco, L.; Zirakian, T.; Boyajian, D. Undergraduate Design and Analysis of a LEED Certified Building. *J. Civ. Eng. Archit.* **2022**, *16*, 227–234.
53. Borkowski, A.S. A Literature Review of BIM Definitions: Narrow and Broad Views. *Technologies* **2023**, *11*, 176. [CrossRef]
54. Masood, R.; Kharal, M.; Nasir, A. Is BIM adoption advantageous for construction industry of Pakistan? *Procedia Eng.* **2014**, *77*, 229–238. [CrossRef]
55. Jankovic, L.; Carta, S. Biozero—Designing nature-inspired net-zero building. *Sustainability* **2021**, *13*, 7658. [CrossRef]
56. Escobar, K.A.; Valles, A.I.A.A.; Campoverde, T.O.C.; Herrera, R.F. Assessment of BIM use in the early stages of implementation. *Rev. Ing. Construcción* **2021**, *36*, 311–321.
57. Solla, M.; Elmesh, A.; Memon, Z.A.; Ismail, L.H.; Kazee, M.F.A.; Latif, Q.B.a.I.; Yusoff, N.I.M.; Alosta, M.; Milad, A. Analysis of BIM-based digitising of Green Building Index (GBI): Assessment method. *Buildings* **2022**, *12*, 429. [CrossRef]
58. Zhang, D.; Zhang, J.; Guo, J.; Xiong, H. A semantic and social approach for real-time green building rating in BIM-based design. *Sustainability* **2019**, *11*, 3973. [CrossRef]
59. Lim, Y.-W.; Chong, H.-Y.; Ling, P.C.; Tan, C.S. Greening existing buildings through Building Information Modelling: A review of the recent development. *Build. Environ.* **2021**, *200*, 107924. [CrossRef]
60. Autodesk. Autodesk Insight. Available online: https://www.autodesk.com/products/insight/overview (accessed on 1 June 2024).
61. Zhao, X.-g.; Gao, C.-P. Research on Energy-Saving Design Method of Green Building Based on BIM Technology. *Sci. Program.* **2022**, *2022*, 2108781. [CrossRef]
62. Arisanti, K.; Latief, Y.; Machfudiyanto, R. Development information system for building maintenance for structural components of government green building using Building Information Modelling (BIM). *IOP Conf. Ser. Mater. Sci. Eng.* **2020**, *830*, 022060. [CrossRef]
63. Pham, D.H.; Kim, B.; Lee, J.; Ahn, Y. An investigation of the selection of LEED version 4 credits for sustainable building projects. *Appl. Sci.* **2020**, *10*, 7081. [CrossRef]
64. Li, L.; Gao, L.; Zhang, X.; Xu, H.; Jiang, L. Research on Building's Carbon Emission Calculation and Reduction Strategy Based on Life Cycle Assessment (LCA) and Building in Formation Modeling (BIM): A Case Study in Beijing, China. *Buildings* **2025**, *15*, 1403. [CrossRef]
65. Long, R.; Li, Y. Analysis of Designing Green Architecture Based on Building Information Modeling (BIM) Technology. *IOP Conf. Ser. Earth Environ. Sci.* **2021**, *827*, 012018. [CrossRef]
66. Sonkamble, R.G.; Bongale, A.M.; Phansalkar, S.; Sharma, A.; Rajput, S. Secure data transmission of electronic health records using blockchain technology. *Electronics* **2023**, *12*, 1015. [CrossRef]
67. Deng, R.; Li, X.; Tian, Y. A Review: The Application of Path Optimization Algorithms in Building Mechanical, Electrical, and Plumbing Pipe Design. *Buildings* **2025**, *15*, 2093. [CrossRef]
68. De Castro, A.V.; Pacheco, G.R.; González, F.J.N. Holistic approach to the sustainable commercial property business: Analysis of the main existing sustainability certifications. *Int. J. Strateg. Prop. Manag.* **2020**, *24*, 251–268. [CrossRef]

energies

MDPI

Article

Influence of Solar Radiation on the Thermal Load of an External Wall Taking into Account Its Material Properties

Joanna Wilk, Artur Nowoświat *, Michał Marchacz , Jerzy Bochen , Janusz Belok and Iwona Pokorska-Silva

Faculty of Civil Engineering, Silesian University of Technology, 44-100 Gliwice, Poland; iwona.pokorska-silva@polsl.pl

* Correspondence: artur.nowoswiat@polsl.pl

Abstract: This study empirically verified the effect of solar radiation on the building envelope, with particular emphasis on the generated surface temperature. A model of a cellular concrete block wall with ETICS (External Thermal Insulation Composite System) was constructed with varying insulation-plaster configurations, followed by tests in a "sun chamber" aging chamber and numerical analyses. The measurement results were compared with those from the numerical simulations, taking into account the thermal properties of the materials used and the radiation exposure conditions. The purpose of the study was to determine to what extent different types of plasters and insulation materials affect the heating of the façades. Computer simulations confirmed the direction of energy flow and the gradual heating of successive layers. Furthermore, the differences between the material variants were consistent with the experimental observations. By modeling perfectly uniform conditions, the numerical analysis allowed us to limit the impact of radiation variability, resulting in results with reduced error.

Keywords: solar radiation; partition temperature; ETICS

1. Introduction

The European Directive 2010/31/E(EPBD) [1] forced the development of research on the dynamic thermal properties of building elements. Thermal characteristics describe the dynamic response of the system to varying loads over time [2]. Heat conduction is one of the main means of heat transfer between the interior and exterior through the building envelope [3], and the key parameters are the building's aspect ratio [4], the window-to-wall ratio [5], and the thermal conductivity of the walls [6,7]. However, in some cases (historic buildings), due to the specific qualities of the façade, the use of thermal insulation is not recommended or hindered. In addition, exterior wall insulation materials are often exposed to adverse weather conditions including solar radiation [8].

The building material used in the construction of the walls, and which is exposed to the direct influence of the external climate, has a direct impact on the temperature and humidity inside the building, which is controlled by the wall structure [9–11]. The causes of material decomposition can be determined from information on changes in temperature and humidity [12], which promote chemical decomposition through dissolution, oxidation, or physical decomposition [13,14] or biodeterioration in the form of microbial colonization [15,16]. Monitoring of the studied parameters is one of the priorities of microclimatic research [17]. It should be noted that the absorption of solar energy by the wall is influenced by factors such as the heat accumulation coefficient of the wall, the heat-transfer coefficient of the south wall's outer surface, the radiation intensity, consecutive sunny days, and the outdoor air temperature [18].

The results also show that the SER is strongly affected by the heat-transfer coefficient of the wall's outer surface, with lower coefficients having a more obvious influence [19]. Generally, all such measures can be said to lead to so-called passive wall cooling [20]. In addition to façades with high thermal inertia [21], passive radiative cooling materials [22], insulating materials [23,24], modular living wall systems [25], ventilated façades [26], and Trombe walls [27], color-changing partitions [28,29], are also used. Giovani's research [29] showed that in desert climates, the maximum surface temperature difference between black and white roofs in summer could reach 30–40 °C, and that high-reflectance roofs made of reflective materials or colors reduced the cooling energy demand and mitigated urban heat islands [30]. Therefore, the authors of this article undertook research on the influence of façade materials, plasters, and paints on surface temperature distribution and heat transport.

The authors of this article, through their research, obtained data to evaluate the influence of the type of plastering and the properties of thermal insulation on the process of heat accumulation and heat transfer through the façade. The results of the experiment may find application in the design of energy-efficient insulation systems as well as in the selection of building materials that provide optimal protection against the overheating of exterior walls under conditions of intense sunlight. The results of the empirical measurements were compared with the results of the simulations. The aim of this comparison was to verify the agreement of the experimental results with theoretical predictions and to identify any discrepancies arising from real-world conditions, which cannot always be fully accounted for in the models. The numerical calculations were based on classical methods for determining the heat flow in the building partitions. In order to carry out the numerical simulation, the partition under study was mapped in the Ansys and THERM programs, which allow for the precise analysis of heat flow in complex material systems. The model took into account the actual thermal properties of the materials used and the boundary conditions corresponding to the values recorded during the laboratory test. The heat flow acting on the surface of a partition was mapped, taking into account the influence of solar radiation and convective heat exchange with the surroundings. Through the use of computer simulation, it was possible to obtain an accurate picture of the temperature distribution in the partition structure. A comparison of the numerical results with those obtained empirically allowed for an assessment to be made of the accuracy of the model used and its applicability in further research into optimizing the thermal insulation of building façades. The added value of the work was the use of a world-unique aging chamber. To simulate the atmospheric environment, a rotating climatic aging chamber was applied, whose stand consisted of four chambers. The core was made up of a central rotating chamber that had four exposition walls, with the dimensions 1.55 × 2.10 m, to mount the test samples.

2. Methods

As part of this study, an experimental verification of the effect of solar radiation on the building envelope was carried out, with particular reference to the temperature generated on its surface.

For the purposes of the experiment, a model two-layer wall with ETICS insulation with different insulation and plaster layer arrangements was created (chapter 2.1).

The experiment was conducted under laboratory conditions, in an aging chamber, a 'sun chamber', which enabled temperature changes to be reproduced precisely and the effect of radiation on the test surfaces to be controlled (chapter 2.2). The scope of the work did not include issues related to the moisture content of the materials, their long-term aging, or the effect of UV radiation. The influence of atmospheric conditions other than solar radiation (precipitation, wind) was also not analyzed.

In addition, numerical calculations were carried out using the Ansys and THERM programs (chapter 2.3), which allowed for precise analysis of the heat flow in complex partition systems.

2.1. Characteristics of Testing Samples

In order to analyze the physical phenomena associated with the heating and heat transfer of building materials, a stand was prepared with a varied combination of insulation materials and renderings.

A sample of a two-layer wall with ETICS insulation with an area of 160 × 202 cm was made. The structural layer of the wall was made of 12 cm thick cellular concrete blocks with adhesive mortar. Then, a 20 cm thick layer of thermal insulation made of polystyrene foam boards fixed with adhesive mortar was attached to the wall layer. For comparison purposes, three types of polystyrene foam were used, laid in 50 cm wide horizontal strips, with different thermal conductivity coefficients λ:

- White EPS with graphite (λ = 0.042 W/m·K);
- Graphite EPS (λ = 0.033 W/m·K);
- White EPS (λ = 0.040 W/m·K).

On the surface of the polystyrene-insulated wall, a reinforcement layer of glass-fiber mesh embedded in adhesive mortar was made and then finished with a plaster coating with a roughcast structure and a grain size of 1.5 mm. Three types of thin-coat plaster were laid in 50 cm wide vertical strips:

- Acrylic render (λ = 0.76 W/m·K, α = 0.55) painted with heat-reflective paint to reduce heat gain (d = 2 mm, λ = 0.053 × 10^{-2} W/m·K, ε = 0.99, α = 0.0996);
- Acrylic render (λ = 0.76 W/m·K, ε = 1, α = 0.55);
- Silicone render (λ = 0.76 W/m·K, ε = 0.98, α = 0.55).

The emissivity ε of the finishing layers was determined using a thermal imaging camera and thermocouple-type sensors connected to a recorder on a separately laid plaster strip outside the test bench.

We denoted the solar absorptivity by α.

The general layout of the wall layers and the location of subsequent partition systems (layers: insulation and plaster) are shown in Figure 1.

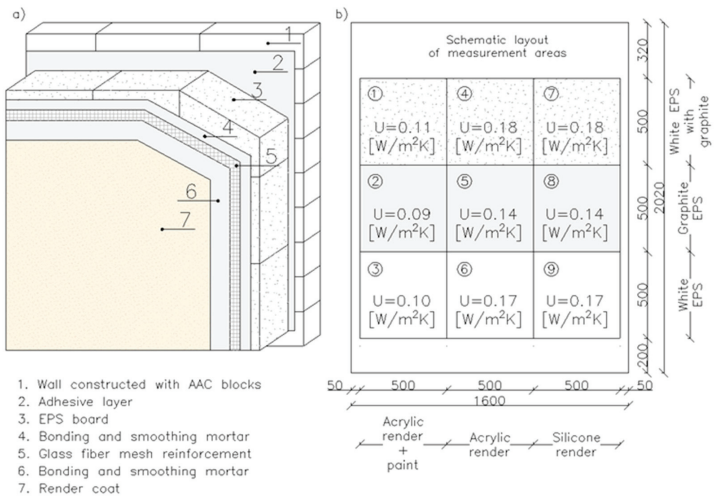

Figure 1. Arrangement of layers: (**a**) diagram of the layers of the partition under consideration and (**b**) the tested arrangements (insulation-plaster) of the partition.

2.2. Tests in the Aging Chamber

Solar heating tests on plaster were carried out in an aging chamber. A test rig designed for atmospheric aging was used to simulate solar radiation. A climate chamber, part of the aging chamber, the so-called 'sun chamber', was used in the study, whose task was to simulate solar performance through illumination.

The 'sun chamber' inflicts radiation close to natural sunlight in the 400–700 nm range through a system of 20 metal-halide (MH) lamps, each with 8 kW of power and 10 UV-mimicking ultraviolet emitters. The MH lamps, with a color temperature of 4500 K and a luminous flux of 35,000 Lm, are characterized by good reproduction in the spectrum of natural solar radiation.

The test specimens were prepared as ETICS (External Thermal Composite Insulation System)-type external wall insulation systems. The prepared system of nine specimens, with different layers of polystyrene and plaster, was built over the entire surface of one of the walls of the central exhibition chamber with an area of 1.6 × 2.1 m (as described in chapter 2.1). In order to collect measurement data of the heating temperature of the plaster in the central point of each sample (50 × 50 cm field), thermocouple-type sensors were installed in the flush-mounted layer and on the render surface (Figures 2 and 3). Individual sensors were connected to an Ahlborn Therm 5500-3 multi-channel recorder (Holzkirchen, Germany). In this way, the test samples, together with the recording system, were prepared for testing.

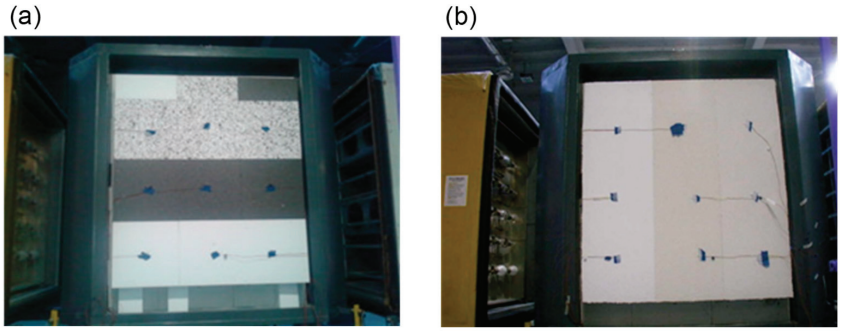

Figure 2. Layering of thermal insulation layers and temperature sensors: (**a**) under the render; (**b**) on the render surface.

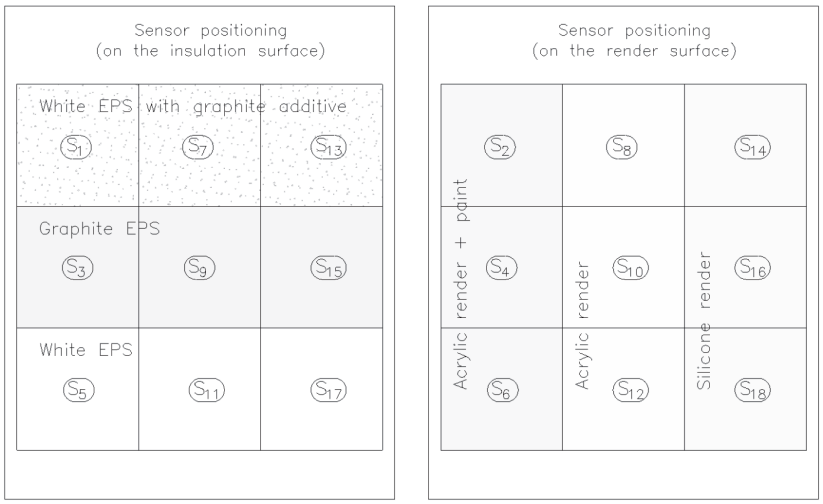

Figure 3. Location and marking of the temperature sensors under the render and on the render surface.

The experimental study was conducted under the following conditions: air temperature near the sample: Meas. I—22.4 °C, Meas. II—33.5 °C, Meas. III—25.3 °C, Meas.

IV—23.5 °C, Meas. V—23.5 °C; air temperature in the laboratory: 17.0 ± 0.2 °C; air humidity: 24%; and air velocity inside the laboratory: 0.1 m/s.

The tests were repeated five times to verify the results and assess the effect of varying the position of the radiation source on the temperature distribution on the partition surface. The distance of the light source from the test surface was changed three times, while the material properties and geometry of the partition were unchanged. The test was carried out with the lamps positioned at distances from the test surface of the partition equal to 66 cm, 23 cm, and 45 cm (Figure 4):

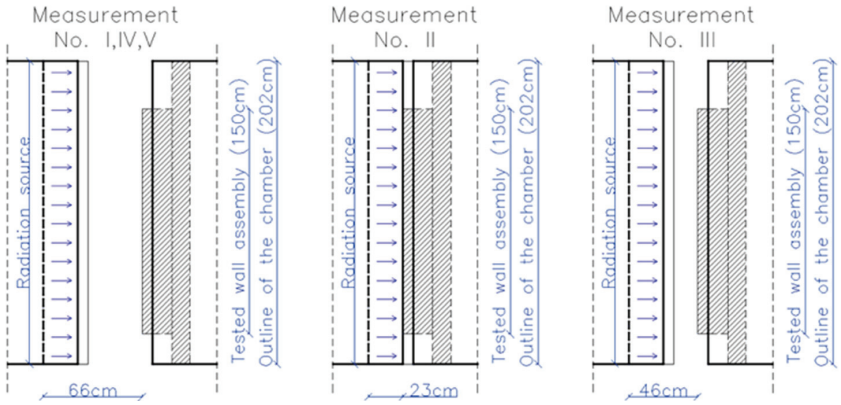

Figure 4. Location of the solar radiation source in relation to the test wall.

Once the aging chamber lamps were switched on, regular temperature readings were taken at 2-min intervals for a period of 2 h. This process allowed the surface temperature changes of the tested materials to be accurately monitored under the influence of the thermal radiation emitted by the lamps. By recording the temperature values at specific measurement points, it was possible to analyze the dynamics of surface heating as a function of time.

At the end of the heating stage, the lamps were switched off, and temperature readings were continued at the same measuring points every 2 min for a further 2 h. This stage was aimed at assessing the cooling process of the surface and determining the time required to reach thermal equilibrium with the surroundings.

2.3. Numerical Analyses

In parallel to the tests in the aging chamber, the experimental situation was also modeled in Ansys, version 2024 R2, and THERM, version 7.6.

In Ansys in the Steady-State Thermal module, 3D analyses were carried out using the finite element method (FEM). The boundary conditions were set so that the specimen was treated as a section of wall (i.e., the width and height of the specimen was not limited). The simulation was based on the introduced geometry, taking into account the material layers and their thermal properties as faithfully as possible, reflecting the specimens used in the experimental studies. The boundary conditions corresponded to the test setup from Measurement IV.

The modeling process in THERM began by importing the geometry of the system under analysis and defining the material parameters and boundary conditions. In THERM, 2D finite-difference analyses were carried out on the created geometry of the analyzed system and after defining the material parameters and boundary conditions.

3. Results and Discussion

The maximum temperatures recorded during the measurement are presented in Figure 5.

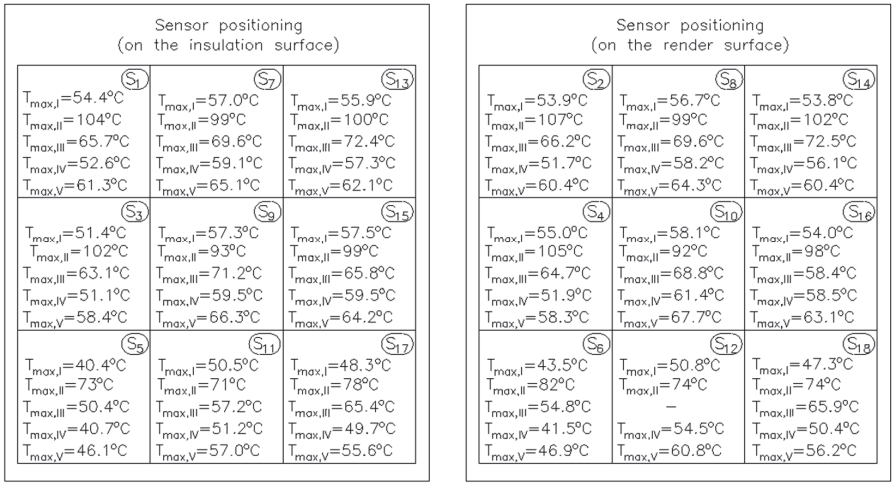

Figure 5. Surface temperatures of render and insulation—Measurements I–V.

During the operation of the aging chamber, the light bulbs generate high temperatures. To prevent emergency situations, the device is equipped with autonomous safety mechanisms that deactivate individual bulbs depending on the temperature. In order to analyze the impact of this aspect, the irradiance level in the central part of the wall, formed by the nine test fields combined, was monitored. The readings were taken over a period of 2.5 h, at 2-minute intervals (Figure 6).

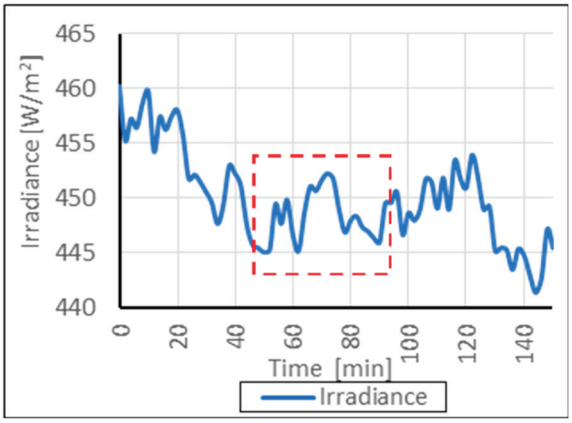

Figure 6. Variation of the solar radiation intensity over time. The area marked in red is enlarged in Figure 7.

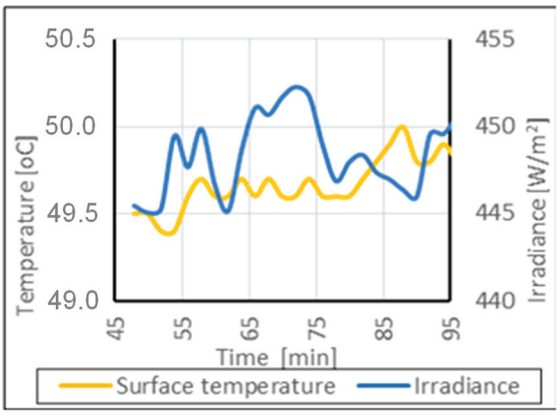

Figure 7. Dependency of temperature variation on the solar radiation intensity over time.

The recorded temperature fluctuations on the surface of the wall section exhibited a clear correlation with the observed variations in irradiance. This relationship is illustrated in Figure 7 (a fragment of the measurement presented in Figure 6), where it is evident that a decrease in irradiance resulted in a temperature drop, while an increase in irradiance led to a renewed rise in surface temperature.

During the 150-minute measurement period, the irradiance levels varied between 441 W/m^2 and 461 W/m^2, representing a fluctuation of less than 5%. These temporal variations—caused by automatic bulb shutoffs—resulted in corresponding fluctuations in the temperature readings; however, the extent of these deviations was considered acceptable.

To ensure the reliability of the measurements, irradiance was verified using a solarimeter across different test fields on the wall. During Measurement I, Field 5 recorded 389.6 W/m^2, while Field 3 showed only 275.8 W/m^2. Even greater discrepancies were observed during Measurement III, with irradiance ranging from a maximum of 499.4 W/m^2 to a minimum of 332.0 W/m^2. The distribution of irradiance across the surface of the wall section is illustrated in Figure 8.

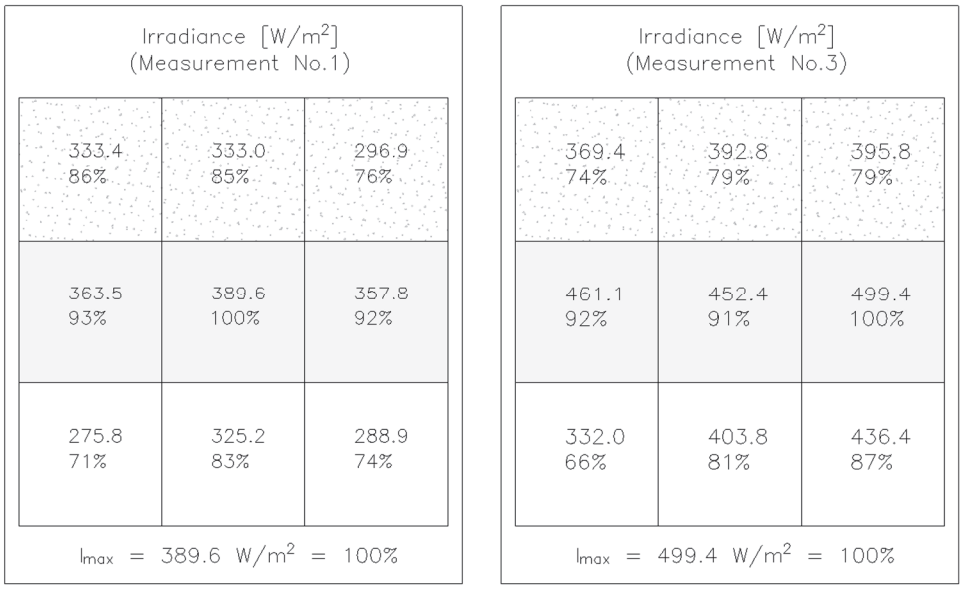

Figure 8. Irradiance values recorded for Measurements I and III.

To assess the significance of this parameter, the measured irradiance values were compared with the corresponding render surface temperatures in Table 1.

Table 1. Summary of the irradiance measurements for individual test fields with corresponding render surface temperatures—Measurements I and III.

Measurement No.	Irradiance [W/m^2]/Temperature [°C] for Subsequent Measurement Areas								
	S1	**S2**	**S3**	**S4**	**S5**	**S6**	**S7**	**S8**	**S9**
I	333.4 53.9	363.5 55.0	275.8 43.5	333.0 56.7	389.6 58.1	325.2 50.8	296.9 53.8	357.8 54.0	288.9 47.3
III	369.4 66.2	461.1 64.7	332.0 54.8	392.8 69.6	452.4 68.8	403.8 -	395.8 72.5	499.4 76.4	436.4 65.9

The study was conducted on fields with different material parameters, making it necessary to determine the relationship between irradiance and temperature.

Based on Table 2, it was found that in the analyzed cases, an irradiance level ranging from 5.5 W/m^2 to 8.6 W/m^2 was required to generate a 1 °C increase in temperature. As

demonstrated in Table 1, the maximum difference in measured irradiance reached nearly 170 W/m^2.

Table 2. Irradiance required to generate a 1 °C temperature rise, depending on the test field on the wall section.

Measurement No.	Required Irradiance per 1 °C Temperature Rise for Each Measurement Area								
	S1	**S2**	**S3**	**S4**	**S5**	**S6**	**S7**	**S8**	**S9**
I	6.2	6.6	6.3	5.9	6.7	6.4	5.5	6.6	6.1
III	5.6	7.1	6.1	5.6	6.6	-	5.5	6.5	6.6

This analysis highlighted that directly comparing different test fields without standardizing the radiation intensity would be methodologically inappropriate. To ensure the reliability and accuracy of the study results, a correction of the temperature readings was necessary. It was assumed that the highest measured irradiance in a given test served as the reference level (100%), and the values for the remaining fields were expressed as a percentage of this reference value. Using this percentage relationship, the recorded temperatures were recalculated accordingly.

Temperature corrections were performed based on the irradiance distribution pattern shown in Figure 8 (where for Measurements I, II, IV, and V: 100% = 389.6 W/m^2, and for Measurement III: 100% = 499.4 W/m^2), with the adjusted results presented in Figure 9.

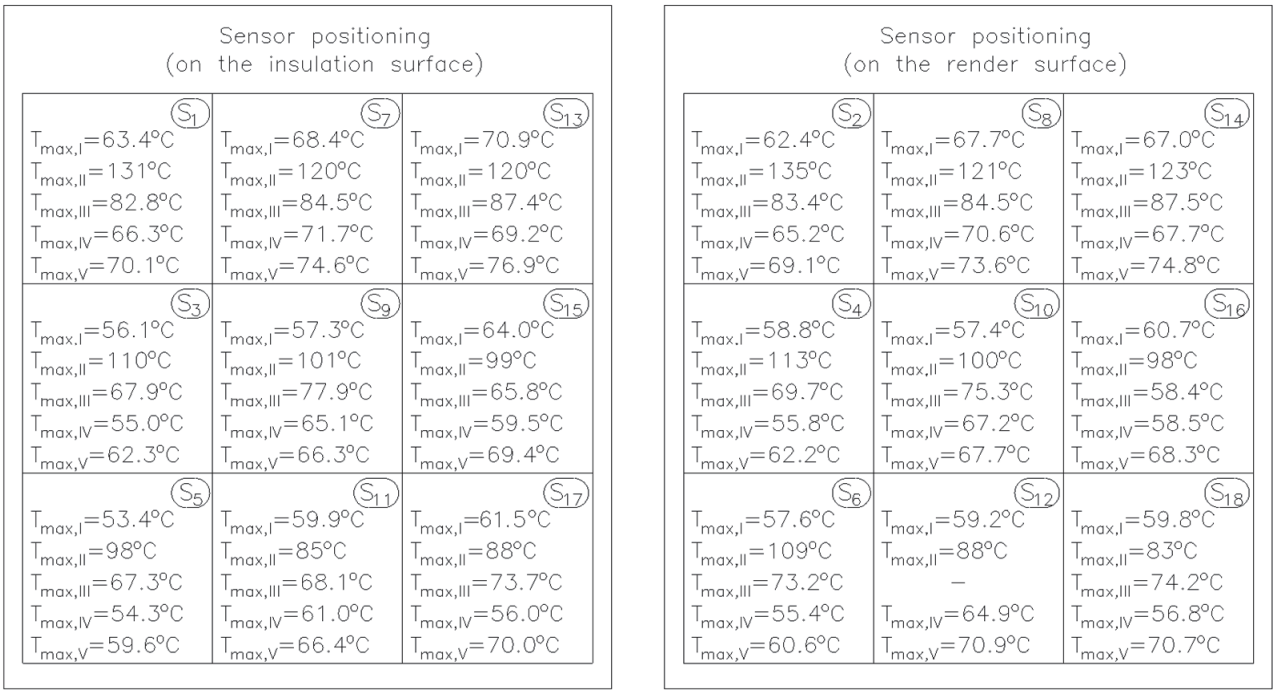

Figure 9. Corrected temperature values based on irradiance uniformity—Measurements I–V.

To illustrate the dynamic impact of radiant exposure on the temperatures at the render surface and within the insulation layer, Figures 10 and 11 present time-dependent temperature profiles for two of the five measurements conducted.

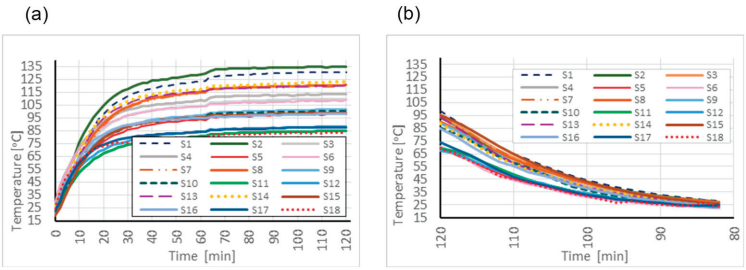

Figure 10. Temperature change over time: (**a**) under solar radiation exposure and (**b**) after switching off the radiation source—Measurement II.

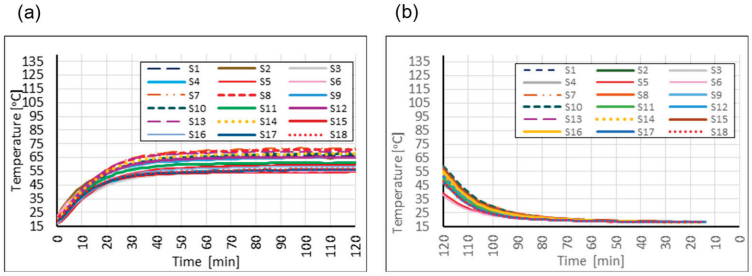

Figure 11. Temperature change over time: (**a**) under solar radiation exposure and (**b**) after switching off the radiation source—Measurement IV.

The graphs captured both the heating phase, resulting from exposure to the radiation source (Figures 10a and 11a), and the cooling phase following its deactivation (Figures 10b and 11b). This dual-phase representation enabled the analysis of both the intensity of the thermal response and the thermal release capability of the tested material assemblies.

It was observed that the temperature differences between the readings taken on the render surface and those on the insulation (EPS) surface varied depending on the position of the measurement points across the tested fields. The results are presented in Figure 12a–e.

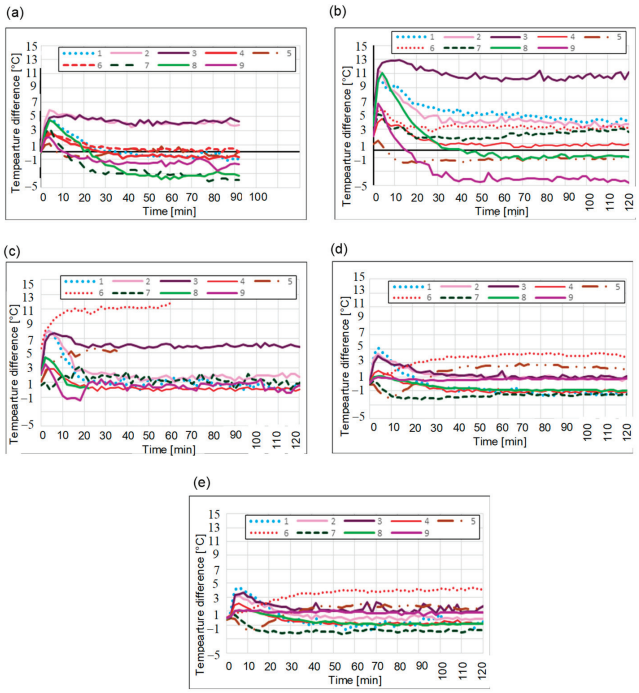

Figure 12. Temperature difference between the render surface and insulation—(**a**) Measurement I, (**b**) Measurement II, (**c**) Measurement III, (**d**) Measurement IV, and (**e**) Measurement V.

The recorded differences in temperature values can, from a physical standpoint, be attributed to varying material properties such as the thermal transmittance coefficient, surface emissivity, or the ability to absorb radiation.

3.1. Influence of Plaster Type and Insulation Material on Temperature Variations

The diagrams presented in the following (Figures 13–15) illustrate the variations in temperature differences between the values measured on the surface of the render (exterior plaster layer) and those recorded on the surface of the thermal insulation over time. The measurements were conducted on samples featuring different finishing systems: acrylic plaster finished with a thermal-insulating paint, standard acrylic plaster, and a silicone plaster.

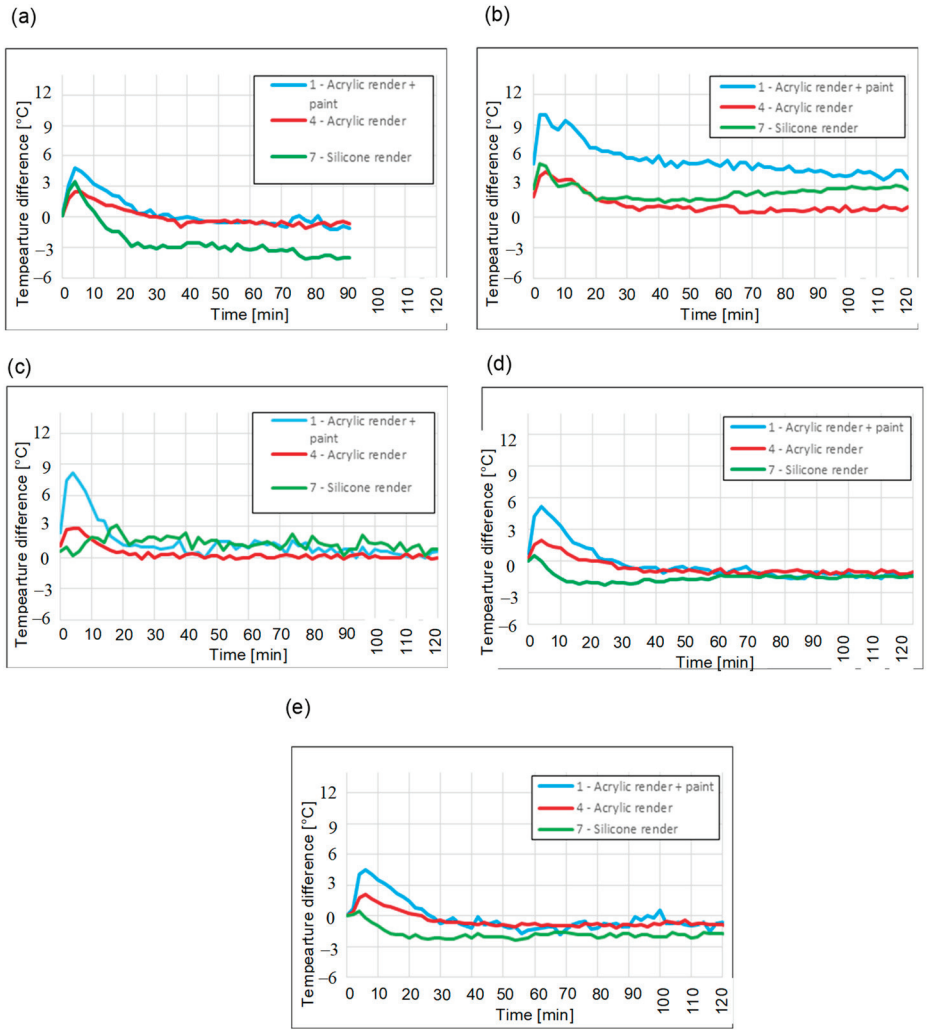

Figure 13. Temperature difference between the render surface and insulation—white polystyrene with graphite, λ = 0.042 W/(m·K)—(**a**) Measurement I, (**b**) Measurement II, (**c**) Measurement III, (**d**) Measurement IV, and (**e**) Measurement V.

To enable comparative analysis, the results were grouped based on the type of thermal insulation used—specifically expanded polystyrene (EPS) variants with different thermal conductivity coefficients.

The tests were carried out under defined atmospheric conditions, with temperature values recorded at consistent time intervals. This ensured a reliable assessment of the thermal characteristics of the tested assemblies.

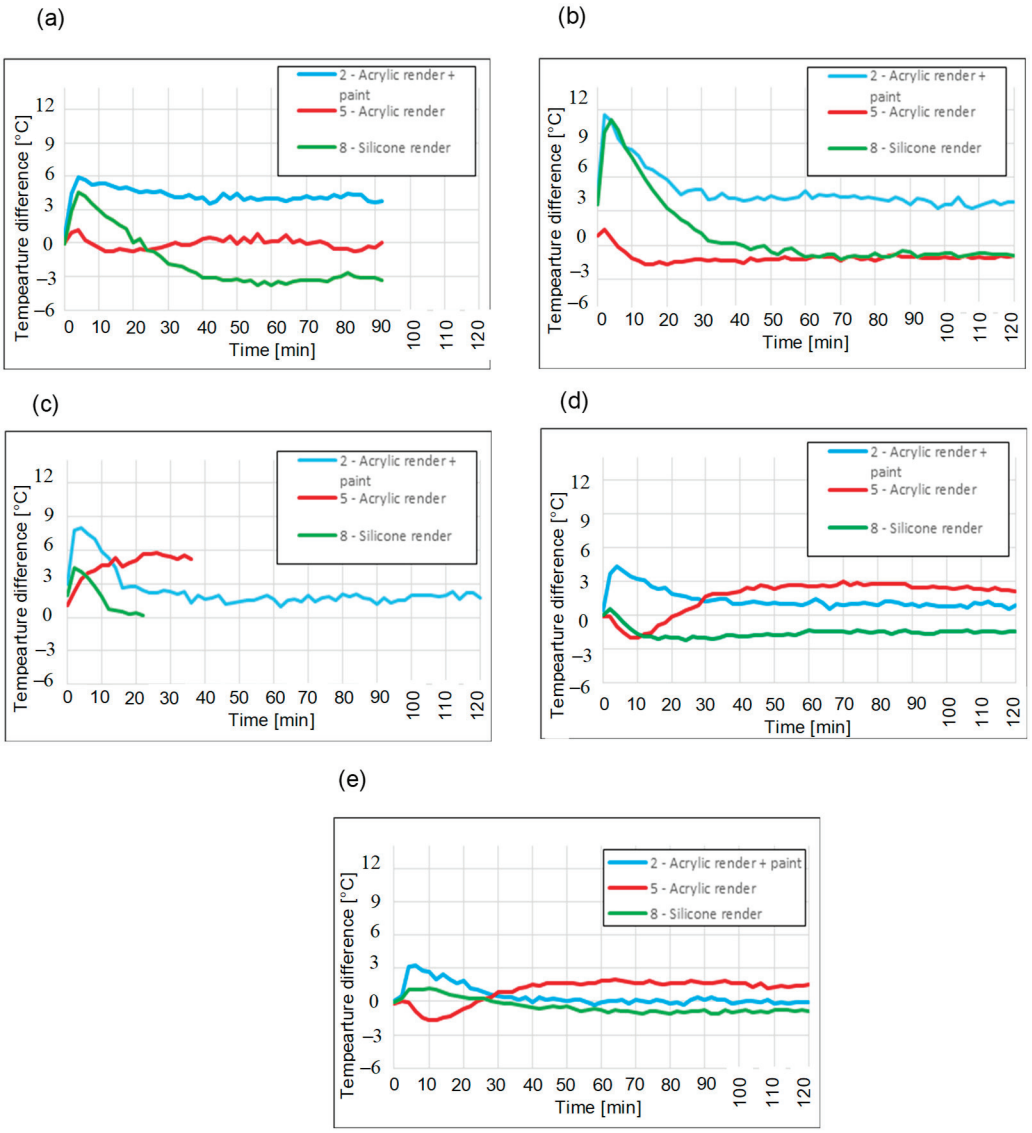

Figure 14. Temperature difference between the render surface and insulation—graphite polystyrene, λ = 0.033 W/(m·K)—(**a**) Measurement I, (**b**) Measurement II, (**c**) Measurement III, (**d**) Measurement IV, and (**e**) Measurement V.

The results for test fields in which white expanded polystyrene with a graphite additive was used as an insulating layer are presented in Figure 13a–e. The acrylic render variant finished with thermochromic paint demonstrated a medium and highest temperature difference—indicating the best thermal properties. The acrylic and silicone render consistently showed low to medium thermal properties.

Figure 14a–e refers to test fields in which graphite polystyrene was used as an insulating layer. The summary of the five measurement series indicates that when using the more thermally efficient graphite-enhanced polystyrene (λ = 0.033 W/m·K), the measurement results changed slightly. The acrylic render with thermal paint more frequently maintained a high temperature differential, which may suggest its more favorable role in preventing heat loss when paired with graphite insulation.

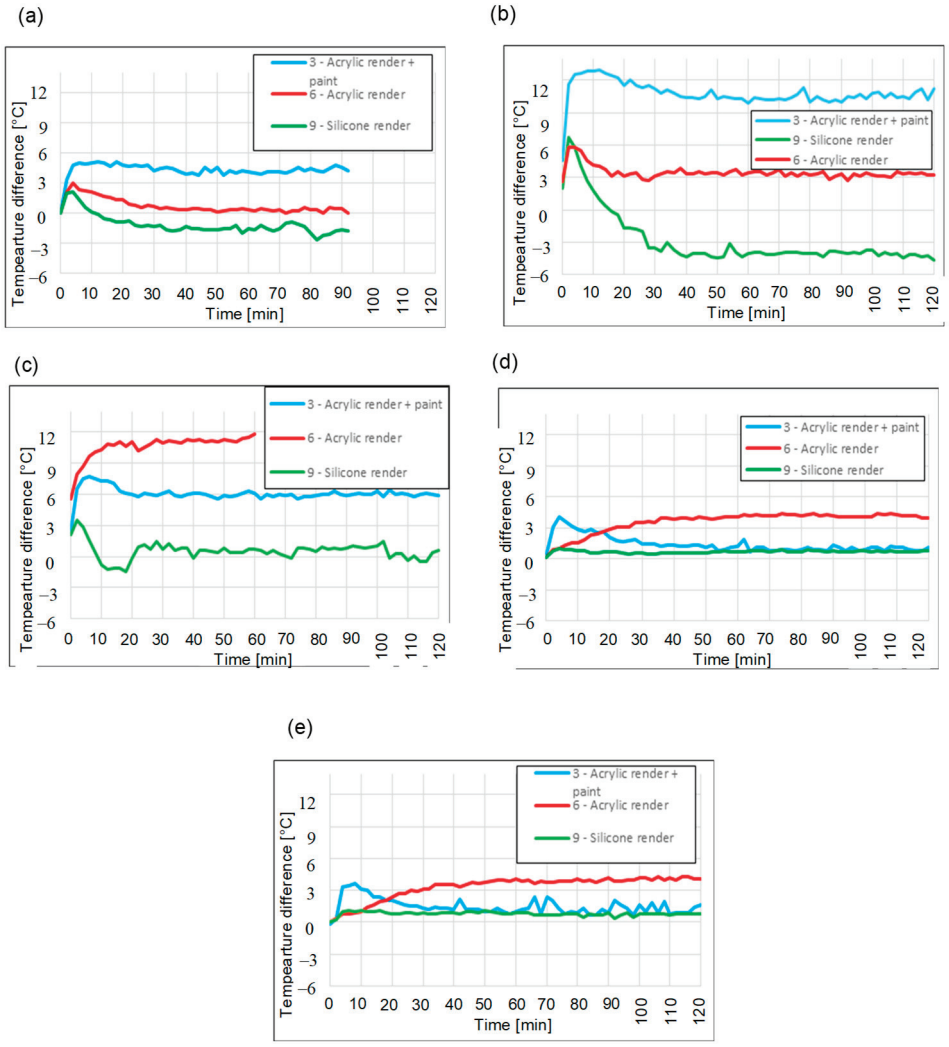

Figure 15. Temperature difference between the render surface and insulation—white polystyrene, λ = 0.040 W/(m·K)—(**a**) Measurement I, (**b**) Measurement II, (**c**) Measurement III, (**d**) Measurement IV, and (**e**) Measurement V.

The measurement data for samples with white polystyrene insulation are shown in Figure 15a–e. For white expanded polystyrene (λ = 0.040 W/m·K), the highest thermal performance was generally exhibited by the acrylic render with thermal paint, which throughout most of the test series achieved the greatest temperature differences, thus providing the highest resistance to heat flow. In this configuration, the acrylic render performed better than when combined with other insulation materials—often demonstrating stable and predictable thermal behavior. In this case, silicone plaster definitely gave way to the others.

Based on the analysis of fifteen graphs depicting the temperature difference between the render surface and the insulation layer for three types of polystyrene—white expanded polystyrene with graphite additive (λ = 0.042 W/m·K), graphite-enhanced polystyrene (Grey EPS) (λ = 0.033 W/m·K), and white expanded polystyrene (λ = 0.040 W/m·K)—clear conclusions can be drawn regarding the behavior of façade systems in response to thermal radiation. Despite the variability in conditions (especially the notable difference in radiation source distance in Measurements II and III), several repeatable tendencies and material-related distinctions were observed.

The silicone render consistently exhibited a characteristic trend of rapidly decreasing temperature differences, often resulting in negative values—indicating that the render

surface became cooler than the insulation surface. This suggests a rapid transfer of thermal energy through the finishing layer, which may be attributed to its low thermal mass and high thermal conductivity, which allow heat to pass through the silicone coating without significant accumulation at the façade level.

The acrylic render demonstrated a more stable and predictable behavior. In most measurements—regardless of insulation type—it maintained moderate temperature differences (~0–5 °C), rarely falling below zero.

The acrylic render with thermal paint almost universally produced the highest temperature differences, indicating high reflectivity, as claimed by the manufacturer. Its overall profile suggests that this render variant most effectively reduced heat transfer to the insulation layer, particularly under intense thermal exposure. This effect was most pronounced in Measurement II (closest heat source), where the acrylic + paint system exhibited temperature differences several times greater than the other render types.

When comparing system performance across insulation types, it is evident that grey EPS, being the most thermally resistant (λ = 0.033 W/m·K), amplified the contrast between the renders—highlighting the poor insulating performance of silicone and the strong barrier effect of acrylic + paint. White EPS with the graphite additive presented a more balanced profile, whereas the silicone render often showed moderate efficiency. Meanwhile, standard white EPS, although theoretically less insulating, demonstrated a surprisingly effective performance when combined with acrylic render—indicating a possible synergistic effect between its moderate conductivity and the thermal mass of the render.

In an ETICS system with a façade plaster, sunlight absorption occurs primarily on the plaster surface, but some long-wave thermal radiation can penetrate the plaster layer, especially thin-layer plaster, and affect the polystyrene. Differences in α between the polystyrene layers may then have a secondary, but measurable, effect on the temperature distribution within the partition, as confirmed by the measurement results.

3.2. Influence of Radiation Source Distance

In order to fully understand the behavior of the tested material systems under thermal exposure, five levels of exposure were analyzed, differing both in the distance between the radiation source and the wall assembly and in radiation intensity. This comparison made it possible to clearly distinguish the impact of external conditions from the intrinsic material properties of the samples and assess how the geometric relationship between the source and the wall influences the heating of façade surfaces. Table 3 presents the summarized measurement data. The reported radiation intensity was the highest among the measured values.

Table 3. Overview of the measurement conditions.

Measurement No.	Distance Between the Radiation Source and the Wall Assembly [cm]	Radiation Intensity [W/m^2]
I	66	389.6
II	23	450.0
III	45	499.4
IV	66	389.6
V	66	389.6

Measurement II was characterized by the shortest distance between the radiation source and the wall, combined with a very high radiation intensity, which allowed for the identification of particularly adverse conditions for envelope systems exposed to local heat sources. Measurement III, despite an even higher intensity, was conducted from a greater distance, which significantly influenced the temperature distribution over time. Measurements I, IV, and V formed a comparative group with standardized exposure conditions.

The graphs do not include the values recorded during measurement disturbances resulting from mechanical interference with the sensor system (e.g., the need to adjust their mounting or restore proper contact with the tested surface). These data were deliberately excluded from the analysis, as they are not representative of the actual thermal response of the system.

In all nine measurement areas, the dominant influence of the distance between the radiation source and the wall assembly on the temperature profile of the tested systems was unequivocally confirmed (Figures 16–18). Measurement II, in which the source was placed closest to the wall—just 23 cm away—at a radiation intensity of 450 W/m^2, resulted in the most rapid and extreme temperature increases across all samples. Under these conditions, the final surface temperatures frequently exceeded 120 °C, regardless of the type of EPS or render used. This clearly indicates that the thermal load intensity outweighs the effect of the material characteristics. In Measurement III, despite an even higher radiation intensity (499.4 W/m^2), the use of a greater source-to-surface distance (45 cm) resulted in notably lower temperatures. This confirms that the efficiency of heat transfer is determined not only by the power of the thermal flux, but above all, by the spatial configuration between the source and the heated surface including both the distance the radiation travels and the presence of obstacles that may restrict free air movement and thus convection.

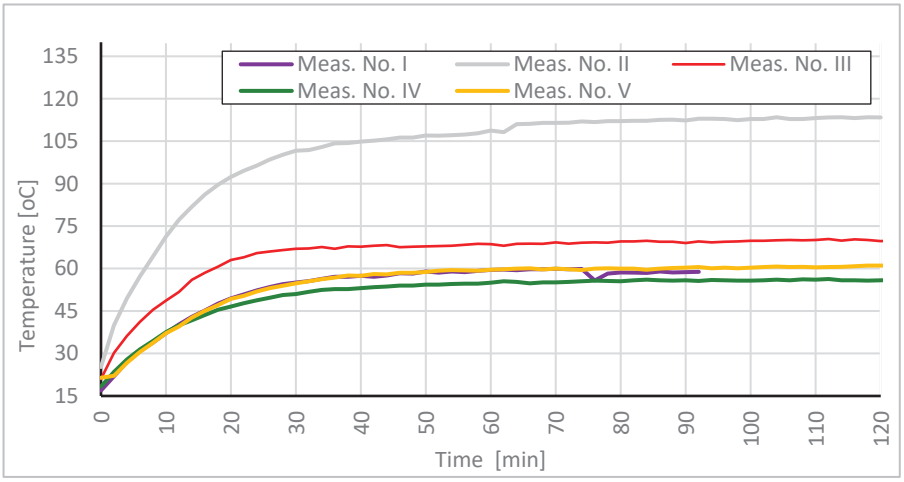

Figure 16. Temperature change over time—comparison of the results on the surface of the finishing layer in Measurement area 2 across consecutive measurements.

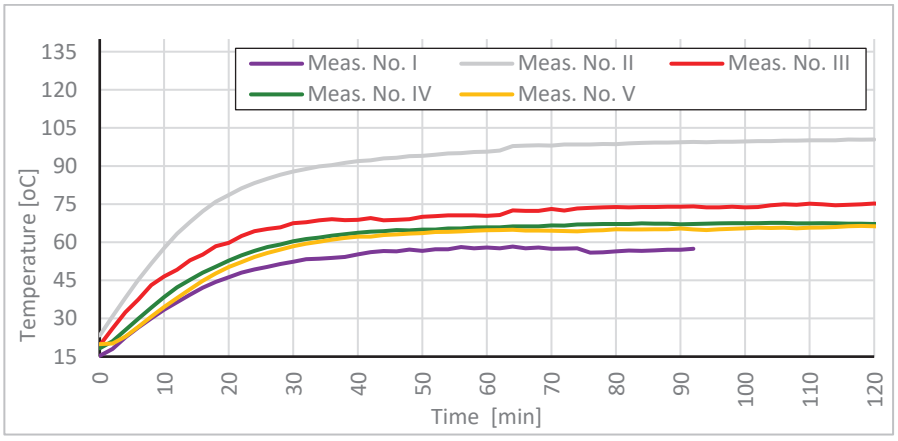

Figure 17. Temperature change over time—comparison of results on the surface of the finishing layer in Measurement area 5 across consecutive measurements.

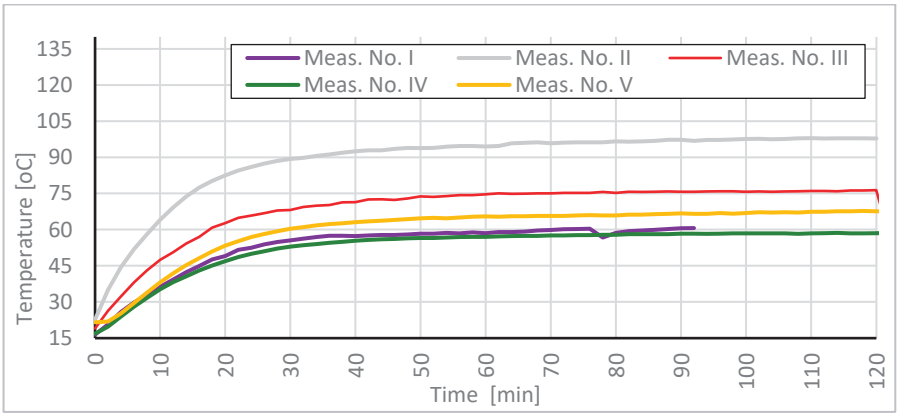

Figure 18. Temperature change over time—comparison of results on the surface of the finishing layer in Measurement area 8 across consecutive measurements.

A key physical phenomenon that further explains the materials' strong response to proximity heating is the limitation of convective heat exchange with the environment. In Measurement II, due to the very small gap between the radiation source and the wall surface, airflow was severely restricted, preventing the efficient displacement of heated air. This limited air circulation caused the formation of a localized layer of warm air that was not effectively replaced by cooler ambient air. The resulting "thermal cushion" effect led to continuous surface heating, as the heat that would otherwise be dissipated by natural convection remained trapped. Consequently, the system exhibited a nonlinear temperature increase in response to reduced distance; despite relatively minor differences in radiation intensity between tests, temperature differences reached several tens of degrees Celsius.

Measurements I, IV, and V, conducted at the greatest distance (66 cm) and a radiation intensity of 389.6 W/m^2, showed the lowest temperatures and the most stable profiles. In these cases, the available space allowed for free airflow and more efficient heat dissipation into the environment, effectively limiting surface temperature rises. Furthermore, under moderate radiation conditions, the differences between the materials became more distinguishable, suggesting that thermal performance characteristics become more apparent when surface phenomena are not overshadowed by extreme radiation exposure.

In summary, reducing the distance between the radiation source and the wall assembly increased both the intensity of heat input and the restriction of heat dissipation through natural convection. These effects act synergistically, producing a pronounced nonlinear rise in the temperature of the material. As a result, even minor changes in exposure geometry may have greater thermal implications than the material parameters themselves. This phenomenon has practical importance in real-world conditions, where wall systems are often subjected to intense, directional solar radiation such as sun-exposed façades, narrow gaps between buildings, or adjacency to heat-emitting surfaces like asphalt. In such scenarios, the thermal protection performance depends not only on the insulation properties, but also on environmental factors that either enable or hinder effective heat exchange with the surroundings.

3.3. Numerical Simulation

In parallel with the experimental study, the scenario was also modeled using Ansys software, version 2024 R2, the Steady-State Thermal module, and THERM software, version 7.6.

THERM is a tool that uses a two-dimensional steady-state heat conduction model, as described.

This program focuses solely on thermal conductivity, without the ability to account for full thermal radiation or dynamic phenomena.

Ansys Steady-State Thermal, on the other hand, is an advanced numerical tool that also uses the Fourier equation in steady-state mode, but in a full 3D or 2D model:

$$\nabla(k\nabla T) + Q = 0 \tag{1}$$

The analysis conducted in both programs focused on the case with one-way heat transfer (from the outer to the inner surface of the partition), which physically implies a 1D model. However, using Ansys allowed for the accurate representation of the influence of solar radiation (through a defined heat flux and emissivity) and the temperature distribution in the layered material, which exceeds the capabilities of THERM.

The numerical modeling conducted included several simplifying assumptions that could have contributed to the differences between the simulation results and the actual measurements. The most important include:

1. Ignoring natural airflows (free convection) around the tested element—the model primarily considered thermal conductivity and radiation, assuming a simplified or constant convection coefficient, without dynamic air exchange with the surroundings.
2. Idealization of contact conditions between the system layers (e.g., plaster—polystyrene)—in reality, micro-gaps, discontinuities, or heat transfer resistances may occur, which were not reflected in the model.
3. Simplified boundary conditions for thermal radiation—the simulation used averaged values of emissivity and radiant flux, ignoring minor differences resulting from surface texture.
4. Assumption of material homogeneity—the model did not account for local inhomogeneities in the insulating material (e.g., in the case of white polystyrene with added graphite), which could have affected the local temperature distribution.
5. Constant ambient conditions—constant ambient temperature and radiation conditions were assumed, ignoring their possible fluctuations during the actual experiment.

The results for the selected test areas are presented in Table 4.

Table 4. Summary of selected results obtained using Ansys and THERM software.

Area No.	Ansys		THERM	
	Maximum Temperature [°C]			
2	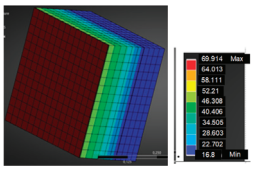	69.91	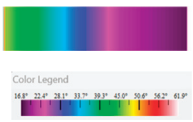	61.88
5	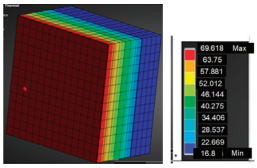	69.62	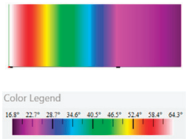	64.30
8	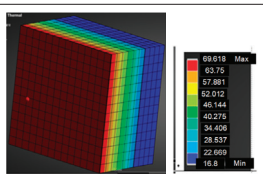	69.62	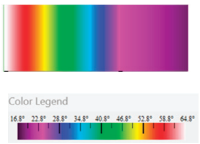	64.80

The analyses took into account the material parameters of the façade renders, the thermal properties of the applied insulation, and the boundary conditions simulating solar exposure (excluding UV radiation) as well as convective and radiative heat exchange with the surrounding environment, consistent with the conditions of Measurement IV.

Table 5 presents the maximum surface temperatures obtained across nine test fields, calculated using different numerical tools: Ansys Steady-State Thermal and THERM. For comparison, these results were juxtaposed with data from the experimental measurements.

Table 5. Summary of results obtained through numerical simulation.

Area No.	Steady-State Thermal			THERM			Measurement IV
	Result	Absolute Error vs. Experimental Reading		Result	Absolute Error vs. Experimental Reading		
	[°C]	[°C]	[%]	[°C]	[°C]	[%]	[°C]
1	69.84	−4.7	−7	61.83	3.3	5	65.2
2	69.91	−14.1	−25	61.88	−6.0	−11	55.8
3	69.85	−14.4	−26	61.80	−6.4	−12	55.4
4	69.42	1.2	2	64.10	6.5	9	70.6
5	69.62	−2.4	−4	64.30	2.9	4	67.2
6	69.46	−4.5	−7	64.20	0.7	1	64.9
7	69.42	−1.7	−2	64.70	3.0	4	67.7
8	69.62	−11.1	−19	64.80	−6.3	−11	58.5
9	69.46	−12.7	−22	64.70	−7.9	−14	56.8

In the comparative analysis of results obtained in the simulation environments Ansys (Steady-State Thermal) and THERM, against the measurement data from the fourth experimental cycle, clear quantitative discrepancies were observed in the recorded surface temperatures. In most cases, the THERM software more accurately reflected the experimental measurements—the absolute deviations were generally within ±5 °C, corresponding to a relative error in the range of 1–11%. The results obtained in Ansys showed larger differences, reaching up to 26% (e.g., Field 3), which may indicate limitations of the applied model or simplifications in the boundary conditions.

The highest relative errors in both simulation environments were observed for Fields 2 and 3, where the differences between the calculated and measured temperatures reached −14.4 °C in Ansys and −6.4 °C in THERM. It should be noted that Fields 1–3 were coated with a thermal insulation paint with reflective properties. This layer could have reduced heat absorption and altered the local thermal balance, which may not have been fully captured in the simulation models—especially in Ansys, where this effect may have been underestimated.

For Fields 4–7, the agreement between the simulation results and the experimental data was significantly better, particularly in the case of THERM. For example, Field 6 exhibited only a 1% error, confirming the reliability of the model when appropriately configured with accurate material and boundary parameters. The discrepancies in Ansys were more pronounced but still within the acceptable range for preliminary analyses.

The largest deviations (up to −14% in THERM and −22% in Ansys) for Field 9 may have resulted from local differences in emissivity, conductivity, or even nonlinear thermal conduction through the layers—effects that are often averaged or omitted in simplified models. This highlights the need for further refinement of the simulation frameworks.

In summary, THERM—due to its simplified but accurately configured two-dimensional model—proved more effective in replicating the experimental results. Ansys, while more suitable for general analysis, requires precise input parameter definitions for comparative

evaluations. Particular attention should be paid to the optical and thermal properties of surface layers—such as reflective coatings—that can significantly affect the temperature distribution within the envelope.

4. Conclusions

The conducted research enabled a comprehensive, multi-faceted evaluation of the influence of thermal radiation on vertical building envelopes, taking into account material variability and exposure geometry. Through five repeated measurement cycles and the application of various finishing and insulation configurations, it was possible to analyze both the dynamic characteristics of wall heating and the long-term effectiveness of thermal protection.

The results recorded across five measurement series clearly demonstrate that both the radiation intensity and the mechanisms of heat dissipation into the environment significantly influence the level of envelope heating as well as the way in which heat is distributed throughout its structure. The most extreme heating conditions occurred during Measurement II, where the smallest distance between the radiation source and the envelope (23 cm) led to the highest recorded surface temperatures on the exterior render, and in many cases, also on the surface of the insulation layer. In contrast, Measurement III, although it had the highest recorded radiation intensity (499.4 W/m^2), resulted in slightly lower temperatures. This can be attributed to the greater distance, which allowed for more efficient heat exchange with the surrounding air, thus reducing the severity of the thermal load. In Measurements I, IV, and V, conducted with the radiation source placed at a greater distance (66 cm), lower temperature values and greater measurement repeatability were observed—creating optimal conditions for comparing the performance of different insulation materials.

A comparison of the maximum temperatures recorded on the surface of the façade render and on the insulation (Figures 19 and 20) revealed significant differences in the thermal behavior of the tested material assemblies. In many cases, the render surface reached higher temperatures during the initial phase of radiation exposure due to its direct exposure to the heat source. However, with prolonged heating and increased thermal load, the temperature on the insulation surface occasionally exceeded that of the render—indicating heat accumulation in the deeper layers of the wall assembly. The final temperature distribution was thus the result of both the individual material properties and their interactions within the entire system.

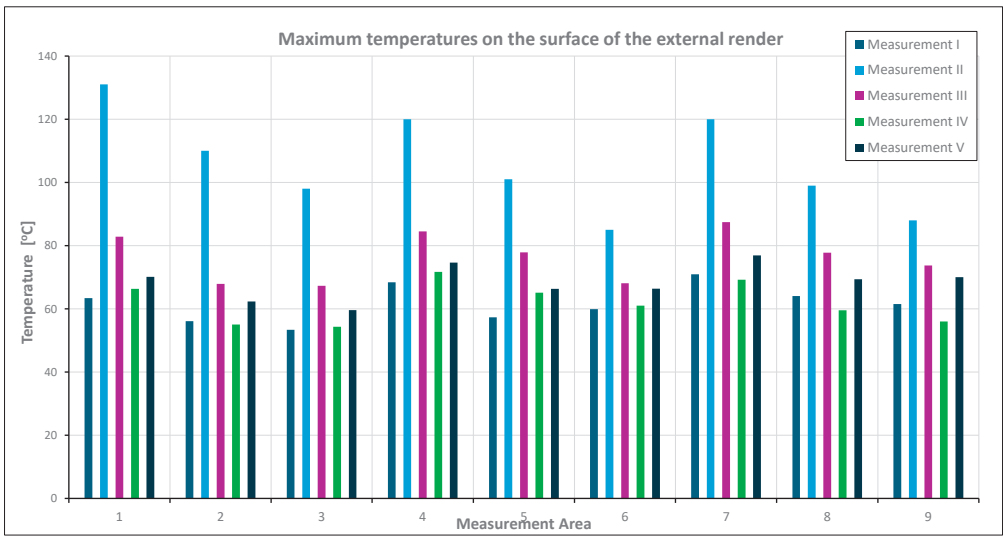

Figure 19. Graph of the maximum temperatures on the surface of the insulation layer for the nine tested areas across five consecutive measurements.

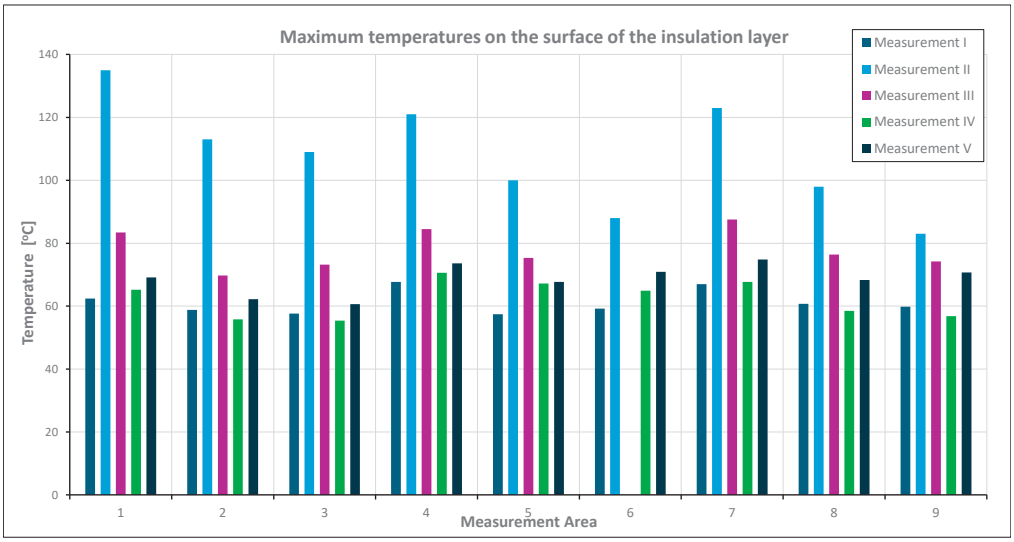

Figure 20. Graph of the maximum temperatures on the surface of the external render for the nine tested areas across five consecutive measurements.

In this study, the distance between the radiation source and the test surface was treated as a model equivalent of real-world conditions with limited heat dissipation such as dense urban settings, poor natural ventilation, or shading. The findings indicate that under such conditions, the envelope is subjected to intensified heating, which should be considered in façade design and the selection of finishing materials.

The inclusion of numerical thermal simulations using dedicated software provided valuable support to the experimental work. Two approaches were employed: a simplified 2D model using THERM to analyze cross-sectional heat conduction, and an advanced 3D simulation using Ansys, enabling the tracking of temperature distribution over time.

The simulations confirmed the direction of energy flow and the progressive heating of successive layers. Differences between material variants observed in the simulation results were consistent with the experimental findings. The numerical approach, based on ideally homogeneous conditions, helped minimize the impact of radiation variability.

From an engineering perspective, the use of two independent simulation methods enabled the cross-validation of results and enhanced the reliability of conclusions. Numerical tools allow for the rapid testing of new material and geometric configurations at the design stage, making them an extremely useful component in optimizing construction solutions. However, it is important to emphasize that experimentally obtained results remain more representative of real-world use and are essential for validating numerical models.

The final analysis confirmed that the effectiveness of a thermal barrier is a function of multiple interacting factors—not only material technical parameters, but also environmental conditions and exposure geometry. Even with identical layer geometries, changes in convective conditions can lead to significant differences in surface heating. The collected measurements, supported by graphical analysis, suggest that insulation surface temperature is one of the key indicators of the thermal protection efficiency of wall assemblies, directly impacting building energy performance and occupant comfort. This work contributes to the broader discussion on the impact of façade materials and colors on the passive cooling of buildings. Our research indicates a need for further development in this area of passive cooling. On the one hand, we presented a research methodology using a rotating chamber to simulate the aging of materials under real-world conditions, which in itself is an original proposal to complement established research methods. On the other hand, we confirmed research results obtained using other research methods known

from the literature, simultaneously identifying gaps in knowledge and proposing further research development in this area.

Author Contributions: Conceptualization, J.W., M.M., J.B. (Jerzy Bochen) and J.B. (Janusz Belok); Methodology, J.W., M.M., J.B. (Jerzy Bochen) and J.B. (Janusz Belok); Software, J.W.; Validation, J.W., M.M. and J.B. (Jerzy Bochen); Formal analysis, J.W., M.M. and A.N., Investigation, J.W., M.M. and A.N.; Data curation, J.W., M.M., J.B. (Jerzy Bochen), J.B. (Janusz Belok) and I.P.-S.; Writing—original draft preparation, J.W., A.N. and I.P.-S.; Writing—review and editing, J.W., A.N. and I.P.-S.; Visualization, J.W., A.N. and I.P.-S. All authors have read and agreed to the published version of the manuscript.

Funding: This research received no external funding.

Data Availability Statement: The data are available through the authors.

Conflicts of Interest: The authors declare no conflicts of interest.

References

1. European Union. Directive 2010/31/EU. European Parliament and of the Council of 19 May 2010 on the Energy Performance of Buildings (receast). *Off. J. Eur. Union L 153* **2010**, 13–35.
2. Mazzeo, D.; Oliveti, G.; Arcuri, N. Mapping of the seasonal dynamic properties of building walls in actual periodic conditions and effects produced by solar radiation incident on the outer and inner surfaces of the wall. *Appl. Therm. Eng.* **2016**, *102*, 1157–1174. [CrossRef]
3. Zhou, Y.; Dang, G.; Zhang, T.; Qi, F. Development of an hourly incidentsolar radiation calculation methodology for building envelopes under ground-object obstruction conditions. *Build. Environ.* **2025**, *282*, 113304. [CrossRef]
4. Lan, Y.; Zhan, Q. How do urban buildings impact summer air temperature? The effects of building configurations in space and time. *Build. Environ.* **2017**, *125*, 88–98. [CrossRef]
5. Sayadi, S.; Hayati, A.; Salmanzadeh, M. Optimization of window-to-wall ratio for buildings located in different climates: An IDA-indoor climate and Energy simulation study. *Energies* **2021**, *14*, 1974. [CrossRef]
6. Wang, Y.; Liu, K.; Liu, Y.; Wang, D.; Liu, J. The impact of temperature and relative humidity dependent thermal conductivity of insulation materials on heat transfer through the building envelope. *J. Build. Eng.* **2022**, *46*, 103700. [CrossRef]
7. Orlik-Kożdoń, B.; Nowoświat, A. Modelling and testing of a granular insulating material. *J. Build. Phys.* **2018**, *42*, 6–15. [CrossRef]
8. Pokorska-Silva, I.; Kadela, M.; Małek, M.; Fedorowicz, L. An assessment of the thermal behavior of envelope surface coatings with different colors. *Polymers* **2021**, *13*, 82. [CrossRef] [PubMed]
9. Tavil, A. Thermal behavior of masonry walls in Istanbul. *Constr. Build. Mater.* **2004**, *18*, 111–118. [CrossRef]
10. Orosa, J.A.; Baaliña, A. Improving PAQ and comfort conditions in Spanish office buildings with passive climate control. *Build. Environ.* **2009**, *44*, 502–508. [CrossRef]
11. Martínez-Garrido, M.I.; Aparicio, S.; Fort, R.; Anaya, J.J.; Izquierdo, M.A.G. Effect of solar radiation and humidity on the inner core walls in historic buildings. *Constr. Build. Mater.* **2014**, *51*, 383–394. [CrossRef]
12. Camuffo, D. Indoor dynamic climatology: Investigations on the interactions between walls and indoor environment. *Atmos. Environ.* **1983**, *17*, 1803–1809. [CrossRef]
13. Espinoza, R.M.; Franke, L.; Deckelmann, G. Phase changes of salts in porous materials: Crystallization, hydronation and deliquescence. *Constr. Build. Mater.* **2008**, *22*, 1758–1773. [CrossRef]
14. Grossi, C.M.; Brimblecombe, P.; Menéndez, B.; Benavente, D.; Harris, I.; Déqué, M. Climatology of salt transitions and implications for stone weathering. *Sci. Total. Environ.* **2011**, *409*, 2577–2585. [CrossRef]
15. Viitanen, H.; Vinha, J.; Salminen, K.; Ojanen, T.; Peuhkuri, R.; Paajanen, L.; Lähdesmäki, K. Moisture and Bio-deterioration Risk of Building Materials and Structures. *J. Build. Phys.* **2009**, *33*, 201–224. [CrossRef]
16. Ito, K. Numerical prediction model for fungal growth coupled with hygrothermal transfer in building materials. *Indoor Built Environ.* **2012**, *21*, 845–856. [CrossRef]
17. Säid, M.N.A.; Brown, W.C.; Shirtliffe, C.J.; Maurenbrecher, A.H.P. Monitoring of the building envelope of a heritage house: A case study. *Energy Build.* **1999**, *30*, 211–219. [CrossRef]
18. Li, H.; Jia, H.; Zhong, K.; Zhai, Z. Analysis of factors influencing actual absorption of solar energy by building walls. *Energy* **2021**, *215*, 118988. [CrossRef]
19. Li, H.; Zhong, K.; Yu, J.; Kang, Y.; Zhai, Z. Solar energy absorption effect of buildings in hot summer and cold winter climate zone, China. *Sol. Energy* **2020**, *198*, 519–528. [CrossRef]
20. Yu, Y.; Ejohwomu, O.; Gallego-Schmid, A. Pssive cooling for circular economy: Building materials and design solutions. *ScienceDirect* **2025**, *135*, 332–337. [CrossRef]

21. Carbonari, A. Retrofit of Italian School Buildings. The Influence of Thermal Inertia and Solar Gains on Energy Demand and Comfort. *Future Cities Environ.* **2019**, *5*, 3. [CrossRef]
22. Geetha, N.B.; Velraj, R. Passive cooling methods for energy efficient buildings with without thermal energy storage—A review. *Energy Educ. Sci. Technol. Part A Energy Sci. Res.* **2012**, *29*, 913–946.
23. Onyenokporo, N.C.; Taki, A.; Montalvo, L.Z.; Oyinlola, M.A. Exploring the Impact of Rice Husk Ash Masonry Blocks on Building Energy Performance. *Buildings* **2024**, *14*, 1290. [CrossRef]
24. Belhous, M.; Boumhaout, M.; Oukach, S.; Hamdi, H. Effects of a Material Based on Dte Palm Fibers on the Thermal Behavior of a Residential Building in the Atlantic Climate of Morocco. *Sustainability* **2023**, *15*, 6314. [CrossRef]
25. Kio, P.; Ali, A.K. In situ experimental evaluation of a novel modular living wall system for industrial symbiosis. *Energy Build.* **2021**, *252*, 111405. [CrossRef]
26. Onyszkiewicz, J.; Sadowski, K. Proposals for the revitalization of prefabricated building facades in terms of the principles of sustainable development and social participation. *J. Build. Eng.* **2022**, *46*, 103713. [CrossRef]
27. Randjelovic, D.; Vasov, M.; Ignjatovic, M.; Stojiljkovic, M.; Bogdanovic, V. Investigation of a passive design approach for a building facility: A case study. *Energy Sources Part A Recovery Util. Environ. Eff.* **2021**, *47*, 8890–8908. [CrossRef]
28. Al-Obaidi, K.M.; Ismail, M.; Rahman, A.M.A. Passive cooling techniques through reflective and radiative roofs in tropical houses in Southeast Asia: A literature review. *Front. Archit. Res.* **2014**, *3*, 283–297. [CrossRef]
29. Giovoni, B. *Passive Low Energy Cooling of Buildings*; John Wiley & Sons: Hoboken, NJ, USA, 1994.
30. Sanchez, E.C.; Diaz, J.R.D.; Kampouropulos, K. Novel Architectural Strategies to Support an nZEB Mediterranean School. *IOP Conf. Ser. Maer. Sci. Eng.* **2019**, *603*, 042012. [CrossRef]

energies

MDPI

Article

Integrated Energy and Social Retrofit Strategies for Lima's Central Market: Balancing Cost and Sustainability

Patricia Aguilera-Benito [1,*] and Karla Soto-Florez [2]

[1] Departamento de Tecnología de la Edificación, Universidad Politécnica de Madrid, 28040 Madrid, Spain
[2] Facultad de Arquitectura, Universidad Peruana de Ciencias Aplicadas, Santiago de Surco 15023, Peru
* Correspondence: patricia.aguilera@upm.es

Abstract: There is an urgent need to implement sustainable solutions in the construction sector, particularly within the Peruvian context, where regulations on energy efficiency and building rehabilitation are still under development. This study addresses the energy and social rehabilitation of the Mercado Central in Lima, with the aim of identifying the most effective interventions from both energy and economic perspectives while promoting urban sustainability. A detailed assessment of the building's original state—covering the thermal envelope and technical systems—was conducted, followed by fifty energy simulations using Ce3X© v.2.3. software. Based on the obtained energy rating, several envelopes and system improvements were proposed and evaluated in terms of energy savings, cost-effectiveness, and social benefits. The most advantageous option, Measure M9, combines interventions in roofs, openings, and installations. It achieved a global energy rating of 17.6 A, with a projected lifespan of 75 years and an investment of EUR 1,642,457.01, recoverable in just 1.4 years. The results highlight the potential of integrated retrofitting strategies to simultaneously improve energy performance and social impact. Measure M9 emerges as the most viable solution, providing a replicable model for sustainable urban rehabilitation in Peru and other regions facing similar challenges.

Keywords: energy simulation; renovation; commercial building; economic analysis

1. Introduction

Sustainability in the construction sector has become a global priority, driven by the urgent need to reduce environmental impacts, conserve natural resources, and promote more responsible and environmentally conscious development [1]. Moreover, the adoption of sustainable practices in construction not only contributes to the protection of the environment but also improves the quality of urban life, creating healthier, more efficient, and comfortable spaces for its inhabitants.

1.1. Challenges in Implementing Sustainable Solutions in Developing Countries

Many developing nations continue to grapple with a complex mix of structural barriers that hamper the adoption of sustainable building practices. Regulatory frameworks for energy efficiency are often fragmented, inconsistently enforced, or underdeveloped. Without clear standards, performance targets, and predictable timelines, investments in efficient technologies and materials struggle to compete with lower upfront costs or quick fixes that yield limited long-term gains. Moreover, incentives such as subsidies, tax benefits, or financing mechanisms are frequently misaligned or inadequately funded, reducing the appeal of retrofitting projects that require higher initial capital.

The retrofitting of existing buildings emerges as a particularly stubborn hurdle. Many structures were designed without energy efficiency in mind, and retrofits involve technical complexities, higher upfront costs, and disruptions to occupants. Inadequate data on building stock, limited technical expertise, and constraints in access to financing further impede progress. Appliances, systems, and envelopes that could dramatically reduce energy use are often outdated or unavailable locally, slowing the pace of modernization. Additionally, the lack of robust consumer awareness and demand for energy-efficient options means that market signals do not sufficiently reward sustainable choices.

These combined challenges hinder cities from fully leveraging the benefits of sustainability. When energy efficiency improvements stagnate, cities miss significant opportunities for energy savings, lower greenhouse gas emissions, and enhanced social well-being, including improved indoor comfort and health. A coherent, well-funded strategy that aligns regulations, incentives, financing, and technical capacity is essential to unlocking the potential of sustainable, resilient buildings and to translating environmental advantages into tangible improvements for residents [2].

A clear example is Peru, a great biosphere for the planet, rich in biodiversity and natural resources, whose environmental dynamics have a global impact. However, it faces an enormous task in moving towards sustainable development and greater energy efficiency. The country has a historical legacy of great heritage value, but its buildings do not always receive the maintenance and rehabilitation they require [3]. When assessing the state of conservation, energy consumption, and efficiency of these properties, many historical structures are found to be prone to deterioration and disproportionate energy consumption. While private companies are significantly driving the construction of new buildings and environments in developed economies, historic centers and national heritage sites, when dependent on public funding, often lag behind, without adequate rehabilitation or energy efficiency upgrades.

This gap between the modernization of new buildings and the conservation of old ones creates significant imbalances: greater vulnerability of historic sites to climatic events, higher maintenance costs, and loss of cultural and tourist value. The lack of incentives and technical capabilities to intervene in historic buildings hinders the implementation of energy efficiency and sustainable rehabilitation solutions that respect architectural identity and heritage value. As a result, sustainability efforts are misaligned with the country's cultural and tourist wealth, limiting the positive impact on emissions reduction and community well-being.

The 2020 pandemic exacerbated the economic situation, causing a recession and relegating sustainability to a secondary level in the face of immediate needs. This blow highlighted the urgency of comprehensive strategies that connect heritage conservation, sustainable urban development, and energy efficiency, supported by public and private financing, clear regulatory frameworks, and technical capabilities. To convert Peru's biospheric potential into tangible benefits for its people, cohesive policies are needed that prioritize the respectful rehabilitation of historic buildings, the modernization of existing infrastructure, and the strengthening of demand for efficient solutions, without losing sight of the cultural wealth that characterizes the country.

1.2. Greater Environmental Impact During the Building's Occupancy Phase

To address these challenges effectively, it is essential to understand at which stage of a building's life the greatest environmental impact occurs. Studies assessing energy costs at each stage of a building's life cycle reveal that, although the material extraction, construction, and demolition phases consume a significant amount of energy, their contribu-

tion to total energy consumption is relatively small compared to the building's occupancy phase [4]. The latter, which includes daily use, maintenance, and operation, accounts for most of the long-term environmental impact. This knowledge is key to guiding design, management, and policy strategies to promote more sustainable and responsible construction [5]. Furthermore, depending on the lifetime of a building, the percentage of energy consumption allocated to the construction phase alone represents 9% of the total for a building with a lifetime of 50 years, and it decreases to 5% for a building with a lifetime of 100 years. This demonstrates the importance of efficient resource management in the occupancy phase of the building [6]. For this reason, it is essential to understand that one of the resources that can decrease the current pressure on the environment is the retrofitting of existing buildings [7].

In this context, retrospective analyses should emphasize the role of heritage-listed and historically significant buildings, which often exhibit architectural features that limit straightforward retrofits yet hold substantial cultural and economic value. Case studies integrating energy retrofits with preservation objectives can illuminate pathways to improve energy performance, without compromising historical integrity, by leveraging passive design principles, high-performance envelope assemblies compatible with conservation guidelines, and targeted retro-commissioning of legacy systems. Such approaches require multidisciplinary collaboration among conservation professionals, engineers, and policymakers to establish adaptable standards and funding mechanisms that align with both conservation ethics and modern energy performance targets [8].

Additionally, adopting a life-cycle assessment framework tailored to historic urban cores can quantify the trade-offs between conservation intervention, retrofit intensity, and long-term energy savings. This involves probabilistic modeling of uncertainty in material durability, climate exposure, and occupancy patterns to optimize retrofit sequences and maintenance scheduling. The resulting evidence base can inform policy instruments—such as targeted subsidies, performance-based financing, and regulatory relief for historic districts—that incentivize progressive energy upgrades while preserving the architectural and cultural identity that drives tourism, education, and community resilience.

1.3. Energy Consumption in Commercial Buildings: Previous Studies

On the other hand, MINEM (2020) [9] has an "Energy efficiency and energy diagnosis guide for large stores", where markets and supermarkets are considered large-scale buildings. These buildings are equipped with more electrical equipment, consume more energy, and have greater demands than other types of buildings. Accordingly, in the informative part on energy efficiency and sector characteristics of this guide, it is mentioned that large shopping centers use electricity as their main source of energy. In addition, the distribution of the energy consumption of electricity that is demanded in a large shopping center may depend on the following factors: type of products it stores, operating hours of refrigeration, and air-conditioning and lighting equipment [10]. The distribution of electrical energy is led by lighting (44%), followed by air conditioning (43%) [9].

The retail sector in Europe is characterized by high energy consumption, with supermarkets being particularly significant, with one of the highest rates of energy consumption in this sector. Given their impact, supermarkets represent a key element in Europe's efforts to meet its greenhouse gas reduction target of 10% by 2020 [11,12]. On the other hand, in the United States, the commercial building sector consumes almost 30% of all energy in the country [13], hence the importance of analyzing this building typology.

In Peru, persistent poverty and economic constraints have significantly conditioned infrastructure and sustainability priorities. Investment in retrofitting existing buildings and in environmental awareness campaigns is low, as the focus is mainly on immediate

economic savings [14]. This reality contrasts with the situation in many European countries, where energy efficiency policies and campaigns are closely linked to environmental awareness and the promotion of sustainable practices [15,16]. In the Peruvian context, especially in the commercial sector, this is reflected in high energy consumption in buildings that, for the most part, have not been refurbished or modernized to improve their efficiency. The lack of investment in upgrading these spaces not only perpetuates high energy consumption but also limits opportunities to reduce costs and reduce environmental impact in the long term. This scenario underlines the need to rethink energy management strategies in Peruvian commercial buildings, considering the economic and social realities of the country, in order to promote a more efficient use of energy and move towards more sustainable development [17–19].

Several international studies have highlighted the potential of retrofitting measures in markets and commercial buildings. For instance, Salgueiro (2021) analyzed the Atarazanas Market in Málaga, focusing on envelope upgrades and system improvements compatible with heritage preservation, achieving reductions in heating demand by 50% and a significant decrease in carbon footprint [20]. Calado (2023) studied the San Cristóbal Market in Madrid, evaluating roof insulation and installation improvements, with payback periods ranging from 1.2 to over 40, depending on the intervention [11]. Echevarría (2023), in turn, examined La Paz Market in Madrid, proposing user behavior changes and envelope optimization, again showing the importance of glazing and skylight interventions [19]. These works confirm that envelope measures and installations can yield meaningful results, yet they also show that cost-effectiveness strongly depends on context [21].

Beyond market typologies, the retail sectors in Europe and the US have been widely studied due to their high energy intensity [13,14,22]. Integrated retrofit approaches—those combining envelope, systems, and renewable generation—are increasingly recommended because they unlock higher savings and better economic returns than isolated measures [15,16]. However, most peer-reviewed evidence for integrated strategies comes from high-income contexts with consolidated regulatory frameworks. By contrast, in Peru, the few existing references highlight the predominance of basic efficiency measures (e.g., LED lighting, improved HVAC) [9,23,24] and show that broader integrated retrofits remain underexplored. Importantly, while previous studies have examined packages of measures targeting a simple element (e.g., only roofs or only façades), there is a lack of systematic analyses of hybrid packages that combine roofs, openings, and installations with explicit economic evaluation in markets of developing countries. This constitutes the specific knowledge gap that the present study addresses.

This research focuses on the energy and social rehabilitation of the Mercado Central of Lima, a landmark building with significant commercial and cultural relevance. The main objective is to identify retrofit strategies that maximize energy savings, economic viability, and social impact. The central hypothesis is that integrated packages combining interventions in roofs, openings, and installations achieve superior performance compared to isolated measures, both in terms of energy efficiency and cost-effectiveness, while also enabling social reuse of building spaces.

Methodologically, the study conducts an initial assessment of the building's envelope and systems, followed by parametric simulations of retrofit measures using Ce3X©. This tool, although simplified, provides an effective basis for comparative energy rating and cost–benefit analysis. Complementary tools include PVGIS for solar potential assessment and CYPE© for cost estimation. We acknowledge, however, the limitations of certification-based software such as Ce3X©, particularly its inability to capture sub-hourly dynamics, occupancy variability, and time-dependent interactions. For this reason, we incorporate a discussion of the value of dynamic simulation and calibrated models, which recent studies

have successfully applied to building retrofit assessments [17,19]. Such approaches can enhance precision in evaluating scenarios with complex temporal interactions, internal loads, or passive strategies and represent an important avenue for future research in the Peruvian context.

The contribution of this article is threefold: it provides the first systematic evaluation of hybrid retrofit packages (roofs + openings + installations) in a Peruvian market; it integrates energy simulations with economic analysis to identify cost-effective and replicable solutions for contexts with limited resources; and it incorporates social rehabilitation considerations, such as the potential reuse of roof and communal spaces, highlighting the broader cultural and economic value of sustainable retrofitting in historic urban centers.

2. Methodology

Modeling required a preliminary analysis of the building, studying its spatial, structural, and architectural configuration. On this basis, the input parameters for the energy simulation were established, as well as the conditions of the building's environment.

2.1. Preliminary Development: Architectural Configuration

The Central Market is located in the district of Cercado de Lima, province and department of Lima, Peru. It was built in 1967. The district of Cercado de Lima is the oldest, most historic and monumental district of Lima, as it is home to a series of monuments of great relevance characterized by their historical, religious, and cultural value.

The mixed building consists of a parallelepiped that occupies the entire block and is surrounded by a commercial perimeter ring. This volume is divided into three main levels, the first of which is subdivided into two platforms separated by half a level; all these levels are connected by ramps. Above the market volume is the nine-story office tower, which is supported by columns that create an open floor plan (Figure 1).

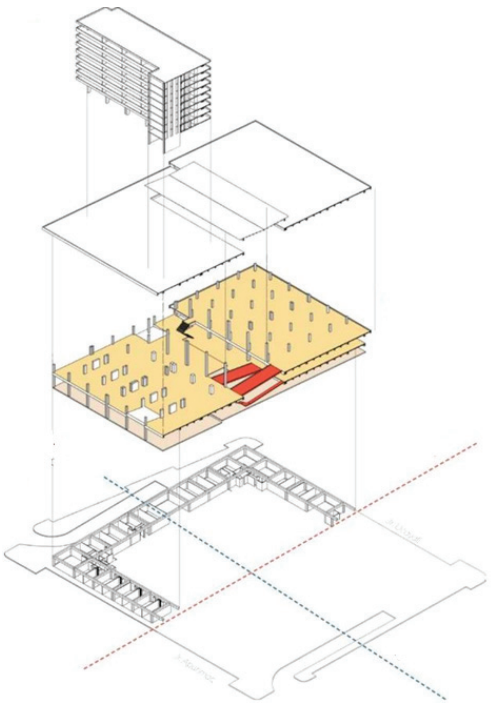

Figure 1. Exploited isometry of formal analysis of the Central Market. Source: Tolentino, 2019 [25].

Inside, the market is composed of a free floor plan with a central triple-height void that becomes the organizer of the main circulation of the complex and where the ramps

connecting the different levels are located. This void is covered by a raised metal roof structure that differs from the concrete roofs used in the rest of the building (Figure 2).

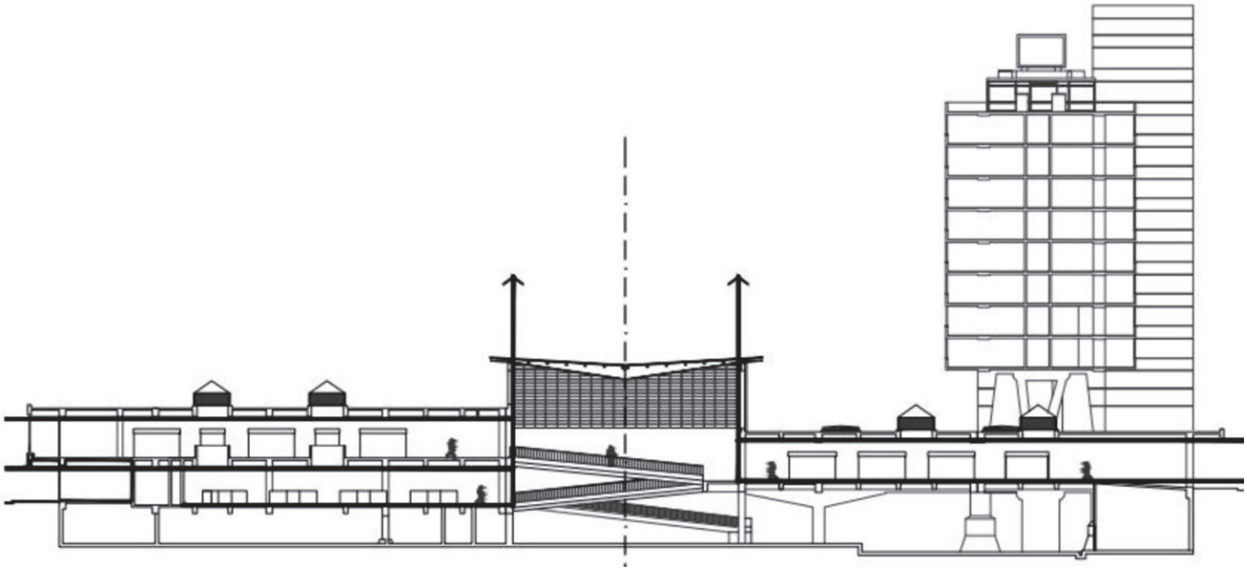

Figure 2. Section of the Central Market. Source: Tolentino, 2019 [25].

In general, the building has an arcade system of reinforced concrete columns and beams. The perimeter walls of the building are also made of this material, while the interior divisions of most of the commercial premises are simple masonry partition walls. The parallelepiped volume is made up of nine blocks separated by 5 m seismic joints. The office tower is supported on blocks A1 and A2, so the columns are replaced in this case by reinforced concrete slabs 60 cm thick and 3 m long (Figure 3).

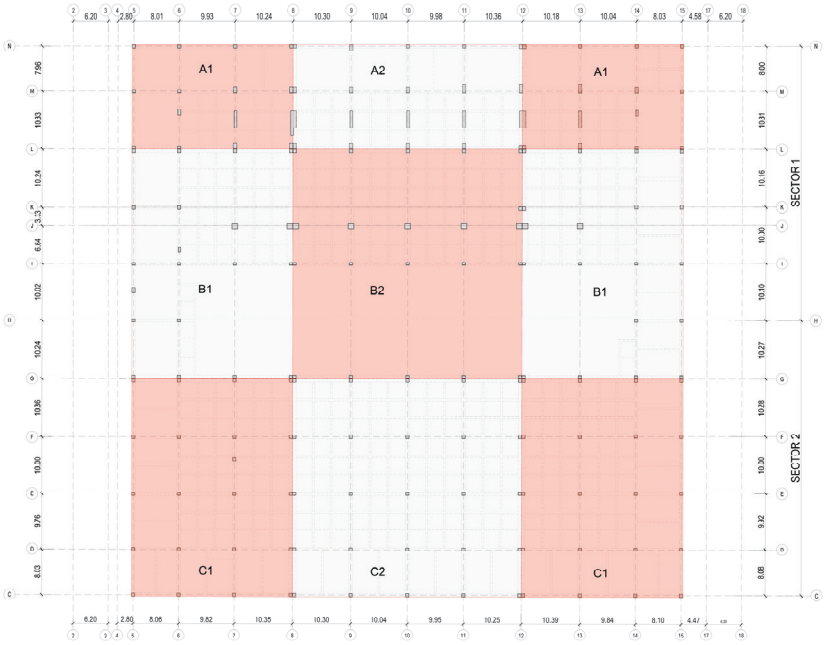

Figure 3. Schematic plan of structural modulation of the Central Market. Source: Tolentino, 2019 [25].

The slabs are 20 cm thick and are supported on secondary beams with a section of 35 × 50 cm. On the other hand, the ramps are structurally supported on trapezoidal section beams that are continuations of the main structure. Likewise, the central void is covered by

a metal roof that rests on a structure made up of full-section steel scissors with a variable section, which in turn rests on reinforced concrete columns.

2.2. Initial Building Analysis

This section outlines the construction characteristics of the building envelope and the facilities available for conducting an initial energy analysis (Tables 1–3).

Table 1. Characteristics of market envelopes.

Elements	Name	Dimensions	Area (m^2)	U (W/m^2k)
Roof	Market flat roof	variable	8745.00	4.23
	Market pitched roof	variable	1838.00	7.04
Walls: Northeast façade Huallaga	F.M. Huallaga first level	variable	550.82	2.36
	F.M. Huallaga central space	variable	517.80	4.00
	F.M. Huallaga skylights	variable	69.30	5.88
	Wall in contact with terrain	variable	576.31	0.66
Walls: Northwest façade Ayacucho	F.M. Ayacucho first level	variable	458.35	2.36
	F.M. Ayacucho second level	variable	215.63	4.00
	F.M. Ayacucho central space	variable	123.55	4.00
Wall in contact with ground	Wall in contact with ground	variable	410.53	0.85
Southwest façade Ucayali	F.M. Ucayali central space	variable	338.44	4.00
	F.M. Ucayali skylights	variable	69.30	5.88
	Wall in contact with ground	variable	302.81	1.01
Walls: Southeast façade Andahuaylas	F.M. Andahuaylas first level	variable	433.72	2.36
	F.M. Andahuaylas second level	variable	215.63	4.00
	F.M. Andahuaylas space central	variable	123.55	4.00
Wall in contact with ground	F.M. Andahuaylas skylights	variable	69.30	5.88
	Wall in contact with ground Andahuaylas	variable	410.53	0.85
Soil	Soil in contact with ground	97.68 × 97.50	9523.80	1.00
	Floor in contact with outside air	variable	1059.00	3.18
Walls	F.M. Ucayali first level	variable	288.19	2.36
	F.M. Ucayali second level	variable	540.09	4.00

Table 2. Characteristics of the office tower enclosures.

Elements	Name	Dimensions	Area (m^2)	U (W/m^2k)
Office flat roof	Office flat roof	variable	1465.00	4.23
Walls: Northeast façade avenida Huallaga	F.O. Huallaga	variable	2501.14	4.00
Walls: Northwest façade avenida Ayacucho	F.O. Ayacucho	variable	722.43	4.00
Walls: Southwest façade avenida Ucayali	F.O. Ucayali	variable	2441.48	4.00
Walls: Southeast façade avenida Andahuaylas	F.O. Andahuaylas	variable	772.43	4.00
Soil	Soil on contact with outside air	variable	1378.00	3.18

Table 3. Characteristics of the office tower enclosures.

Characteristics of Office Tower Enclosures	
Heating	It does not have a heating system because the temperatures are not very low, so this equipment is not indispensable.
Cooling	The building does not have this type of system; however, some premises on the perimeter ring on the first level have air-conditioning equipment for private use.
Sanitary Hot Water	The building does not have domestic hot water (DHW). The commercial stalls belonging to the semi-wet and wet areas, as well as the toilets, only have cold water.
Ventilation	There is no ventilation system, so no data is entered in the program for this.
Lighting	In terms of lighting equipment, linear fluorescent-type luminaires predominate in the market, both in the whole of the outer perimeter and in most of the interior of the market. It is estimated that 80% of the surface area of this area has these types of luminaires. The remaining parts of the interior of the market, specifically the sales stalls located near the main entrances, have linear LED tube luminaires, covering 20% of the area's surface. The office tower, which is currently used as a warehouse, has incandescent luminaires due to the age of this sector.

The openings have different thermal properties that vary according to their typology, which is defined according to the type of enclosure they have. In order to organize their typologies, they have been named as follows: ROM, nomenclature for openings with a roll-up enclosure; REM, nomenclature for openings with a static vertical louvered or slatted enclosure; HM, nomenclature for openings without a defined enclosure; VO and VM, for window openings with a glass enclosure; and MO and MM, for partition openings with a glass enclosure. The thermal properties of the openings are defined as estimated values.

The building has been designated for commercial use, which predetermines its occupancy. Its intensity of use has been estimated as high, and its daily operating hours have been set at 12 h. All of this data is crucial for defining its operation. The equipment that affects the building's operation is detailed below.

2.3. Instruments for Evaluating Energy and Economic Improvements

In order to carry out this study, several tools and approaches were used to comprehensively assess possible energy improvements in the building under analysis. Firstly, the Ce3X© software was used, a platform specialized in energy analysis of buildings, in which all the data related to the thermal envelope of the building was entered, including walls, windows, doors, and other construction elements, as well as the existing installations. This process allowed an initial energy rating of the building to be obtained, serving as a baseline for future improvements.

Ce3X© was selected because it is widely applied for preliminary energy certification and retrofit assessment, especially in contexts where comprehensive building energy datasets are scarce and regulatory frameworks are under development, such as in Peru. Compared to dynamic simulation tools [26–29], such as Energy Plus©, TRNSYS©, or Design builder©, Ce3X© offers simplified calculations with reduced computational time, which allowed the evaluation of fifty different retrofit scenarios. Its limitations include the monthly resolution of results, the absence of sub-hourly dynamics, simplified internal load representation, and lack of advanced control strategies. These limitations are acknowledged in the discussion as potential sources of uncertainty.

Although Ce3X© provides a simplified and certification-oriented assessment of building energy performance, it does not capture the time-dependent dynamics of occupancy, climate, and internal loads. In the broader context of building energy analysis, dynamic simulation tools calibrated with real data can provide more accurate insights, especially

when evaluating retrofit scenarios involving passive strategies and complex interactions over time. Nevertheless, the choice of Ce3X© in this study is based on feasibility, data availability, and its certification-driven purposes.

Subsequently, different individualized improvement measures, such as additional insulation, window replacement, lighting improvements, and more efficient air-conditioning and ventilation systems, were incorporated into Ce3X©. In addition, combinations of these measures were analyzed to identify the most favorable configurations in terms of efficiency and energy savings. To assess the economic viability of each option, the costs associated with each measure and combination were entered, using data provided by the program itself, which calculated the corresponding payback years, thus facilitating a comparison between the different alternatives.

In addition, the SketchUp© software (v.2023) was used to carry out a detailed study of the building's sunlight. This analysis made it possible to determine which façades receive the greatest amount of solar radiation throughout the day, which is crucial information for defining improvement measures related to orientation and solar protection, thus optimizing the efficiency of solar installations and other passive strategies. To dimension the PV installation, the PVGIS-5 application© was used, which provides precise data on solar yields based on geographical location and climatic conditions. With this tool, the required power of the solar panels to cover the energy demands of the building was determined, ensuring that the proposed solutions are technically feasible and efficient.

Finally, the CYPE© software, a price generator that allows for obtaining the updated costs of the different improvement measures proposed, was used. This resource facilitated the accurate estimation of the budgets required for the implementation of each alternative, thus complementing the technical analysis with a sound economic evaluation. Together, these tools and methodologies allowed for a comprehensive and informed analysis for the selection of the best energy improvement strategies for the building under study.

According to all of the above, the integration of the software tools followed sequential logic. SketchUp© was employed to create the 3D model and conduct the solar incidence study. Geometric and envelope data were transferred into Ce3X© for energy simulations. PVGIS© was used to estimate solar photovoltaic potential, and its results were incorporated into Ce3X© for renewable energy scenarios. Finally, CYPE© was applied to calculate the implementation costs of each measure, ensuring that technical and economic analyses were consistently integrated.

2.4. Climate Data

The district of Cercado de Lima is located in the Lima region. In the report "Climas del Perú: Mapa de clasificación climática Nacional", the climate is classified as E (d)B, which means that this province is located in a desert with an annual rainfall of 8 mm in the form of drizzle, mainly between July and September. Temperatures are influenced by the adjacent sea to the west, with maxima between 18 °C in August and 26.7 °C in February, and minima between 13.5 °C in August and 19 °C in February [30]. With respect to altitude, the city of Lima has an altitude of 101 m above sea level. According to Weather Spark, the average relative humidity in Lima is 81%, while the average minimum humidity is 66% and the maximum humidity is 92% [20].

In addition, a sunlight study of the building was carried out to evaluate the incidence of the sun on the dates of the autumn equinox, 21 March 2024; the spring equinox, 23 September; the summer solstice, 21 December 2024; and the winter solstice, 21 June. Through the project modeled in 3D in the Sketchup©, its geolocation and data such as latitude of −12.0453 and latitude 12°02′57′ South and longitude 77°01′31′ West can be entered in this file, and the following is obtained:

- The northeast façade receives more hours of light and sunshine in the morning at the autumn equinox, spring equinox, and winter solstice.
- The southeast façade receives more hours of daylight and morning sun at the autumnal equinox, spring equinox, and summer solstice.
- The northwest façade receives more hours of light and sunshine in the afternoon at the autumn equinox, spring equinox, and winter solstice.
- The southwest façade receives more hours of daylight and afternoon sun at the autumn equinox, spring equinox, and summer solstice.

2.5. Model Verification and Limitations

The model was not calibrated with measured energy consumption data, as no historical utility records were available for Mercado Central. Nevertheless, internal consistency checks were performed, such as verifying energy balances within Ce3X© and comparing demand values with benchmark studies of similar commercial markets in Peru and Spain. These cross-checks suggest that the model produces results of reasonable magnitude. We acknowledge, however, that the absence of a quantitative validation or calibration process represents a limitation of this study.

3. Results

This section presents the results obtained in the evaluation of the energy improvement measures. Firstly, an individual analysis of each improvement measure is carried out, assessing its impact on the energy consumption, emissions, and demand of the building. Subsequently, those measures that have shown the best results for these parameters are selected and combined to form different intervention configurations. Finally, an economic and payback analysis of the combinations with the best energy performance is carried out, considering the associated costs and payback periods. This process makes it possible to identify the most efficient and viable solution from a technical and economic point of view, thus optimizing the improvement strategies for the building under study.

3.1. Evaluation of Individual Improvement Measures with the Ce3X© Software

In this first stage of evaluation of individual improvement measures, the objective is to determine which of these proposals will be the ones that can be finally implemented in the project. In this case, only those measures that have the highest percentage of savings and qualification compared to the original situation of the building will be prioritized. For improvement measures involving the thermal envelope, i.e., roofs, façades, and openings, the percentage of demand savings is more important; on the contrary, for improvement measures involving installations, the percentage of consumption savings will be the determining factor for the choice of the most suitable improvements.

3.1.1. Roof Improvement Measures

The results with respect to these measures show that, individually, the ones that produce the greatest savings in terms of consumption, emissions, and demand are those that have thicker thermal insulation. Regarding the proposals for improvements in the flat roof of the market, it can be determined that the proposal to install XPS thermal insulation with a walkable finish in one sector and a vegetation finish in another sector generates greater savings than the proposal to install thermal insulation with a non-walkable finish. With regard to the pitched roof on the market, it can be seen that incorporating PUR thermal insulation of the sandwich panel type does not generate any energy savings for the building, at least as an individual measure, and worsens the rating in the three factors analyzed (Table 4).

Table 4. Savings and rating of individual improvement measures on roofs.

Savings and Ratings of Individual Improvement Measures on Roofs Compared to Original Situation			
Measures	**Consumption**	**Emissions**	**Demand**
Original Rating	487.5 E	129.4 E	78.5 D
Incorporate 80 mm thick XPS thermal insulation in flat market roof with walkable and vegetated finish.	Cooling: 4.8% Lighting: - 481.98 E	Cooling: 4.8% Lighting: - 127.91 E	Cooling: 4.8% 74.73 C
Incorporate 40 mm thick XPS thermal insulation in flat market roof with walkable and vegetated finish.	Cooling: 4.5% Lighting: - 482.24 E	Cooling: 4.5% Lighting: - 127.98 E	Cooling: 4.5%. 74.91 C
Incorporate 80 mm thick XPS thermal insulation in flat roof of market with non-trafficable finish.	Cooling: 3.4% Lighting: - 483.55 E	Cooling: 3.4% Lighting: - 128.33 E	Cooling: 3.4% 75.8 C
Incorporate 40 mm thick XPS thermal insulation in flat roof of market with non-trafficable finish.	Cooling: 3% Lighting: - 484.01 E	Cooling: 3% Lighting: - 128.45 E	Cooling: 3% 76.12 C
Incorporate 80 mm thick XPS thermal insulation in flat roof of offices with non-trafficable finish.	Cooling: 0.4% Lighting: - 486.91 E	Cooling: 0.4% Lighting: - 129.22 E	Cooling: 0.4% 78.1 D
Incorporate 40 mm thick XPS thermal insulation in flat roof of offices with non-trafficable finish.	Cooling: 0.4% Lighting: - 486.96 E	Cooling: 0.4% Lighting: - 129.24 E	Cooling: 0.4% 78.1 D
Incorporate 80 mm thick PUR (sandwich panel) thermal insulation in pitched market roof.	Cooling: −0.2% Lighting: - 487.62 E	Cooling: −0.2% Lighting: - 129.41 E	Cooling: −0.2% 78.59 D
Incorporate thermal insulation of PUR (sandwich panel) of 30 mm thickness in pitched market roof.	Cooling: −0.3% Lighting: - 487.72 E	Cooling: −0.3% Lighting: - 129.44 E	Cooling: −0.3% 78.66 D

The most suitable improvement measures are to incorporate 80 mm thick XPS thermal insulation into the flat roof of the market, with one sector with a walkable finish and another sector with a vegetated finish, and to incorporate 80 mm thick XPS thermal insulation into the flat roof of the offices with a non-walkable finish. All the chosen measures are then carried out (Tables 5 and 6).

In this case, if all the improvement measures are carried out on roofs with 40 mm thermal insulation, the savings and ratings in terms of consumption, emissions, and demand improve by 1% compared to the original situation. This means that for the climatic conditions in which the building is located, it is preferable to have improvement measures with thinner insulation, because when the temperature rises, a thicker thermal insulation material retains more heat inside the building and therefore causes a greater cooling demand.

According to the analyses indicated, in building envelopes, the greatest savings come from measures that increase thermal inertia and reduce heat gains and cooling demand, with insulation thickness being the key factor. The greater the insulation thickness, the lower the heat gain, and when accompanied by a thermal mass, it can moderate temperature peaks and reduce demand, while in the flat roof of the market, the combination of 80 mm of XPS with a walkable finish in one zone and a vegetated finish in another generates greater savings than a non-walkable finish. In gable roofs, the incorporation of PUR sandwich panel

insulation does not provide significant savings and can worsen the ratings by increasing the interior heat gain without improving the overall thermal resistance; therefore, the optimal sizes are 80 mm of XPS in the market's flat roof with a walkable and a vegetated sector, and 80 mm of XPS in the office's flat roof with a non-walkable finish, balancing demand and heat gains through permeability and solar exposure. If all the improvements are applied to roofs with 40 mm, the improvements in consumption, emissions, and demand are around 1% with respect to the original situation, indicating that, under these climatic conditions, it is preferable to seek greater thickness when the outside temperature rises to avoid greater cooling needs. As indicated in the limitations, this value could be adjusted with a heat flow and interaction analysis.

Table 5. Savings and ratings of the set of improvement measures for roofs, case 1.

Savings and Rating of All Roof Improvement Measures Compared to the Original Situation Original Situation			
Measures	**Consumption**	**Emissions**	**Demand**
Original Rating	487.5 E	129.4 E	78.5 D
Incorporate XPS insulation Roof thickness 80 mm Market flat roof Passable finish and garden	Cooling: −1.3% Lighting: - 488.96 E	Cooling: −1.3% Lighting: - 129.77 E	Refrigeration: −1.3% 79.51 D
Incorporate insulation XPS insulation 80 mm thick in flat roof Flat roof of offices with non-trafficable finish			

Table 6. Savings and ratings of the set of improvement measures for roofs, case 2.

Savings and Ratings of Combined Improvement Measures on Roofs Compared to Original Situation Original Situation			
Measures	**Consumption**	**Emissions**	**Demand**
Original Rating	487.5 E	129.4 E	78.5 D
Incorporate 40 mm thick XPS thermal insulation in flat market roof with walkable and vegetated finish.	Cooling: 1% Lighting: - 486.23 E	Cooling: 1% Lighting: -	Cooling: 1% 77.63 C
Incorporate 40 mm thick XPS thermal insulation in flat roof of offices with non-trafficable finish.			

3.1.2. Façade Improvement Measures

The results with respect to these improvement measures show that, individually, those that contribute the most are the incorporation of 60 mm thick XPS thermal insulation on the inside for both the northwest and southwest façades, which generates savings of 1.2% in consumption, emissions, and demand (Table 7).

The best-performing improvements involve interior installation of 60 mm of XPS thermal insulation on the northwest and southwest façades. Their effectiveness stems from enhanced thermal inertia, which dampens temperature fluctuations and reduces conduction losses, coupled with a higher overall thermal resistance that moderates solar gains and convective heat losses. By increasing effective permeability and thermal mass,

these measures lower cooling demand and, in turn, reduce energy consumption and associated emissions.

Table 7. Savings and ratings of individual improvement measures on façades.

Savings and Ratings of Individual Improvement Measures on Façades Compared to Original Situation			
Measures	**Consumption**	**Emissions**	**Demand**
Original Rating	487.5 E	129.4 E	78.5 D
Incorporate 60 mm thick XPS thermal insulation on the inside of NW and SW façades (most solar radiation received).	Cooling: 1.2% Lighting: - 486.03 E	Cooling: 1.2% Lighting: - 128.99 E	Cooling: 1.2% 77.5 D
Incorporate 20 mm thick XPS thermal insulation on the inside of the NW and SW façades (more solar radiation received).	Cooling: 1% Lighting: - 486.32 E	Cooling: 1% Lighting: - 129.07 E	Cooling: 1% 77.7 D
Incorporate 60 mm thick XPS thermal insulation on the inside of NE and SE façades (less solar radiation received).	Cooling: 0.2% Lighting: - 487.16 E	Cooling: 0.2% Lighting: - 129.29 E	Cooling: 0.2% 78.27 D
Incorporate 20 mm thick XPS thermal insulation on the inside of NE and SE façades (less solar radiation received).	Cooling: 0.2% Lighting: - 487.22 E	Cooling: 0.2% Lighting: - 129.3 E	Refrigeration: 0.2% 78.32 D

3.1.3. Improvement Measures in Openings

The results with respect to these improvement measures show that, individually, those that contribute the most are replacing the glass and frames of the northwest and southwest façades with low-emissivity 4-12-4 double glazing in the vertical position that has a thermal transmittance of 1.6/Wm^{2}k and PVC frames with three air chambers that have a thermal transmittance of 1.8/Wm^{2}k, generating savings of 6.7%. Regarding skylights, the measure that generates the greatest savings, exactly 2.6%, is the replacement of the current material with low-emissivity 4-6-4 double glazing in the horizontal position that has a thermal transmittance of 2.6/Wm^{2}k and PVC frames with three air chambers that have a thermal transmittance of 1.8/Wm^{2}k. Finally, the replacement of the building's static vertical louvers with movable louvers has a better result if only applied on the northwest and southwest façades, producing savings of 7.8% in building consumption, emissions, and demand (Table 8).

Table 8. Savings and ratings of individual improvement measures in opening.

Savings and Ratings of Individual Improvement Measures in Openings Compared to Original Situation			
Measures	**Consumption**	**Emissions**	**Demand**
Original Rating	487.5 E	129.4 E	78.5 D
Replace windows and screens with low-emissivity 4-6-4 double glazing and PVC frames with three air chambers on NW and SW façades.	Cooling: 6.5% Lighting: - 479.97 E	Cooling: 6.5% Lighting: - 127.38 E	Cooling: 6.5% 73.35 C
Replace windows and partitions with low-emissivity 4-6-4 double glazing and PVC frames with three air chambers on NE and SE façades.	Cooling: 4.6% Lighting: - 482.15 E	Cooling: 4.6% Lighting: - 127.96 E	Cooling: 4.6% 74.85 C

Table 8. *Cont.*

Savings and Ratings of Individual Improvement Measures in Openings Compared to Original Situation			
Measures	**Consumption**	**Emissions**	**Demand**
Replace windows and partitions with low-emissivity 4-12-4 double glazing and PVC frames with three air chambers on NW and SW façades.	Cooling: 6.7% Lighting: - 479.76 E	Cooling: 6.7% Lighting: - 127.32 E	Cooling: 6.7% 73.21 C
Replace windows and partitions with low-emissivity 4-12-4 double glazing and PVC frames with three air chambers on NE and SE façades.	Cooling: 4.4% Lighting: - 482.43 E	Cooling: 4.4% Lighting: - 128.03 E	Cooling: 4.4% 75.04 C
Replace skylights with low-emissivity 4-6-4 double glazing and PVC frames with three air chambers.	Cooling: 2.6% Lighting: - 484.4 E	Cooling: 2.6% Lighting: - 128.55 E	Cooling: 2.6% 76.39 C
Replace skylights with low-emissivity 4-12-4 double glazing and PVC frames with three air chambers.	Cooling: 2.6% Lighting: - 484.44 E	Cooling: 2.6% Lighting: - 128.57 E	Cooling: 2.6% 76.41 C
Replace static louvers with movable louvers on NW and SW façades.	Cooling: 7.8% Lighting: - 478.54 E	Cooling: 7.8% Lighting: - 127.0 E	Cooling: 7.8% 72.37 C
Replace static louvers with movable louvers on NE and SE façades.	Cooling: 7.1% Lighting: - 479.32 E	Cooling: 7.1% Lighting: - 127.21 E	Cooling: 7.1% 72.91 C

Table 9 presents the ratings after selecting the measures that maximise savings for the building, focusing on the openings.

Table 9. Savings and qualification of the set of improvement measures in openings.

Savings and Qualification of the Set of Improvement Measures in Openings			
Measures	**Consumption**	**Emissions**	**Demand**
Original Rating	487.5 E	129.4 E	78.5 D
Replace windows and partitions with low-emissivity 4-12-4 double glazing and PVC frames with three-chambered glass on NW and SW façades.	Cooling: 17.4% Lighting: - 467.45 E	Cooling: 17.4% Lighting: - 124.06 E	Cooling: 17.4% 64.79 C
Replace skylights with low-emissivity 4-6-4 double glazing and PVC frames with three air chambers.			
Replace static louvers with movable louvers in in NW and SW façades.			

The most notable improvements come from modifications to key openings, such as replacing the glazing and frames on the northwest and southwest façades with low-emissivity double glazing. This change reduces unwanted solar heat gains and lowers the total transmittance of the envelope, moderating thermal peaks and reducing conduction losses. The result is a lower cooling demand and, therefore, savings of about 6.7% in consumption, emissions, and demand.

As for skylights, the most cost-effective improvement is to replace the current material with low-emissivity double glazing, which operates by reducing both excessive solar gain and thermal losses, achieving approximately 2.6% savings.

Replacing static vertical louvers with movable louvers offers the highest performance when applied on the northwest and southwest façades only, with an estimated 7.8% savings in consumption, emissions, and demand, by improving solar gain control and ventilation (air intake) according to orientation.

The combination of these improvements in openings achieves total savings of 17.4% for consumption, emissions, and demand by achieving solar gain reductions, reduced transmission through the openings, and increased dynamic ventilation control capability.

3.1.4. Improvement Measures in Installations

The results with respect to these improvement measures show that individually, those that contribute most are the incorporation of an air-conditioning system, with savings of 80.3% in cooling consumption and 100% in lighting; the incorporation of solar panels, which generates savings of 47.8% in cooling consumption and 100% in lighting; and, finally, the replacement of current luminaires with LED luminaires, a measure that allows savings of 42.1% in cooling and 88% in lighting (Table 10).

Table 10. Savings and qualification of individual improvement measures in installations.

Savings and Rating of Individual Improvement Measures in Installations Compared to the Original Situation			
Measures	**Consumption**	**Emissions**	**Demand**
Original Rating	487.5 E	129.4 E	78.5 D
Incorporate air-conditioning equipment	Cooling: 80.3%. Illumination: 100%. 27.14 A	Cooling: 80.3%. Lighting: 100% 6.96 A	Cooling: 47.8% 40.98 C
Incorporate ventilation equipment	Refrigeration: 37.5% Lighting: 100% 75.65 C	Cooling: 37.5% Lighting: 100% 19.86 C	Cooling: 37.5% 49.05 C
Replace existing luminaires with LED luminaires	Cooling: 42.1% Lighting: 88% 115.06 A	Cooling: 42.1% Lighting: 88% 30.32 A	Cooling: 42.1% 45.46 B
Incorporate solar panels	Cooling: 47.8% Lighting: 100% 59.73 C	Cooling: 47.8% Cooling: 47.8% 15.61 C	Cooling: 47.8% 40.98 C

Once the measures with the greatest savings for the building in terms of installations have been chosen, these are then taken as a whole (Table 11).

Table 11. Savings and ratings of all improvement measures for installations.

Savings and Ratings of Set of Improvement Measures in Installations Compared to Original Situation			
Measures	**Consumption**	**Emissions**	**Demand**
Original Rating	487.5 E	129.4 E	78.5 D

Table 11. *Cont.*

Savings and Ratings of Set of Improvement Measures in Installations Compared to Original Situation			
Measures	**Consumption**	**Emissions**	**Demand**
Incorporate air-conditioning equipment	Cooling: 78.1% Lighting: 88	Cooling: 78.1% Lighting: 88%	Cooling: 42.1%
Replace existing luminaires with LED luminaires	68.96 A	18.09 A	45.46 B
Incorporate solar panels			

Together, these improvements in installations produce savings of 78.1% and 88% in cooling and lighting consumption and emissions, respectively. The savings in cooling demand are 42.1%.

3.2. Analysis of Combined Improvement Measures with the Ce3X© Software

Table 12 analyzes all combinations derived from the previously obtained sets for each thermal envelope element and installation, identifying those that optimize consumption, emissions, and demand reductions alongside the measure rating.

The table above shows that eleven possible combinations of all sets of improvement measures can be obtained, which are M1, improvement measures in roofs and façades; M2, improvement measures in roofs and openings; M3, improvement measures in roofs and installations; M4, improvement measures in façades and openings; M5, improvement measures in façades and installations; M6, measures to improve openings and installations; M7, measures to improve roofs, façades, and openings; M8, measures to improve roofs, façades, and installations; M9, measures to improve roofs, openings, and installations; M10, measures to improve façades, openings, and installations; and finally, M11, measures to improve roofs, façades, openings, and installations. Below is a table showing the eleven proposed improvement measures combined; the percentage of savings in consumption, emissions, and demand compared to the original situation; and the new rating that would be obtained after applying each average (Table 13) for subsequent analysis.

- M1: Improvement measures on roofs and façades

It can be seen that if the improvement measures on roofs and façades are combined, the percentage of savings in cooling is −10.1%. This means that it generates greater demand than the current situation, which is reflected in the negative ratings of the three factors analyzed; therefore, the overall rating worsens to 132.4 E. One of the most important factors is the use of the roof and façade improvement measures.

One of the reasons for this is that warm air tends to rise, as it is less dense air, concentrating on the roofs and inside the building. While it is true that the set of individual measures on roofs generated savings of 1%, which in itself is a low percentage, when combined with the set of individual measures on façades, the hot air concentrated in the building becomes very high, creating a greater need for cooling in the building. From an energy point of view, this combination is not favorable for retrofitting. It should be mentioned that, as analyzed in the previous section, the two sets of improvements in this combination represent the lowest percentage savings in cooling demand for the building.

Table 12. Combined improvement measures.

ELEMENTS		FACADE	ROOMS	FACILITIES
MEASURES		- Incorporate 60 mm thick XPS thermal insulation on the inside of the NO and SO façades.	- Replace windows and partitions with low emissivity 4-12-4 double glazing and PVC frames with three air chambers on NO, SO façades. - Replace skylights with low-emissivity 4-6-4 double glazing and PVC frames with three air chambers. - Replace static louver with movable louver on - façades NW, SW	- Incorporate air conditioning equipment - Replace existing luminaires with LED luminaires. - Incorporate solar panels
ROOF	- Incorporate 40 mm thick XPS thermal insulation on flat market roof with walkable and vegetated finish. - Incorporate 40 mm thick XPS thermal insulation in flat roof of offices with non-trafficable finish.	●M1	●M2	●M3
FACADE	- Incorporate 60 mm thick XPS thermal insulation on the inside of NW and SW façades.		●M4	●M5
ROOMS	- Replace windows and screens with low-emissivity 4-12-4 double glazing and PVC frames with three air chambers on NW, SW façades. - Replace skylights with low emissivity 4-6-4 double glazing and PVC frames with three air chambers. - Replace static louver with movable louver on NW, SW facades			●M6
ROOF-FAÇADE	- Incorporate 40 mm thick XPS thermal insulation in flat market roof with trafficable and vegetation finish. - Incorporate 40 mm thick XPS thermal insulation in flat roof of offices with non-trafficable finish. - Incorporate 60 mm thick XPS thermal insulation on the inside of the NW and SW facades.		●M7	●M8

Table 12. *Cont.*

ELEMENTS		FACADE	ROOMS	FACILITIES
ROOF-OPENINGS	- Incorporate 40 mm thick XPS thermal insulation in flat roof of market with trafficable and vegetation finish - Incorporate 40 mm thick XPS thermal insulation in flat roof of offices with non-trafficable finish. - Replace windows and partitions with low emissivity 4-12-4 double glazing and PVC frames with three air chambers on NW, SW façades. - Replace skylights with low emissivity 4-6-4 double glazing and PVC frames with three air chambers. - Replace static louver with movable louver on NW, SW façades.			•M9
FAÇADE-OPENINGS	- Incorporate 60 mm thick XPS thermal insulation on the inside of NW and SW facades. - Replace windows and partitions with low emissivity 4-12-4 double glazing and PVC frames with three air chambers in NO, SO façades. - Replace skylights with low emissivity double glazing 4-6-4 and PVC frames with three air chambers. - Replace static louver with movable louver on NW, SW façades.			•M10
ROOF-FAÇADE-OPENINGS	- Incorporate 40 mm thick XPS thermal insulation in flat market roof with walkable and green finish. - Incorporate 40 mm thick XPS thermal insulation in flat roof of offices with non-trafficable finish. - Incorporate 60 mm thick XPS thermal insulation on the inside of NO and SO façades. - Replace windows and partitions with low-emissivity 4-12-4 double glazing and PVC frames with three air chambers in NW and SO façades. - Replace skylights with low-emissivity 4-6-4 double glazing and PVC frames with three air chambers. - Replace static louver with movable louver in NO, SW façades.			•M11

Table 13. Savings and ratings of the combinations of improvement packages compared to the original situation.

	Consumption (%)	Emissions (%)	Demand (%)	Energy Rating ($KgCO_2/m^2$)
Original	114.7	30.4	78.5	129.4
M1	−10.1	−10.1	−10.1	132.4
M2	2.8	2.8	2.8	128.5
M3	78.9	78.9	44.1	18.1
M4	18.8	18.8	18.8	123.6
M5	78.4	78.4	42.6	18.9
M6	82.4	82.4	36.5	17.6
M7	−6.8	−6.8	−6.8	131.4
M8	77.0	77.0	39.1	18.6
M9	80.5	80.5	48.4	17.6
M10	82.9	82.9	54.7	17.3
M11	78.9	78.9	44.2	18.1

Note: The blue rows show the best solutions.

- M2: Roof and cavity improvement measures

In this case, combining roof and cavity improvements generates cooling demand savings of 2.8%; consequently, the overall rating improves, and a rating of 128.5 E is obtained. Although this rating is an improvement, it is not a combination that generates high energy efficiency in the building, as the difference from the original rating of 129.4 is small. In any case, it can be determined that the set of measures that contributes the most in this combination is the one applied to the openings, which prevents solar gain towards the interior in summer, thus representing savings in cooling demand. From an energy point of view, this combination is favorable for the renovation of the building.

- M3: Improvement measures on roofs and installations

Combining the set of roof improvement measures with the roof installation measures results in savings of 78.9% and 87% in cooling and lighting consumption and emissions, respectively; on the other hand, the cooling demand has savings of 44.1%. In addition, the overall rating improves to a value of 18.1 A. It can be determined that, despite the fact that this combination includes the set of measures on roofs, which leads to 1% savings in the three factors analyzed, the improvements in installations make the greatest contribution in this combination and tend to improve the energy efficiency and therefore the overall rating of the building much more. On the other hand, although implementing roof improvements can concentrate heat inside the building and generate greater cooling demand, incorporating energy-efficient air-conditioning equipment helps to counteract this demand; i.e., it minimizes the need for cooling and, in the process, helps to maintain the building's internal comfort conditions. In addition, this cooling equipment generates a percentage savings in the energy consumed. In terms of lighting, the contribution of solar panels and new LED luminaires also means that less energy is consumed from non-renewable sources. From an energy point of view, this combination is favorable for building refurbishment.

- M4: Improvement measures in façades and openings

It is observed that combining the improvement measures in façades and openings generates savings of 18.8% in energy consumption and cooling demand. This is reflected in the overall rating improvement to 123.6 E. In this combination, the set of measures that contributes the most is the one applied to the building's openings, as analyzed in

the previous section. From an energy point of view, this combination is favorable for the renovation of the building.

- M5: Improvement measures on façades and installations

Combining the façade improvement measures with the installation measures results in savings of 78.4% and 87% in cooling and lighting consumption and emissions, respectively; on the other hand, cooling demand has savings of 42.6%. In addition, the overall rating improves to a value of 18.9A. In this case, similar to Measure M3, a set of improvements in the thermal envelope is proposed, this time in façades, which, despite showing savings of 1.2% in cooling demand, when combined with the improvements in installations, greatly improves the energy efficiency and therefore the overall rating of the building. On the other hand, although implementing façade improvements can prevent heat from entering the building, if only this measure is applied, there is still a considerable cooling demand that is countered by the incorporation of energy-efficient air-conditioning equipment, thus minimizing the need for cooling and, at the same time, helping to maintain the internal comfort conditions of the building. In addition, these cooling units generate a percentage savings in energy consumed, as do the panels and the new LED luminaires. From an energy point of view, this combination is favorable for building refurbishment.

- M6: Improvement measures in openings and installations

In this case, combining improvements in openings and installations generates savings of 82.4% and 87% in cooling and lighting consumption and emissions, respectively; on the other hand, cooling demand has savings of 53.5%. These high savings percentages are reflected in the overall rating of the building, which improves to 17.6A. It is worth mentioning that, as discussed in the previous section, the two sets of improvements in this combination represent the highest percentage savings in cooling demand for the building. From an energy point of view, this combination is favorable for the refurbishment of the Central Market.

- M7: Improvement measures on roofs, façades, and openings

It can be seen that, if the improvement measures on roofs, façades, and openings are combined in the building, the percentage saving in cooling demand is −6.8%. This means that it generates greater demand than the current situation, which is reflected in the negative ratings of the three factors analyzed; hence, the overall rating worsens to 131.4 E. As mentioned in the analysis of the previous measures, this is due to the fact that hot air tends to rise and concentrate on the roof, which, having thermal insulation, causes it to concentrate more inside the building. This, together with the thermal insulation applied to the façades, means that the hot air concentrated in the building is very high, creating a greater need for cooling in the building. In this case, the measures applied to the openings, which prevent solar gains towards the interior, are not sufficient to obtain better cooling of the building.

- M8: Improvement measures on roofs, façades, and installations

If all the improvement measures on roofs, façades, and installations are combined, savings of 77% and 87% in cooling and lighting consumption and emissions, respectively, are obtained; on the other hand, the cooling demand has savings of 39.1%. In addition, the overall rating improves to a value of 18.6A. In this case, similar to Measures M3 and M5, a set of improvements in the thermal envelope is proposed, this time in roofs and façades, which, despite showing savings of 1% and 1.2%, respectively, in cooling demand, when combined with the improvements in installations, greatly improve the energy efficiency and therefore the overall rating of the building. On the other hand, it was determined that hot air from inside the building is concentrated on the roofs and that the thermal insulation of the façades, while preventing heat from entering the building, also retains

the heat that has already been generated. These two situations mean that there is still a considerable demand for cooling, which is counteracted by the incorporation of energy-efficient air-conditioning equipment, thus minimizing the need for cooling, while at the same time helping to maintain the internal comfort conditions of the building. In addition, these cooling units generate a percentage savings in energy consumed, as do the panels and the new LED luminaires. From an energy point of view, this combination is favorable for building refurbishment.

- M9: Improvement measures in roofs, openings, and installations

It can be observed that, if all the improvement measures in roofs, openings, and installations are combined, savings of 80.5% and 87% in cooling and lighting consumption and emissions, respectively, are obtained; on the other hand, cooling demand has savings of 48.4%. In addition, the overall rating improves to a value of 17.6A. In this case, similar to Measures M3, M5, and M8, a set of improvements in the thermal envelope is proposed, this time in roofs, which, despite demonstrating savings of 1% in cooling demand, when combined with the improvements in installations, achieves a much greater improvement in energy efficiency and therefore the overall rating of the building. It should be noted that, as analyzed in the previous section, it is the combined improvements to openings and installations that represent the highest percentage of savings in cooling demand. For this reason, although this combination includes the roof improvement package, which, if applied individually, still creates a considerable cooling demand, this time it is offset by the incorporation of energy-efficient air-conditioning equipment, thus minimizing the need for cooling and, at the same time, helping to maintain the internal comfort conditions of the building. In addition, these cooling units generate a percentage savings in energy consumed, as do the panels and the new LED luminaires. From an energy point of view, this combination is favorable for building refurbishment.

- M10: Improvement measures in façades, openings, and installations

This time, if all the improvement measures in façades, openings, and installations are combined, savings of 82.9% and 87% in cooling and lighting consumption and emissions, respectively, are obtained; on the other hand, the cooling demand has savings of 54.7%. In addition, the overall rating improves to a value of 17.3 A, the best rating of the eleven proposed. As with Measures M3, M5, M8, and M9, a set of improvements to the thermal envelope is proposed, this time in façades, which, despite showing savings of 1.2% in cooling demand, when combined with the improvements in installations, greatly improves the energy efficiency and therefore the overall rating of the building. As analyzed in the previous section, it is the combined improvements to openings and installations that represent the greatest percentage of savings in cooling demand. Although this combination includes the façade improvement package, which, when applied individually, still has a considerable cooling demand, this time it is offset by the incorporation of energy-efficient air-conditioning equipment, thus minimizing the need for cooling and contributing to maintaining the building's internal comfort conditions. In addition, these cooling units generate a percentage savings in energy consumption, as do the panels and the new LED luminaires.

- M11: Improvement measures on roofs, façades, openings, and installations

This last proposal is the combination of the four sets of measures applied to the roof, façades, openings, and installations. If applied, savings of 78.9% and 87% in cooling and lighting consumption and emissions, respectively, can be obtained; on the other hand, cooling demand has savings of 44.2%. In addition, the overall rating improves to a value of 18.1 A. In this case, the set of measures that contribute most to this combination are those applied to openings and installations, which allow for counteracting the hot air contained

inside the building that is generated by the thermal insulation applied in façades and roofs, thus reducing cooling demand. In addition, the cooling equipment, solar panels, and new LED luminaires allow high savings in energy consumption. From an energy point of view, this combination is favorable for building renovation.

The roof and façade improvement measures, when evaluated in isolation or combined, show that the roof–façade combination tends to increase cooling demand and reduce its overall energy performance, with a negative variation of −10.1% in cooling demand and an overall rating that drops to 132.4 E. This result is explained by the tendency of warm air to accumulate indoors when combining roof insulation with façade insulation, increasing the need for cooling despite slight individual reductions (1% in roofs). Therefore, this combination is not favorable for renovation from an energy point of view and should be avoided or managed with complementary strategies (Figure 4).

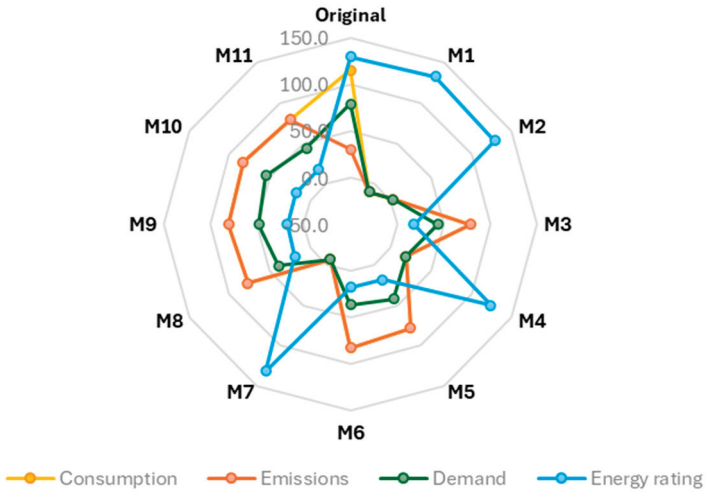

Figure 4. Radial graph of percentage improvement in consumption, emissions, and demand (%). Energy rating ($KgCO_2/m^2$).

In contrast, combinations that apply improvements to openings and installations (M6) or installations with the thermal envelope (M3, M5, M8, M9, M10, and M11) show significant improvements in cooling demand and overall performance (supported by ratings between 17.3 A and 18.6 A). In particular, the synergy between openings and installations produces the greatest cooling savings (53.5% in M6) and a notable decrease in energy consumption thanks to efficient HVAC equipment, solar panels, and LED luminaires, suggesting that strategies that prioritize improvements in installations and solar control of openings are the most effective for energy renovation.

3.3. Economic and Cost–Benefit Analysis

In this section, the economic and payback aspects for each combined measure will be analyzed in order to determine which is the most convenient and feasible according to these parameters. The criterion for this selection is that the combined measures analyzed have a low number of years of amortization, i.e., that the investment to be made to implement the measure can be recovered in a few years.

In addition, it is necessary to specify that, as this is a study on the energy and social rehabilitation of a building located in Peru, the study of the economic cost of the improvement measures will be carried out in the nuevo sol currency, which is the one used in this country, but later the conversion to euros will be carried out. The prices will be obtained through the CYPE price generator and the budget sheets of the products that will be used as

part of the improvement measures. The prices of the rehabilitation measures have been set in accordance with the Peruvian economy (data provided by local construction company).

Below is a table showing the eleven proposed improvement measures combined, their useful life, their implementation costs, the years of amortization, and the new rating that would be obtained after applying each measure (Table 14), for later analysis.

Table 14. Data on the useful life, costs, and years of amortization of the combinations of the sets of measures.

Data on the Useful Life, Costs, and Years of Amortization of the Combinations of the Sets of Measures				
Combination of Measure Sets	**Useful Life (Years)**	**Implementation Cost**	**Amortization (Years)**	**New Rating**
M1 ROOF + FAÇADES	60	EUR 416,912.51	−12.9	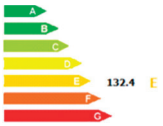
M2 ROOF + OPENINGS	60	EUR 633,087.44	69.3	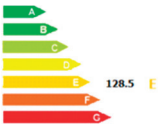
M3 ROOF + FACILITIES	50	EUR 1,383,089.79	1.2	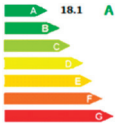
M4 FAÇADES + OPENINGS	50	EUR 302,559.52	5	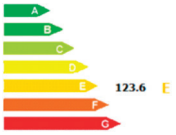
M5 FAÇADES + INSTALLATIONS	40	EUR 1,052,261.88	0.9	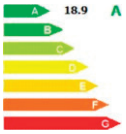
M6 ROOMS + FACILITIES	40	EUR 1,268,736.80	1.1	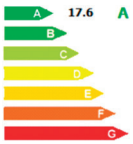
M7 ROOF + FAÇADES+ OPENINGS	85	EUR 676,279.74	−31.1	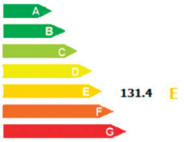
M8 ROOF + FAÇADES + INSTALLATIONS	75	EUR 1,426,282.09	1.2	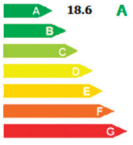

Table 14. *Cont.*

Data on the Useful Life, Costs, and Years of Amortization of the Combinations of the Sets of Measures				
Combination of Measure Sets	**Useful Life (Years)**	**Implementation Cost**	**Amortization (Years)**	**New Rating**
M9 ROOF + OPENINGS + INSTALLATIONS	75	EUR 1,642,457.01	1.4	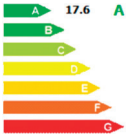
M10 FAÇADES+ OPENINGS + INSTALLATIONS	65	EUR 1,311,929.10	1.1	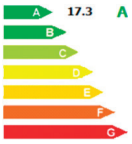
M11 ROOF + FAÇADES+ OPENINGS + INSTALLATIONS	100	EUR 1,685,649.31	1.4	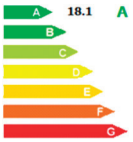

- M1: Improvement measures on roofs and façades

This combined improvement measure has a useful life of 60 years, which is the sum of 35 years of useful life of the roof measures plus 25 years of useful life of the façade measures. The cost involved in this proposal is 416,912.51, making it the second-cheapest measure, which could be amortized over −12.9 years. This means that, all in all, if these two measures are combined, it would not be worth investing in this one because it is not cost-effective.

- M2: Improvement measures on roofs and openings

The second combined improvement measure also has a useful life of 60 years, which is the sum of 35 years of useful life of the roof measures plus 25 years of useful life of the measures in the openings of the building. The cost of this proposal is EUR 633,087.43, being the third-cheapest measure, which could be amortized over 69.3 years. It can be seen that the amortization period is very high, so in principle, this would not be a favorable measure.

- M3: Improvement measures on roofs and installations

This combined improvement measure has a useful life of 50 years, which is the result of the sum of 35 years of useful life of the measures applied to roofs plus 15 years of useful life of the measures applied to the facilities of the project. The cost of this proposal is EUR 1,383,089.79, which could be amortized over 1.2 years. This measure requires a higher amount of investment because it is composed of the two most expensive measures, which are the implementation of new roofs and installations. However, the years of amortization are ideal, as the investment could be recovered in a very short time, which indicates that it is a measure worth investing in because it is profitable.

- M4: Improvement measures for façades and openings

This fourth combined improvement measure has a useful life of 50 years, which is the sum of 25 years of useful life of the measures applied to the façades plus 25 years of useful life of the measures applied to the openings of the building. The cost of this proposal is EUR 302,559.52, which could be amortized over 5 years. The cost of this measure is the cheapest of all the options considered; the number of years of amortization is a reasonable

number to be able to recover the investment made, so it would be worthwhile to invest in the measure.

- M5: Improvement measures for façades and installations

The fifth combined improvement measure has a useful life of 40 years, which is the sum of 25 years of useful life of the façade measures and 15 years of useful life of the facility measures of the project. The cost involved in this proposal is EUR 1,052,261.88, which could be amortized over 0.9 years. This measure also has a high cost because it contains improvements to installations; however, the number of years of amortization is a reasonable time to be able to recover the investment made; therefore it would be convenient to invest in the measure.

- M6: Improvement measures for openings and installations

This sixth combined improvement measure has a useful life of 40 years, which is the sum of 25 years of useful life of the measures applied to the openings of the building plus 15 years of useful life of the installation measures. The cost of this proposal is EUR 1,268,736.80 euros, which could be amortized over 1.1 years. Although it is true that the cost of the measure is high, the years of amortization are few, which means that it is worth investing in this measure.

- M7: Improvement measures for roofs, façades, and openings

The seventh combined improvement measure has 85 years of useful life, which is the sum of 35 years of useful life of the measures on roofs, 25 years of the measures on façades, and 25 years of useful life of the measures applied to the openings. The cost of this proposal is EUR 676,279.74, which could be amortized over −31.1 years. This measure is one of the cheapest of all the proposals; however, the payback period is long, so it would not be advisable to invest in the measure because it is not cost-effective.

- M8: Improvement measures for roofs, façades, and installations

The eighth combined improvement measure has a useful life of 75 years, which is the sum of 35 years of useful life of the roof measures, 25 years of the façade measures, and 15 years of useful life of the installation measures. The cost of this proposal is EUR 1,426,282.09, which could be amortized over 1.2 years. This measure has the third-highest cost; however, this amount of money could be recovered in a few years, which means that it is worth investing in this measure.

- M9: Improvement measures for roofs, openings, and installations

The ninth combined improvement measure has 75 years of useful life, which is the sum of 35 years of useful life of the roof measures, 25 years of the measures applied to the openings of the building, and 15 years of useful life of the measures applied to the installations. The cost of this proposal is EUR 1,642,457.01, which could be amortized over 1.4 years. This measure has the second-highest cost; however, the amount of money invested could be recovered in a few years, making it a favorable measure.

- M10: Improvement measures for façades, openings, and installations

This combined improvement measure has 65 years of useful life, which is the sum of 25 years of useful life of the façade measures, 25 years of the measures applied to the openings of the building, plus 15 years of useful life of the measures applied in the installations. The cost of this proposal is EUR 1,311,929.10, which could be amortized over 1.1 years. The cost of this measure is high, but the years of amortization are few; therefore, it is advisable to invest in this measure.

- M11: Improvement measures on roofs, façades, openings, and installations

The last combined improvement measure has 100 years of useful life, which is the result of the sum of 35 years of useful life of roof measures, 25 years of façade measures, 25 years of the measures applied to the openings of the building, and 15 years of useful life of the measures applied to installations. The cost of this proposal is EUR 1,685,649.31, which could be amortized over 1.4 years. This measure is the most expensive of the eleven proposals because it combines all the possible improvements in the different elements of the building; despite this, the payback years are few, so it would be feasible and advisable to invest in this measure.

3.4. Energy and Economic Comparison Between the Initial State and the Adopted Solution

The rating of the building's thermal envelope and installations in the initial state is 129.4 $KgCO_2/m^2$ (E), and in the final state, after the selected improvements, it is 17.6 $KgCO_2/m^2$ (A).

The demand and emissions for heating and DHW are considered unquantifiable, as the program has not defined reference values for these demands. This is due to the climatic characteristics of the location, which, as it does not experience very low temperatures, does not require these systems. The opposite is true for the building's cooling demand, which is rated at 78.5 kWh/m^2 in its initial state and drops to 40.5 kWh/m^2 in its improved state. The emissions produced by the cooling system drop from 30.4 Kg CO_2/m^2 to 5.9 Kg CO_2/m^2. On the other hand, with regard to the emissions produced by the lighting system, in the initial state, they are 98.9 kg CO_2/m^2 due to the low efficiency and inadequate characteristics of the installations, and they go down to a value of 12.9 kg CO_2/m^2.

The differences between the initial characteristics of the envelope and installations and the characteristics with the improvement measures analyzed can be seen in the following Figures 5 and 6.

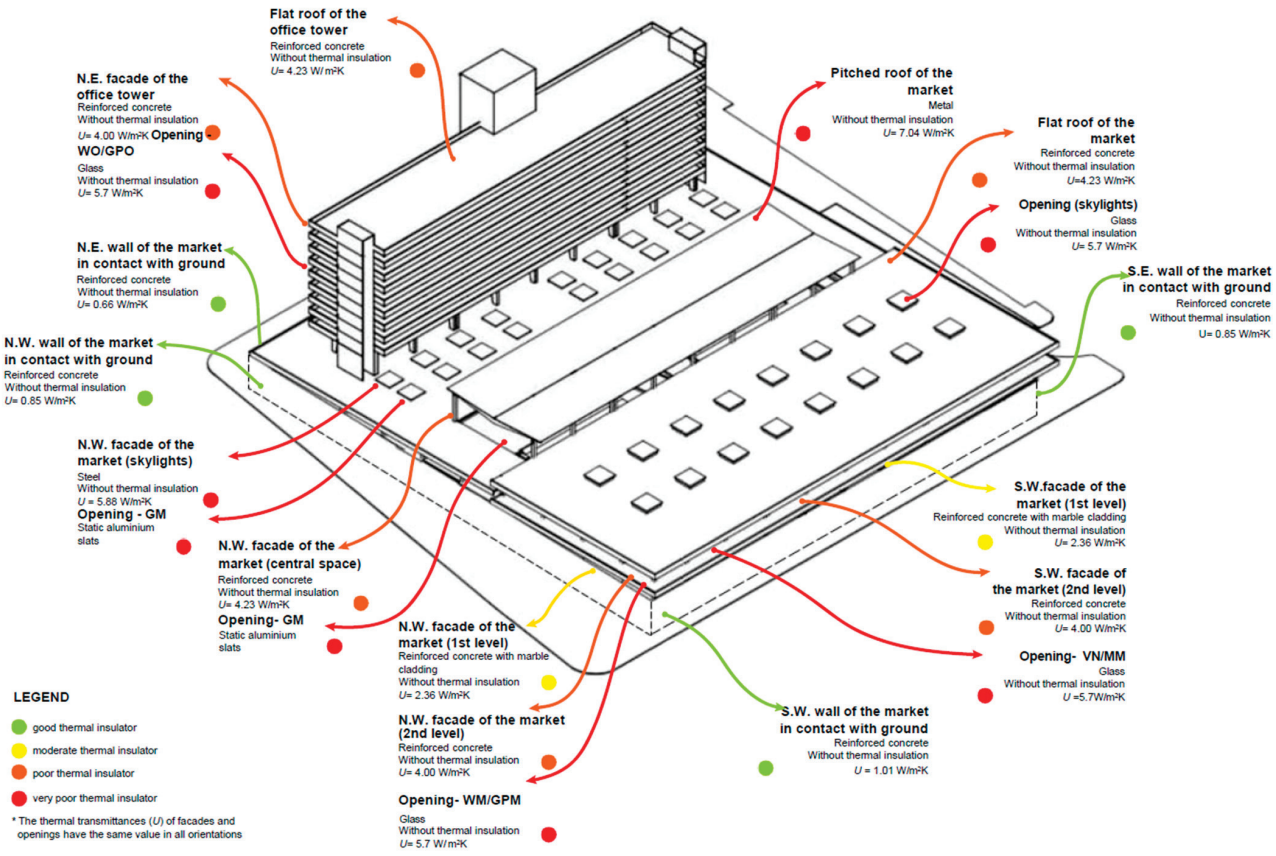

Figure 5. Isometry explaining the energy rating of the current state of the building.

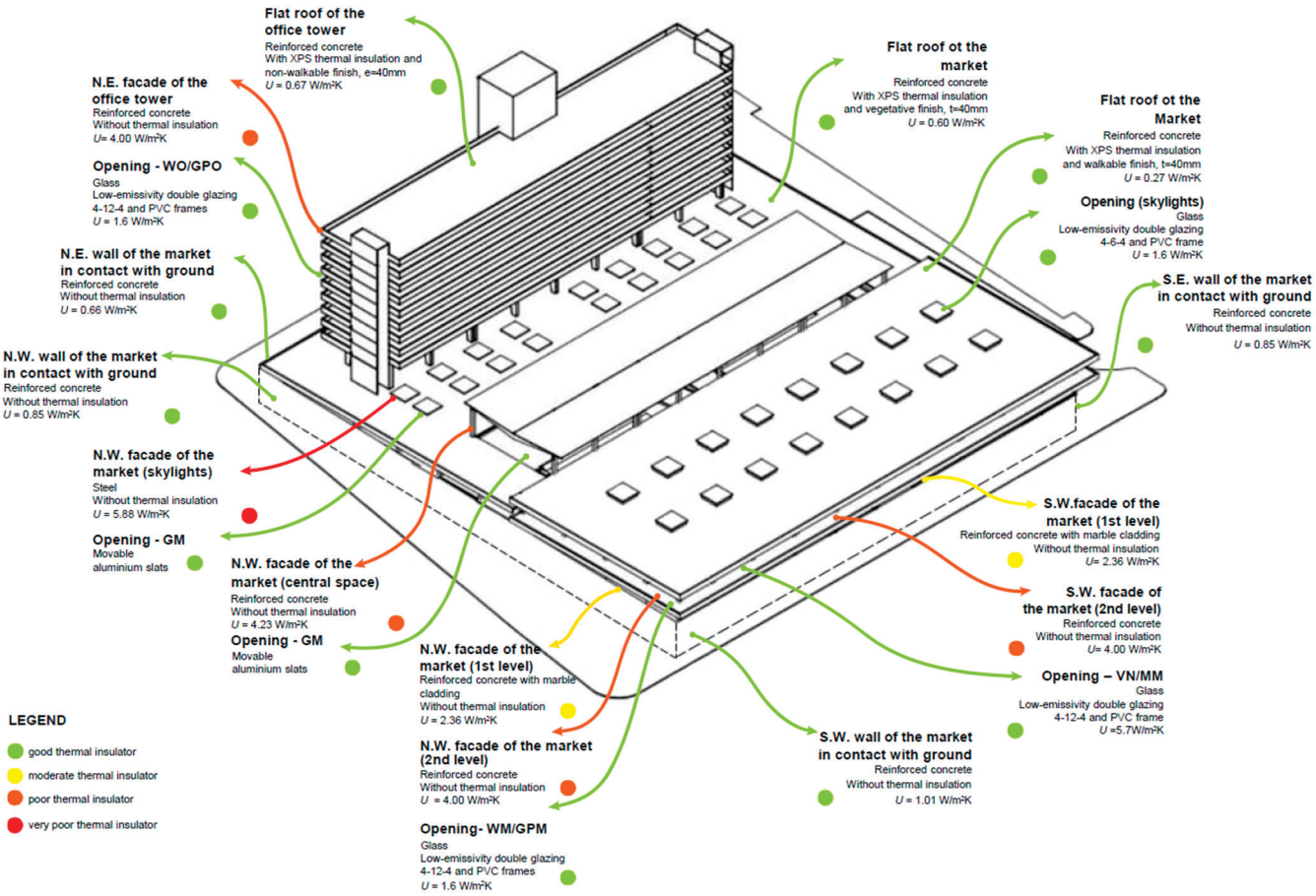

Figure 6. Explanatory isometry of the energy rating obtained by applying Measure M9.

The most energetically advantageous measure and, at the same time, the most economically viable that fits the objective of this work—to achieve energetic and social rehabilitation—is M9. This measure has an overall energy rating of 17.6 A, combines improvement measures applied to roofs, openings, and installations, has 75 years of useful life, and requires an investment of EUR 1,642,457.01, which can be amortized over 1.4 years. Although it is true that some measures also improve the overall energy rating of the building and can be amortized over a few years, this combination is considered the most favorable of all because it includes two improvement measures that are in line with the social rehabilitation of the building, which are the improvements to the roof and the installations, with the office tower refurbished by replacing the LED lights and adding an air-conditioning system.

The results demonstrate significant energy and economic gains by focusing interventions on openings and installations, especially with Measure M9, which obtains a rating of 17.6 A, a payback period of 1.4 years, and a useful life of 75 years. The evidence is consistent with similar studies, such as Salgueiro [22] and Calado [31], showing that envelope improvements and especially installations generate substantial reductions in demand and emissions when properly combined. While Salgueiro highlights the impact of insulation and renewable energy systems in reducing demand and carbon footprint, our analysis shows that improvements in windows, frames, and movable louvers can achieve similar or greater reductions in cooling demand, complemented by improvements in roofs and systems. In both cases, integrated interventions outperform isolated measures.

In terms of analysis and transferability, the results reinforce the idea that interventions targeting openings and systems are often the most energy-cost-effective, even when initial costs are high. This aligns with the findings of Calado and Echeverría [23,31], who note

that improvements in installations can offer quick wins, but sustained efficiency is best achieved when acting on the envelope and combining measures. It is also noted that, as in the Spanish studies cited above, consideration of local climatic contexts is crucial to avoid solutions that, while efficient elsewhere, do not offer the same cost-effectiveness in the Peruvian location. Ultimately, the integrated strategy M9 demonstrates consistency with the literature, highlighting the need for packages of measures that combine the envelope, openings, and installations to maximize energy and social benefits.

4. Discussion

After conducting multiple energy and economic analyses in the Central Market of Lima (Peru), it is possible to conclude that the improvement measures applied to the building's openings and installations, although representing the most costly investments, are the ones that contribute most significantly to the project, since they result in a higher energy rating thanks to savings in consumption and demand for refrigeration and lighting. This highlights the importance of prioritizing these interventions to achieve optimal energy efficiency. The analysis of the thermal envelope and installations showed that interventions on openings and installations generate the greatest energy and economic impacts of all the measures evaluated. In particular, the replacement of glazing and frames on the northwest and southwest façades, the optimization of skylights, and the adoption of movable louvers offer significant reductions in unwanted solar gain, lower overall transmittance, and better control of air intakes, which translates into lower cooling demand and, consequently, lower emissions and operating costs.

On the other hand, improvements to the thermal envelope, such as façades and roofs, on their own, do not generate considerable savings in cooling demand and, in terms of cost-effectiveness, are not as efficient. However, when combined with facility measures, their impact is enhanced. In addition, roof improvements can have an important social benefit, as they can be transformed into meeting and leisure spaces or even generate economic income, thus increasing the social and economic value of the property.

In the case of roofs, it was observed that a lower thickness of thermal insulation can favor a better energy rating in certain contexts, as a greater thickness can retain more heat and increase cooling demand. This underlines the need to adapt improvement measures to the specific climatic conditions of the site in order to maximize energy benefits.

Peruvian regulations currently focus mainly on improvements in installations, such as LED lighting or air-conditioning systems. However, this study shows that interventions in openings, such as the replacement of glass or frames or the incorporation of movable louvers, also offer great potential for energy savings and should be considered in efficiency policies.

The limitations of the research are concentrated in several dimensions. On the one hand the estimates of demand and emissions for heating and domestic hot water are presented as non-quantifiable within the current framework due to the absence of reference values; sensitivity analyses and long-term simulations were not performed to capture seasonal variations and cost evolution. On the other hand, no sensitivity analyses or long-term simulations were performed to capture seasonal variations and cost evolution, and furthermore, the evaluation framework could be expanded to incorporate social and economic metrics (rental value, quality of life, and use of rehabilitated spaces) and to analyze impacts on the community.

The numerical results, on the other hand, should be interpreted according to the climatic and design conditions of the site; the magnitude of benefits may vary according to orientation, occupancy, and air-conditioning demand; furthermore, the model was not calibrated with measured energy consumption data (there were no historical records of

the Central Market), although internal consistency checks and comparisons with reference studies in Peru and Spain were performed; the absence of quantitative validation represents a significant limitation that will be addressed in future research. However, the proposed approach combines improvements in the thermal envelope, openings, and systems and incorporates a social dimension into decision making, demonstrating that efficiency policies can generate multiple benefits, such as energy savings, cost reductions, improvements in comfort, and opportunities for social use of rehabilitated spaces.

5. Conclusions

The conclusions reached in this research indicate that the optimal scenario is M9, which integrates improvements in roofs, openings, and installations. It emerged as the most favorable option from energy and economic points of view, with an overall energy rating of 17.6 A, an estimated payback period of 1.4 years, and a useful life of 75 years. This scenario also has a social dimension, as it provides recreational and leisure space for users, in addition to improving the comfort of the building. This result reflects the synergy between technical interventions and their appropriate alignment with the objectives of social and economic rehabilitation.

Finally, this study highlights the importance of adopting a holistic approach that combines technical improvements with social interventions. Building retrofitting should focus not only on energy efficiency but also on enhancing the social and economic environment of the building. The reconversion of spaces such as the office tower and the creation of meeting and leisure areas in renovated areas can generate a positive social impact, promoting cultural change and improving the quality of life in the community.

Author Contributions: Conceptualization, K.S.-F.; Methodology, P.A.-B.; Software, K.S.-F.; Validation, P.A.-B.; Formal analysis, K.S.-F.; Investigation, P.A.-B.; Resources, K.S.-F.; Writing—original draft, K.S.-F.; Writing—review & editing, P.A.-B.; Supervision, P.A.-B. All authors have read and agreed to the published version of the manuscript.

Funding: This research received no external funding.

Data Availability Statement: The data are not publicly available due to privacy or ethical restrictions.

Conflicts of Interest: The authors declare no conflict of interest.

References

1. Wang, X.; Wang, S.; Li, T. Research on the Performance and Energy Saving of Solar-Coupled Air Source Heat Pump Heating System: A Case Study of College Dormitory in Hot Summer and Cold Winter Zone. *Energies* **2025**, *18*, 3794. [CrossRef]
2. Álvarez, A.M. Challenges for Latin America: The Agenda for Sustainabale Development and Negotiations in the Twenty-First Century. *Probl. Desarro.* **2016**, *47*, 9–30. [CrossRef]
3. Angrisano, M.; Fabbrocino, F.; Iodice, P.; Girard, L.F. The evaluation of historic building energy retrofit projects through the life cycle assessment. *Appl. Sci.* **2021**, *11*, 7145. [CrossRef]
4. Mousavi, E.; Bhattacharya, A.; Betz, F.; Lautz, R. Evolution of Ventilation Measures and Energy Performance in Buildings with High Ventilation Demands: A Critical Review. *Energies* **2025**, *18*, 3603. [CrossRef]
5. Cáceres, A.L. Análisis de Ciclo de Vida Comparativo de Edificaciones Multifamiliares en Lima. Bachelor's Thesis, Pontificia Universidad Católica del Perú, Limá, Peru, 2016; pp. 1–69. Available online: http://tesis.pucp.edu.pe/repositorio/handle/123456789/6682 (accessed on 14 January 2023).
6. Ruiz, E. El Análisis de Ciclo de Vida. Metodología de Decisión y Evaluación Ambiental en El Sector de la Edificación. Grado en Arquitectura Técnica, Universidad de Los Andes, Bogotá, Colombia, 2016. Available online: http://hdl.handle.net/10251/66016 (accessed on 16 March 2023).
7. Schittich, C. *Rehabilitación*; Walter de Gruyter: Berlin, Germany, 2013.
8. Verónica, E.; Farroñán, R.; Christiam, G.; Chilicaus, F.; Edgardo, L.; Salinas, C.; Rojas, L.C.; Katherine, L.; Cotrina, C.; Licaparedolfo, G.S.; et al. Green Finance and the Energy Transition: A Systematic Review of Economic Instruments for Renewable Energy Deployment in Emerging Economies. *Energies* **2025**, *18*, 4560. [CrossRef]

9. Caneppele, L.B.; Nogueira de J, M.C.; de Vasconcellos, A.B. Avaliação Da Eficiência Energética E Custo Benefício No Uso De Coberturas Metálicas Em Supermercados Empregando O Software Energyplus. *Rev. Eletrônica Em Gestão, Educ. e Tecnol. Ambient.* **2013**, *9*, 1971–1979. [CrossRef]
10. Ministerio de Energía y Minas. Guía de Orientación del Uso Eficiente de la Energía y de Diagnóstico Energético. *Dir. Gen. Efic. Energética.* **2020**, *2*, 1–2. Available online: https://eficienciaenergetica.minem.gob.pe/Content/fileman/Uploads/Documents/Gu%C3%ADas%202022/GUIA%20SECTOR%20RESIDENCIAL_VF3.pdf (accessed on 3 March 2023).
11. Ríos-Fernández, J.C. Economic and environmental improvements using high energy efficiency HVAC in supermarkets. *Clean Technol. Environ. Policy.* **2020**, *22*, 1417–1429. [CrossRef]
12. Cecchinato, L.; Corradi, M.; Minetto, S. Energy performance of supermarket refrigeration and air conditioning integrated systems. *Appl. Therm. Eng.* **2010**, *30*, 1946–1958. [CrossRef]
13. Sherman, R.; Naganathan, H.; Parrish, K. Energy savings results from small commercial building retrofits in the us. *Energies* **2021**, *14*, 6207. [CrossRef]
14. Cordano, A.L.V.; Balistreri, E.J. The marginal cost of public funds of mineral and energy taxes in Peru. *Resour. Policy* **2010**, *35*, 257–264. [CrossRef]
15. De la Cruz Torres, D.G.; Mazadiego, L.F.; Bolonio, D.; Pons-Esparver, R.R. Long-Term Forecast of Energy Demand towards a Sustainable Future in Renewable Energies Focused on Geothermal Energy in Peru (2020–2050): A LEAP Model Application. *Sustainability* **2024**, *16*, 4964. [CrossRef]
16. Colina-Calvo, A.O. A Comprehensive Review of Peru's Energy Scenario: Advancing Energy Access, Sustainability, and Policy Implications. *Rev. Kawsaypacha Soc. y Medio Ambient.* **2024**, *2024*, 1–24. [CrossRef]
17. Never, B.; Kuhn, S.; Fuhrmann-Riebel, H.; Albert, J.R.; Gsell, S.; Jaramillo, M.; Sendaza, B. Energy saving behaviours of middle class households in Ghana, Peru and the Philippines. *Energy Sustain. Dev.* **2022**, *68*, 170–181. [CrossRef]
18. Alva, G.; Liu, L.; Huang, X.; Fang, G. Thermal energy storage materials and systems for solar energy applications. *Renew. Sustain. Energy Rev.* **2017**, *68*, 693–706. [CrossRef]
19. Liu, P.; Pistikopoulos, E.N.; Li, Z. An energy systems engineering approach to the optimal design of energy systems in commercial buildings. *Energy Policy* **2010**, *38*, 4224–4231. [CrossRef]
20. Ren, Z. A Literature Review on the Use of Weather Data for Building Thermal Simulations. *Energies* **2025**, *18*, 3653. [CrossRef]
21. Evangelisti, L.; De Cristo, E.; De Lieto Vollaro, R. In Situ Winter Performance and Annual Energy Assessment of an Ultra-Lightweight, Soil-Free Green Roof in Mediterranean Climate: Comparison with Traditional Roof Insulation. *Energies* **2025**, *18*, 4581. [CrossRef]
22. Salguiero, M.J. *Mercados de Hierro en España: Rehabilitación y Mejora Energética*; E.T.S. Arquitectura (UPM): Madrid, Spain, 2021; pp. 49–111.
23. Echevarria, M. *Eficiencia Energética en el Mercado de la Paz (Madrid)*; E.T.S. Arquitectura (UPM): Madrid, Spain, 2022.
24. Escrivá-Escrivá, G. Basic actions to improve energy efficiency in commercial buildings in operation. *Energy Build* **2011**, *43*, 3106–3111. [CrossRef]
25. Cosio, F.P.T. *Nuevo Mercado Central de Lima: Centro Gastronómico y Residencia Para Estudiantes en el Centro Histórico de Lima*; Pontificia Universidad Católica del Perú: Lima, Peru, 2019.
26. De Cristo, E.; Evangelisti, L.; Guattari, C.; De Lieto Vollaro, R. An Experimental Direct Model for the Sky Temperature Evaluation in the Mediterranean Area: A Preliminary Investigation. *Energies* **2024**, *17*, 2228. [CrossRef]
27. González, V.G.; Bandera, C.F. A building energy models calibration methodology based on inverse modelling approach. *Build. Simul.* **2022**, *15*, 1883–1898. [CrossRef]
28. Hong, T.; Langevin, J.; Sun, K. *Building Simulation: Ten Challenges*; Springer: Berlin/Heidelberg, Germany, 2018. [CrossRef]
29. Gómez, G.; Soto, S.; Suástegui, J.A.; Acuña, A. A New Proposal for the Use of Cooling Degree Hours for the Energy Simulation of Residential Buildings in Mexico. *Energies* **2025**, *18*, 4554. [CrossRef]
30. SERVICIO NACIONAL DE METEOROLOGÍA E HIDROLOGÍA DEL PERÚ—SENAMHI, Climas del Perú—Mapa de Clasificación Climática Nacional. 2010. Available online: https://www.senamhi.gob.pe/?p=mapa-climatico-del-peru (accessed on 20 March 2023).
31. Bonnin, C.C. *Rehabilitación Energética del Mercado de San Cristóbal*; E.T.S. Arquitectura (UPM): Madrid, Spain, 2023.

energies

MDPI

Article

Long-Term Performance of Thermal Insulating Composite Systems Based on Water Resistance and Surface Multifunctionality

Giovanni Borsoi [1,2], João L. Parracha [1,2], Jéssica D. Bersch [1], Ana R. Garcia [3,4], Amélia Dionísio [5], Paulina Faria [6], Rosário Veiga [2] and Inês Flores-Colen [1,*]

[1] Civil Engineering Research and Innovation for Sustainability (CERIS), Department of Civil Engineering, Architecture and Environment (DECivil), Instituto Superior Técnico, University of Lisbon, Av. Rovisco Pais, 1049-001 Lisbon, Portugal; giovanni.borsoi@gmail.com (G.B.); jparracha@lnec.pt (J.L.P.); jessica.d.bersch@tecnico.ulisboa.pt (J.D.B.)
[2] National Laboratory for Civil Engineering (LNEC), Av. do Brasil, 101, 1700-066 Lisbon, Portugal; rveiga@lnec.pt
[3] Centro de Química Estrutural, Instituto Superior Técnico, University of Lisbon, Av. Rovisco Pais, 1049-001 Lisbon, Portugal; argarcia@ualg.pt
[4] Department of Chemistry and Pharmacy, Faculty of Science and Technology, University of Algarve, Campus de Gambelas, 8005-139 Faro, Portugal
[5] Centro de Recursos Naturais e Ambiente (CERENA), Departamento de Engenharia de Recursos Minerais e Energéticos (DER), Instituto Superior Técnico, University of Lisbon, Av. Rovisco Pais, 1049-001 Lisbon, Portugal; amelia.dionisio@tecnico.ulisboa.pt
[6] Civil Engineering Research and Innovation for Sustainability (CERIS), Department of Civil Engineering (DECivil), NOVA School of Science and Technology, NOVA University Lisbon, 2829-516 Caparica, Portugal; paulina.faria@fct.unl.pt
* Correspondence: ines.flores.colen@tecnico.ulisboa.pt

Abstract: External Thermal Insulation Composite Systems (ETICSs) are increasingly applied in both new construction and energy retrofitting, where long-term durability under environmental exposure is critical to preserving thermal efficiency. Moisture ingress represents a key degradation factor, reducing insulation performance and undermining energy savings promoted by the ETICS. The effectiveness of these systems is strongly influenced by surface protection, which also reflects aesthetic and biological resistance. This study investigates the influence of three commercial protective surface coatings, characterized by hydrophobicity, photocatalytic activity, and resistance to biological growth, on ETICS finishes based on acrylic, natural hydraulic lime (NHL), and silicate binders. An artificial aging protocol was employed to evaluate coating stability and compatibility with the finishing layers. Results show that acrylic-based finishes provided superior durability and protection, while coatings on NHL and silicate substrates exhibited lower performance. Notably, a TiO_2 enriched photocatalytic coating, despite improved self-cleaning potential, demonstrated the least durability. The findings highlight that optimal ETICS protection requires coatings that combine low water absorption, effective drying, and biological resistance, thereby ensuring sustained thermal and energy performance over time.

Keywords: ETICS; multifunctional coatings; durability; hydrophobicity; self-cleaning; biocidal

1. Introduction

External Thermal Insulation Composite Systems (ETICSs), also known as Exterior Insulation Finishing Systems (EIFSs) or Exterior Wall Insulation Systems (EWIs), consist

of thermal insulation materials, such as expanded polystyrene (EPS), mineral wool (MW), or insulation cork board (ICB), bonded and/or mechanically fixed to façades and coated with a reinforced rendering (a base coat with a glass fiber mesh) and a finishing coat (e.g., paint) [1–3]. Since the 1960s, ETICSs have been widely used worldwide for new constructions and retrofitting [4] due to their contributions to thermal insulation, building envelope protection [5], and reductions in energy consumption and CO_2 emissions [6].

However, ETICSs are continuously exposed to environmental and anthropogenic agents [7] that affect their durability and in-service life, including wind-driven rain, solar radiation, atmospheric pollutants, and biocolonization [8–11]. Water accumulation or condensation can lead to several anomalies, including aesthetic changes and runoff stains, thermo-mechanical stresses and microcracks [12,13], biological growth (e.g., algae, fungi, bacteria, lichens) [14,15], and increased thermal conductivity of the insulation layer and the whole system [6].

Applying protective products to ETICS surfaces can help reduce degradation and enhance their durability. Multifunctional coatings and paints, which encompass biocide, hydrophobic, and self-cleaning properties, can provide a suitable maintenance strategy [16]. Nevertheless, the coexistence of these functions raises concerns about the materials' long-term performance and the suitability of their protection function.

Hydrophobic binders or additives (e.g., siloxane, silicates, silane, aliphatic or fluorinated compounds) provide a water-repellent barrier on façades, preventing the penetration of water and harmful ions (e.g., chlorides or sulfates) [17] and thus preserving the thermal resistance of ETICSs. Silicon-based water repellents can form covalent bonds with the substrate, resulting in a barrier at the air-substrate interface and/or nanoscale roughness [18]. These features induce low surface energy and increase the water contact angle. However, a lack of data on the durability of hydrophobic emulsion coatings is often reported in the literature [19,20].

Biocide additives in infinitesimal percentages (e.g., terbutryn, isothiazole, zinc pyrithione) within surface protective coatings can hinder biological growth [15]. Biocidal action generally includes enzymatic inactivation (disturbance of selected metabolic or energetic processes by disintegration or chemical modification of antimicrobial agents), reduced intracellular accumulation, specific reactions, and physicochemical alterations at the cellular target sites (i.e., mutational changes, chemical modification, and protection) [21].

Photocatalytic additives (e.g., titanium or zinc oxides, cadmium sulfide) provide self-cleaning, air-purifying, and antimicrobial properties [22] when applied to façades. Photocatalysts, activated by UV irradiation, accelerate photoinduced reactions and lead to a heterogeneous advanced oxidation process (formation of free radicals) [23,24], decomposing organic molecules and forming superhydrophilic surfaces that can facilitate the removal of contaminants [16,23,25–30].

A competitive effect between hydrophobic (water contact angle (θ) > 90° between drops and the surface due to water-repellent additives) and superhydrophilic properties (with $\theta \sim 0°$, induced by the photocatalytic products) can lead to a lack of long-term effectiveness [25,26]. Similarly, the durability of biocides is a significant concern for façades [31]. Although their use has been increasingly limited [32], leaching phenomena and degradation byproducts are rarely reported [33,34].

Most previous studies have addressed hydrophobic coatings, biocidal treatments, and photocatalytic additives independently. Comprehensive data on their combined long-term performance after aging remain limited [35–37]. In particular, the potential interactions between these functionalities when applied to commercial ETICS [38] should be further clarified. Addressing this gap is essential not only for developing sustainable maintenance

strategies for façades but also for advancing the scientific understanding of multifunctional coatings in building envelopes.

Therefore, this paper aims to investigate the performance of three commercially available multifunctional coatings with biocidal, hydrophobic, and photocatalytic properties when applied to four different widely used commercial ETICS. Their long-term efficacy was assessed by correlating moisture transport properties, mold growth, and photocatalytic activity to identify synergistic or competitive effects among the different additives. Additionally, incompatibilities between additives and some of the coatings were found. A recently developed innovative accelerated aging procedure [13], involving hygrothermal cycles, ultraviolet (UV) radiation, and exposure to air pollutants (SO_2), was conducted, including examining the chemical and morphological changes that occurred during aging.

2. Materials and Methods

2.1. Materials

2.1.1. ETICS

Four commercially available ETICSs, with a European Technical Approval (ETA), were selected based on the most common systems available on the market. The products feature various thermal insulation materials (including EPS, ICB, and MW), base coats (formulated with cement or natural hydraulic lime (NHL)), and finishing coats (acrylic-, lime-, or silicate-based), as shown in Table 1.

Table 1. Constituent layers and thicknesses of the studied ETICSs.

System Acronym	Thermal Insulation	Base Coat (BC) [1]	Finishing Coat (FC)		Thickness (mm)
			Key-Coat	Finishing	
S1	EPS	Cement, synthetic resins, mineral additives	Water-based acrylic dispersion	Water-based acrylic co-polymer, pigments, marble powder, and additives	40.6
S2	ICB	NHL, cement, mineral fillers, resins, and synthetic fibers	Air lime, hydraulic binder, and organic additives		65.8
S3	MW	Cement, synthetic resins, mineral fillers, and additives	Water-based acrylic co-polymer and mineral additives	Water-based acrylic paint, mineral aggregates, pigments, and additives	61.3
S4	ICB	NHL, cement, mixed binders, and cork aggregates	Water-based dispersion of silicate	Water-based silicate paint, organic additives, and pigments	43.9

[1] BC includes a reinforcement glass fiber mesh.

2.1.2. Multifunctional Coatings

Three commercial multifunctional coatings (MC) (Table 2) were applied to the dry surface of ETICS in two successive layers using a brush, following the manufacturers' guidelines. A 24 h interval was maintained between applications to allow for complete solvent evaporation. The coated ETICS specimens were stored under controlled conditions (T = 20 ± 3 °C, RH = 50 ± 5%) for three weeks to ensure complete polymerization of the coatings.

Table 2. Technical data for the multifunctional coatings (MCs), as reported in the manufacturers' technical and safety sheets.

Product Identification	Color	Density (g/cm^3) at T = 20 °C/ RH% = 60	pH	Drying Residue (g/L)	Application Yield (L/m^2)	Flash Point (°C)
HW	Whitish	0.99 ± 0.02	9.3 ± 0.5	59 ± 6	0.166–0.25 (no dilution)	64
NS	Whitish	0.98 ± 0.05	9.2 ± 0.5	30 ± 2	0.1–0.125 (no dilution)	>23
AQ	Transparent (opal)	1.31 ± 0.09	8.5 ± 0.5	718 ± 21	0.26–0.27 (10% dilution in water)	>100

According to the technical documentation, HW consists of an aqueous silane/siloxane emulsion with hydrophobic performance and biocidal additives (isothiazole). NS is an ethyl silicate-based coating with reduced percentages of silane, incorporating nanostructured TiO_2 particles that enable photocatalytic self-cleaning and antimicrobial properties. AQ is a multifunctional coating with hydrophobic, self-cleaning, and biocidal properties based on an acrylic aqueous dispersion (methyl methacrylate and butyl acrylate), also containing nano- to microstructured TiO_2 particles (10%), $CaCO_3$ (5 to 10%), quartz, ZnO, and biocidal additives (terbutryn, isothiazole).

2.2. Methods

2.2.1. Moisture Transport Properties

Capillary water absorption was tested according to EAD 040083-00-0404 [3]. Two specimens (with dimensions 150 mm × 150 mm × thickness, Table 1) of each "ETICS + MC" were used. The specimens were conditioned in a controlled environment (T = 23 ± 2 °C, RH = 65 ± 5%) for seven days before testing, and their lateral faces were sealed with metallic adhesive tape. The external surface of the specimens was placed in contact with water at approximately a 3 mm depth, and weight was recorded at selected intervals (i.e., after 3 min, 1, 2, 4, 8, and 24 h).

The capillary water absorption coefficient (Cc) was determined from the initial linear portion of the absorption curve, obtained by plotting the mass of absorbed water per unit area in contact with the water, kg/m^2, against the square root of time, min$^{0.5}$ [7]. Specifically, Cc was calculated as the slope of the absorption curve during the first 3 min of testing, by dividing the absorbed water mass per specimen area at 3 min by the square root of the time at this point. In addition, the mean water absorption of the specimens after 1 h and 24 h was considered for comparative purposes [3].

Drying kinetics were evaluated immediately after the capillarity test, following EN 16322 [39]. Weight loss was monitored until stabilization (defined as mass variation < 1%), under the same controlled environment (T = 23 ± 2 °C, RH = 65 ± 5%) [7]. The drying index (DI) was calculated with Equation (1), which describes the cumulative extent of water release during drying relative to the maximum possible water content and theoretical drying potential over time. In Equation (1), M_x is the mass of the specimen measured during the drying process (g), M_1 is the mass of the oven-dried specimen (g), M_3 the initial mass at the beginning of drying (g), t_0 (h) the initial test time and t_f (h) the ending time of

the drying process [40]. A lower *DI* value indicates faster water release and drying kinetics. For comparison, the same t_f was adopted for all samples.

$$DI = \frac{\int_{t_0}^{t_f} f\left(\frac{M_x - M_1}{M_1}\right) dt}{\left(\frac{M_3 - M_1}{M_1}\right) \times t_f} \quad (1)$$

2.2.2. Photocatalytic Efficacy and Color Change

Rhodamine B (RhB), functionalized diethylammonium chloride, $C_{28}H_{31}ClN_2O_3$) was selected for the photocatalytic assessment of the multifunctional coatings over time. A 0.05 g/l RhB water-based solution was prepared and applied with a micropipette to the specimen surface (80 mm × 45 mm × Thickness, Table 1), producing stains of approximately 2 cm in diameter [41]. Three stained specimens per set of "ETICS + MC" system were exposed in a UV-light chamber with three lamps (60 W/m^2, λ = 315–400 nm, UV-A), placed 5 cm away from the samples.

Color coordinates (*L**, *a**, and *b** from the CIELab color space) were measured using a Chroma Meter Minolta CR-410 chromameter (Konica Minolta, Inc., Tokyo, Japan). *L** indicates lightness (0 = black, 100 = white), *a** represents the red (+*a**) to green (−*a**) axis, and *b** the yellow (+*b**) to blue (−*b**) [16,42]. The equipment operated in specular component included mode (SCI) with D_{65} illuminant, 2° observer angle, and a 50 mm measurement area. Measurements were collected immediately after RhB application and after 4, 8, 24, 48, 72, 96, and 168 h of UV exposure.

Color change (ΔE, dimensionless) was calculated with Equation (2) [43], which expresses the overall difference in color between two measurements in the CIELab color space. In Equation (2), Δ*L**, Δ*a**, and Δ*b** are the mean differences in the corresponding coordinates (lightness L*, red-green a*, and yellow-blue b*, dimensionless) between the RhB-stained specimens at a time of interest (t) and their initial stained state at the beginning of the test (t = 0) [15,43,44]. A higher ΔE value indicates a more pronounced magnitude of color change.

$$\Delta E = \sqrt{(\Delta L^*)^2 + (\Delta a^*)^2 + (\Delta b^*)^2} \quad (2)$$

Color variations and/or preservation were further assessed by comparing the CIELab coordinates of unstained specimens before and after accelerated aging cycles. For this purpose, three specimens of each setting were studied, and six measurements were collected from each specimen.

2.2.3. Biological Colonization

The susceptibility to mold growth was examined on both unaged multifunctional coatings (tested alone) and "ETICS + MC" settings after completing the accelerated aging procedure (hygrothermal cycles, UV radiation, and SO_2 exposure, Section 2.2.4). A method adapted and previously validated for ETICS [7] was used in the analysis.

Unaged coatings (HW, NS, and AQ) were applied in three layers to both sides of Whatman three n° 1 filter paper (45 mm diameter), in accordance with the technical data sheets (see Table 2). Furthermore, three coated ETICS specimens of each system (50 mm × 50 mm × 20 mm) were tested after the complete aging procedure.

All specimens were steam-sterilized in an autoclave for 20 min, then placed on test flasks containing culture media (4% malt, 2% agar). A mixed aqueous spore suspension (2 mL) of *Aspergillus niger* and *Penicillium funiculosum* was evenly spread across the specimens and surrounding medium. The test flasks were placed for four weeks in a culturing chamber (T = 22 ± 1 °C, RH = 70 ± 5 %) [13]. A control group (three Whatman n° 1 filter papers and three *Pinus pinaster* wood samples) was included for validation [45].

Mold development was visually assessed weekly using the ASTM D5590-17 [46] rating scale: 0 for no apparent growth (0% of contaminated surface); 1 for traces of growth (<10% of contaminated surface); 2 for light growth (10–30% of contaminated surface); 3 for moderate growth (30–60% of contaminated surface); 4 for heavy growth (>60% of contaminated surface). After four weeks, specimens were removed, and the percentage of contaminated surface was confirmed under an Olympus B061 stereo microscope.

2.2.4. Accelerated Aging Procedure

Accelerated aging involved sequential exposure of "ETICS + MC" to hygrothermal cycles (HT), UV radiation (UV), and air pollutants (SO_2) [13,47]. After each type of exposure, all tests described in Sections 2.2.1–2.2.3 were performed, except for absorption and drying after SO_2 exposure (due to the reduced specimen size).

Hygrothermal aging was conducted following EAD 040083-00-0404 [3] in a FitoClima 10,000 ELC climatic chamber (Aralab, Rio de Mouro, Portugal). The insulation and basecoat layers (150 mm × 150 mm × Thickness—Table 1) were previously sealed with metallic tape and a sealing adhesive. Specimens were exposed to sprinklers with a water flux of 1 L/(m^2·min) and thermal IR lamps (8 × 250 W). 80 heat/rain cycles were carried out (for a total of 320 h), alternating 3 h at T = 70 ± 5 °C and RH = 10–30%, and 1 h of continuous water spray at T = 15 ± 5 °C. Specimens were left to drain for 2 h and then conditioned for 48 h at room temperature (T = 20 ± 5 °C, RH ≥ 50%). After this, five heat/cold cycles were performed (totaling 120 h): 8 h at T = 50 ± 5 °C and RH ≤ 30%, followed by 16 h at T = −20 ± 5 °C.

ISO 16474-3 [48] was followed for UV cycles, using a Q-Panel UV-light chamber. Specimens were exposed to 125 cycles (totaling 1000 h) of alternating 4 h of UV-A radiation (λ = 315–400 nm, 60 W/m^2) at T = 60 °C and 4 h of moisture at T = 50 °C, RH = 80%.

Air pollutant cycles were conducted in a FitoClima 300EDTU climatic chamber (Aralab). Specimens were in an SO_2-rich environment of 25 ppm (3% dilution in 3000 ppm of nitrogen). A total of 60 cycles (720 h) were carried out, alternating 6 h at T = 40 °C and RH = 30%, with 6 h at T = 15 °C and RH = 85% [13].

2.2.5. DRIFT and SEM-EDS Analyses

Diffuse Reflectance Infrared Fourier Transform (DRIFT) spectroscopy was performed to detect possible physical-chemical alterations and/or degradation in coated and uncoated ETICS surfaces. Measurements were conducted using a Bruker VERTEX 70 spectrophotometer (Bruker Optics GmbH & Co. KG, Ettlingen, Germany), equipped with an MCT broadband detector (spectral range: 4000–500 cm^{-1}) and a resolution of 4 cm^{-1}. Each spectrum was obtained from 200 accumulated single-beam scans, which were divided by the KBr spectrum (FTIR grade, background), and then converted to Kubelka-Munk units. Baseline correction was performed in OPUS software (version OPUS 9.0). Deconvolution was carried out in the 1915–1100 cm^{-1} region to study adsorbed water and coating carbonation [13].

Morphological and microchemical analyses were carried out using a ThermoScientific Phenom ProX G6 scanning electron microscope (SEM) (Thermo Fisher Scientific Inc., Waltham, MA, USA), equipped with a CsB6 filament and a light elements energy-dispersive spectroscopy (EDS) detector. Specimens were previously placed on Al stubs with double-sided carbon tape and sputtered with an Au-Pd (80:20) film using a Quorum Technologies Q150T ES system (Quorum Technologies Ltd., Laughton, UK).

3. Results

3.1. Moisture Transport Properties

Figure 1 illustrates the capillary water absorption coefficients (Cc) for all settings studied along the aging cycles. The three multifunctional coatings reduced water absorption by capillarity in the acrylic-finished ETICS S1 with EPS insulation, and the system generally maintained these values after undergoing artificial aging cycles. The hygrothermal cycles induced even a higher Cc reduction with the application of the hydrophobic silane/siloxane emulsion HW and the acrylic-based AQ, possibly due to a reduction in the pore size distribution and thus in wettability [13]. Conversely, the UV cycles led to a slight Cc increase, which can be attributed to the UV activation of photocatalytic additives (and thus formation of surfaces with higher hydrophilicity) [49].

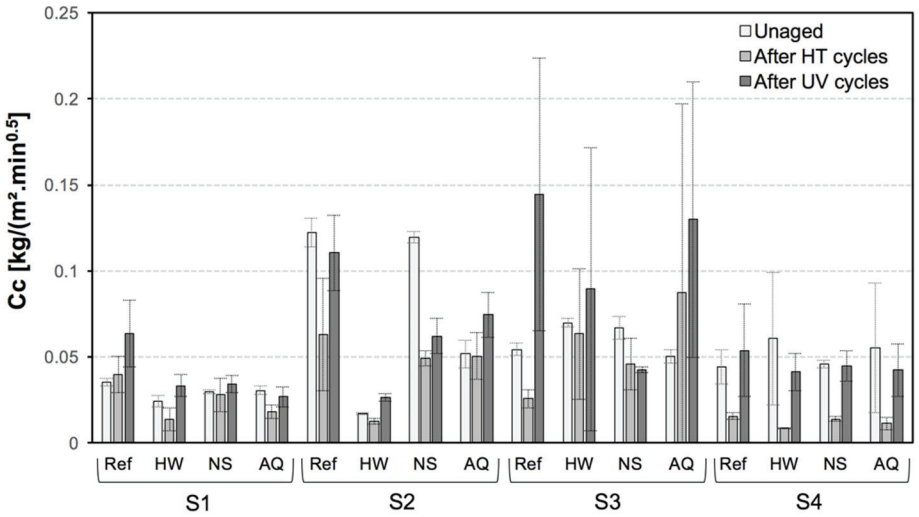

Figure 1. Average results and relative standard deviations for capillary water absorption coefficients (Cc) of the studied ETICS (S1–S4) without (Ref) and with protective treatments (HW, NS, and AQ), unaged and after hygrothermal (HT) and ultraviolet (UV) artificial aging cycles.

Concerning the NHL-based finished S2 ETICS with ICB insulation, which has noticeably higher water absorption compared to S1, the protective coatings reduced the Cc values. The application of the highly hydrophobic silane/siloxane emulsion (HW) induced the highest Cc reduction, in accordance with previous studies [20]. In contrast, slightly higher values were observed when the acrylic-based hydrophobic, self-cleaning, and biocidal AQ coating was applied. This latter product exhibited low wettability (Cc < 0.1 kg/(m^2·h)) after the aging cycles; however, its values are rather similar to those of the silicate-based NS, possibly due to the inclusion of hydrophilic nano- or micro-structured TiO_2 additives.

In the acrylic-finished ETICS S3 with MW insulation, no initial increase in Cc was observed with the application of protective coatings. The HT cycles had a moderate effect on the Cc values, whereas a significant rise in Cc was observed after the UV cycles. This variation can be attributed to the partial photodegradation of the acrylic-based surface and coatings during UV irradiation [50], which is associated with the use of a hydrophilic insulation layer (mineral wool). This layer can facilitate water absorption and retention, thereby reducing the effectiveness of protective products. The thermal conductivity is directly proportional to the water or moisture content [7].

The application of protective products did not significantly affect the Cc of the silicate-finished S4 system with ICB. The remarkable Cc reduction after hygrothermal cycles might indicate reduced compatibility and bonding among the silicate substrate and the waterborne products. Finally, an increase in water absorption is observed again after the UV cycles, due to the activation of the photocatalytic and thus hydrophilic additives.

Therefore, all the settings studied had a relevant reduction in Cc values after hygrothermal cycles. These data agree with previous works on hydrophobic treatments [20,51], which also identified lower Cc values after heat-cold and freeze–thaw cycles due to modifications in the pore size distribution of the substrates and/or physical-chemical alterations in the polymeric matrix of the multifunctional coatings. On the contrary, the UV cycles led to an increase in absorption in some cases, due to an increase in hydrophilicity and thus a decrease in the water contact angle [13,52–54].

Figure 2 shows the mean water absorption values of the studied settings after one hour. All unaged ETICS, with and without multifunctional coatings, met the requirement of EAD 040083-00-0404 [3], i.e., a water absorption of less than 1 kg/m^2 within one hour. However, S2-AQ considerably surpassed this threshold after hygrothermal cycles, as was also the case for S3-REF, S3-HW, and S3-AQ after hygrothermal and UV cycles. Conversely, the aged acrylic-finished S1 and silicate-finished S4 fulfilled the requirements in all conditions, with and without multifunctional coatings.

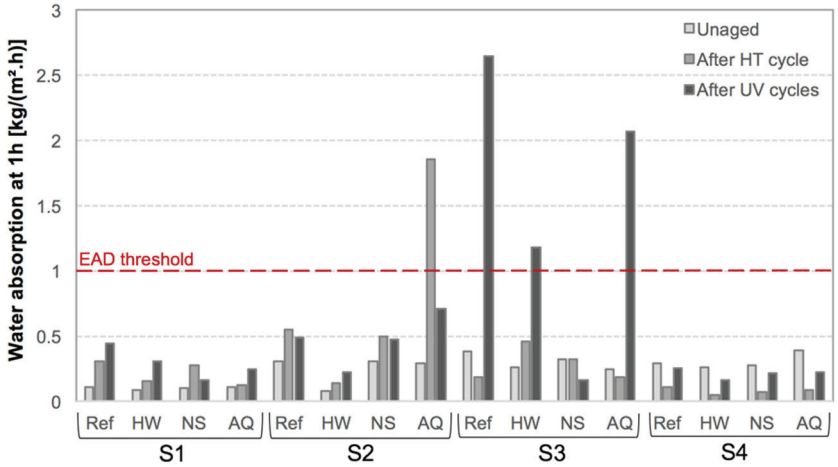

Figure 2. Mean water absorption at one hour of the studied ETICS S1–S4, without (Ref) or with protective treatments (HW, NS, AQ), unaged, and after HT and UV artificial aging cycles.

Figure 3 presents the drying index (DI) values obtained for the ETICS before and after the aging cycles. In the unaged state, it can be observed that the application of the hydrophobic, self-cleaning, and biocidal AQ coating induced the highest DI increase (i.e., slower drying rate), which is noticeable in the case of the NHL-finished S2 system.

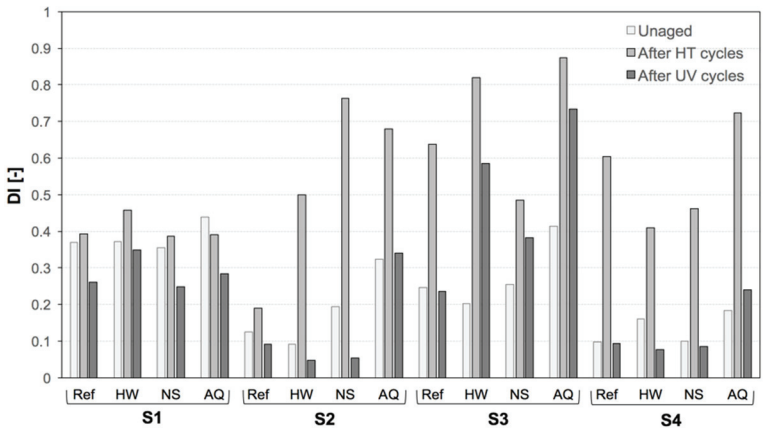

Figure 3. Average results for the drying index (DI) of the studied ETICS (S1–S4) without (Ref) and with protective coatings (HW, NS, AQ), unaged and after HT and UV aging cycles.

In contrast, HW and, more notably, the photocatalytic and antimicrobial coating NS caused minor changes, with values closer to those of the reference specimen. These data can be related to the significantly higher density and dry residual of the acrylic-based AQ product (Table 2), if compared to the silane-siloxane and ethyl silicate compositions of HW and NS, respectively. These data are in accordance with previous research [51], which indicated an increase in drying index results with acrylic-based hydrophobic products, characterized by low water vapor permeability, whereas siloxane-based products reduced the drying resistance.

Results showed that the hygrothermal cycles significantly affected the drying capacity of the products, with an increase in the DI values, especially when applied to ETICS S2, S3, and S4. This can indicate a relevant abrasion and alteration of the surface induced by the combined action of heat-cold and freeze–thaw cycles, affecting water loss in the liquid state (step I of drying) as well as water vapor permeability (step II of drying) [13,51].

On the other hand, a significant DI reduction (i.e., faster water evaporation) was observed after the UV cycles, with values closer to those of the unaged specimens. The NHL-finished S2 and silica-finished S4 systems with ICB insulation showed the lowest DI values, in accordance with previous studies [55]. Furthermore, the UV activation of photocatalytic additives (TiO_2) leads to hydrophilic properties, which can also enhance water vapor permeability and thus facilitate evaporation [16,56].

3.2. Color Change and Photocatalytic Efficacy

3.2.1. Chromatic Coordinates

The application of the NS and AQ products led to light whitening. In contrast, almost no chromatic variation (with a slightly glossier surface) was observed in the case of the hydrophobic/biocidal emulsion HW. When considering the color changes in the pristine specimens throughout the accelerated aging procedure (Figure 4), it can be observed that the NHL-finished ETICS S2 was the most chromatically affected (yellowish tone) after hygrothermal aging, both in the untreated specimens and the specimens with HW or NS. Conversely, the UV cycles induced a chromatic alteration not visible to the naked eye (i.e., $\Delta E < 2$) [57] in almost all specimens. In the case of aging cycles with SO_2, ΔE values were generally lower than 4 CIELab units, resulting in only a slight color variation.

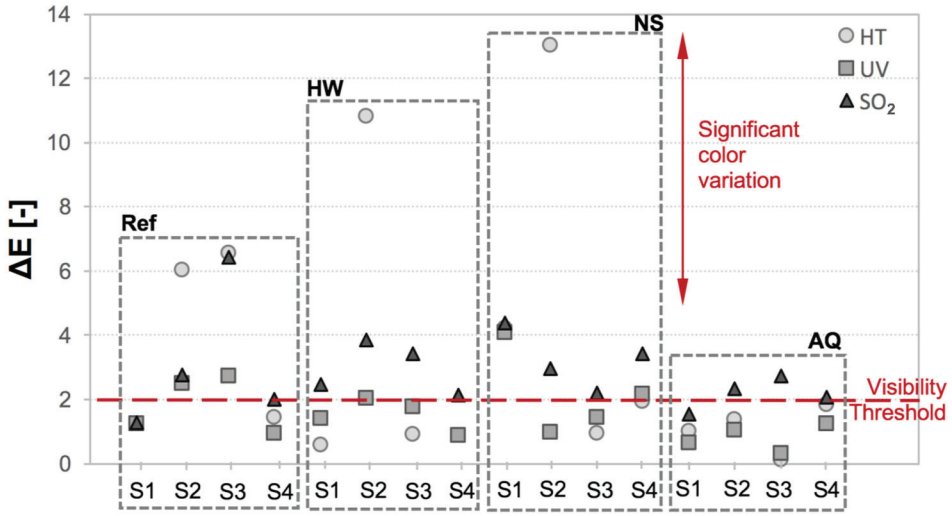

Figure 4. Average results for the color change (ΔE) of the studied ETICS S1–S4 without (Ref) and with protective coatings (HW, NS, AQ), after HT, UV, and SO_2 aging cycles.

No significant color variation was observed on the acrylic-finished ETICS (S1 with EPS and S3 with MW insulation) after aging, indicating proper chromatic compatibility of

the multifunctional protective coatings with these ETICS. NS and AQ provided the lowest chromatic alteration, possibly due to their photocatalytic properties, which may have contributed to maintaining the lightness and solar reflectance over time [49]. Indeed, TiO_2 nanoparticles possess unique amphiphilic (both hydrophilic and oleophilic) properties, which are based on their photocatalytic activation [16]. The photocatalytic properties led to a whitening of the surface, thereby contributing to maintaining the lightness and solar reflectance over time [49], and ensuring self-cleaning effectiveness, particularly in acrylic- (S1, S3) and silicate-finished (S4) ETICS.

It can be concluded that the NHL-finishing S2 system was the most chromatically affected by the aging cycles, while silicate-based finishing S4 ETICS presented the highest resistance, with or without multifunctional coatings. Hygrothermal cycles were the most invasive artificial aging process, particularly in the case of the protective products HW and NS, and with the untreated system S3.

3.2.2. Photocatalysis Evaluation

Regarding photocatalytic efficacy, Figure 5 illustrates the RhB decomposition (ΔE) over time for specimens along the aging protocol, compared to the initial values on RhB-dyed surfaces. In all cases, the color variation was significantly higher after 1 week of exposure to the UV-A lamp compared to a short-term (4 h) exposure. It is worth noting that 80% to 90% of the value obtained after one week (168 h) was achieved within 2 to 3 days of UV-A lamp exposure, confirming a relatively fast photocatalytic activity of the treatments.

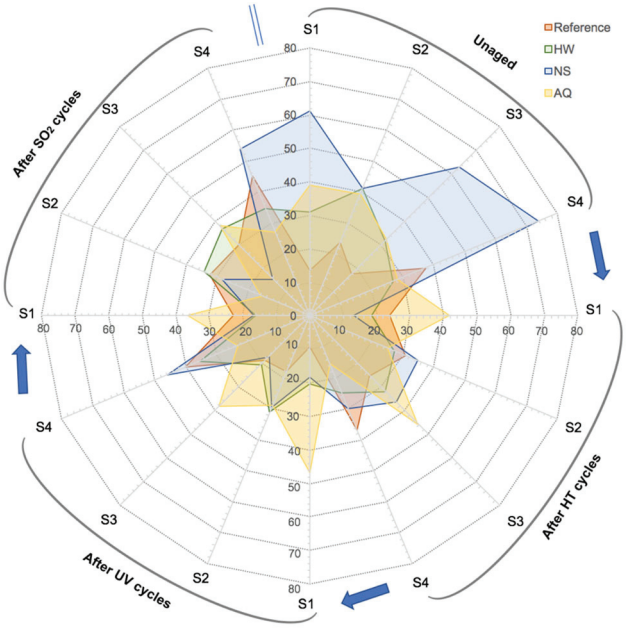

Figure 5. Average results for the color changes (ΔE), related to RhB decomposition after 168 h of UV-A lamp exposure of unaged and aged (after HT, UV, and SO_2 cycles) systems, with or without protective coatings.

Concerning the ETICS with no protective products, a significantly reduced self-cleaning capacity was observed in the acrylic-finished systems (S1 and S3), if compared to the NHL-finished (S2) and silicate-finished (S4) ICB ETICS. RhB also presents a dye-sensitized process, in addition to its degradation by TiO_2 particles under UV radiation [58]. The different aging cycles have a reduced effect on RhB degradation and, consequently, on the color change in the systems, confirming the relatively high resistance of the studied systems to aging (as observed in [13]).

In the unaged state, the most significant self-cleaning properties and, therefore, photocatalytic efficiencies were observed in the specimens treated with the photocatalytic and antimicrobial coating NS (Figure 5), due to the incorporation of TiO_2 nanoparticles with photoinduced properties [30]. The highest values were obtained for the ETICSs finished with acrylic and silicate products, rather than NHL. The application of AQ, which also presented considerable percentages of TiO_2 and ZnO, induced a higher photocatalytic effect in the acrylic- (S1, S3) and NHL-finished (S2) systems, if compared to the untreated specimens. Therefore, in the unaged state, an order NS > AQ > HW can be defined for self-cleaning effectiveness (Figure 5).

After artificial aging, the systems treated with NS showed a considerable reduction in ΔE after the hygrothermal cycles. Except for the silicate-finished S4 ETICS, the UV and SO_2 cycles resulted in even lower ΔE variations, thereby reducing photocatalytic activity and highlighting the reduced durability of NS to artificial aging. Acrylic-finished ETICS (S1 and S3) were generally more affected when compared to the inorganic finished (silicate or NHL) ETICS. It is worth noting that the association of wet and dry cycles, as well as prolonged exposure to UV radiation, can lead to partial removal of the protective product and/or the formation of micro-defects on the coating's surface [50]. Although TiO_2 nanoparticles are generally encapsulated (in e.g., SiO_2, Al_2O_3, or ZrO_2 as shell materials) to prevent the contact between the degradable organics and the photoactive TiO_2 surface, the photoinduced hydrophilicity and self-cleaning effectiveness of the treatment with nano-engineered TiO_2 can be partially reduced by weathering [44,59], with discoloration, loss of gloss, or chalking coatings.

The effect of the aging cycles was less significant in the case of the systems treated with HW and AQ, exhibiting considerable resistance to hygrothermal cycles, UV radiation, and SO_2-rich cycles. In accordance with previous studies [20,51], silane/oligomeric siloxane presented lower modification of their properties after aging, when compared to SiO_2-TiO_2 nanostructured treatments. The treatments with AQ showed significant resistance, also due to its considerable thickness, if compared to the other treatments (Table 1).

3.3. Biological Colonization

The average results of mold development on the coatings after four weeks of incubation on the unaged multifunctional products showed traces of mold growth in all three types of coatings, with slightly higher values for the indicated photocatalytic and antimicrobial NS product (Figure 6a–c). The test was validated by considering the results obtained for the paper control, in which all specimens were rated 4 out of 4 (heavy growth, exceeding 60% of the contaminated surface) after the third week of testing.

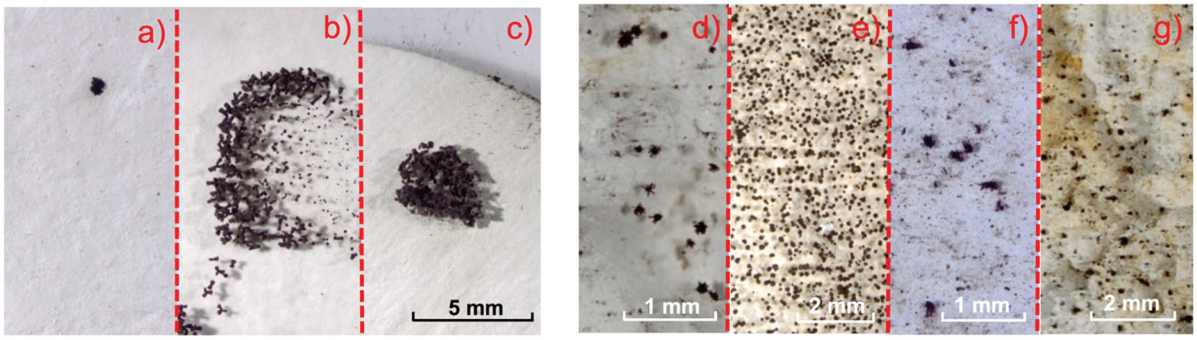

Figure 6. Traces of *A. niger* growth on the unaged multifunctional protective products: (**a**) HW, (**b**) NS, and (**c**) AQ after four weeks of testing. Mold growth observed with NS applied on ETICS: (**d**) S1 and (**e**) S2; (**f**) Mold growth observed with HW applied on ETICS S4; (**g**) ETICS S3 without protective coating.

The results of the average rate of mold development on ETICS after the complete accelerated aging procedure are presented in Figure 7. For the acrylic-finished ETICS S1 and S3 (with EPS and MW insulation, respectively), the application of NS led to an increase in mold development, with moderate mold growth: 30 to 60% of contaminated surface (Figure 6d). Conversely, the application of protective products HW (hydrophobic and biocidal emulsion) and AQ (hydrophobic, self-cleaning and biocidal coating) in ETICS S1 and S3 slightly increased the mold resistance of the system after aging, with only traces of mold growth (<10% of the contaminated surface). In the case of ETICS S3, the surface of this system gained a considerable yellowish tone after accelerated aging (Figure 6f), regardless of the application of protective coatings, mainly due to the use of mineral wool (i.e., thin yellow microfiber) as thermal insulation layer, which was possible partially leached to the drying surface after the HT cycles (e.g., [13]).

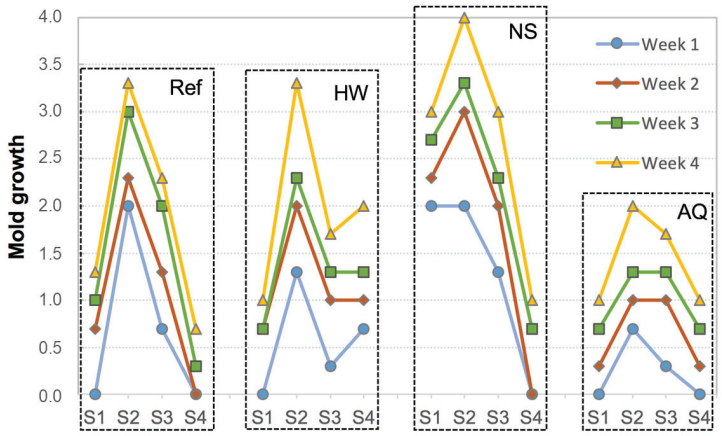

Figure 7. Average results of mold development up to 4 weeks of the untreated (Ref) and treated (HW, NS, and AQ) systems S1–S4. Rating scale: 0—no growth; 1—traces of growth; 2—light growth; 3—moderate growth; 4—heavy growth.

Heavy mold growth (>60% of contaminated surface) was observed with the application of NS (Figure 6e) on the NHL-finished S2 ETICS. In contrast, product AQ slightly increased the resistance to mold development (light growth with 10% to 30% of contaminated surface) in this system after aging. Results showed that the application of HW did not enhance the mold growth resistance of system S2.

Finally, the application of multifunctional products in silicate-finished ETICS S4 contributed to a decrease in mold resistance after aging. In this case, the highest mold development was observed with the application of the siloxane-based HW (Figure 6g), indicating a possible incompatibility between the silicate-based surface and this product.

Although product NS is formulated with remarkable amount of TiO_2 nanoparticles, which might decompose biological macromolecules (DNA) and thus inhibit biological growth [60], as observed in previous studies [61–63], the highest mold growth was generally observed with the application of this product, mainly after artificial aging, with heavy growth in the ETICS with acrylic- (S1 and S3) and NHL-based coating (S2). Conversely, the application of the AQ product slightly increased the resistance to mold growth in ETICSs S1, S2, and S3. Finally, the application of HW did not affect the mold growth resistance of the systems, and in some cases, even induced an increase in bio-susceptibility, as seen with ETICS S4.

3.4. Chemical and Morphological Analyses

3.4.1. SEM-EDS

Results showed that the silicate-based NS protective products formed a thin coating (10–50 μm) when applied to all systems. However, after drying and complete polymerization, the product tended to shrink when applied on the acrylate-finished system (S1 and S3), with a diffuse cracking and a partial detachment of the resulting plate-like clusters [64] (Figure 8a). EDS spectra confirmed a notable amount of titanium, attributed to the photocatalytic TiO_2 nanoparticles (Figure 8c).

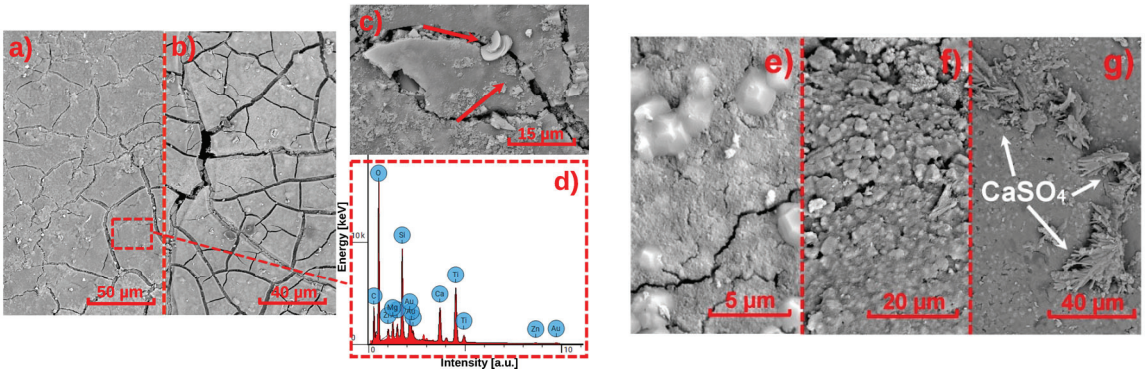

Figure 8. SEM microphotographs of NS product applied on ETICS S1 (**a**) before aging and (**b**) after HT cycles; (**c**) neoformation products (arrows) after SO_2 cycles; (**d**) software-generated EDS elemental spectra of a spot of (**b**); NS product applied on system S2 (**e**) before aging, (**f**) after HT cycles and (**g**) after SO_2 cycles, with acicular gypsum neoformation (arrows).

Cracking generally increased along the aging protocol, mainly after hygrothermal cycles (Figure 8b), with further micro-detachment, dirtiness, and neoformation products observed both after UV and SO_2 cycles (Figure 8d). This trend can be attributed to a combined leaching of the finishing and basecoat of the systems, as well as $CaCO_3$ dissolution-reprecipitation processes [13].

The NS product had a heterogeneous distribution and thus possible lack of compatibility when applied on the NHL-finished S2 system (Figure 8e). The product formed a heterogeneously distributed coating with clusters and suffered an almost complete removal during the hygrothermal cycles (Figure 8f). After the SO_2 cycles, the acicular formation is consistent with gypsum-based clusters (Figure 8g) [65–67], possibly obtained by sulfation, i.e., combination of sulfur dioxide from the pollutant chamber, and the $Ca(OH)_2$ and $CaCO_3$ neoformation [68] after hygrothermal aging. When applied to silicate-finished S4 ETICS, the NS product demonstrated poor physical-chemical compatibility with the substrate, characterized by heterogeneous distribution and material detachment, which consistently increased after artificial aging.

As observed in previous works [69], the high reactivity of the NS silicate binder in an alkaline environment provided by the aqueous medium and the NHL of the substrate (ETICS S2 and S4), and the presence of a relevant amount of $CaCO_3$ can favor the development of shorter linear chains of tetrahedral silica and linear silicate structure, forming colloidal silica gel with plate-like shape [70]. Cracks and surface abnormalities have also been previously reported as a result of a lack of compatibility between protective coatings and the applied substrates [71].

The silane/siloxane emulsion hydrophobic HW product formed a highly compact and homogeneous coating on the acrylate-finished ETICS (S1 and S3) (Figure 9a). Nevertheless, partial decohesion and material loss, and even neoformation products (i.e., calcium carbonate and gypsum) at the surface (Figure 9b), can be noted after the hygrothermal

cycles. A relatively homogeneous and durable HW treatment was observed in the case of the silicate-finished ETICS S4, which can indicate proper compatibility between the product and this rather durable system [15]. Conversely, the application of HW on the NHL-finished S2 system led to a heterogeneous coating, which was seriously damaged after hygrothermal cycles (severe loss of material) (Figure 9c), and again with the formation of carbonate- and sulfate-based clusters after aging cycles with SO_2 (Figure 9d).

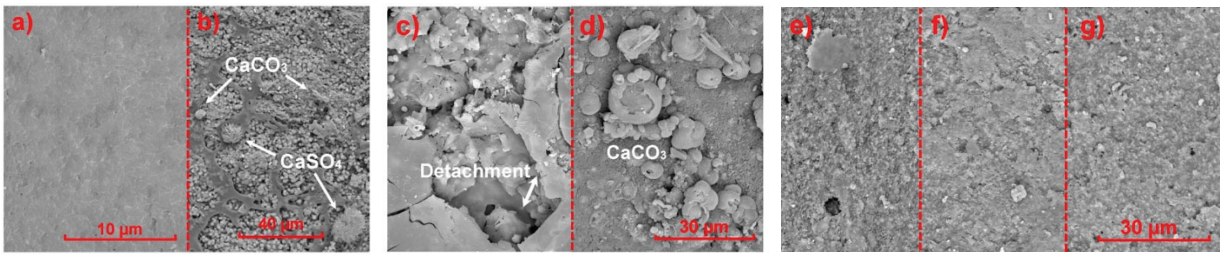

Figure 9. SEM microphotographs of HW product applied on ETICS: S1 (**a**) before aging and (**b**) after SO_2 cycles; S2 (**c**) after HT cycles and (**d**) after SO_2 cycles; AQ product applied on ETICS: (**e**) S1 after SO_2 cycles; (**f**) S2 after SO_2 cycles; (**g**) S4 after HT cycles.

The application of AQ also resulted in a homogeneous coating, with some porosity at the microscale. The coating exhibited high resistance to various aging cycles across all systems (Figure 9e,f) [40,51], possibly due to its enhanced thickness compared to other products. The hygrothermal aging cycles were confirmed to be the most invasive aging procedure, leading to the washing and thus micro-abrasion of the surface, mainly in the case of the NHL-finished S4 system (Figure 9g).

3.4.2. DRIFT

The DRIFT spectra of the finishing coating of ETICS S1, S2, and S4 (untreated), used as reference (Figure 10), showed generally considerable amounts of cement-based or lime-based compounds, as well as additives (inert sands or acrylic resins), in agreement with previous results [13].

After the artificial aging cycles, a higher intensity of the carbonate bands (overlapped $\nu CO_3^{2-}/\delta_{as}CH_3$ mode at ~1400 cm^{-1}; ωCO_3^{2-} mode at 876 cm^{-1}) was observed for ETICS S1 (Figure 10a) and ETICS S2 (Figure 10b,c) after UV cycles, when compared to the unaged ETICS, confirming the presence of leached clusters and additives on the aged substrate. Additionally, an intensity increase in the hydroxyl bands (νOH at ~3300 cm^{-1}, δHOH of adsorbed water at ~1640 cm^{-1}), partially attributed to the presence of $Ca(OH)_2$ [72], confirmed the neoformation of calcium-based products observed in the SEM-EDS analysis (in Section 3.4.1). In the case of ETICS S4, with or without protective products, no significant changes were observed in the spectra after artificial aging with UV and SO_2 cycles, indicating the high stability of the silicate-finished ETICS.

In the DRIFT spectra, a doublet band is observed at ~1795 and ~1740 cm^{-1} that can be assigned to $\nu_s CO_3^{2-}$ modes overlapped with νC=O modes, or to combination bands of the two modes, for the acrylic-finished (ETICS S1) or for polymeric additives (ETICS S2 and S4). A significant change in those bands is observed for ETICS S2, with an inverse evolution to that of carbonates, and therefore can be associated with a possible degradation process.

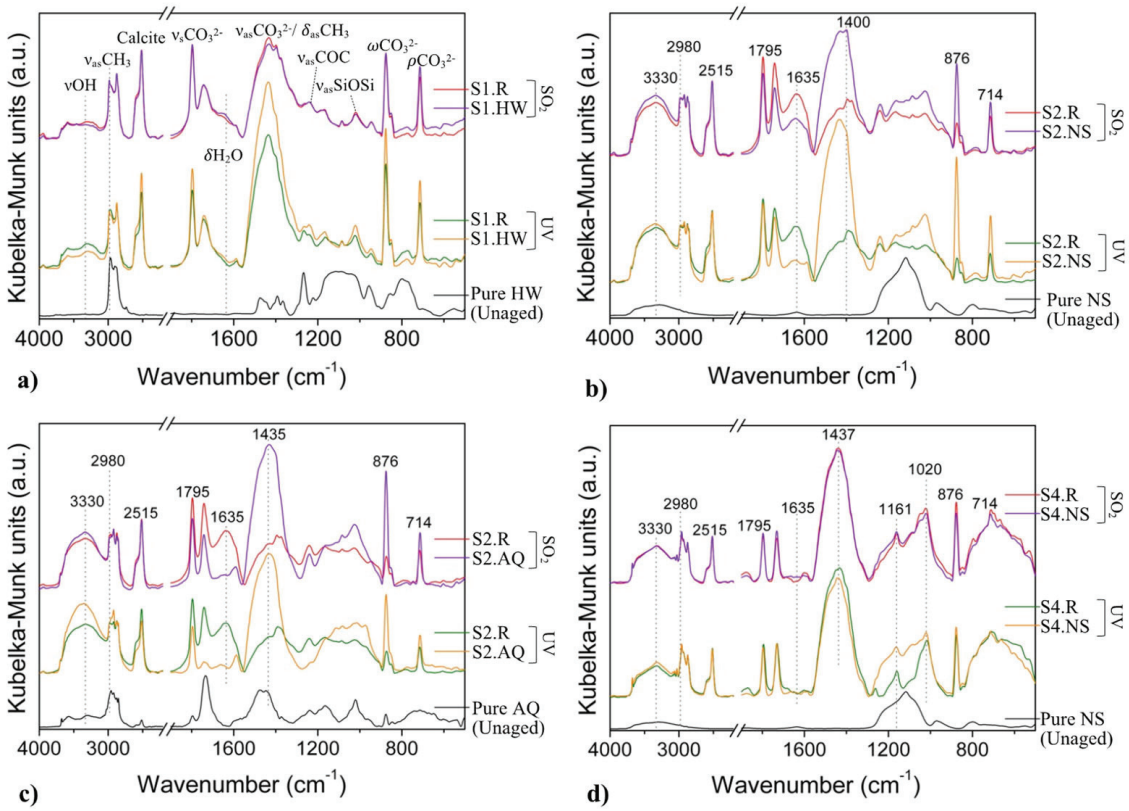

Figure 10. Comparison of DRIFT spectra of the protective coating (unaged) and ETICS without (R) and with protective products (HW, NS, and AQ), after UV and SO_2 aging cycles: (**a**) ETICS S1 with HW; ETICS S2 with (**b**) NS and (**c**) AQ; (**d**) ETICS S4 with NS. The coating spectra are normalized at 2981 cm^{-1}, and the protective coating spectra are normalized at maximum.

Moreover, the decrease in the band at ~3330 cm^{-1} (νOH mode) with an increase in the band at ~1795 cm^{-1} for ETICS S1 after UV irradiation, might arise from the photo-oxidation reaction of –OH, leading to the formation of oxidized products containing C=O chromophores and, thus, a slight yellowish of the surface, in accordance with the results of color change and photocatalytic efficacy (Section 3.2.1) [73]. Finally, a band of the silicate (ν_{as}Si-O-Si mode at ~1020 cm^{-1}) was observed in all ETICS, with the intensity increasing for ETICS S4 (Figure 10d).

When analyzing the ETICS with the protective products, a possible mixture of the signals from the protective product and the reference system materials (finishing and basecoat) can be observed, also due to the method of sample collection, which involves scraping the surface. The bands of the protective products' spectra (pure HW, NS, or AQ) overlap with those of the finishing and basecoat of the ETICS (Figure 10a–d), hindering a clear identification of alterations or degradation of the protective products along the aging protocol. However, the decrease in the δHOH mode (1640 cm^{-1}) can be attributed to the decrease in adsorbed water resulting from the artificial aging cycles of ETICS S2, if accompanied by a reduction in the νOH band, or confirms the possibility of some degradation product formation.

Regarding the acrylate polymers (in the finishing coat of ETICS S1, or the protective product AQ), the presence of monomer acrylic groups can be associated with a νC=C band in the infrared spectrum that can be observed in the same region of the δHOH mode (adsorbed water). Since no changes were observed in the δHOH mode region (at 1640 cm^{-1}) in the spectra of ETICS S1, degradation throughout the aging processes can be excluded, confirming the high durability of the ETICS S1 acrylate coating. In the case of

ETICS S2, the band in the region of the δHOH mode decreased significantly, and the νOH band region increased with artificial aging. Following previous work [14], no partial repair or degradation reversion of the polymer paint was observed, particularly after exposure to UV radiation. The decrease in the relative intensity of the δHOH band may be attributed to a drying process or, more likely, to a chemical reaction between water and a coating component, which increases the number of OH groups and consequently enhances the relative intensity of the νOH band.

Concerning ETICS S4, a relative intensity increase in the band at 1161 cm^{-1} is observed in the sample after UV cycles, which may be due to the presence of the protective product, resulting in an overlap of the finishing coat and protective product bands.

4. Discussion

The photocatalytic and antimicrobial NS treatment (ethyl silicate-based with TiO_2) produced a thin coating with extensive microcracking, which was considered to have poor compatibility with the NHL (S2) and silicate-finished (S4) ETICS. In these systems, the distribution of the coating components was heterogeneous, with cluster-like deposition. Although the formulation included hydrophobic ethyl silicate, the improvement in water repellency was negligible. Hygrothermal aging significantly affected this coating, resulting in partial detachment or surface yellowing. However, the product possibly filled the nano- and micro-porosities of the systems [16], thereby reducing water uptake even after aging. Exposure to UV light activated the TiO_2 particles within the product, resulting in a slightly more hydrophilic surface, which can also favor water vapor permeability and thus evaporation [51].

Although the SO_2 cycles did not seriously affect the coating, with a grayish tone which is only slightly visible to the naked eye, the reduced durability of NS can affect the self-cleaning features over time, with a partial release of TiO_2 nanoparticles during the aging cycles [50,74], followed by a reduction in the photoactivity after exposure to UV radiation and condensation cycles [75]. Investigating the degradation of TiO_2-modified paints under low-radiation conditions, a study observed a rather opposite effect, as microcracks arising from this type of exposure enhanced photocatalytic performance due to a larger exposure area [76]. Therefore, the importance of analyzing different weathering agents is straightforward.

Furthermore, the presence of microcracks influenced the bioreceptivity of the coating, providing potential anchoring points for mold growth and, thus, compromising the expected antimicrobial attribute of the surface [77]. The increase in the drying index after hygrothermal aging can further aggravate this matter, because if drying is not fast enough, the presence of moisture for more extended periods favors biological growth in ETICS [4]. Taken together, the limited stability, durability, and weak compatibility make it unsuitable for long-term use on the studied systems.

The silane/siloxane HW emulsion created a compact, water-repellent coating that was durable and compatible with acrylic-finished S1 and S3 ETICS. In contrast, its distribution was heterogeneous when applied to the NHL-finished S2 system and showed no substantial benefit on the silicate-finished ETICS (S4). However, partial photodegradation of the coatings was observed during UV irradiation [78]. Additionally, the aging of this product can affect the drying rate, especially in the case of highly rough, acrylic-finished surfaces (e.g., S3), where poor self-cleaning properties were observed both before and after aging. HW is therefore suitable for acrylic ETICS, but its application to lime- and silicate-based systems is not recommended.

The acrylic AQ dispersion formed a thicker, more microporous coating than the other products. Its chemical affinity to acrylic ETICS enhanced the compatibility and durability

of the hydrophobic features in S1 and S3, whereas a slight improvement was observed in lime- and silicate-based systems (S2 and S4). The coexistence of hydrophobic acrylic components with hydrophilic TiO_2 resulted in a competitive effect [79], reducing overall water repellency. Additionally, UV further increased surface hydrophilicity due to the activation of photocatalytic additives. Indeed, hydrophobicity is reported to be dependent on the TiO_2 loads within the development of protective coatings [80], requiring fine-tuning to achieve the desired performance.

Compared to NS, the self-cleaning effect of AQ was less pronounced; however, the coating exhibited superior resistance to hygrothermal, UV, and SO_2 aging, particularly when used on acrylic-finished ETICS. Poor results were observed when applied to silicate-finished ETICS S4, possibly due to the lack of a coupling agent (e.g., silane) in the acrylic polymer, which could have increased the physical-chemical compatibility between the organic and inorganic phases [81]. Furthermore, the acrylic AQ coating slowed down the drying rate, compared to the NS and (ethyl silicate) HW products.

Overall, the results indicate apparent differences in performance depending on both the protective product and the ETICS finish. NS provided initial self-cleaning capabilities but failed in terms of durability and compatibility. HW was effective only on acrylic systems, and AQ also combined good durability with moderate self-cleaning in acrylic ETICS, albeit at the expense of drying time. Analogously, in another study, hydrophobic products were also identified as having differing effectiveness and durability when applied to limestone or cementitious mortars [20], thereby underscoring the importance of an integrated assessment.

When selecting between hydrophobic and photocatalytic properties for ETICS, the trade-offs must be weighed. Hydrophobicity reduces water uptake and, thus, can prevent moisture degradation, but it can also limit drying and self-cleaning. Photocatalysis can support surface whitening and pollutant degradation by leveraging increased hydrophilicity; however, this effect is not sustained if low durability is identified, as in the case of NS. For this reason, the selected treatments must be case-oriented, considering the product quality, substrate compatibility, and environmental conditions. Indeed, other research indicates that exposure conditions significantly impact on maintenance needs for ETICS [82].

Although the performance of ETICS has already been investigated in other European contexts, material formulations, construction practices, and aging methodology vary significantly, and these factors strongly influence the durability and compatibility of surface treatments. In addition, most earlier works considered individual parameters, whereas the present study employs a comprehensive set of artificial aging cycles, allowing for a systematic comparison of multifunctional products. This approach provides data that are directly relevant to local building practice and expands the understanding of ETICS performance under different climates.

5. Conclusions

This study evaluated the performance of three commercial multifunctional protective coatings applied to thermal insulating composite systems (ETICS) surfaces, focusing on their effects on moisture transport, photocatalytic activity, color stability, and mold growth before and after accelerated aging. Thus, the research aimed to provide a comprehensive overview of long-term performance and address pressing challenges in building façades. The results underline that the long-term effectiveness of protective treatments is strongly influenced by their chemical compatibility with the underlying ETICS finishes.

Through surface multifunctionality, including water resistance features, different lines of behavior were observed for the four types of ETICS throughout the accelerated aging procedure, which are directly related to the long-term performance of the whole system.

The relevance of the interconnection between moisture transfer, biological colonization, and photocatalytic activity was especially evident for the ethyl-silicate-based coating with TiO_2 applied to NHL finishing ETICS. Poor compatibility, resulting in surface microcracks, may have facilitated mold growth, which can also be favored through an increase in the drying index with hygrothermal aging.

The results were indeed found to be highly dependent on the chemical compatibility between the coatings and the ETICS finishes (acrylic, hydraulic lime, or silicate). On silicate substrates, the application of the protective products led to worse moisture transport properties (i.e., higher water absorption and slower drying) and higher biological colonization, due to reduced compatibility and bonding between the silicate substrate and the waterborne organic products (without a coupling agent). Hydrophobic and/or photocatalytic coatings were somewhat effective and durable on acrylic/finished thermal insulating systems due to their chemical compatibility, which also favors extended long-term performance. On the contrary, low durability and low performance were observed when applied to the hydraulic lime-finished thermal insulating systems.

Concerning durability, both ETICS and protective products were primarily affected by hygrothermal aging, resulting in physical-chemical alterations to the polymeric matrix of the multifunctional coatings or changes in the pore size distribution of the systems. Conversely, the UV cycles led to activation of the photocatalytic and hydrophilic additives, slightly favoring the wettability of the substrates.

Regarding the individual commercial products investigated:

- HW (silane/siloxane emulsion) ensured good water repellency and durability on acrylic ETICS, but showed reduced performance on lime- and silicate-based systems and limited self-cleaning;
- NS (ethyl silicate with TiO_2) offered initial photocatalytic and self-cleaning properties, but a negative performance in terms of biocidal effect, durability, and effectiveness over time;
- AQ (acrylic dispersion with TiO_2) combined acceptable durability and moderate self-cleaning on acrylic systems but increased drying resistance and showed weak performance on mineral-based ETICS.

From a practical standpoint, none of the tested coatings is recommended for silicate-based ETICS, while the ethyl silicate—TiO_2 product should generally be avoided. Protective treatments for acrylic-based ETICS showed more promising results, particularly with HW and AQ. However, the study emphasizes that performance cannot be assessed based on a single property; successful solutions must ensure multifunctionality, combining water repellency, drying capacity, and biological resistance, while avoiding incompatibility that could compromise the hygrothermal balance of the system. In some cases, reapplying the original compatible finish may represent the most reliable strategy to safeguard ETICS durability, insulation efficiency, and long-term energy performance.

Author Contributions: Conceptualization, G.B., J.L.P., R.V., A.D., P.F. and I.F.-C.; methodology, G.B., J.L.P., R.V., A.D., P.F. and I.F.-C.; validation, G.B., J.L.P., A.R.G., A.D., P.F., R.V. and I.F.-C.; formal analysis, G.B., J.L.P., A.R.G., A.D., P.F., R.V. and I.F.-C.; investigation, G.B., J.L.P., A.D. and A.R.G.; data curation, G.B., J.L.P., J.D.B. and A.R.G.; writing—original draft preparation, G.B., J.L.P., J.D.B. and A.R.G.; writing—review and editing, A.R.G., R.V., A.D., P.F. and I.F.-C.; funding acquisition, I.F.-C. and R.V. All authors have read and agreed to the published version of the manuscript.

Funding: This research was funded by FUNDAÇÃO PARA A CIÊNCIA E A TECNOLOGIA (FCT), within the research project WGB_Shield (PTDC/ECI-EGC/30681/2017). The authors acknowledge the financial support of the FCT through the project UIDB/04625/2025 of the research unit CERIS and UIDB/04028/2020 of CERENA. The third author acknowledges the FCT grant number 2023.05316.BD (DOI: https://doi.org/10.54499/2023.05316.BD).

Data Availability Statement: The raw data supporting the conclusions of this article will be made available by the authors on request.

Acknowledgments: In Memoriam of Dr. Lina Nunes, who actively collaborated in this and several previous projects.

Conflicts of Interest: The authors declare no conflicts of interest.

Abbreviations

The following abbreviations are used in this manuscript:

θ	Contact Angle
ΔE	Color Change
a*	Color Coordinate (red-green)
AQ	Hydrophobic, Self-cleaning and Biocidal Coating
b*	Color Coordinate (yellow-blue)
BC	Base Coat
Cc	Capillary Water Absorption Coefficient
DI	Drying Index
DRIFT	Diffuse Reflectance Infrared Fourier Transform
EDS	Energy Dispersive Spectroscopy
EIFS	Exterior Insulation Finishing System
EPS	Expanded Polystyrene
ETA	European Technical Approval
ETICS	External Thermal Insulation Composite Systems
EWI	Exterior Wall Insulation Systems
FC	Finishing Coat
HT	Hygrothermal Cycles
HW	Hydrophobic and Biocidal Coating
ICB	Insulation Cork Board
L*	Lightness
MC	Multifunctional Coatings
MW	Mineral Wool
NHL	Natural Hydraulic Lime
NS	Photocatalytic Self-Cleaning and Antimicrobial Coating
Ref	Without Protective Treatment
RH	Relative Humidity
RhB	Rhodamine B
S1	System 1
S2	System 2
S3	System 3
S4	System 4
SCI	Specular Component Included
SEM	Scanning Electron Microscope
SO_2	Air Pollutant Cycles
T	Temperature
UV	Ultraviolet Radiation Cycles

References

1. Malanho, S.; Veiga, M.R. Bond strength between layers of ETICS—Influence of the characteristics of mortars and insulation materials. *J. Build. Eng.* **2020**, *28*, 101021. [CrossRef]
2. Amaro, B.; Saraiva, D.; De Brito, J.; Flores-Colen, I. Inspection and diagnosis system of ETICS on walls. *Constr. Build. Mater.* **2013**, *47*, 1257–1267. [CrossRef]
3. *EAD 040083-00-0404*; External Thermal Insulation Composite Systems (ETICS) with Rendering. EOTA (European Organisation for Technical Approvals): Brussels, Belgium, 2020; pp. 1–88.
4. Barreira, E.; de Freitas, V.P. Experimental study of the hygrothermal behaviour of External Thermal Insulation Composite Systems (ETICS). *Build. Environ.* **2013**, *63*, 31–39. [CrossRef]
5. Xu, H.; Wang, H.; Huo, Q.; Qin, Y.; Zhou, H. Comparative study of Chinese, European and ISO external thermal insulation composite system (ETICS) standards and technical recommendations. *J. Build. Eng.* **2023**, *68*, 105687. [CrossRef]
6. Malanho, S.; Veiga, R.; Farinha, C. Global Performance of Sustainable Thermal Insulating Systems with Cork for Building Facades. *Buildings* **2021**, *11*, 83. [CrossRef]
7. Parracha, J.L.; Borsoi, G.; Flores-Colen, I.; Veiga, R.; Nunes, L.; Dionísio, A.; Gomes, M.G.; Faria, P. Performance parameters of ETICS: Correlating water resistance, bio-susceptibility and surface properties. *Constr. Build. Mater.* **2021**, *272*, 121956. [CrossRef]
8. Zhou, X.; Kubilay, A.; Derome, D.; Carmeliet, J. Comparison of wind-driven rain load on building facades in the urban environment and open field: A case study on two buildings in Zurich, Switzerland. *Build. Environ.* **2023**, *233*, 110038. [CrossRef]
9. Bauer, E.; Souza, A.L.R. Failure patterns associated with facade zones and anomalies in the initiation and propagation of degradation. *Constr. Build. Mater.* **2022**, *347*, 128563. [CrossRef]
10. Ren, H.; Koshy, P.; Chen, W.F.; Qi, S.; Sorrell, C.C. Photocatalytic materials and technologies for air purification. *J. Hazard. Mater.* **2017**, *325*, 340–366. [CrossRef] [PubMed]
11. De la Rosa, J.M.; Miller, A.Z.; Pozo-Antonio, J.S.; González-Pérez, J.A.; Jiménez-Morillo, N.T.; Dionisio, A. Assessing the effects of UVA photocatalysis on soot-coated TiO_2-containing mortars. *Sci. Total Environ.* **2017**, *605–606*, 147–157. [CrossRef]
12. Amaro, B.; Saraiva, D.; De Brito, J.; Flores-Colen, I. Statistical survey of the pathology, diagnosis and rehabilitation of ETICS in walls. *J. Civ. Eng. Manag.* **2014**, *20*, 511–526. [CrossRef]
13. Parracha, J.L.; Borsoi, G.; Veiga, R.; Flores-Colen, I.; Nunes, L.; Garcia, A.R.; Ilharco, M.; Dionísio, A.; Faria, P. Effects of hygrothermal, UV and SO_2 accelerated ageing on the durability of ETICS in urban environments. *Build. Environ.* **2021**, *204*, 108151. [CrossRef]
14. Veigas, C.A.; Borsoi, G.; Moreira, L.M.; Parracha, J.L.; Nunes, L.; Malanho, S.; Veiga, R.; Flores-Colen, I. Diversity and distribution of microbial communities on the surface of External Thermal Insulation Composite Systems (ETICS) facades in residential buildings. *Int. Biodeterior. Biodegrad.* **2023**, *184*, 105658. [CrossRef]
15. Vega-Garcia, P.; Lok, C.S.C.; Marhoon, A.; Schwerd, R.; Johann, S.; Helmreich, B. Modelling the environmental fate and behavior of biocides used in façades covered with mortars and plasters and their transformation products. *Build. Environ.* **2022**, *216*, 108991. [CrossRef]
16. Silva, A.S.; Borsoi, G.; Parracha, J.L.; Flores-Colen, I.; Veiga, R.; Faria, P.; Dionísio, A. Evaluating the effectiveness of self-cleaning products applied on external thermal insulation composite systems (ETICS). *J. Coat. Technol. Res.* **2022**, *19*, 1437–1448. [CrossRef]
17. Wang, L.; Zhang, J.; Wang, F.; Liu, Z.; Su, W.; Chen, Z.; Jiang, J. Investigation on the effects of polyaniline/lignin composites on the performance of waterborne polyurethane coating for protecting cement-based materials. *J. Build. Eng.* **2023**, *64*, 105665. [CrossRef]
18. Heib, F.; Hempelmann, R.; Munief, W.M.; Ingebrandt, S.; Fug, F.; Possart, W.; Groß, K.; Schmitt, M. High-precision drop shape analysis (HPDSA) of quasistatic contact angles on silanized silicon wafers with different surface topographies during inclining-plate measurements: Influence of the surface roughness on the contact line dynamics. *Appl. Surf. Sci.* **2015**, *342*, 11–25. [CrossRef]
19. Chen, Y.; Wang, R.; Wang, H.; Hu, F.; Jin, P. Study on PVA-siloxane mixed emulsion coatings for hydrophobic cement mortar. *Prog. Org. Coat.* **2020**, *147*, 105775. [CrossRef]
20. Borsoi, G.; Esteves, C.; Flores-Colen, I.; Veiga, R. Effect of hygrothermal aging on hydrophobic treatments applied to building exterior claddings. *Coatings* **2020**, *10*, 363. [CrossRef]
21. van Duijkeren, E.; Schink, A.K.; Roberts, M.C.; Wang, Y.; Schwarz, S. Mechanisms of Bacterial Resistance to Antimicrobial Agents. *Microbiol. Spectr.* **2018**, *6*, 2. [CrossRef]
22. Castro-Hoyos, A.M.; Rojas Manzano, M.A.; Maury-Ramírez, A. Challenges and Opportunities of Using Titanium Dioxide Photocatalysis on Cement-Based Materials. *Coatings* **2022**, *12*, 968. [CrossRef]
23. Riaz, S.; Park, S.J. An overview of TiO_2-based photocatalytic membrane reactors for water and wastewater treatments. *J. Ind. Eng. Chem.* **2020**, *84*, 23–41. [CrossRef]
24. Hot, J.; Dasque, A.; Topalov, J.; Mazars, V.; Ringot, E. Titanium valorization: From chemical milling baths to air depollution applications. *J. Clean. Prod.* **2020**, *249*, 119344. [CrossRef]

25. Padmanabhan, N.T.; Thomas, R.M.; John, H. Antibacterial self-cleaning binary and ternary hybrid photocatalysts of titanium dioxide with silver and graphene. *J. Environ. Chem. Eng.* **2022**, *10*, 107275. [CrossRef]
26. La Russa, M.F.; Ruffolo, S.A.; Rovella, N.; Belfiore, C.M.; Palermo, A.M.; Guzzi, M.T.; Crisci, G.M. Multifunctional TiO_2 coatings for Cultural Heritage. *Prog. Org. Coat.* **2012**, *74*, 186–191. [CrossRef]
27. Celia, E.; Darmanin, T.; Taffin de Givenchy, E.; Amigoni, S.; Guittard, F. Recent advances in designing superhydrophobic surfaces. *J. Colloid. Interface Sci.* **2013**, *402*, 1–18. [CrossRef]
28. Nath, R.K.; Zain, M.F.M.; Jamil, M. An environment-friendly solution for indoor air purification by using renewable photocatalysts in concrete: A review. *Renew. Sustain. Energy Rev.* **2016**, *62*, 1184–1194. [CrossRef]
29. Higashimoto, S. Titanium-dioxide-based visible-light-sensitive photocatalysis: Mechanistic insight and applications. *Catalysts* **2019**, *9*, 201. [CrossRef]
30. Munafò, P.; Goffredo, G.B.; Quagliarini, E. TiO_2-based nanocoatings for preserving architectural stone surfaces: An overview. *Constr. Build. Mater.* **2015**, *84*, 201–218. [CrossRef]
31. Vega-Garcia, P.; Schwerd, R.; Scherer, C.; Schwitalla, C.; Johann, S.; Rommel, S.H.; Helmreich, B. Influence of façade orientation on the leaching of biocides from building façades covered with mortars and plasters. *Sci. Total Environ.* **2020**, *734*, 139465. [CrossRef]
32. European Union. Regulation (EU) No 528/2012 of the European Parliament and of the Council of 22 May 2012 concerning the Making Available on the Market and Use of Biocidal Products. *Off. J. Eur. Union* **2022**, *167*, 1–123.
33. Schoknechta, U.; Sommerfelda, T.; Borhob, N.; Bagdab, E. Interlaboratory comparison for a laboratory leaching test procedure with façade coatings. *Prog. Org. Coat.* **2013**, *76*, 351–359. [CrossRef]
34. Bollmann, U.E.; Minelgaite, G.; Schlüsener, M.; Ternes, T.; Vollertsen, J.; Bester, K. Leaching of Terbutryn and Its Photodegradation Products from Artificial Walls under Natural Weather Conditions. *Environ. Sci. Technol.* **2016**, *50*, 4289–4295. [CrossRef] [PubMed]
35. La Russa, M.F.; Rovella, N.; Alvarez De Buergo, M.; Belfiore, C.M.; Pezzino, A.; Crisci, G.M.; Ruffolo, S.A. Nano-TiO_2 coatings for cultural heritage protection: The role of the binder on hydrophobic and self-cleaning efficacy. *Prog. Org. Coat.* **2016**, *91*, 1–8. [CrossRef]
36. Diamanti, M.V.; Luongo, N.; Massari, S.; Lupica Spagnolo, S.; Daniotti, B.; Pedeferri, M.P. Durability of self-cleaning cement-based materials. *Constr. Build. Mater.* **2021**, *280*, 122441. [CrossRef]
37. Bersch, J.D.; Flores-Colen, I.; Masuero, A.B.; Dal Molin, D.C.C. Photocatalytic TiO_2-Based Coatings for Mortars on Facades: A Review of Efficiency, Durability, and Sustainability. *Buildings* **2023**, *13*, 186. [CrossRef]
38. Goffredo, G.B.; Terlizzi, V.; Munafò, P. Multifunctional TiO_2-based hybrid coatings on limestone: Initial performances and durability over time. *J. Build. Eng.* **2017**, *14*, 134–149. [CrossRef]
39. *EN 16322:2013*; Conservation of Cultural Heritage—Test Methods—Determination of Drying Properties. CEN: Brussels, Belgium, 2013.
40. Parracha, J.L.; Borsoi, G.; Veiga, R.; Flores-Colen, I.; Nunes, L.; Viegas, C.A.; Moreira, L.M.; Dionísio, A.; Glória Gomes, M.; Faria, P. Durability assessment of external thermal insulation composite systems in urban and maritime environments. *Sci. Tot. Environ.* **2022**, *849*, 157828. [CrossRef]
41. *UNI 11259*; Determination of the Photocatalytic Activity of Hydraulic Binders—Rhodamine Method (in Italian). UNI: Milan, Italy, 2008.
42. Krishnan, P.; Zhang, M.H.; Yu, L.; Feng, H. Photocatalytic degradation of particulate pollutants and self-cleaning performance of TiO_2-containing silicate coating and mortar. *Constr. Build. Mater.* **2013**, *44*, 309–316. [CrossRef]
43. *ASTM-D2244*; Standard Practice for Calculation of Color Tolerances and Color Differences from Instrumentally Measured Color Coordinates. ASTM International: West Conshohocken, PA, USA, 2022.
44. Munafò, P.; Quagliarini, E.; Goffredo, G.B.; Bondioli, F.; Licciulli, A. Durability of nano-engineered TiO_2 self-cleaning treatments on limestone. *Constr. Build. Mater.* **2014**, *65*, 218–231. [CrossRef]
45. *ASTM C1338-19*; Standard Test Method for Determining Fungi Resistance of Insulation Materials and Facings. ASTM: West Conshohocken, PA, USA, 2019.
46. *ASTM D5590-17*; Standard Test Method for Determining the Resistance of Paint Films and Related Coatings to Fungal Defacement by Accelerated Four-Week Agar Plate Assay. ASTM: West Conshohocken, PA, USA, 2017.
47. Parracha, J.L.; Borsoi, G.; Flores-Colen, I.; Veiga, R.; Nunes, L. Impact of natural and artificial ageing on the properties of multilayer external wall thermal insulation systems. *Constr. Build. Mater.* **2022**, *317*, 125834. [CrossRef]
48. *ISO 16474-3*; Paints and Varnishes—Methods of Exposure to Laboratory Light Sources—Part 3, Fluorescent UV Lamps. ISO: Geneva, Switzerland, 2013.
49. Diamanti, M.V.; Paolini, R.; Rossini, M.; Aslan, A.B.; Zinzi, M.; Poli, T.; Pedeferri, M.P. Long term self-cleaning and photocatalytic performance of anatase added mortars exposed to the urban environment. *Constr. Build. Mater.* **2015**, *96*, 270–278. [CrossRef]
50. Graziani, L.; Quagliarini, E.; Bondioli, F.; D'Orazio, M. Durability of self-cleaning TiO_2 coatings on fired clay brick façades: Effects of UV exposure and wet & dry cycles. *Build. Environ.* **2014**, *71*, 193–203. [CrossRef]

51. Roncon, R.; Borsoi, G.; Parracha, J.L.; Flores-Colen, I.; Veiga, R.; Nunes, L. Impact of water-repellent products on the moisture transport properties and mould susceptibility of external thermal insulation composite systems. *Coatings* **2021**, *11*, 554. [CrossRef]
52. Ghaee, A.; Ghadimi, A.; Sadatnia, B.; Ismail, A.F.; Mansourpour, Z.; Khosravi, M. Synthesis and characterization of poly(vinylidene fluoride) membrane containing hydrophobic silica nanoparticles for CO_2 absorption from CO_2/N_2 using membrane contactor. *Chem. Eng. Res. Des.* **2017**, *120*, 47–57. [CrossRef]
53. Quéré, D. Non-sticking drops. *Rep. Prog. Phys.* **2005**, *68*, 2495–2532. [CrossRef]
54. Sadat-Shojai, M.; Ershad-Langroudi, A. Polymeric coatings for protection of historic monuments: Opportunities and challenges. *J. Appl. Polym. Sci.* **2009**, *112*, 2535–2551. [CrossRef]
55. Feltes, J.; Borsoi, G.; Caiado, P.; Dionísio, A.; Parracha, J.; Flores-Colen, I. Graffiti removal on external thermal insulation composite systems through chemical-mechanical methods: A feasible protocol? *J. Build. Eng.* **2023**, *66*, 105872. [CrossRef]
56. Lu, T.; Solis-Ramos, E.; Yi, Y.; Kumosa, M. UV degradation model for polymers and polymer matrix composites. *Polym. Degrad. Stab.* **2018**, *154*, 203–210. [CrossRef]
57. Gil, B.C.; Borsoi, G.; Parracha, J.L.; Dionísio, A.; Veiga, R.; Flores-Colen, I. Effectiveness and durability of anti-graffiti products applied on ETICS: Towards a compatible and sustainable graffiti removal protocol. *Environ. Sci. Pollut. Res.* **2023**, *30*, 65160–65176. [CrossRef] [PubMed]
58. Folli, A.; Pade, C.; Hansen, T.B.; De Marco, T.; MacPhee, D.E. TiO_2 photocatalysis in cementitious systems: Insights into self-cleaning and depollution chemistry. *Cem. Concr. Res.* **2012**, *42*, 539–548. [CrossRef]
59. Calia, A.; Lettieri, M.; Masieri, M. Durability assessment of nanostructured TiO_2 coatings applied on limestones to enhance building surface with self-cleaning ability. *Build. Environ.* **2016**, *110*, 1–10. [CrossRef]
60. Solovyeva, M.; Selishchev, D.; Cherepanova, S.; Stepanov, G.; Zhuravlev, E.; Richter, V.; Kozlov, D. Self-Cleaning Photoactive Cotton Fabric Modified with Nanocrystalline TiO_2 for Efficient Degradation of Volatile Organic Compounds and DNA Contaminants. *Chem. Eng. J.* **2020**, *388*, 124167. [CrossRef]
61. Guo, M.-Z.; Ling, T.-C.; Poon, C.-S. Nano-TiO_2-based architectural mortar for NO removal and bacteria inactivation: Influence of coating and weathering conditions. *Cem. Concr. Compos.* **2013**, *36*, 101–108. [CrossRef]
62. Maury-Ramirez, A.; De Muynck, W.; Stevens, R.; Demeestere, K.; De Belie, N. Titanium dioxide based strategies to prevent algal fouling on cementitious materials. *Cem. Concr. Compos.* **2013**, *36*, 93–100. [CrossRef]
63. Hegyi, A.; Grebenişan, E.; Lăzărescu, A.; Stoian, V.; Szilagyi, H. Influence of TiO_2 Nanoparticles on the Resistance of Cementitious Composite Materials to the Action of Fungal Species. *Materials.* **2021**, *14*, 4442. [CrossRef] [PubMed]
64. Borsoi, G.; Veiga, R.; Santos Silva, A. Effect of nanostructured lime-based and silica-based products on the consolidation of historical renders. In Proceedings of the 3rd Historic Mortars Conference, Glasgow, Scotland, 11–14 September 2013.
65. Kim, J.; Kim, D.; Yun, T.S. Containment of sulfate in leachate as gypsum ($CaSO_4 \cdot 2H_2O$) mineral formation in bio-cemented sand via enzyme-induced carbonate precipitation. *Sci. Rep.* **2023**, *13*, 10938. [CrossRef]
66. Kistanova, N.S.; Chashchukhina, A.D.; Kudryashova, O.S.; Khayrulina, E.A. Influence of polyacrylamide on the precipitation of gypsum in sodium chloride solutions. *Environ. Earth Sci.* **2023**, *82*, 565. [CrossRef]
67. İnceoğlu, F.; Mermer, N.K.; Kırmızı, V.; Tombaş, G. Influence of cement with different calcium sulfate phases on cementitious tile adhesive mortars: Microstructure and performance aspects. *Int. J. Adhes. Adhes.* **2021**, *104*, 102744. [CrossRef]
68. Biedunkova, O.; Kuznietsov, P.; Gandziure, V. Behaviour of dissolved inorganic salts in the cooling water of a nuclear power plant open recirculation system and formation of water discharge. *R. Soc. Open Sci.* **2024**, *11*, 240492. [CrossRef]
69. Borsoi, G.; Tavares, M.; Veiga, R.; Santos Silva, A. Microstructural characterization of consolidant products for historical renders: An innovative nanostructured lime dispersion and a more traditional ethyl silicate limewater solution. *Microsc. Microanal.* **2012**, *18*, 1181–1189. [CrossRef]
70. Zendri, E.; Biscontin, G.; Nardini, I.; Rialto, S. Characterization and reactivity of silicatic consolidants. *Constr. Build. Mater.* **2007**, *21*, 1098–1106. [CrossRef]
71. Hashim, H.; Dias, L.; Martins, S.; Pires, V.; Costa, M.; Barrulas, P. Optimization of the Application of Commercial Hydrophobic Coatings for Natural Stone Protection and Preservation. *Heritage* **2024**, *7*, 3495–3510. [CrossRef]
72. Hoyos-Montilla, A.A.; Puertas, F.; Molina Mosquera, J.; Tobón, J.I. Infrared spectra experimental analyses on alkali-activated fly ash-based binders. *Spectrochim. Acta A Mol. Biomol. Spectrosc.* **2022**, *269*, 120698. [CrossRef]
73. Shanti, R.; Hadi, A.N.; Salim, Y.S.; Chee, S.Y.; Ramesh, S.; Ramesha, K. Degradation of ultra-high molecular weight poly(methyl methacrylate-co-butyl acrylate-coacrylic acid) under ultra violet irradiation. *RSC Adv.* **2017**, *7*, 112. [CrossRef]
74. Olabarrieta, J.; Zorita, S.; Peña, I.; Rioja, N.; Monzón, O.; Benguria, P.; Scifo, L. Aging of photocatalytic coatings under a water flow: Long run performance and TiO_2 nanoparticles release. *Appl. Catal. B* **2012**, *123–124*, 182–192. [CrossRef]
75. Carmona-Quiroga, P.M.; Martínez-Ramírez, S.; Viles, H.A. Efficiency and durability of a self-cleaning coating on concrete and stones under both natural and artificial ageing trials. *Appl. Surf. Sci.* **2018**, *433*, 312–320. [CrossRef]
76. Kalinowski, M.; Chilmon, K.; Kuziak, J.; Łukowski, P. Photocatalytically Induced Degradation of Nano-TiO_2-Modified Paint Coatings Under Low-Radiation Conditions. *Coatings* **2025**, *15*, 281. [CrossRef]

77. Sanmartín, P.; Noya-Pintos, D.; Fuentes, E.; Pozo-Antonio, J.S. Cracks in consolidants containing TiO_2 as a habitat for biological colonization: A case of quaternary bioreceptivity. *Mat. Sci. Eng. C* **2021**, *124*, 112058. [CrossRef] [PubMed]
78. Wojciechowski, K.; Skowera, E.; Pietniewicz, E.; Zukowska, G.Z.; Van Der Ven, L.G.J.; Korczagin, I.; Malanowski, P. UV stability of polymeric binder films used in waterborne facade paints. *Prog. Org. Coat.* **2014**, *77*, 298–304. [CrossRef]
79. Fukaya, N.; Ogi, S.; Sotome, H.; Fujimoto, K.J.; Yanai, T.; Bäumer, N.; Fernández, G.; Miyasaka, H.; Yamaguch, S. Impact of Hydrophobic/Hydrophilic Balance on Aggregation Pathways, Morphologies, and Excited-State Dynamics of Amphiphilic Diketopyrrolopyrrole Dyes in Aqueous Media. *J. Am. Chem. Soc.* **2022**, *144*, 22479–22492. [CrossRef]
80. Colangiuli, D.; Calia, A.; Bianco, N. Novel multifunctional coatings with photocatalytic and hydrophobic properties for the preservation of the stone building heritage. *Const. Build. Mat.* **2015**, *93*, 189–196. [CrossRef]
81. Ribeiro, T.; Baleizão, C.; Farinha, J.P. Functional Films from Silica/Polymer Nanoparticles. *Materials* **2014**, *7*, 3881–3900. [CrossRef] [PubMed]
82. Ferreira, C.; Barrelas, J.; Silva, A.; De Brito, J.; Dias, I.S. Impact of Environmental Exposure Conditions on the Maintenance of Facades' Claddings. *Buildings* **2021**, *11*, 138. [CrossRef]

energies

MDPI

Article

Influence of Web-Perforated Cold-Formed Steel Studs on the Heat Transfer Properties of LSF External Walls

Saranya Ilango , Anthony Ariyanayagam * and Mahen Mahendran

Faculty of Engineering, Queensland University of Technology (QUT), Brisbane, QLD 4000, Australia; saranya.ilango@hdr.qut.edu.au (S.I.); m.mahendran@qut.edu.au (M.M.)
* Correspondence: a.ariyanayagam@qut.edu.au

Abstract: Thermal bridging through cold-formed steel (CFS) studs significantly reduces the thermal performance of light gauge steel frame (LSF) wall systems, particularly in climates demanding higher thermal resistance (R-value). While thermal breaks are commonly used, they increase material costs and construction complexity. According to NCC 2022, the minimum total R-value requirement for external walls ranges between 2.8 and 3.8 m^2·K/W depending on the climate zone and building class. This study therefore evaluated web-perforated steel studs as a passive strategy to enhance thermal resistance of LSF walls, analysing 120 configurations with validated 3D finite element models in Abaqus and benchmarking in THERM. The results showed that web perforations consistently improved R-values by 14 to 20%, as isotherm contours and heat flux vectors demonstrated disruption of direct heat flow through the stud, thereby mitigating thermal bridging. Although the axial compression capacity of web-perforated CFS studs decreased by 29.5%, the use of 4 mm hole-edge stiffeners restored 96.8% of the original capacity. The modified NZS 4214:2006 and ASHRAE Modified Zone methods, incorporating steel area reduction and heat flux redistribution, closely matched Abaqus predictions, with coefficients of variation (COV) below 0.009, corresponding to less than 1% relative deviation between analytical and numerical R-values. Furthermore, application of web-perforated CFS studs in five external wall systems demonstrated improved thermal resistance, ensuring compliance with NCC 2022 R-value requirements across all Australian climate zones. Overall, the findings establish web-perforated studs as an effective solution for improving the energy performance of LSF building envelopes.

Keywords: light gauge steel framing; cold-formed steel; web perforations; thermal bridging; ASHRAE Modified Zone Method; energy efficiency; thermal resistance; heat flux analysis

1. Introduction

Thermal losses in light gauge steel framed (LSF) buildings account for approximately 20 to 40% of total energy loss through the building envelope. Of these, external wall assemblies contribute 10 to 25%, primarily due to thermal bridging through high-conductivity steel components such as studs, noggings, and plates, which have conductivities exceeding 50 W/m·K. In contrast, adjacent materials such as insulation and sheathing typically exhibit conductivities below 0.05 W/m·K [1]. While internal LSF walls contribute minimally to building envelope heat transfer, external walls provide dominant conductive pathways and exert substantial influence on heating, ventilation, and air conditioning (HVAC) loads [2,3]. The thermal performance of LSF systems is characterised by thermal transmittance (U-value, W/m^2·K) and thermal resistance (R-value, m^2·K/W), which are inversely related

(R = 1/U) [4]. The thermal performance of LSF wall assemblies is influenced by parameters such as stud spacing, flange geometry, insulation configuration, cladding type, thermal breaks, and web perforations [5]. Insulation layout can influence thermal resistance, as Santos et al. [6] and Rajanayagam et al. [7] demonstrated that varying insulation placement can result in efficiency differences exceeding 60%. Francis et al. [8] and Martins et al. [9] reported that cold-framed LSF walls produced U-values up to 0.432 $W/m^2 \cdot K$, with R-value reductions approaching 65%, whereas warm-framed systems with continuous insulation achieved U-values as low as 0.295 $W/m^2 \cdot K$. Stud spacing and flange width also modulate thermal performance, as closer spacing (e.g., 300 mm) increases the steel fraction, raising U-values by 0.10 to 0.16 $W/m^2 \cdot K$ and reducing R-values by up to 25%, whereas wider spacing with continuous insulation can improve R-values by about 20% [10,11]. Also, flange width reduction from 50 mm to 35 mm has been shown to improve R-values by up to 15% [5]. Additional strategies including staggered studs, optimised cavity insulation, and composite sheathing have produced R-value increases of over 22%, with some configurations exceeding 3.5 $m^2 \cdot K/W$ [12,13]. Among various passive strategies, web perforations offer an effective approach to mitigating thermal bridging by reducing conductive cross-sectional area and introducing air voids as shown in Figure 1. Sovetova and Calautit [14] reported heat transfer reductions of 50% using air-filled perforations. Yang et al. [15] reported U-value reductions from 0.697 to 0.428 $W/m^2 \cdot K$ using slotted studs, with further reduction to 0.329 $W/m^2 \cdot K$ achieved by increasing slot number and length. Alekperov et al. [16] found triangular and dumbbell-shaped slots lowered thermal conductivity by up to 19% versus rectangular slots. Further, Martins et al. [9] recorded an 8.3% drop in U-value using 10 mm thermal break strips on 28% web slotted studs. Langner et al. [17] demonstrated that slotting alone could match the resistance benefit of reducing stud thickness sixfold. Furthermore, Höglund and Burstrand [18] identified flanges and webs as primary heat conduction paths and confirmed that web perforations effectively reduce through-stud conduction. Combined, these methods improve R-values by 15 to 20%, supporting compliance with ISO 6946:2017 [19] and the National Construction Code (NCC) [20] while reducing HVAC energy demand. However, such web perforations in steel studs may introduce structural capacity concerns caused by premature buckling [21].

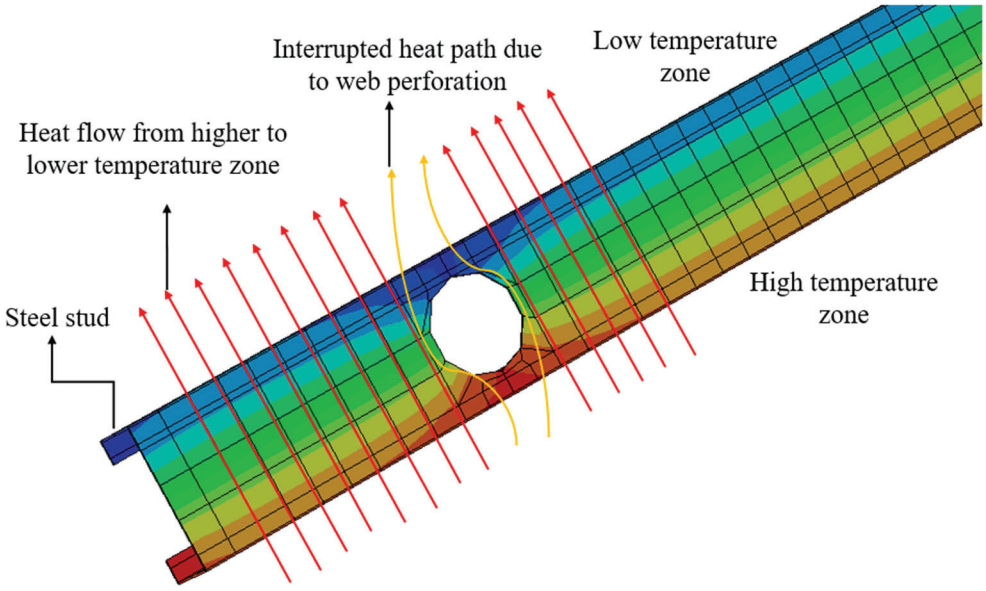

Figure 1. Heat flow distribution in a web-perforated steel stud.

Globally, energy efficiency regulations have become increasingly stringent, mandating higher R-values in steel-framed building envelopes. The International Energy Conservation Code 2021 [22] requires total R-values between 2.29 and 3.52 $m^2 \cdot K/W$, supplemented by energy rated cavity insulation. According to the American Society of Heating, Refrigerating and Air-Conditioning Engineers (ASHRAE) [23], above-grade LSF walls in cold climate zones (Zones 5 to 8) must not exceed a U-value of 0.064 $W/m^2 \cdot K$. In Europe, national standards aligned with the European Union directive prescribe external wall R-values ranging from 2.8 to 6.0 $m^2 \cdot K/W$, depending on the climate zone [24]. Australia's NCC 2022 mandates total R-values between 2.8 and 3.8 $m^2 \cdot K/W$ based on climate zone and building class and requires thermal breaks with a minimum resistance of R 0.2 for direct-fix cladding. However, current provisions across these standards do not explicitly address passive enhancements such as web perforations in steel studs. In this context, to assess regulatory compliance, several analytical methods are employed, including ISO 6946:2017 [19], NZS 4214:2006 [25] and the ASHRAE Modified Zone Method [26], which estimate thermal resistance under steady-state conditions. ISO 6946:2017, although widely used for conventional walls, explicitly states that its combined method is not valid for cold and hybrid LSF walls due to the strong metal bridging effect. While NZS 4214:2006, based on the isothermal planes approach, is suitable for low R-value assemblies, it tends to overestimate performance of highly thermally bridged systems such as CFS frames, limiting its applicability. The ASRAE Modified Zone Method addresses some of these limitations by incorporating zone factors that account for lateral heat flow, offering improved accuracy for cold-framed or discontinuously insulated assemblies [27]. However, both NZS 4214 and the Modified Zone Method assume homogeneous steel framing and do not consider geometric disruptions such as web perforations, limiting their applicability to perforated LSF systems. Also, even with cavity insulation rated at R 2.5 $m^2 \cdot K/W$, thermal bridging can reduce effective resistance to between R 1.1 and R 1.4 $m^2 \cdot K/W$, resulting in performance losses exceeding 50%, depending on climate zone [28,29]. Although thermal breaks are mandated for cladding systems, passive strategies such as web perforations remain unacknowledged in existing regulations, and current calculation methods continue to overlook internal voids and discontinuities in steel geometry [30].

Previous research on LSF walls has primarily examined solid studs and, in some cases, slotted studs, focusing on insulation strategies, thermal breaks, and cavity design, which achieved only incremental gains. However, systematic strategies that alter the stud geometry to directly interrupt heat transfer pathways remain limited. In particular, the role of circular web perforations in passively enhancing the energy performance of LSF walls has not been investigated. This study addresses this gap through a comprehensive numerical and analytical evaluation of web-perforated CFS studs, incorporating thermal efficiency, structural performance in terms of load carrying capacity of the CFS studs, and compliance with NCC 2022 requirements. Full-scale 3 m LSF wall assemblies with 1.15 mm lipped-channel CFS studs were modelled for steady-state heat transfer using 3D Abaqus and 2D THERM under a 35 °C gradient (40 °C external, 5 °C internal) and validated against guarded hot-box experiments [31]. To capture the influence of geometry, 120 stud configurations were developed by systematically varying web hole diameters between 36 and 68 mm and spacings between 200 and 450 mm, consistent with the limits prescribed in AS/NZS 4600 and NASH provisions. The structural capacity of web-perforated studs was benchmarked against the experimental results of Gunalan et al. [32], ensuring that axial load-carrying performance was reliably represented. Perforations redistributed heat flux through the insulation, increasing thermal resistance by up to 20% relative to solid studs. This gain was initially accompanied by reduced axial capacity, but the addition of 4 mm web-hole stiffeners restored the performance with no significant loss of strength

while retaining a 15% R-value improvement. The optimised perforated stud was further examined within five representative façade systems, confirming consistent thermal benefits at the envelope level. Finally, modified forms of NZS 4214 and the ASHRAE Zone Method were developed to account for discontinuous steel geometries, achieving close agreement with Abaqus and THERM predictions, and the resulting R-values were mapped against NCC 2022 thermal requirements across multiple climate zones.

2. Methodology

2.1. Model Validation

Experimental investigations into the thermal performance of LSF walls have played a critical role in validating numerical models used in estimating R-values. The benchmark study by Santos and Mateus [31] utilised a mini hot-box apparatus under quasi-steady-state conditions to evaluate the thermal resistance of both load-bearing and non-load-bearing LSF wall assemblies. The configuration of their load-bearing wall comprised three C90 × 43 × 15 × 1.5 mm steel studs at 400 mm spacing, with a 90 mm mineral wool core (λ = 0.035 W/m·K), 12 mm OSB on both faces, and an internal 12.5 mm gypsum plasterboard layer, resulting in a total thickness of 126.5 mm as shown in Figure 2. It measured 1030 mm × 1060 mm and included three symmetrically placed studs. The measured surface-to-surface thermal resistance was R = 1.558 m^2·K/W. In this study, this reference load-bearing LSF wall was numerically modelled to evaluate its thermal performance using three-dimensional steady-state (3D) heat transfer analysis in Abaqus as shown in Figure 3. The 3D approach was adopted to better represent realistic heat flow in all spatial directions. Material conductivities were taken as 50 W/m·K for steel, 0.100 W/m·K for OSB, and 0.175 W/m·K for plasterboard. A temperature gradient of 35 °C was applied (40 °C hot side, 5 °C cold side), with heat fluxes recorded using four sensors positioned across the stud and cavity regions. The developed model was validated against measured surface-to-surface R values reported in [31].

A parallel simulation was performed in THERM as shown in Figure 4, which, in addition to providing validation, facilitated a clearer understanding of the distinctions between 2D and 3D thermal behaviour, particularly in relation to the influence of geometric dimensionality on predicted R-values.

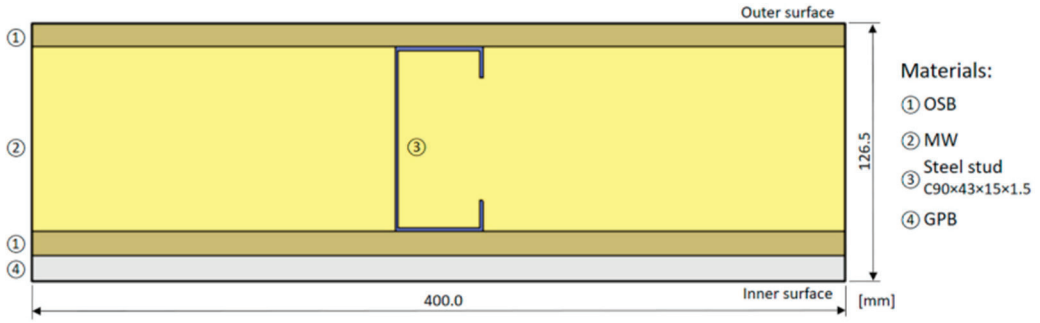

Figure 2. Load-bearing LSF Wall investigated in [31].

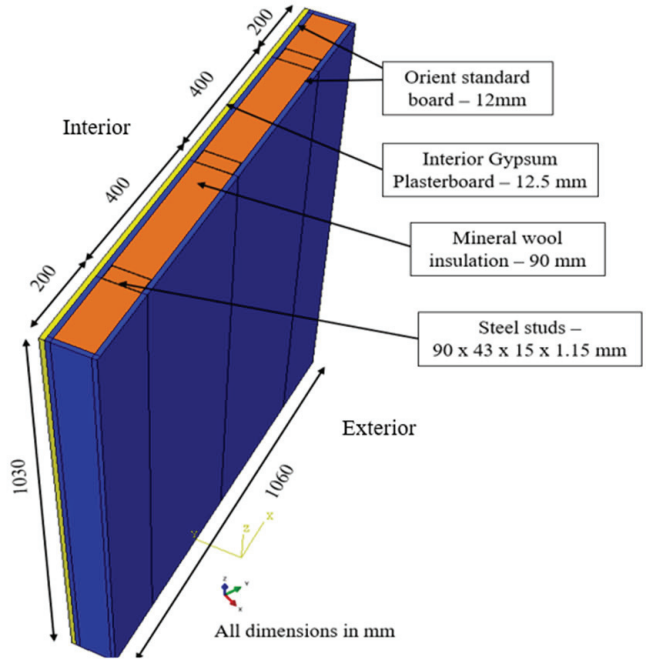

Figure 3. Three-dimensional Abaqus model of the reference wall.

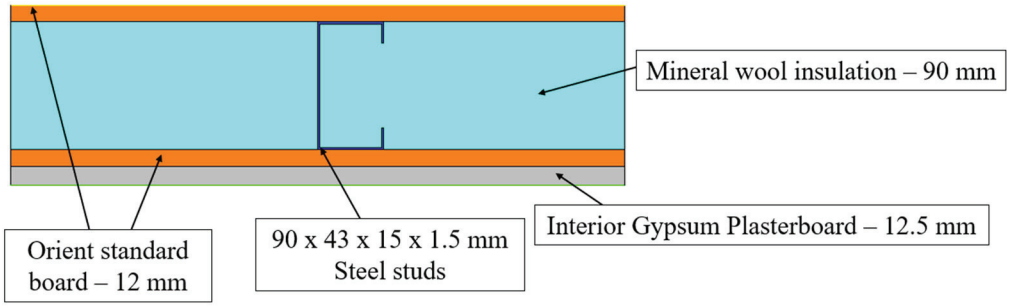

Figure 4. THERM model of the reference wall.

2.2. Studied Cases—Thermal Resistance of LSF Wall and Structural Capacity of CFS Stud

Following model validation, web perforations were introduced to the studs of the same LSF wall configuration to mitigate thermal bridging and investigate their influence on conductive heat transfer pathways. Five perforations with a diameter of 45 mm were introduced with a clear spacing of 160 mm between adjacent holes. The resulting effects on isotherm alignment and heat flux redistribution were investigated. Furthermore, a 1200 mm × 3000 mm wall with non-perforated CFS stud was developed in Abaqus to represent full scale LSF construction, as shown in Figure 5. Previous studies show that wall width has minimal impact on thermal resistance under steady-state conditions due to predominantly one-dimensional heat flow [33,34]. The 3 m height was adopted to enable axial conduction study along solid studs, followed by assessment of the potential thermal impact of introducing web perforations and the associated reduction in steel cross-sectional area. The R-value obtained from this configuration was used as a reference for subsequent analyses. To assess the influence of geometric modifications on thermal resistance, the model was then extended by incorporating circular web openings in the steel studs (Figure 5).

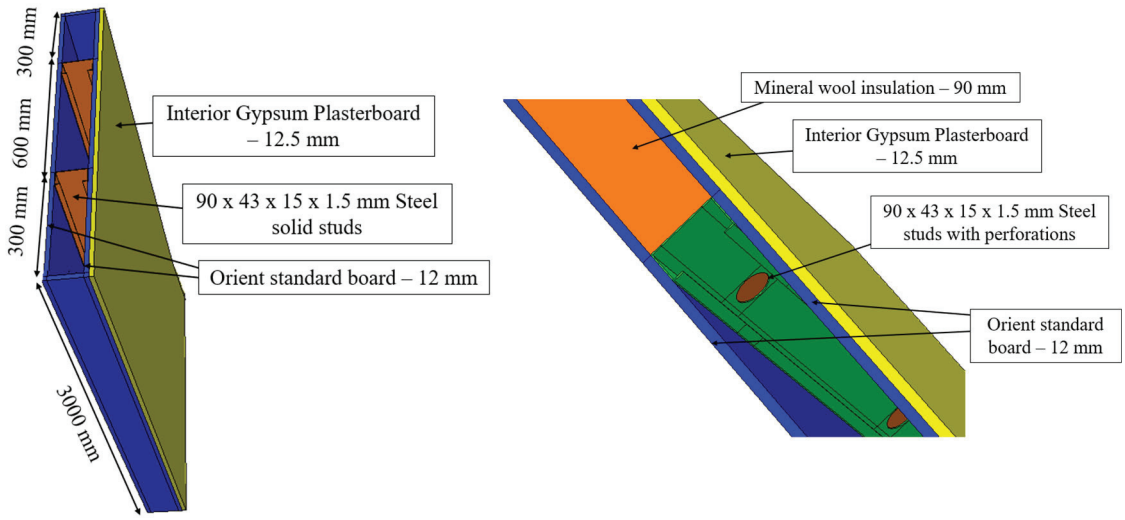

Figure 5. Abaqus model of 1200 mm × 3000 mm LSF wall with solid and web-perforated CFS studs.

Moreover, the 1.5 mm thick CFS stud reported in the literature was replaced with a 1.15 mm thick section, consistent with the 3 m lipped channel stud experimentally investigated by Gunalan et al. [32] to allow structural capacity assessment. A parametric study was undertaken numerically in Abaqus, adopting the modelling methodology of Vy et al. [35] to evaluate the influence of web perforation geometry and spacing on the thermal and structural performance of CFS studs, aiming to enhance the thermal resistance of LSF walls. A total of 120 LSF configurations were evaluated by varying the web hole diameter to web depth ratio between 0.40 and 0.76, consistent with the limits defined in AS/NZS 4600 [36], National Association of Steel-Framed Housing (NASH) [37] and the NCC. Hole diameters ranged from 36 mm to 68 mm, with spacing between 120 mm and 450 mm along a 3000 mm stud length (Figure 6).

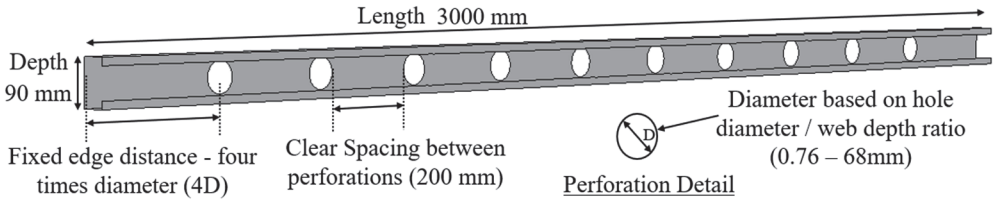

Figure 6. Locations and sizes of web perforations modelled in Abaqus.

The analysis revealed that increases in thermal resistance were consistently accompanied by reductions in load-bearing capacity. To address this capacity reduction, the same configuration was refined by using 4 mm long hole-edge stiffeners, with material property identical to the base CFS stud material. This modification maintained the thermal improvement while enhancing load-bearing capacity, with the stiffened configuration substantially increasing the capacity compared to the unstiffened stud and recovering most of the capacity lost due to web perforations. The wall assembly, integrating web perforations and web-hole stiffeners, was used to evaluate the thermal performance of fire-rated external LSF walls. Five full-scale ventilated façade systems were modelled, each integrating a dedicated air cavity along with a distinct external cladding type: autoclaved aerated concrete panels, corrugated steel sheeting, non-combustible aluminium composite panels, fire-rated glass façades, and ventilated clay brick veneer. Thermal resistance was evaluated at each stage based on the required R-values for different Australian climate zones given in Table 1.

Table 1. Required total R-Values for external walls from NCC [20].

Climate Zone	Class of Building		
	1	**2, 5, 6, 7, 8 or 9b or 9a Excluding Ward Area**	**3 or 9c or 9a Ward Area**
1	2.8	2.4	3.3
2	2.8	1.4	1.4
3	2.8	1.4	3.3
4	2.8	1.4	2.8
5	2.8	1.4	1.4
6	2.8	1.4	2.8
7	2.8	1.4	2.8
8	3.8	1.4	3.8

Additionally, external LSF wall performance was assessed by varying stud spacing, insulation configuration, plasterboard layers, and thermal break inclusion, benchmarked against R-value targets for extreme climates. Analytical methods, including NZS 4214 and the ASHRAE Modified Zone method, were adapted for web-perforated studs by recalculating frame fractions based on net steel area. The analytical expressions for thermal resistance were modified to account for the reduced steel cross-sectional area introduced by web perforations. Table 2 provides an overview of the present study on web-perforated CFS studs in LSF walls.

Table 2. Overview of the present study on web-perforated CFS studs in LSF walls.

Study Component	Details	Scope/Configurations	Purpose
Model Validation	Reference LSF wall by Santos & Mateus [31] (guarded hot-box)	1 wall (R = 1.558 m^2·K/W)—Heat transfer model	Benchmark validation of LSF wall using Abaqus and THERM
	Gunalan et al. [32] 3 m lipped channel CFS stud	1 stud (81 kN vs. 79 kN (experimental).)—Structural capacity model	Structural validation of CFS stud model in Abaqus
Numerical Study	Validated LSF walls with and with-out web-perforated CFS studs	THERM (2D), Abaqus (3D), and analytical methods (NZS 4214, ASHRAE)	Evaluate the role of web-perforations in thermal capacity enhancement
Parametric Study (CFS studs)	Lipped channel stud 90 × 40 × 15 × 1.15 mm, 3 m height	120 CFS studs: Hole Ø 36–68 mm, spacing 120–450 mm (d/h = 0.40–0.76)	Evaluate thermal R-values and load capacity
	Edge stiffeners (4 mm plates)	1 CFS stud with 68 mm Ø holes with 200 mm clear spacing	Restore structural capacity of perforated studs
Analytical Methods	Modified NZS 4214 & ASHRAE MZM	Compared with Abaqus & THERM	Develop reliable predictive models
Façade Systems (External Walls)	AAC panels	1 case (THERM (2D), Abaqus (3D), and analytical methods (NZS 4214, ASHRAE))	High thermal mass façade
	Corrugated steel sheeting	1 case (THERM (2D), Abaqus (3D), and analytical methods (NZS 4214, ASHRAE))	Lightweight, high conductivity façade

Table 2. *Cont.*

Study Component	Details	Scope/Configurations	Purpose
	Aluminium composite panels (ACP)	1 case (THERM (2D), Abaqus (3D), and analytical methods (NZS 4214, ASHRAE))	Insulated lightweight façade
	Fire-rated glass façade	1 case (THERM (2D), Abaqus (3D), and analytical methods (NZS 4214, ASHRAE))	Transparent, fire-resistant façade
	Ventilated brick veneer	1 case (THERM (2D), Abaqus (3D), and analytical methods (NZS 4214, ASHRAE))	Brick veneer with ventilated cavity
Enhancements	Thermal breaks	Applied in all external walls considered in study	Reduce thermal bridging
	Hybrid insulation (partial cavity fill + sheathing)	Applied in all external walls considered in study	Improve thermal efficiency
	Double plasterboard	Applied in all external walls considered in study	Increase thermal mass & fire performance
Climate Zone Analysis	NCC 2022 Australian climate zones (Z1–Z8)	Applied in all external walls considered in study	Demonstrate compliance with R-value requirements

3. Three-Dimensional Heat Transfer Simulation Using Abaqus Finite Element Models

3.1. Model Description

A 3D steady-state heat transfer model was developed in Abaqus/CAE 2023 [38] to evaluate the R-values of LSF wall assemblies, following the modelling framework of Ariyanayagam and Mahendran [39]. Several wall configurations were analysed, including (a) LSF wall specimens reported in the literature, measuring 1060 mm × 1030 mm with and without web perforations (Figure 3); (b) 1200 mm × 3000 mm walls with and without perforations (Figure 5); and (c) external wall assemblies with cladding, also measuring 1200 mm × 3000 mm. Configurations (b) and (c) incorporated two C90 × 43 × 15 × 1.5 mm LSF studs spaced at 600 mm, while configuration (a) used 400 mm spacing and were connected by top and bottom tracks. In configurations involving external walls, CFS battens were included. Components were assembled with spatial alignment and tie constraints ensured thermal continuity at all interfaces. All materials, including LSF framing, oriented strand board (OSB), gypsum plasterboard (GPB), and mineral wool insulation, were modelled as 3D homogeneous deformable solids using 3D eight-node linear brick elements with first-order temperature interpolation. A mesh independence study was performed to ensure accuracy of both thermal and structural simulations. Five mesh densities were examined: coarse (8 mm), medium (4 mm), and fine (2 mm). The predicted R-values for the reference wall varied by less than 1.2% between medium and fine meshes, while the axial capacity of the perforated stud differed by only 0.9%. Very fine mesh led to longer numerical simulation time. The final scheme applied a 20 mm global mesh to bulk regions such as insulation and stud bodies, 4 mm refinement through plasterboard and OSB layers, 5 mm elements at material interfaces, and 6 to 8 mm refinement around perforation zones to resolve heat-flux redistribution and stress concentrations. Mesh sensitivity analysis confirmed that further refinement produced negligible changes in the R-value, validating the mesh strategy. The final mesh configuration is illustrated in Figure 7. A steady-state heat transfer analysis was conducted to compute the temperature distribution and determine the R-value.

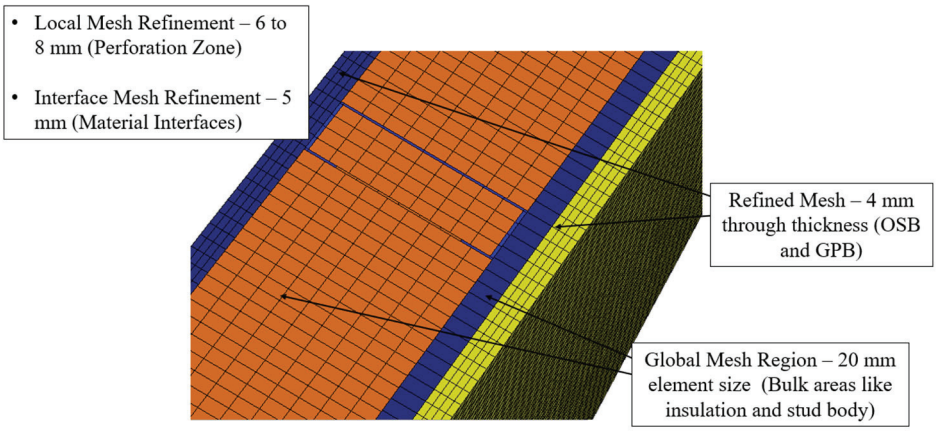

Figure 7. Final mesh configuration.

3.2. Constraints, Boundary Conditions and Contact Interactions

Thermal boundary conditions and heat transfer processes were defined following established finite element (FE) methods for LSF walls [40], as shown in Figure 8. Heat transfer was modelled by incorporating conduction through solid materials and convection at internal and external surfaces, while radiation was neglected under the steady-state assumption. Interfaces between LSF framing, OSB, plasterboard, and insulation were modelled using tie constraints with a tolerance of 0.0001 mm, automatically assigned through the contact detection algorithm in Abaqus. Surface film coefficients of 10 $W/m^2 \cdot K$ on the interior OSB surface and 25 $W/m^2 \cdot K$ on the exterior plasterboard face were applied, consistent with ASHRAE guidelines for vertical surfaces under natural convection, consistent with ASHRAE guidelines for vertical surfaces under natural convection [3]. To reflect the imposed temperature difference in experimental setups, boundary temperatures of 40 °C and 5 °C were used to simulate the experimental thermal gradient. Subsequently, a steady-state heat transfer step was employed with solver settings optimised for numerical stability. Surface heat flux results were used to calculate the R-value based on ISO 10211 2017 [34], and the modelling framework complied with NZS 4214 2006 for thermal resistance evaluation in LSF systems.

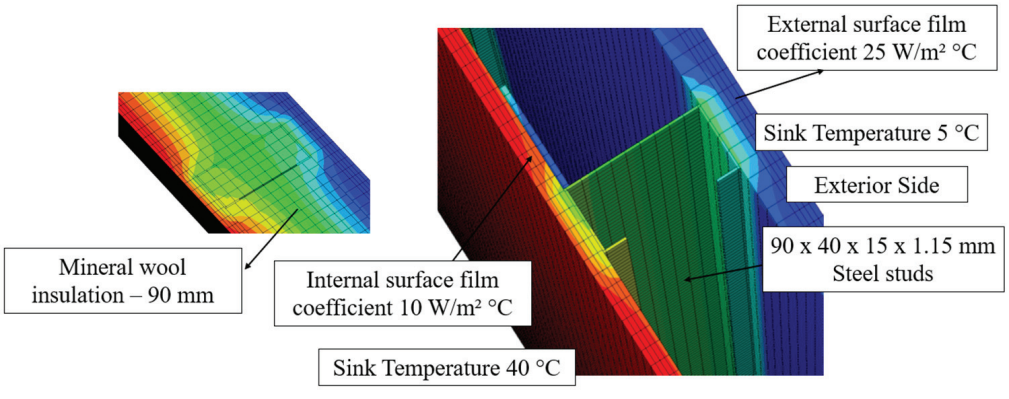

Figure 8. Thermal boundary conditions and material interactions in LSF Walls.

3.3. Thermal Resistance Calculation Using Heat Flux Measurement

The steady-state thermal performance (R-value) of the LSF wall system was evaluated in Abaqus by extracting nodal heat fluxes from five thermally critical regions: corners, cavity centre, stud location, web perforation zones, and continuous steel segments. These regions were selected to capture variations in heat transfer due to geometric and material discontinuities. Abaqus solves the steady-state heat conduction equation based on Fourier's

law, from which nodal heat fluxes (ϕ_i) are derived. These were averaged to obtain the representative surface heat flux ϕ assuming fine meshing and uniform surface distribution, as shown in Equation (1):

$$\phi \frac{1}{N} \sum_{i=1}^{N} \phi_i \quad (1)$$

The thermal transmittance (U-value) was then computed by dividing the average heat flux by the applied temperature gradient ΔT (Equation (2)):

$$U = \frac{\phi}{\Delta T} \quad (2)$$

The total thermal resistance (R_T) of the assembly, representing its global resistance to conductive heat flow, was determined by Equation (3):

$$R_T = 1/U \quad (3)$$

The total thermal resistance obtained from Abaqus aligns with the ISO 6946 formulation, comprising the internal and external surface resistances (R_{si}, R_{se}) and the sum of individual layer resistances, as expressed by Equation (4):

$$R_T = R_{si} + \sum_{x=1}^{n} \frac{d_j}{k_j} + R_{se} \quad (4)$$

Here, d_j and k_j are the thickness and thermal conductivity of the jth layer, n is the number of material layers in the assembly while R_{si} and R_{se} correspond to internal and external surface resistances, typically taken as 0.13 and 0.04 $m^2 \cdot K/W$.

The thermal results obtained from Abaqus are based on steady-state heat conduction governed by total heat transfer derived as in Equation (5) and Fourier's law, shown in Equation (6).

$$Q = \overline{\phi} \cdot A \quad (5)$$

where Q is the total heat transfer in Watts and A is the surface area of the wall in m^2. The underlying heat flux distribution is defined by Equation (6),

$$\overline{q} = -k.\ \Delta T, \quad (6)$$

where $\overline{q}$ is the heat flux vector (W/m^2).

These formulations, applied under isotropic and homogeneous material assumptions, enabled robust calculation of the U and R-values while capturing directional thermal bridging effects introduced by CFS framing and web perforations using Abaqus as shown in Figure 9. Furthermore, Abaqus simulations incorporated appropriate thermal boundary conditions and calibrated material properties, with the resulting heat flux output (ϕ), used to compute the U-value and total thermal resistance of the LSF wall system.

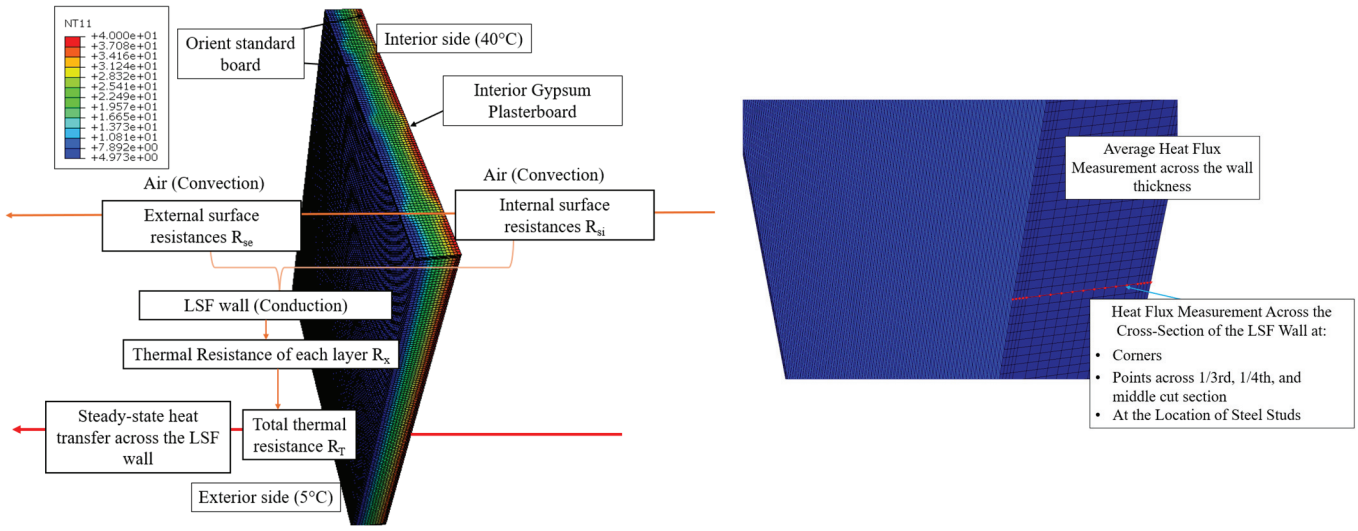

Figure 9. Measurement of total thermal resistance in LSF wall assemblies.

4. Two-Dimensional Thermal Modelling of Load-Bearing LSF Walls Using THERM

Two-dimensional steady-state thermal analysis was conducted in THERM (v7.8.2) to complement the 3D simulations in Abaqus (Figure 10). THERM was selected due to its widespread application in modelling planar conductive heat transfer in layered building envelopes. It was used alongside Abaqus to compare 2D and 3D thermal behaviour in the LSF wall assembly. The cross-sectional geometry and material properties were identical to those used in Abaqus and based on validation against experimental data from [31]. All materials were modelled as homogeneous and isotropic, with constant thermal conductivities assigned from standard references. Boundary conditions included fixed surface temperatures (40 °C interior, 5 °C exterior), and surface resistances were applied in accordance with ISO 6946:2017. These were applied as inputs but subtracted from the results to isolate the surface-to-surface R-value, in accordance with the referenced method. Mesh refinement was applied near material interfaces to capture thermal gradients while maintaining computational efficiency. Radiative and transient effects were neglected under the steady-state assumption. R-values were obtained directly from the simulation output. For perforated configurations, the thermal resistance was determined using a weighted average across perforated and adjacent solid web regions to account for the planar geometric simplification inherent to 2D THERM modelling.

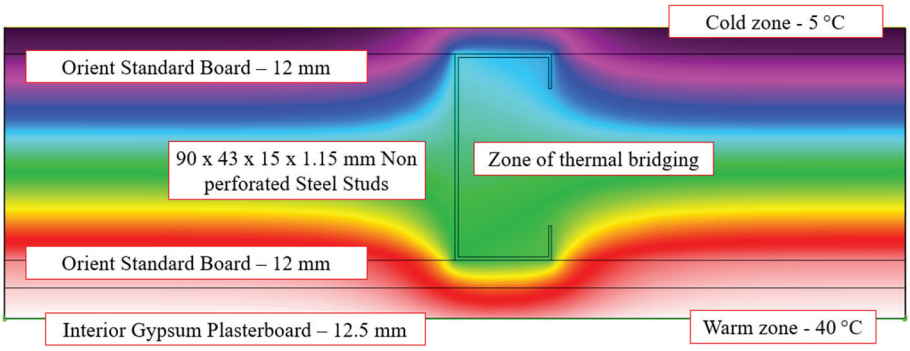

Figure 10. Model validation of THERM simulations based on thermal gradient analysis and resistance evaluation.

5. Modified Analytical Methods for Calculating Thermal Resistance of LSF Walls with Web-Perforated Studs

5.1. Model-Based Validation of R-Values for Web-Perforated LSF Walls Using the NZS 4214 Analytical Framework

To overcome the limitations of conventional analytical methods in estimating the thermal resistance of web-perforated LSF walls, this study introduces an enhanced framework calibrated against 120 validated 3D FE simulations in Abaqus. As illustrated in Figure 11, standard approaches such as NZS 4214:2006 rely on the isothermal plane's method, assuming uninterrupted axial conduction through continuous steel studs. These models simplify the stud as a thermally equivalent solid rectangle with effective conductivity, which fails to account for the disrupted conduction paths caused by web perforations. The equivalent rectangle conductivity expressing the equivalent thermal conductivity of the stud when simplified into an enclosing solid rectangle under the isothermal planes method is given by Equation (7):

$$K = \frac{d}{a} k_m \tag{7}$$

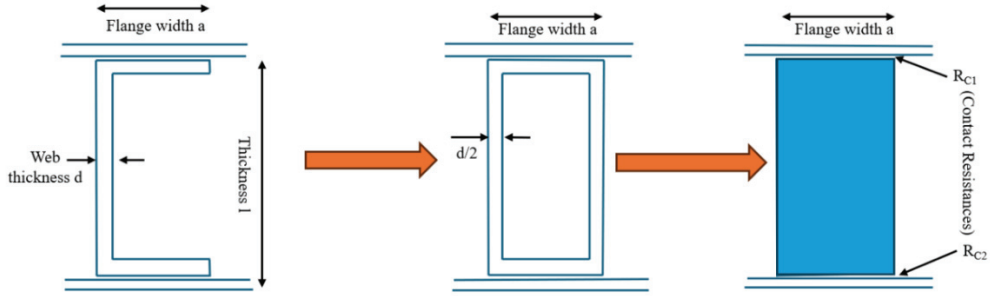

Figure 11. Steel frame elements replaced with an enclosing equivalent solid rectangle in conventional NZS 4214-based analytical configuration.

Also, the thermal resistance of the equivalent rectangle R is given by Equation (8):

$$R = \frac{L}{k} = \frac{a * l}{d * k_m} + R_{c1} + R_{c2} \tag{8}$$

where k is the overall thermal conductivity (W/m·K) of the wall section through the metal path, d is web thickness, a is flange width, l is wall thickness, and k_m is the thermal conductivity of steel. However, this formulation fails to account for heat flow disruption caused by perforations, leading to overestimation of thermal bridging and underestimation of overall thermal resistance of web-perforated LSF wall. To overcome this, two corrections were introduced. First, the effective steel area was reduced by using a perforation-adjusted frame fraction and the modified frame fraction (f'_s) is shown in Equation (9):

$$f\prime_s = f_s \times \left(1 - \frac{A_p}{A_s}\right) \tag{9}$$

where A_p and A_s denote the perforated and gross web areas and f_s is the frame fraction of the LSF wall. Second, a flux redistribution factor (C_f) was developed using heat flux data from Abaqus to represent the alteration of conduction paths induced by web perforations. This factor quantifies the ratio of axial heat flux in perforated studs to that in solid studs, effectively capturing the reduction in axial conduction caused by geometric discontinuities. The correction factor is defined as shown in Equation (10):

$$C_f = \frac{Q_P}{Q_{NP}} \tag{10}$$

where Q_P and Q_{NP} are the surface heat fluxes for perforated and solid studs obtained from Abaqus simulations, respectively. Based on the results, the C_f ranged from 0.5 to 0.9, with lower values corresponding to greater perforation size and density. The corrected stud thermal resistance incorporating this factor is expressed in Equation (11):

$$R_{Web-perforated\ steel} = \frac{a * l}{C_f * d * k_m} + R_{Contact1} + R_{Contact2} \quad (11)$$

This dual-modified expression captures both conduction loss due to cross-sectional voiding and the thermodynamic effects of lateral flux redistribution. The bridged layer resistance ($R_{b,\ corrected}$) was corrected using a perforation-adjusted frame fraction and corrected stud thermal resistance, as shown in Equation (12):

$$R_b = \frac{f\prime_s}{R_{Web-perforated\ steel}} + \frac{f_{ins}}{R_{ins}} \quad (12)$$

The total thermal resistance of the whole system (R_T), including the corrected bridged layer resistance, is given by Equation (13):

$$R_T = R_{se} + R_1 + R_2 \ldots + R_n + R_{Web-perforated\ steel} + R_{si} \quad (13)$$

where R_{si} and R_{se} correspond to internal and external surface resistances, and R_1 to R_n represent the thermal resistances of homogeneous material layers. The equation shows close alignment with FE predictions and extends the applicability of NZS 4214 to geometrically discontinuous LSF wall systems, offering improved accuracy in R-value estimation under realistic thermal conditions.

5.2. Modified ASHRAE Zone Method Incorporating Perforation-Based Heat Flux and Area Corrections

The Modified ASHRAE Zone Method was employed across all 120 web-perforated and non-perforated LSF wall configurations to evaluate R-values [13]. This method partitions the wall into two regions: a thermally bridged zone around the steel stud, Section W, and the insulated cavity, Section CAV, as shown in Figure 12. The influence zone width, w (m), is calculated by Equation (14):

$$w = f_l + z_f * d_{sheath} \quad (14)$$

where f_l is the stud flange width, d_{sheath} is the thicker sheathing thickness, and z_f is a geometry and resistivity dependent factor derived from empirical charts.

For walls where at least one sheathing exceeds 16 mm, z_f is derived from fitted power-law trendlines specific to each stud size. When both sheathings are thinner than 16 mm, a simplified rule assigns $z_f = -0.5$ for $r_{sheathing} \leq 10.4$ m·K/W and $z_f = -0.5$ for $r_{sheathing} > 10.4$ m·K/W, where $r_{sheathing}$ is the sheathing resistivity. The overall thermal resistance is then computed using a parallel path formulation shown in Equation (15):

$$\frac{1}{R_{total}} = \frac{w}{ss} * \frac{1}{R_w} + \left(1 - \frac{w}{ss}\right) * \frac{1}{R_{Cav}} \quad (15)$$

where ss is the stud spacing, R_w (m^2·K/W) is the resistance in Section W, which is the zone influenced by the stud, and R_{Cav} is the resistance of the remaining cavity layers. In Section W, the resistance of each wall layer is computed as a parallel conduction path between steel and insulation given by Equation (16):

$$\frac{1}{R_j} = \frac{f_j^{(met)}}{R_j^{(met)}} + \frac{f_j^{(ins)}}{R_j^{(ins)}} \tag{16}$$

where $f_j^{(met)}$ and $f_j^{(ins)}$ are the area fractions of metal and insulation in layer j, and $R_j^{(met)}$ and $R_j^{(ins)}$ are their respective resistances ($m^2 \cdot K/W$). To capture the impact of web perforations, two corrections were introduced. First, the metal area fraction was reduced to reflect the loss of steel cross-section using Equation (17):

$$f_j^{(met,\ corrected)} = f_j^{(met)} * \left(1 - \frac{A_p}{A_s}\right) \tag{17}$$

where A_p is the total perforated area (m^2) and A_s is the gross web area of the stud (m^2). Second, a heat flux correction factor was introduced to represent the reduction in heat conduction capacity due to perforations as shown in Equation (18):

$$C_f = \frac{Q_P}{Q_{NP}} \tag{18}$$

where Q_P and Q_{NP} are the average surface heat fluxes through perforated and non-perforated studs (W/m^2), respectively, extracted from steady-state FE simulations. The resistance of the steel conduction path was then corrected using Equation (19):

$$R_j^{(met,\ corrected)} = \frac{R_j^{(Solid)}}{C_f} \tag{19}$$

Finally, the corrected total resistance for the stud-influenced zone is expressed by Equation (20):

$$\frac{1}{R_j^{(Web-peroated\ steel)}} = \frac{f_j^{(met)} * \left(1 - \frac{A_p}{A_s}\right)}{\frac{R_j^{(Solid)}}{C_f}} + \frac{f_j^{(ins)}}{R_j^{(ins)}} \tag{20}$$

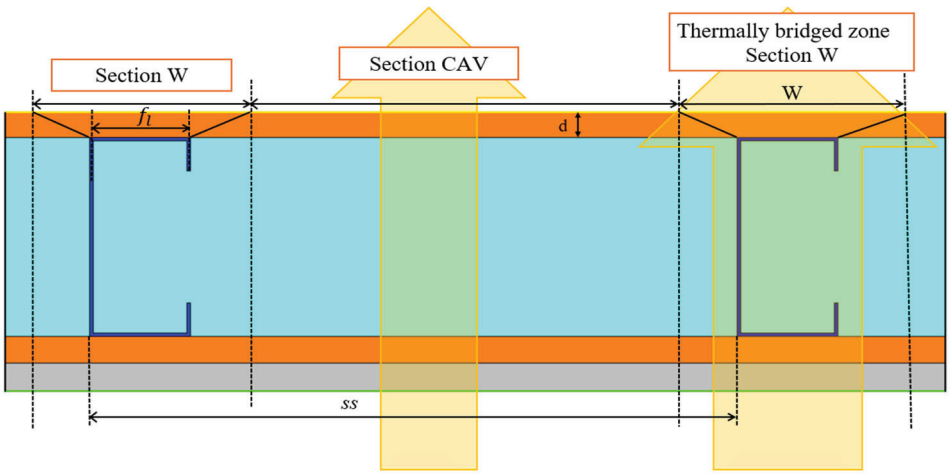

Figure 12. Regions of Section W and Section CAV in LSF wall based on ASHRAE method [13].

The total thermal resistance of the whole system (R_T), is given by Equation (13). This dual correction accounts for both geometric perforation-induced reductions in steel area and flux-based attenuation of thermal conduction, enabling the Modified ASHRAE Zone Method to deliver physically accurate and analytically efficient R-value predictions for discontinuous steel-framed wall systems.

6. Analysis of Results

6.1. Validation of Numerical Models

The developed numerical heat transfer thermal models were validated against the test results from a reference LSF wall specimen (1030 mm × 1060 mm) under steady-state conditions. As shown in Table 3, all predicted R-values (surface-to-surface) deviated by less than 5% from the experimental values, confirming the reliability of the modelling approaches. The Abaqus 3D FE model accurately simulated steady-state heat conduction by resolving 3D heat flux vectors, including anisotropic conduction through steel studs and thermal interface resistances. In contrast, the 2D THERM simulation, constrained by planar assumptions, slightly overestimated thermal resistance by neglecting through-thickness conduction paths and localised multidirectional fluxes near geometric discontinuities. Analytical methods based on NZS 4214 (Isothermal Planes Method) and the ASHRAE Modified Zone Method applied layer-based approximations and frame correction factors to estimate thermal bridging effects. Despite their geometric simplifications, both analytical approaches produced R-values within an acceptable margin of experimental results. The validated models, particularly the 3D Abaqus model, demonstrated sufficient spatial resolution to capture complex thermal bridging phenomena, including localised resistance zones. This good agreement across experimental, numerical, and analytical results establishes a robust basis for evaluating advanced thermal mitigation strategies in LSF wall systems.

Table 3. Validation of R-values against experimental results.

Method	R Value–Non-Perforated LSF Walls (m^2·K/W)	Deviation from Experiment (%)
Experimental reference	1.558	—
Abaqus	1.570	0.77%
THERM	1.632	4.75%
NZS 4214:2016	1.591	2.12%
ASHRAE Modified Zone method	1.579	1.35%

6.2. Thermal Resistance Enhancement in LSF Walls with Perforated Studs

To mitigate thermal bridging in LSF walls, five web perforations were introduced, with a hole diameter of 45 mm and a spacing of 160 mm. The experimentally measured R-value for non-perforated studs was 1.558 m^2·K/W. Numerical simulations incorporating web perforations predicted enhanced R-values in the range of 1.813 to 1.896 m^2·K/W, depending on the evaluation method, as shown in Table 4. These correspond to relative improvements of approximately 15.4% to 16.2%. The enhancement is attributed to a reduction in effective thermal conductivity (k_{eff}), resulting from the replacement of thermally conductive steel sections with air voids in the web region. This alteration elongates the conduction path and interrupts direct heat flow [33]. Consequently, the net heat flux (q) across the wall assembly decreased. The Biot number remained well below unity, confirming a conduction-dominated regime. The efficiency of web perforations in improving thermal resistance is illustrated by the results of the 2D THERM and 3D Abaqus simulations shown in Figure 13.

Among the numerical methods, the highest R value of 1.896 m^2·K/W was achieved by the 2D THERM simulation, representing a 16.18% improvement over its non-perforated counterpart (Figure 14). NZS 4214 and the ASHRAE Modified Zone methods predicted R values of 1.845 and 1.833 m^2·K/W, corresponding to respective improvements of 15.96% and 16.09%. The 3D Abaqus model produced an R value of 1.813 m^2·K/W, indicating a 15.48% increase. Although 2D and analytical models offer computational efficiency, they assume planar conduction and uniform cross-sections, thereby overlooking multidirectional

heat transfer effects that are critical in perforated configurations. In contrast, the 3D modelling approach resolves cross-plane heat fluxes, localized thermal bridging zones, and multiaxial conduction paths, offering a more accurate representation of the thermal behaviour of perforated LSF wall systems [41].

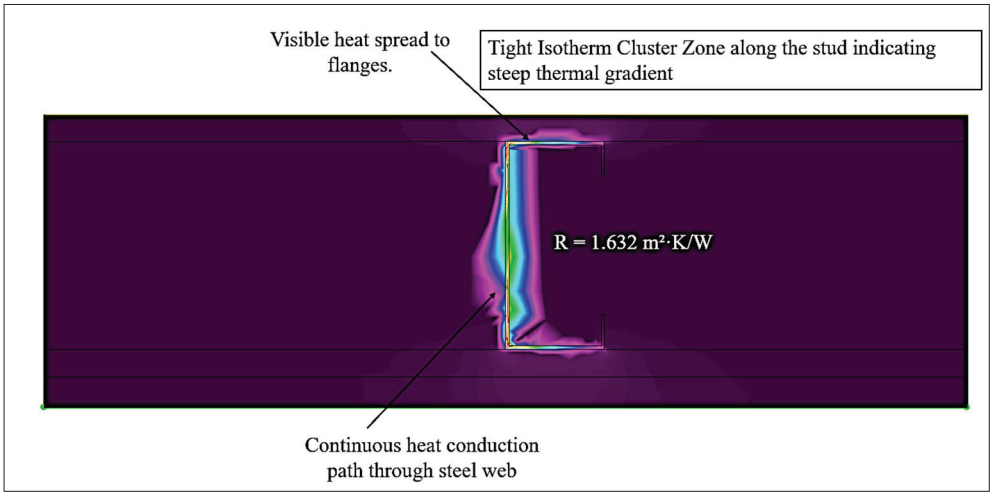

(**a**)

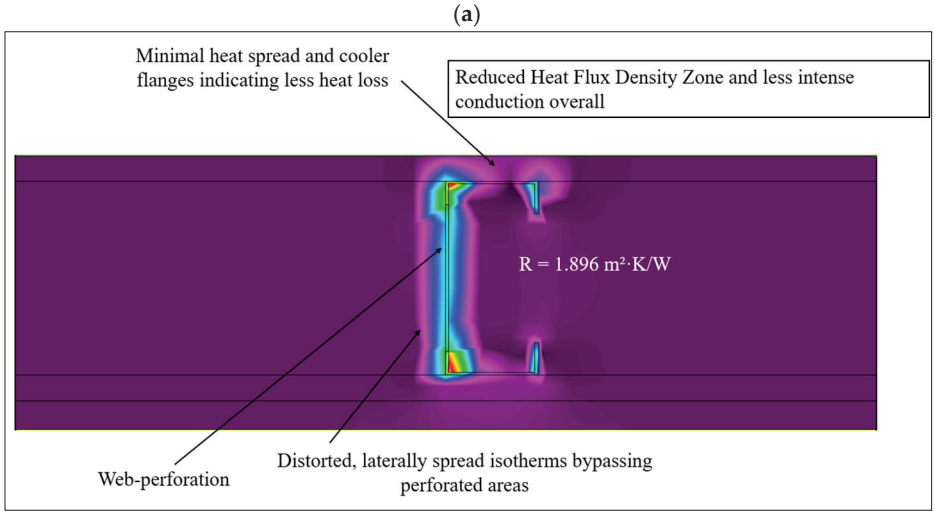

(**b**)

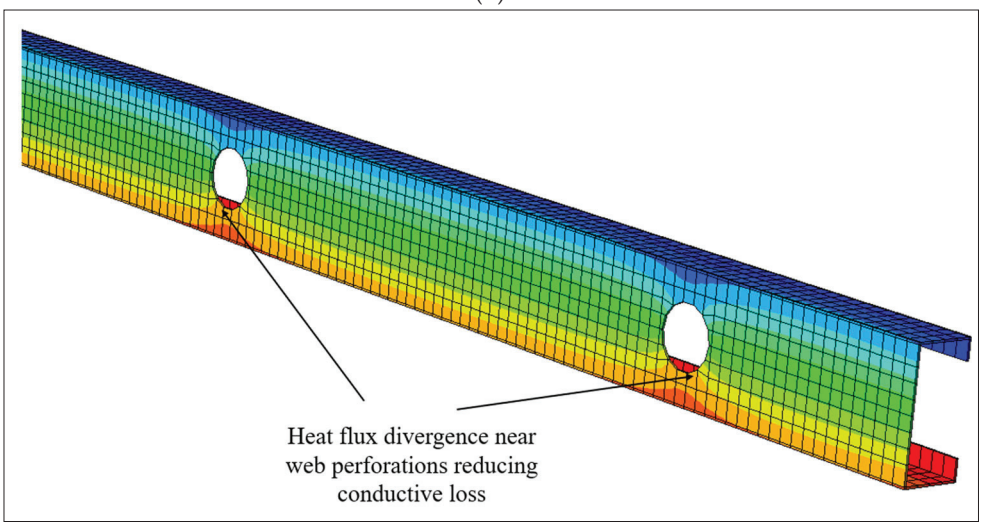

(**c**)

Figure 13. Results of LSF walls: (**a**,**b**) 2D Isotherm and heat flux distribution of a solid and web-perforated stud in THERM model; (**c**) 3D localized resistance zones in Abaqus model.

Table 4. Enhanced R-values of perforated stud walls.

Method	R Value–Web-Perforated LSF Walls ($m^2 \cdot K/W$)	% Improvement of R Value Due to Web-Perforation
Abaqus	1.813	15.48%
THERM	1.896	16.18%
NZS 4214	1.845	15.96%
ASHRAE Modified Zone	1.833	16.09%

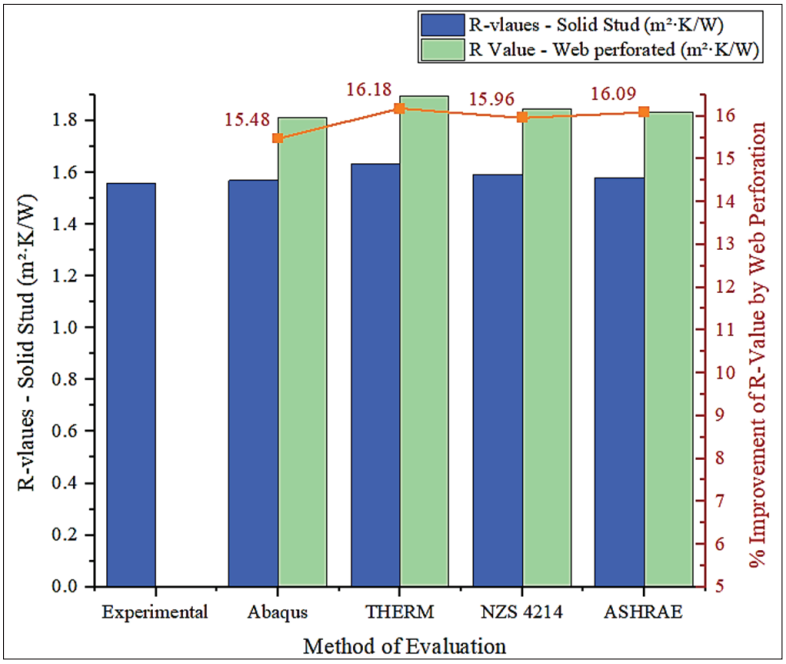

Figure 14. Comparison of R-values.

Figure 15 depicts the thermal response of the non-perforated LSF wall, where uniformly spaced, orthogonal isotherms in the insulation zones signify idealised one-dimensional conduction governed by Fourier's law ($q = -k \nabla T$). As the isotherms approach the steel stud, they bend sharply and become highly compressed, especially within the web, reflecting steep thermal gradients and concentrated axial heat flux. This distortion illustrates anisotropic conduction and confirms the formation of a pronounced thermal bridge, as the high-conductivity steel provides a low-resistance path that short-circuits the surrounding insulation. In contrast, Figure 16 (perforated stud) reveals a disruption in isotherm alignment through the web, where geometric discontinuities attenuate axial conduction and redistribute heat laterally into the adjacent insulation. The contours are more widely spaced within the web zone, indicating increased local resistance and diminished gradient magnitude.

Heat flux vectors in the LSF wall with web perforations demonstrate redistribution of heat flow around the openings, reducing flux density along the stud web and thereby diminishing the strong conduction pathway observed in the non-perforated case. Compared with the directional flux convergence evident in the solid-stud wall, the perforated profile promotes lateral dispersion into the insulation and reduces thermal short-circuiting. Collectively, these behaviours confirm that web perforations shift the conduction balance from stud-dominated to insulation-dominated, thereby enhancing overall thermal resistance.

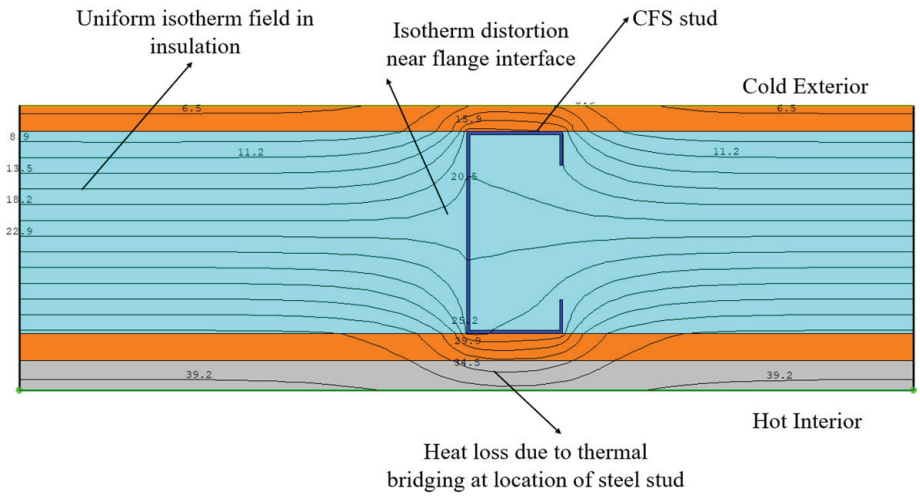

Figure 15. Temperature contours for LSF walls without web perforations in THERM.

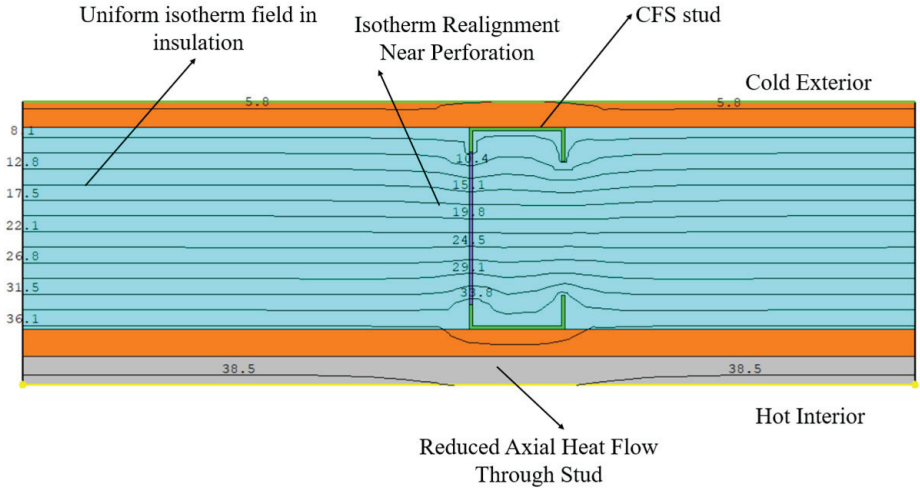

Figure 16. Temperature contours for LSF walls with web perforations in THERM.

6.3. Thermal Performance of 3 m High LSF Walls

6.3.1. Walls with Non-Perforated Steel Studs

To simulate actual construction conditions and extend thermal analysis beyond laboratory scale, a 3 m high and 1.2 m wide LSF wall with non-perforated steel studs was modelled using the same configuration as the validated 1030 mm × 1060 mm wall assembly. Material layers, sheathing, and stud spacing were held constant. The Abaqus model predicted an R-value of 1.55 m^2·K/W, showing a slight reduction compared to the 1030 mm wall which recorded 1.57 m^2·K/W. The THERM model yielded 1.621 m^2·K/W for both cases, while the NZS 4214 and ASHRAE Modified Zone methods reported values of 1.59 and 1.583 m^2·K/W, respectively. The marginal decrease observed in Abaqus model is attributed to enhanced numerical resolution of temperature gradients along the extended steel conduction path. Greater nodal density enabled the model to capture localised flux intensification near steel and sheathing interfaces, increasing the computed heat flow and slightly reducing net resistance. Analytical methods, which apply simplified planar assumptions, remained unaffected by stud height variation. These findings validate the thermal scalability of non-perforated LSF walls and established a reference case for subsequent evaluation of web-perforated configurations in full-height assemblies.

6.3.2. Walls with Perforated Steel Studs

Following the validation of the 3 m high non-perforated LSF wall, a similar wall with web-perforated steel studs was modelled to assess the impact of perforations on thermal resistance. Various configurations of web perforations were analysed with diameters (d) varying from 36 mm to 68 mm, spacing from 200 mm to 450 mm, and the number of perforations ranging from 5 to 12 per stud using Abaqus FE simulations, as well as comparative assessments through THERM, NZS 4214 and ASHRAE Modified Zone methods. In all cases, the edge distance from the hole centre was maintained between 3d to 4d based on AS/NZS 4600 and NASH guidelines. Among all configurations, the layout comprising 68 mm diameter holes spaced at 200 mm with 10 perforations as shown in Figure 17, produced the highest thermal resistance of 1.892 $m^2 \cdot K/W$, corresponding to a 20.06% increase compared to the non-perforated reference wall.

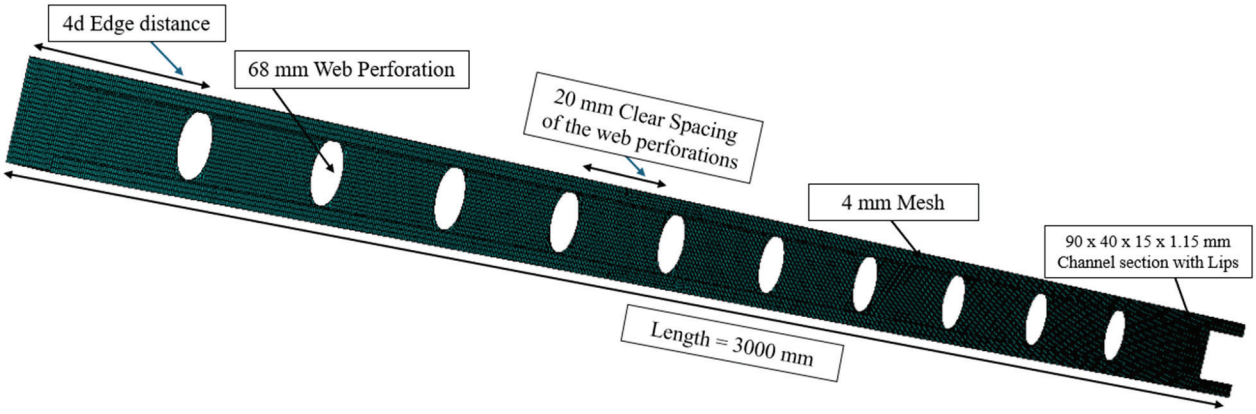

Figure 17. Stud configuration yielding maximum thermal resistance in Abaqus.

The R-value results from NZS 4214 and ASHRAE Modified Zone methods, as well as THERM 2D simulations, were compared against the 3D Abaqus FE simulations for 120 configurations. The models accounted for perforation-induced changes in cross-sectional area and flux distribution. Validation followed ISO 10211 using mean and coefficient of variation (COV) metrics. THERM and Abaqus results closely matched with a mean ratio of 1.0003 and COV of 0.0116. NZS 4214 and ASHRAE slightly overpredicted R-values, with mean values of 1.0277 and 1.0146, and COVs of 0.0085 and 0.0075, respectively. This confirms good agreement and low variability for configurations as shown in Figure 18. The error in R-value predictions across models was small. THERM and Abaqus results matched closely, with a mean deviation below 0.05% (ratio = 1.0003). The NZS 4214 method slightly overpredicted, with an average error of 2.8%, while the ASHRAE Modified Zone method showed a 1.5% overestimation. The coefficients of variation ($\leq$0.012) confirm that the variability across the 120 configurations was negligible.

Furthermore, to assess the structural performance of 3 m high LSF walls under compression, structural FE models were developed using Abaqus using an established method used by several researchers [35,42]. An experimentally tested non-perforated stud lined on both sides was selected as the reference [32], and its geometry and boundary conditions were replicated in the model as shown in Figure 19. Elastic buckling analysis was first conducted, using which appropriate geometric imperfections were incorporated, followed by a nonlinear analysis. The non-perforated stud achieved a load capacity of 82.13 kN, showing good agreement with the experimental result of 79 kN and confirming the validity of the structural FE model.

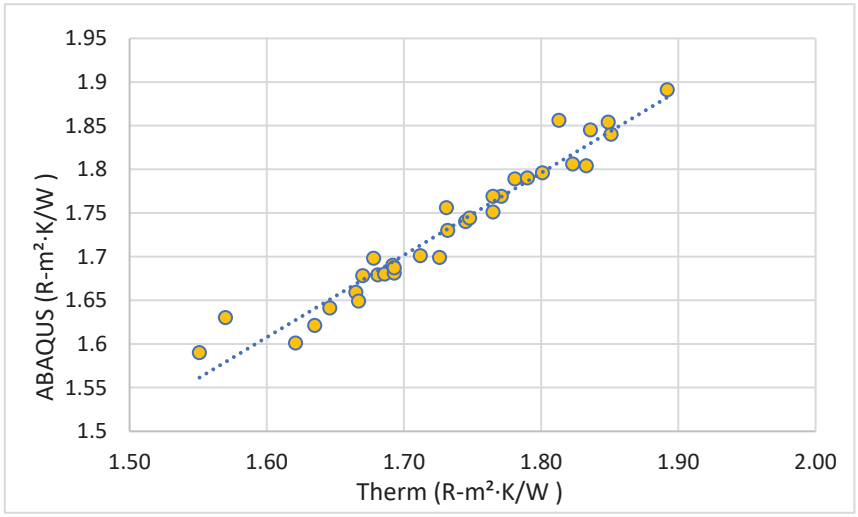

(**a**)

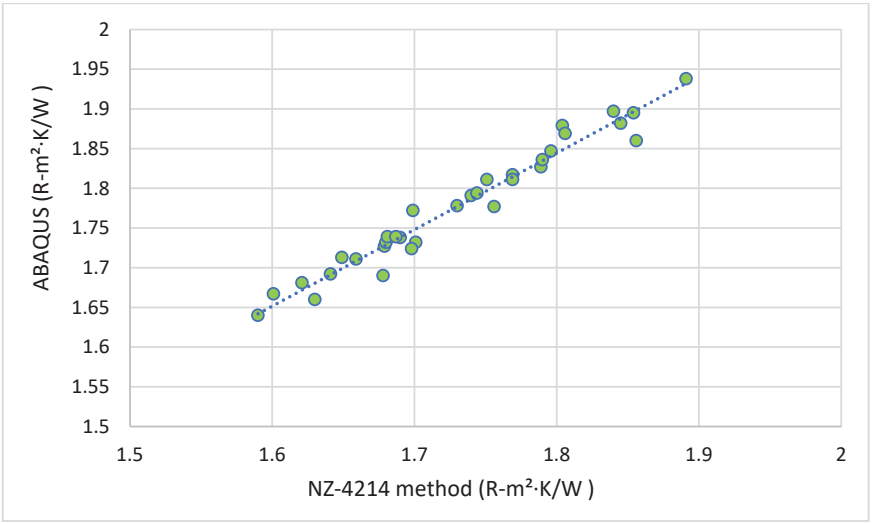

(**b**)

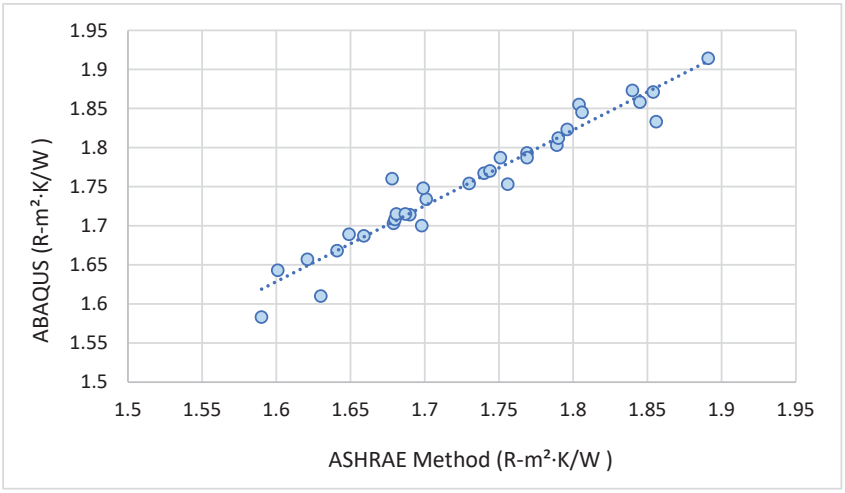

(**c**)

Figure 18. Comparison of R-values of web-perforated stud walls between Abaqus model and (**a**) THERM models (**b**) modified NZ4214 method (**c**) modified ASHRAE method.

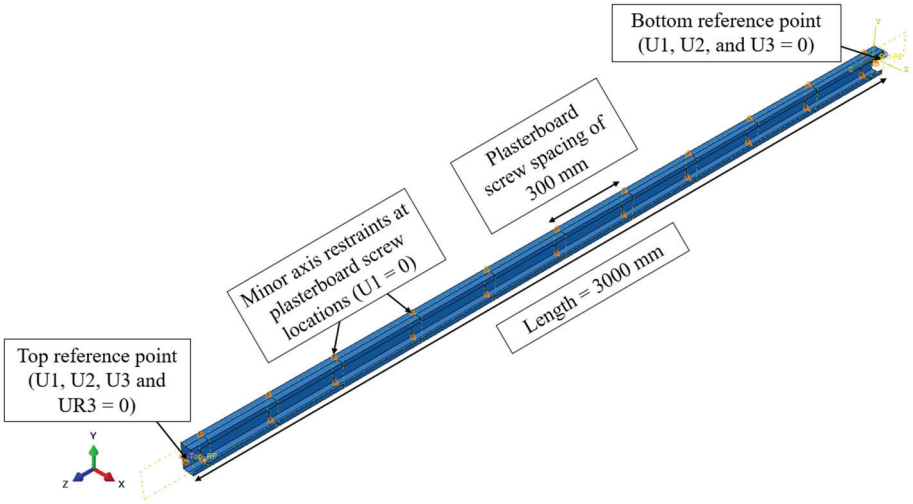

Figure 19. Structural FE model of non-perforated stud.

Following this validation, the same stud geometry was modified to incorporate web perforations. The thermally optimised configuration, incorporating 68 mm diameter holes spaced at 200 mm and comprising 10 perforations, reduced the axial compression load capacity to 57.89 kN, i.e., 29.51% reduction compared to non-perforated stud. This reduction was primarily due to the removal of web material and the associated increase in local buckling susceptibility around the perforated regions. To address this issue, 4 mm long stiffeners were used around the holes, as shown in Figure 20. This modification preserved thermal gains, maintaining a 15.3% increase in R-value, while significantly improved the axial capacity to 78.36 kN, i.e., with only 3.2% reduction.

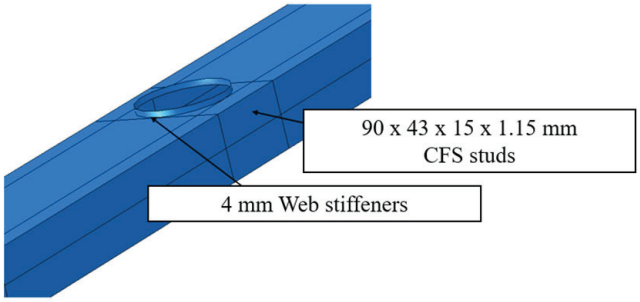

Figure 20. Studs with 4 mm web-hole stiffeners.

6.4. Thermal Performance of External LSF Walls with Fire-Rated Facades and Web-Perforated Studs

The thermal performance of five external LSF wall systems was evaluated to determine the effectiveness of web-perforated CFS studs in enhancing R values under Australian climatic conditions. Each wall configuration included a fire-rated external façade systems as shown in Figure 21, consisting of 75 mm Autoclaved aerated concrete (AAC) panel, 0.42 mm profiled steel sheeting, 5 mm aluminium composite panel (ACP), 25 mm fire-rated glass, and 110 mm brick veneer. The façade systems considered in this study represent a broad spectrum of practical applications: AAC panels are widely used in lightweight masonry construction for their insulation and fire resistance; corrugated steel sheeting is common in residential and industrial claddings for its durability; ACP's are prevalent in commercial façades as lightweight, non-combustible cladding with architectural flexibility; fire-rated glass is employed in façades and curtain walls to provide natural lighting while maintaining fire protection; and ventilated clay brick veneer is used in residential and institutional buildings, combining the appearance of traditional masonry with cavity ventilation for

improved thermal and moisture performance. They were selected based on their prevalence in contemporary Australian facade systems and compliance with NCC 2022 fire and energy efficiency requirements. Their material properties are summarised in Table 5. All wall systems were constructed using a 3 m high LSF wall assembly with CFS framing and cavity insulation to ensure consistency across simulations. Steady-state thermal simulations were conducted in Abaqus using validated FE models of external LSF walls under a temperature gradient of 35 °C, with 40 °C applied externally and 5 °C internally. The studied configuration incorporated 68 mm diameter web perforations at 200 mm spacing, each locally stiffened with 4 mm edge plates to preserve load-bearing capacity.

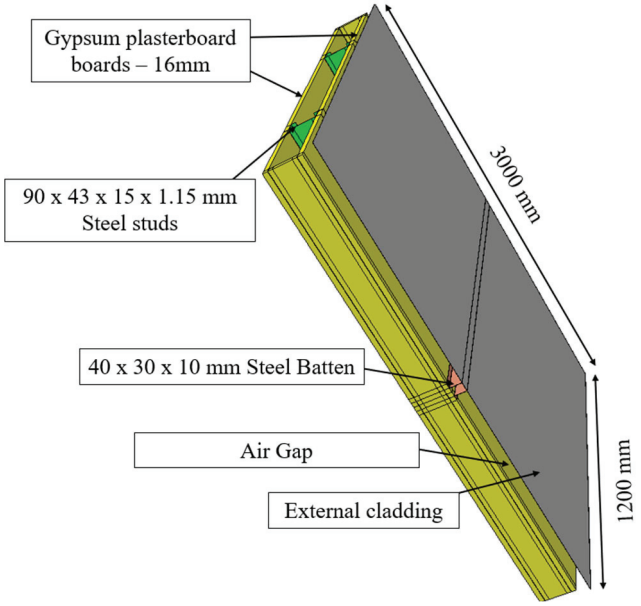

Figure 21. External LSF wall with cladding in Abaqus.

Table 5. Physical and material properties of external cladding materials.

Material	Description	Thickness (mm)	Thermal Conductivity (W/m·K)
AAC	Lightweight cellular concrete panel	75	0.14
Profiled Steel Cladding	Zinc-coated profiled steel cladding (BMT 0.42 mm)	0.42	51
ACP	Non-combustible A1-grade panel with mineral core	5.0 (total)	0.40 (effective)
Fire-Rated Glazing	Laminated fire-resistive glass with intumescent core	25	1.0 (overall)
Brick Veneer	External clay brick masonry	110	0.7

As shown in Tables 6–10 and Figures 22–31, five external wall types were assessed using Abaqus, THERM, NZS 4214, and the ASHRAE Modified Zone Method. Both perforated and non-perforated stud wall assemblies were analysed to evaluate the influence of web openings on thermal resistance. R-values for non-perforated walls ranged from 2.05 to 2.83 m^2·K/W, increasing to values between 2.65 and 3.27 m^2·K/W for perforated walls. THERM consistently predicted higher values due to its 2D simplification, while Abaqus produced lower but more representative results by including multidirectional conduction. NZS 4214 and ASHRAE methods yielded intermediate values consistent with composite wall behaviour under steady-state conditions.

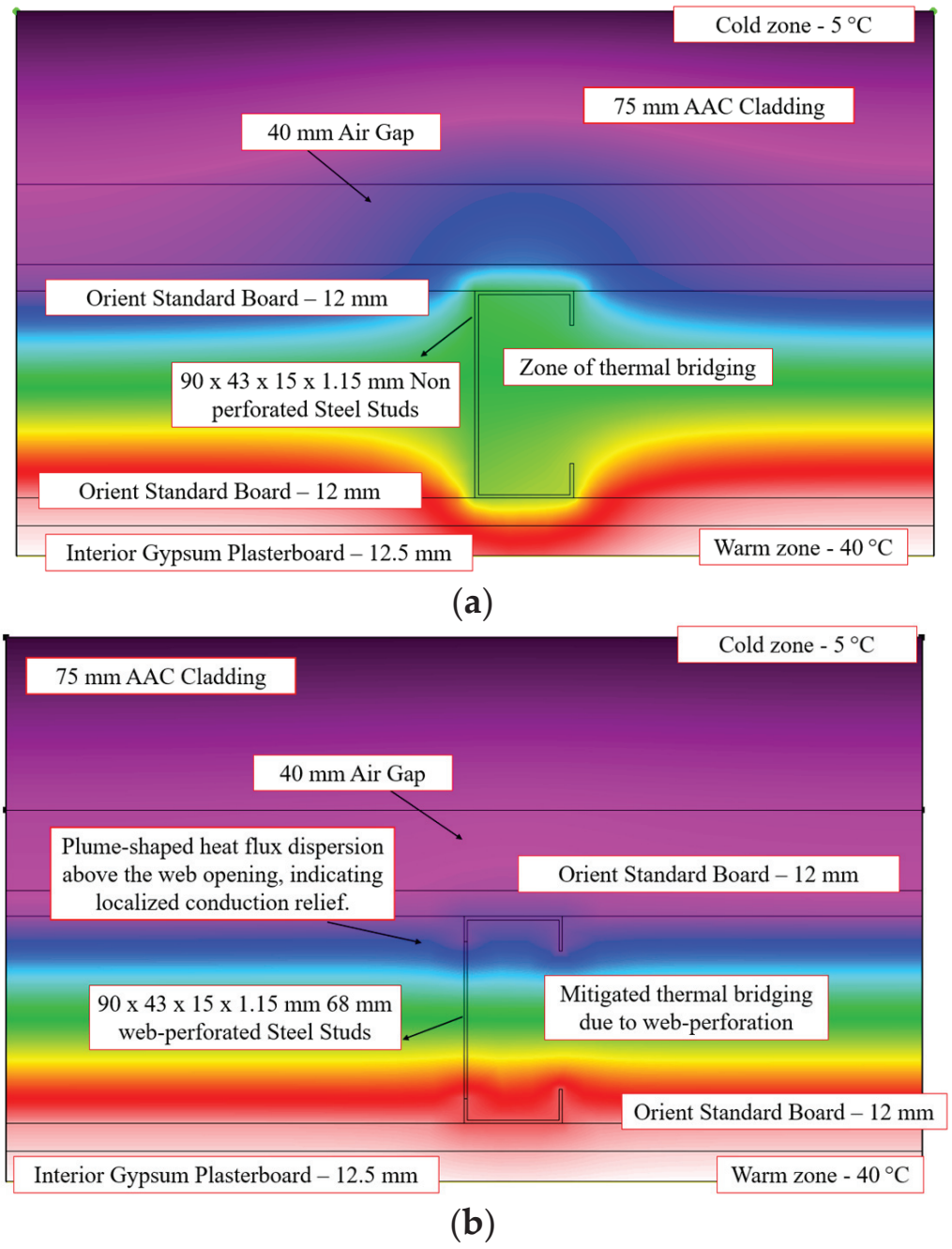

Figure 22. Heat flux behaviour in AAC-Clad external LSF wall with (**a**) non-perforated and (**b**) web-perforated studs.

Table 6. Thermal resistance of AAC-Clad LSF walls with and without web perforations.

External Wall Type	Method	R (Non-Perforated) (m^2·K/W)	R (Perforated) (m^2·K/W)	% Improvement
AAC Cladding	Abaqus	2.71	3.12	15.13
	THERM	2.83	3.27	15.50
	NZS 4214	2.77	3.21	15.88
	ASHRAE Modified Zone	2.73	3.18	16.48

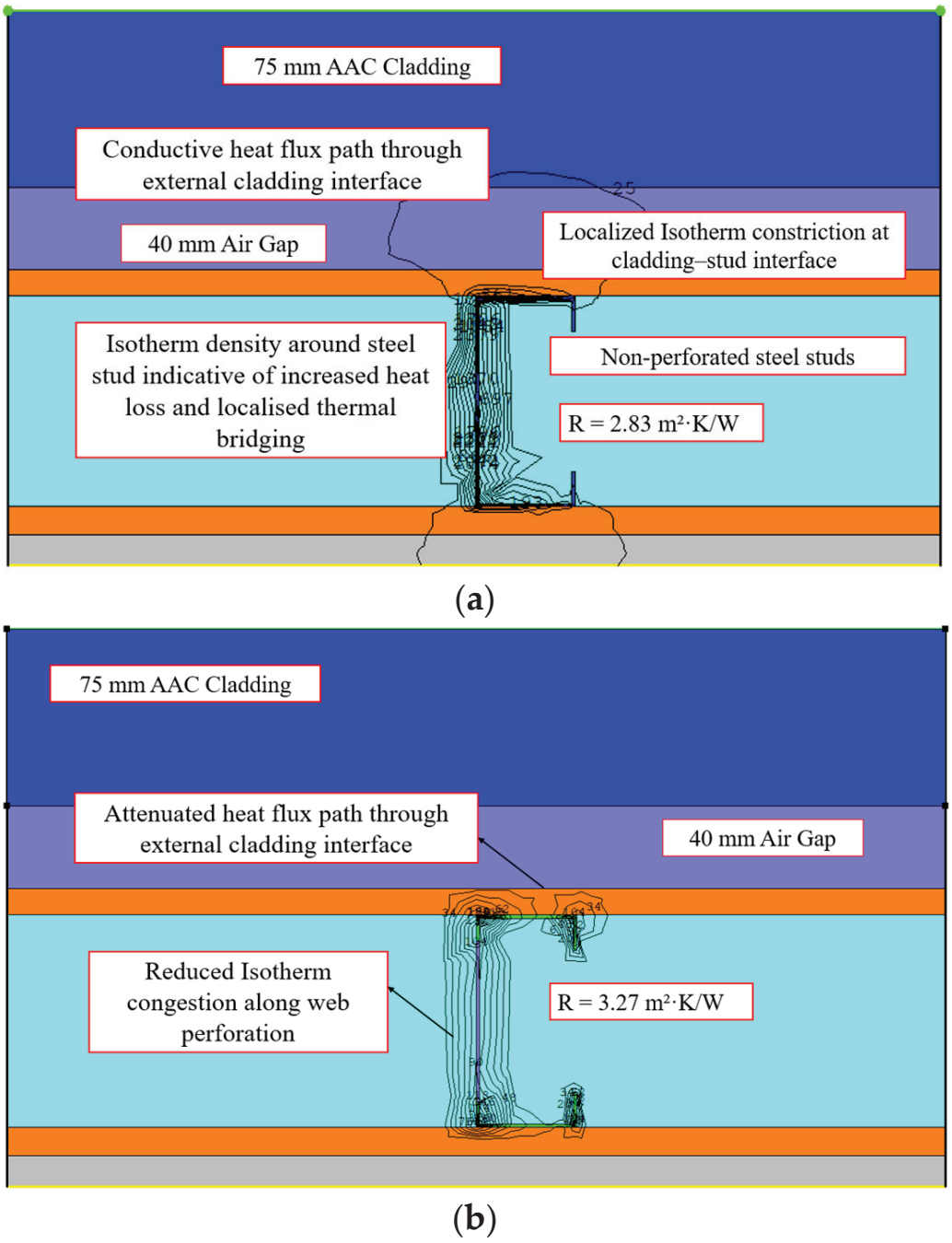

Figure 23. Isotherm distribution in AAC-Clad external LSF Wall with (**a**) non-perforated and (**b**) web-perforated studs.

Table 7. Thermal resistance of profiled steel-clad LSF walls with and without web perforations.

External Wall Type	Method	R (Non-Perforated) (m^2·K/W)	R (Perforated) (m^2·K/W)	% Improvement
Profiled Steel Cladding	Abaqus	2.32	2.67	15.09%
	THERM	2.41	2.79	15.77%
	NZS 4214	2.35	2.75	17.02%
	ASHRAE Modified Zone	2.33	2.74	17.60%

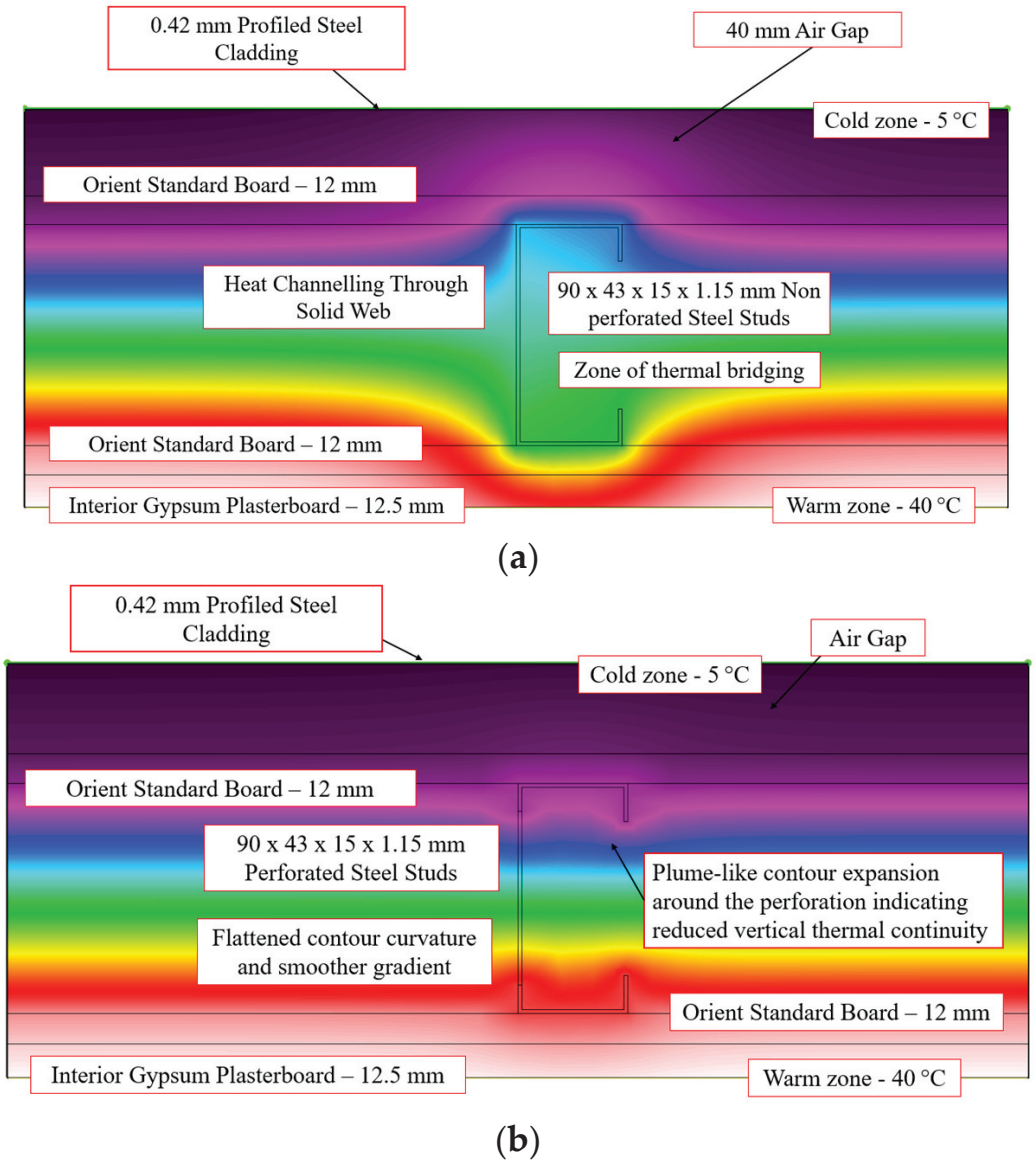

Figure 24. Heat flux behaviour in profiled steel-clad external LSF wall with (**a**) non-perforated and (**b**) perforated studs.

Table 8. Thermal resistance of ACP-clad LSF walls with and without web perforations.

External Wall Type	Method	R (Non-Perforated) ($m^2 \cdot K/W$)	R (Perforated) ($m^2 \cdot K/W$)	% Improvement
ACP Cladding	Abaqus	2.68	3.109	15.99%
	THERM	2.76	3.2	15.94%
	NZS 4214	2.71	3.16	16.61%
	ASHRAE Modified Zone	2.67	3.14	17.60%

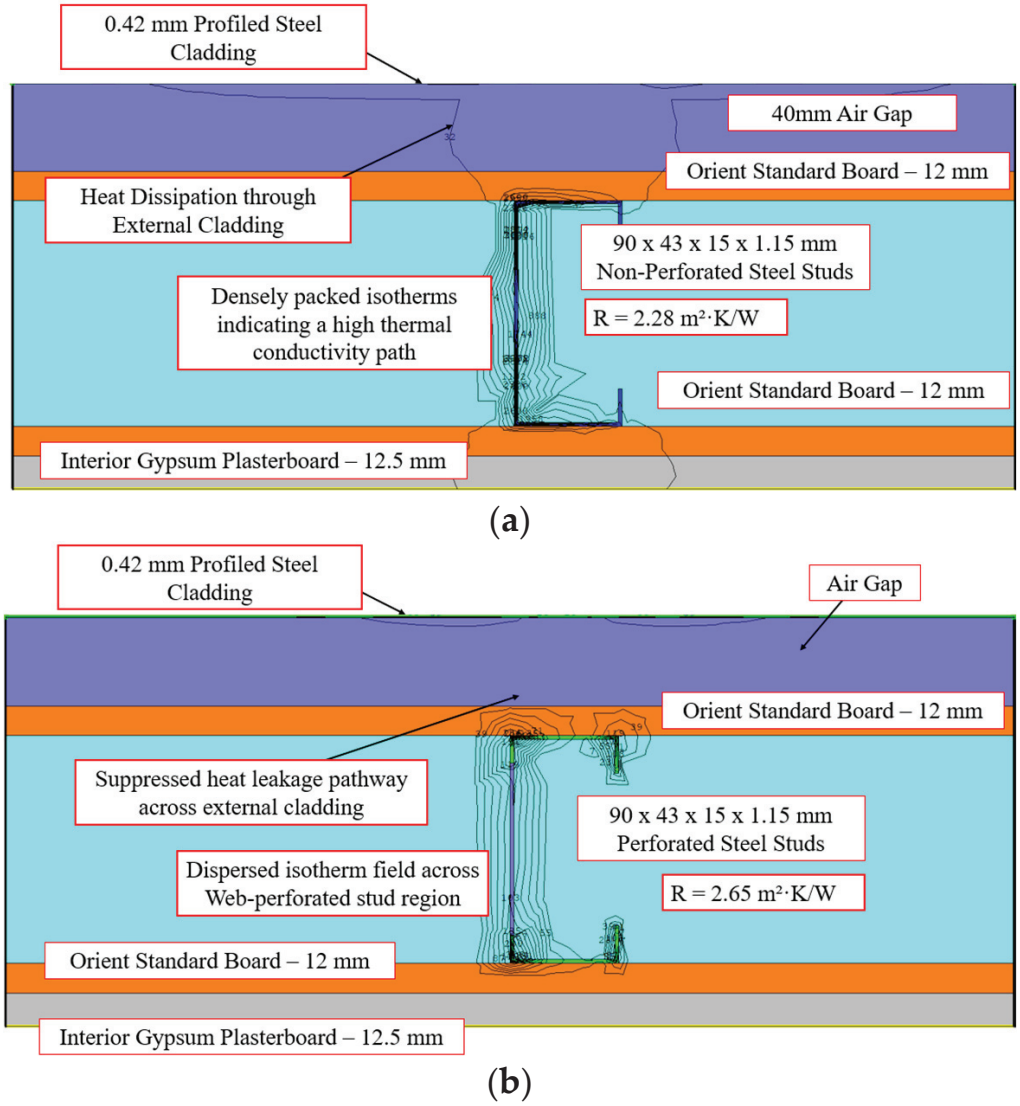

Figure 25. Isotherm distribution in profiled steel-clad external LSF wall with (**a**) non-perforated and (**b**) web-perforated studs.

Table 9. Thermal resistance of fire-rated glazing-clad LSF walls with and without web perforations.

External Wall Type	Method	R (Non-Perforated) (m^2·K/W)	R (Perforated) (m^2·K/W)	% Improvement
Fire-Rated Glazing Cladding	Abaqus	2.61	3	14.94%
	THERM	2.71	3.14	15.87%
	NZS 4214	2.65	3.09	16.60%
	ASHRAE Modified Zone	2.61	3.08	17.62%

Table 10. Thermal resistance of brick veneer-clad LSF walls with and without web perforations.

External Wall Type	Method	R (Non-Perforated) (m^2·K/W)	R (Perforated) (m^2·K/W)	% Improvement
Fire-Rated Glazing Cladding	Abaqus	2.57	2.95	14.79%
	THERM	2.70	3.13	15.93%
	NZS 4214	2.67	3.11	16.48%
	ASHRAE Modified Zone	2.64	3.10	17.42%

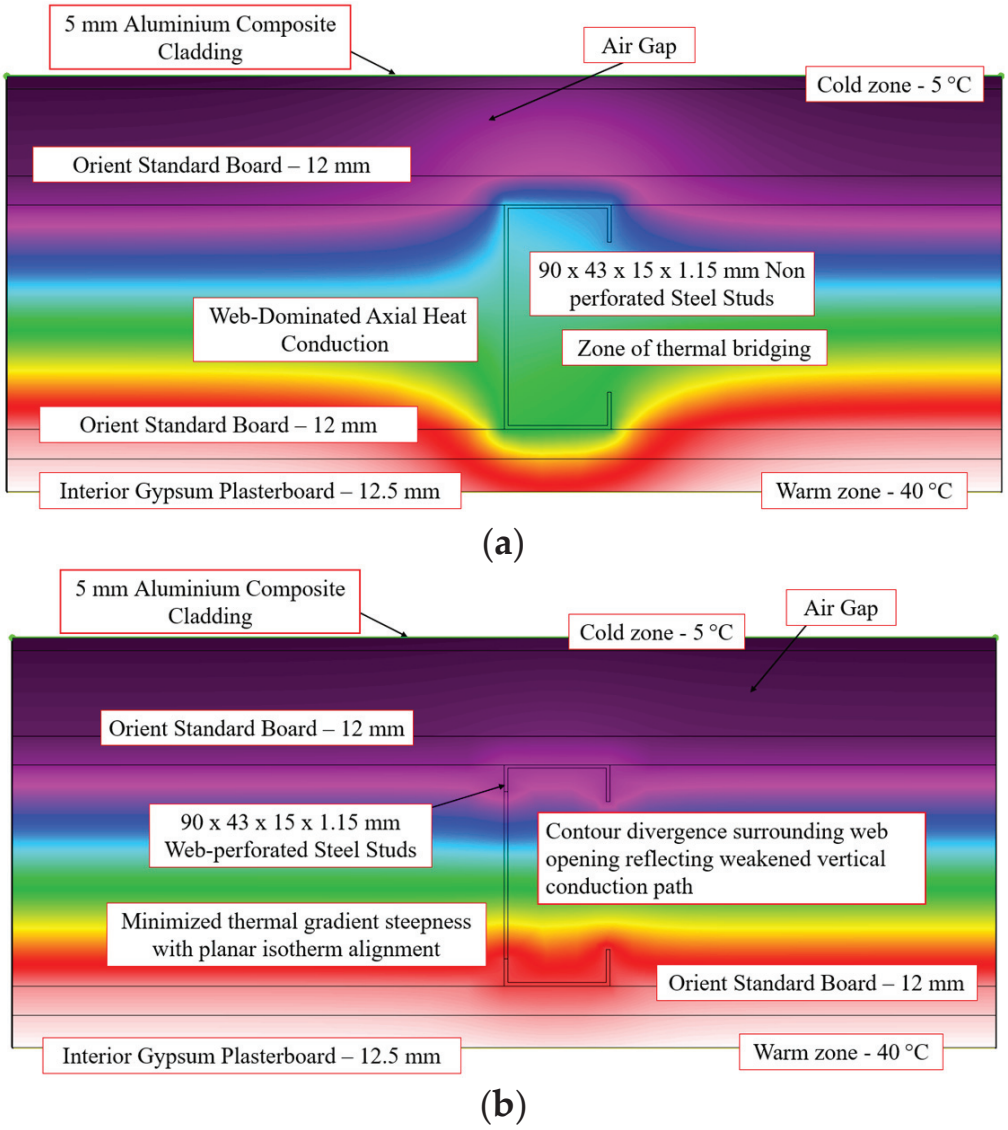

Figure 26. Heat flux behaviour in ACP-clad external LSF Wall with (**a**) non-perforated and (**b**) perforated studs.

6.4.1. External LSF Wall with AAC External Cladding

In AAC-clad LSF walls, the 75 mm aerated concrete layer attenuates surface heat flux through low-conductivity, high-porosity material, suppressing conductive transport at the cladding-cavity interface. In the non-perforated case, the 90 × 43 × 15 × 1.15 mm steel stud acts as a dominant thermal bridge, concentrating axial conduction through the web, as evidenced by steep gradients and compressed isotherms at the AAC–stud and flange–cladding junctions (Figure 22). R-values across methods range from 2.71 to 2.83 m^2·K/W.

Introducing 68 mm web perforations interrupts the longitudinal heat pathway, promoting lateral flux redistribution into adjacent insulation. As shown in Figure 23, perforations induce plume-shaped diffusion fields and smoother isothermal gradients across the stud–cavity domain. This geometry increases thermal resistance to 3.12–3.27 $m^2 \cdot K/W$, reflecting a 15.13 to 16.48% improvement. Perforations thus reduce directional conduction continuity, enabling more uniform energy transport and enhancing the thermal resistance of the wall system.

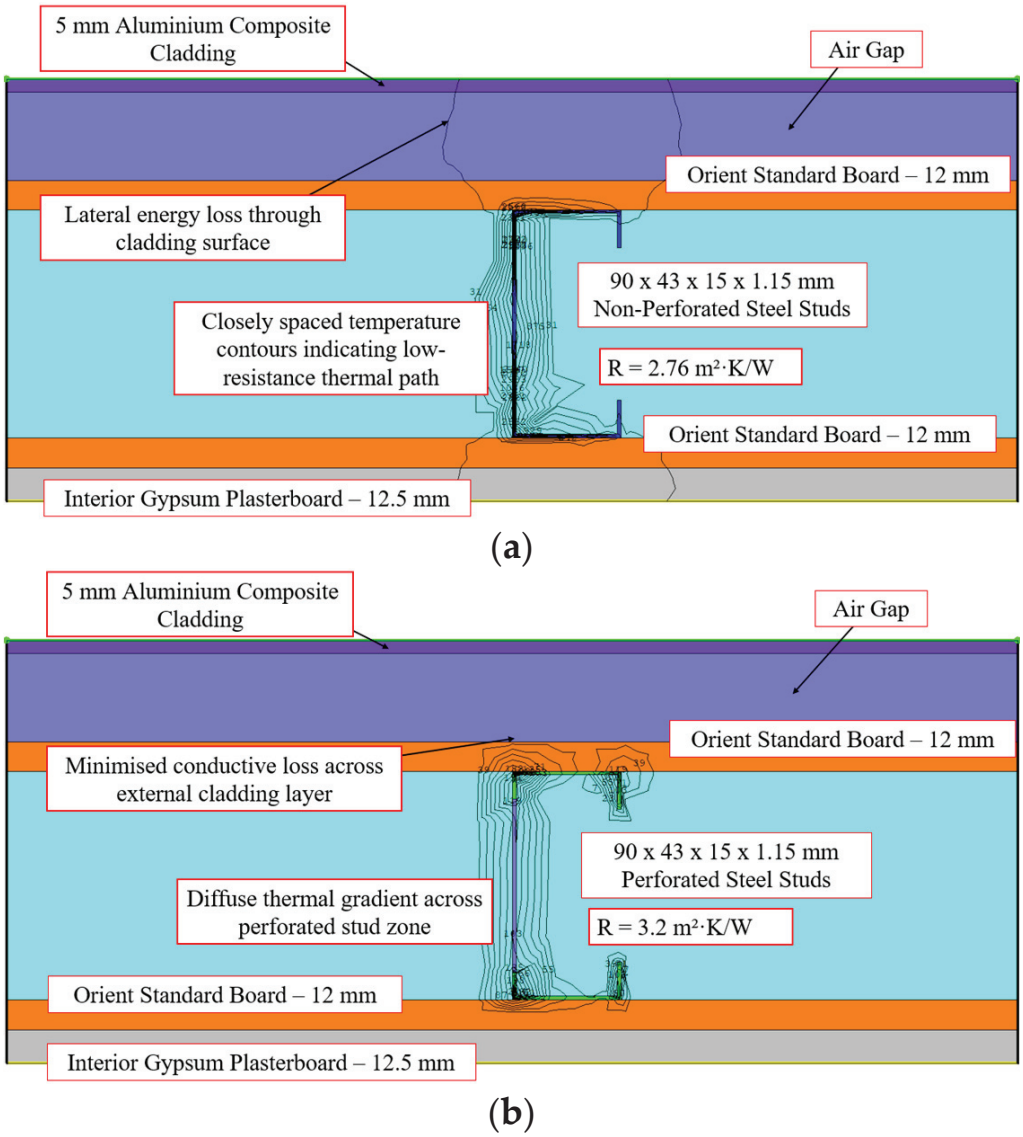

Figure 27. Isotherm distribution in ACP-clad external LSF wall with (**a**) non-perforated and (**b**) web-perforated studs.

In profiled steel-clad LSF walls, heat transfer is dominated by axial conduction through the steel frame. In the non-perforated stud configuration, vertically aligned isotherms and steep gradients at the cladding–flange and base junctions indicate strong directional heat flow and concentrated thermal bridging (Figure 24). This yields R-values between 2.32 and 2.41 $m^2 \cdot K/W$. Introducing 68 mm web perforations disrupts the primary conduction path, promoting lateral thermal diffusion into the insulation. As shown in Figure 25, this results in flattened isotherms, reduced flux density, and suppressed thermal plumes at boundary zones. Thermal resistance increases to 2.67–2.79 $m^2 \cdot K/W$, reflecting a 15.09 to

17.60% improvement. The enhancement stems from geometric redirection of heat flux, reducing anisotropic conduction and improving overall energy attenuation.

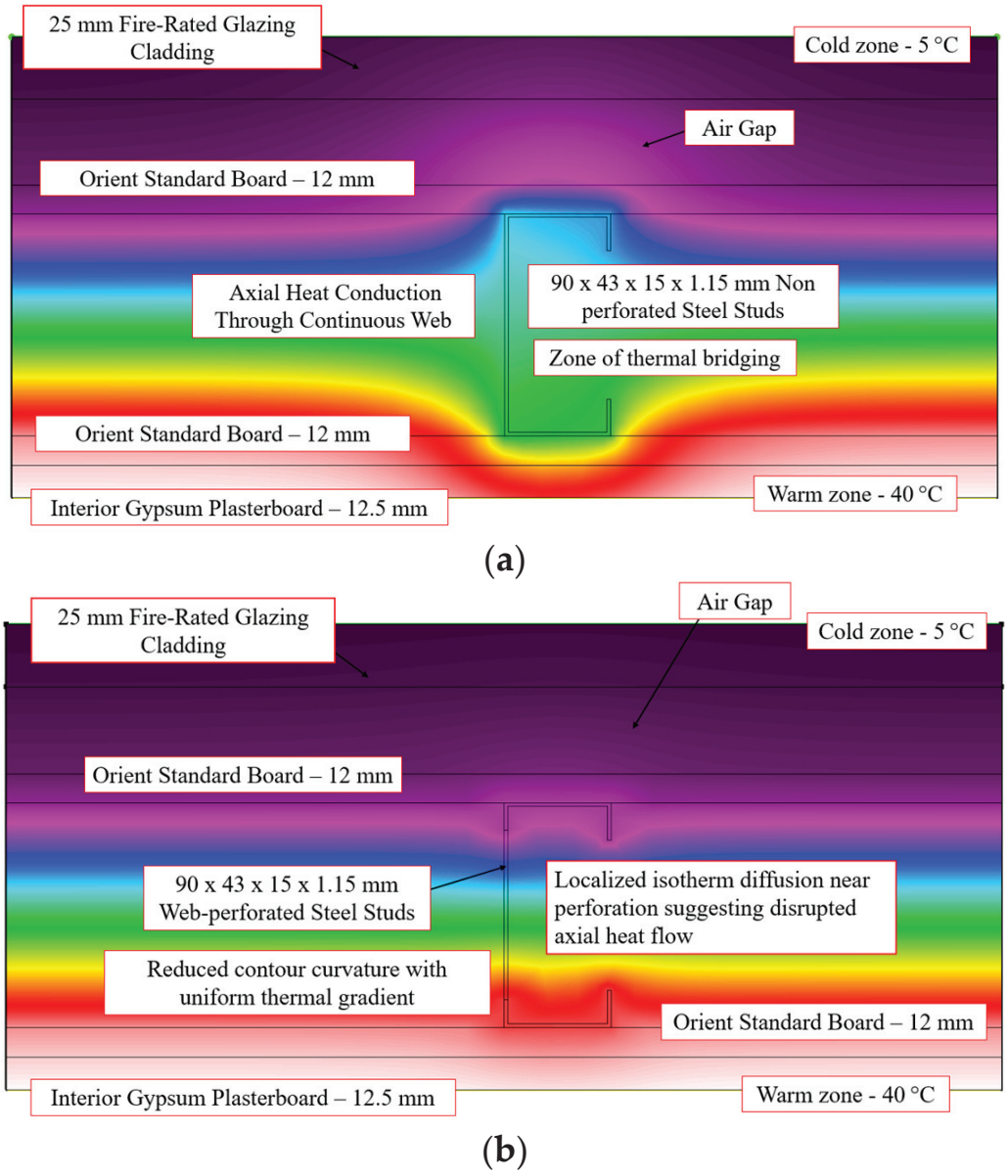

Figure 28. Heat flux behaviour in fire-rated glazing-clad external LSF wall with (**a**) non-perforated and (**b**) perforated studs.

6.4.2. External LSF Wall with 0.42 mm Profiled Steel Cladding

6.4.3. External LSF Wall with 5 mm Aluminium Composite Panel (ACP) Cladding

In ACP-clad LSF walls, the 5 mm high-conductivity external layer facilitates lateral heat dissipation, particularly at batten–cladding interfaces. In the non-perforated configuration, axial conduction dominates through the continuous steel web as shown in Figure 26, producing steep thermal gradients and compressed isotherms across the stud zone. This concentrated flux pathway lowers thermal resistance, yielding R-values from 2.67 to 2.76 $m^2 \cdot K/W$. Introducing 68 mm web perforations disrupts this vertical conduction path, promoting planar isotherm alignment and lateral diffusion into the insulation layer. As shown in Figure 27 the resulting thermal field, plume suppression and distributed flux patterns emerge around the perforations. This geometric interruption enhances the thermal performance, raising R-values to 3.109–3.20 $m^2 \cdot K/W$ and achieving a 15.94% to 17.60% in-

crease. These results confirm that web perforations act as passive thermal breaks, reducing axial conduction and enhancing lateral energy attenuation across the steel–ACP interface.

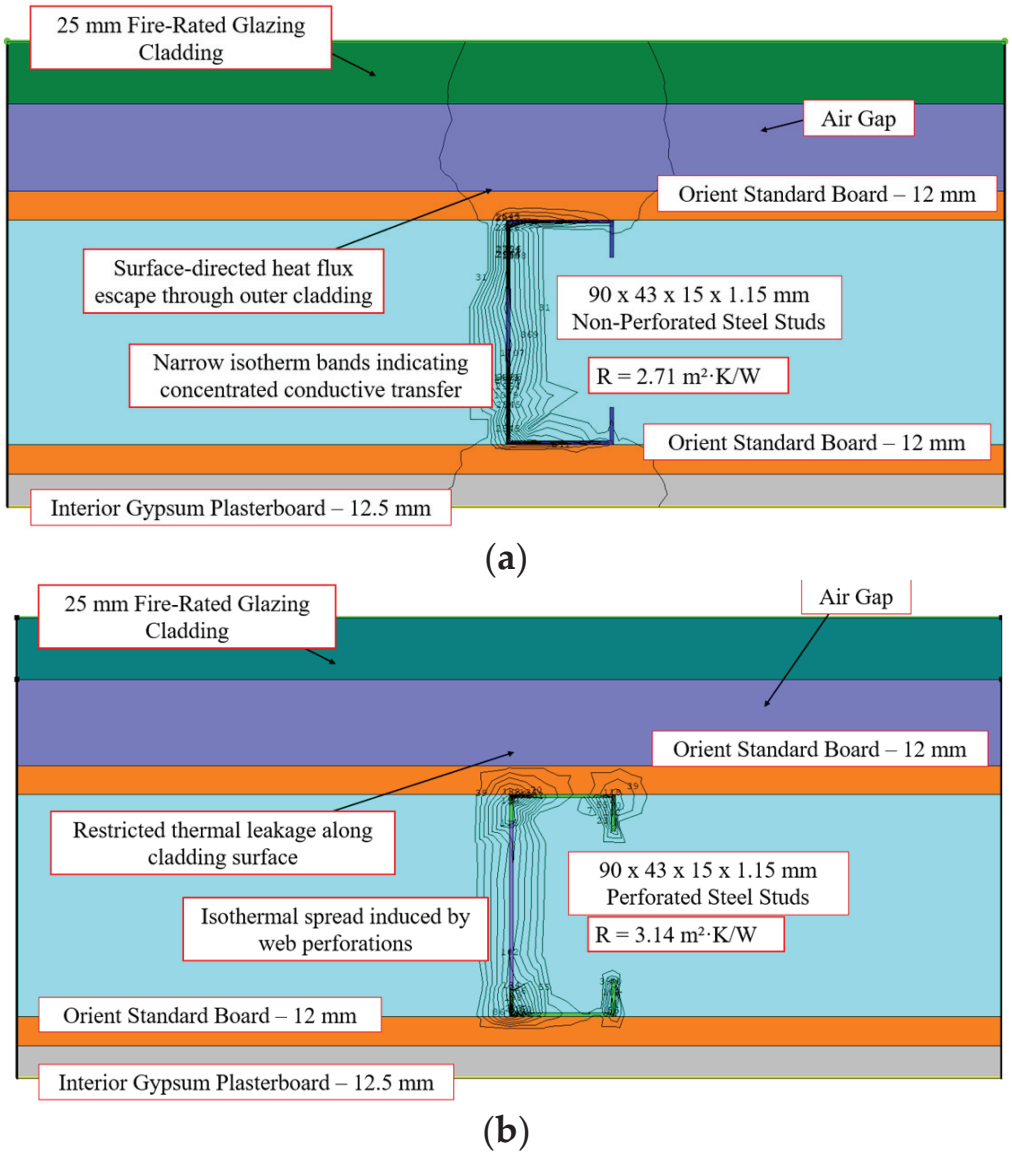

Figure 29. Isotherm distribution in fire-rated glazing-clad external LSF Wall with (**a**) non-perforated and (**b**) web-perforated studs.

6.4.4. External LSF Wall with 25 mm Fire-Rated Glazing Cladding

In fire-rated glazing-clad LSF walls, the 25 mm glass layer provides moderate thermal resistance, but permits considerable heat transmission due to its relatively high thermal conductivity. In the non-perforated configuration, vertically stratified isotherms concentrate along the stud web, with peak thermal gradients at the flange–cladding interface and stud base (Figures 28a and 29a), indicating dominant axial conduction. This constrained thermal field yields R-values between 2.61 and 2.71 $m^2 \cdot K/W$. Introducing 68 mm web perforations interrupts the vertical conduction stream, promoting lateral heat diffusion into surrounding insulation. As shown in Figures 28b and 29b, the isotherm field becomes less aligned and more dispersed, with reduced curvature near perforations. Plume suppression at critical junctions and reoriented thermal gradients enhance energy attenuation across the stud–glazing interface. The resultant R-values increase to 3.00–3.14 $m^2 \cdot K/W$, corresponding to a 14.94–17.62% improvement. This confirms the role of perforations in

redistributing flux, mitigating axial conduction, and improving the thermal performance of fire-glazed assemblies.

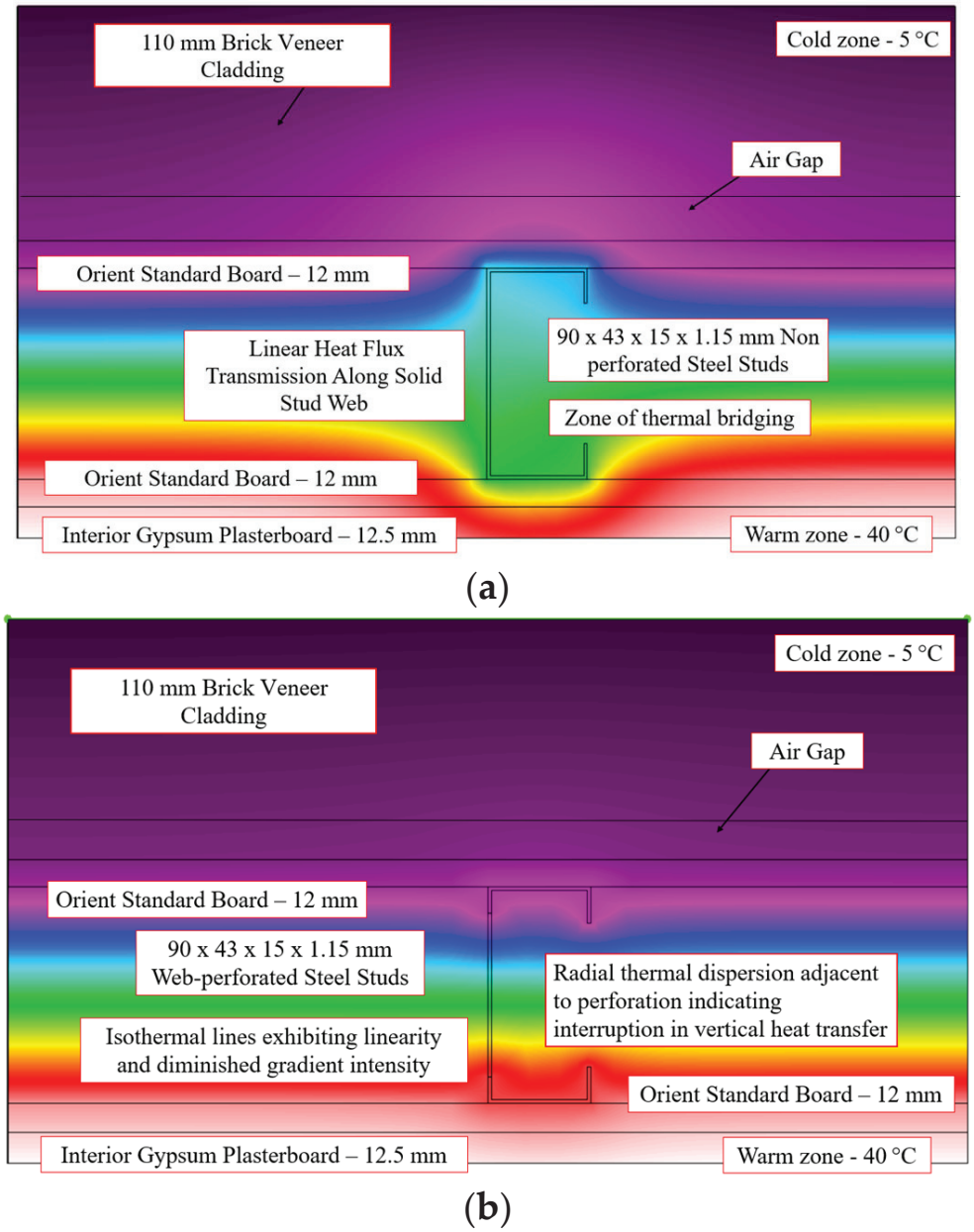

Figure 30. Heat flux behaviour in brick veneer-clad external LSF wall with (**a**) non-perforated and (**b**) perforated studs.

6.4.5. External LSF Wall with 110 mm Brick Veneer Cladding

In brick veneer-clad LSF walls, the thermal field is shaped by the high thermal mass and moderate conductivity of the 110 mm external masonry layer. In the non-perforated configuration, axial conduction dominates along the steel web, with dense isotherms and steep gradients forming a narrow conduction channel from exterior to interior (Figures 30 and 31). These concentrated flux pathways yield R-values between 2.57 and 2.70 $m^2 \cdot K/W$. Introducing 68 mm web perforations interrupts this direct conduction stream, enhancing lateral thermal diffusion into the surrounding insulation. As shown in Figures 30b and 31b, isotherms exhibit radial dispersion around the perforations, reduced curvature, and broadened thermal contours, especially near flange and floor junctions. These modifications redistribute the thermal gradient and suppress interface

leakage. The improved energy spread raises R-values to 2.95–3.13 m^2·K/W, corresponding to a 14.79–17.42% improvement. This confirms that geometric disruption of axial heat paths enhances thermal resistance, even under heavy cladding conditions where mass effects dominate.

Comparative thermal analysis of five external LSF wall systems demonstrates that incorporating web-perforated studs consistently enhances thermal resistance across all cladding types. Among them, AAC and profiled steel exhibited high R-value gains. Overall, web-perforated CFS studs act as effective thermal modifiers by altering conduction path geometry and promoting distributed flux, delivering R-value gains based on the results of Abaqus, THERM, NZS4214 and ASHRAE Modified Zone methods.

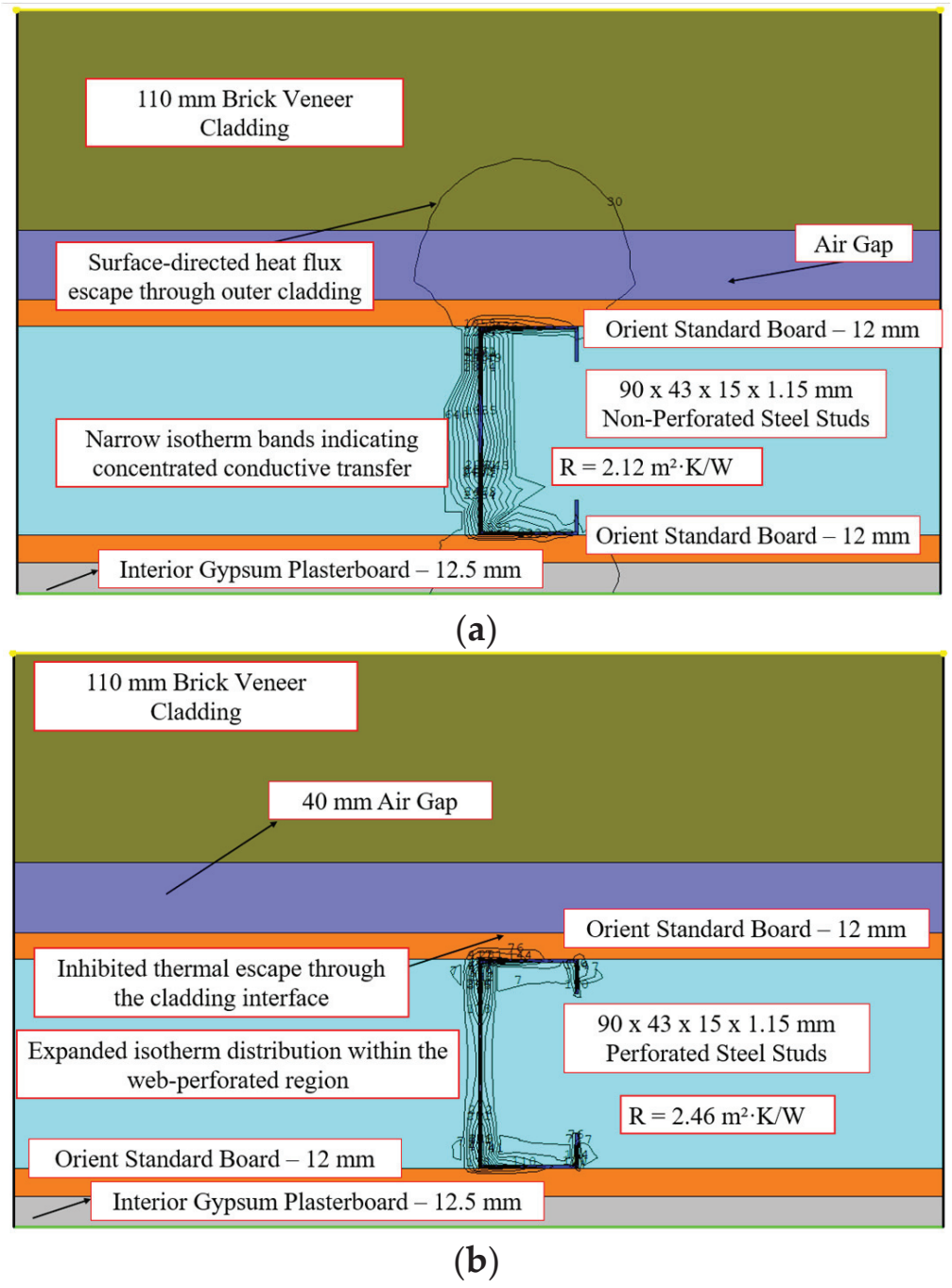

Figure 31. Isotherm distribution in brick veneer-clad external LSF wall with (**a**) non-perforated and (**b**) web-perforated studs.

7. Heat Transfer Modulation Through Web Perforations in Previously Published LSF Wall Assemblies

Previous research has demonstrated the use of passive measures such as thermal breaks, additional insulation layers, and double lining systems to increase the thermal resistance (R-value) of LSF wall systems. In this study, reference wall configurations with non-perforated CFS studs reported in the literature were modelled using THERM to establish baseline performance. To quantify the influence of web perforations, circular web openings of 68 mm diameter were introduced at the stud centre, and the R-values were recalculated. The results showed that the inclusion of perforations increased thermal resistance by reducing direct heat transfer across the steel web. The outcomes of these modifications are presented in Table 11.

Table 11. Thermal performance improvements from web perforations based on literature.

Wall Configuration	R (Non-Perforated) (m^2·K/W)	R (Perforated) (m^2·K/W)	% Improvement	Source
12.5 mm gypsum plasterboard (both sides) + 90 mm mineral wool + single C90 stud (400 mm spacing)	1.78	2.06	15.73%	Francis et al. [8] *Journal of Building Engineering*, 2025.
12.5 mm gypsum plasterboard (both sides) + 90 mm mineral wool + back-to-back C90 studs (400 mm spacing)	1.45	1.64	13.10%	Francis et al. [8] *Journal of Building Engineering*, 2025,
12.5 mm gypsum + 12 mm OSB + 90 mm mineral wool + C90 × 43 × 15 × 1.5 mm stud (400 mm spacing) + 50 mm EPS + ETICS finish (no Thermal breaks -TBS)	3.204	3.648	13.87%	Santos et al. [43] *Energies*, 2023.
12.5 mm gypsum + 12 mm OSB + 90 mm mineral wool + C90 × 43 × 15 × 1.5 mm stud + 1 TBS (10 mm, λ = 7.5 mW/m·K) + 50 mm EPS + ETICS finish	3.842	4.487	16.78%	Santos et al. [43] *Energies*, 2023.
12.5 mm gypsum + 12 mm OSB + 90 mm mineral wool + C90 × 43 × 15 × 1.5 mm stud + 2 TBS (5 mm each, λ = 7.5 mW/m·K) + 50 mm EPS + ETICS finish	4.444	5.219	17.43%	Santos et al. [43] *Energies*, 2023.
12.5 mm gypsum plasterboard + 90 mm mineral wool + single C90 stud (600 mm spacing) + 15 mm flange indentation filled with aerogel	1.906	2.135	12.00%	Santos et al. [5] *Sustainability*, 2021.
12.5 mm gypsum + 90 mm MW + C90 (600 mm) + 15 mm indentation (aerogel) + ETICS	3.499	3.954	13.00%	Santos et al. [5] *Sustainability*, 2021.
12.5 mm gypsum + 90 mm MW + C150 (600 mm) + 15 mm indentation (aerogel) + ETICS	4.301	5.032	17.00%	Santos et al. [5] *Sustainability*, 2021.

Table 11. *Cont.*

Wall Configuration	R (Non-Perforated) (m^2·K/W)	R (Perforated) (m^2·K/W)	% Improvement	Source
12.5 mm gypsum + 90 mm MW + C90 (400 mm) + 15 mm indentation (aerogel) + ETICS	3.203	3.812	19.00%	Santos et al. [5] *Sustainability*, 2021.
12.5 mm plasterboard + 10 mm OSB + 150 mm RW between steel studs + 15 mm OSB + 5 mm ETICS (C1—Cold Construction)	2.317	2.595	12.00%	Santos et al. [44] *Buildings*, 2017.
12.5 mm plasterboard + 10 mm OSB + 150 mm steel studs + 15 mm OSB + 75 mm RW (internal) + 75 mm EPS (external) + 5 mm ETICS (H1—Hybrid Construction)	3.744	4.249	13.50%	Santos et al. [44] *Buildings*, 2017.
12.5 mm plasterboard + 10 mm OSB + 150 mm steel studs + 15 mm OSB + 150 mm EPS (fully external) + 5 mm ETICS (W1—Warm Construction)	4.779	5.496	15.00%	Santos et al. [44] *Buildings*, 2017.

Among the reviewed configurations shown in Table 11, web perforations consistently disrupt axial heat conduction through steel studs, promoting lateral thermal diffusion into adjacent insulation layers such as mineral wool, EPS, and aerogel. In conventional C90 assemblies, both single and back-to-back, perforations fragment the continuous steel conduction path, yielding improvements of 13.10 to 15.73%. In walls with thermal breaks (TBS) or high-resistance materials, such as aerogel or ETICS, perforations further suppress axial gradients and redistribute concentrated flux zones, with thermal gains rising to 16.79 and 17.44%. Heavier steel sections like C150 studs exhibit enhanced benefit (up to 17.0%) as perforations mitigate intensified directional conduction by redirecting heat laterally. Systems with continuous external insulation, such as hybrid and warm constructions, also experience 13.49 to 15.00% increases, as perforations reorient residual conduction into low-conductivity exterior envelopes. Overall, the use of web perforations enhances transverse heat dispersion, weakens axial flux continuity, and delivers up to 19.01% improvement in R-values, confirming their role as effective geometric modifiers for thermal optimization in LSF wall systems.

8. Climate Zoning Assessment of Enhanced Web-Perforated LSF Wall Systems

The climate zoning assessment was undertaken to evaluate whether web-perforated LSF wall systems, with and without supplementary measures, could achieve compliance with the minimum R-value requirements of NCC 2022 across Australia's eight climate zones. In this study, external wall configurations reported in the previous section were modelled in THERM. Sequential enhancements were then systematically introduced, beginning with the addition of web perforations, followed by perforations combined with external and dual flange thermal breaks, hybrid insulation, and double plasterboard linings, as shown in Table 12. These configurations were selected because they represent the most widely adopted strategies in the literature for improving thermal resistance in steel-framed walls [39,43]. This modelling approach enabled a direct comparison of the performance

of perforated studs against mandated solutions and demonstrated the effectiveness of combined strategies in reducing thermal bridging.

Table 12. R-Values of LSF external wall systems with web-perforated studs and various enhancement configurations.

External Wall Type	Method	R (Non-Perforated) (m^2·K/W)	R (Perforated) (m^2·K/W)	Web-Perforated + Thermal Break (External Flange)—R (m^2·K/W)	Web-Perforated + Thermal Break (Both Flanges)—R (m^2·K/W)	Web-Perforated + Hybrid Insulation—R (m^2·K/W)	Web-Perforated + Double Plasterboards—R (m^2·K/W)
AAC	Abaqus	2.71	3.12	3.915	4.365	4.19	3.78
	THERM	2.83	3.27	4.065	4.515	4.34	3.93
	NZS 4214	2.77	3.21	4.005	4.455	4.28	3.87
	ASHRAE Mod. Zone	2.73	3.18	3.975	4.425	4.25	3.84
Profiled Steel	Abaqus	2.32	2.67	3.401	3.389	3.7	3.33
	THERM	2.41	2.79	3.521	3.509	3.82	3.45
	NZS 4214	2.35	2.75	3.481	3.469	3.78	3.41
	ASHRAE Mod. Zone	2.33	2.74	3.471	3.459	3.77	3.4
ACP	Abaqus	2.68	3.109	3.815	3.863	4.192	3.769
	THERM	2.76	3.2	3.906	3.954	4.283	3.86
	NZS 4214	2.71	3.16	3.866	3.914	4.243	3.82
	ASHRAE Mod. Zone	2.67	3.14	3.846	3.894	4.223	3.8
Fire-Rated Glass	Abaqus	2.61	3	3.782	3.873	4.0923	3.66
	THERM	2.71	3.14	3.922	4.013	4.2323	3.8
	NZS 4214	2.65	3.09	3.872	3.963	4.1823	3.75
	ASHRAE Mod. Zone	2.61	3.08	3.862	3.953	4.1723	3.74
Brick Veneer	Abaqus	2.57	2.95	3.32	3.72	4.114	3.61
	THERM	2.7	3.13	3.45	3.9	4.294	3.79
	NZS 4214	2.67	3.11	3.42	3.88	4.274	3.77
	ASHRAE Mod. Zone	2.64	3.1	3.39	3.87	4.264	3.76

Figure 32 presents the thermal resistance outcomes summarised in Table 12 for external LSF wall systems incorporating web-perforated studs, evaluated across five cladding types and four analytical methods (Abaqus, THERM, NZS 4214, ASHRAE Modified Zone). Table 12 quantifies R-values for each system under five enhancement configurations: baseline perforated, external thermal break, dual-side thermal break, hybrid insulation, and internal double plasterboards. Across all cladding types, web perforations consistently improved R-values by 14–18% compared to their non-perforated counterparts, primarily by attenuating axial conductive flux through the steel webs and introducing thermal discontinuities that reduce effective conductivity. The highest thermal resistance values up to 4.515 m^2·K/W were achieved in AAC-clad systems with dual thermal breaks, owing to suppressed lateral conduction and increased surface resistance. While hybrid insulation and double plasterboards yielded incremental gains, the dominant improvement mech-

anism was the conduction-path interruption induced by perforation, which aligns with Fourier-driven heat transport theory. These results confirm that in specific climates, wall designs optimised with perforations and moderate enhancements may deliver sufficient thermal resistance, potentially reducing the need for mandatory thermal breaks.

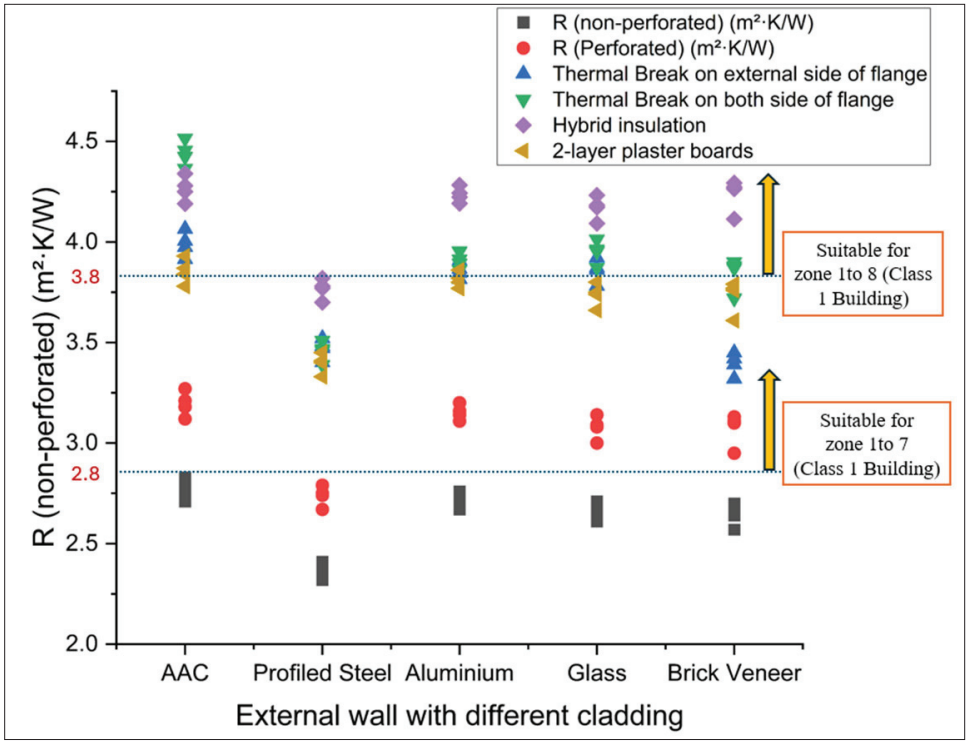

Figure 32. Comparison of R-values of external LSF walls with web-perforated studs across different cladding types with thermal enhancement strategies.

Table 13 presents the climate zone applicability of external LSF wall types incorporating web-perforated studs under a range of thermal enhancement configurations. R-values were mapped to Australian climate zones (Z1 to Z8) based on minimum required thermal resistance for energy efficiency compliance. Across all wall types, the baseline perforated configuration extended zone coverage beyond the non-perforated case, most notably, AAC walls expanded from Zones Z1 to Z7 (R = 2.71 to 2.83 m^2·K/W) to the same zone range with increased resistance (R = 3.12 to 3.27 m^2·K/W). ACP, brick veneer, and fire-rated glass systems also exhibited improvements, qualifying for up to Z7 under perforated or enhanced conditions. Configurations with thermal breaks (both external and dual-sided) enabled all wall types to meet R-value thresholds across Zones Z1 to Z8, achieving values up to 4.5 m^2·K/W. Hybrid insulation and double-layer plasterboards further supported full climatic applicability, with most systems exceeding 4.0 m^2·K/W. Profiled steel-clad walls, while initially limited to Z4 to Z5 in the non-perforated state, were rendered zone-compliant across Z1 to Z8 when enhanced. These results highlight the critical role of perforations in achieving broader climatic compatibility, particularly when paired with passive resistive strategies.

Table 13. Climate zone applicability of external LSF wall systems with web-perforated studs under diverse thermal enhancement configurations.

External Wall Type	R (Non-Perforated)	Zones	R (Perforated)	Zones	Thermal Break-Ext	Zones	Thermal Break-Both	Zones	Hybrid Insulation	Zones	Double Plasterboards	Zones
AAC	2.71–2.83	Z1–7	3.12–3.27	Z1–7	3.9–4.1	Z1–8	4.4–4.5	Z1–8	4.19–4.34	Z1–8	3.78–3.93	Z1–8
ACP	2.67–2.76	Not suitable for any zone	3.10–3.2	Z1–7	3.8–3.9	Z1–8	3.9–3.95	Z1–8	4.19–4.3	Z1–8	3.769–3.86	Z1–8
Brick Veneer	2.57–2.7	Not suitable for any zone	2.95–3.13	Z1–7	3.3–3.5	Z1–7	3.72–3.9	Z1–8	4.1–4.3	Z1–8	3.61–3.79	Z1–8
Fire-Rated Glass	2.61–2.71	Not suitable for any zone	3.00–3.14	Z1–7	3.8–3.9	Z1–8	3.9–4.0	Z1–8	4.1–4.2	Z1–8	3.66–3.8	Z1–8
Profiled Steel	2.32–2.41	Not suitable for any zone	2.67–2.79	Not suitable for any zone	3.4–3.5	Z1–8	3.39–3.5	Z1–8	3.7–3.82	Z1–8	3.33–3.45	Z1–8

9. Conclusions

This study has assessed the thermal and structural performance of web-perforated cold-formed light steel frame walls using validated numerical models and analytical methods. Based on the results, the following conclusions were drawn.

- Web perforations in CFS studs function as a passive thermal optimization strategy, delivering consistent R-value enhancements of 14.79 to 20.06% across all tested wall systems. R-values increased from 2.57–2.83 $m^2 \cdot K/W$ (non-perforated) to 2.95–3.27 $m^2 \cdot K/W$ (perforated), with a peak gain of 0.54 $m^2 \cdot K/W$ in AAC-clad walls.
- By reducing the steel web cross-sectional area, perforations interrupted the continuous through-stud conduction path and promoted lateral heat flux redistribution into the insulation. Heat flux vectors along the stud web decreased by 23.6–37.5%, with 2D and 3D isotherm analyses in THERM and Abaqus confirming flux redistribution and attenuated thermal bridging.
- The maximum R-value of 1.892 $m^2 \cdot K/W$ was achieved in a 3 m wall with 68 mm diameter holes at 200 mm spacing, improving thermal resistance by 20.06%.
- Although the axial compression capacity reduced by 29.51% in perforated studs (from 82.13 to 57.1 kN), it was restored to within 3.2% of the non-perforated stud capacity using 4 mm long edge stiffeners around the holes (78.31 kN).
- Web-perforated studs increased thermal resistance across all façade systems, with perforations alone sufficient to satisfy NCC 2022 R-value thresholds in several zones. As NCC mandates thermal breaks ($R \geq 0.2$) for metal-framed external walls and roofs where cladding and lining are directly fixed, combined systems with 19 mm thermal breaks or hybrid insulation achieved 4.2–4.5 $m^2 \cdot K/W$, ensuring compliance across all climate zones (Z1–Z8).
- Adapted NZS 4214 and ASHRAE Modified Zone methods accurately predicted the R-values of perforated walls using frame fraction and flux correction adjustments.
- Across selected façade systems, web-perforated LSF wall designs achieved R-values of 3.14 to 3.27 $m^2 \cdot K/W$, demonstrating that in certain climates, thermal breaks can be excluded where cladding or insulation sufficiently limits heat transfer.
- Heat flux correction factors (C_f= 0.52 to 0.89) derived from the 120 Abaqus models allow accurate R-value estimation without full 3D FE simulations, supporting practical design and compliance with NCC, ASHRAE, and ISO 6946.
- Furthermore, the climate zoning analysis demonstrated that web-perforated LSF wall systems, either alone or in combination with moderate enhancements such as thermal breaks or hybrid insulation, satisfied the NCC 2022 R-value requirements across all Australian climate zones (Z1–Z8).

Overall, web perforations offer a geometry-driven, energy-efficient, and structurally viable solution to mitigating thermal bridging in steel-framed wall systems, scalable across assemblies and climates without reliance on costly thermal breaks.

Author Contributions: S.I.: Conceptualization, Data curation, Formal analysis, Investigation, Methodology, Visualization, Writing—original draft. A.A.: Conceptualization, Methodology, Project administration, Resources, Supervision, Validation, Writing—review & editing. M.M.: Conceptualization, Project administration, Supervision, Validation, Writing—review & editing. All authors have read and agreed to the published version of the manuscript.

Funding: This research received no external funding.

Data Availability Statement: The datasets generated or analysed during the current study are available from the corresponding author upon reasonable request.

Acknowledgments: The authors acknowledge the Queensland University of Technology (QUT) for providing a PhD scholarship to the first author and the necessary facilities to undertake this research project.

Conflicts of Interest: The authors declare that there are no conflicts of interest related to this work.

References

1. Song, J.-H.; Kim, H.-W. Performance Evaluation of Low Thermal Bridging Drywall System with Separating Clips for C-Studs. *Buildings* **2024**, *14*, 3032. [CrossRef]
2. Qi, X.; Tan, Y.; Tan, J.; Li, X. Methods for improving the thermal performance of thermal bridges of lightweight steel-framed buildings. *PLoS ONE* **2024**, *19*, e0314634. [CrossRef]
3. Soares, N.; Santos, P.; Gervásio, H.; Costa, J.J.; da Silva, L.S. Energy efficiency and thermal performance of lightweight steel-framed (LSF) construction: A review. *Renew. Sustain. Energy Rev.* **2017**, *78*, 194–209. [CrossRef]
4. Soares, N.; Martins, C.; Gonçalves, M.; Santos, P.; da Silva, L.S.; Costa, J.J. Laboratory and in-situ non-destructive methods to evaluate the thermal transmittance and behavior of walls, windows, and construction elements with innovative materials: A review. *Energy Build* **2019**, *182*, 88–110. [CrossRef]
5. Santos, P.; Poologanathan, K. The importance of stud flanges size and shape on the thermal performance of lightweight steel framed walls. *Sustainability* **2021**, *13*, 3970. [CrossRef]
6. Santos, P. Energy Efficiency of Lightweight Steel-Framed Buildings. In *Energy Efficient Buildings*; InTech: London, UK, 2017. [CrossRef]
7. Rajanayagam, H.; Upasiri, I.; Poologanathan, K.; Gatheeshgar, P.; Sherlock, P.; Konthesingha, C.; Nagaratnam, B.; Perera, D. Thermal Performance of LSF Wall Systems with Vacuum Insulation Panels. *Buildings* **2021**, *11*, 621. [CrossRef]
8. Francis, E.; Gatheeshgar, P.; Santos, P. Thermal transmittance of single and double stud LSF walls: Parametric study and simplified models. *J. Build. Eng.* **2025**, *102*, 111939. [CrossRef]
9. Martins, C.; Santos, P.; da Silva, L.S. Lightweight steel-framed thermal bridges mitigation strategies: A parametric study. *J. Build. Phys.* **2016**, *39*, 342–372. [CrossRef]
10. Santos, P.; Abrantes, D.; Lopes, P.; Mateus, D. Experimental and Numerical Performance Evaluation of Bio-Based and Recycled Thermal Break Strips in LSF Partition Walls. *Buildings* **2022**, *12*, 1237. [CrossRef]
11. Gorgolewski, M. Developing a simplified method of calculating U-values in light steel framing. *Build Environ.* **2007**, *42*, 230–236. [CrossRef]
12. Chandrasiri, D.; Gatheeshgar, P.; Ahmadi, H.M.; Simwanda, L. Numerical Study of Thermal Efficiency in Light-Gauge Steel Panels Designed with Varying Insulation Ratios. *Buildings* **2024**, *14*, 300. [CrossRef]
13. Santos, P.; Lemes, G.; Mateus, D. Analytical Methods to Estimate the Thermal Transmittance of LSF Walls: Calculation Procedures Review and Accuracy Comparison. *Energies* **2020**, *13*, 840. [CrossRef]
14. Sovetova, M.; Calautit, J.K. Thermal and energy efficiency in 3D-printed buildings: Review of geometric design, materials and printing processes. *Energy Build.* **2024**, *323*, 114731. [CrossRef]
15. Yang, Z.; Sun, L.; Nan, B.; Wei, S. Thermal Performance of Slotted Light Steel-Framed Composite Wall. *Energies* **2023**, *16*, 2482. [CrossRef]
16. Alekperov, R.; Aksenov, I. Decrease of cold-formed slotted studs heat conductivity by slots shape modification. *E3S Web Conf.* **2019**, *97*, 06009. [CrossRef]
17. Langner, M.; Soares, T.A.; Figueiredo, A.; Almeida, R.M.S.F.; Vicente, R. Parametric Analysis of Steel Studs to Reduce Thermal Bridges in Light Steel Framing Construction Systems. *Buildings* **2025**, *15*, 194. [CrossRef]
18. Höglund, T.; Burstrand, H. Slotted steel studs to reduce thermal bridges in insulated walls. *Thin-Walled Struct.* **1998**, *32*, 81–109. [CrossRef]
19. *BS EN ISO 6946:2017*; Building Components and Building Elements. Thermal Resistance and Thermal Transmittance. Calculation Methods. British Standards Institute: London, UK, 2017.
20. NCC 2022 Volume Two—Building Code of Australia Class 1 and 10 Buildings. Available online: http://ncc.abcb.gov.au/editions/ncc-2022/adopted/volume-two (accessed on 1 April 2025).
21. Liang, H.; Roy, K.; Fang, Z.; Lim, J.B.P. A Critical Review on Optimization of Cold-Formed Steel Members for Better Structural and Thermal Performances. *Buildings* **2022**, *12*, 34. [CrossRef]
22. 2021 International Energy Conservation Code (IECC) and ANSI/ASHRAE/IES Standard 90.1-2022. Available online: https://www.energycodes.gov/sites/default/files/2024-02/Standard_90.1-2022_Final_Determination_TSD.pdf (accessed on 1 March 2025).
23. ASHRAE. *Handbook of Fundamentals, American Society of Heating*; Refrigeration and Air-Conditioning Engineers, Inc.: Atlanta, GA, USA, 2021.

24. European Commission. Directive (EU) 2018/844 on the Energy Performance of Buildings (EPBD). *Off. J. Eur. Union* **2018**, *L156*, 75–91.
25. *NZS 4214*; Methods of Determining the Total Thermal Resistance of Parts of Buildings. New Zealand Standard: Wellington, New Zealand, 2006.
26. Santos, P.; Ribeiro, T. Thermal Performance of Double-Pane Lightweight Steel Framed Walls with and without a Reflective Foil. *Buildings* **2021**, *11*, 301. [CrossRef]
27. Kempton, L.; Kokogiannakis, G.; Green, A.; Cooper, P. Evaluation of thermal bridging mitigation techniques and impact of calculation methods for lightweight steel frame external wall systems. *J. Build. Eng.* **2021**, *43*, 102893. [CrossRef]
28. A Review of Thermal Bridging Mitigation Provisions and Thermal Break Provisions NCC 2022. Available online: https://www.abcb.gov.au/sites/default/files/resources/2023/LittleShrub%20Report%20-%20Thermal%20Bridging%20and%20Thermal%20Break.pdf (accessed on 1 February 2025).
29. Department of Climate Change, Energy, the Environment and Water. *Trajectory for Low Energy Buildings*; Department of Climate Change, Energy, the Environment and Water: Canberra, Australia, 2019.
30. ationwide House Energy Rating Scheme. Software Accreditation Protocol—New Homes 2025. Available online: https://www.nathers.gov.au/sites/default/files/2025-02/Software%20Accreditation%20Protocol%20-%20New%20Homes%2020250227.pdf (accessed on 1 March 2025).
31. Santos, P.; Mateus, D. Experimental assessment of thermal break strips performance in load-bearing and non-load-bearing LSF walls. *J. Build. Eng.* **2020**, *32*, 101693. [CrossRef]
32. Gunalan, S.; Kolarkar, P.; Mahendran, M. Experimental study of load bearing cold-formed steel wall systems under fire conditions. *Thin-Walled Struct.* **2013**, *65*, 72–92. [CrossRef]
33. Incropera, F.P.; DeWitt, D.P.; Bergman, T.L.; Lavine, A.S. *Fundamentals of Heat and Mass Transfer*, 6th ed.; Wiley: Hoboken, NJ, USA, 2007.
34. *ISO 10211:2017*; Thermal Bridges in Building Construction—Heat Flows and Surface Temperatures—Detailed Calculations. International Organization for Standardization: Geneva, Switzerland, 2017.
35. Vy, S.T.; Mahendran, M.; Ariyanayagam, A. Numerical modelling and investigation of CFS built-up stud walls in fire. *Fire Saf. J.* **2024**, *144*, 104102. [CrossRef]
36. *AS/NZS 4600:2005*; Cold-Formed Steel Structures. Standards Australia: Sydney, Australia; Standards New Zealand: Wellington, New Zealand, 2018.
37. Clayton, T.G. Design of Steel Wall Studs with Service Holes; Senior Research Engineer, BlueScope Steel Research. Available online: https://www.nash.asn.au/wp-content/uploads/2022/04/303_1330395018.pdf (accessed on 1 April 2023).
38. *ABAQUS*; Dassault Systèmes: Providence, RI, USA, 2023.
39. Keerthan, P.; Mahendran, M. Thermal Performance of Composite Panels Under Fire Conditions Using Numerical Studies: Plasterboards, Rockwool, Glass Fibre and Cellulose Insulations. *Fire Technol.* **2013**, *49*, 329–356. [CrossRef]
40. Perera, D.; Upasiri, I.R.; Poologanathan, K.; Gatheeshgar, P.; Sherlock, P.; Hewavitharana, T.; Suntharalingam, T. Energy performance of fire rated LSF walls under UK climate conditions. *J. Build. Eng.* **2021**, *44*, 103293. [CrossRef]
41. Auwerda, G.J.; Zheng, Y.H.; Kloosterman, J.L.; Lathouwers, D. Comparison of 2D and 3D heat transfer models around the coolant channels in the HTR-PM side reflector. *Nucl. Eng. Des.* **2014**, *271*, 465–471. [CrossRef]
42. Peiris, M.; Mahendran, M. Behaviour of cold-formed steel lipped channel sections subject to eccentric axial compression. *J. Constr. Steel Res.* **2021**, *184*, 106808. [CrossRef]
43. Santos, P.; Lopes, P.; Abrantes, D. Thermal Performance of Lightweight Steel Framed Facade Walls Using Thermal Break Strips and ETICS: A Parametric Study. *Energies* **2023**, *16*, 1699. [CrossRef]
44. Roque, E.; Santos, P. The Effectiveness of Thermal Insulation in Lightweight Steel-Framed Walls with Respect to Its Position. *Buildings* **2017**, *7*, 13. [CrossRef]

energies

MDPI

Article

Analysis on the Insulation Improvements in Dutch Houses

Joel Alpízar-Castillo * and Laura Ramírez-Elizondo

DC Systems, Energy Conversion and Storage, Delft University of Technology, 2628 CD Delft, The Netherlands; l.m.ramirezelizondo@tudelft.nl
* Correspondence: j.j.alpizarcastillo@tudelft.nl

Abstract: Thermal comfort accounts for significant residential energy consumption in high latitudes; however, quantitative information about insulation improvements is not widely available. First, we performed a study to quantify the effects of improving the insulation in walls, roofs, and windows of typical dwellings in the Netherlands (a studio, an apartment, and a stand-alone house). Our results indicate that improving from single- to double-glazing is the most significant change, reducing gas consumption up to 50%, whereas the difference between double- and triple-glazing is less than 7%. Improving the roof insulation, filling cavity walls with insulation, or adding external wall insulation did not show attractive business cases, as the payback time was too high. Second, we evaluated upgrading the dwelling energy label by improving the insulation or adding a PV system and a heat pump. The results showed that, for energy labels C or above, the insulation reached a saturation point where it is not attractive to improve it before its end-of-life proactively. Instead, investing in the energy system by adding a PV system and a heat pump has better payback times. Our results allow policymakers and project developers to focus on the most relevant changes to accelerate the energy transition.

Keywords: building envelope; building insulation; building performance simulation; heat pumps; energy efficiency

1. Introduction

Space heating to ensure thermal comfort is one of the major sources of energy consumption in residential buildings in the Netherlands [1]. In general, countries at higher latitudes require a significant amount of energy to face the lower temperatures, typically supplied by gas (although electricity, biomass, and district heating networks are also used in some cases). For instance, the spacial heating demand was 85 TWh during 2016 [2] in the Netherlands, with a kilogram of oil equivalent of approximately 7 kgOE/m^2, which remained somewhat constant until 2021 [3]. However, proactive measures must be taken to meet international climate goals, since 75% of the building stock in the European Union is considered energy inefficient [4]. On the one hand, heating electrification has been widely adopted in the form of heat pumps, surpassing the 17% of Dutch households by 2023 [5], with an expected acceleration in adoption towards 2030 [1]. Nevertheless, massive deployments of heating electrification create significant pressure on the electric infrastructure, as system operators must supply an increasingly growing demand. On the other hand, improvements in insulation techniques tackle the demand, not from the energy source, but by reducing the overall consumption. These two measures are not mutually exclusive, but the best way they are implemented (either individually or together) would depend on the case.

Current research recommends studying what kind of insulation improvements are optimal for different types of buildings [6,7]. From a technical perspective, understanding the effects of the insulation on the thermal demand could reduce building improvement investments by adequately designing the insulation required for walls, roof, and windows [8], avoiding under- or over-dimensioning. Similarly, from a cost perspective, an analytical background would allow data-driven business cases, since tractable and reproducible simulations and cases can be performed. This way, project developers and policymakers could understand when it is better to invest in insulation and when it is better to invest in heating electrification, based on a techno-economic assessment [9].

1.1. Literature Review

Recent works can be found in the literature that focus on studying how the thermal properties of buildings affect the heating demand for different countries or regions. For instance, the work in [10] studied how the thermal transmittance coefficients approved in the Polish law during the last decade affect the energy demand for heating in residential buildings. Their results suggest a decrease in the thermal demand between 11% and 32.6%, which translates into yearly savings between €43 and €67. Similarly, ref. [11] used 18 years of energy consumption measurements of existing buildings in Poland to compare the consumption before and after insulation improvements were carried out using large slabs, demonstrating that the method results in energy savings between 16% and 23%.

The European Union-level study performed by [12] indicated that improving the insulation of walls and roofs can lead to energy savings of up to 48%. Nevertheless, the results show a high sensitivity to the current insulation levels. In addition, it showed the importance of a baseline for energy efficiency (required heating degree days (HDD) or U-values) when comparing the results among countries. These results are congruent with [13], who compared the regulations for residential building stock between Finland and Türkiye, suggesting that the current insulation in Finnish buildings is likely above the optimal, whereas Turkish insulation limits must be improved. In [14], a case study was carried out for a single-family house from 2012 in Ontario, Canada, modeled using eQUEST. It was concluded that energy improvements could lead to energy savings of up to 78%, where window and door upgrades accounted for only 13 % of the energy savings and required an investment of between 14,620 CAD and 18,292 CAD, and the PV system and the heat pump account for 33% and 20%, with costs around 18,000 CAD each.

Polystyrene thermal insulation in walls and roofs was studied by [15] in a case study in Chalous city, Northern Iran, using DesignBuilder. The results suggested heat loss reduction of up to 54.8% in walls and 53.5% in roofs and highlighted the importance of adequate insulation to minimize thermal losses and costs. A comparison of the impact of different U-values for walls, windows, roofs, and floors in Palestine, considering different climatic zones following the ASHRAE standard 90.1-2019 using the software DesignBuilder, was conducted in [16]. Using the current Palestinian building energy code as a reference, improving the insulation resulted in a reduction between 43% and 83% when compared with other international building energy codes. However, their study is limited to the building types and materials used in Palestine.

Different optimization strategies have also been proposed in the literature to obtain the ideal insulation thickness. For example, in [17], a human thermal comfort index (predicted mean vote) was used to optimize the insulation thickness of the external walls and roof for two case scenarios (Greece and Cyprus), without considering economic indicators. The simulations conducted in TRNSYS show an improvement in the yearly comfortable hours from below 60% to 97%, while reducing the heating load 66% compared to a non-insulated house, when using wall insulation between 2.9 and 3.2 cm and roof insulation

between 13.9 and 14 cm. The work in [18] focused on optimizing the EPS insulation thickness of brick walls for a case study in Algeria to minimize energy costs using TRNSYS, suggesting an optimal range between 1 and 2.5 cm. The effect of insulating the walls of buildings from different construction methods (gray brick, hollow clay block, LECA block, and AAC block) and regions is compared in [19] to optimize the insulation thickness based on energy savings. As expected, the optimal insulation would depend on regional climatic conditions; however, the results indicated that walls made with AAC block would not require additional insulation in regions where the other wall types do. This way, in the cold regions, insulating gray brick (optimal insulation of 1.5–2 cm) or hollow clay block (optimal insulation of 1.5–2 cm) walls would reduce energy consumption by up to 53%, and LECA block (optimal insulation of 0.5–1 cm) walls by up to 26%, but AAC block would not show any significant benefit (no insulation needed). These strategies provide insight into the optimal thickness of the insulation based on different objective functions; thus, future work should compare or implement their results with the available market.

Alternatively, other works have focused on analyzing heating electrification adoption from a cost perspective, since changing the source of heating supply would not necessarily mean a change in the heating demand. A case study in three Italian cities suggests that replacing gas boilers with a heat pump leads to significant reductions in energy costs [20]. Using TRNSYS, it was determined that combining a heat pump, a PV system, and a battery, together with improved insulation, results in up to 52% primary energy savings. Similar results were obtained by [21] for a case study in Ireland, where replacing the gas boilers in residential buildings reduced the overall primary energy consumption between 45% and 72% (or up to 128 kWh/(m^2·year)). Similarly, ref. [22] evaluated the energy and economic performance of different combinations of insulation and energy system improvements for a case scenario in Greece. Their results demonstrated that adding a high-efficiency heat pump and improving the window glazing have the highest impact on reducing the thermal demand of space heating in a residential building.

More complex systems have also been proposed in the literature. Different multi-carrier energy system configurations were simulated using TRNSYS 17.2 [23]. Combining a heat pump with a PV system resulted in a self-consumption rate of 34.1%, adding a battery energy storage system and a thermal energy storage system improved the self-consumption rate to 69.4%, but did not noticeably change the overall energy demand. Instead, using a photovoltaic-thermal system coupled to the heat pump led to the best performance, with a self-consumption rate of 96.2%, but with a considerably higher investment cost. The results in [24] also suggest that combining electric and thermal storage together with heat pumps in residential dwellings allows higher heating electrification adoptions if aggregated at the neighborhood level, compared to using only a system comprised of a PV and a heat pump, at the cost of very unattractive business cases for the prosumers. Both results are consistent with the review performed by [25], which demonstrated that highly efficient heat pumps do not lead to the best economic scenario due to their higher upfront costs and relatively low difference in consumption when compared to others with lower energy labels.

Specifically in the Netherlands, some works have examined the Dutch context to understand pathways for reducing residential energy demand and achieving climate targets. A bottom-up dynamic building stock model was developed by [26] to simulate the evolution of Dutch residential buildings under the national control scenario. Their analysis showed that improvements in insulation, together with heating electrification and PV deployment, could reduce space heating demand by two-thirds and cut operational GHG emissions by up to 90% by 2050, but material-related emissions will gain relative importance. In their work, ref. [27] studied the temporal dynamics of space heating demand, using hourly gas consumption data from 8077 dwellings during 2020 to model thermostat

behavior and its dispersion across households. It was demonstrated that occupant-driven thermostat settings significantly influence peak loads, highlighting the need for demand-side flexibility and accurate district-level heat demand profiles. The cost-optimal retrofit for typical Dutch housing archetypes was addressed by [28], emphasizing that upgrading to current regulation standards combined with heat recovery ventilation can reduce spatial heat demand up to 60%, while investments in insulation improvement led to thermal demand reductions of only 12%.

1.2. Research Gap

Based on the literature review, the following research gaps were found:

- many studies provide results based on insulation improvements without detailing the initial insulation condition of the buildings nor the insulation measures taken (including their costs), and
- most of the literature focus either on insulation or on heating electrification techniques but does not compare them directly.

Therefore, the contributions of this paper are

- a quantitative assessment of available thermal insulation improvement methods from an energy consumption and cost-effective perspective, considering different initial insulation levels, and
- a techno-economic comparison between insulation improvement and a heating electrification adoption scenario.

2. Thermal Losses Mathematical Description

To estimate the thermal demand in buildings, one can use building performance standards (BPS), as well as standardized methods, such as ISO 52016-1 [29] . However, these methods often require detailed input data and computational resources. As a response, the work in [30] provided an analytical framework to model the thermal losses of a Dutch house. The model accounts for the losses due to conduction, convection, infiltration, and ventilation for a specific type of window, roof, and wall. External radiative heating effects are not considered (e.g., heating through the windows due to solar irradiance). This section is dedicated to adapting the models for the window, roof, and wall losses to include additional insulation, allowing us to perform a more comprehensive analysis on the most common house insulation methods used in the Netherlands.

The ventilation ($\dot{Q}_v$) and infiltration ($\dot{Q}_i$) losses were calculated based on the American Society of Heating, Refrigerating and Air-Conditioning Engineers (ASHRAE) Handbook [31]. The ventilation losses can be estimated with

$$\dot{Q}_v(k) = c_a \rho_a q_v \Delta T(k)\,, \tag{1}$$

where c_a and ρ_a are the specific heat capacity and density of the air, $\Delta T(k)$ is the temperature difference between the outside and inside of the house (in degrees Fahrenheit), and q_v is the required ventilation airflow (in cubic feet per minute), given by

$$q_v = 0.03 A_{\text{cf}} + 7.5(N_{\text{br}} + 1)\,, \tag{2}$$

where A_{cf} is the building conditioned area (in feet squared) and N_{br} is the number of bedrooms in the house.

The infiltration losses can be estimated with

$$\dot{Q}_i(k) = c_a \rho_a q_i \Delta T(k)\,. \tag{3}$$

where q_i is the infiltration airflow, given by

$$q_i(k) = A_{\text{es}} A_u \sqrt{C_s |\Delta T(k)| + C_w u^2(k)}\,, \tag{4}$$

where A_{es} is the building's exposed area (in feet squared), A_u is the unit leakage area (in inches squared per foot squared), C_s is the stacking coefficient, C_w is the wind coefficient, and u is the wind speed (in miles per hour). Internal sources of heat, such as inhabitants, lighting, and appliances, were neglected, as high-efficiency appliances were considered [31].

2.1. Windows Insulation

Three types of glazing are modeled in this section: single-, double-, and triple-glazing. On the one hand, a single-glazed window behaves as a solid wall, without intermediate convective mechanisms. On the other hand, double- and triple-glazing, thanks to their air gaps, prevent convective-only heat flows, increasing the window's thermal resistance. The thermal circuits considered for single-, double-, and triple-glazed windows are shown in Figure 1. This way, the thermal losses for each type of glazing can be represented as

$$\dot{Q}_{\text{window, single}}(k) = \left(\frac{1}{h^{\text{conv}}_{\text{out, window}}} + \frac{L_{\text{glass}}}{k_{\text{glass}}} + \frac{1}{h^{\text{conv}}_{\text{in, window}}} \right)^{-1} A_{\text{window}} \left[T_{\text{in}}(k) - T_{\text{out}}(k) \right], \tag{5}$$

$$\dot{Q}_{\text{window, double}}(k) = \left(\frac{1}{h^{\text{conv}}_{\text{out, window}}} + 2\frac{L_{\text{glass}}}{k_{\text{glass}}} + \frac{1}{h^{\text{conv}}_{\text{gap, window}}} + \frac{1}{h^{\text{conv}}_{\text{in, window}}} \right)^{-1} A_{\text{window}} \left[T_{\text{in}}(k) - T_{\text{out}}(k) \right], \tag{6}$$

and

$$\dot{Q}_{\text{window, triple}}(k) = \left(\frac{1}{h^{\text{conv}}_{\text{out, window}}} + 3\frac{L_{\text{glass}}}{k_{\text{glass}}} + 2\frac{1}{h^{\text{conv}}_{\text{gap, window}}} + \frac{1}{h^{\text{conv}}_{\text{in, window}}} \right)^{-1} A_{\text{window}} \left[T_{\text{in}}(k) - T_{\text{out}}(k) \right], \tag{7}$$

where $h^{\text{conv}}_{\text{out, window}}$ and $h^{\text{conv}}_{\text{in, window}}$ are the convective heat transfer coefficients between the window and the outdoor and indoor air, respectively; $h^{\text{conv}}_{\text{gap, window}}$ is the convective heat transfer coefficient of the air gap between the glass layers, and L_{glass} and k_{glass} are the thickness and thermal conductivity of the glass, respectively. A_{window} is the window area, and T_{in} and T_{out} are the indoor and outdoor temperatures, respectively. We assumed that for double- and triple-glazed windows, the glass and air gaps have the same thickness per layer.

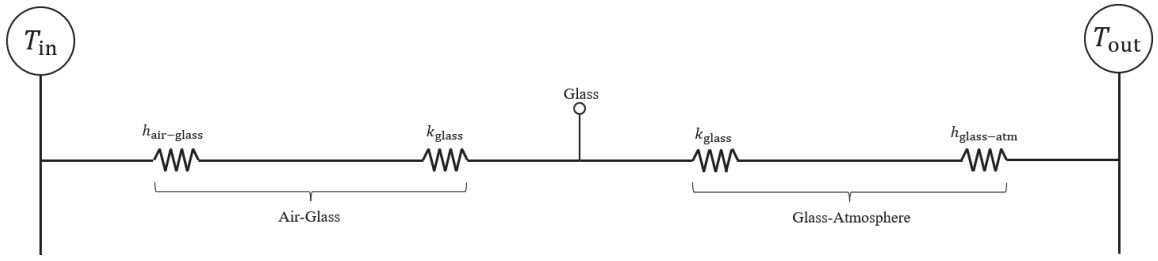

(**a**)

Figure 1. *Cont.*

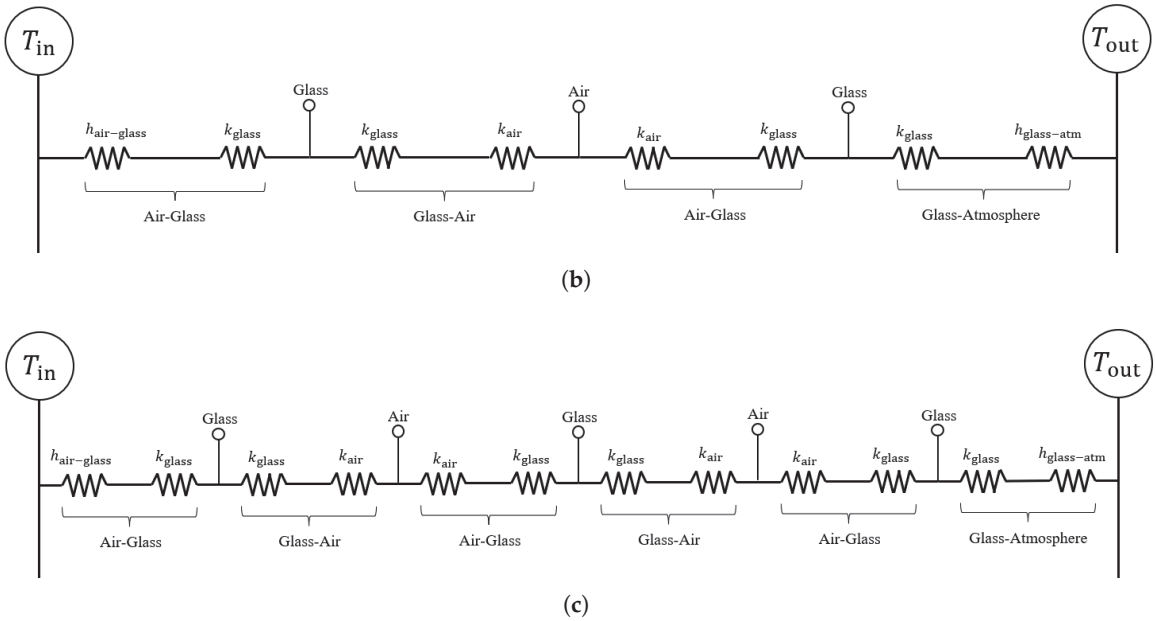

Figure 1. Equivalent thermal circuit considered for a (**a**) singgle-, (**b**) double- and (**c**) triple-glazed window.

2.2. Roof Insulation

The improvements of the roof consist of increasing the conductive thermal resistance by increasing the thickness of a layer of insulation material, resulting in the thermal circuit shown in Figure 2. This way, the thermal losses through the roof are

$$\dot{Q}_{\text{roof}}(k) = \left(\frac{1}{h^{\text{conv}}_{\text{out, roof}}} + \frac{L_{\text{roof}}}{k_{\text{roof}}} + \frac{L_{\text{insulation}}}{k_{\text{insulation}}} + \frac{1}{h^{\text{conv}}_{\text{in, roof}}} \right)^{-1} A_{\text{roof}} \left[T_{\text{in}}(k) - T_{\text{out}}(k) \right], \quad (8)$$

where $h^{\text{conv}}_{\text{out, roof}}$ and $h^{\text{conv}}_{\text{in, roof}}$ are the convective heat transfer coefficients between the roof and the outdoor and indoor air, respectively, L_{roof} and $L_{\text{insulation}}$, and k_{roof} and $k_{\text{insulation}}$ are the thickness and thermal conductivity of the roof and insulation layers, respectively. A_{roof} is the roof area, and T_{in} and T_{out} are the indoor and outdoor temperatures, respectively.

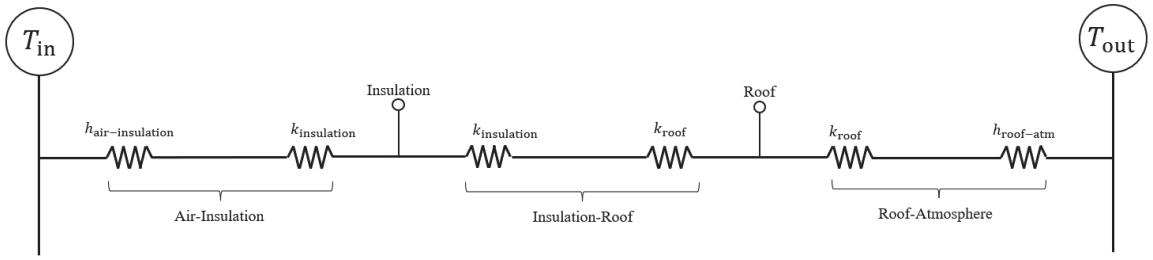

Figure 2. Equivalent thermal circuit considered for the roof.

2.3. Walls Insulation

For the walls, we considered two separated insulation mechanisms, namely external wall covering and wall gaps, as shown in Figure 3. For the latter, two fillings are considered: air and insulation material. The external wall covering consists of a layer of insulation material placed against the wall, increasing the conductive thermal resistance. The wall gap effect, however, would depend on the filling. In the case of air, the cavity would increase the overall thermal resistance by adding a convective heat transfer coefficient, as shown in Figure 3a, whereas filling the air gap with insulation material would replace the convective

effect by a conductive resistance, as shown in Figure 3b. This way, the expressions for a wall with an air or filled gap are

$$\dot{Q}_{\text{wall, air}}(k) = \left(\frac{1}{h^{\text{conv}}_{\text{out, wall}}} + \frac{L_{\text{wall, cover}}}{k_{\text{wall, cover}}} + \frac{L_{\text{wall}}}{k_{\text{wall}}} + \frac{1}{h^{\text{conv}}_{\text{gap, wall}}} + \frac{1}{h^{\text{conv}}_{\text{in, wall}}} \right)^{-1} A_{\text{wall}} \left[T_{\text{in}}(k) - T_{\text{out}}(k) \right], \tag{9}$$

and

$$\dot{Q}_{\text{wall, fill}}(k) = \left(\frac{1}{h^{\text{conv}}_{\text{out, wall}}} + \frac{L_{\text{wall, cover}}}{k_{\text{wall, cover}}} + \frac{L_{\text{wall}}}{k_{\text{wall}}} + \frac{L_{\text{gap, wall}}}{k_{\text{gap, wall}}} + \frac{1}{h^{\text{conv}}_{\text{in, wall}}} \right)^{-1} A_{\text{wall}} \left[T_{\text{in}}(k) - T_{\text{out}}(k) \right], \tag{10}$$

respectively, where $h^{\text{conv}}_{\text{out, wall}}$ and $h^{\text{conv}}_{\text{in, wall}}$ are the convective heat transfer coefficients between the walls and the outdoor and indoor air, respectively, $L_{\text{wall, cover}}$, L_{wall} and $L_{\text{gap, wall}}$, and $k_{\text{wall, cover}}$, k_{wall} and $k_{\text{gap, wall}}$ are the thickness and thermal conductivity of the wall insulation cover, the wall itself and the wall filling layers, respectively. $h^{\text{conv}}_{\text{gap, wall}}$ is the convective heat transfer coefficient of the air gap within the wall, A_{wall} is the wall area, and T_{in} and T_{out} are the indoor and outdoor temperatures, respectively.

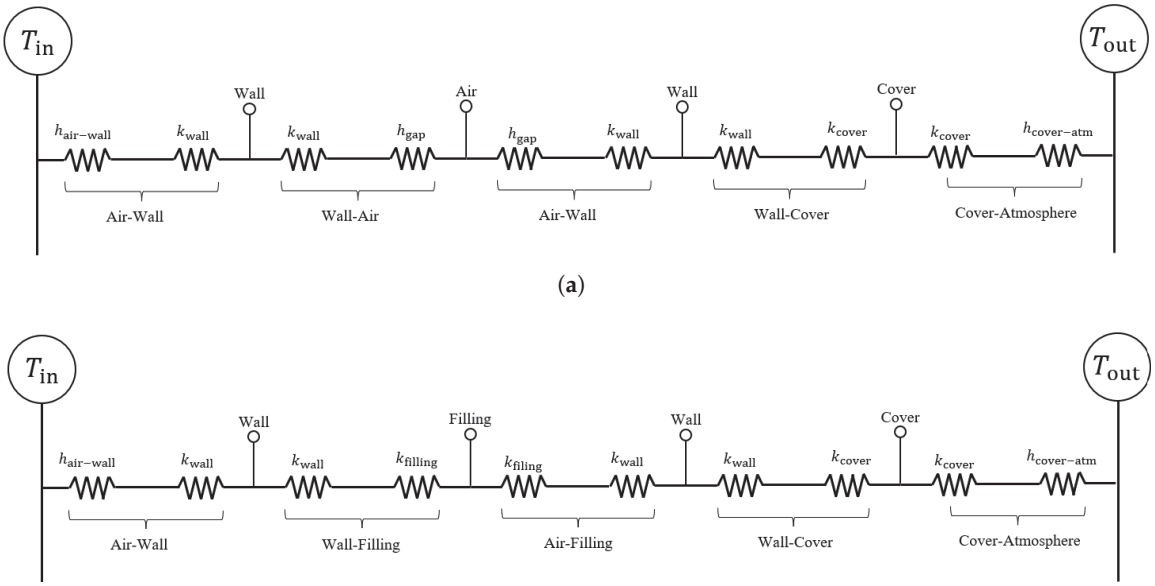

Figure 3. Equivalent thermal circuit considered for an (**a**) air-filled cavity wall and (**b**) insulation-filled cavity wall.

3. Case Description

This work provides a quantitative assessment of the influence of different insulation techniques applied to Dutch residential buildings. Two different case scenarios are considered. First, the insulation techniques are analyzed individually, considering the insulation of a house energy label C (following the Dutch energy label standard NTA 8800:2024 [32]) as reference for the other insulation elements (see Table 1). Second, different insulation parameters were chosen to replicate houses with energy labels between G and A, as shown in Table 1. The thermodynamic models used were taken from [30].

Table 1. Parameters considered for each energy label.

	G	F	E	D	C	B	A
Windows type	Single	Single	Single	Double	Double	Double	Triple
Roof insulation	3 cm	5 cm	10 cm	15 cm	15 cm	20 cm	30 cm
Inner wall insulation	Solid wall	3 cm (air)	5 cm (air)	5 cm (air)	8 cm (air)	8 cm (EPS)	10 cm (EPS)
External wall insulation	-	-	-	-	-	-	10 cm (EPS)
Heating type	Boiler	Boiler	Boiler	Boiler	Boiler	Boiler	Heat pump
RES	-	-	-	-	-	-	PV

The individual analysis considers improvements on the windows (dingle-, double-, and triple-glazed), roof (3 cm, 5 cm, 10 cm, 15 cm, 20 cm, and 30 cm insulation), and walls (no cavity, cavities of 3 cm, 5 cm, 8 cm, and 10 cm filled with air and EPS; and 10 cm of external wall insulation). In addition, three types of houses are considered: a studio, an apartment, and a stand-alone house, whose parameters are shown in Table 2. These values were obtained through an exploratory search carried out in the housing platform Funda, which hosts approximately 97% of the housing market listings in the Netherlands [33]. The weather data for ambient temperature and solar irradiance were taken from the KNMI database. For our simulations, we used the open-source library available in [34], built in Python 3.12.11 (see the block diagram in Figure 4), considering a timestep of 15 min for a whole year.

Table 2. Description of the houses considered.

	Windows [m^2]	Roof [m^2]	Walls [m^2]	Consumption [kWh]
Studio	4	56.2	76.6	1000
Apartment	8	120.3	111.6	2500
Stand-alone	12	120.3	219.5	5000

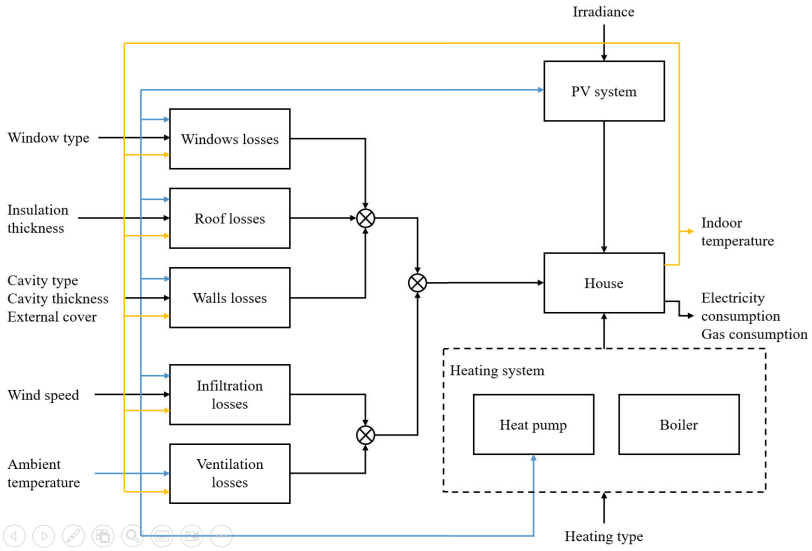

Figure 4. Flow diagram of the components used for the simulation.

Four metrics are considered to compare the performance of the insulation improvements:

- Thermal demand [kWh]: considered as the amount of thermal energy used to maintain the indoor temperature.
- Gas consumption [m^3]: considered as the gas used by the boiler to deliver thermal power for space heating.

- CAPEX: [€] considered as the total cost of improving the insulation.
- OPEX: [€] considered as the total energy cost (electricity and gas) by the household.
- Payback: [years] considered as the time it would take to cover the CAPEX based on the change in OPEX after an improvement.

Note that the cost considered for the insulation improvements, as well as the PV system and the heat pump, was obtained through quotes requested from local contractors in the Netherlands.

Three different types of windows were considered, namely single-, double-, and triple-glazed. Each glass layer is assumed to be 4 mm thick with a thermal conductivity of 0.8 $WK^{-1}m^{-1}$, and with air gaps of 1.4 cm for double- and triple-glazed windows. The costs considered are shown in Table 3. In this case, we considered a single-glazed window as the base; therefore, no cost is associated, since it is assumed that such glazing would already exist in the building. Note that these costs are only for the window upgrade (materials and labor) and exclude any improvement or replacements of the frames; therefore, no changes in the infiltration rates are considered when changing the glazing. Also, it was assumed that the frames, regardless of the glazing type, are in good quality and there are no considerable leakages (aside from what is estimated using the ASHRAE method detailed in (3)) through the frame or air gaps in the case of multiple-glazed windows.

Table 3. Costs considered for the windows insulation.

Glaze	Cost [€/m^2]
Single	-
Double	700
Triple	1000

For the roof insulation analysis, it was assumed that the improvement would be made by insulation panels with a thickness of 10 cm or 15 cm. For insulation thinner than 10 cm, no capital expenses were considered, since the available insulation is a minimum of 10 cm, and it is assumed that, for the cases with insulation thinner than 10 cm, it would already be placed in the building. The cost per thickness is shown in Table 4. Note that these costs include only materials and labor related to the insulation alone; thus, finishings are excluded.

Table 4. Costs considered for the roof insulation.

Thickness [cm]	Cost [€/m^2]
0–5	-
10	35
15	40
20	50
30	60

Two different methods were considered to improve the insulation of walls: cavity filling through granulated EPS and external covering. On the one hand, air (thermal conductivity 0.0257 $WK^{-1}m^{-1}$) and EPS fillings (thermal conductivity 0.035 $WK^{-1}m^{-1}$) were considered for cavity widths between 3 cm and 10 cm. For walls with air cavities, no CAPEX was considered, as it was assumed that the building was initially constructed with the cavity. For EPS filling, a fixed cost of €40/m^2 was considered. It is important to mention that the cavity gap is often between 3 cm and 5 cm, which is the reason why contractors often quote based on area instead of volume. In our work, we extended the cavity gap up to 10 cm to evaluate if thicker gaps would have a noticeable improvement,

but no changes in the cost are assumed. On the other hand, 10 cm thick EPS panels were considered as external covering, with a cost of €150/m^2.

After the individual analysis, a comparison of different combinations of insulation levels associated with an energy label, as shown in Table 1, was done. The PV system was sized to cover the base electric load of the household, excluding the heat pump. This is because, typically, the usage of space heating indoors is more significant during low-irradiance periods, both seasonal (mostly winter) and hourly (early in the morning or during the evening) [1]. Therefore, adding the heat pump electric consumption to the sizing of the PV system, albeit resulting in a net-zero house, would probably exchange a large part of the generation with the grid due to the mismatch between solar generation and electric consumption, leading to local congestion in the residential distribution networks [24]. The cost and peak power for the PV system are shown in Table 5. For the heat pump, a fixed cost of €10,000 was considered.

Table 5. Costs considered for the PV system.

	Peak Power [kW]	Cost [€]
Studio	2	2469.6
Apartment	4.8	6148.5
Stand-alone	10	12,272.4

4. Results

4.1. Windows Insulation

The results are shown in Figure 5. In general, one can notice a significant change from single- to double-glazed windows in terms of thermal demand reduction (Figure 5a) and, thus, gas consumption and energy cost (Figure 5b). Nevertheless, the change from double- to triple-glazed is less noticeable, improving the overall thermal performance around 10% for stand-alone houses, while being almost 40% more expensive than double-glazing (Figure 5).

The performance behavior can be explained given the total window area for the different house types, as apartments and studios have less window area and, thereby, fewer losses through the windows. Similarly, the single air gap can significantly reduce the thermal loss, leaving only cooling mechanisms via convective effects, which are minimal when there is no air flow (within the air gap). Thus, a second air gap, despite reducing the convective and radiative heat transfer mechanisms, has a significantly lower impact.

From a cost perspective, it was mentioned that improving from single- to double- or triple-glazed windows might result in a more attractive scenario for both cost and performance perspectives than improving from double- to triple-glazed windows. Table 6 shows the payback for these upgrades for studios, apartments, and stand-alone houses, respectively. These results show that, despite triple-glazed windows resulting in lower gas consumption, they would only be attractive when upgrading single-glazed windows. This is because the reduction in gas consumption from double- to triple-glazed windows is one order of magnitude smaller, as shown in Table 7. Nevertheless, if the double-glazed windows are deteriorated and require a replacement after their lifetime, it might be worth replacing them with triple-glazed windows, based on the household owner's criteria.

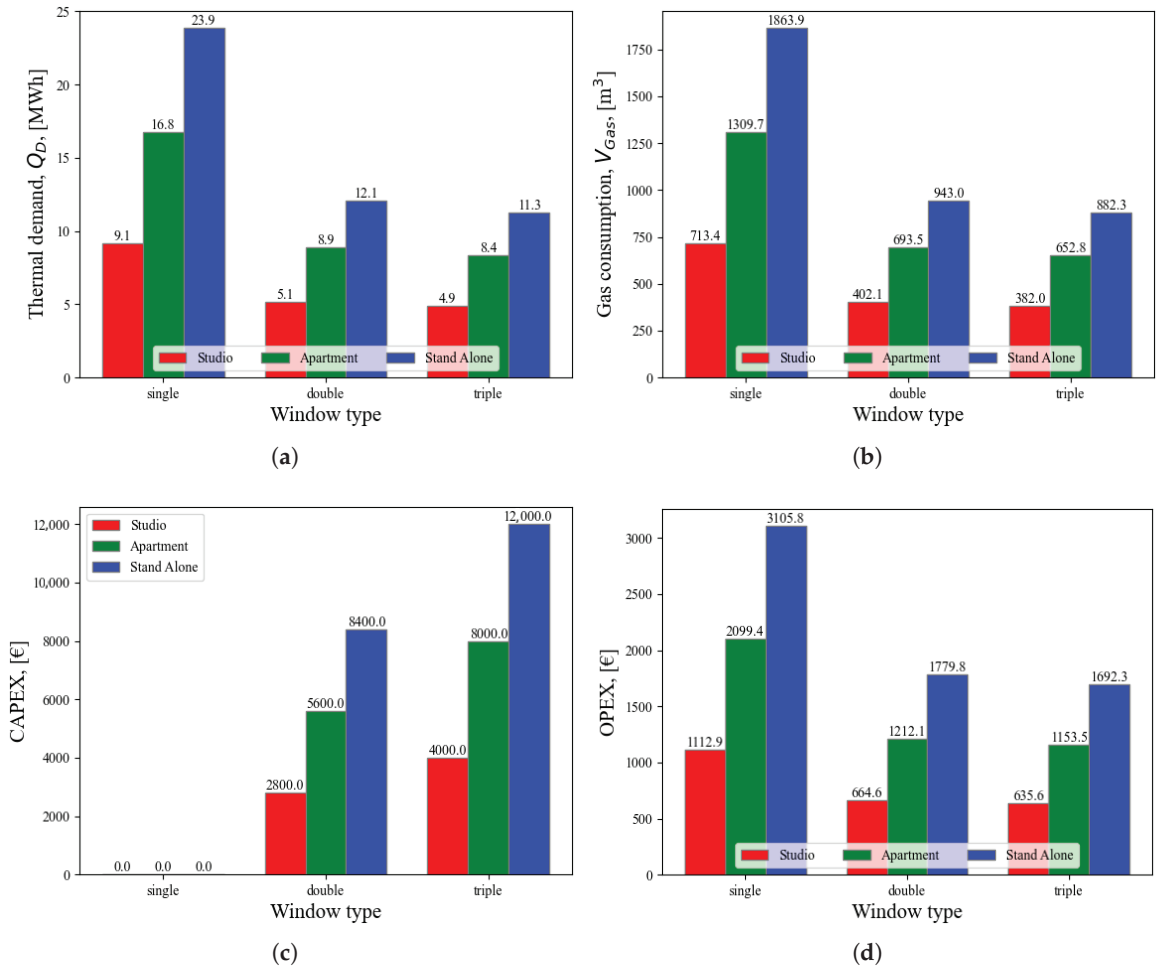

Figure 5. Results for different window insulation, comparing (**a**) thermal demand, (**b**) gas consumption, (**c**) capital expenses, and (**d**) operative expenses, for a representative studio, apartment, and stand-alone house.

Table 6. Payback [years] for the windows insulation improvement for a representative studio, apartment, and stand-alone house.

Glaze	Single	Double	Triple
Single	-	6.2/6.3/6.3	8.4/8.5/8.5
Double	-	-	138/137/137
Triple	-	-	-

Table 7. Gas reduction [m^3] for the windows insulation improvement for a representative studio, apartment, and stand-alone house.

Glaze	Single	Double	Triple
Single	-	331.3/616.2/920.9	331.4/656.9/981.6
Double	-	-	20.1/40.7/60.7
Triple	-	-	-

4.2. Roof Insulation

The results shown in Figure 6 demonstrate that, as expected, thicker insulation results in better thermal demand and gas consumption performance (Figure 6a,b). Still, the performance difference decreases when the thickness increases, i.e., the performance would reach

a saturation point. This way, as shown in the windows analysis, depending on the current status, it might not be worth improving the roof insulation until it has reached its lifetime.

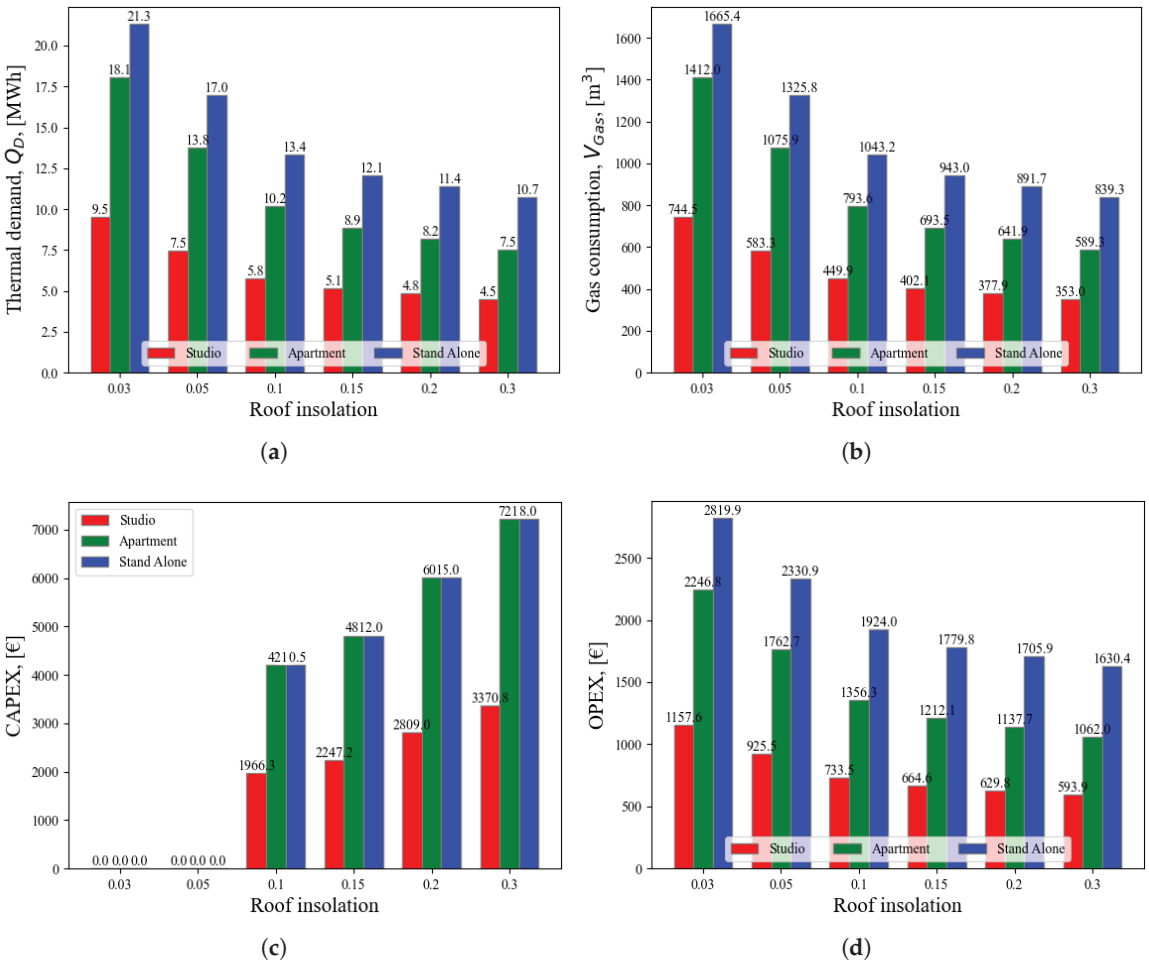

Figure 6. Results for different roof insulation thicknesses, comparing (**a**) thermal demand, (**b**) gas consumption, (**c**) capital expenses, and (**d**) operative expenses, for a representative studio, apartment, and stand-alone house.

Table 8 shows the payback time when upgrading the roof insulation. As shown, proactively upgrading insulation below 10 cm is relatively attractive for homeowners. However, improving insulation from 10 cm would have very high paybacks (around 33 years), despite resulting in gas reductions up to 21.5% (96.9 m^3), 25.7% (204.3 m^3), and 19.5% (203.9 m^3) when upgrading from 10 cm to 30 cm for studios, apartments, and stand-alone houses, respectively, as shown in Table 9.

Table 8. Payback [years] for the roof insulation improvement for a representative studio, apartment, and stand-alone house.

Thickness [cm]	3	5	10	15	20	30
3	-	-	4.6/4.7/4.7	4.6/4.7/4.6	5.3/5.4/5.4	6.0/6.1/6.1
5	-	-	10.2/10.4/10.3	8.6/8.7/8.7	9.5/9.6/9.6	10.2/10.3/10.3
10	-	-	-	32.6/33.4/33.4	27.1/27.5/27.6	24.2/24.5/24.6
15	-	-	-	-	80.8/80.9/81.4	47.7/48.1/48.3
20	-	-	-	-	-	93.9/95.35/95.6
30	-	-	-	-	-	-

Table 9. Gas reduction [m^3] for the roof insulation improvement for a representative studio, apartment, and stand-alone house.

Thickness [cm]	3	5	10	15	20	30
3	-	-	294.6/618.4/622.2	342.4/718.5/722.4	366.6/770.1/773.7	391.5/822.7/826.1
5	-	-	133.4/282.3/282.6	181.2/382.4/382.8	205.4/434.0/434.1	230.3/486.6/486.5
10	-	-	-	47.8/100.1/100.2	72.0/151.7/151.5	49.1/104.2/103.7
15	-	-	-	-	24.2/51.6/51.3	49.1/104.2/103.7
20	-	-	-	-	-	24.9/52.6/52.4
30	-	-	-	-	-	-

4.3. Walls Insulation

The results for the air cavity wall are shown in Figure 7. From a thermal performance perspective, adding an air cavity of only 3 cm already reduces the gas consumption by around 9% (see Figure 7b). However, increasing the width of the cavity, despite decreasing the thermal demand, has a small influence on the thermal performance, as shown in Figure 7a. Filling the cavities with materials whose thermal conductivity is similar to air would result in similar behaviors. In this case, EPS was considered, and the results are shown in Figure 8.

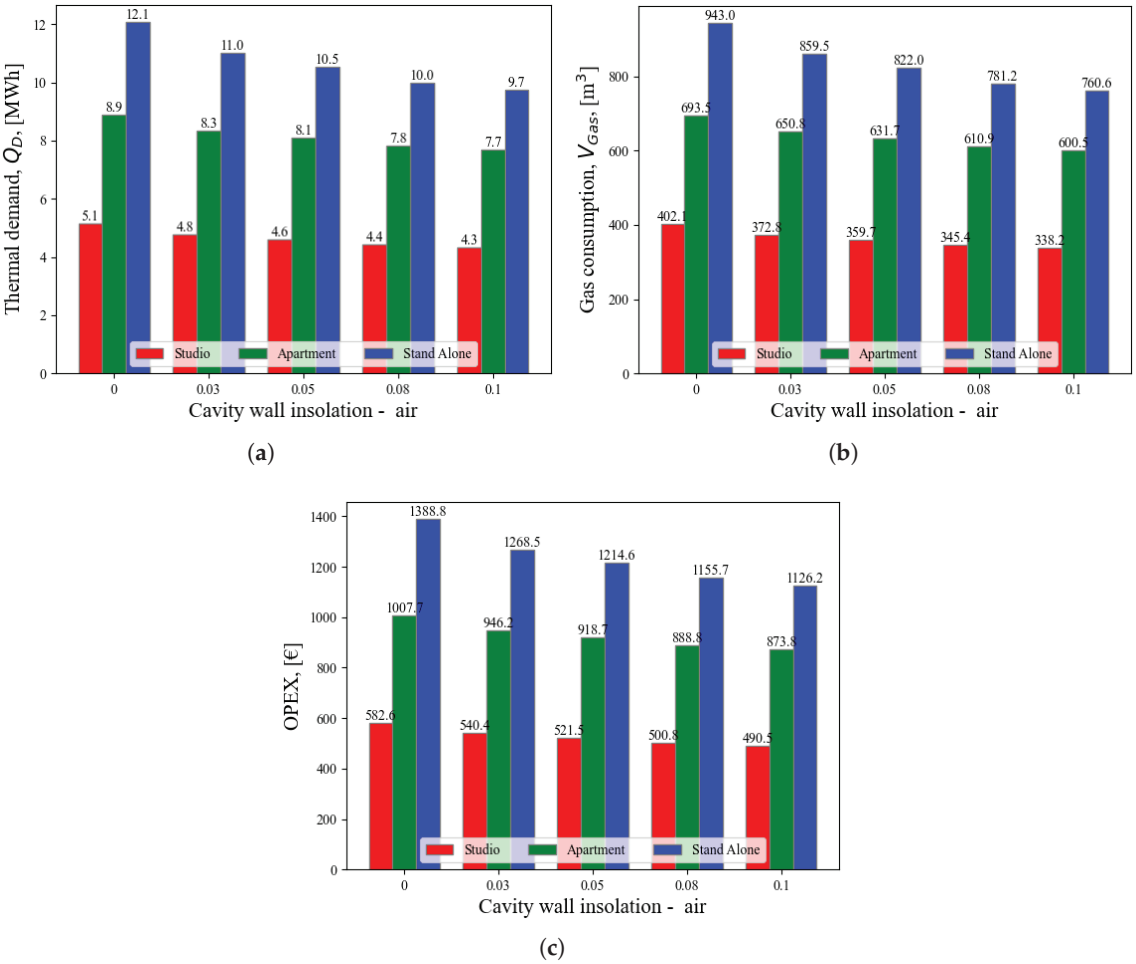

Figure 7. Results for different thicknesses of air-gap cavity walls, comparing (**a**) thermal demand, (**b**) gas consumption, and (**c**) operative expenses, for a representative studio, apartment, and stand-alone house.

As EPS has a higher thermal conductivity than air (0.035 $WK^{-1}m^{-1}$ and 0.0257 $WK^{-1}m^{-1}$, respectively), the EPS filling results in slightly lower thermal performance due to the way the cavity is modelled. In this case, the cavity is assumed to be

isolated from the environment (acting as a double-glazed window); therefore, the air gap has no convective nor infiltration losses, whereas in reality, such losses would decrease the thermal insulation performance of the air gap. Nevertheless, the results for the filled cavity are, in fact, more accurate than the results for the air gap, as conductive losses are indeed taken into consideration.

Adding an external layer of isolation had a similar effect on the thermal performance. Figure 9 shows the performance comparison between having or not having the wall external cover. As shown, including the insulation panels can reduce the gas consumption between 11.3% and 16.4% (Figure 8b, Tables 10 and 11). However, the high cost of this kind of insulation makes it unattractive for houses with some degree of insulation.

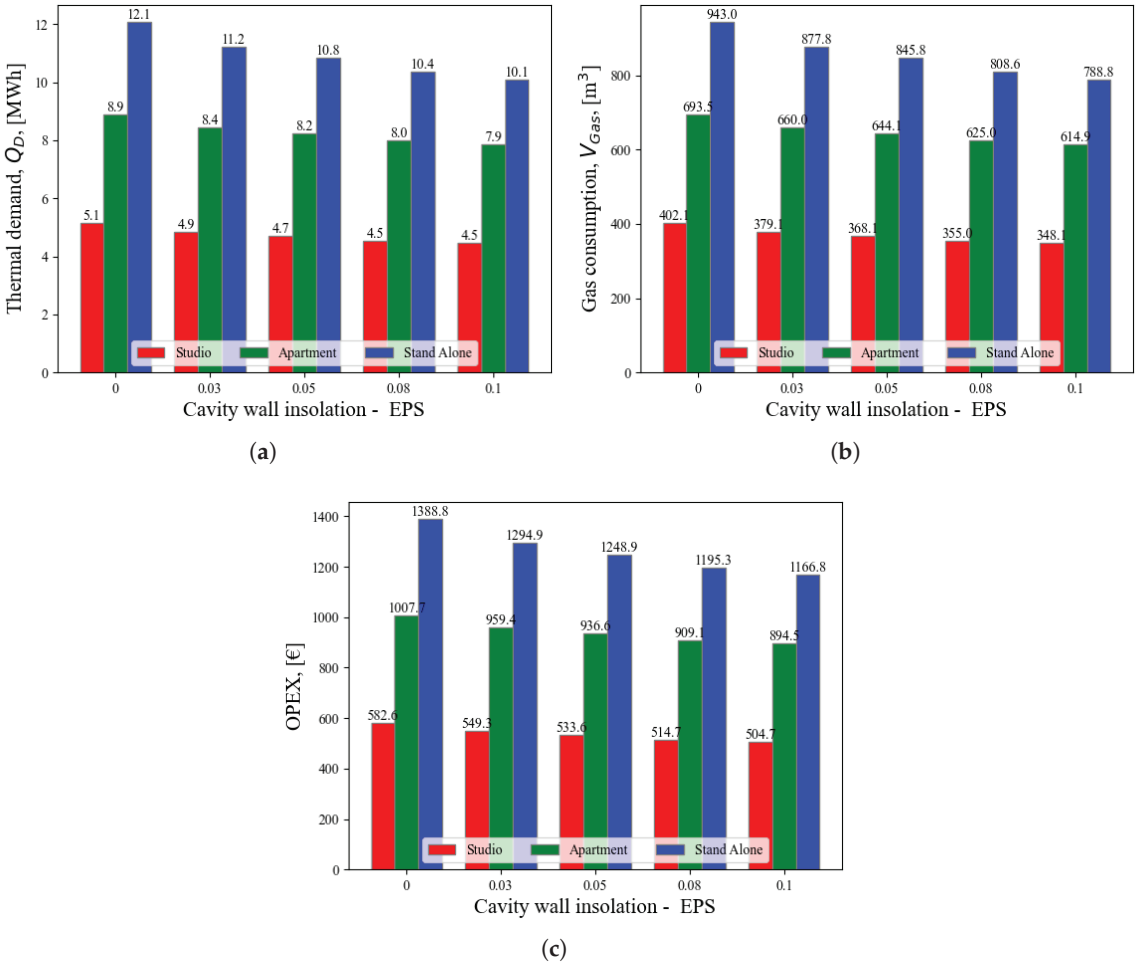

Figure 8. Results for different thickness of EPS-filled cavity walls, comparing (**a**) thermal demand, (**b**) gas consumption, and (**c**) operative expenses, for a representative studio, apartment, and stand-alone house.

Table 10. Gas reduction [m^3] for the air cavity wall width for a representative studio, apartment, and stand-alone house.

Thickness [cm]	No Cavity	3	5	8	10
No cavity	-	29.3/42.7/83.5	42.4/61.8/121.0	56.7/83.0/161.8	63.9/93.0/182.4
3	-	-	13.1/19.1/37.5	27.4/40.3/78.3	34.7/50.3/98.9
5	-	-	-	14.3/21.2/40.8	21.5/31.2/61.4
8	-	-	-	-	7.2/10.0/20.6
10	-	-	-	-	-

Table 11. Gas reduction [m^3] for the EPS-filled cavity wall width for a representative studio, apartment, and stand-alone house.

Thickness [cm]	No Cavity	3	5	8	10
No cavity	-	23.1/33.5/65.2	34.0/61.8/97.2	47.1/82.6/134.4	54.1/93.0/154.2
3	-	-	10.9/15.9/32.0	24.1/35.0/69.2	31.1/45.1/89.0
5	-	-	-	22.8/19.1/37.2	30.0/29.2/57.0
8	-	-	-	-	7.0/10.1/19.8
10	-	-	-	-	-

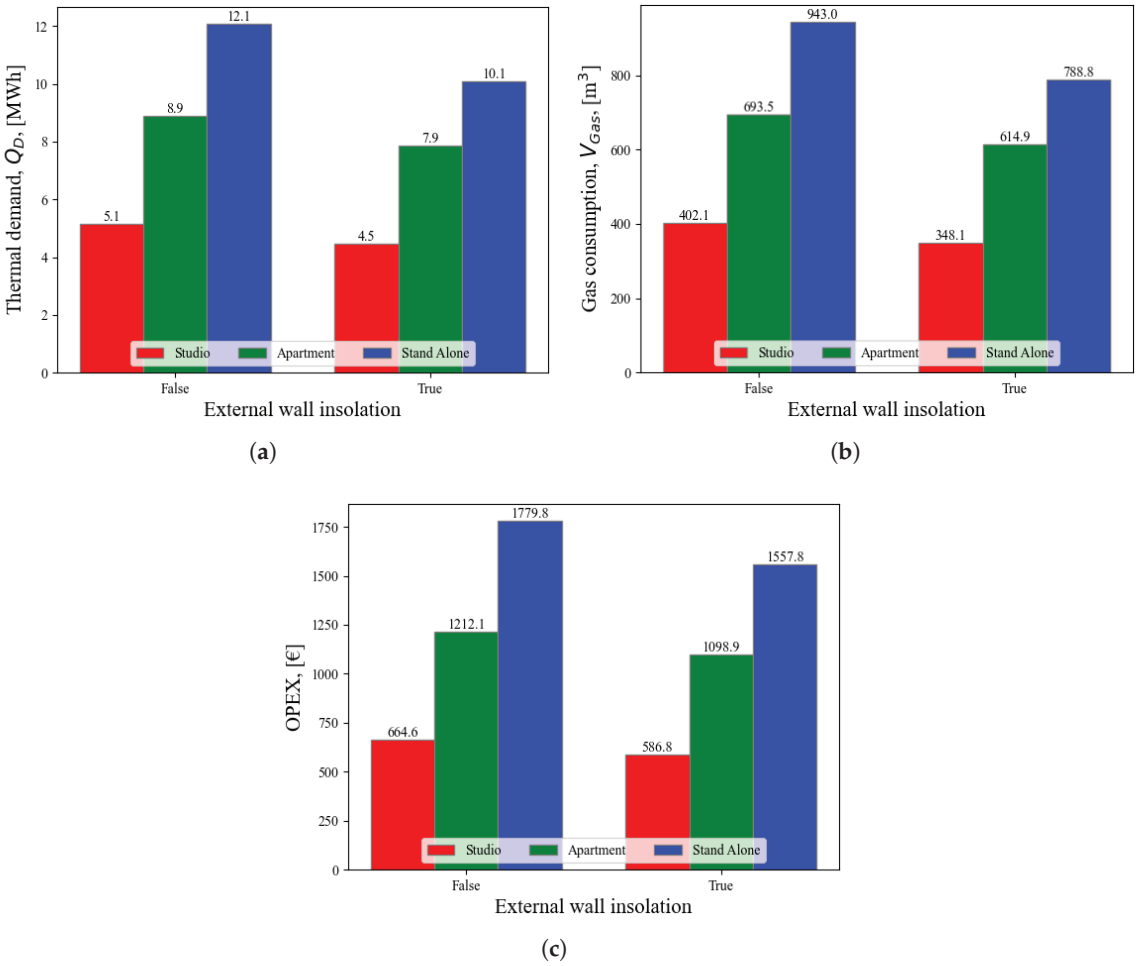

Figure 9. Results for presence and absence of external wall insulation, comparing (**a**) thermal demand, (**b**) gas consumption, and (**c**) operative expenses, for a representative studio, apartment, and stand-alone house.

4.4. Energy Label Analysis

The results in Figure 10 are consistent with the previous sections. As can be seen in Figure 10a, the thermal demand decreases significantly from energy label G to E thanks to the improvement in roof insulation and cavity walls. Also, there is a major increase in thermal performance from label E to label D thanks to the improvement from single- to double-glazing windows. Then, from label D to B, the thermal performance of the building increases around 10%.

The other noticeable change is the gas consumption from energy label B to A thanks to the heat pump (see Figure 10b). Such decrease is also reflected in the OPEX in Figure 10c. The heat pump reduced to zero the gas consumption for space heating, and the PV system compensates for a significant proportion of the electrical consumption, reducing the energy

costs. A smaller improvement is noted in the thermal demand from energy labels B to A thanks to the inclusion of triple-glazed windows and external wall covering (see Figure 10a), but as shown earlier, since the overall insulation is already highly efficient, the accumulated effect is less significant.

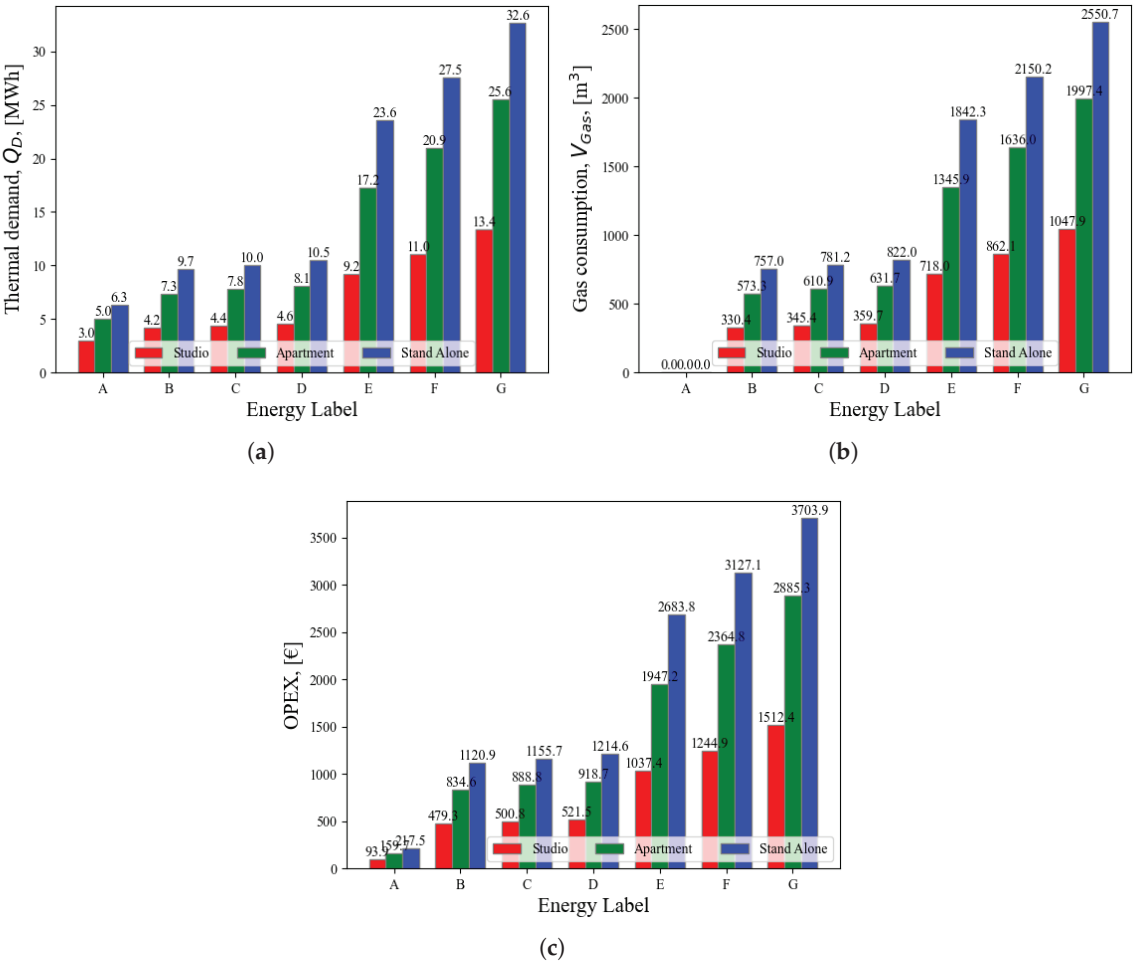

Figure 10. Results for different typical energy label insulation, comparing (**a**) thermal demand, (**b**) gas consumption, and (**c**) operative expenses, for a representative studio, apartment and stand-alone house.

From a cost perspective, Table 12 shows the required investment to improve from one energy label to another. In this case, the same equipment was considered as the previous sections (i.e., roof insulation panels of 10 cm and 15 cm and wall insulation improvement only possible by filling the already existing cavities or adding external insulation); thus, for some cases it is not possible to change from one energy label to the other (e.g., from G to F) or the costs are the same for several energy labels in a row (e.g., when the improvement from one to the next is the width of the wall cavity that cannot be changed).

The resulting payback after improving the energy labels is shown in Table 13. The results suggest that the improvements starting from the worst-performing energy labels results in more attractive scenarios thanks to the larger difference in the OPEX before and after the improvement. However, in better-insulated houses, as the change in OPEX is not as considerable, the payback is consistently higher.

Table 12. CAPEX required [k€] to improve the energy labels for a representative studio, apartment and stand-alone house.

Energy Label	G	F	E	D	C	B	A
G	-	N/A	1.97/4.21/4.21	5.05/10.41/13.21	5.05/10.41/13.21	8.57/16.08/23.52	33.90/52.57/84.745
F	-	-	1.97/4.21/4.21	5.05/10.41/13.21	5.05/10.41/13.21	8.57/16.08/23.52	33.90/52.57/84.745
E	-	-	-	5.05/10.41/13.21	5.05/10.41/13.21	8.57/16.08/23.52	33.90/52.57/84.745
D	-	-	-	-	NA	8.57/16.08/23.52	33.90/52.57/84.745
C	-	-	-	-	-	8.57/16.08/23.52	33.90/52.57/84.745
B	-	-	-	-	-	-	33.90/52.57/84.745
A	-	-	-	-	-	-	-

Table 13. Payback [years] to improve the energy labels for a representative studio, apartment and stand-alone house.

Energy Label	G	F	E	D	C	B	A
G	-	N/A	4.14/4.49/4.13	5.09/5.29/5.31	4.99/5.22/5.18	8.30/7.84/9.11	23.90/19.27/24.31
F	-	-	9.48/10.08/9.50	6.98/7.20/6.91	6.78/7.05/6.70	11.19/10.51/11.72	29.45/23.82/29.13
E	-	-	-	9.78/10.12/8.99	9.41/9.84/8.65	15.35/14.45/15.05	35.93/29.38/34.36
D	-	-	-	-	N/A	136.7/124.5/161.4	79.28/69.08/84.99
C	-	-	-	-	-	268.4/193.0/434.53	83.31/71.91/90.33
B	-	-	-	-	-	-	87.96/77.68/93.81
A	-	-	-	-	-	-	-

Finally, a building label D for each type was considered and, instead of improving the insulation, a PV system and a heat pump were added. This energy label was chosen based on the previous results, where a relative stability in the performance was displayed, so a comparison between improving the insulation and the energy system was done. The results are summarized in Table 14. As can be seen, improving a building with an energy label D with a PV system and a heat pump, excluding improvements in the insulation, results in more attractive economic scenario than improving the insulation. In addition, thanks to the heat pump, the heating system will no longer consume gas for space heating. Despite no complex analyses being performed on the energy market, coupling a local generator, such as a PV, with an electric heat source, in this case the heat pump, can result in a robust strategy against volatile energy prices, eliminating the dependency on gas prices, but relying on the electricity prices.

Table 14. Results of adding a PV system and a heat pump a studio, apartment and stand-alone house with an energy label D.

	Thermal Demand [MWh]	CAPEX [€]	Change in OPEX [€]	Payback [Years]
Studio	4.15	12,470	393.63	31.7
Apartment	7.07	16,149	699.07	23.1
Stand alone	9.06	22,274	922.40	24.2

5. Discussion

Previously, Section 4 presented and briefly discussed the results obtained. First, the individual analysis of insulation improvement for windows, roofs, and walls was presented. Second, the results of typical insulation associated with the energy labels, together with their performance improvement and associated costs, were shown. This section elaborates on the meaning of the results and compare them with recent works as validation.

Starting with the windows improvements, Figure 5 shows how adding a second layer of glass drastically reduces the thermal demand (up to 50%). This is because double- and triple-glazed windows add a convective element in the heat transfer, drastically reducing the overall thermal conductivity of the window. However, the improvement from double- to triple-glazed in new windows is not that noticeable, as one convective layer already decreases the thermal conductivity close to a saturation point. These results are consistent with [35], which reported a thermal performance increase lower than 5% when upgrading from double- to triple-glazed windows when the former is in good state, close to our results for studios, apartments and stand-alone houses (3.9%, 5.6%, and 6.6%, respectively).

This way, the performance improvement does not justify the overall investment expenses of changing from double- to triple-glazed windows, as shown in Table 6. Even when the windows have already reached their end-of-life, the payback achieved by double-glazed windows is still lower than triple-glazed due to the small difference in performance but considerable difference in price, making double-glazed windows the more attractive solution. Note that evaluating the additional benefits of increased glazing, such as acoustic insulation and condensation prevention, is outside of the scope of this work but can provide additional value.

Increasing the insulation thickness in the roofs did not drastically change the thermal demand. Despite significant changes shown in Figure 6 when comparing insulations below 10 cm, most houses in the Netherlands already have 10 cm of insulation or more [1]. Then, as shown in Table 8, it is not economically attractive to improve the roof insulation, results aligned with [36], who highlighted the small effect of the roof insulation improvement in the overall thermal demand. Similarly, ref. [12] also showed some saturation in the economic indicators when increasing the thickness of insulation layers.

The saturation effect was also noticed in the walls. On the one hand, it was shown that a wall with an air gap does reduce the thermal demand of the house (see Figure 7), but it has to be added during the construction; hence, improvement is possible. Similarly, filling the air gaps with EPS does not directly affect the thermal demand, as shown in Figure 8. Nonetheless, it might add additional benefits not included in our analysis, for instance, reduced infiltration losses. On the other hand, adding an external layer of insulation can reduce the thermal demand between 10% and 20%, but the costs are still a major drawback.

Depending on the combination of insulation conditions, a particular dwelling is assigned an energy label, as shown in Table 1. Based on our previous analysis, it can be expected that improving the insulation to move from a lower to a higher energy label might not always be an attractive business case. In fact, Table 13 shows how improving from low-efficiency energy labels to C is attractive, as the payback time is below 10 years for all types of buildings.

Improving a house with an energy label of C or above, however, requires very high investment costs, with small performance improvements. For those cases, the results in Table 14 show that, instead of investing in improving the insulation, it would be more attractive to invest in the energy system itself, in our case, by including a PV system and a heat pump. It must be noted that our results do not include any subsidy or similar aids, as they would largely vary among countries and cases. Nevertheless, it is expected that such benefits largely improve the business cases.

6. Conclusions

This paper performed two separate analysis. First, a parametric analysis was performed for each insulation strategy (windows, roofs, and walls). Second, the performance of a typical residential building (studio, apartment and stand-alone house) for each energy label, from G to A. The main conclusions are:

- The windows are the main source of thermal losses in residential buildings. In addition, they present the best payback time among the insulation strategies. As such, they should be prioritized when improving the insulation of a house, followed by the roof and, at last, the walls.
- Replacing the windows from single- to double-glazed windows can reduce gas consumption up to 50%. However, replacing double- to triple-glazed windows only reduces the gas consumption by up to 7%.
- Improving roof insulation from 3 cm to 30 cm can reduce gas consumption up to 50%. However, for houses with 10 cm of insulations or more, the gas consumption is reduced only up to 20%.
- Adding an air or filled cavity to the walls slightly improves its thermal performance. However, no major benefits were observed. Similar to adding external insulation to the walls.
- Some upgrades are not attractive to homeowners if completed proactively, i.e., while the insulation has not reached its end-of-life. This is the case for double- to triple-glazed windows and roof insulations, starting from 10 cm. For those cases, the payback time is too high, and it would be better to wait until the insulation shows signs of aging or damage.
- Improving the overall energy label of a house by upgrading its insulation is more attractive for lower energy labels (namely from G to D). For energy labels D and above, it is more attractive to invest in improving the energy system itself, e.g., adding a PV system or replacing the gas boiler with a heat pump. However, adding such systems might have a negative effect on the grid.

Future work can focus on multi-domain optimization of the insulation levels for specific case studies, which can benefit from the Python library developed, available on GitHub on its version 2.1 (Python 3.12.11).Also, it could be interesting to study the insulation improvements in non-residential buildings.

Author Contributions: Conceptualization, J.A.-C.; methodology, J.A.-C.; software, J.A.-C.; validation, J.A.-C. and L.R.-E.; formal analysis, J.A.-C.; investigation, J.A.-C.; resources, L.R.-E.; writing—original draft preparation, J.A.-C.; writing—review and editing, L.R.-E.; visualization, J.A.-C.; supervision, L.R.-E.; project administration, L.R.-E.; funding acquisition, L.R.-E. All authors have read and agreed to the published version of the manuscript.

Funding: The project was carried out with a Top Sector Energy subsidy from the Ministry of Economic Affairs and Climate, carried out by the Netherlands Enterprise Agency (RVO). The specific subsidy for this project concerns the MOOI subsidy round 2020.

Data Availability Statement: No additional data were used in this paper. The software for the simulations used can be find here https://github.com/jjac13/LV_network_simulator_public, last accessed on 28 July 2025.

Conflicts of Interest: The authors declare no conflicts of interest.

References

1. de Wind, J.; Alpízar-Castillo, J.; Visser, J.; Ramírez-Elizondo, L. An in-depth analysis of residential E-cooling demand in The Netherlands. *Case Stud. Therm. Eng.* **2025**, *73*, 106469. [CrossRef]
2. Centraal Bureau voor de Statistiek. Energieverbruik van Particuliere Huishoudens. 2018. Available online: https://www.cbs.nl/nl-nl/achtergrond/2018/14/energieverbruik-van-particuliere-huishoudens (accessed on 5 July 2025) .
3. ODYSSEE-MURE. *Netherlands | Energy Profile: Energy Efficiency Trends and Policies*; Technical Report; ODYSSEE-MURE: Grenoble, France, 2023.
4. European Environment Agency. *Annual European Union Greenhouse Gas Inventory 1990–2023 and Inventory Report 2025*; Report; European Environment Agency: Copenhagen, Denmark, 2025.

5. Centraal Bureau voor de Statistiek. Warmtepompen; Aantallen, Thermisch Vermogen en Energiestromen. 2024. Available online: https://opendata.cbs.nl/#/CBS/nl/dataset/85523NED/table (accessed on 7 July 2025).
6. Citadini de Oliveira, C.; Catão Martins Vaz, I.; Ghisi, E. Retrofit strategies to improve energy efficiency in buildings: An integrative review. *Energy Build.* **2024**, *321*, 114624. [CrossRef]
7. Aslan, A. Effect of thermal insulation on building energy efficiency in Turkey. *Proc. Inst. Civ. Eng.-Energy* **2022**, *175*, 119–139. [CrossRef]
8. Kapoor, G.; Singhal, M. Impact of innovative thermal insulation materials in the building envelope on energy efficiency of residential buildings. *Mater. Today Proc.* **2024** . [CrossRef]
9. Kadrić, D.; Aganovic, A.; Martinović, S.; Delalić, N.; Delalić-Gurda, B. Cost-related analysis of implementing energy-efficient retrofit measures in the residential building sector of a middle-income country – A case study of Bosnia and Herzegovina. *Energy Build.* **2022**, *257*, 111765. [CrossRef]
10. Jezierski, W.; Sadowska, B.; Pawłowski, K. Impact of Changes in the Required Thermal Insulation of Building Envelope on Energy Demand, Heating Costs, Emissions, and Temperature in Buildings. *Energies* **2021**, *14*, 56. [CrossRef]
11. Cieśliński, K.; Tabor, S.; Szul, T. Evaluation of Energy Efficiency in Thermally Improved Residential Buildings, with a Weather Controlled Central Heating System. A Case Study in Poland. *Appl. Sci.* **2020**, *10*, 8430. [CrossRef]
12. Filippi Oberegger, U.; Prina, M.G.; Hummel, M.; Kranzl, L.; Pezzutto, S.; Lollini, R.; Sparber, W. Bottom-up method to derive cost curves for space heating savings in residential buildings for all European countries. *J. Build. Eng.* **2024**, *98*, 111303. [CrossRef]
13. Kınay, U.; Laukkarinen, A.; Vinha, J. Renovation wave of the residential building stock targets for the carbon-neutral: Evaluation by Finland and Türkiye case studies for energy demand. *Energy Sustain. Dev.* **2023**, *75*, 1–24. [CrossRef]
14. Heidari, M.; Rahdar, M.H.; Dutta, A.; Nasiri, F. An energy retrofit roadmap to net-zero energy and carbon footprint for single-family houses in Canada. *J. Build. Eng.* **2022**, *60*, 105141. [CrossRef]
15. Amani, N. Energy efficiency of residential buildings using thermal insulation of external walls and roof based on simulation analysis. *Energy Storage Sav.* **2025**, *4*, 48–55. [CrossRef]
16. Haj Hussein, M.; Monna, S.; Abdallah, R.; Juaidi, A.; Albatayneh, A. Improving the Thermal Performance of Building Envelopes: An Approach to Enhancing the Building Energy Efficiency Code. *Sustainability* **2022**, *14*, 16264. [CrossRef]
17. Axaopoulos, P.J.; Sakellariou, E.I.; Panayiotou, G.P.; Kalogirou, S. Evaluation of the optimum insulation thickness of building external walls and roof based on human thermal comfort criterion. *Renew. Energy* **2025**, *247*, 123058. [CrossRef]
18. Derradji, L.; Imessad, K.; Amara, M.; Boudali Errebai, F. A study on residential energy requirement and the effect of the glazing on the optimum insulation thickness. *Appl. Therm. Eng.* **2017**, *112*, 975–985. [CrossRef]
19. Rosti, B.; Omidvar, A.; Monghasemi, N. Optimal insulation thickness of common classic and modern exterior walls in different climate zones of Iran. *J. Build. Eng.* **2020**, *27*, 100954. [CrossRef]
20. Calise, F.; Cappiello, F.L.; Cimmino, L.; Dentice d'Accadia, M.; Vicidomini, M. Dynamic modelling and thermoeconomic analysis for the energy refurbishment of the Italian building sector: Case study for the "Superbonus 110%" funding strategy. *Appl. Therm. Eng.* **2022**, *213*, 118689. [CrossRef]
21. Saffari, M.; Keogh, D.; De Rosa, M.; Finn, D.P. Technical and economic assessment of a hybrid heat pump system as an energy retrofit measure in a residential building. *Energy Build.* **2023**, *295*, 113256. [CrossRef]
22. Kitsopoulou, A.; Bellos, E.; Lykas, P.; Vrachopoulos, M.G.; Tzivanidis, C. Multi-objective evaluation of different retrofitting scenarios for a typical Greek building. *Sustain. Energy Technol. Assess.* **2023**, *57*, 103156. [CrossRef]
23. Gagliano, A.; Tina, G.M.; Aneli, S. Improvement in Energy Self-Sufficiency in Residential Buildings Using Photovoltaic Thermal Plants, Heat Pumps, and Electrical and Thermal Storage. *Energies* **2025**, *18*, 1159. [CrossRef]
24. Alpízar-Castillo, J.; Ramírez-Elizondo, L.; van Voorden, A.; Bauer, P. Aggregated residential multi-carrier energy storage as voltage control provider in low-voltage distribution networks. *J. Energy Storage* **2025**, *132*, 117507. [CrossRef]
25. Yu, F.; Feng, W.; Luo, M.; You, K.; Ma, M.; Jiang, R.; Leng, J.; Sun, L. Techno-economic analysis of residential building heating strategies for cost-effective upgrades in European cities. *iScience* **2023**, *26*, 107541. [CrossRef]
26. Yang, X.; Hu, M.; Tukker, A.; Zhang, C.; Huo, T.; Steubing, B. A bottom-up dynamic building stock model for residential energy transition: A case study for the Netherlands. *Appl. Energy* **2022**, *306*, 118060. [CrossRef]
27. Koene, F.F.; Eslami-Mossallam, B.B. Space heating demand profiles of districts considering temporal dispersion of thermostat settings in individual buildings. *Build. Environ.* **2023**, *228*, 109839. [CrossRef]
28. Alavirad, S.; Mohammadi, S.; Hoes, P.J.; Xu, L.; Hensen, J.L. Future-Proof Energy-Retrofit strategy for an existing Dutch neighbourhood. *Energy Build.* **2022**, *260*, 111914. [CrossRef]
29. *ISO 52016-1:2017*; Energy Performance of Buildings—Energy Needs for Heating and Cooling, Internal Temperatures and Sensible and Latent Heat Loads Part 1: Calculation Procedures. International Organization for Standardization (ISO): Geneva, Switzerland, 2017.
30. Alpízar-Castillo, J.; Ramírez-Elizondo, L.M.; Bauer, P. Modelling and evaluating different multi-carrier energy system configurations for a Dutch house. *Appl. Energy* **2024**, *364*, 123197. [CrossRef]

31. American Society of Heating, Refrigerating and Air-Conditioning Engineers, Inc. (ASHRAE). *2021 ASHRAE® Handbook—Fundamentals (SI Edition)*; American Society of Heating, Refrigerating and Air-Conditioning Engineers, Inc. (ASHRAE): Peachtree Corners, GA, USA, 2021.
32. *NTA 8800:2024 nl*; Energieprestatie van Gebouwen—Bepalingsmethode. Royal Netherlands Standardization Institute (NEN): Delft, The Netherlands, 2024.
33. Funda. *Jaarverslag 2024*; Technical Report; Funda: Amsterdam, The Netherlands, 2025.
34. Alpízar-Castillo, J. LV Network Simulator Public. 2025. Available online: https://github.com/jjac13/LV_network_simulator_public (accessed on 28 July 2025).
35. Fereidoni, S.; Nabisi, M.; Fereidooni, L.; Javidmehr, M.; Zirak, N.; Kasaeian, A. An assessment of the impact of building envelope design on the tradeoff between embodied and operating energy. *Energy Build.* **2023**, *298*, 113542. [CrossRef]
36. Kirschbaum, J.; Divkovic, D.; Meschede, H. From demand to action: Analysing building emissions and refurbishment scenarios towards climate neutrality. *Appl. Energy* **2025**, *396*, 126302. [CrossRef]

MDPI AG
Grosspeteranlage 5
4052 Basel
Switzerland
Tel.: +41 61 683 77 34

Energies Editorial Office
E-mail: energies@mdpi.com
www.mdpi.com/journal/energies

Academic Open
Access Publishing

mdpi.com

ISBN 978-3-7258-5914-6